Springer Series in Materials Science 218

M. Parans Paranthaman
Winnie Wong-Ng
Raghu N. Bhattacharya *Editors*

Semiconductor Materials for Solar Photovoltaic Cells

Springer

Springer Series in Materials Science

Volume 218

The Springer Series in Materials Science covers the complete spectrum of materials physics, including fundamental principles, physical properties, materials theory and design. Recognizing the increasing importance of materials science in future device technologies, the book titles in this series reflect the state-of-the-art in understanding and controlling the structure and properties of all important classes of materials.

More information about this series at http://www.springer.com/series/856

M. Parans Paranthaman · Winnie Wong-Ng
Raghu N. Bhattacharya
Editors

Semiconductor Materials for Solar Photovoltaic Cells

Springer

Editors
M. Parans Paranthaman
Chemical Sciences Division
Oak Ridge National Laboratory
Oak Ridge, TN
USA

Raghu N. Bhattacharya
National Renewable Energy Laboratory
Golden, CO
USA

Winnie Wong-Ng
Material Measurement Laboratory
NIST
Gaithersburg, MD
USA

ISSN 0933-033X ISSN 2196-2812 (electronic)
Springer Series in Materials Science
ISBN 978-3-319-20330-0 ISBN 978-3-319-20331-7 (eBook)
DOI 10.1007/978-3-319-20331-7

Library of Congress Control Number: 2015943837

Springer Cham Heidelberg New York Dordrecht London

Printed on acid-free paper

Springer International Publishing AG Switzerland is part of Springer Science+Business Media (www.springer.com)

Preface

This essential reference provides the most comprehensive presentation of the state of the art in the field of solar photovoltaics (PV). This growing field of research and applications is currently being supported by numerous governmental, industrial, and educational initiatives in the United States, Asia, and Europe to overcome solar grid parity. The technology is particularly intended for increasing the usage of renewable energy resources for energy production. The next-generation solar PV is focused on improving the single junction cell conversion efficiency to near the Shockley-Queisser limit and also working toward reducing the gap between cell and module efficiencies while reducing the cost of the present process lines for existing flexible PV. This book can be used as a research and professional reference for teaching earth-abundant and inorganic-organic hybrid solar photovoltaics. World-renowned authors explore the topic in nine engaging chapters: (1) 3D Geometries: Enabling Optimization Toward the Inherent Limits of Thin-Film Photovoltaics; (2) Earth-Abundant $Cu_2ZnSn(S,Se)_4$ (CZTSSe) Solar Cells; (3) Cu_2ZnSnS_4, $Cu_2ZnSnSe_4$ and Related Materials; (4) ZnO Doping and Defect Engineering—A Review; (5) Hydrogen Production and Photodegradation at TiO_2/Metal/CdS Sandwich Using UV-Visible Light; (6) Organic Photovoltaics; (7) Nanophase Engineering of Organic Semiconductor-Based Solar Cells; (8) Solar Cell Characterization; and (9) Applications.

The first article by Debnath et al. provides an overview and outlook of 3D geometries with the promise of improved efficiency. A number of 3D nano and microscale approaches based on silicon (Si), cadmium telluride (CdTe), copper indium sulfide (CIS), copper indium gallium selenide (CIGS), gallium arsenide (GaAs), and Zinc oxide (ZnO) absorbers are discussed. The approaches attempt to decouple conflicting criteria for optimization of performance, eliminate particular criteria, modify materials properties, or achieve some combination thereof. Significant challenges do exist for scaling-up the current designs based on nano and micro-manufacturing. Research on 3D geometries for light management are also presented, as are developments of back contacts. A number of third-generation 3D PV devices are approaching double digit efficiencies, and there is a significant crosstalk between planar and 3D solar cell developments.

The main challenge in solar PV technology is to reduce the cost and use earth-abundant elements for manufacturing reliable, efficient PV devices for global clean energy needs. A promising pathway to reduce PV cost is the use of thin-film technologies in which thin layers of earth-abundant photoactive materials are deposited on large-area substrates. One of the most promising thin-film PV technologies is based on earth-abundant copper-zinc-tin-chalcogenide-based kesterites, Cu_2ZnSnS_4 (CZTS), $Cu_2ZnSnSe_4$ (CZTS(Se)). These materials are presented in great detail in the next two contributions. Significant developments have been made on CZTS(Se) devices in the past few years, reporting $\sim$11 %-efficient solar cell. However, CZTS(Se) PV technology is currently in its amateur state and requires extensive research to become marketable in the near future. The chapter by Das et al. covered a limited overview of the technologies employed to prepare CZTS-based materials. CZTS absorbers have been prepared by a variety of physical vapor deposition techniques such as evaporation, sputtering, and pulsed laser deposition. In addition, they have been prepared by a variety of nonvacuum deposition techniques such as solution processing, nanocrystal-based deposition, electrodeposition, screen printing, spray pyrolysis, and chemical bath deposition. CZTS thin-film technologies can be deposited on a wide variety of substrate materials making it possible to manufacture very lightweight, flexible solar cells on metals, sodalime glass, and plastic substrates, and thus have correspondingly lower cost. This CZTS has a direct bandgap of 1.4–1.5 eV and high optical absorption coefficient for photon energies higher than the bandgap such that only a few microns of material are needed to absorb most of the incident light, and hence material and production costs are reduced. Thin-film CZTS solar cells can be 100 times thinner than silicon-wafer cells. The CZTS cells consist of at least five layers: (i) substrate (soda-lime glass); (ii) back contact (Mo); (iii) CZTS absorber; (iv) CdS emitter; and (v) front contact (ZnO, ITO).

The article by Shiyou Chen introduces the fundamental material properties of CZTS, CZTS(Se), and related quaternary compound semiconductors, including how they are derived from binary II–VI semiconductors, crystal structures, electronic structure, alloys, thermodynamic stability, secondary phases, defects, and surfaces. Their influence on electrical, optical, and photovoltaic performance is discussed. As a result of the increased chemical and structural freedom of these quaternary semiconductors, these properties are much more flexible and complicated than those of simple elemental and binary semiconductors, and are also critical for understanding the limiting mechanism to the solar cell performance. Detailed band structure calculations for CZTS-related materials are also reported. Growth and fundamental understanding of the photoactive CZTS layers with reduced defect density, compositional variations, grain boundary doping, and microstructure and their correlation with photovoltaic properties are necessary to increase the cell efficiency further.

The current status of ZnO n-type and p-type doping is comprehensively reviewed in the chapter by Xiu and Xu, including the different doping methods and dopant sources. ZnO is inexpensive, nontoxic, and compatible with semiconductor manufacturing processes. Also, ZnO has been synthesized with a variety of

nanostructures. The nanoscale p–n junctions can increase the injection rate of carriers many times more than that for a planar ZnO diode. Based on these advantages, ZnO has seen a surge of research interest aimed at achieving high efficiency for ultrabright LEDs, laser diodes, and ultrafast photodetectors. However, the main obstacle hindering ZnO application is a reliable method for fabricating p-type ZnO material with a high hole concentration, high mobility, and low resistivity. The current state of p-type doping of ZnO seems to be similar to that of p-type doping of GaN more than 20 years ago. Therefore, it is believed that, with continuing innovation, the p-doping difficulty in ZnO could be solved in the near future.

As clean energy resources, sunlight and water are abundant and universally available, and hence there is immense interest for energy applications. Hydrogen production utilizing sunlight and water is a sustainable and logical approach for constant energy generation. This is an example of a conversion of solar energy into chemical energy. As a well-known photocatalyst, TiO_2 is of interest and has been examined persistently for water splitting for a range of reasons, including its wide-ranging pH stability, nontoxicity, and good photoactivity in the presence of UV light. The chapter by Manivannan et al. discusses a wet chemical approach to synthesize anatase-only TiO_2, incorporate platinum group metals (PGMs), and subsequently deposit a chalcogenide to form a unique high surface area nanocomposite. Optical, microstructural, and photoelectrochemical studies have shown that the as-prepared TiO_2 has a particle size of 20 nm, demonstrates 60 % higher surface area compared to the commercial TiO_2, and exhibits superior photoelectrochemical responses (e.g., 60 % increase in photocurrent) indicating that it is a promising base material for preparing visible light active composites. Among the three PGMs studied for photocatalytic hydrogen generation, $\sim$0.79 wt% of Pt on as-synthesized TiO_2 is noted to be most useful: attributable at least in part to its known stability relative to other PGMs during photocatalysis. To conclude, metal oxides such as TiO_2 can be used as a replacement for polysulfide stabilizers with the dual benefit of its photodegradation as well as hydrogen generation.

The contribution by Delongchamp provides details about the origin of organic photovolatics (OPV) and the future outlook of these solar cell devices. The active layer of an OPV solar cell is composed of hydrocarbon-based organic materials. OPV occupies a special niche among solar energy technologies in that it could potentially satisfy the growing energy needs of the world with a product that is sustainable, elementally abundant, and cheaply manufactured. OPV cells have recently seen a dramatic uptick in reported efficiencies, with power conversion efficiencies reaching $\approx$11 %. These increases in power conversion efficiency have largely been driven by the development and discovery of new OPV active layer materials and new ways to process them. The technology has gained significant commercial attention over the past decade, as its unique attributes merit consideration for a place in the landscape of distributed energy generation devices. Some of OPV's advantages include a flexible form factor and facile processing, either from fluids or from vacuum deposition.

The chapter by Yang et al. describes chemical synthesis approaches to tune the electronic energy levels in low bandgap polymers to match the energy levels of fullerene derivative acceptors for optimized charge transfer. They also review recent progress in tuning the film morphologies with solvent annealing, thermal annealing, processing additives, and compatibilizers. The development of OPVs toward future commercialization is still underway. Very recently, the organometal halide perovskite solar cells have shown great promise with efficiency of over 15 %. The remarkable success of organic–inorganic hybrid perovskites is based on the combination of the advantages of organic materials, such as low cost, solution processing capability, and flexibility, with the advantages of inorganic semiconductors, such as high crystallinity and excellent charge transport properties.

The solar cell characterizations covered in the chapter by Hamadani and Dougherty address the electrical power generating capabilities of the cell. Some of these covered characteristics pertain to the workings within the cell structure (e.g., charge carrier lifetimes) while the majority of the highlighted characteristics help establish the macro performance of the finished solar cell (e.g., spectral response, maximum power output). Specific performance characteristics of solar cells are summarized in this article, while the method(s) and equipment used for measuring these characteristics are also emphasized.

Lastly, the various solar cell applications are reviewed in the chapter by Chen et al. The important applications in space are discussed first, including the history, development, and materials consideration of solar panels in space. Among terrestrial applications, the most widely used is solar power generation for grid utilities. Building-integrated photovoltaics (BIPV) have been identified as a fast growth application with a large market, and the latest developments in hybrid solar, transparent solar panel are discussed. In addition, solar cells have also been used in automotives, public electric facilities, such as road lighting, water pumps, vending machines, and various consumer electronics such as watches and hand calculators. The solar cell efficiency, life cycle, and cost of these various applications are reviewed. Finally, this chapter provides an overview of the latest solar panel technology and the major solar panel manufacturers worldwide, as well as a broad look at the current solar market and the outlook for the future.

Overall, the nine chapters in this book provide the reader an excellent resource for understanding materials for solar photovoltaics over a wide range of topical areas.

We acknowledge Ms. Sara Kate Heukerott for her involvement in editing and producing this book. Special thanks are due to the authors and manuscript reviewers for their contributions.

Oak Ridge, USA M. Parans Paranthaman
Gaithersburg, USA Winnie Wong-Ng
Golden, USA Raghu N. Bhattacharya

Contents

About the Editors

Dr. M. Parans Paranthaman is a Distinguished Research Staff Member and a Group Leader of Materials Chemistry at the Chemical Sciences Division at the Oak Ridge National Laboratory (ORNL), a Distinguished Inventor at ORNL, and fellow of ASM International and the Institute of Physics, London, UK. He earned his Ph.D. degree in solid state chemistry and materials science from the Indian Institute of Technology, Madras in 1988. He has co-edited and written several book chapters related to his area of research, authored or co-authored more than 350 publications, and holds 30 U.S. patents related to superconductivity, energy storage, and solar cells. His present research focuses on the development of flexible thin film solar cells, radiation resistant polymer composites, coated conductors, additive manufacturing of permanent magnets, lithium separation from geothermal brine, and energy storage materials. He has won several awards, including four R&D 100 awards. Currently, he is an associate editor for the *Journal of American Ceramic Society*.

Dr. Winnie Wong-Ng is a senior Research Chemist at the Materials Science Measurement Division of the National Institute of Standards and Technology (NIST). She received a B.Sc. degree in Chemistry from the Chinese University of Hong Kong and a Ph.D. degree in Inorganic Chemistry from Louisiana State University. She has about 350 scientific publications. She is a fellow of the American Crystallographic Association, the American Ceramic Society (ACerS), and the International Centre for Diffraction Data (ICDD). She received two Bronze Medals from the United States Department of Commerce, the McMurdie Award from ICDD, and the Spriggs Phase Equilibria Award from the American Ceramic Society. She was on the Board of Directors of ICDD from 2010 to 2014 and was the past chair of the Electronics Division of the American Ceramic Society (2005). Currently, she is an associate editor for the *Journal of American Ceramic Society* and for *Powder Diffraction*.

Dr. Raghu N. Bhattacharya is a senior scientist at the National Renewable Energy Laboratory (NREL). He received his Ph.D. degree in the field of Electronic Materials from the Indian Institute of Technology, Kharagpur, in 1982. He has published over 170 technical papers in the field of processing PV materials and superconductors and has been awarded 22 patents. Dr. Bhattacharya made original contributions to the field of thin film photovoltaics and high T_c superconducting materials and devices. In the field of photovoltaics he has made major advances in the development of low-cost processes for the fabrication and characterization of thin film Cu(In,Ga)Se_2 and CdZnS solar cell materials. By using electrodeposition and chemical bath deposition techniques he has overseen the development of 19.5 %-efficient thin film solar cells. Similarly, he has employed electrodeposition as a low-cost approach to the fabrication of the state-of-the-art Tl-oxide superconducting materials. Dr. Bhattacharya has also worked with several industrial groups (e.g., Solo Power, Super Power Inc., American Superconductor, Oxford Superconducting Technology, UES, Inc., and Dasstech. Inc.). Dr. Bhattacharya is an Editorial Board Member for the *International Journal of Photoenergy*, *The Open Surface Science Journal, Bentham Science Publishers*, and *Journal of Advanced Chemical Engineering*.

Contributors

Raghu N. Bhattacharya National Renewable Energy Laboratory, Golden, CO, USA

Craig A. Bridges Oak Ridge National Laboratory, Oak Ridge, TN, USA

F.L. Chen Columbia University, New York, USA

Shiyou Chen Key Laboratory for Polar Materials and Devices (MOE), East China Normal University, Shanghai, China; Key Laboratory for Computational Material Sciences (MOE), Department of Physics, Fudan University, Shanghai, China

Sandip Das Department of Electrical Engineering, Kennesaw State University, Marietta, GA, USA

R. Debnath Materials Science and Engineering Division, National Institute of Standards and Technology, Gaithersburg, MD, USA

Dean M. DeLongchamp Materials Science and Engineering Division, National Institute of Standards and Technology, Gaithersburg, MD, USA

Brian Dougherty National Institute of Standards and Technology, Gaithersburg, MD, USA

David Geohegan Center for Nanophase Materials Sciences, Oak Ridge National Laboratory, Oak Ridge, TN, USA

Behrang H. Hamadani National Institute of Standards and Technology, Gaithersburg, MD, USA

C.M. Hangarter Materials Science and Engineering Division, National Institute of Standards and Technology, Gaithersburg, MD, USA

D. Josell Materials Science and Engineering Division, National Institute of Standards and Technology, Gaithersburg, MD, USA

Pooran C. Joshi Oak Ridge National Laboratory, Oak Ridge, TN, USA

Jong Keum Center for Nanophase Materials Sciences, Oak Ridge National Laboratory, Oak Ridge, TN, USA

Krishna C. Mandal Department of Electrical Engineering, University of South Carolina, Columbia, SC, USA

A. Manivannan Thermal Sciences Division, National Energy Technology Laboratory, US Department of Energy, Morgantown, WV, USA; Mechanical and Aerospace Engineering, West Virginia University, Morgantown, WV, USA

Bratindranath Mukherjee Chemical and Materials Engineering, University of Nevada, Reno, NV, USA

M. Parans Paranthaman Oak Ridge National Laboratory, Oak Ridge, TN, USA

Aaron Peterson Chemical and Materials Engineering, University of Nevada, Reno, NV, USA

Ming Shao Center for Nanophase Materials Sciences, Oak Ridge National Laboratory, Oak Ridge, TN, USA

Vaidyanathan Ravi Subramanian Chemical and Materials Engineering, University of Nevada, Reno, NV, USA

Winn Wilson Civil and Environmental Engineering, University of Nevada, Reno, NV, USA

Kai Xiao Center for Nanophase Materials Sciences, Oak Ridge National Laboratory, Oak Ridge, TN, USA

Faxian Xiu State Key Laboratory of Surface Physics and Department of Physics, Fudan University, Shanghai, China

Jun Xu Oak Ridge National Laboratory, Oak Ridge, TN, USA

Bin Yang Center for Nanophase Materials Sciences, Oak Ridge National Laboratory, Oak Ridge, TN, USA

D.J. Yang OmniVison Technologies, Inc., Santa Clara, CA, USA

H.M. Yin Columbia University, New York, USA

Chapter 1
3D Geometries: Enabling Optimization Toward the Inherent Limits of Thin-Film Photovoltaics

R. Debnath, C.M. Hangarter and D. Josell

1.1 Introduction

Three dimensionally patterned photovoltaic (3D PV) geometries are the subject of modeling and experimental study because theory indicates such devices could outperform traditional one-dimensional planar devices. The proposed functional improvements possible through the 3D geometry broadly arise from (1) decoupling of conflicting criteria for performance optimization, (2) elimination or relaxation of criteria for performance optimization, and (3) enhancement of performance through material or device properties that are not observed with bulk materials. Examples of 3D PV research focused on assessing and/or improving the performance of inorganic thin-film PV devices through each of these three approaches are detailed in this chapter.

In the principal examples where 3D geometries are used to decouple conflicting criteria for optimization, the conflict lies in the requirements for thicker absorber to improve capture of light and thinner absorber to improve collection of generated carriers. Decoupling these conflicting length scale criteria is the goal of studies with cadmium selenide/cadmium telluride (CdSe/CdTe) and cadmium sulfide/cadmium telluride (CdS/CdTe) devices with micro- and nanopillar geometries for which the length scales for light absorption and carrier collection are independently controllable.

For 3D approaches that eliminate or relax criteria for optimization, the principle example is elimination of requirements that the conducting contact layer, for example, indium tin oxide (ITO) or aluminum doped zinc oxide in planar devices with p-type CdTe as well as p-type copper indium sulfide (CIS) or copper indium gallium selenide (CIGS) absorbers, be highly transparent as well as highly con-

R. Debnath · C.M. Hangarter · D. Josell (✉)
Materials Science and Engineering Division, National Institute of Standards and Technology, Gaithersburg, MD 20899, USA
e-mail: daniel.josell@nist.gov

M.P. Paranthaman et al. (eds.), *Semiconductor Materials for Solar Photovoltaic Cells*, Springer Series in Materials Science 218,
DOI 10.1007/978-3-319-20331-7_1

ductive. Devices with back contact geometries are detailed that entirely eliminate the need for the transparent conducting layer, rear side placement permitting high-density arrays of interdigitated metal electrodes. The restriction on optically transparent n-type junction material is also lifted as it is also moved behind the absorber layer.

Approaches to enhance materials' properties through 3D patterning are captured in a summary of recent efforts to understand photonics of 3D structures. Studies are described whereby the small-scale structuring in the 3D devices leads to enhanced optical coupling of light and thereby potentially more effective utilization of material.

One might anticipate that the most successful approaches accomplish more than one of these goals. Indeed, this is almost inherent in 3D geometries, which can impact performance all the way from light absorption through carrier transport to current collection. Thus, the pillar geometries will be detailed as an approach to decouple conflicting criteria for light absorption and current collection as well as a means to enhance light absorption. Such overlap is, however, not always the case. Thus, modeling of fine metal structures for plasmonics control of light absorption suggests no significant role with regard to carrier transport or current collection, leaving discussion of this approach entirely in the third section of the review.

1.2 Broader Background

While this chapter is focused on 3D inorganic *thin-film* devices, it is worth noting that 3D geometries are already ubiquitous in commercial silicon (Si) solar cells. Albeit typically in more limited form, these 3D implementations provide functional improvement by reducing or eliminating conflicting optimization criteria; they do not enhance or modify material properties. Metallization wrap through technologies are one example, reducing front contact shading without degrading carrier collection. Back contact Si devices with localized rear surface positive and negative contacts [1–5] are another example. The back contact geometry relaxes the conflicting requirements on absorber thickness dictated by light absorption and carrier collection, albeit absorber thickness still influences both. Although there are no commercial devices, Si nanowire and micro-column devices with dimensions that more fully decouple the length scales of absorption and collection are the subjects of numerous studies.

The 3D approaches addressed are broadly relevant across materials. Organic devices, albeit having efficiencies that are generally lower and degrade more quickly than those of inorganic devices, are frequently based on structures that are highly 3D in nature. They are subject to issues of material heterogeneity that can factor as heavily into device performance as intentional 3D micro-, and even nano-, structuring. While there are numerous studies of hybrid PV devices incorporating

dispersed nanodots, nanorods, and nanowires (NWs), interpretation of observed behavior is complicated by the need to account for variations in size, orientation, geometry, and percolation between particles in addition to consideration of the orientations of polymers and other organic compounds around them. For this reason, this overview is limited to studies of thin-film inorganic devices with well-defined geometries.

1.3 Conflicting Requirements

Significantly, pillar and related 3D geometries that seek to decouple conflicting criteria for optimization have achieved only 6 % efficiency to date, despite their success in decoupling light absorption from carrier collection, the latter length scale being reduced to lengths to less than 500 nm [6]. A major factor limiting their performance is the new complication introduced by the pillars of CdS themselves. These thick light absorbing structures necessitate undesirable illumination through the metal contact on the CdTe side and increase the interface area on which carriers can recombine. The example thus illustrates what is commonly called the law of unintended consequences. However, it also highlights the benefits of alternative approaches, e.g., back contact devices that decouple light absorption from carrier collection but do so without requiring illumination through the metal contact (or any contact) and can reduce interface areas even below those in planar devices.

The direct bandgap thin-film CdTe, CIS, and CIGS absorbers, of interest as thinner alternatives to indirect bandgap Si in planar devices, introduce a number of unintended consequences. Unlike Si, which can be readily doped n-type and p-type to make homojunction devices, these compound semiconductor absorbers are typically p-type. Heterojunction devices in these systems thus require an n-type material, typically a CdS layer. The n-type layer must be thin to minimize absorption of light within it but sufficiently thick that there are no pinholes that shunt the junction. One must therefore optimize the window layer thickness to balance the conflicting criteria of minimal absorption and a pinhole-free layer, commonly resulting in substantial loss of UV response with commercial panels. The use of a larger bandgap layer is used to relax these conflicting requirements. However, this approach limits the choice of window materials, and consideration must be given to possible influence on the device performance through the nature of the p-n junction.

Micrometer-scale recombination lengths in polycrystalline thin-film materials are not associated with finger electrodes of similar pitch on the front surface of thin-film devices only because the transparent conducting oxide (TCO) layer on this surface carries the current. In the absence of TCO, such thin-film devices would require finger electrodes with pitch fine enough to both accommodate the recombination length of the underlying materials and provide tolerable series resistance. Unfortunately, increasing the conductivity of an oxide by doping generally makes it less transparent. Similar to the case with the n-type window layer, the TCO

composition, doping, and thickness must balance the competing criteria of high transparency and high conductivity.

Clearly, the front TCO and n-type semiconductor layers, while integral to operation of traditional 1D geometry thin-film devices, bring with them a number of conflicting criteria for device optimization. Low open-circuit voltage (V_{oc}) of CdTe/CdS planar devices (900 mV, well below the ≈1.5 eV CdTe bandgap as well as V_{oc} values for devices based on GaAs, which has a similar bandgap) indicates that performance in these devices is far from ideal. Approaches that eliminate conflicting criteria present the possibility to overcome associated limitations and thus achieve a more optimal value.

1.4 Optical Modeling and Simulation of 3D Geometries

Like planar devices, NW and other nanostructured PV devices include regions of layered materials, the optical properties of each material affecting the transmission of light through all the layers. The optical properties of the materials are represented by their complex refractive indices, $\tilde{n} = n + jk$ (where n is the refractive index and k is the extinction coefficient) or by the complex relative permittivity ε_r defined by $\tilde{n} = \sqrt{\varepsilon_r}$ for nonmagnetic substances. As the spectrum of interest for PV applications is broadband in nature, $\tilde{n}$ and ε_r typically depend on the wavelength of the irradiating light (λ). The intensity of light is typically presumed to decrease exponentially with propagation distance x according to the Beer–Lambert equation $I(\lambda) = I_0(\lambda)e^{-\alpha(\lambda)x}$ where the absorption coefficient in the material α can also be expressed in terms of the extinction coefficient as $\alpha = \frac{4\pi k}{\lambda}$. Reflection and transmission at interfaces, as defined by the optical properties of the adjacent materials, also affect light propagation through a PV cell. This frequently begins with the reflection of a significant portion of the incident light from the device surface due to the substantial mismatch of the refractive indices of most materials from that of air. The benefits of one-dimensional (1D) optical modeling for thin-film PV devices pale in comparison with those derived from the application of two-dimensional (2D) and/or 3D optical models to devices containing relevant materials' distributions or surface texturing. With light management critical to device performance, accurate understanding of light scattering and absorption in nanostructured devices that incorporate novel optical concepts and device architectures through optical modeling is often crucial. 3D solar cells can, of course, be analyzed using rigorous 3D optical modeling to properly understand the optical behavior of the system [7]. However, substantial understanding can frequently be obtained from consideration of simpler subcomponents (e.g., surface textures or metal nanoparticles) bringing together 1D, 2D, and 3D modeling concepts in order to reduce computational requirements.

Methods developed to solve the electromagnetic wave equations in PV devices include the finite element method, finite difference time domain (FDTD), and

rigorous coupled-wave analysis. The methods have their own advantages and are applied to solve electromagnetic problems accordingly. Typically, subwavelength spatial discretization of the PV structure is employed in modeling wave propagation and wave interaction with the PV materials. When the dimensions of the structure are smaller than the relevant wavelengths of light, geometric ray optics cannot be applied to model light scattering and other modeling approaches are utilized. With the optical properties defined and boundary conditions imposed, the light source is added and the electric and magnetic fields are evaluated in the simulation domain in order to generate the desired light reflection and absorption and associated carrier generation. With their simplifying periodicity and relevance to numerous systems, nanopillar geometries have been the subject of a number of such models [6, 8–10]. Models that evaluate both optical and electrical response have been used to understand light trapping [10, 11] and device physics of nanostructured solar cells [12]. For plasmonic solar cells, such models predict how nanoparticles within a PV device influence the electronic response of the system [13, 14].

1.5 Nano-/Micro-pillars

Developments in nanotechnology have yielded nanostructured materials with demonstrated potential for high-performance electronic devices [15–17]. In particular, NW-based solar cells possess a number of potential advantages over planar wafer-based thin-film solar cells. The advantages arise from the unique characteristics of these nanomaterials: (i) superior light trapping, (ii) excellent absorption and anti-reflection, (iii) enhanced radial charge separation making them less sensitive to defect states, and (iv) single-crystal growth on non-epitaxial low-cost substrates being more structurally relaxed due to their reduced dimensionality. With the efficiencies of crystalline Si devices already incorporated into commercial solar panels exceeding 23 % as of the submission of this chapter, limited improvement toward the single-junction limit is possible through 3D redesign. Nonetheless, while NW-based PV devices have yet to supersede the efficiency limit of their planar crystalline Si counterparts, these unique characteristics may provide less expensive processing options and enable use of a wider range of geometries as well as materials, organic or inorganic.

1.5.1 Advantages of NW Geometry

High efficiency solar cells transmit incident photons into the device, absorb them in the appropriate location, and then efficiently collect generated photocurrent. The tailored geometries of NW-based devices can minimize the losses in each photo-conversion step, permitting low reflectivity, high absorption, and reduced carrier diffusion lengths.

1.5.1.1 Broadband Absorption and Anti-reflection

Because the refractive indices of device materials impact detrimental light reflection, a quarter wavelength transparent layer is typically used as an anti-reflective coating for thin-film solar cells; however, such a layer is effective only for a narrow range of wavelengths. In contrast, a gradual change in refractive indices can suppress reflection for a wide range of wavelength, with such impedance matching achievable through engineered nanostructures on the device surface. NWs in particular and their geometry determining the local absorption of photons as well as the efficiency of photogenerated carrier collection at the electrodes appear ideal in this regard. As such, there has been substantial exploration in the last decades of NW materials of different shapes and sizes fabricated using vapor–liquid–solid (VLS) methods, template-assisted growth, colloidal lithography, etc. [18–21]. Smoother transition between air and material can be achieved using arrays of NWs/pillars or multi-diameter micro-wires with gradually changing diameter [22], different aspect ratio [23], or pitch [24] where they can deliver absorption approaching, or even exceeding, the Lambertian limit.

Nanocones or tapered NW structures exhibit more efficient broadband absorption than planar thin-film samples due to refractive index matching with air that suppresses Fresnel reflection [25, 26]. Figure 1.1a shows scanning electron micrograph (SEM) of a-Si:H nanocone arrays fabricated by a scalable low-temperature nanosphere lithography process [27]. For wavelengths between

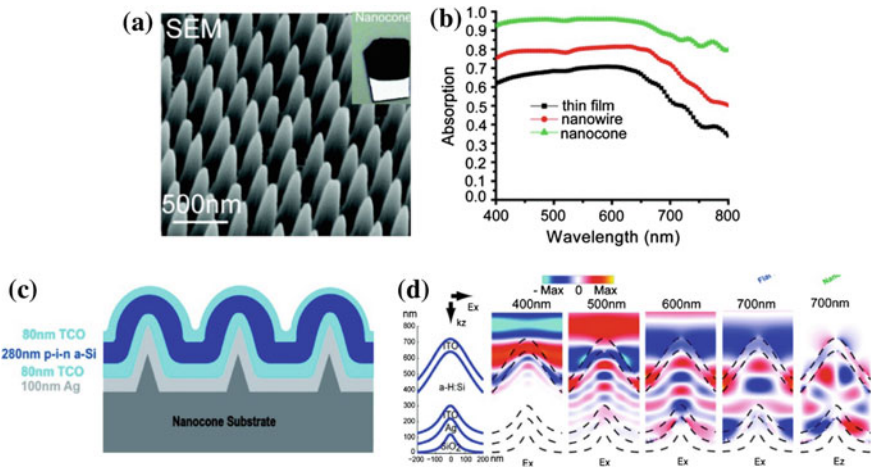

Fig. 1.1 **a** SEM images of Si:H nanocones fabricated by nanosphere lithography. Inset shows the nanocone solar cell. **b** Comparison of absorption data from a-Si:H thin film, nanowire arrays, and nanocones at normal incident over a broad range of wavelengths. Adapted with permission from Ref. [27]. Copyright © 2009, American Chemical Society. **c** Schematic showing the cross-sectional structure of nanodome solar cells. **d** FDTD simulation of electric field of the nanodome structure at different wavelengths. Incident plane wave is polarized in the *x* direction. Adapted with permission from Ref. [29]. Copyright © 2010, American Chemical Society

400 and 800 nm, absorption is significantly higher than that of either NW arrays or thin films (Fig. 1.1b). Even for thin active layers, absorption is improved due to the broadband suppression of front surface reflection over a wide range of incident angles [28, 29]. The same phenomenon has been observed with nanodome solar cells in which the a-Si:H solar cell is conformably deposited on top of the nanocone-patterned substrate (Fig. 1.1c). Enhanced absorption arises from both decreased reflection, due to refractive index matched with air, and increased optical path length due to scattering of reflected light along the in-plane direction. 3D FDTD simulations indicate that nanodome structures can absorb 93 % of normally incident sunlight over the spectral range from 400 to 800 nm, with single-pass absorption of shorter wavelength light and multi-pass absorption of longer wavelength light (Fig. 1.1d). In an analogous manner, Ge nanopillars with reduced diameter toward the top exhibit improved broadband absorption by decoupling reflection of light at different wavelengths as shown in Fig. 1.2 [22]. Other materials such as Si, InP, GaP, and CdS also show much reduced reflection with both tapered and untapered NW configurations [6, 30, 31]. Ordered nanopillar arrays with appropriately well-controlled geometries can be readily synthesized by template-assisted growth.

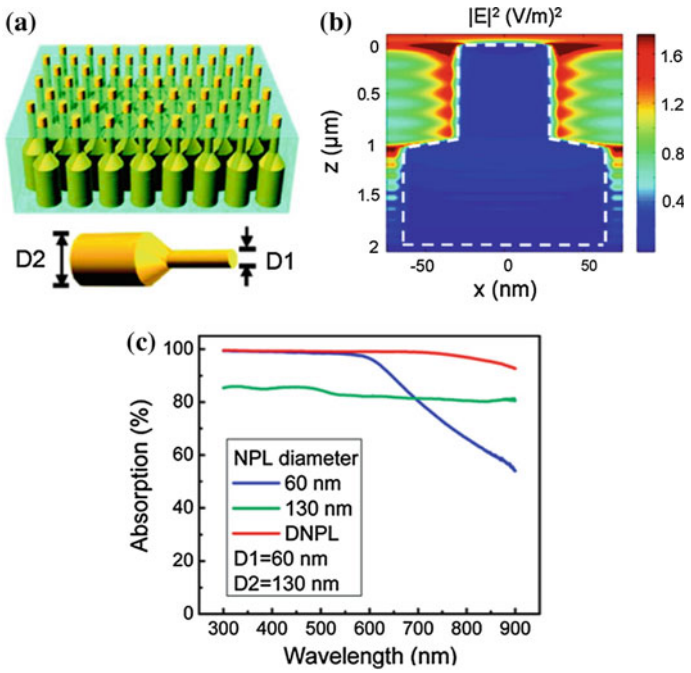

Fig. 1.2 **a** Schematics of Ge dual diameter nanopillar arrays. **b** Simulated electric field intensity distribution at 800 nm, which decays axially as the absorption of photons in Ge takes place. **c** Broadband absorption spectra showing the enhancement. Adapted with permission from Ref. [22]. Copyright © 2010, American Chemical Society

1.5.1.2 Improvement in Charge Separation and Collection

In addition to improvements in optical absorption, optimally designed NW devices can significantly improve charge collection efficiency. While one may improve light absorption in the active region of planar devices by increasing their thickness, minority carrier diffusion ultimately becomes a bottleneck, with reduced photo-carrier collection efficiency. For single-crystalline material such as Si, the minority carrier diffusion length is hundreds of micrometers so that increased thickness is less of a problem in this respect. However, for polycrystalline materials, smaller minority carrier diffusion lengths impose real thickness limitations on planar device architectures. 3D structures can overcome these limitations both by separating the charges laterally and by collecting them more quickly through band conduction. When the carrier collection distance is significantly reduced, such devices are more defect-tolerant. Examples include enhanced carrier collection from Cd (Se,Te) [32] and CdS/CdTe [6] 3D nanorod array solar cells, manifesting as higher quantum yield in the red and higher fill factor than devices with planar configurations.

1.5.2 Single-Nanowire/Micro-wire Devices

Consistent with nominal expectations for application, NWs are typically assembled and integrated as arrays in experimental PV devices. However, a number of efforts have studied single-NW (or micro-wire) devices to elucidate fundamental understanding of surface recombination, minority carrier diffusion, doping effects, etc., in such systems. The NWs in such devices typically have one of two structural geometries that are defined by the modulation of dopants within them, axial [33–36] and radial (core-shell) [34, 35, 37–39], although there has been study of single dopant NW devices [40]. The standard motif is the p-i-n configuration shown in Fig. 1.3a. In the axial configuration, the dimensions of the p-i-n regions are controlled during the NW synthesis, and the doped (n and p) regions can be made arbitrarily small near the metal contact at either end. The architecture can impose limits on carrier collection efficiency due to enhanced bulk recombination for NW lengths greater than the comparatively small minority carrier diffusion lengths of most semiconductors. These shortcomings can be circumvented in radially modulated p-i-n device (Fig. 1.3c) in which carrier separation takes place over much reduced distances in the radial direction, making photogenerated carrier collection more efficient.

PV properties of axial and radial Si NW diodes are shown in Fig. 1.3b, d. Dark current–voltage (*I–V*) curves of the axial p-i-n Si NW diodes show the rectifying nature of the junction for different lengths of the i region. Under AM1.5 solar illumination, the PV nature is evident with improved diode quality factor as compared to its p-n counterpart and 0.5 % efficiency in which the (projected) area is approximated as the length of the intrinsic region and the depletion widths in the p- and n-regions multiplied by the NW diameter [33]. However, the efficiency is only 0.15 % considering the entire length between the contacts of the p-i-n axial device.

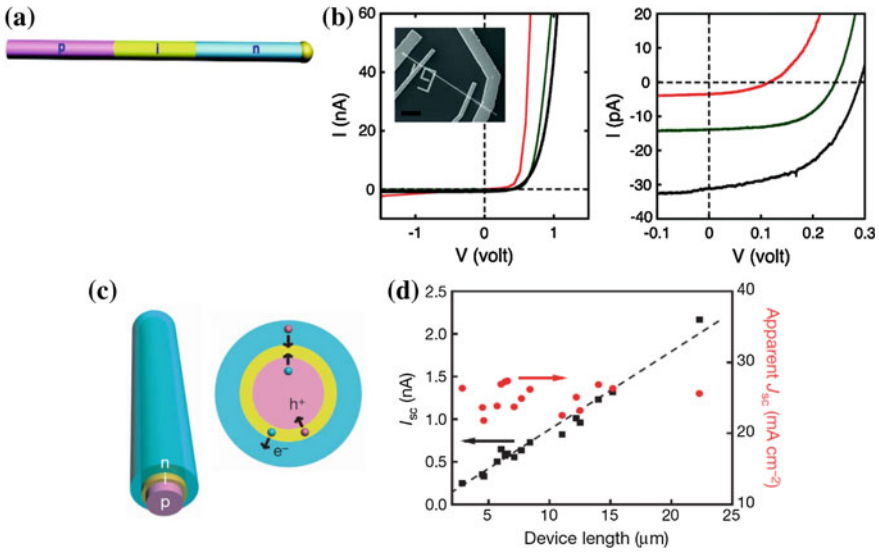

Fig. 1.3 Schematic of **a** axial p-i-n Si NWs with **b** current–voltage (*I–V*) characteristics under dark (*first plot*) and AM1.5G illumination (*second plot*). *Red*, *green*, and *black curves* correspond to i-segment lengths of 0, 2, and 4 μm, respectively. SEM image of the Si NW device (inset). The scale bar indicates 4 μm. Adapted with permission from Ref. [33]. Copyright © 2008, American Chemical Society. **c** Illustration of coaxial Si NW structure showing the photogenerated electrons (e^-) and holes (h^+) are swept into the n-shell and p-core, respectively, due to the built-in electric field. **d** Linear increase of short-circuit current of the NW PV device at 0.6 sun as a function of device length suggesting that the photogenerated carriers are collected uniformly along the radial structure. Adapted with permission from Ref. [37]. Copyright © 2007, Macmillan Publishing Limited

The Si core–shell single-NW diode in the radial p-i-n configuration exhibits an apparent upper bound short-circuit current density of 24 mA/cm^2, a substantial improvement over the axial version as well as close to that of polycrystalline Si solar cells [41]. This implies very good absorption of light within the material as well as efficient charge collection/separation. Short-circuit current that scales linearly with the device length indicates uniformly efficient charge separation along the entire length of such core–shell structures (Fig. 1.3d).

When the NW diameter is similar to the wavelength of the light, optical interference effects can play a major role in the absorption spectra. For high absorption coefficient direct bandgap III–V material like GaAs in particular, resonances can occur that significantly increase the total absorption [38]. When a single GaAs NW solar cell with radial p-i-n configuration is vertically oriented, the short-circuit current becomes one order of magnitude higher than predicted from the Lambert–Beer law. Due to the high absorption cross section, light gets concentrated in the standing NW (Fig. 1.4) resulting in an optimal GaAs p-n junction diode that exceeds the solar cell efficiency set forth by the Shockley–Queisser limit based on its actual physical area.

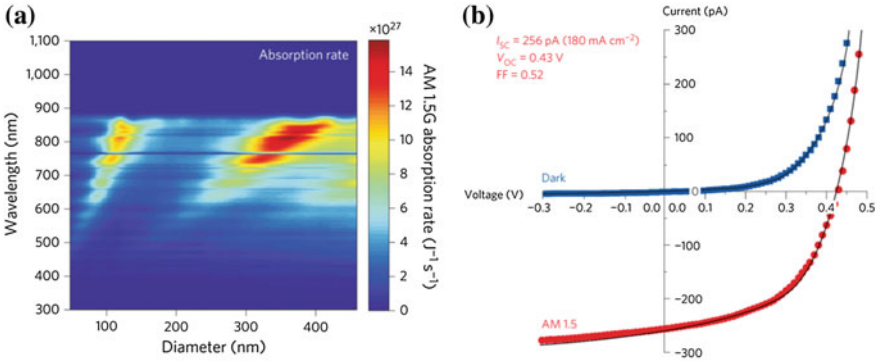

Fig. 1.4 **a** Simulation of light absorption in GaAs NW (2.5 μm) under solar AM1.5G illumination. The absorption rate depends on the diameter and wavelength. Optimal light absorption leads to solar cell efficiency above the Shockley–Queisser limit. **b** Short-circuit current density exceeds by more than one order of magnitude that predicted using the Lambert–Beer rule under 1 sun. Adapted with permission from Ref. [38]. Copyright © 2013, Macmillan Publishing Limited

1.5.3 3D Absorber Solar Cells

In traditional thin-film PV, the active layers should be thick enough to absorb all the incident photons, but the limited minority carrier diffusion length of many semiconducting materials imposes a thickness limitation on the device architecture. This conflict can be overcome either by using p-n radial junction as explained earlier or introducing nanopillars (NPs) within the thin film. By optimally designing the dimension of the NPs, the latter architecture can take full advantage of high photon absorption and efficient carrier collection in this 3D configuration as compared to it planar counterpart.

1.5.3.1 Chalcogenide Absorbers

CdS/CdTe devices in which polycrystalline CdTe thin film was deposited by chemical vapor deposition (CVD) on arrays of CdS NPs have demonstrated enhanced absorption as well as efficient carrier collection [6, 42, 43]. Highly periodic anodic alumina membranes (AAM) have been used to template the high-density, single-crystalline CdS NP arrays, the device efficiency depending on the embedded nanopillar lengths (Fig. 1.5). The volumetric recombination of photogenerated carriers is substantially reduced as the carrier collection volume near the n-p junctions is increased beyond that of the conventional planar structure, overcoming the small minority diffusion length that limits planar CdS/CdTe solar cells. The 3D geometry exhibits enhanced optical absorption and has permitted fabrication on a flexible substrate, although the efficiency of these devices only

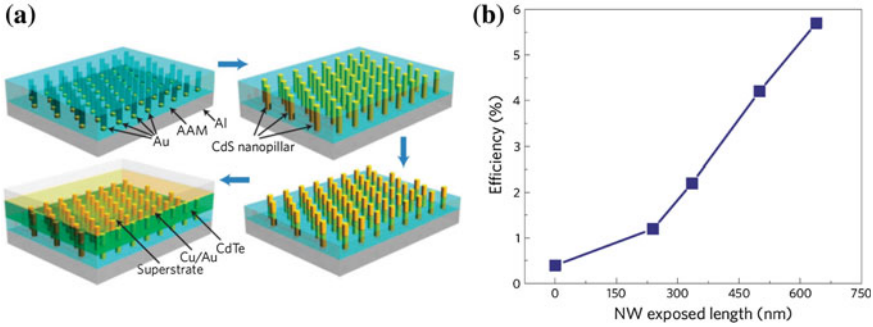

Fig. 1.5 **a** Fabrication process flow of CdS/CdTe 3D nanopillar solar cells. Highly periodic anodized aluminum is used as the template for the direct synthesis of single-crystalline n-CdS nanostructures. A p-type CdTe thin film is then deposited by CVD followed by thermal evaporation of the Cu/Au metal contact on top. **b** Efficiency of the cells as a function of the embedded nanopillar height in which the CdTe film thickness is maintained constant. Adapted with permission from Ref. [6]. Copyright © 2009, Macmillan Publishing Limited

reached ≈6 %. Similar efficiency was obtained from devices with high-density randomized CdS NWs grown on fluorine-doped tin oxide/soda lime glass substrates via low-temperature liquid-phase synthesis and electrochemically deposited CIGS [44].

1.5.3.2 Si Micro- and Nanowires

Using a VLS growth process, arrays of Si micro-wires with minority carrier diffusion lengths and surface recombination velocities similar to those of single-crystal materials can be grown on different substrates [45]. These arrays can provide significant photon absorption using a very small fraction of the materials used in wafer-based PV devices with significant improvements in effective optical concentration and charge collection [46]. Solar cells fabricated with wires whose diameter is of the order of the minority carrier diffusion length have been predicted to achieve efficiencies up to 17 % [45].

Arrays of disordered NWs grown by a VLS method on low-cost substrates such as glass and surrounded by a thin transparent conductive oxide have both low diffuse and specular reflection. These anti-reflective properties enhance infrared absorption in the core–shell NWs, with additional enhancement in external quantum efficiency (EQE) obtained with overlying nanocrystalline Si [47].

Nanostructured 3D "*folded cell*" amorphous/microcrystalline Si multi-junction solar cells (micromorph) have also been proposed for improved efficiency over planar a-Si devices [48]. Monte Carlo optical modeling indicates a stable efficiency of amorphous Si p-i-n solar cells of over 12 % range is possible. For the micromorph cells, efficiency over 15 % is predicted given thicknesses of amorphous Si below 200 nm and of microcrystalline Si around 500 nm.

1.5.3.3 Oxides

A design that uses solution processed vertically oriented n-type ZnO NWs and p-type cuprous oxide (Cu_2O) nanoparticles combines the ideal of a NW-based solar cell with the concept of environment friendly, inexpensive, scalable, and durable semiconducting PV [49]. Cu_2O–ZnO heterojunctions are formed electrochemically, and the device performance is compared with that of a bilayer structure for different active layer thickness and NW dimensions [50]. Although these NW heterojunction devices show improved charge collection, a blocking layer of TiO_2 reducing shunting and enabling long-term stability [51], the efficiency is less than that of a bilayer structure.

1.6 3D Structures for Light Management

The traditional means to increase light absorption in solar cells has been to increase absorber thickness, previously noted to underlie the conflict between optimization of light absorption and charge collection. Barring the related light management schemes of anti-reflective coatings and multi-junction cells, the primary approach to mitigate this tradeoff in Si solar cells has been surface texturing. The roughened surface scatters light internally to increase propagation distances. Utilizing ray optics, the conventional limit on absorption enhancement has been determined to be $4n^2/\sin\theta$ [52], where n is the index of refraction.

Light management has been long recognized as a strategy to increase the efficiency of solar cells and light-emitting diodes. In solar cells, this approach aims to fully absorb light in a particular spectral region with a much thinner absorber layer than that dictated by material absorption coefficients. Thus, with proper design, absorbers can be made to be "optically thick" for increased efficiency while being physically thin. The advantage is twofold in that the thinner absorber reduces material costs even as it mitigates, or eliminates, the tradeoff between the diffusion length and absorption length thickness criteria.

This section explores 3D structures and surfaces that fall under the umbrella of light management. This excludes the important, related schemes of transparent anti-reflective coatings and multi-junction cells and focuses upon techniques that can be loosely categorized as surface texturing and micro-/nanoscale photonic architectures. Surface texturing is introduced from the classic ray optic approach, before briefly surveying more recent developments in nano- and microscale topologies, already covered to a greater extent, that push absorption beyond the ray optic limit. In the latter, a host of structures, including plasmonic and reflector designs, will be described for light trapping. Recent examples in the literature are used to illustrate advances.

1.6.1 Surface Texturing

While the original motivation behind surface texturing was to improve the response of Si photodiodes, the concept has since been adopted by the PV community as a means to increase the propagation length of light in Si solar cells [53, 54]. The basic premise is that a textured surface can randomize the direction of light with a maximum absorption enhancement factor of $4n^2/\sin(\theta)$ assuming an ideal back reflector with total internal reflectance [55]. For diffusely scattering surfaces (Lambertian), derived path lengths are nearly double that of a planar surface [56].

1.6.1.1 Nanocones

In the previous section, a fine scale patterned adaptation of this approach was examined with several NW studies finding optical absorption enhancement over planar counterparts. Hydrogenated amorphous Si nanocones were shown to absorb light more efficiently over a larger angle of incidence than cylindrical wires due to the graded effective refractive index associated with the cone sidewalls shown in Fig. 1.6 [27]. This work demonstrated considerable improvement in absorption

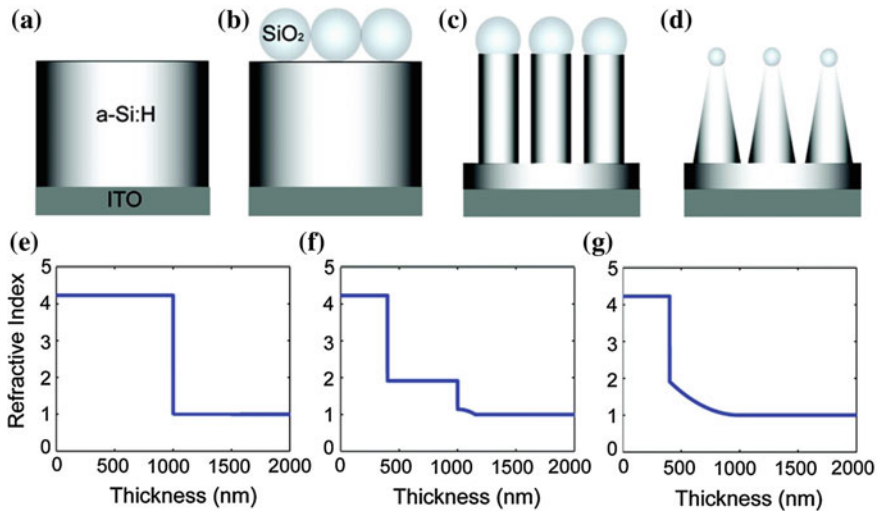

Fig. 1.6 **a–d** Schematic illustration of 1-μm-thick a-Si:H on ITO-coated glass substrate, a monolayer of silica nanoparticles on top of a-Si:H thin film, NW arrays, and NC arrays. The effective refractive index profiles of the interfaces between air and **e** a-Si:H thin film, **f** 600 nm a-Si:H NW arrays, and **g** 600 nm a-Si:H NC arrays. Adapted with permission from Ref. [27]. Copyright © 2009, American Chemical Society

could be achieved with nanoscale patterned geometries, setting the stage for short-circuit current density (J_{SC}) gains in devices.

Subsequent studies with nanopillar textured Si thin films realized a nearly three-fold improvement over the Lambertian limit depending on the nanopillar length [9]. Despite the increased absorbance exhibited by nanopillar patterned films, the patterned film exhibited a similar value in J_{SC}. This was rationalized as increased surface recombination on the large area of the unpassivated nanopillar surface, both the fill factor and open-circuit voltage degrading with extended pillar length. VLS-grown Si micro-wire arrays, reported almost concurrently, were also shown to display near ideal absorption and photoelectrochemical internal quantum efficiency [46]. Similar solid-state solar cells have been limited to single-wire devices that are difficult to correlate to bulk performance due to configurational differences [45].

1.6.1.2 Mei Resonators

A separate class of surface-textured structures known as Mei resonators has also been recently identified as a means to substantially reduce reflection through NW-type gratings and low aspect ratio morphologies [57, 58]. This approach, applicable to any high index material, is based on the large absorption cross section of Mie resonances in nanostructured absorbers [59]. The behavior was first demonstrated with Ge NWs, illustrating the size-dependent absorption efficiency and weak dependence on illumination angle [60]. Absorption efficiency and coupling of Mei resonances into Si substrates was shown to be strongly dependent on cross-sectional geometry. The angular insensitivity of the grating structure was also improved upon by utilizing discretely patterned particles on a Si substrate [57]. The general scheme of light trapping with Mie resonators and a patterned wafer is shown in Fig. 1.7 along with images of bare and Mie resonator patterned wafers.

While this first step in photon management has been demonstrated in several systems [9, 22, 46, 61], translation into improved power conversion efficiency is still challenging as contacts play a crucial role in realizing the completed device and absorbance behavior. As mentioned previously, recombination at both contacts and exposed surfaces is problematic in these high surface area structures. Although exposed surfaces can be passivated to reduce recombination, surface roughness factors can still elevate surface recombination velocities to detrimental values. Additionally, high surface area contacts may present additional challenges as heavy doping is usually employed to mitigate contact recombination. Low aspect ratio Mie resonators may offer a disruptive surface texturing route to increase absorption with minimal increase in surface recombination.

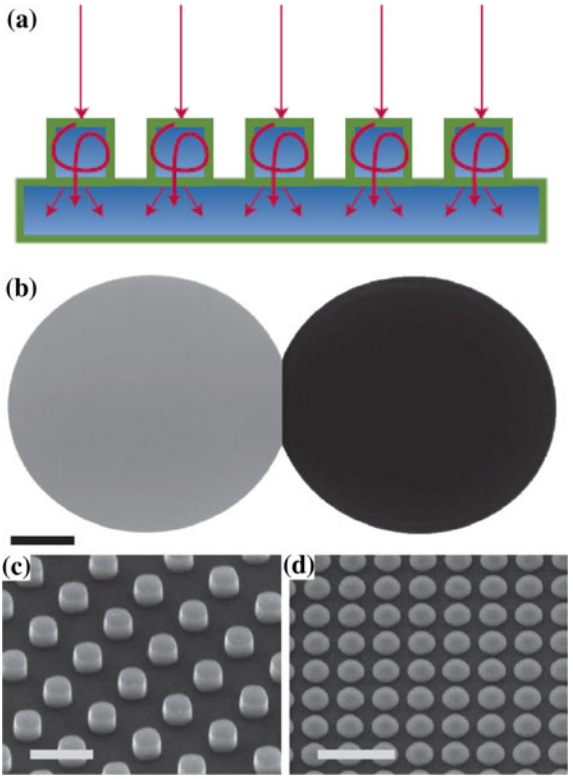

Fig. 1.7 **a** Mie scattering surface nanostructure for light trapping. **b** Photograph of a bare flat 4-inch Si wafer (*left*) and a 4-inch Si wafer fully imprinted with an optimized (250 nm diameter, 150 nm height, 450 nm pitch) Si NP array overcoated with a 60-nm-thick Si_3N_4 layer (*right*). Scale bar represents 1 inch. **c** Oblique scanning electron microscope image of a bare Si NP array (scale bar represents 500 nm) and **d** a Si NP array coated with a 60-nm-thick Si_3N_4 layer (scale bar represents 1 μm). Adapted with permission from Ref. [57]. Copyright © 2012 Macmillan Publishing Limited

1.6.2 Plasmonic Structures

1.6.2.1 Plasmonic Scattering

For nearly two decades, plasmonic structures have been utilized as a means to enhance scattering in solar cells. The impact of these metallic particles resides in localized surface plasmons, polarized oscillations of conduction electrons, whose enhanced local electromagnetic field increases the light-active cross section of the particle beyond that of its geometric cross section. Incident light near the surface plasmon resonance frequency is absorbed while off-resonant light is scattered. For solar cells, light absorbed by plasmonic structures is dissipated as heat and considered detrimental. However, the off-resonant scattering can increase absorption in the solar cell absorber and consequently increase current collection. These interactions with light can be easily tailored in PV devices as the particle shape, size, material, and refractive index of the surrounding medium can impact the dipole surface plasmon resonance frequency [62]. Three different key plasmonic solar cell geometries, shown in Fig. 1.8, including both particle and grating structures, have been identified as promising routes to significantly increase light trapping [63] and will be discussed next.

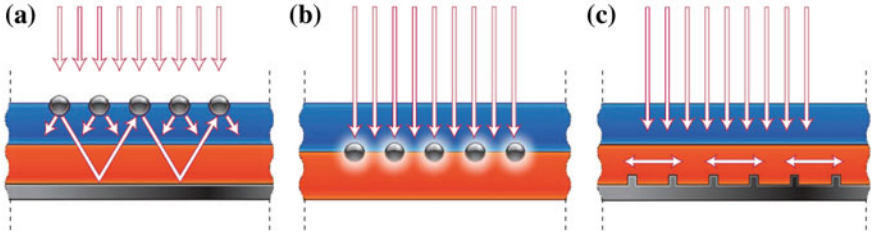

Fig. 1.8 Plasmonic light-trapping geometries for thin-film solar cells. **a** Light trapping by scattering from metal nanoparticles at the surface of the solar cell. Light is preferentially scattered and trapped into the semiconductor thin film by multiple and high-angle scattering, causing an increase in the effective optical path length in the cell. **b** Light trapping by the excitation of localized surface plasmons in metal nanoparticles embedded in the semiconductor. The excited particles' near field causes the creation of electron–hole pairs in the semiconductor. **c** Light trapping by the excitation of surface plasmon polaritons at the metal/semiconductor interface. A corrugated metal back surface couples light to the surface plasmon polariton or photonic modes that propagate in the plane of the semiconductor layer. Adapted with permission from Ref. [63].

Early experiments with plasmonically coupled semiconductor explored the use of Cu, Ag, and Au particle decorated surfaces with Si-on-insulator (SOI) photodiodes [64, 65]. These efforts demonstrated over an order of magnitude gain in photocurrent over that of particle-free devices at 800 nm. Importantly, the particles were separated from the absorber by a thin insulating film to provide electrical isolation and prevent detrimental surface recombination. This general scheme was revisited by several groups for SOI, Si, a-Si, and GaAs solar cells with I_{SC} enhancement factors that spanned 8–33 % [66–68]. The particle size, shape, and material were also shown to play an important role in front decorated forward scattering configurations [66]. These parameters were explored through simulation, which correlated scattering from cylindrical and hemispherical Ag particles to path length enhancement over that of Au and spherical geometries. More recently, rear plasmonic designs with an underlying back reflector have yielded a 25 % increase in power efficiency attributable to strong scattering and reduced parasitic absorption by the Ag particles [69].

Since reduced materials usage is an important theme for plasmonic solar cells, a natural extension of this work is coupling plasmonic designs with waveguide structures, which have been utilized to increase propagation of light in thin solar cells. In this architecture, the plasmonic particles/grating is placed on the front or backside of the solar cell waveguide, consisting of a solar cell sandwiched between low refractive index dielectric layers. In some cases, these dielectric layers are conducting metal oxides that function as contact layers, while in others, they are simply passivation layers. In the latter case, metal contacts must penetrate the passive layer to make contact to the absorber. In plasmonic waveguide solar cells, including SOI devices, the plasmon resonance can couple light into the waveguide modes, which traps light in the absorber. Hence, design of the plasmonic resonance should take into consideration the waveguide modes for efficient coupling [64].

1.6.2.2 Near-Field Coupling

Plasmonic nanoparticles can also enhance near-field coupling with the semiconductor. Since light absorption is proportional to the electromagnetic field, the enhanced local field around the particle increases absorption in the semiconductor material near the particle. These particles consequently act as light concentrators and are generally smaller to reduce emission. The behavior can be exploited with several different geometries, front, back, and embedded, but most demonstrations incorporate particles near the junction as a means to enhance absorption in materials with low diffusion lengths (e.g., polymers). Inorganic efforts applicable to direct bandgap semiconductors are less developed as scattering has yielded more promising results. Although difficult to isolate experimentally, near-field coupling has also been suggested to directly excite carriers without phonon assistance [70].

1.6.2.3 Surface Plasmon Polaritons

The last scenario in Fig. 1.8c illustrates the use of corrugated back contacts to couple light into surface plasmon polariton (SPP) and photonic modes. SPPs are electromagnetic waves that travel along the metal–insulator interface with propagation lengths that can reach 100 μm in the infrared region for some systems. SPP modes are tightly bound to the interface with depths (tens of nanometers) that facilitate absorption in the semiconductor. In theory, the concept is easily assimilated into current thin-film designs as metallic back contacts are existing components in all solar cells. Several reports have examined the use of patterned back contacts, exploring the impact of particle order, size, pitch, and material [10, 12, 61, 71]. These studies have shown that patterned back contacts provide substantial short-circuit current enhancement, albeit primarily due to photonic modes arising from the metal/conducting metal oxide interface as the metal oxide interlayer reduces SPP modes [10]. Attention to this geometry, with a dielectric interlayer between the absorber and patterned metal, may speak to the recombination challenges associated with a high surface area metal contact as well as pragmatic barriers to SPP modes. In an alternative structure, the interfacial area between the absorber and metal is reduced by introducing a dielectric in the recess regions of the corrugated metal contact.

Although study of plasmonic solar cells has seen a surge in recent years, one of the most significant challenges they face is material based. Nearly all studies to date have focused on Ag because of its high scattering cross section. However, the cost of Ag can be significant in some designs and alternative metals such as Al and Cu compromise performance. It is also quite clear that improved absorption does not translate into an equal improvement in current density, and other considerations, such as recombination and contact configuration, must be addressed before practical utility can be assessed. Moreover, extension of the demonstrated power conversion efficiency improvements of 1–3 % in poorly performing devices to more efficient,

commercially relevant solar cells must be questioned. That being said, the rapid rate of progress in plasmonic solar cells provides significant impetus for continued development.

1.7 Back Contact Geometry Devices

Back contact devices such as that pictured in Fig. 1.9 place the n-type "window" layer behind the absorber so that light strikes the absorber without passing through a window layer. The back contact geometry thus permits optimization of the window layer without concern for light transmission.

However, research on back contact thin-film solar cells is far more limited than that just summarized for pillar and plasmonic-type devices. The referenced texts would seem to encompass the only publications focused on devices with this geometry. The majority detail geometrically ordered structures and inorganic materials, all CdTe-based, including CdTe homojunction [72, 73] and CdTe/CdS [74] and CdTe/CdSe [75, 76] heterojunction devices.

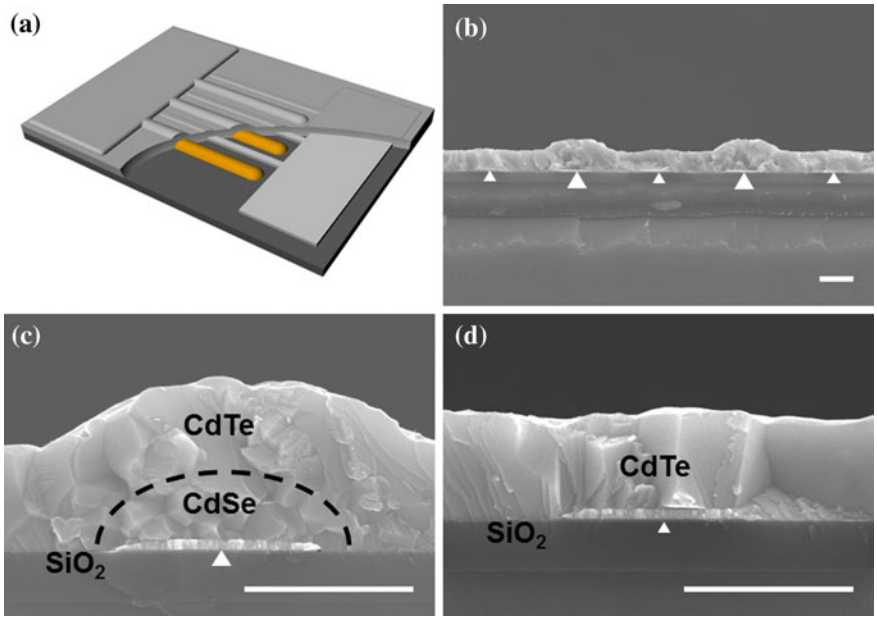

Fig. 1.9 **a** Schematic of the windowless interdigitated CdSe/CdTe solar cells, including removal of the CdTe from a portion to show the CdSe-coated wire and bare wire contacts. **b** Cross-sectional SEM image of a CdSe/CdTe device exhibits periodicity at a length scale twice that of the electrode pitch due to the CdSe deposit on every other wire. Arrows mark the locations of the wire contacts. **c** Higher magnification images of a CdSe-coated wire contact with overlying CdTe and the heterojunction delineated, and **d** the CdTe wire contact. Scale bars are 1 μm. Adapted with permission from Ref. [75]. Copyright © 2013, American Chemical Society

The relative paucity of study in this area finds an interesting analog in the dominance of 1D Si panels despite higher performance of back contact Si panels (due to higher cost per watt).

Particularly in light of present commercial market conditions that include a capacity glut and commodity-like pricing pressures, scalability concerns and associated cost of the complicated manufacturing procedures required for many 3D geometries are constraints on even far-sighted research efforts. The back contact geometries are intermediate in this respect, as the steps in manufacture can be similar to those presently used for manufacture of some types of planar devices, with the main changes being in the order in which the steps are conducted.

1.7.1 Back Contact Manufacturing Approaches

A key difference between manufacture for thin-film and Si back contact PV devices is the sequence in which semiconductor and metallization are fabricated. With Si devices, the semiconductor serves as the substrate upon which all processing is executed. This need not be the case with thin-film devices. Indeed, for the back contact thin-film devices manufactured to date, the metallization for both the positive and negative contacts is deposited first (on an insulating substrate), the semiconducting components being deposited subsequently onto the metallization (s). The sequence of manufacture can be inferred from the schematic and scanning electron microscope images of actual devices in Fig. 1.9.

It has been previously noted that the back contact geometry eliminates conflicting criteria for device optimization by placing the n-type window layer behind the absorber and eliminating the need for a transparent current collector layer. A benefit of the manufacturing approach used for the devices in Fig. 1.9a is that only a single patterning process, to fabricate both the positive and negative interdigitated electrodes, is required for device fabrication; this is a point of some practical significance for manufacture of micrometer-scale features. Differentiation of the two electrodes is achieved by electrodeposition, application of different potentials to the two electrodes enabling selective, highly conformal deposition onto only the desired electrode.

1.7.2 Back Contact Heterojunction CdS/CdTe Devices

The first inorganic heterojunction devices fabricated in this manner were based on the commercial CdTe/CdS system [72]. Fabrication involved CdS electrodeposition on one electrode followed by CdTe electrodeposition on both electrodes through impingement of the deposits, with annealing after each process. Devices exhibited efficiencies of less than 1 % with a correlation of performance and the pitch of the electrodes. Modeling suggested extremely low carrier concentrations in the intrinsic electrodeposited CdTe. Additional factors negatively impacting performance

included recombination on the unpassivated surface, the use of identical contact metallizations for both n-type CdS and p-type CdTe, and low aspect ratio contacts.

Taking advantage of the flexibility introduced by the back contact geometry, devices were also fabricated using n-type material, CdSe, selected without consideration of light absorption (i.e., bandgap). Devices with CdSe electrodeposition on one electrode followed by CdTe electrodeposition on both electrodes through impingement of the deposits reached efficiency of only ≈2 % after annealing, likely still limited by the same issues as the CdS/CdTe devices.

Devices were also fabricated with pulse laser deposited (PLD) CdTe. Fabrication involved CdSe electrodeposition on one electrode followed by PLD of CdTe over the entire surface of the device. Device efficiencies reached ≈2.8 % after annealing. Subsequent passivation of the devices by immersion in ammonium sulfate increased the maximum device efficiency to ≈4.3 % [75], the improvement largely associated with increase of V_{oc} by ≈150 mV (such devices have since reached ≈5.1 % efficiency, while devices with modified contacts widths have reached 5.9 % efficiency.

1.7.3 *Laser Beam-Induced Current Mapping of Device Performance*

The spatial variation of device performance has been explored using laser beam-induced current measurements. The spatial variation of short-circuit current collection as the laser beam was rastered over the device surface is shown in Fig. 1.10 for back contact devices with PLD CdTe absorber. The 3D aspects of device performance are evident, in particular reduced collection for illumination over the contacts.

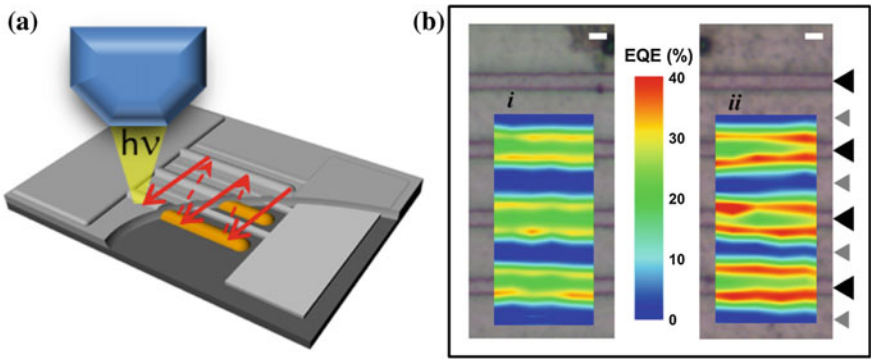

Fig. 1.10 **a** Schematic of scanning photocurrent microscopy. **b** External quantum efficiency maps obtained by scanning photocurrent microscopy (focused 532 nm laser) of part of a back contact CdSe/CdTe PV device (i) before and (ii) after surface passivation treatment. Locations of wire contacts are indicated. Scale bars are 1 μm. Adapted with permission from Ref. [75]. Copyright © 2013, American Chemical Society

1.8 Summary and Outlook

3D PV is the subject of substantial exploration, in part, because such devices present the promise of improved efficiency. A number of 3D nano- and microscale approaches to solar cell efficiency enhancement have been discussed. The approaches attempt to decouple conflicting criteria for optimization of performance, eliminate particular criteria, modify materials properties, or achieve some combination thereof. Examples of 3D devices based on each approach have been captured herein.

While the scientific rational for such approaches is sound and initial results are promising for the most part, processing complexity and cost-to-performance ratios do not presently yield significant commercial value. Significant challenges exist for nano- and micro-manufacturing that prevent current designs from being implemented on a macro scale with high parallelism. Additionally, contacts are proving to be quite critical in these designs and frequently are not addressed despite being of the utmost importance in commercial planar solar cells. Performance problems are exacerbated by high surface area structures that require significantly reduced surface recombination velocities, not to mention understanding and control of doping gradients at submicrometer length scale, to be competitive with thin-film devices.

A number of third-generation 3D PV devices are approaching double-digit efficiencies and have done so in a relatively short period of time. Furthermore, as the field matures, continued cross talk between planar and 3D solar cell development can be expected to expedite efficiency gains. That said, if thin-film progress is an indicator of the 3D PV road map, progress will become slower and more incremental as efficiencies continue to improve.

References

1. Schwartz, R.J., Lammert, M.D.: IEEE International Electron Devices Meeting. Washington DC (1975)
2. Lammert, M.D., Schwartz, R.J.: Interdigitated back contact solar-cell—silicon solar-cell for use in concentrated sunlight. IEEE Trans. Electron Devices **24**(4), 337–342 (1977)
3. Sinton, R.A., et al.: Silicon point contact concentrator solar cells. Electron Device Letters IEEE **6**(8), 405–407 (1985)
4. Sinton, R.A., Swanson, R.M.: Recombination in highly injected silicon. Electron Devices IEEE Trans. **34**(6), 1380–1389 (1987)
5. Kerschaver, E.V., Beaucarne, G.: Back-contact solar cells: a review. Prog. Photovoltaics Res. Appl. **14**(2), 107–123 (2006)
6. Fan, Z., et al.: Three-dimensional nanopillar-array photovoltaics on low-cost and flexible substrates. Nat. Mater. **8**(8), 648–653 (2009)
7. Isabella, O., et al.: 3-D optical modeling of thin-film silicon solar cells on diffraction gratings. Prog. Photovoltaics Res. Appl. **21**(1), 94–108 (2013)
8. Lin, Q., et al.: Efficient light absorption with integrated nanopillar/nanowell arrays for three-dimensional thin-film photovoltaic applications. ACS Nano **7**(3), 2725–2732 (2013)
9. Garnett, E., Yang, P.D.: Light trapping in silicon nanowire solar cells. Nano Lett. **10**(3), 1082–1087 (2010)

10. Ferry, V.E., Polman, A., Atwater, H.A.: Modeling light trapping in nanostructured solar cells. ACS Nano **5**(12), 10055–10064 (2011)
11. Grandidier, J., et al.: Simulations of solar cell absorption enhancement using resonant modes of a nanosphere array. J. Photonics Energy **2**(1), 024502-1–11 (2012)
12. Deceglie, M.G., et al.: Design of nanostructured solar cells using coupled optical and electrical modeling. Nano Lett. **12**(6), 2894–2900 (2012)
13. Li, X., et al.: Bridging electromagnetic and carrier transport calculations for three-dimensional modelling of plasmonic solar cells. Opt. Express **19**(S4), A888–A896 (2011)
14. Li, X.F., et al.: Multi-dimensional modeling of solar cells with electromagnetic and carrier transport calculations. Prog. Photovoltaics **21**(1), 109–120 (2013)
15. Xiang, J., et al.: Ge/Si nanowire heterostructures as high-performance field-effect transistors. Nature **441**(7092), 489–493 (2006)
16. Xu, S., et al.: Self-powered nanowire devices. Nat. Nanotechnol. **5**(5), 366–373 (2010)
17. Tian, B., et al.: Three-dimensional, flexible nanoscale field-effect transistors as localized bioprobes. Science **329**(5993), 830–834 (2010)
18. Wu, Y., et al.: Controlled growth and structures of molecular-scale silicon nanowires. Nano Lett. **4**(3), 433–436 (2004)
19. Gudiksen, M.S., Wang, J., Lieber, C.M.: Synthetic control of the diameter and length of single crystal semiconductor nanowires. J. Phys. Chem. B **105**(19), 4062–4064 (2001)
20. Wu, Z.H., et al.: Growth of Au-catalyzed ordered GaAs nanowire arrays by molecular-beam epitaxy. Appl. Phys. Lett. **81**(27), 5177–5179 (2002)
21. Wang, X., Summers, C.J., Wang, Z.L.: Large-scale hexagonal-patterned growth of aligned ZnO nanorods for nano-optoelectronics and nanosensor arrays. Nano Lett. **4**(3), 423–426 (2004)
22. Fan, Z., et al.: Ordered arrays of dual-diameter nanopillars for maximized optical absorption. Nano Lett. **10**(10), 3823–3827 (2010)
23. Jeong, S., et al.: Hybrid silicon nanocone-polymer solar cells. Nano Lett. **12**(6), 2971–2976 (2012)
24. Hua, B., et al.: Rational geometrical design of multi-diameter nanopillars for efficient light harvesting. Nano Energy **2**(5), 951–957 (2013)
25. Li, Y., Zhang, J., Yang, B.: Antireflective surfaces based on biomimetic nanopillared arrays. Nano Today **5**(2), 117–127 (2010)
26. Zhu, J., et al.: Nanostructured photon management for high performance solar cells. Mater. Sci. Eng. R: Rep. **70**(3–6), 330–340 (2010)
27. Zhu, J., et al.: Optical absorption enhancement in amorphous silicon nanowire and nanocone arrays. Nano Lett. **9**(1), 279–282 (2009)
28. Wang, K.X., et al.: Absorption Enhancement in Ultrathin Crystalline Silicon Solar Cells with Antireflection and Light-Trapping Nanocone Gratings. Nano Lett. **12**(3), 1616–1619 (2012)
29. Zhu, J., et al.: Nanodome solar cells with efficient light management and self-cleaning. Nano Lett. **10**(6), 1979–1984 (2010)
30. Muskens, O.L., et al.: Design of Light Scattering in Nanowire Materials for Photovoltaic Applications. Nano Lett. **8**(9), 2638–2642 (2008)
31. Tsakalakos, L., et al.: Silicon nanowire solar cells. Appl. Phys. Lett. **91**(23), 233117-1–3 (2007)
32. Spurgeon, J.M., Atwater, H.A., Lewis, N.S.: A Comparison Between the Behavior of Nanorod Array and Planar Cd(Se, Te) Photoelectrodes. J. Phys. Chem. C **112**(15), 6186–6193 (2008)
33. Kempa, T.J., et al.: Single and tandem axial p-i-n nanowire photovoltaic devices. Nano Lett. **8** (10), 3456–3460 (2008)
34. Li, Y., et al.: Nanowire electronic and optoelectronic devices. Mater. Today **9**(10), 18–27 (2006)
35. Tian, B., Kempa, T.J., Lieber, C.M.: Single nanowire photovoltaics. Chem. Soc. Rev. **38**(1), 16–24 (2009)
36. Pan, C., et al.: Enhanced Cu_2S/CdS coaxial nanowire solar cells by piezo-phototronic effect. Nano Lett. **12**(6), 3302–3307 (2012)

37. Tian, B., et al.: Coaxial silicon nanowires as solar cells and nanoelectronic power sources. Nature **449**(7164), 885–889 (2007)
38. Krogstrup, P., et al.: Single-nanowire solar cells beyond the Shockley-Queisser limit. Nat. Photonics **7**(4), 306–310 (2013)
39. Tang, J., et al.: Solution-processed core-shell nanowires for efficient photovoltaic cells. Nat. Nanotechnol. **6**(9), 568–572 (2011)
40. Kelzenberg, M.D., et al.: Photovoltaic measurements in single-nanowire silicon solar cells. Nano Lett. **8**(2), 710–714 (2008)
41. Green, M.A., et al.: Solar cell efficiency tables (version 31). Prog. Photovoltaics Res. Appl. **16** (1), 61–67 (2008)
42. Fan, Z., et al.: Challenges and prospects of nanopillar-based solar cells. Nano Res. **2**(11), 829–843 (2009)
43. Kapadia, R., Fan, Z.Y., Javey, A.: Design constraints and guidelines for CdS/CdTe nanopillar based photovoltaics. Appl. Phys. Lett. **96**(10), 103116-1–3 (2010)
44. Kwak, W.-C., et al.: Electrodeposition of Cu(In, Ga)Se_2 crystals on high-density CdS nanowire arrays for photovoltaic applications. Cryst. Growth Des. **10**(12), 5297–5301 (2010)
45. Kelzenberg, M.D., et al.: High-performance Si microwire photovoltaics. Energy Environ. Sci. **4**(3), 866–871 (2011)
46. Kelzenberg, M.D., et al.: Enhanced absorption and carrier collection in Si wire arrays for photovoltaic applications. Nat. Mater. **9**(3), 239–244 (2010)
47. Adachi, M.M., Anantram, M.P., Karim, K.S.: Core-shell silicon nanowire solar cells. Sci. Rep. **3**, 1546-1–6 (2013)
48. Vanecek, M., et al.: Nanostructured three-dimensional thin film silicon solar cells with very high efficiency potential. Appl. Phys. Lett. **98**(16), 163503-1–3 (2011)
49. Musselman, K.P., et al.: Strong efficiency improvements in ultra-low-cost inorganic nanowire solar cells. Adv. Mater. **22**(35), E254–E258 (2010)
50. Musselman, K.P., et al.: Incompatible length scales in nanostructured Cu_2O solar cells. Adv. Funct. Mater. **22**(10), 2202–2208 (2012)
51. Yuhas, B.D., Yang, P.: Nanowire-based all-oxide solar cells. J. Am. Chem. Soc. **131**(10), 3756–3761 (2009)
52. Yu, Z.F., Raman, A., Fan, S.H.: Fundamental limit of nanophotonic light trapping in solar cells. Proc. Natl. Acad. Sci. U.S.A. **107**(41), 17491–17496 (2010)
53. Campbell, P., Green, M.A.: Light trapping properties of pyramidally textured surfaces. J. Appl. Phys. **62**(1), 243–249 (1987)
54. Zhao, J.H., et al.: 19.8 % efficient "honeycomb" textured multicrystalline and 24.4 % monocrystalline silicon solar cells. Appl. Phys. Lett. **73**(14), 1991–1993 (1998)
55. Yablonovitch, E.: Statistical ray optics. J. Opt. Soc. Am. **72**(7), 899–907 (1982)
56. Green, M.A.: Lambertian light trapping in textured solar cells and light-emitting diodes: Analytical solutions. Prog. Photovoltaics **10**(4), 235–241 (2002)
57. Spinelli, P., Verschuuren, M.A., Polman, A.: Broadband omnidirectional antireflection coating based on subwavelength surface Mie resonators. Nat. Commun. **3**, 692-1–5 (2012)
58. Cao, L.Y., et al.: Semiconductor nanowire optical antenna solar absorbers. Nano Lett. **10**(2), 439–445 (2010)
59. Bohren, C.F., Huffman, D.R.: Absorption and scattering of light by small particles, xiv, p. 530. Wiley, New York (1983)
60. Cao, L.Y., et al.: Engineering light absorption in semiconductor nanowire devices. Nat. Mater. **8**(8), 643–647 (2009)
61. Zhu, J., et al.: Nanodome solar cells with efficient light management and self-cleaning. Nano Lett. **10**(6), 1979–1984 (2010)
62. Kreibig, U., Vollmer, M.: Optical properties of metal clusters. Springer series in materials science, xx, p. 532. Springer, Berlin (1995)
63. Atwater, H.A., Polman, A.: Plasmonics for improved photovoltaic devices. Nat. Mater. **9**(3), 205–213 (2010)

64. Stuart, H.R., Hall, D.G.: Island size effects in nanoparticle-enhanced photodetectors. Appl. Phys. Lett. **73**(26), 3815–3817 (1998)
65. Stuart, H.R., Hall, D.G.: Absorption enhancement in silicon-on-insulator waveguides using metal island films. Appl. Phys. Lett. **69**(16), 2327–2329 (1996)
66. Nakayama, K., Tanabe, K., Atwater, H.A.: Plasmonic nanoparticle enhanced light absorption in GaAs solar cells. Appl. Phys. Lett. **93**(12), 121904-1–3 (2008)
67. Pillai, S., et al.: Surface plasmon enhanced silicon solar cells. J. Appl. Phys. **101**(9), 093105-1–8 (2007)
68. Derkacs, D., et al.: Improved performance of amorphous silicon solar cells via scattering from surface plasmon polaritons in nearby metallic nanoparticles. Appl. Phys. Lett. **89**(9), 093103-1–3 (2006)
69. Tan, H.R., et al.: Plasmonic light trapping in thin-film silicon solar cells with improved self-assembled silver nanoparticles. Nano Lett. **12**(8), 4070–4076 (2012)
70. Kirkengen, M., Bergli, J., Galperin, Y.M.: Direct generation of charge carriers in c-Si solar cells due to embedded nanoparticles. J. Appl. Phys. **102**(9), 0193713-1–5 (2007)
71. Li, T., Dai, L., Jiang, C.: Design of efficient plasmonic thin-film solar cells based on mode splitting. J. Opt. Soc. Am. B Opt. Phys. **28**(8), 1793–1797 (2011)
72. Josell, D., et al.: Three dimensionally structured CdTe thin-film photovoltaic devices with self-aligned back-contacts: electrodeposition on interdigitated electrodes. J. Electrochem. Soc. **156**(8), H654–H660 (2009)
73. Josell, D., et al.: Three-dimensionally structured thin film heterojunction photovoltaics on interdigitated back-contacts. ECS Trans. **28**, 521–532 (2010)
74. Hangarter, C.M., et al.: Three dimensionally structured interdigitated back contact thin film heterojunction solar cells. J. Appl. Phys. **109**(7), 073514-1–8 (2011)
75. Hangarter, C.M., et al.: Photocurrent mapping of 3D CdSe/CdTe windowless solar cells. ACS Applied Materials & Interfaces **5**(18), 9120–9127 (2013)
76. Kim, D.U., et al.: Backcontact CdSe/CdTe windowless solar cells. Sol. Energy Mater. Sol. Cells **109**, 246–253 (2013)

Chapter 2
Earth-Abundant $Cu_2ZnSn(S,Se)_4$ (CZTSSe) Solar Cells

Sandip Das, Krishna C. Mandal and Raghu N. Bhattacharya

2.1 Introduction

Current benchmark thin film solar cell (TFSC) technologies based on polycrystalline $CuIn_xGa_{1-x}S(Se)_2$ (CIGS) and CdTe absorber materials have reached record efficiencies of 20.8 and 19.6 % for laboratory-scale devices and have already reached the commercial production stage [1]. However, these thin film photovoltaic (PV) technologies suffer from serious issues of toxicity, skyrocketing material cost, and/or low abundance of raw materials, which are predicted to severely limit the production, mass deployment, and economic sustainability of these solar cells [2–9]. Indium (In), gallium (Ga), and tellurium (Te) supply have been categorized as "critical" by the US Department of Energy (DOE) and the European Commission (EC) [10, 11]. Particularly, In supply for CIGS production could be stringent as more than 80 % of In produced worldwide is consumed by the flat panel display (FPD) industry and with ever-increasing demand of such displays, sustainability and economic viability of CIGS PV technology could be in great danger in upcoming years [12]. Also, due to the environmental health concerns, use of toxic cadmium (Cd) hinders the mass production and deployment of CdTe solar cells [13]. Thus, an intense research effort has been triggered to develop alternative thin film solar absorber materials comprising of earth-abundant, low-cost, and non-toxic elements which can yield high-efficiency devices, be economically

S. Das
Department of Electrical Engineering, Kennesaw State University, Marietta, GA 30060 USA

K.C. Mandal
Department of Electrical Engineering, University of South Carolina, Columbia, SC 29208 USA

R.N. Bhattacharya (✉)
National Renewable Energy Laboratory, Golden, CO 80401, USA
e-mail: Raghu.Bhattacharya@nrel.gov

M.P. Paranthaman et al. (eds.), *Semiconductor Materials for Solar Photovoltaic Cells*, Springer Series in Materials Science 218,
DOI 10.1007/978-3-319-20331-7_2

competitive with the conventional energy sources, and support terawatt (TW)-scale PV generation in the near future.

Copper (Cu)-based I_2–II–IV–VI_4 quaternary kesterite compounds—Cu_2ZnSnS_4 (CZTS), $Cu_2ZnSnSe_4$ (CZTSe), and mixed chalcogenide $Cu_2ZnSn(S_xSe_{1-x})_4$ (CZTSSe) have emerged as the potential alternative to the existing CIGS and CdTe absorbers in thin film solar cells. CZTS(Se) is an attractive choice for thin film solar cell absorber material owing to its tunable direct bandgap of 1.0–1.5 eV with a large optical absorption coefficient ($>10^4$ cm^{-1}) and p-type conductivity [14–19]. The constituent elements of CZTS(Se) are earth abundant, inexpensive, and environmentally benign. The reserve of Cu, Zn, Sn, and sulfur on earth's crust is 68 ppm, 79 ppm, 2.2 ppm, and 420 ppm, respectively, compared to 0.16 ppm of In, 0.15 ppm of Cd, and 0.001 ppm of Te [20].

The availability of Zn and Sn is about 500 and 14 times higher, and the annual global production is 20 times and 340 times more compared to the scarce and expensive In [21]. Also, the Zn price is nearly two orders and Sn price is one order of magnitude less than indium, while the In price is sharply rising [21, 22]. Abundance and recent cost of the constituent elements for CZTS(Se), CIGS, and CdTe compounds are illustrated in Fig. 2.1.

Calculations according to the Shockley–Queisser photon balance have estimated the theoretical conversion efficiency of single-junction CZTS(Se) solar cells to be as high as 32.2 % [23]. In light of the above-mentioned advantages, CZTS(Se) shows extreme promise to be the ideal thin film solar cell material for low-cost, sustainable, high-efficiency, and environment-friendly PV technology.

Significant developments have been made on CZTS(Se)-based thin film photovoltaic solar cells in the past few years, reporting solar cell with ~11 % efficiency [24]. However, CZTS(Se) PV technology is currently in its amateur state and requires extensive research to become marketable in the near future. This

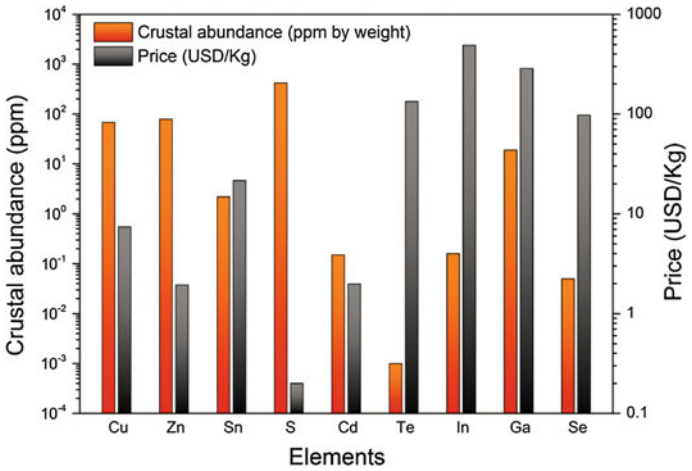

Fig. 2.1 Abundance on earth's crust and cost of constituent elements for CIGS, CdTe, and CZTS (Se) absorber materials for thin film solar cells

chapter presents an overview of the various techniques employed to prepare CZTS (Se) absorber material, physical properties of the material, defect physics, and photovoltaic performances of selected high-efficiency solar cells achieved following different absorber preparation routes.

2.2 Crystal Structure

$Cu_2ZnSn(S,Se)_4$ belongs to the I_2–II–IV–VI_4 quaternary material system with similar structure to that of ternary chalcopyrite material $CuInSe_2$ (space group $I\bar{4}2d$) (Fig. 2.2a), in which one half of In atoms (group III) are replaced by Zn (group II) and other half by Sn atoms (group IV). $Cu_2ZnSn(S,Se)_4$ crystallizes in two primary crystalline structures known as kesterite (space group $I\bar{4}$) and stannite (space group $I\bar{4}2m$) [25–28]. These two crystal structures are very similar; both have cations located at tetrahedral sites but differ in the stacking arrangement of Cu and Zn atoms along the *c*-axis [26–31]. The crystal structure and atomic arrangements for the kesterite and stannite structures are illustrated in Fig. 2.2b and c, respectively.

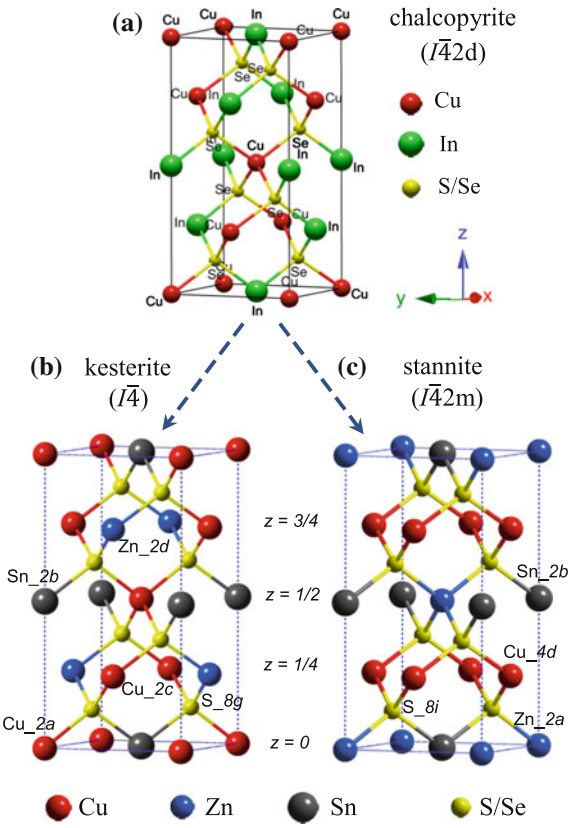

Fig. 2.2 Crystal structure of **a** chalcopyrite $CuInSe_2$, **b** kesterite Cu_2ZnSnS_4, and **c** stannite Cu_2ZnSnS_4

In kesterite structure, the cationic layers along the *c*-axis are arranged in the Cu–Sn, Cu–Zn, Cu–Sn, and Cu–Zn fashion. One Cu atom is located at *2a* position; Zn atom and the other Cu atom are located at *2d* and *2c* positions, respectively, with corresponding Madelung potentials of −15.04, −21.88, and −15.21 V. In stannite structure, a periodic arrangement of Zn–Sn cationic layer sandwiched in between Cu–Cu layers is repeated, where both Cu atoms are located at *4d* position and the Zn atom at *2a* position with Madelung potentials of −15.30 and −21.62 V, respectively. Sn atom site is located at *2b* position in both structures [32, 33]. Theoretical studies have predicted that the kesterite phase has slightly lower energy compared to the stannite phase and therefore should be thermodynamically more stable than stannite counterpart [33–40]. As predicted theoretically, most of CZTS samples have been reported to have kesterite structure.

Due to the similar structural properties and isoelectronic nature of Cu^{+} and Zn^{2+}, it is very difficult to distinguish between the kesterite and stannite phases experimentally by X-ray diffraction. Recently, neutron diffraction [31] and anomalous diffusion [41] studies confirmed that $Cu_2ZnSn(S,Se)_4$ compounds crystallize in kesterite structure and are dominant at temperature <876 °C. It is suggested that observations of stannite structure for $Cu_2ZnSn(S,Se)_4$ compounds were due to the existence of partial disorders of Cu and Zn sites in the I–II (001) layer of the kesterite phase [31, 42, 43]. This disorder could be due to the formation of both kesterite and stannite phases during crystallization process since there is only a negligible difference in the lattice parameters and the total energy.

2.3 Solar Cell Structure

The well-studied CIGS thin film solar cell structure is usually inherited for CZTS-based devices. The schematic structure of a typical CZTS solar cell is shown in Fig. 2.3a, and a corresponding cross-sectional SEM image showing the device

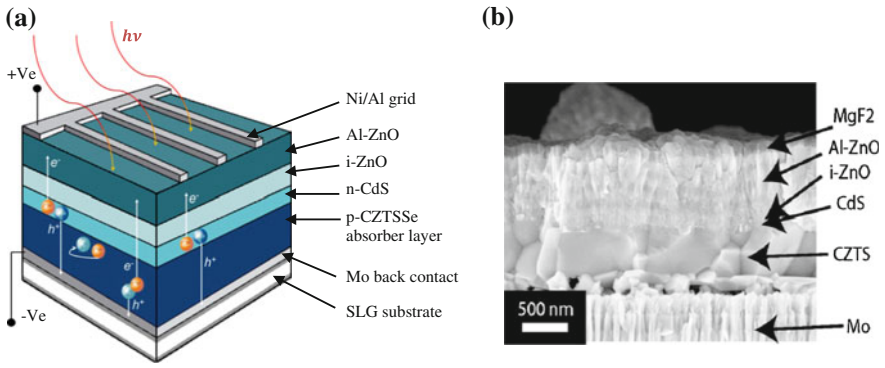

Fig. 2.3 **a** Schematic device structure of a typical CZTSSe thin film solar cell, **b** cross-sectional SEM image showing all layers of the device [17]

structure is presented in Fig. 2.3b. Sputtered bilayer molybdenum (Mo) film with a thickness of ~0.5–1.0 μm deposited on soda-lime glass (SLG) substrate is used as the standard back contact. The p-type CZTS absorber layer with thickness ranging from ~0.6 to 2.0 μm is grown on the Mo film. A thin n-type CdS layer of 50–100 nm thickness is deposited on the p-CZTS film, usually by chemical bath deposition to fabricate the heterojunction. Subsequently, the device structure is completed by deposition of a 50–90-nm high-resistive intrinsic ZnO (i-ZnO) buffer layer followed by the deposition of a transparent conducting oxide (TCO) layer as the front contact. Typically, 0.5–1.0 μm thick Al-doped n-type ZnO (Al-ZnO) or indium tin oxide (ITO) is used as the TCO. Finally, Ni/Al grid lines are deposited on the TCO layer for improved current collection. The typical device configuration of a CZTS-based solar cell is as follows: SLG/Mo/CZTS/CdS/i-ZnO/Al:ZnO/Al/Ni. In order to reduce the loss of reflection, MgF_2 antireflection coating is often deposited on top of the cell to capture the incident light more efficiently.

2.4 Composition and Phase Diagram

It is extremely challenging to grow pure single-phase kesterite $Cu_2ZnSnS(Se)_4$. CZTS(Se) can be grown via solid-state chemical reactions between Cu_2S, ZnS, and SnS_2 (or Cu_2Se, ZnSe, and $SnSe_2$). Due to the complexity of the quaternary material system, several binary and ternary sulfides (or selenides) including $Zn_xS(Se)$, $Cu_xS(Se)$, $Sn_xS(Se)$, and $Cu_xSnS(Se)_y$ phases can easily form during the CZTS(Se) film growth which may adversely affect the photovoltaic performance of the resulting device. The ternary phase diagram of the Cu_2S–ZnS–SnS_2 (or Cu_2Se–ZnSe–$SnSe_2$) system exhibits very narrow region of stability for single-phase kesterite CZTS(Se) crystals (Fig. 2.4) [44–47]. Kesterite structure is highly sensitive to composition compared to the chalcopyrite structure [48–51]. Only 1–2 %

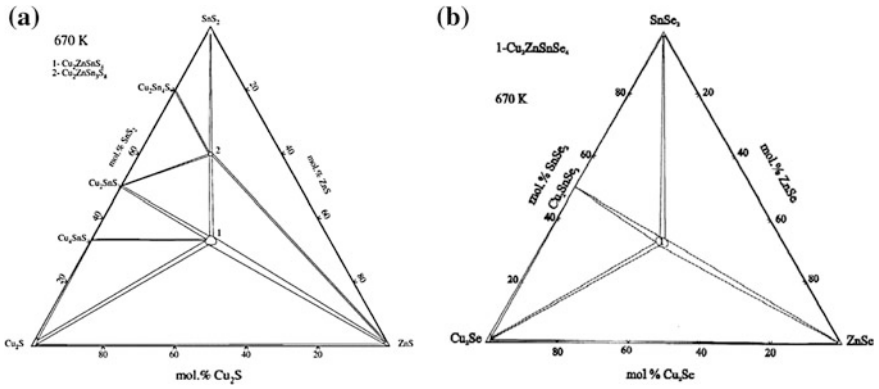

Fig. 2.4 Phase diagrams of **a** Cu_2S–ZnS–SnS_2 [44] and **b** Cu_2Se–ZnSe–$SnSe_2$ pseudo-ternary systems at 670 K [45]

deviation from the ideal stoichiometric composition is allowed compared to ~4 % deviation in chalcopyrites [52]. Also, the stability region of Cu_2ZnSnS_4 for Cu-rich condition in the chemical potential μ_{Sn}–μ_{Zn} diagram is about 0.1 eV wide stability region [48, 49, 53] compared to the 0.5 eV wide stability region for $CuInSe_2$ [54]. Based on ab initio calculations and experimental results, it is considered that single-phase kesterite is far more difficult to prepare compared to chalcopyrites.

So far, high-efficiency CZTS-based solar cells were found to have slightly Cu-poor and Zn-rich composition in general. It is observed that irrespective of the deposition technique or absorber preparation method, the best solar cells were obtained around a composition ratio of ~0.8–0.9 for Cu/(Zn + Sn) and ~1.1–1.2 for Zn/Sn. From selected published literature data, an efficiency map is generated against the Cu/(Zn + Sn) and Zn/Sn ratios as shown in Fig. 2.5a. Experimental data plotted in the ternary phase diagram as shown in Fig. 2.5b provides a clear idea of the confined composition space to realize high-efficiency CZTS-based solar cells. It is observed that the stoichiometric CZTS(Se) devices were limited to only ~5 % efficiency range, suggesting that Zn-rich composition is favorable.

During the absorber layer fabrication process, secondary phases such as ZnS(Se) and $Cu_2SnS(Se)_3$ may form in the Zn-rich regime. Nagoya et al. [48] and Maeda et al. [55] have theoretically predicted ZnS to be the predominant impurity phase under the Cu-poor and Zn-rich growth condition with Cu_{Zn} antisite being the most stable defect in the entire stability region of CZTS [53].

Existence of the ZnSe secondary phase in $Cu_2ZnSnSe_4$ films has been experimentally confirmed [56, 57]. ZnS(Se) has a wider bandgap and is usually less conductive and therefore is not considered to be responsible for reduced open-circuit voltage or reduced shunt resistance, but can lead to high series resistance of the solar cell [30, 56]. Other secondary phases such as $SnS(Se)_x$, $CuS(Se)_x$, or Cu–Sn sulfide(selenide) are considered to be more detrimental because of their lower bandgap and high conductivity, which can significantly reduce the

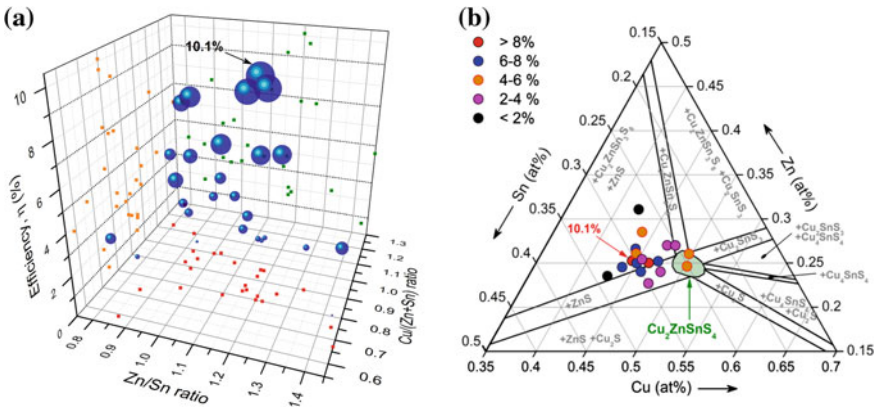

Fig. 2.5 **a** Efficiency map for CZTS-based solar cells plotted against Cu/(Zn + Sn) and Zn/Sn composition ratios and **b** solar cell efficiencies plotted in the ternary phase diagram

open-circuit voltage and decrease the shunt resistance leading to much inferior photovoltaic performance of the cell [42].

2.5 Etching

Surface preparation of semiconductors is important to achieve improved junction properties, reducing the recombination at the interface. For CZTS absorbers, KCN etching has been regularly performed to remove $Cu_{2-x}S$ phases from the surface, improving the device performance. Influence of KCN etching on the chemical and electronic structure of CZTS films has been studied by Bär et al. [58]. It was observed that KCN preferentially etches Cu and some amount of Sn, changing the surface composition of CZTS films and widening the surface bandgap from 1.53 to 1.91 eV. However, air voids are often formed after the etching.

Katagiri et al. [59] have introduced a simple and non-hazardous etching process by soaking the absorber film in DI water. The CZTS/CdS heterojunction was fabricated after 10-min DI water soaking of the absorber, resulting in improved efficiency. The authors concluded that metal oxide particles on the absorber surface were removed in this process. Electron probe micro analysis (EPMA) showed that oxygen concentration on the film surface was significantly reduced as a result of the DI water soaking (Fig. 2.6).

Timmo et al. [60] studied the effect of different etching agents on $Cu_2ZnSn(S,Se)_4$ monograins including HCl, KCN, NH_4OH, and Br-methanol. They observed that HCl could effectively etch Sn and Se, KCN has a preferential etching effect on Cu, Sn, and chalcogens, whereas NH_4OH preferentially etched copper and chalcogens. A tin-rich CZTS surface was obtained by Br-methanol etching.

Fairbrother et al. [61] showed that HCl etching drastically enhanced the device efficiency almost twofold compared to a device without any etching. The process was less hazardous and more effective than KCN etching. Experiments were carried out on CZTS films with Cu-poor and Zn-rich composition, which typically show

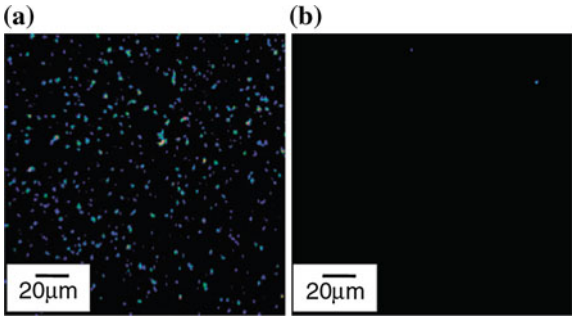

Fig. 2.6 Oxygen distribution (*bright points*) on CZTS surface: **a** before DI water soaking and **b** after 4 h DI water soaking [59]

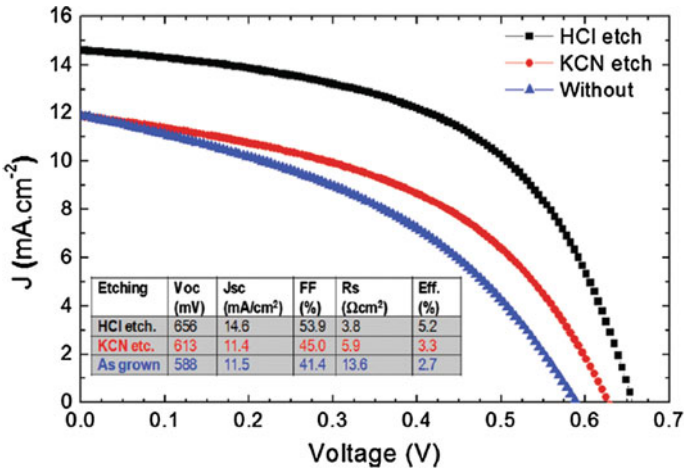

Fig. 2.7 *J–V* characteristics of the solar cells prepared using HCl-etched, KCN-etched, and without etched CZTS absorber layers [61]

superior photovoltaic performance. The authors suggested that HCl preferentially removes the Zn-rich secondary phases formed on the film surface leading to low series resistance, improved fill factor, and enhanced conversion efficiency. A device efficiency of 5.2 % was achieved with HCl etching compared to 3.3 and 2.7 % for KCN and unetched samples, respectively (Fig. 2.7).

2.6 Defects

Defects play an important role in the resulting optoelectronic properties of semiconductor materials. There are thirteen possible isolated intrinsic point defects in kesterite structure that may form during the CZTS(Se) thin film/bulk crystal growth including vacancies (V_{Cu}, V_{Zn}, V_{Sn}, and V_S), antisites (Cu_{Zn}, Zn_{Cu}, Cu_{Sn}, Sn_{Cu}, Zn_{Sn}, and Sn_{Zn}), and interstitial defects (Cu_i, Zn_i, and Sn_i). Existence of point defects and deviation from the ideal stoichiometry lead to the self-doping and intrinsic p-type conductivity of CZTS(Se).

Several theoretical defect studies based on density functional theory (DFT)/first-principle calculations have been employed to investigate the defect mechanism and formation energies of different possible point defects in kesterites [48, 49, 51, 53, 55, 62–64]. Chen and co-workers have thoroughly studied the defect characteristics of CZTS(Se) [38, 53, 65, 66]. The polyhedron for the stable region of CZTS and CZTSe in the (μ_{Cu}–μ_{Zn}–μ_{Sn}) three-dimensional space with $\mu_{Cu} = -0.2$ eV is shown in Fig. 2.8 [65], and the calculated defect formation energies of various isolated point defects (vacancies, antisites, and interstitials) as a function of Fermi energy at the chemical potential point ***P*** of the polyhedron is

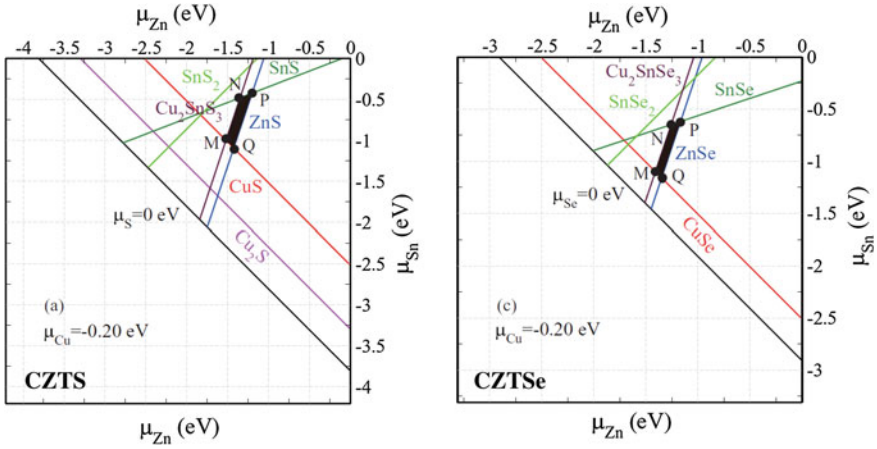

Fig. 2.8 Stable chemical potential area (*black*) of Cu_2ZnSnS_4 (CZTS) and $Cu_2ZnSnSe_4$ (CZTSe) in (μ_{Zn}, μ_{Sn}) planes with $\mu_{Cu} = -0.20$ eV in (μ_{Cu}, μ_{Zn}, μ_{Sn}) three-dimensional chemical potential space [65]

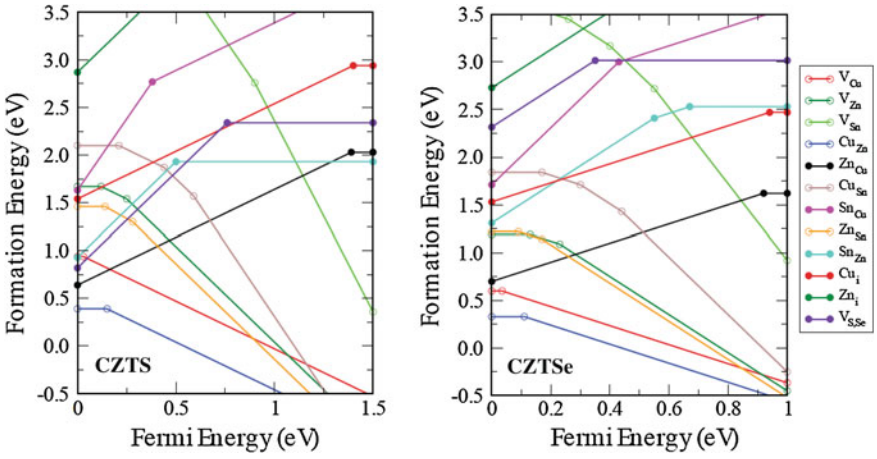

Fig. 2.9 Change of defect formation energies in Cu_2ZnSnS_4 (*left*) and $Cu_2ZnSnSe_4$ (*right*) as a function of the Fermi energy at the chemical potential point ***P*** (see Fig. 2.8). For the same Fermi energy, only the most stable charge state is plotted, and the charge state changes at the *circles* (open for acceptors and filled for donors), which show the transition energy levels [65]

represented in Fig. 2.9. Out of the possible 13 point defects mentioned above, the lowest five formation energies in ascending order correspond to Cu_{Zn}, V_{Cu}, Zn_{Sn}, V_{Zn}, and Cu_{Sn}, respectively, for Cu-poor kesterite as represented in Fig. 2.9.

All investigations converge to the general agreement that the acceptor defects such as Cu_{Zn} or Cu_{Sn} antisites and the Cu vacancy (V_{Cu}) have lower energy of formation with the lowest formation energy for Cu_{Zn} antisite defect (Fig. 2.9). The

donor defects such as the S vacancy (V_S) and the Zn_{Cu} antisite have much higher energy of formation. Such low formation energies of the acceptor defect levels, particularly Cu_{Zn} antisite, suggest the favorable formation of acceptors and are generally attributed to the evolution of p-type characteristics of Cu_2ZnSnS_4 [67–75] and $Cu_2ZnSnSe_4$ [76–79]. This explains why CZTS(Se) has always been reported to be of p-type regardless of the deposition method, and CZTS(Se) films for high-efficiency solar cells have shown Cu-poor and Zn-rich stoichiometry.

The Cu_{Zn} acceptor level is predicted to lie about 0.1 eV above the valence band maximum (VBM) compared to the shallower acceptor V_{Cu} at $\sim$0.02 eV above the VBM [53]. It is suggested that Cu vacancy (V_{Cu}) is preferred than the Cu_{Zn} antisite for high-performance solar cells, since Cu_{Zn} antisite produces deeper acceptor level than that of the V_{Cu} [53]. The Cu_{Sn} antisite energy level lying near the mid-gap ($\sim$0.6 eV above the VBM) is predicted to be the most active deep recombination center for the charge carriers [53, 80].

The Cu_{Zn} substitution occurs at the *2d* site, and Zn_{Cu} substitutions occur at the *2c* site [81, 82]. The existence of charge-compensated electrically neutral defect complexes such as $[Cu_{Zn}^{-} + Zn_{Cu}^{+}]^0$ and $[V_{Cu}^{-} + Zn_{Cu}^{+}]^0$ are also predicted for Cu-rich, Zn-poor and Cu-poor, Zn-rich CZTS, respectively [49]. However, such electrically benign defect pairs are believed to help in screening and electronic passivation of the deep levels, thus reducing the charge carrier recombination resulting in improved device performance [48, 53, 55].

In addition, two deep defect levels corresponding to activation energies of 0.12 and 0.167 eV have been experimentally identified via admittance spectroscopy of monograin CZTS solar cells which were attributed to Cu_{Zn} deep acceptor level and to interface states, respectively [83].

2.7 Deposition Techniques

Several physical and chemical deposition methods have been investigated for the fabrication of CZTS(Se) thin film absorber layer including thermal evaporation, electron beam evaporation, atom beam sputtering, RF/DC magnetron sputtering, hybrid sputtering, pulsed laser deposition (PLD), electrochemical deposition, solution-processed, nanoparticle-based synthesis, sol–gel spin coating, spray pyrolysis, chemical bath deposition (CBD), open-atmosphere chemical vapor deposition (OACVD), successive ion layer adsorption and reaction (SILAR), and screen printing. The main driving force for exploring different deposition methods is to develop a suitable absorber preparation technique to realize commercially viable low-cost and high-efficiency CZTS(Se) thin film solar cells. Such deposition techniques can be broadly classified as vacuum-based and non-vacuum deposition methods. The vacuum-based techniques are categorized as the methods requiring sophisticated instrumentation for deposition of precursor materials or absorber film fabrication under high vacuum. All physical vapor deposition (PVD) techniques—thermal evaporation, e-beam evaporation, atom beam sputtering, RF/DC magnetron

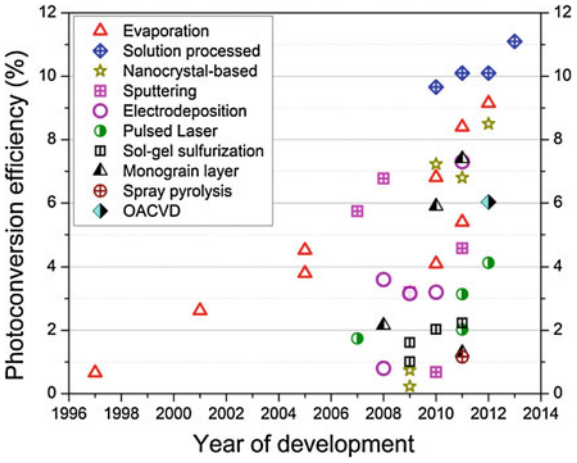

Fig. 2.10 Evolution of CZTS (Se)-based solar cell efficiency using different deposition techniques

sputtering, hybrid sputtering, and pulsed laser deposition (PLD) fall into this category. On the other hand, the non-vacuum absorber deposition techniques promise high-throughput roll-to-roll production opportunity at reduced cost. Deposition techniques such as electrochemical deposition, solution processing, nanoparticle-based synthesis, sol–gel spin coating, spray pyrolysis, chemical bath deposition (CBD), open-atmosphere chemical vapor deposition (OACVD), successive ion layer adsorption and reaction (SILAR), and screen printing are classified as non-vacuum deposition methods.

Efficiency of the CZTS(Se)-based thin film solar cells has been improved significantly over the past decade since the first report by Katagiri et al. in 1997 [73]. The evolution of efficiency using different deposition techniques is illustrated in Fig. 2.10. All types of deposition methods have realized noticeable improvement over the years. Details of the deposition methods and corresponding solar cell device characteristics are summarized in Table 2.1.

So far, the best photovoltaic performance has been achieved by Se-enriched CZTS absorber layer (CZTSSe) deposited using a non-vacuum solution-processed technique developed by IBM. A solar cell efficiency of 11.1 % was reported for CZTSSe-based device [24]. Only sulfur-containing (Se free) CZTS solar cell has reached an efficiency of 8.4 %, and only Se-containing CZTSe solar cell has been reported with an efficiency of 9.15 %, respectively, employing vacuum-based evaporation technique [14, 84]. The efficiencies > 3 %, achieved by different vacuum and non-vacuum methods for CZTS, CZTSe, and CZTSSe absorbers, are depicted in Fig. 2.11.

2.7.1 Vacuum-Based Deposition Methods

Vacuum-based absorber layer fabrication techniques can be subclassified into one-step or two-step processes. Unlike CIGS, the vacuum-based CZTS(Se) absorber layer fabrication technique had been exclusively the two-step process. In a

Table 2.1 Summary of various deposition methods Table of various deposition methods and device characteristics and their corresponding absorber composition and device characteristics taken from selected published literature

Deposition technique	V_{OC} (mV)	J_{SC} (mA/cm^2)	Fill factor (FF)	Efficiency	Year	Compositional details			References
						Absorber type	Cu/(Zn + Sn)	Zn/Sn	
Evaporation	400	6.0	27.7	0.66	1997	CZTS	–	–	[73]
	522.4	14.11	35.54	2.62	2001	CZTS	–	–	[74]
	661	19.5	65.8	8.4	2011	CZTS	–	–	[84]
	629	12.53	58.0	4.53	2005	CZTS	–	–	[86]
	436	6.0	41.0	1.1	2008	CZTS	–	–	[96]
	587	17.8	65.0	6.81	2010	CZTS	0.82	1.2	[17]
	377	37.4	64.9	9.15	2012	CZTSe	0.86	1.15	[14]
	652	9.6	61.0	3.8	2005	CZTS	0.84	1.16	[151]
	541	13.0	59.8	4.1	2010	CZTS	1.01	1.02	[87]
	272	36.8	38.2	3.82	2011	CZTSe	0.59	0.86	[152]
	497	20.0	–	5.4	2011	CZTSSe	0.78	0.97	[91]
	478	9.78	38.0	1.79	2008	CZTS	0.96	1.18	[85]
	422	29.5	60.0	7.51	2011	CZTSSe	–	–	[153]
	247	26.84	43.5	2.88	2013	CZTSe	0.57	2.35	[154]
Sputtering	610	17.9	62.0	6.77	2008	CZTS	0.85	1.25	[59]
	662	15.7	55.0	5.74	2007	CZTS	–	–	[109]
	545	15.44	54.6	4.59	2011	CZTS	0.67	1.45	[99]
	359	20.7	43.0	3.2	2009	CZTSe	0.83	1.15	[100]
	523	15.1	38.0	3.01	2011	CZTS	0.89	0.96	[101]
	718	10.9	41.0	3.2	2011	CZTS	0.92	0.93	[155]
	345	4.42	44.3	0.68	2010	CZTS	–	–	[102]
	620	11.8	63.0	4.5	2012	CZTS			[156]
	462	22.8	62.1	6.6	2012	CZTSSe	0.73	1.1	[157]

(continued)

Table 2.1 (continued)

Deposition technique	V_{OC} (mV)	J_{SC} (mA/cm^2)	Fill factor (FF)	Efficiency	Year	Compositional details			References
						Absorber type	Cu/(Zn + Sn)	Zn/Sn	
Pulsed laser deposition (PLD)	651	8.76	55.0	3.14	2011	CZTS	–	–	[116]
	546	6.78	48.4	1.74	2007	CZTS	0.73	0.86	[112]
	585	6.74	51.0	2.02	2011	CZTS	–	–	[117]
	700	10.01	59.0	4.13	2012	CZTS	–	–	[118]
Solution processing	517	30.8	63.7	10.1	2011	CZTSSe			[135]
	516	28.6	65.0	9.66	2010	CZTSSe	0.8	1.22	[134]
	422.8	38.7	61.9	10.1	2012	CZTSSe	0.8	1.2	[15]
	516.9	18.9	52.8	5.14	2012	CZTS	0.99	0.93	[158]
	459.8	34.5	69.8	11.1	2013	CZTSSe	–	–	[24]
	400	24.9	41.2	4.1	2011	CZTSSe	0.8	1.13	[159]
Nanocrystal-based synthesis	430	31.2	53.9	7.23	2010	CZTSSe	0.79	1.1	[18]
	321	1.95	37.0	0.23	2009	CZTS	–	–	[123]
	451	29.0	64.9	8.5	2012	CZTSSe			[126]
	640	21.5	49.0	6.8	2011	CZTGeS			[160]
Sol-gel sulfurization	529	10.2	41.6	2.23	2011	CZTS	0.9	1.32	[161]
	575	9.69	36.4	2.03	2010	CZTS	0.92	1.17	[162]
	554	6.7	43.4	1.61	2009	CZTS	0.96	1.17	[163]
	390	7.8	33.0	1.01	2009	CZTS	–	–	[164]
	358	5.06	34.7	0.63	2011	CZTS	0.75	1.43	[165]
	381	15.8	42.1	2.76	2012	CZTSe	0.79	1.39	[166]
Monograin layer (MGL)	582.4	7.13	32.0	1.3	2011	CZTS	–	–	[83]
	622	15.87	60.0	5.9	2010	CZTSSe	–	–	[148]
	422	15.5	44.0	2.16	2008	CZTSe	–	–	[149]
	720	18.4	60.0	7.4	2011	CZTSSe	0.89	1.1	[150]

(continued)

Table 2.1 (continued)

Deposition technique	V_{OC} (mV)	J_{SC} (mA/cm^2)	Fill factor (FF)	Efficiency	Year	Compositional details			References
						Absorber type	Cu/(Zn + Sn)	Zn/Sn	
Electrodeposition	567	22.0	58.1	7.3	2011				[138]
	529	15.9	42	3.6	2009	CZTS	0.97	1.08	[139]
	540	12.6	46.4	3.16	2009	CZTS	–	–	[140]
	540	16.9	40	3.6	2013	CZTSSe	–	–	[145]
Screen printing	386	4.76	27.0	0.49	2010	CZTS	–	–	[167]
	250	8.76	27.0	0.6	2012	CZTS	–	–	[168]
Spray pyrolysis	410	8.0	35.5	1.16	2011	CZTS	–	–	[169]
	175	0.46	24.5	0.154	2012	CZTS	–	–	[170]
OACVD	658	16.5	55.0	6.03	2012	CZTS	0.78	1.29	[136]
Chemical bath deposition	210	2.4	–	0.16	2010	CZTS	–	–	[171]
SILAR	280.5	0.637	62.0	0.396	2012	CZTS	–	–	[104]

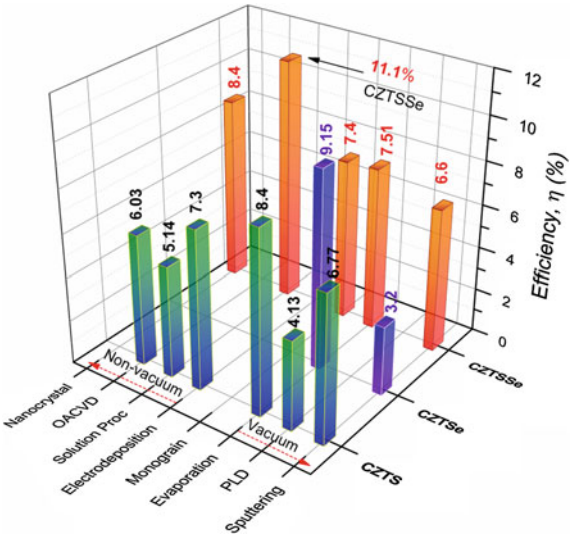

Fig. 2.11 Best photoconversion efficiencies achieved via different vacuum and non-vacuum deposition techniques using pure CZTS, pure CZTSe, and mixed CZTSSe solar absorber layers

two-step process, the first step involves the deposition of constituent elements of CZTS(Se) compound onto a substrate by deposition of pure elemental metals (Cu/Zn/Sn) or a combination of elemental and binary chalcogenides (such as Cu/ZnS/SnS). They can be either deposited in a stacked layer fashion or co-deposited together to achieve the desired composition in the final film. In the second step, the CZTS(Se) film growth and incorporation of balance chalcogen atoms (S/Se) are achieved by an atmospheric thermal processing of the substrate under S/Se vapor or $H_2S(Se)$ gas flow. Recently, a one-step absorber layer fabrication process had been reported for CZTSe solar cell, where the deposition and film growth were achieved in a single step by controlled evaporation of all constituent elements (Cu, Zn, Sn, and Se) inside the vacuum chamber under elevated substrate temperature yielding 9.15 % champion cell [14]. The one-step process can be considered superior compared to the two-step process from commercial point of view, as it eliminates the hazardous thermal processing step, reducing the time and cost of fabrication. This section will review the various vacuum-based deposition techniques employed to prepare CZTS(Se) solar cells and the notable results reported in the literature.

2.7.1.1 Evaporation

Evaporation is a well-established technique for the fabrication and development of thin film solar cells. Various types of evaporation technologies such as electron beam evaporation, thermal evaporation including co-evaporation, and fast evaporation have been investigated to fabricate CZTS(Se) absorber layer [14, 17, 73, 74, 84–97].

In 1997, the first photovoltaic performance of a CZTS-based thin film solar cell was reported by Katagiri et al. with an open-circuit voltage (V_{OC}) of 400 mV, short-circuit current density (J_{SC}) of 6 mA/cm^2, and a photoconversion efficiency of 0.66 % [73]. The absorber layer was fabricated by sequential deposition of Zn/Sn/Cu elemental stacked precursor layers on Mo-coated soda-lime glass (SLG) substrate by electron beam evaporation at 150 °C substrate temperature followed by sulfurization of the precursor layers under N_2 + H_2S (5 %) flow at 500 °C for 1–3 h. The heterojunction was formed by the deposition of n-CdS window layer on the p-type CZTS film. Since then, evaporation technique has been intensively used in the development of CZTS (Se) solar cells.

The same year, Friedlmeier et al. [88] reported CZTS solar cell with 2.3 % efficiency, fabricated by thermal evaporation of elemental metals and binary chalcogenides under high vacuum. Later, in 2001, Katagiri et al. [74] further improved the efficiency by replacing the elemental Zn with ZnS in the precursor layer and subsequent sulfurization at an increased temperature of 550 °C under H_2S flow for 1 h. The substrate temperature was also elevated up to 400 °C during the precursor layer deposition. Absorbers with different thicknesses from 0.95 to 1.63 μm were fabricated to study the effect on the photovoltaic response of the resulting devices. XRD peaks corresponding to (112), (200), (220/204), and (312/116) planes with a preferential orientation along [112] were observed and attributed to the kesterite structure. Film compositions were found slightly Cu-poor and Zn-rich with an optical absorption coefficient >10^4 cm^{-1} and a bandgap of 1.45 eV for the best performing cell. A significant decrease of the short-circuit current density and fill factor were observed with increasing thickness of the CZTS active layer, leading to drastically reduced efficiency. The best solar cell with Al/ZnO:Al/CdS/CZTS/Mo-SLG device configuration showed a photoconversion efficiency of 2.62 % [74]. By optimization of the sulfurization process and the device structure, the same group of researchers developed a device with 5.45 % efficiency in 2003 with a reported V_{OC} = 582 mV, J_{SC} = 15.5 mA/cm^2, and 60 % fill factor [89].

Large dependence of Cu/(In + Ga) ratio on the optoelectronic properties of CIGS thin film motivated the investigation of such dependence in CZTS solar cells by varying the Cu/(Zn + Sn) ratio [98]. Kobayashi et al. [86] studied the effect of Cu/(Zn + Sn) and the sulfurization temperature on the resulting film properties prepared via e-beam evaporation. CZTS absorbers were prepared with the varying Cu/(Zn + Sn) ratio ranging from 0.49 to 1.18 in the final film, and the sulfurization temperature was varied from 510 to 550 °C. The best photovoltaic performance was obtained for the CZTS film sulfurized at 520 °C with measured elemental ratios of Cu/(Zn + Sn) = 0.85, Zn/Sn = 1.03, and S/metal = 1.18. The best solar cell exhibited an efficiency of 4.53 % with V_{OC} = 629 mV, J_{SC} = 12.53 mA/cm^2, and FF = 58 %. Araki et al. [85] studied the influence of different stacking orders of elemental Zn, Sn, and Cu in the precursor layer on the film properties. Stacked precursor layers with six possible sequences were fabricated by e-beam evaporation on Mo-coated borosilicate glass and subsequently sulfurized at 560 °C for 2 h under the flow of elemental sulfur vapor to form CZTS films. Surface morphology,

composition, and electronic properties of the resulting films were found to be highly dependent on the precursor layer stacking order. The best cell was obtained for the precursor with a Mo/Zn/Cu/Sn stacking configuration yielding a photoconversion efficiency of 1.79 %. It was observed that considerably higher efficiency is achieved for the films with Cu and Sn layers placed adjacent to each other.

Wang et al. developed a simple two-step method where film processing time was significantly reduced to few minutes compared to the previous reports of H_2S processing requiring hours of annealing. They prepared high-quality PV-grade CZTS films by thermal co-evaporation of constituent elements on Mo/SLG substrates held at 110 °C followed by a hot-plate annealing for 5 min at 540 °C under sulfur vapor [17]. Absorber layers with different thicknesses ranging from 0.65 to 1.2 μm were fabricated. Raman spectra showed the CZTS characteristic peaks corresponding to 287, 338, and 368 cm^{-1} without the presence of any secondary phases. Similar to the observation made by Katagiri et al. [74], a significant reduction in efficiency was observed with increasing absorber thickness mainly due to degraded fill factor. The completed device had a configuration of SLG/700 nm Mo/CZTS absorber/70 nm CdS/80 nm i-ZnO/460 nm Al:ZnO or 180 nm ITO/Ni–Al metal fingers. A 105 nm MgF_2 antireflection coating was applied on top of the cell. The champion device (device D in Fig. 2.12a) showed a photoconversion efficiency of 6.8 % (V_{OC} = 587 mV, J_{SC} = 17.8 mA/cm^2, and FF = 65 %) with an absorber layer thickness of 0.65 μm. The *J–V* characteristics of the cells with different absorber layer thickness are presented in Fig. 2.12a.

The device performance was limited by high series resistance (R_S). A strong temperature dependence of R_S indicated the existence of a back-contact blocking layer (Schottky barrier) at the Mo/CZTS interface, suppressing the hole transport from the absorber to the Mo back contact. A barrier height of 0.32 eV for the blocking back contact was estimated from temperature-dependent measurement of the series resistance, and an activation energy of 1.05 eV corresponding to the

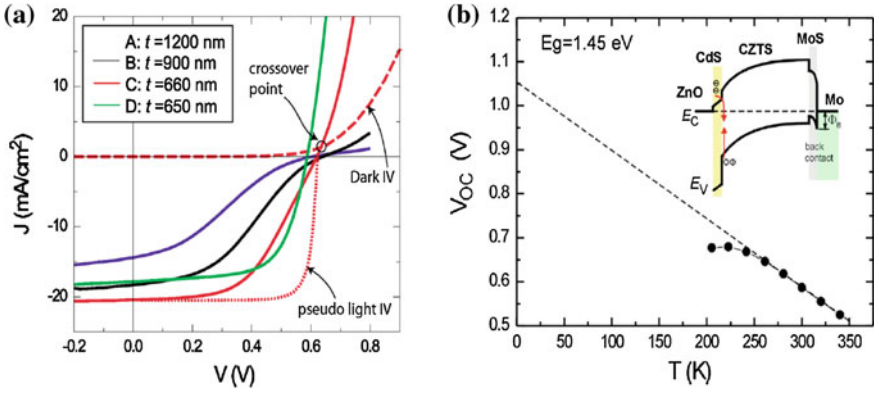

Fig. 2.12 **a** *J–V* curves of solar cells with different CZTS absorber thickness. The *dark J–V* and the pseudo *J–V* correspond to device C, **b** open-circuit voltage (V_{OC}) versus temperature plot of device C. A hypothetical band diagram showing the dominant recombination pathway at the CdS buffer/CZTS absorber interface and presence of a blocking back contact [17]

dominant recombination loss was extracted from the temperature-dependent V_{OC} measurement. A hypothetical band diagram was proposed based on these measurements, and the authors suggested that the subbandgap activation energy corresponds to the interfacial recombination at the CdS/CZTS interface, leading to lower open-circuit voltage (Fig. 2.12b).

Following the same procedure developed by Wang et al. [17], an 8.4 % efficient CZTS solar cell was reported by Shin et al. [84]. CZTS films were fabricated by thermal co-evaporation of constituent elements and 5 min atmospheric annealing at 570 °C. The device structure was as follows: Mo-coated SLG/ ~ 600 nm CZTS/90–100 nm CdS/80 nm i-ZnO/450 nm Al:ZnO/Ni–Al metal fingers/100 nm MgF_2. A bimodal grain size distribution was observed with larger grains comparable to the film thickness in the bulk of the film and much smaller grains at the immediate vicinity of the Mo back contact (Fig. 2.13a). The EDX line scan data perpendicular to the substrate (shown by the red arrow in Fig. 2.13a) revealed that the smaller grains correspond to an interfacial ZnS layer near the Mo back contact, whereas the larger grains in the bulk of the film are CZTS compound (Fig. 2.13b).

A depletion layer width of 180 nm and minority carrier diffusion length larger than 350 nm was estimated from time-resolved photoluminescence (TRPL) measurements and drive-level capacitance measurements. The champion cell exhibited V_{OC} = 661 mV, J_{SC} = 19.5 mA/cm^2, and a fill factor of 65.8 % (Fig. 2.14).

Loss of Sn under high vacuum during the annealing process for the Cu–Zn–Sn–S, Cu–Sn–S, and Sn–S material systems was investigated by Weber et al. [90]. Experimental results showed that Sn loss occurs in these systems as volatile SnS above 350 °C at a pressure of 1×10^{-2} Pa and the rate of Sn loss is increased significantly at temperatures above 550 °C. Decomposition of ternary Cu_2SnS_3 and Cu_4SnS_4 and quaternary Cu_2ZnSnS_4 phases leaves Cu_xS and ZnS solid phases in the annealed films. They suggested the decomposition reaction to take place following the reaction paths as summarized in (2.1)–(2.3). The authors suggested CZTS film processing at temperatures less than 550 °C under an inert gas ambient to minimize high degree of Sn loss and decomposition of CZTS.

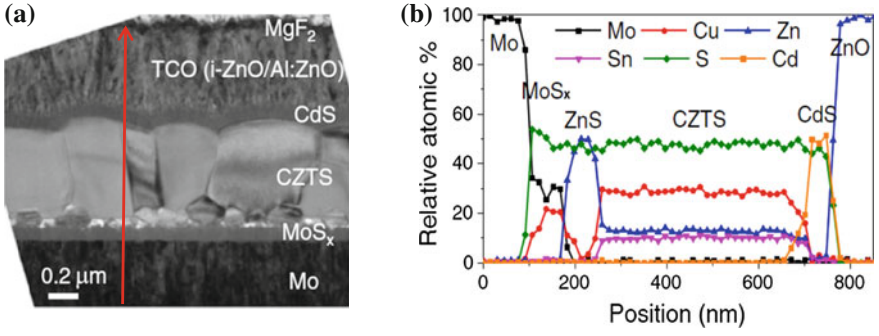

Fig. 2.13 **a** Bright-field cross-sectional TEM image of the champion CZTS device (Se free) and **b** EDX line scan along the *red arrow* in Fig. 2.13a showing the elemental profile [84]

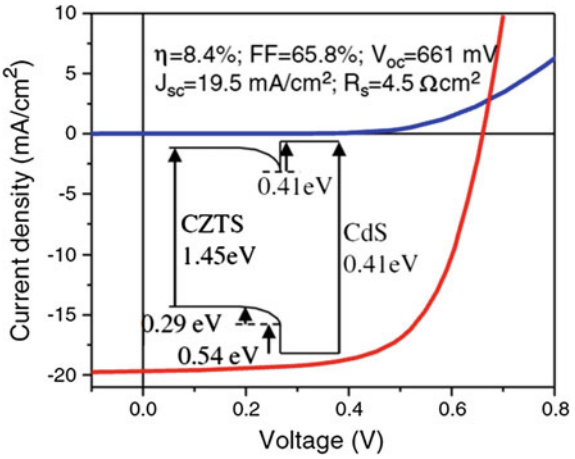

Fig. 2.14 *J–V* characteristics of the solar cell with 8.4 % efficiency *under dark* and under 1 sun illumination. Band alignment of CdS buffer with the CZTS absorber layer is depicted in the *inset* [84]

$$2Cu_2SnS_3(s) \rightarrow Cu_4SnS_4(s) + SnS(g) + S(g) \tag{2.1}$$

$$Cu_4SnS_4(s) \rightarrow 2Cu_2S(s) + SnS(g) + S(g) \tag{2.2}$$

$$Cu_2ZnSnS_4(s) \rightarrow Cu_2S(s) + ZnS(s) + SnS(g) + S(g) \tag{2.3}$$

Redinger et al. addressed this issue by introducing extra Sn along with excess sulfur during the annealing process [91]. They prepared the CZTSe films by co-evaporation of Cu, Zn, Sn, and Se under high vacuum followed by annealing at 560 °C for 2 h under elemental S vapor. A dramatic increase of the device efficiency from 0.02 to 5.4 % was achieved with the addition of Sn in the annealing chamber. It was suggested that Sn in the presence of excess sulfur forms SnS during high-temperature processing of CZTS films and the partial pressure of volatile SnS creates a dynamic equilibrium with its solid-state counterpart in the film, resulting in suppression of Sn loss in the form of SnS from the CZTS precursor layer. The authors modified the proposed decomposition reaction path suggested by Weber et al. [90] to a reversible reaction mechanism under the improved annealing conditions in the presence of excess Sn.

In 2006, Tanaka et al. [92] reported on the growth of CZTS film by co-evaporation of elemental Cu, Zn, Sn, and sulfur simultaneously deposited for 3 h on quartz substrates held at 400–600 °C. Notably, this was the first report on the one-step film fabrication approach, although no photovoltaic performance was investigated. All films showed p-type conductivity with a strong preferred orientation along [112] plane. The grain sizes increased with increasing substrate temperature, and large columnar grains were reported to form at 550 °C. Later, in 2008, Oishi et al. adopted the similar approach to grow CZTS thin films on (110) Si wafers by one-step co-evaporation technique [93]. Films were fabricated by simultaneous deposition of Cu, ZnS, Sn, and sulfur for 3 h at substrate temperatures

from 430 to 500 °C. All films showed slightly Cu-rich and highly Zn-rich stoichiometry. XRD pattern revealed that the (112) peak intensity is decreased and (004)/(200) peak intensity is increased for the films grown at elevated temperature, suggesting a temperature-induced orientational growth at higher temperatures. Tanaka et al. [94] studied the influence of Cu/(Zn + Sn) on the physical properties of CZTS thin films prepared by one-step co-evaporation technique. CZTS films were grown by multisource evaporation of the constituent elements at 550 °C substrate temperature for 2 h. Cu/(Zn + Sn) ratio was varied from 0.82 to 1.06 keeping the constant Zn/Sn ratio at 1.1, and in a second set, Cu/(Zn + Sn) was varied from 0.82 to 1.28 with a constant Zn/Sn ratio of 0.95, while S/metal ratio was kept constant at 0.93 for all films. Structural, morphological, and electrical characteristics of the films were correlated with the film compositions. For Zn-rich films, the resistivities of the films were found to be highly dependent on the Cu/(Zn + Sn) ratio, but Sn-rich films did not show such dependency. An increase of the (112) peak intensity and a narrower FWHM in the X-ray diffraction pattern with increasing Cu/(Zn + Sn) ratio suggested an improved crystallinity which was supported by the larger grains evidenced in SEM micrographs. This important observation suggested that growth of high-quality larger grain CZTS film can be promoted by a Cu-rich growth condition similar to the benchmark CIGS films obtained by multistage evaporation, where the deposition process begins with Cu-rich condition and is controlled to terminate with a Cu-poor stoichiometry.

A fast (16 min) co-evaporation technique was introduced by Schubert et al. to fabricate CZTS absorber in one-step process [87]. Cu, ZnS, Sn, and sulfur were co-evaporated on Mo-coated SLG substrates held at 550 °C under constant sulfur partial pressure of $2–3 \times 10^{-3}$ Pa. Due to the formation of a secondary CuS phase as evidenced from X-ray diffraction pattern, the as-grown films were highly Cu-rich with a Cu/(Zn + Sn) ratio of 1.42. The absorber layer was etched with aqueous KCN solution before CdS deposition to remove the excess CuS. As a result of KCN etching, the Cu/(Zn + Sn) ratio decreased to 1.01, resulting in nearly stoichiometric films. The best cell with a SLG/Mo/CZTS/CdS/Al:ZnO/Ni/Al device configuration showed a total area efficiency of 4.1 % with V_{OC} = 541 mV, J_{SC} = 13.0 mA/cm^2, and FF = 59.8 %. So far, this holds the record for the high-efficiency CZTS solar cell produced via one-step vacuum co-evaporation technique.

Repins et al. [14] fabricated $Cu_2ZnSnSe_4$ (CZTSe) solar cell with 9.15 % efficiency by co-evaporation. The CZTSe absorber layer was grown by four-source (Cu, Zn, Sn, and Se) thermal co-evaporation. A 15 nm NaF layer was deposited on Mo-coated SLG substrate by e-beam evaporation before the CZTSe film fabrication. The NaF layer was used to compensate the low out-diffusion of sodium. It was argued that the NaF deposition helped to improve the V_{OC}, J_{SC}, and the fill factor. Deposition flux of each source and the substrate temperature were precisely controlled during the film growth (Fig. 2.15a). A Cu-rich growth was carried out for initial 12.5 min to favor larger grain growth, and the Cu source was turned off thereafter. Formation of Cu_xSe_y is expected during this period which further reacts with continuing Zn and Sn flux to form kesterite CZTSe film.

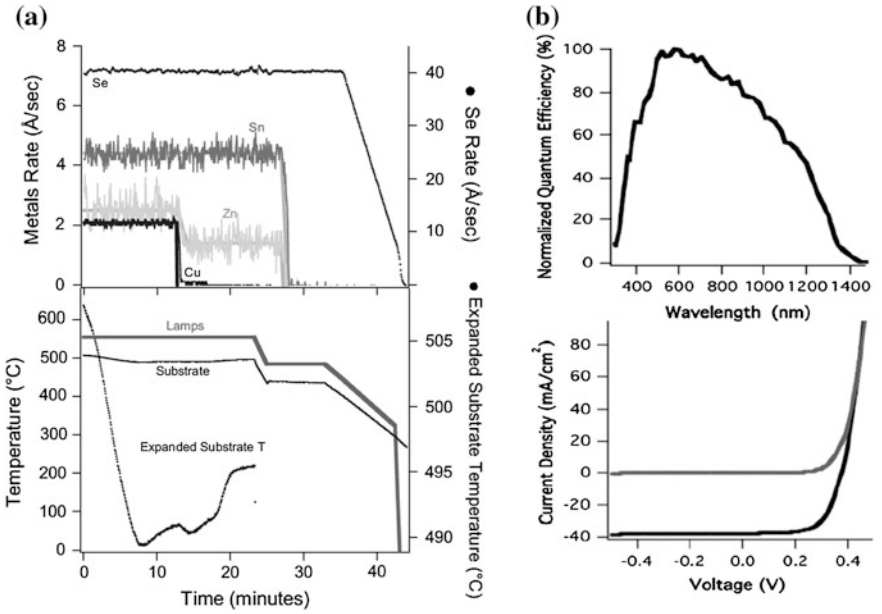

Fig. 2.15 **a** Deposition rate of source materials (*top*) and substrate temperature profile (*bottom*); **b** external quantum efficiency (*top*) and the illuminated *J–V* characteristic of the CZTSe device with 9.15 % efficiency (*bottom*) [14]

The film composition was slightly Zn-rich and Cu-poor and was found to be uniform throughout the bulk with a Cu-poor surface. Void-free, large 0.5–1.0-μm columnar grains with faceted surfaces extending the entire absorber thickness were observed. Single-phase kesterite CZTSe without any secondary phases were detected by XRD and Raman measurements. The best solar cell with $\sim$0.42 cm^2 total area exhibited V_{OC} = 377 mV, J_{SC} = 37.4 mA/cm^2, and FF = 64.9 %, yielding an efficiency of 9.15 % (Fig. 2.15b).

A high diode ideality factor of 1.8 and lower V_{OC} indicated dominant recombination in the device which was further confirmed by small carrier lifetime of 1–2 ns calculated from TRPL measurements. Notably, unlike the high-efficiency CZTS device reported by Wang et al. [17], no evidence of a blocking back contact was observed for the solar cells obtained in this process. Therefore, it can be concluded that formation of such blocking barrier is dependent on the particular deposition process and not an intrinsic issue related to the kesterite material system.

Controlling the deposition parameters play key role to obtain single-phase kesterite compound. Even a small presence of secondary phases could be highly detrimental to the resulting photovoltaic performance and by choosing the right deposition parameters, the undesired secondary Sn chalcogenides can be avoided in the resulting film [95]. XRD data showed that binary Sn chalcogenides can easily form at lower deposition temperature or if the Sn flux is continued below 450 °C during cooling down of the substrate. Similarly, control of Cu flux and Zn flux is

also important to obtain the absorber layer without binary Cu/Zn chalcogenides which can severely limit the solar cell performance.

A multistage evaporation technique was experimented by Weber et al. [96] to fabricate CZTS thin film absorber. Two different batches of samples were produced. In the first one, Cu–Sn–S (CTS) precursor was reacted with ZnS, and in the second one, ZnS precursor was reacted with Cu–Sn–S phase to promote CZTS growth. Both types of samples showed kesterite-type structure. Densely packed larger grains were observed for the second sample, and the highest efficiency of 1.1 % (V_{OC} = 436 mV, J_{SC} = 6.0 mA/cm^2, and FF = 41 %) was achieved for this batch compared to the 0.7 % efficiency (V_{OC} = 501 mV, J_{SC} = 4.2 mA/cm^2, and FF = 35 %) obtained from the first batch of samples with CTS precursor.

2.7.1.2 Sputtering

Sputtering is another well-established high-vacuum deposition technique widely used in the semiconductor industry to fabricate high-quality thin film devices. Different variations of sputtering technologies have been investigated to prepare CZTS(Se) thin film absorber materials including argon beam sputtering, DC/RF magnetron sputtering, and hybrid and reactive sputtering [68, 71, 99–108]. Similar to evaporation, CZTS(Se) film fabrication approach by sputtering techniques also could be subclassified into one-step or two-step processes.

Historically, the first report on the preparation and characterization of CZTS thin films made by Ito and Nakazawa in 1988 [71] employed sputtering technique. The absorber layer was deposited on Corning 7059 glass substrates at different temperatures by atom beam sputtering of quaternary target material synthesized by heating elemental powders to 1050 °C in a vacuum-sealed quartz ampoule. The deposited polycrystalline films showed a strong diffraction peak from (112) plane at substrate temperature higher than 90 °C, and the authors have suggested the crystal structure to be stannite type. An increase of the grain sizes and decrease of resistivity were observed for the films deposited at higher substrate temperatures due to the higher mobility of sputtered particles. A direct bandgap of 1.45 eV was measured for the film deposited at substrate temperature of 120 °C, and the absorption coefficient was in the range of 10^4 cm^{-1}. Photovoltaic cells were fabricated on CZTS films deposited on stainless steel substrate at 160 °C. The heterodiode formed by the deposition of cadmium tin oxide window layer on CZTS absorber showed an open-circuit voltage of 165 mV. Shortly after, they improved the V_{OC} to 265 mV with a short-circuit current density of 0.1 mA/cm^2 by atmospheric annealing of the deposited film [103].

In 2003, Seol et al. [105] reported on CZTS thin films prepared by RF magnetron sputtering at room temperature using a cold-pressed target made of Cu_2S, ZnS, and SnS_2 powders. The as-deposited films were sulfur-deficient and were subsequently annealed under Ar + S(g) atmosphere at 250–400 °C for 2 h to improve the S content. The ratio of Cu_2S, ZnS, and SnS_2 was kept at 2:1.5:1 and the RF power between 50 and 100 W to obtain a stoichiometric CZTS film after

sulfurization. The films became Sn-rich and Cu-deficient as the RF power was increased over 100 W. XRD results showed strong diffraction peaks corresponding to (112), (200), (220), and (312) planes with a preferential orientation along (112) and showed improved crystallinity at higher annealing temperatures. The crystal structure was identified as kesterite type and the measured bandgap was 1.51 eV with an optical absorption coefficient of 1×10^4 cm^{-1}.

Tanaka et al. [68] experimented with a hybrid sputtering system equipped with Cu and Sn sputtering sources and Zn and S effusion cells inside a high-vacuum chamber to achieve sequential deposition of Cu/Zn/Sn precursor layer followed by annealing under incident S flux to prepare CZTS films. Sn layer was deposited by DC sputtering, Zn layer by evaporation, and Cu layer was deposited by RF sputtering at different substrate temperatures from 300 to 500 °C. A decrease in film thickness was observed at higher substrate temperatures, which was attributed to reduced sticking coefficient and/or increased density due to improved crystallization. At lower substrate temperature (<350 °C), binary Cu_xS compounds were formed as identified from XRD analysis. Formation of stannite CZTS compound along with binary Cu sulfides started above 350 °C as evidenced by the evolution of CZTS (112) peak in the diffraction pattern. At 400 °C, single-phase stoichiometric CZTS film was obtained without the presence of any significant secondary phases. Above 450 °C, films were Zn-poor due to high vapor pressure of Zn, resulting in substantial Zn loss. Replacing Zn by ZnS or by introducing S flux during Zn deposition to form zinc sulfide was suggested to mitigate the Zn loss at higher substrate temperatures. The film obtained at 400 °C showed a direct bandgap of 1.5 eV with an optical absorption coefficient $>10^4$ cm^{-1}. The films exhibited p-type conductivity with a carrier concentration of 8×10^{18} cm^{-3}.

In order to avoid the effect of moisture adsorption from atmosphere during the film fabrication process, Jimbo et al. [109] developed an inline-type vacuum apparatus consisting of two interconnected chambers: one for precursor deposition by RF co-sputtering and the other for sulfurization of the precursor. Cu, ZnS, and SnS targets were co-sputtered to deposit the precursor film. After the precursor layer fabrication, the substrate was transferred to the annealing chamber without breaking the vacuum. Annealing was performed under $N_2 + H_2S$ (20 %) environment at 580 °C for 3 h. The best solar cell showed $V_{OC} = 662$ mV, $I_{SC} = 15.7$ mA/cm^2, and a fill factor of 55 %, leading to 5.74 % conversion efficiency. The composition of the CZTS absorber was found to be slightly Cu-deficient and Zn-rich with compositional ratios of Cu/(Zn + Sn) = 0.87 and Zn/Sn = 1.15, respectively. An external quantum efficiency of 65 % at $\lambda = 480$ nm and bandgap of 1.45 eV were measured.

Later in 2008, the same group of researchers further improved the efficiency by soaking the CZTS absorber in DI water prior to CdS window layer deposition [59].

The metal oxide particles in the film were removed by DI water, resulting in an improved device performance. The stoichiometry of the films was found to be Cu-poor and Zn-rich with elemental composition ratios of Cu/(Zn + Sn) = 0.85, Zn/Sn = 1.25, and S/metal = 1.1, respectively. The champion cell showed an open-circuit voltage of 610 mV, short-circuit current density of 17.9 mA/cm^2, and a fill factor of 62 %, leading to an efficiency of 6.77 % after light soaking for 5 min

under AM 1.5 illumination. This is the highest efficiency cell fabricated by sputtering technique till date. An incident photon to current efficiency (IPCE) of >70 % was observed at ~550 nm. The *J–V* characteristic and the IPCE curve showing the photovoltaic response of the device in the visible spectrum are shown in Fig. 2.16.

Similar to the study of Araki et al. [85], the effect of precursor layers' staking order on the physical properties of resulting CZTS thin films was investigated by Fernandes et al. [104]. CZTS films were prepared with Mo/Zn/Cu/Sn and Mo/Zn/Sn/Cu initial metallic precursor stacking orders deposited by DC magnetron sputtering. Sulfurization of the precursor layer was performed in N_2 + S(g) atmosphere at 525 °C for 10 min. However, contrary to the results obtained by Araki et al., the authors concluded the best precursor order to be Mo/Zn/Sn/Cu. It was argued that top Cu layer helped to reduce the Zn and Sn loss during the annealing process, leading to a better composition. Binary Cu_xS was detected on the film surface which was subsequently removed by KCN etching. The resulting films had a kesterite structure as confirmed by Raman spectroscopy. A sharp absorption edge at 1.43 eV and a carrier concentration of 3.3×10^{18} cm^{-3} were measured.

Yoo et al. [107] studied the influence of Cu-rich, Cu-correct, and Cu-poor precursor on the structural and morphological properties of CZTS films. Stacked Cu, Zn, and Sn elemental precursor layers with different Cu content and various stacking sequences were prepared by RF magnetron sputtering and sulfurized at 570 °C under S vapor. Cu_xS phase was observed in the films with precursors containing excess Cu and stoichiometric amount of Cu, but was free from such impurity phases in films produced from Cu-poor precursor. Also, a smoother morphology was obtained for the Cu-poor films.

Liu et al. [108] have reported on a single-step CZTS film fabrication approach by DC reactive sputtering. A Cu–Zn–Sn alloy target with stoichiometric Cu:Zn:Sn molar ratio of 2:1:1 and 98 % H_2S was used as the reactive gas for sputtering. The substrate was held at 500 °C during the film deposition. As-prepared films showed a preferential orientation along (112) plane with densely packed columnar grains. However, undesired secondary phases such as $Cu_{2-x}S$ and Cu_3SnS_4 were detected

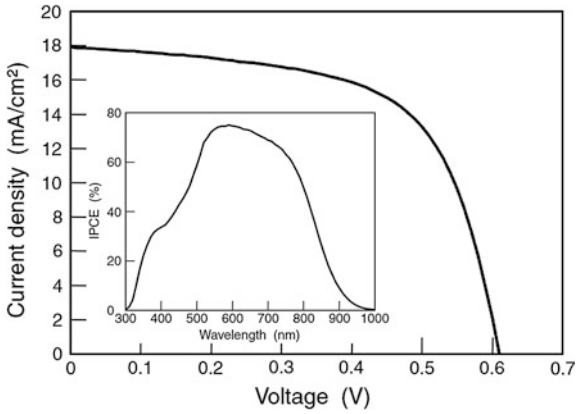

Fig. 2.16 *J–V* characteristics of the CZTS cell with 6.77 % efficiency prepared by co-sputtering and (*inset*) IPCE curve of the corresponding device [59]

in the film alongside CZTS. The films exhibited p-type conductivity with a carrier concentration of 2.2×10^{18} cm^{-3}.

Momose et al. [101] reported on a CZTS solar cell with 3.7 % device efficiency prepared by co-sputtering of elemental metal precursors from a single target followed by sulfurization. The target was constructed by placing Zn and Sn plates on a Cu disk, exposing the top surfaces of each metal according to the required stoichiometry. The best cell was obtained by sulfurization of the deposited precursor for 7 min at 590 °C under 1.5 atmospheric pressure of S vapor. A V_{OC} of 425 mV, J_{SC} = 16.5 mA/cm^2, and a fill factor of 53 % were recorded for the best performing cell with a SLG/MO/CZTS/CdS/In_2O_3 device configuration. The absorber layer of the corresponding device showed a Cu-poor and Zn-rich composition with Cu/(Zn + Sn) = 0.89 and Zn/Sn = 1.15. Chalapathy et al. [99] used DC sputtering to deposit Cu/ZnSn/Cu stacked layer on Mo-coated SLG substrate at room temperature and subsequent 30 min sulfurization at 560 °C and 580 °C under S vapor to grow CZTS absorber layer. The atomic concentration of the ZnSn target was kept at Zn:Sn = 60:40. The completed device with a SLG/Mo/CZTS/CdS/i-ZnO/Al:ZnO/Al configuration prepared on the CZTS film fabricated at 560 °C showed a conversion efficiency of 4.59 % (V_{OC} = 545 mV, J_{SC} = 15.44 mA/cm^2, and FF = 54.6 %). A quantum efficiency of 65 % at λ = 520 nm and an optical bandgap of 1.46 eV were reported. In situ XRD and Raman data were collected during the annealing ramp-up cycle at different temperatures to understand the growth mechanism. Below 470 °C, only binary metal sulfides ($Cu_{2-x}S$, ZnS, and SnS_2) were observed. Kesterite CZTS compound was found to form at 470 °C. At 560 °C and 580 °C sharp CZTS peaks were observed in Raman spectra. However, small amount of $Cu_{2-x}S$ still exists which disappeared after 30-min annealing. Contrary to the other reports of high-efficiency CZTS(Se) solar cells, the absorber film composition in this study was highly Cu-depleted and excess in zinc. The corresponding elemental ratios were measured to be 0.67 and 1.45 for Cu/(Zn + Sn) and Zn/Sn, respectively. One important structural feature observed in the best absorber film in this study was the presence of a bilayer grain distribution with dense small grain microstructure near the Mo back contact and grooved larger grains on the top, similar to the observation made by Shin et al. [84] for the CZTS solar cell with 8.4 % efficiency.

Katagiri et al. [106] employed RF co-sputtering to fabricate CZTS thin films using Cu, ZnS, and Sn/SnS targets. The influence of the film composition was directly correlated with the photovoltaic performance of the solar cells. The compositional ratios of Cu/(Zn + Sn) and Zn/Sn were varied in a wide range from 0.75 to 1.25 and 0.8 to 1.35, respectively. The annealing was performed under N_2 + H_2S environment at 580 °C for 3 h with different H_2S concentrations from 5 to 20 %. No significant difference in the film properties were observed between the films annealed at different H_2S concentrations. The device with 5 % H_2S-treated absorber showed an open-circuit voltage, V_{OC} = 612 mV, short-circuit current density, J_{SC} = 10.6 mA/cm^2, and FF = 62.3 %, resulting in an efficiency (η) of 4.1 % compared to V_{OC} = 634 mV, J_{SC} = 9.5 mA/cm^2, FF = 62.7 %, and η = 3.8 % of the device obtained by sulfurization under 20 % H_2S concentration. To study the

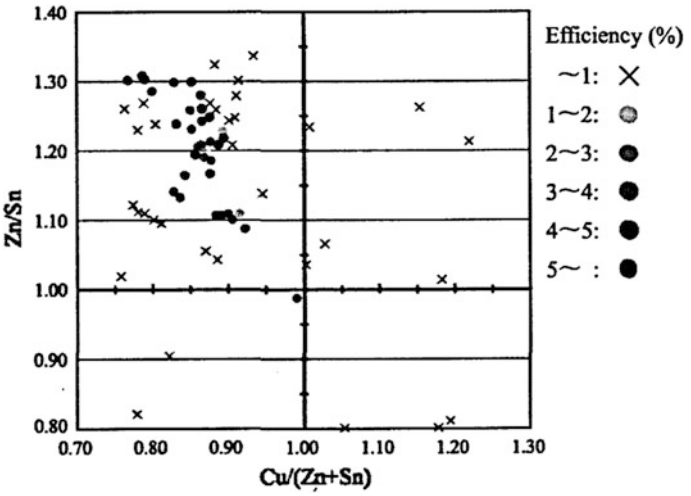

Fig. 2.17 Device efficiency versus composition of the CZTS absorber layer [106]

dependence of photovoltaic performance on the film composition, device efficiency data were plotted against the absorber layer composition, collected from a series of solar cells prepared with varying elemental ratios as shown in Fig. 2.17. Clearly, superior devices lie in a confined space within the composition map in Fig. 2.17, having a Zn/Sn ratio in the range of 1.1–1.3 and a Cu/(Zn + Sn) ratio in the range of 0.8–0.9. This study supports the observation of Cu-poor and Zn-rich stoichiometry evidenced in best performing CZTS-based devices prepared by any deposition technique and suggests the compositional range to obtain high-efficiency cells.

2.7.1.3 Pulsed Laser Deposition (PLD)

Pulsed laser deposition (PLD) is a relatively new method explored for the deposition of high-quality thin films and fabrication of interconnections in integrated circuits. This method offers flexible and controlled deposition of highly crystalline thin films under high vacuum with great reproducibility [110]. The film is deposited by physical ablation of the target material onto a substrate by a high-power pulsed laser radiation, and the film properties can be easily controlled by altering various deposition parameters, such as laser power, pulse rate, duration, distance from the substrate to the target, and substrate temperature. Although PLD has been proved to be a versatile and competent technique to grow different thin film materials, application of this technique for commercial manufacturing of large-area photovoltaic devices is currently limited mainly due to the small deposition area achievable by present laser technology.

In 2006, Sekiguchi et al. [111] have reported on the growth of epitaxial CZTS films on n-type (100)-oriented GaP substrates using pulsed laser deposition. CZTS

target was synthesized by solid-state reaction of equimolar amounts of Cu_2S, ZnS, and SnS_2 powders in a quartz ampoule sintered at 750 °C for 24 h. Deposition was carried out at a constant laser power of 0.85 J/cm^2 using a KrF laser source with varying substrate temperatures from 300 to 400 °C. Structural, compositional, and optical properties of the as-deposited films were reported. X-ray diffraction peaks corresponding to reflections from CZTS (112), (020)/(004), and (040)/(008) planes were observed. Films were found to be slightly S-deficient with nearly stoichiometric metal composition. Best crystallinity was obtained for the film deposited at 400 °C substrate temperature showing a bandgap of 1.5 eV.

Photovoltaic cells employing PLD technique for absorber layer deposition were first reported by Moriya et al. in 2007 [112]. The target CZTS pellet was synthesized by adopting the similar recipe used by Sekiguchi et al. [111]. KrF excimer laser (248 nm) with 1.5 J/cm^2 energy density and 10 ns pulse width at a repetition rate of 30 Hz was used for the deposition. CZTS film was deposited onto Mo-coated SLG substrate at room temperature and subsequently annealed under inert N_2 ambient at 300–500 °C for 1 h. The films annealed at 500 °C exhibited improved crystallinity with strong (112) orientation. XRD peaks corresponding to (112), (200), (220), and (312) planes of CZTS were identified. Contrary to the widely reported Cu-poor and Zn-rich stoichiometry for PV-grade CZTS films, all films under this study showed Cu-poor, Sn-rich, and S-poor stoichiometry with elemental ratios of Zn/Sn = 0.86, Cu/(Zn + Sn) = 0.73, and S/metal = 0.92 for the film annealed at 500 °C. The best device was obtained from the film annealed at 500 °C. The resulting solar cell showed V_{OC} = 546 mV, J_{SC} = 6.78 mA/cm^2, and FF = 48 %, leading to a conversion efficiency of 1.74 %.

Later in 2008, the same group of researchers changed the annealing environment from N_2 to N_2 + H_2S (5 %) in order to improve the S content of the CZTS films [113]. Also, the laser power was varied from 0.7 to 1.5 J/cm^2 to optimize the ablation process. Films deposited at 1.5 J/cm^2 incident laser power showed formation of Cu–Sn–S grains on the film surface, while a smoother and better quality film was obtained at 0.7 J/cm^2 incident laser power. As a result of annealing in the presence of H_2S, the films became nearly stoichiometric. However, the cell performance was inferior compared to the earlier report [112]. The best solar cell efficiency of 0.64 % was reported with V_{OC} of 336 mV, J_{SC} = 6.53 mA/cm^2, and a fill factor of 46 %.

The influence of incident laser power on the resulting CZTS film properties was further studied in detail by Pawar et al. [114]. The density of laser energy was varied from 1.0 to 3.0 J/cm^2, and corresponding structural, morphological, and optical properties of the films were investigated. Preparation of CZTS target was similar to that of the earlier reports by Moriya et al. [113]. A KrF excimer laser source (248 nm) operated at 25 ns pulse width at a frequency of 10 Hz was used to deposit CZTS thin films on glass substrates. As-deposited films were annealed under N_2 + H_2S (5 %) ambient at 400 °C for 1 h. Structural, morphological, and optical properties of the as-deposited films improved with increased laser power up to 2.5 J/cm^2, but degraded at higher energy density of 3.0 J/cm^2. Improvement of crystallinity was evidenced from the evolution of larger diffraction peak intensity

with increasing power till 2.5 J/cm^2, which slightly decreased at 3.0 J/cm^2. A consistent enhancement of grain size and a decrease in optical bandgap were observed with higher laser energy. However, the bandgap increased slightly when the laser power increased beyond 2.5 J/cm^2.

Influence of the substrate temperature on the resulting film properties was carried out by Sun et al. [115]. Only the substrate temperature (T_{sub}) was varied from 300 to 450 °C without changing other deposition parameters. As-deposited films were characterized for structural, optical, and compositional analysis. All CZTS films showed kesterite structure with strong (112) orientation and had a Cu-rich and S-deficient composition. At lower temperatures, isolated island-like crystallites were formed, whereas larger clusters were formed at higher temperature due to higher surface mobility leading to coalescence of islanded structures. Raman spectroscopy showed formation of $Cu_{2-x}S$ compound at 350 and 400 °C, which disappeared at higher deposition temperature. A gradual decrease of the bandgap from 1.98 to 1.53 eV was observed with increasing T_{sub}. From XRD and Raman analysis, the authors suggested existence of internal compressive strain in the as-deposited films.

The research group of Moholkar et al. [116–118] made consistent progress over last few years on the development of CZTS solar cells made by PLD technique. Without altering the device architecture and the target synthesis recipe, a gradual improvement of efficiency was achieved by optimization of the absorber layer properties and the deposition process parameters. In 2011, they studied the influence of pulse frequency on the film properties and a conversion efficiency of 2.02 % was reported [117]. The pulse repetition rate was modulated from 2 to 20 Hz with a constant laser power of 1.5 J/cm^2. As-deposited films were annealed in $N_2 + H_2S$ (5 %) at 400 °C for 1 h. Annealed films showed improved crystallinity with increasing pulse rate with strong (112) orientation. Thickness of the deposited films also increases up to 18 Hz, but noticed to fall at 20 Hz. Composition of the annealed films deposited at 10 Hz pulse frequency was nearly stoichiometric with Cu:Zn:Sn:S = 2.04:0.8:1.0:4.16. The optical bandgap of the films after annealing was in the range of 1.5–1.8 eV. Solar cell with a glass/Mo/CZTS/CdS/Al:ZnO/Al device structure fabricated with the absorber layer deposited at 10 Hz exhibited V_{OC} = 585 mV, J_{SC} = 6.74 mA/cm^2, and a fill factor of 51 %, resulting in an efficiency of 2.02 %. A maximum 32 % quantum efficiency was recorded at λ = 530 nm.

In the same year, an enhanced efficiency of 3.14 % was reported for pulsed laser deposited CZTS solar cells [116]. CZTS absorber film deposition was carried out at a fixed laser power of 2.5 J/cm^2 pulsed at 10 Hz with varying deposition time from 5 to 45 min. The best device prepared with an absorber layer thickness of $\sim$2.9 μm obtained by 30 min of deposition followed by 1 h of annealing at 400 °C under 5 % H_2S showed V_{OC} = 651 mV, J_{SC} = 8.76 mA/cm^2, and FF = 55 %, yielding an efficiency of 3.14 %. An optical bandgap of 1.54 eV for the absorber and a peak quantum efficiency of 34 % at 530 nm were measured for the respective device.

In 2012, the photoconversion efficiency was further improved to 4.13 % by optimization of chemical composition of the deposited CZTS films [118]. So far, it

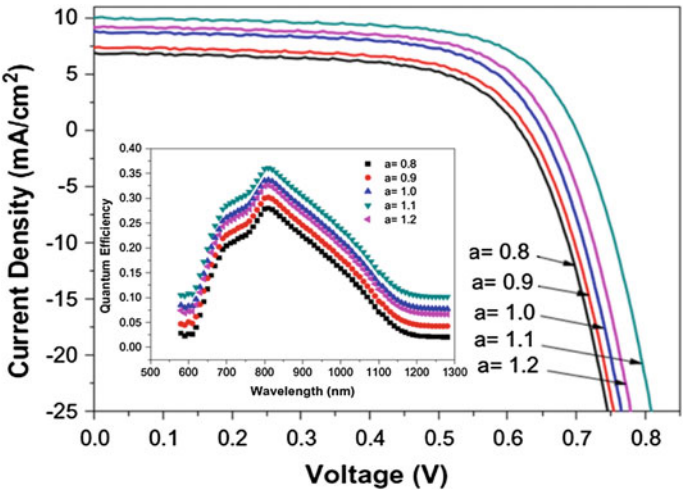

Fig. 2.18 *J–V* characteristics of the CZTS solar cells obtained by PLD technique deposited with various target compositions of a = Cu/(Zn + Sn) = 0.8–1.2 and (*inset*) the quantum efficiency curves of the respective devices [118]

is the highest efficiency CZTS-based device obtained by PLD technique. The composition ratio of Cu/(Zn + Sn) in the target material was varied from 0.8 to 1.2, keeping a constant Zn/Sn ratio. The *J–V* characteristics of the best devices obtained from CZTS films deposited using different chemical composition of the target are shown in Fig. 2.18, where "a" denotes the Cu/(Zn + Sn) ratio of the target material.

It was found that the chemical composition of the deposited films can be gradually varied by changing the composition of the target. Crystallinity of the films was improved and larger grains were obtained by increasing Cu/(Zn + Sn) ratio from 0.8 to 1.1, indicating promotion of grain growth under Cu-rich and Zn-poor condition. However, structural and morphological degradation is observed for higher Cu/(Zn + Sn) ratio of 1.2. The absorber layer thickness was found to increase with increasing Cu/(Zn + Sn) ratio up to 1.1. Bandgap (E_g) of the films shifted to lower energy, changing from 1.79 to 1.53 eV for increased Cu/(Zn + Sn) from 0.8 to 1.2. The champion cell obtained from a target composition of Cu/(Zn + Sn) = 1.1 corresponding to the absorber with E_g = 1.54 eV showed V_{OC} = 700 mV, J_{SC} = 10.01 mA/cm^2, FF = 0.59, and η = 4.13 %. The maximum quantum efficiency of the champion cell was measured to be 36 % at 810 nm.

2.7.2 Non-vacuum Deposition Methods

The PVD technique is expensive and challenging to scale up because of film non-uniformity and low material utilization. Sputtering techniques are suitable for large-area deposition; however, they require expensive vacuum equipment and

sputtering targets. The PLD technique is also very expensive and has not demonstrated high-efficiency devices yet. Some of the many disadvantages of vacuum technology are complicated instrumentation, materials waste, high cost per surface area of deposition, and instability of some compounds at the high deposition temperature. Recently, the record efficiency of 11.1 %-CZTS(Se) thin film solar cell has been achieved by a non-vacuum hybrid solution-particle processing technique developed by IBM [24]. In the past decade, various non-vacuum deposition techniques have been investigated to prepare CZTS-based solar absorbers and photovoltaic solar cell fabrication including electrochemical deposition, hybrid solution-particle processing, nanoparticle-based synthesis, sol–gel spin coating, spray pyrolysis, chemical bath deposition (CBD), open-atmosphere chemical vapor deposition (OACVD), successive ion layer adsorption and reaction (SILAR), and screen printing. In this section, different non-vacuum approaches for CZTS(Se) absorber fabrication are discussed.

2.7.2.1 Nanocrystal-Based Approach

Recent developments of semiconductor nanoparticle synthesis have opened up new opportunities to fabricate thin films using the nanocrystals and construct solar cells with novel device architecture. Owing to tunable optoelectronic properties and easy composition control capability, nanocrystal-based approach for solar absorber fabrication is an attractive choice. In recent years, a significant research effort has been dedicated for the synthesis of I–III–VI_2 nanocrystals for photovoltaic applications [119–122].

In 2009, three individual research groups reported on the synthesis of CZTS nanocrystals, out of which two reported on solar cell properties, prepared using the nanocrystals [123–125]. All of these reports investigated solution-based colloidal hot-injection method for nanocrystal synthesis.

Riha et al. [125] synthesized homogeneous, nearly monodisperse CZTS nanocrystals and characterized their structural, compositional, and optical properties. Stoichiometric amounts of metal salts (copper(II) acetylacetonate, zinc acetate, and tin(IV) acetate) dissolved in oleylamine and elemental sulfur powder separately mixed in oleylamine were used as precursor solutions. Both precursors were quickly injected into trioctylphosphine oxide (TOPO) solution heated to 300 °C, initiating the nucleation and growth of CZTS nanocrystals. As-synthesized triangular and round-shaped nanocrystals were stoichiometric in composition and showed single-crystalline tetragonal structure with an average diameter of 12.8 ± 1.8 nm. Diffraction spots corresponding to (112), (200), (220), (312), (008), and (332) planes of kesterite CZTS phase were identified from selected-area electron diffraction (SAED) pattern. Phase purity of the nanocrystals was further confirmed by differential thermal analysis (DTA). The CZTS nanocrystals exhibited an optical bandgap of 1.5 eV.

Sheinhagen et al. [123] reported photovoltaic properties of devices prepared using CZTS nanocrystals synthesized by arrested precipitation at high temperature.

Copper acetylacetonate, zinc acetate, tin chloride dihydrate, and elemental sulfur were used as precursor materials. Oleylamine was solely used as the coordinating solvent for the precursors. Nanocrystal growth was carried out for 1 h under an inert atmosphere at elevated precursor solution temperature of 280°C. As-synthesized irregular-shaped CZTS nanocrystals had an average particle size of 10.6 ± 2.9 nm with slightly Sn-rich and S-poor stoichiometry. An optical bandgap of 1.3 eV was estimated and powder XRD pattern revealed characteristic peaks of kesterite CZTS structure. TEM and SEM micrographs of the as-prepared CZTS nanocrystals are shown in Fig. 2.19. The nanocrystals dispersed in toluene were used as an ink to deposit CZTS absorber layer by spray coating. A solar cell fabricated with SLG/Au/CZTS/CdS/ZnO/ITO configuration exhibited an open-circuit voltage, V_{OC} = 321 mV, short-circuit current density, J_{SC} = 1.95 mA/cm^2, and a fill factor of 37 %, yielding an efficiency of 0.23 %.

Guo et al. [124] fabricated CZTSSe solar cells by drop-casting of CZTS nanocrystals prepared by a hot-injection method followed by selenization of the films under Se vapor. Copper(II) acetylacetonate, zinc acetylacetonate, tin(IV) bis (acetylacetonate) dibromide, and elemental sulfur at 2:1:1:4 molar ratios were used as precursors and oleylamine as the solvent for nanocrystal synthesis. The growth reaction was initiated by swift injection of the sulfur solution into the mixed metal precursor solution at 225 °C, and the reaction was continued for 30 min. As-grown nanocrystals were purified by successive precipitation and decantation using organic solvents. Absorber film was fabricated by drop-casting of the CZTS nanocrystal ink on Mo-coated SLG substrate forming ~0.75 μm thick film. A thicker film was obtained by repeating the drop-casting process two times and

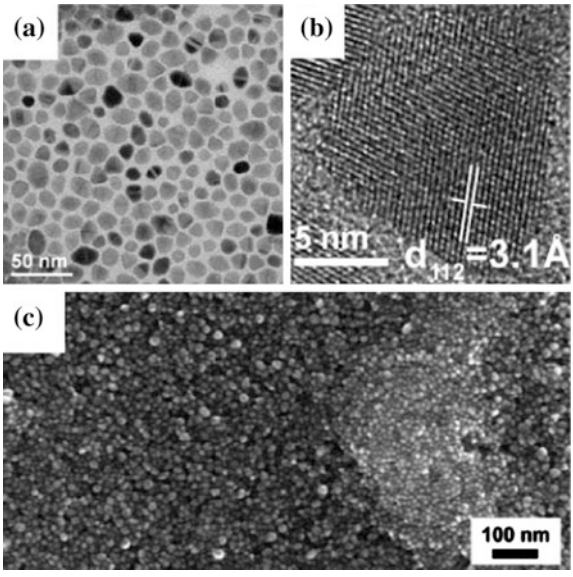

Fig. 2.19 **a** TEM image of the as-synthesized CZTS nanocrystals, **b** high-resolution TEM image of a single nanocrystal, and **c** SEM image of the dispersed CZTS nanocrystals [123]

each layer was annealed under Ar at 350 °C for 1 h, removing any organic ligands attached to the nanocrystal surface. As-prepared CZTS films were further annealed under Se vapor at 400–500 °C to form CZTSSe absorber layer used for final device fabrication. Powder XRD pattern of the as-synthesized CZTS nanocrystals showed a kesterite structure with lattice parameters of a = 5.421 Å and c = 10.816 Å. A Cu-rich and Zn-poor stoichiometry was observed from EDX measurement. The size range of the nanocrystals was between 15 and 25 nm, and the bandgap was measured to be 1.5 eV. Solar cell with a SLG/Mo/$CZTS_xSe_{1-x}$/CdS/i-ZnO/ITO configuration obtained using the CZTS film selenized at 500 °C showed the best power conversion efficiency of 0.74 % with V_{OC} = 210 mV, J_{SC} = 11.5 mA/cm^2, and a fill factor of 33.1 %.

Following the same approach, later in 2010, Guo et al. [18] made a significant improvement of the solar cell performance, reporting 7.23% photoconversion efficiency by optimizing the composition of CZTS nanocrystals.

A Cu-poor and Zn-rich composition of the nanocrystals was achieved by adjusting the amounts of metal salts in the precursor (1.332 mmol, 0.915 mmol, and 0.75 mmol for Cu, Zn, and Sn, respectively) keeping the synthesis methodology essentially same as before [124]. Absorber layer of ~1 μm was deposited on Mo-coated SLG substrate by knife-coating of the nanocrystal ink prepared by dispersion of the purified nanocrystals in hexanethiol. Selenization of the as-deposited CZTS film was carried out in the presence of Se vapor at 500 °C for 20 min, forming CZTSSe film with large, densely packed grains. Selenized films used for cell fabrication exhibited a Cu-poor and Zn-rich stoichiometry with compositional ratios of Cu/(Zn + Sn) = 0.79 and Zn/Sn = 1.11. The best solar cell fabricated with a device configuration of SLG/Mo/$CZTS_xSe_{1-x}$/CdS/i-ZnO/ITO/Ni/Al showed V_{OC} = 420 mV, J_{SC} = 30.4 mA/cm^2, FF = 52.7 %, and a total area efficiency of 6.73 % which was further improved to 7.23 % (V_{OC} = 430 mV, J_{SC} = 31.2 mA/cm^2, FF = 53.9 %) after 15-min light soaking under AM 1.5 G

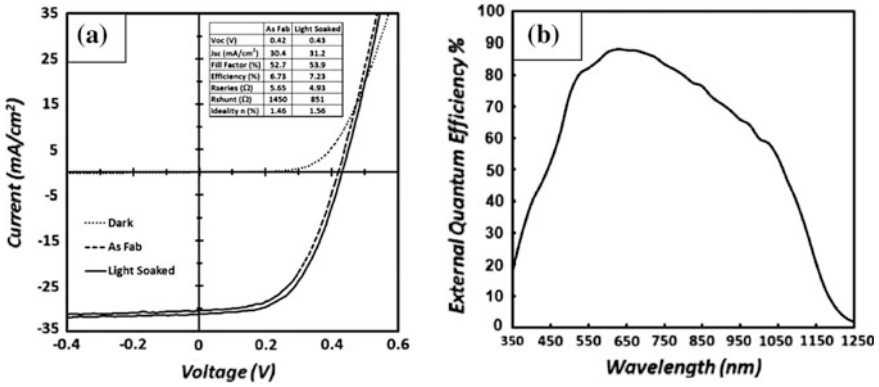

Fig. 2.20 **a** *J–V* characteristics of the best CZTSSe solar cell without and with 15-min light soaking and **b** external quantum efficiency of the corresponding device [18]

illumination (Fig. 2.20). The device showed ~90 % quantum efficiency in the visible spectrum corresponding to a bandgap of 1.05 eV.

The photoconversion efficiency was further improved to 8.5 % by Cao et al. at DuPont [126]. Binary and ternary metal sulfide nanoparticles, such as copper-tin-sulfide (CTS), ZnS, SnS, and Cu_xS_y, were synthesized by reacting metal–oleylamine complexes with sulfur in a solution of oleylamine and TOPO at high temperature (>200 °C). As-synthesized metal chalcogenide nanocrystals mixed with desired proportions and dispersed in hexanethiol were used as the precursor ink for CZTSSe absorber film fabrication by spin coating. This method allowed easy composition control of the final film by changing the ratio of different metal sulfide nanocrystals in the precursor ink. Spin-coated films were annealed under Se vapor at 560 °C for 20 min to form a robust CZTSSe absorber layer. The best solar cell with a device configuration of SLG/Mo/CZTSSe/CdS/i-ZnO/ITO/Ag showed a V_{OC} = 451 mV, J_{SC} = 29.0 mA/cm^2, and FF = 64.9 % and a photoconversion efficiency of 8.5 % without any antireflection coating. The CTS and ZnS nanoparticles used in preparing the precursor ink for absorber layer formation are shown in Fig. 2.21a. Cross-sectional SEM revealed a bilayer microstructure of the CZTSSe absorber comprising of a fine-grained bottom layer near the back contact and the top layer consisting of larger grains (Fig. 2.21b). Similar bimodal structure was observed for high-efficiency solar cells prepared by vacuum-based thermal evaporation and DC sputtering techniques [84, 99]. The carbon-rich nanometer-sized grains in the bottom layer were the incompletely selenized initial precursor film. The micrometer-sized highly crystalline and densely packed larger grains on top were formed as a result of selenization and were carbon free. The elemental composition of the larger grain CZTSSe was estimated to be $Cu_{1.7}Zn_{1.2}SnS_{0.6}Se_{5.0}$. The authors suggested that highly crystalline top layer contributed to high photogeneration of carriers and the bottom carbon-rich layer acted as a low resistive interface to the Mo back contact, resulting in superior device performance. This is the best performing CZTSSe device obtained by nanocrystal-based approach.

Kameyama et al. carried out the hot-injection synthesis at various temperatures to assess the effect of temperature on the growth and crystallization of CZTS

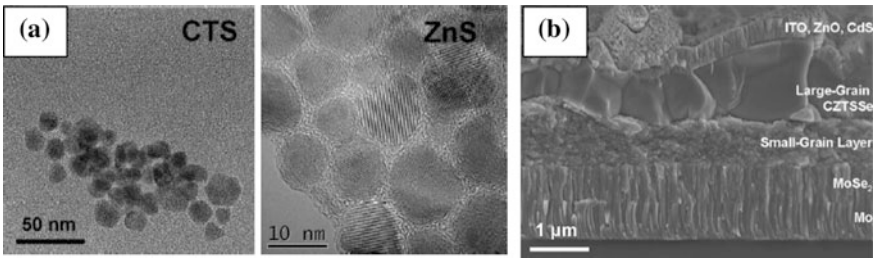

Fig. 2.21 **a** TEM images of the as-synthesized copper-tin-sulfide and ZnS nanocrystals and **b** cross-sectional SEM image of the completed device structure [126]

nanocrystals. Metal acetate salts and elemental sulfur in oleylamine were used as the precursors [127]. At growth temperature below 180 °C, secondary CuS phase was detected, whereas pure CZTS nanocrystals were formed at temperature above 240 °C. Contrary to the general growth statistics observed for semiconductor nanocrystals grown in colloidal solution, size of the nanocrystals under this study was found to decrease at increased reaction temperature with average particle diameter of ~6.6 ± 1.5 nm at 120 °C, 6.6 ± 1.3 nm at 180 °C, 5.6 ± 1.2 nm at 240 °C, and 5.1 ± 1.2 nm at 300 °C. Photoelectrochemical characterization of immobilized layer-by-layer deposited CZTS nanocrystals on ITO-coated glass exhibited p-type nature. Comparable to the bulk counterpart, a bandgap of 1.5 eV was estimated for the as-prepared nanocrystals showing no quantum confinement effect. The conduction band edge (E_{CB}) and the valence band edge (E_{VB}) potentials of the CZTS nanocrystals were estimated to lie at +0.3 and −1.2 eV, measured against a saturated Ag/AgCl electrode.

Riha et al. [128] fabricated a CZTS-based photoelectrochemical cell following the hot-injection synthesis technique reported earlier. Stoichiometric and Zn-rich CZTS thin films were prepared by dip coating the FTO substrates in respective nanocrystal solutions. As-deposited films were annealed in Ar atmosphere at 350 °C for 1.5 h. A redox electrolyte containing Eu^{3+} was used for the cell fabrication. Incident photon to current efficiency (IPCE) of 1.8 and 2.8 % at 500 nm was recorded for the as-deposited films prepared from stoichiometric and Zn-rich nanoparticles, respectively, which were further improved to 3.1 and 10.1 % after annealing.

Shavel et al. [129] prepared CZTSe ($Cu_2Zn_xSn_ySe_{1+x+2y}$) nanocrystals for the first time via hot-injection colloidal synthetic route by reacting amine complexes of the metal salts with elemental Se in trioctylphosphine (TOP). The synthesized nanocrystals were nearly monodisperse with an average particle size of 20 ± 2 nm, showing highly faceted polyhedral geometries (Fig. 2.22a). X-ray diffraction analysis revealed a tetragonal stannite structure ($I\bar{4}2m$) and compositional analysis

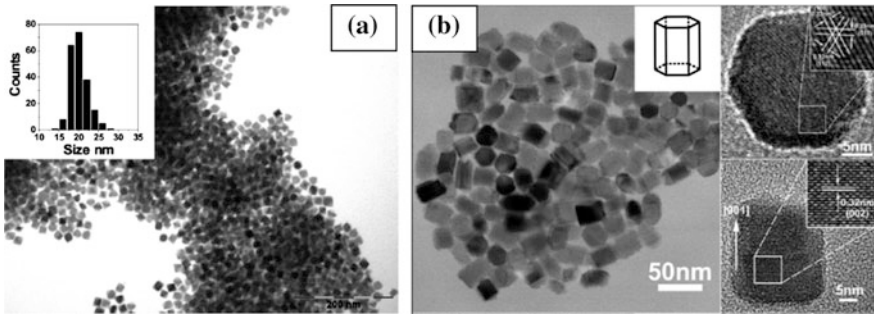

Fig. 2.22 **a** TEM image of stannite CZTSe nanocrystals grown via hot-injection method at 295 °C for 5 min [129]; **b** TEM and HRTEM images of wurtzite CZTS nanocrystals prepared in dodecanethiol and oleylamine [130]

showed a homogeneous elemental distribution with Zn-poor and Sn-poor stoichiometry.

In general, CZTS has been reported to crystallize in tetragonal kesterite and stannite structures. Lu et al. reported CZTS nanocrystals with a new wurtzite phase, synthesized by a hot-injection method [130]. Metal–thiolate complexes prepared by dissolving metal salts in dodecanethiol were reacted with elemental sulfur in oleylamine or oleic acid at 240 °C for 1 h to grow the CZTS nanocrystals. The authors implied that dodecanethiol plays a key role in balancing the reactivities of different cations in the reaction mixture and promoted wurtzite phase CZTS growth. The new wurtzite phase CZTS nanocrystals showed a highly crystalline hexagonal structure (Fig. 2.22b), and the bandgap was measured to be 1.4 eV.

Dai et al. [131] investigated a solvothermal route for the synthesis of compositionally tunable $(Cu_2Sn)_{x/3}Zn_{1-x}S$ ($0 \le x \le 0.75$) nanocrystals. The obtained nanocrystals showed a sphalerite structure with tunable bandgap from 3.48 to 1.23 eV. As-prepared CZTS nanocrystals with a chemical composition of $(Cu_2Sn)_{0.01}Zn_{0.97}S$ were used as the photoactive agent in a quantum dot-sensitized solar cell structure. An open-circuit voltage, V_{OC} = 283 mV, a short-circuit current density, J_{SC} = 0.36 mA/cm^2, a fill factor of 28.6 %, and a photoconversion efficiency of 0.03 % were reported.

Cao et al. [132] also investigated a solvothermal method to synthesize CZTS nanocrystals. $CuCl_2$, $(CH_3CO_2)_2Zn$, $SnCl_4$, and sulfur were autoclaved in ethylenediamine at 180 °C for 15 h to obtain CZTS nanocrystals with 5–10 nm diameter. As-synthesized nanocrystals showed a bandgap of 1.5 eV with slightly Cu-poor, Sn-rich, and S-deficient composition. However, wurtzite ZnS phase was detected along with kesterite CZTS crystals which was removed by annealing the nanocrystal thin film under Ar + H_2S (5 %) atmosphere at 550 °C for 1 h, resulting in improved crystallinity.

Single-crystalline CZTS and CZTSe nanowires have been fabricated by Shi et al. [133] using an anodic aluminum oxide (AAO) template. AAO templates (200 nm pore diameter) were immersed in the precursor solution containing metal chloride salts and sulfur/selenium in anhydrous ethylenediamine and successively autoclaved at 230 °C for 70 h to grow the nanowires. Highly ordered template-directed several micrometer-long nanowires were obtained with predominant growth direction along [110, 111] (Fig. 2.23). As-grown CZTS nanocrystals showed kesterite structure with a near-stoichiometric composition ratio of Cn:Zn:Sn:S = 2.2:0.9:0.8:4.1. An optical bandgap of ~1.5 eV for CZTS and ~1.3 eV for CZTSe nanowires was determined. This investigation showed possibility of designing and fabrication of three-dimensional CZTS solar cells using nanowires. However, CZTS nanowire-based photovoltaic device has not been reported.

2.7.2.2 Processing of Hydrazine-Based Solution-Particle

At IBM, Todorov et al. [134] developed a hydrazine-based hybrid solution-particle processing technique for CZTS(Se) film fabrication. A hybrid solution-particle

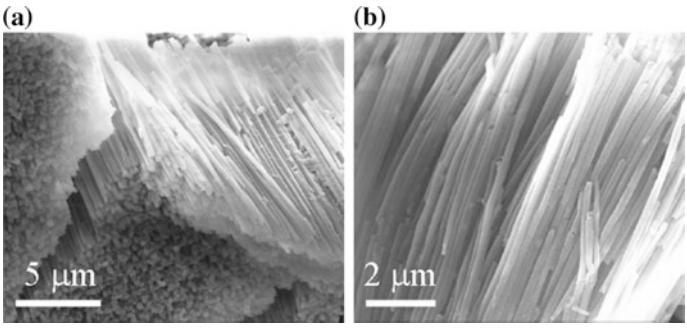

Fig. 2.23 SEM micrographs of the as-prepared CZTS nanowires: **a** Top view and **b** side view after etching the AAO template using NaOH [133]

slurry containing copper-tin-chalcogenide mixed in hydrazine and $ZnSe(N_2H_4)$ or $ZnS(N_2H_4)$ was deposited layer by layer via spin coating and successively annealed at 540 °C to form the absorber layer. By varying the amount of chalcogens, highly Se-rich, mixed sulfoselenide, and pure sulfide (Se free) absorbers were prepared.

A Zn-rich and Cu-poor stoichiometry was maintained for the films with the composition ratios of Cu/(Zn + Sn) = 0.8 and Zn/Sn = 1.22, respectively. Final films showed micrometer-scale large grains. High-efficiency device performance was reported for solar cells fabricated from sulfoselenide (S/chalcogen = 0.4) and high Se-content (S/chalcogen = 0.08) absorbers. A remarkable conversion efficiency of 9.66 % was achieved with the sulfoselenide absorber having V_{OC} = 516 mV, J_{SC} = 28.6 mA/cm^2, and FF = 65 %, while the device from Se-rich absorber exhibited a conversion efficiency of 9.30 % with V_{OC} = 412 mV, J_{SC} = 36.4 mA/cm^2, and FF = 62 % (Fig. 2.24a). An optical bandgap of 1.0 eV for Se-rich sample and 1.2 eV for the sulfoselenide sample was estimated from the corresponding IPCE data (Fig. 2.24b).

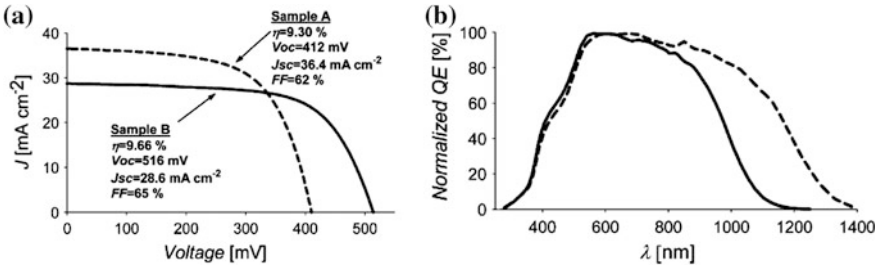

Fig. 2.24 **a** *J–V* characteristics of solar cells prepared from highly Se-rich (sample A) and sulfoselenide (sample B) CZTSSe absorbers and **b** normalized quantum efficiency of the corresponding devices (*dashed line* Se-rich and *straight line* sulfoselenide) [134]

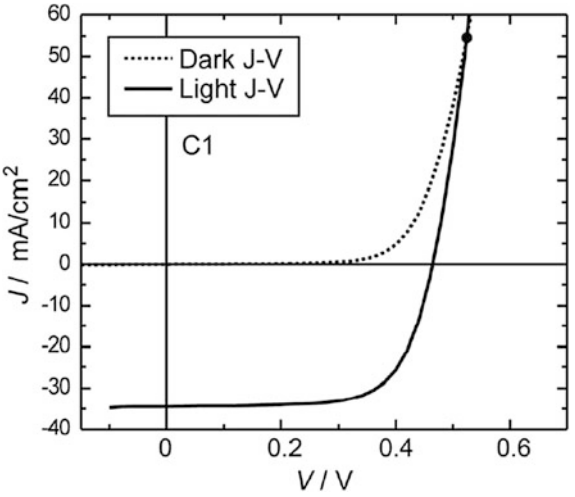

Fig. 2.25 *J–V* characteristics of the benchmark CZTSSe device with 11.1 % efficiency [24]

Shortly after this report, the same group of researchers improved the device efficiency above 10 % following the same approach [135]. The enhanced cell performance was attributed to improved short-circuit current density and fill factor. The best solar cell exhibited an open-circuit voltage, VOC = 517 mV, short-circuit current density, J_{SC} = 6 mA/cm^2, FF =63.7 %, leading to a photoconversion efficiency of 10.1 % corresponding to an absorber bandgap of 1.15 eV.

The benchmark CZTS-based solar cell exceeding 11 % power conversion efficiency was reported by the same group of researchers following the hydrazine-based hybrid solution-particle processing route developed earlier [24]. The enhancement of efficiency was mainly attributed to the improved short-circuit current density and fill factor. CZTSSe films with thickness of 1.5–2.2 μm were fabricated. Larger grains with the dimension of entire absorber layer thickness were observed with a thin (~200 nm) $MoSe_2$ interfacial layer at the Mo back contact. Completed device stack had a glass/Mo/CZTSSe/CdS/ZnO/ITO/Ni–Al structure with 0.45 cm^2 active area. The benchmark device showed a V_{OC} = 459.8 mV, J_{SC} = 34.5 mA/cm^2, and FF = 69.8 %, resulting in an efficiency of 11.1 % under AM 1.5 G illumination with an antireflection coating (Fig. 2.25). This is the maximum power conversion efficiency achieved with kesterite CZTS-based devices inclusive of all deposition methods. Existence of a near-bandgap activation energy indicated that the cell performance was limited by Schottky–Read–Hall (SRH) recombination process occurring within the depletion region. Investigation of the device inhomogeneity within the active area using light beam-induced current (LBIC) measurement showed a minimal 5 % standard deviation of photogenerated current which is ascribed to the inhomogeneity of the absorber layer bandgap across the device.

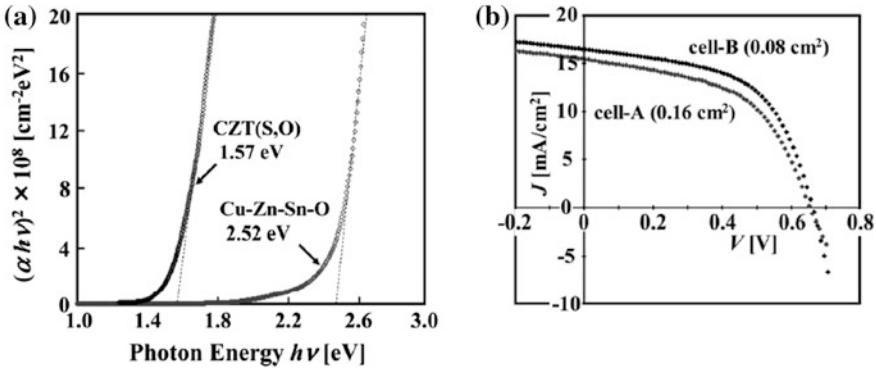

Fig. 2.26 **a** $(\alpha h\nu)^2$ versus hν plot of the as-deposited oxide precursor film and CZTS film after sulfurization and **b** *J–V* characteristics of the champion CZTS solar cells prepared by OACVD technique [136]

2.7.2.3 Open-Atmosphere Chemical Vapor Deposition (OACVD)

An open-atmosphere chemical vapor deposition (OACVD) method for CZTS film fabrication has been reported by Washio et al. [136]. They reported that the CZTS thin film device with an active area of 0.08 cm^2 showed a V_{OC} = 658 mV, J_{SC} = 16.5 mA/cm^2, FF = 55 %, and a power conversion efficiency of 6.03 % under AM 1.5 illumination (Fig. 2.26b).

CZTS thin films were prepared by sulfurization of an oxide precursor layer annealed at 520–560 °C under 5 % H_2S for 3 h. The oxide precursor film deposited by spraying vaporized $Cu(C_5H_7O_2)_2$, $Zn(C_5H_7O_2)_2$, and $Sn(C_5H_7O_2)_2$ sources directly onto Mo-coated SLG substrates held at 250–450 °C using N_2 as the carrier gas. Sulfurized CZTS films showed X-ray diffraction peaks corresponding to kesterite structure. Optical bandgap of the as-deposited oxide precursor film was 2.52 eV and decreased to 1.57 after sulfurization (Fig. 2.26a). Solar cells with a SLG/Mo/CZTS/CdS/Al:ZnO/Al device structure was fabricated. The best photovoltaic performance was obtained by the cell prepared with an absorber composition of Cu/(Zn + Sn) = 0.78 and Zn/Sn = 1.29.

2.7.2.4 Electrodeposition

This section presents the electrodeposition of CZTS(Se) materials. Electroplating is a potentially suitable preparation method to obtain low-cost precursor films. The electrodeposition process could provide (a) high-quality film with very low capital investment; (b) a low-cost, high-rate process; (c) use of very low-cost starting materials (e.g., low-purity salts or solvents), based on automatic purification of the deposited materials during plating; (d) a large-area, continuous, multicomponent, low-temperature deposition method; (e) deposition of films on a variety of shapes

and forms (wires, tapes, coils, and cylinders); (f) controlled deposition rates and effective material use (as high as 98 %); and (g) minimum waste generation (i.e., the solution can be recycled) [137]. The major drawback for electrodeposition is that it requires conductive substrates, which limits the application of this process in several key technologies.

Electrodeposition uses electrolysis to deposit a coating of desired form on conducting substrates from a solution ("bath") containing the ions of interest (e.g., Cu^{2+}, Sn^{2+}, Zn^{2+}). Almost without exception, one of the two phases contributing to an interface of interest in electrodeposition will be an electrolyte, which is a phase through which charge is carried by the movement of ions. The second phase at the boundary is the substrate, through which charge is carried by electronic movement. In cathodic electrodeposition, when the potential of the substrate (electrode) is moved from its equilibrium value toward negative potentials, the cation that will be reduced first is the one with the least negative (or most positive) redox potential E^0. In a solution containing Cu^{2+}, Sn^{2+}, and Zn^{2+}, all three ions can be co-deposited on the surface of the substrate (cathode) when the potential is sufficiently negative. Interestingly, Se also co-deposits with Cu, Sn, and Zn under certain conditions even though it is expected to deposit on the counter electrode (anode). The conditions of electrodeposition of CZTS thin films are related to the individual electrochemical reactions that correspond with the following Nernst equation, leading to the deposition of Cu, Sn, Zn, and Se. In this case, the electrodeposition of CZTS films on the cathode is most probably caused by the combination of electrochemical and chemical reactions as follows:

$$M^{n+} + ne^- \rightarrow M \tag{2.4}$$

$$Cu^{2+} + 2e^- \rightarrow Cu(s) \tag{2.5}$$

$$E = E^0_{Cu} + RT/2F \ln\left[Cu^{2+}\right] = 0.337 + 0.0295 \log\left[Cu^{2+}\right] \tag{2.6}$$

$$Sn^{2+} + 2e^- \rightarrow Sn(s) \tag{2.7}$$

$$E = E^0_{Sn} + RT/2F \ln\left[Sn^{2+}\right] = -0.136 + 0.0295 \log\left[Sn^{2+}\right] \tag{2.8}$$

$$Zn^{2+} + 2e^- \rightarrow Zn(s) \tag{2.9}$$

$$E = E^0_{Zn} + RT/2F \ln\left[Zn^{2+}\right] = -0.763 + 0.0295 \log\left[Zn^{2+}\right] \tag{2.10}$$

$$H_2SeO_3 + 4H^+ + 4e^- \rightarrow Se + 3H_2O \tag{2.11}$$

$$E = 0.741 - 0.0591\ pH + 0.0148 \log[H_2SeO_3] \tag{2.12}$$

$$HSeO_3^- + 5H^+ + 4e^- \rightarrow Se + 3H_2O \tag{2.13}$$

$$E = 0.778 - 0.0739\ \mathrm{pH} + 0.0148\ \log\left[\mathrm{HSeO_3^-}\right] \tag{2.14}$$

$$\mathrm{SeO_3^{2-}} + 6\mathrm{H^+} + 4\mathrm{e^-} \rightarrow \mathrm{Se} + 3\mathrm{H_2O} \tag{2.15}$$

$$E = 0.875 - 0.0886\ \mathrm{pH} + 0.0148\ \log\left[\mathrm{SeO_3^{2-}}\right] \tag{2.16}$$

$$xM + y\mathrm{Se} \rightarrow \mathrm{M}_x\mathrm{Se}_y \tag{2.17}$$

where E is the electrode equilibrium potential with respect to the standard hydrogen electrode (SHE) and E^0_{Cu}, E^0_{Sn}, and E^0_{Zn} are the standard electrode potentials of Cu, Sn, and Zn, respectively. F is Faraday's constant equal to 96,485 Coulomb/mole. Concentration of H^+ is converted to pH scale and shown in the equations. The logarithm of concentrations of different chemical species shifts the electrode equilibrium potential at the specific concentration.

Several research group reported successful electrodeposition of CZTS materials [138–147]. Ennaoui et al. [139] fabricated electrodeposited Cu_2ZnSnS_4 device with 3.4 % efficiency, with a V_{OC} = 0.56 V, J_{SC} = 14.8 mA/cm^2, and FF = 0.41. The absorber layers were prepared by solid-state reaction in H_2S atmosphere of electrodeposited Cu–Zn–Sn precursors. Araki et al. [140] fabricated electrodeposited Cu_2ZnSnS_4 device with 3.16 % efficiency, with a V_{OC} = 0.54 V, J_{SC} = 12.6 mA/cm^2, and FF = 0.46. The absorber layers were prepared by annealing the electrodeposited Cu–Zn–Sn precursors with sulfur in N_2 atmosphere. Farinella et al. [146] reported the fabrication of quaternary Cu_2ZnSnS_4 thin films on flexible ITO substrates supported by polyethylene terephthalate (PET) by co-electrodeposition of all elements from a sulfate solution potentiostatically. Bhattacharya [147] electrodeposited multilayered Cu–Sn–Zn metal films on Mo/glass substrates. Cu and Zn thin films were prepared from aqueous solution, and Sn was prepared from ionic liquid solvent. Cu/Sn/Zn stacked layers were annealed in a tube furnace in elemental sulfur and selenium at 570 °C. The device efficiency of such electrodeposited CZTSS thin film was 3.6 % with a V_{OC} = 0.54 V, J_{SC} = 16.9 mA/cm^2, and FF = 0.40. Higher-performance Cu_2ZnSnS_4 photovoltaic devices were fabricated by Ahmed et al. [138] using stacked electrodeposited Cu/Zn/Sn or Cu/Sn/Zn layers. The stacked layers were first annealed at low temperature (210–350 °C) in an N_2 environment in order to produce homogeneous (Cu, Zn) and (Cu, Sn) alloys and subsequently annealed at 550–590 °C in a sulfur atmosphere for 5–15 min. The electrodeposited device (Fig. 2.27) showed a power conversion efficiency of 7.3 %, with open-circuit voltage (V_{OC} = 567 mV), photocurrent (J_{SC} = 22 mA cm^{-2}), and the fill factor (FF = 58.1 %).

2.7.2.5 Monograin Layer Cell

Recently, a new type of device structure known as monograin layer (MGL) solar cell has emerged as a potential alternative to realize low-cost large-area

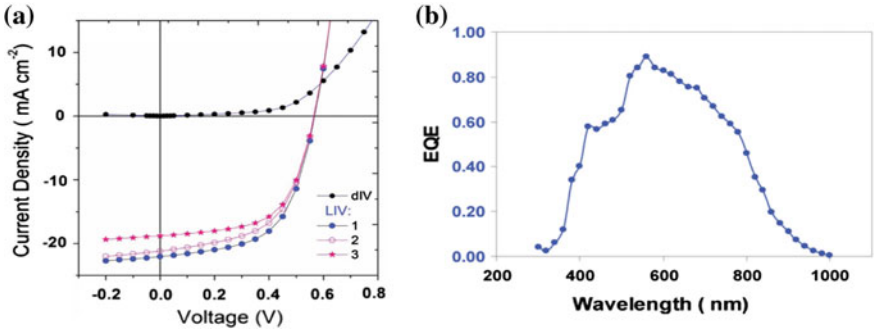

Fig. 2.27 **a** *I–V* characteristics of electrodeposited CZTS solar cell under *dark* (*black*) and 1 sun (lines 1, 2, and 3) illumination for a champion CZTS cell, showing efficiencies of 7.3, 6.74, and 6.86 %, respectively. **b** The quantum efficiency (QE) curve. LIV and dIV mean light and dark current–voltage curve, respectively [138]

photovoltaic devices [83, 148–150]. In this method, monocrystalline granular powders of the absorber material are embedded in an epoxy layer for the absorber layer fabrication. Each monocrystalline particle makes an islanded junction with the top CdS layer to form the effective heterojunction. The schematic of the MGL cell structure is depicted in Fig. 2.28a.

The monocrystalline powders are usually produced by recrystallization of binary chalcogenides: CuS(Se), ZnS(Se), and SnS(Se) in an evacuated quartz ampoule at high temperature. This device structure offers several advantages including simple and low-cost fabrication process and allows the possibility of flexible solar cells to be fabricated without degradation of the absorber layer due to mechanical stress retaining the superior optoelectronic properties of the single-crystalline absorber. Researchers at Tallinn University have pioneered this technology and prepared $Cu_2ZnSn(Se_{1-x}S_x)_4$ solar cells with varying S/Se ratios. The best cell showed an open-circuit voltage of 622 mV, short-circuit current density of 15.87 mA/cm^2, and

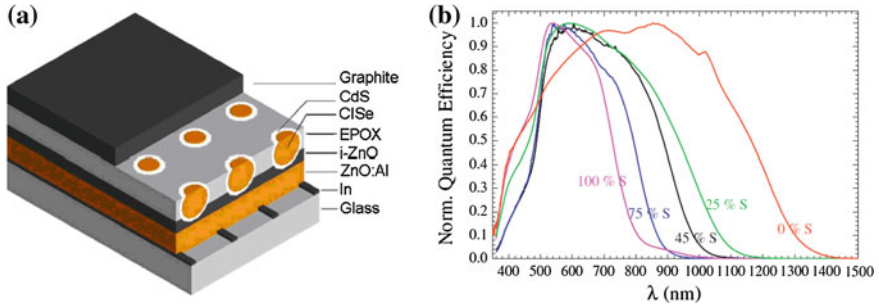

Fig. 2.28 **a** Schematic of a monograin layer (MGL) solar cell structure [149] and **b** quantum efficiencies of MGL cells with varying S/Se ratios [148]

fill factor of 60 %, leading to an efficiency of 5.9 % with absorber layer containing 75 mol% of sulfur and 25 mol% of Se [148]. The quantum efficiencies of solar cells with different S/Se compositions are shown in Fig. 2.28b.

References

1. Green, M.A., Emery, K., Hishikawa, Y., Warta, W., Dunlop, E.D.: Solar cell efficiency tables (version 42). Prog. Photovoltaics Res. Appl. **21**, 827–837 (2013)
2. Green, M.A.: Estimates of Te and In prices from direct mining of known ores. Prog. Photovoltaics Res. Appl. **17**, 347–359 (2009)
3. Tao, C.S., Jiang, J., Tao, M.: Natural resource limitations to terawatt-scale solar cells. Sol. Energy Mater. Sol. Cells **95**, 3176–3180 (2011)
4. Feltrin, A., Freundlich, A.: Material considerations for terawatt level deployment of photovoltaics. Renew. Energy **33**, 180–185 (2008)
5. Zuser, A., Rechberger, H.: Considerations of resource availability in technology development strategies: the case study of photovoltaics. Resour. Conserv. Recycl. **56**, 56–65 (2011)
6. Fthenakis, V.: Sustainability of photovoltaics: the case for thin-film solar cells. Renew. Sustain. Energy Rev. **13**, 2746–2750 (2009)
7. Wadia, C., Alivisatos, A.P., Kammen, D.M.: Materials availability expands the opportunity for large-scale photovoltaics deployment. Environ. Sci. Technol. **43**, 2072–2077 (2009)
8. Candelisea, C., Speirsa, J.F., Grossa, R.J.K.: Materials availability for thin film (TF) PV technologies development: a real concern? Renew. Sustain. Energy Rev. **15**, 4972–4981 (2012)
9. Green, M.A.: Consolidation of thin-film photovoltaic technology: the coming decade of opportunity. Prog. Photovoltaics Res. Appl. **14**, 383–392 (2006)
10. U.S. Department of Energy, *Critical Materials Strategy*, (2010)
11. European Commission, *Critical Raw Materials for the EU*, (2010)
12. O'Neill, B.: Indium market forces, a commercial perspective. In: Photovoltaic specialists conference (PVSC), 35th IEEE, pp. 000556–000559 (2010)
13. Fthenakis, V.M., Moskowitz, P.D.: Thin-film photovoltaic cells: health and environmental issues in their manufacture use and disposal. Prog. Photovoltaics Res. Appl. **3**, 295–306 (1995)
14. Repins, I., Beall, C., Vora, N., DeHart, C., Kuciauskas, D., Dippo, P., To, B., Mann, J., Hsu, W.-C., Goodrich, A., Noufi, R.: Co-evaporated $Cu_2ZnSnSe_4$ films and devices. Sol. Energy Mater. Sol. Cells **101**, 154–159 (2012)
15. Bag, S., Gunawan, O., Gokmen, T., Zhu, Y., Todorov, T.K., Mitzi, D.B.: Low band gap liquid-processed CZTSe solar cell with 10.1 % efficiency. Energy Environ. Sci. **5**, 7060–7065 (2012)
16. Olekseyuk, I.D., Gulay, L.D., Dydchak, I.V., Piskach, L.V., Parasyuk, O.V., Marchuk, O.V.: Single crystal preparation and crystal structure of the Cu_2Zn/Cd, $Hg/SnSe_4$ compounds. J. Alloy. Compd. **340**, 141–145 (2002)
17. Wang, K., Gunawan, O., Todorov, T., Shin, B., Chey, S.J., Bojarczuk, N.A., Mitzi, D., Guha, S.: Thermally evaporated Cu_2ZnSnS_4 solar cells. Appl. Phys. Lett. **97**, 143508 (2010)
18. Guo, Q., Ford, G.M., Yang, W.-C., Walker, B.C., Stach, E.A., Hillhouse, H.W., Agrawal, R.: Fabrication of 7.2 % efficient CZTSSe solar cells using CZTS nanocrystals. J. Am. Chem. Soc. **132**, 17384–17386 (2010)
19. Willoughby, A.: Solar Cell Materials: Developing Technologies, Wiley Series in Materials for Electronic & Optoelectronic Applications, pp. 186. Wiley, Chichester (2014)
20. http://www.webelements.com/
21. U.S. geological survey, http://minerals.usgs.gov/minerals/pubs/commodity/

22. http://www.metalprices.com/
23. Shockley, W., Queisser, H.J.: Detailed balance limit of efficiency of p-n junction solar cells. J. Appl. Phys. **32**, 510 (1961)
24. Todorov, T.K., Tang, J., Bag, S., Gunawan, O., Gokmen, T., Zhu, Y., Mitzi, D.B.: Beyond 11 % efficiency: characteristics of state-of-the-Art $Cu_2ZnSn(S,Se)_4$ solar cells. Adv. Energy Mater. **3**, 34–38 (2013)
25. Bernardini, G.P., Borrini, D., Caneschi, A., Di Benedetto, F., Gatteschi, D., Ristori, D., Romanelli, M.: EPR and SQUID magnetometry study of Cu_2FeSnS_4 (stannite) and Cu_2ZnSnS_4 (kesterite). Phys. Chem. Miner. **27**, 453–461 (2000)
26. Hall, S.R., Szymanski, J.T., Stewart, J.M.: Kesterite, $Cu_2(Zn,Fe)SnS_4$, and stannite, $Cu_2(Fe,Zn)SnS_4$, structurally similar but distinct minerals. Can. Mineral. **16**, 131–137 (1978)
27. Brockway, L.O.: The crystal structure of stannite Cu_2FeSnS_4, Zeitschrift für Kristallographie—Crystalline Materials, 89, 434–441 (1934)
28. Bonazzi, P., Bindi, L., Bernardini, G.P., Menchetti, S.: A model for the mechanism of incorporation of Cu, Fe and Zn in the stannite—kesterite series, Cu_2FeSnS_4—Cu_2ZnSnS_4. Can. Mineral. **41**, 639–647 (2003)
29. Schorr, S.: Structural aspects of adamantine like multinary chalcogenides. Thin Solid Films **515**, 5985–5991 (2007)
30. Mitzi, D.B., Gunawan, O., Todorov, T.K., Wang, K., Guha, S.: The path towards a high-performance solution-processed kesterite solar cell. Sol. Energy Mater. Sol. Cells **95**, 1421–1436 (2011)
31. Schorr, S.: The crystal structure of kesterite type compounds: a neutron and X-ray diffraction study. Sol. Energy Mater. Sol. Cells **95**, 1482–1488 (2011)
32. Catlow, C.R.A., Guo, Z.X., Miskufova, M., Shevlin, S.A., Smith, A.G.H., Sokol, A.A., Walsh, A., Wilson, D.J., Woodley, S.M.: Advances in computational studies of energy materials. Philos. Trans. Roy. Soc. A **368**, 3379–3456 (2010)
33. Persson, C.: Electronic and optical properties of Cu_2ZnSnS_4 and $Cu_2ZnSnSe_4$. J. Appl. Phys. **107**, 053710 (2010)
34. Chen, S., Gong, X.G., Walsh, A., Wei, S.-H.: Crystal and electronic band structure of Cu_2ZnSnX_4 (X = S and Se) photovoltaic absorbers: first-principles insights. Appl. Phys. Lett. **94**, 041903 (2009)
35. Paier, J., Asahi, R., Nagoya, A., Kresse, G.: Cu_2ZnSnS_4 as a potential photovoltaic material: a hybrid Hartree-Fock density functional theory study. Phys. Rev. B **79**, 115–126 (2009)
36. Walsh, A., Chen, S., Gong, X.G., Wei, S.H.: Crystal structure and defect reactions in the kesterite solar cell absorber Cu_2ZnSnS_4 (CZTS): theoretical insights. AIP Conf. Proc. **1399**, 63 (2011)
37. Walsh, A., Wei, S.H., Chen, S.Y., Gong, X.G.: Design of quaternary chalcogenide photovoltaic absorbers through cation mutation. In: 34th IEEE Photovoltaic Specialists Conference, 1–3, pp. 1803–1806 (2009)
38. Walsh, A., Chen, S., Wei, S., Gong, X.: Kesterite thin film solar cells: advances in materials modelling of Cu_2ZnSnS_4. Adv. Energy Mater. **2**, 400–409 (2012)
39. Zhang, Y., Sun, X., Zhang, P., Yuan, X., Huang, F., Zhang, W.: Structural properties and quasiparticle band structures of Cu-based quaternary semiconductors for photovoltaic applications. J. Appl. Phys. **111**, 063709 (2012)
40. Raulot, J.M., Domain, C., Guillemoles, J.F.: Ab initio investigation of potential indium and gallium free chalcopyrite compounds for photovoltaic application. J. Phys. Chem. Solids **66**, 2019–2023 (2005)
41. Nozaki, H., Fukano, T., Ohta, S., Seno, Y., Katagiri, H., Jimbo, K.: Crystal structure determination of solar cell materials: Cu_2ZnSnS_4 thin films using X-ray anomalous dispersion. J. Alloy. Compd. **524**, 22–25 (2012)
42. Siebentritt, S., Schorr, S.: Kesterites—a challenging material for solar cells. Prog. Photovoltaics Res. Appl. **20**, 512–519 (2012)

43. Chen, S., Gong, X.G., Walsh, A., Wei, S.H.: Electronic structure and stability of quaternary chalcogenide semiconductors derived from cation cross-substitution of II–VI and I–III–VI_2 compounds. Phys. Rev. B **79**, 165211 (2009)
44. Oleksyuk, I.D., Dudchar, I.V., Piskach, L.V.: Phase equilibria in the Cu_2S–ZnS–SnS_2 system. J. Alloy. Compd. **368**, 135–143 (2004)
45. Dudchak, I.V., Piskach, L.V.: Phase equilibria in the Cu_2SnSe_3–$SnSe_2$–ZnSe system. J. Alloy. Compd. **351**, 145–150 (2003)
46. Das, S., Krishna, R.M., Ma, S., Mandal, K.C.: Single phase polycrystalline Cu_2ZnSnS_4 grown by vertical gradient freeze technique. J. Cryst. Growth **381**, 148–152 (2013)
47. Das, S., Mandal, K.C.: $Cu_2ZnSnSe_4$ photovoltaic absorber grown by vertical gradient freeze technique. Jpn. J. Appl. Phys. **52**, 125502 (2013)
48. Nagoya, A., Asahi, R., Wahl, R., Kresse, G.: Defect formation and phase stability of Cu_2ZnSnS_4 photovoltaic material. Phys. Rev. B **81**, 113202 (2010)
49. Chen, S.Y., Gong, X.G., Walsh, A., Wei, S.H.: Appl. Phys. Lett. **96**, 021902 (2010)
50. Dale, P.J., Hoenes, K., Scragg, J., Siebentritt, S.: A review of the challenges facing kesterite based thin film solar cells. In: Photovoltaic Specialists Conference (PVSC), 34th IEEE, pp. 002080–002085 (2009)
51. Maeda, T., Nakamura, S., Wada, T.: First-principles calculations of vacancy formation in In-free photovoltaic semiconductor $Cu_2ZnSnSe_4$. Thin Solid Films **519**, 7513–7516 (2011)
52. Gödecke, T., Haalboom, T., Ernst, F.: Phase equilbiria of Cu–In–Se. I. Stable states and non-equilibrium states of the In_2Se_3–Cu_2Se subsystem. Zeitschrift für Metallkunde, **91**, 622–634 (2000)
53. Chen, S., Yang, J.-H., Gong, X.G., Walsh, A., Wei, S.-H.: Intrinsic point defects and complexes in the quaternary kesterite semiconductor Cu_2ZnSnS_4. Phys. Rev. B **81**, 245204 (2010)
54. Persson, C., Lany, S., Zhao, Y.-J., Zunger, A.: n-type doping of $CuInSe_2$ and $CuGaSe_2$. Phys. Rev. B **72**, 035211 (2005)
55. Maeda, T., Nakamura, S., Wada, T.: First principles calculations of defect formation in in-free photovoltaic semiconductors Cu_2ZnSnS_4 and $Cu_2ZnSnSe_4$. Jpn. J. Appl. Phys. **50**, 04DP07 (2011)
56. Redinger, A., Berg, D.M., Dale, P.J., Djemour, R., Gütay, L., Eisenbarth, T., Valle, N., Siebentritt, S.: Route toward high-efficiency single-phase $Cu_2ZnSn(S,Se)_4$ thin film solar cells: model experiments and literature review. IEEE J. Photovoltaics **1**, 200–206 (2011)
57. Redinger, A., Hönes, K., Fontané, X., Izquierdo-Roca, V., Saucedo, E., Valle, N., Pérez-Rodríguez, A., Siebentritt, S.: Detection of a sZnSe secondary phase in coevaporated $Cu_2ZnSnSe_4$ thin films. Appl. Phys. Lett. **98**, 101907 (2011)
58. Bär, M., Schubert, B.-A., Marsen, B., Krause, S., Pookpanratana, S., Unold, T., Weinhardt, L., Heske, C., Schock, H.-W.: Impact of KCN etching on the chemical and electronic surface structure of Cu_2ZnSnS_4 thin film solar cell absorbers. Appl. Phys. Lett. **99**, 152111 (2011)
59. Katagiri, H., Jimbo, K., Yamada, S., Kamimura, T., Maw, W.S., Fukano, T., Ito, T., Motohiro, T.: Enhanced conversion efficiencies of Cu_2ZnSnS_4-based thin film solar cells by using preferential etching technique. Appl. Phys. Exp. **1**, 041201 (2008)
60. Timmo, K., Altosaar, M., Raudoja, J., Grossberg, M., Danilson, M., Volobujeva, O., Mellikov, E.: Chemical etching of $Cu_2ZnSn(S,Se)_4$ monograin powder. In: Photovoltaic Specialists Conference (PVSC), 35th IEEE, pp. 001982–001985 (2010)
61. Fairbrother, A., García-Hemme, E., Izquierdo-Roca, V., Fontané, X., Pulgarín-Agudelo, F. A., Vigil-Galán, O., Pérez-Rodríguez, A., Saucedo, E.: Development of a selective chemical etch to improve the conversion efficiency of Zn-Rich Cu_2ZnSnS_4 solar cells. J. Am. Chem. Soc. **134**, 8018–8021 (2012)
62. Biswas, K., Lany, S., Zunger, A.: The electronic consequences of multivalent elements in inorganic solar absorbers: multivalency of Sn in Cu_2ZnSnS_4. Appl. Phys. Lett. **96**, 201902 (2010)

63. Siebentritt, S., Igalson, M., Persson, C., Lany, S.: The electronic structure of chalcopyrites—bands, point defects and grain boundaries. Prog. Photovoltaics Res. Appl. **18**, 390–410 (2010)
64. Nagoya, A., Asahi, R., Kresse, G.: First-principles study of Cu_2ZnSnS_4 and the related band offsets for photovoltaic applications. J. Phys. Condens. Matter **23**, 404203 (2011)
65. Chen, S., Walsh, A., Gong, X.-G., Wei, S.-H.: Classification of lattice defects in the Kesterite Cu_2ZnSnS_4 and $Cu_2ZnSnSe_4$ earth-abundant solar cell absorbers. Adv. Mater. **25**, 1522–1539 (2013)
66. Zhai, Y.-T., Chen, S., Yang, J.-H., Xiang, H.-J., Gong, X.-G., Walsh, A., Kang, J., Wei, S.-H.: Structural diversity and electronic properties of Cu_2Snx_3 (X = S, Se): a first-principles investigation. Phys. Rev. B **84**, 075213 (2011)
67. Friedlmeier, T.M., Wieser, N., Walter, T., Dittrich, H., Schock, H.W.: 14th European photovoltaic solar energy conference, vol. 1, p. 1242 (1997)
68. Tanaka, T., Nagatomo, T., Kawasaki, D., Nishio, M., Guo, Q.X., Wakahara, A., Yoshida, A., Ogawa, H.: Preparation of Cu_2ZnSnS_4 thin films by hybrid sputtering. J. Phys. Chem. Solids **66**, 1978–1981 (2005)
69. Zhang, J., Shao, L.X., Fu, Y.J., Xie, E.Q.: Cu_2ZnSnS_4 thin films prepared by sulfurization of ion beam sputtered precursor and their electrical and optical properties. Rare Met. **25**, 315–319 (2006)
70. Leitao, J.P., Santos, N.M., Fernandes, P.A., Salome, P.M.P., da Cunha, A.F., Gonzalez, J.C., Ribeiro, G.M., Matinaga, F.M.: Photoluminescence and electrical study of fluctuating potentials in Cu_2ZnSnS_4-based thin films. Phys. Rev. B **84**, 024120 (2011)
71. Ito, K., Nakazawa, T.: Electrical and optical properties of Stannite-type quaternary semiconductor thin films. Jpn. J. Appl. Phys. **27**, 2094–2097 (1988)
72. Nakayama, N., Ito, K.: Sprayed films of stannite Cu_2ZnSnS_4. Appl. Surf. Sci. **92**, 171–175 (1996)
73. Katagiri, H., Sasaguchi, N., Hando, S., Hoshino, S., Ohashi, J., Yokota, T.: Preparation and evaluation of Cu_2ZnSnS_4 thin films by sulfurization of E-B evaporated precursors. Sol. Energy Mater. Sol. Cells **49**, 407–414 (1997)
74. Katagiri, H., Saitoh, K., Washio, T., Shinohara, H., Kurumadani, T., Miyajima, S.: Development of thin film solar cell based on Cu_2ZnSnS_4 thin films. Sol. Energy Mater. Sol. Cells **65**, 141–148 (2001)
75. Katagiri, H., Ishigaki, N., Ishida, T., Saito, K.: Characterization of Cu_2ZnSnS_4 thin films prepared by vapor phase sulfurization. Jpn. J. Appl. Phys. **40**, 500–504 (2001)
76. Matsushita, H., Maeda, T., Katsui, A., Takizawa, T.: Thermal analysis and synthesis from the melts of Cu-based quaternary compounds Cu–III–IV–VI_4 and Cu_2–II–IV–VI_4 (II = Zn, Cd; III = Ga, In; IV = Ge, Sn; VI = Se). J. Cryst. Growth **208**, 416–422 (2000)
77. Wibowo, R.A., Kim, W.S., Lee, E.S., Munir, B., Kim, K.H.: Single step preparation of quaternary $Cu_2ZnSnSe_4$ thin films by RF magnetron sputtering from binary chalcogenide targets. J. Phys. Chem. Solids **68**, 1908–1913 (2007)
78. Wibowo, R.A., Lee, E.S., Munir, B., Kim, K.H.: Pulsed laser deposition of quaternary $Cu_2ZnSnSe_4$ thin films. Phys. Status Solidi A **204**, 3373–3379 (2007)
79. Friedlmeier, T.M., Dittrich, H., Schock, H.W.: 11th international conference on ternary and multinary compounds. ICTMC-11 Institute of Physics Publishing, Salford, UK (1998)
80. Repins, I., Vora, N., Beall, C., Wei, S.-H., Yan, Y., Romero, M., Teeter, G., Du, H., To, B., Young, M., Noufi, R.: Kesterites and chalcopyrites: a comparison of close cousins. In: MRS proceedings, vol. 1324 (2011)
81. Schorr, S., Hoebler, H.J., Tovar, M.: A neutron diffraction study of the stannite-kesterite solid solution series. Eur. J. Mineral. **19**, 65–73 (2007)
82. Washio, T., Nozaki, H., Fukano, T., Motohiro, T., Jimbo, K., Katagiri, H.: Analysis of lattice site occupancy in kesterite structure of Cu_2ZnSnS_4 films using synchrotron radiation X-ray diffraction. J. Appl. Phys. **110**, 074511 (2011)
83. Kask, E., Raadik, T., Grossberg, M., Josepson, R., Krustok, J.: Deep defects in Cu_2ZnSnS_4 monograin solar cells. Energy Procedia **10**, 261–265 (2011)

84. Shin, B., Gunawan, O., Nestor, Y.Z., Bojarczuk, A., Chey, S.J., Guha, S.: Thin film solar cell with 8.4 % power conversion efficiency using an earth-abundant Cu_2ZnSnS_4 absorber. Prog. Photovoltaics Res. Appl. **21**, 72–76 (2013)
85. Araki, H., Mikaduki, A., Kubo, Y., Sato, T., Jimbo, K., Maw, W.S., Katagiri, H., Yamazaki, M., Oishi, K., Takeuchi, A.: Preparation of Cu_2ZnSnS_4 thin films by sulfurization of stacked metallic layers. Thin Solid Films **517**, 1457–1460 (2008)
86. Kobayashi, T., Jimbo, K., Tsuchida, K., Shinoda, S., Oyanagi, T., Katagiri, H.: Investigation of Cu_2ZnSnS_4-based thin film solar cells using abundant materials. Jpn. J. Appl. Phys. **44**, 783–787 (2005)
87. Schubert, B.-A., Marsen, B., Cinque, S., Unold, T., Klenk, R., Schorr, S., Schock, H.-W.: Cu_2ZnSnS_4 thin film solar cells by fast coevaporation. Prog. Photovoltaics Res. Appl. **19**, 93–96 (2011)
88. Friedlmeier, T.M., Wieser, N., Walter, T., Dittrich, H., Schock, H.-W.: Heterojunctions based on Cu_2ZnSnS_4 and $Cu_2ZnSnSe_4$ thin films. In: Proceedings of the 14th European PVSEC and Exhibition, P4B.10, 1242 (1997)
89. Katagiri, H., Jimbo, K., Moriya, K., Tsuchida, K.: Solar cell without environmental pollution by using CZTS thin film. In: Proceedings of the 3rd World conference on photovoltaic energy conversion, Osaka, pp. 2874–2879 (2003)
90. Weber, A., Mainz, R., Schock, H.W.: On the Sn loss from thin films of the material system Cu–Zn–Sn–S in high vacuum. J. Appl. Phys. **107**, 013516 (2010)
91. Redinger, A., Berg, D.M., Dale, P.J., Siebentritt, S.: The consequences of Kesterite equilibria for efficient solar cells. J. Am. Chem. Soc. **133**, 3320–3323 (2011)
92. Tanaka, T., Kawasaki, D., Nishio, M., Guo, Q., Ogawa, H.: Fabrication of Cu_2ZnSnS_4 thin films by co-evaporation, physica status solidi C. **3**, 2844–2847 (2006)
93. Oishi, K., Saito, G., Ebina, K., Nagahashi, M., Jimbo, K., Maw, W.S., Katagiri, H., Yamazaki, M., Araki, H., Takeuchi, A.: Growth of Cu_2ZnSnS_4 thin films on Si (100) substrates by multisource evaporation. Thin Solid Films **517**, 1449–1452 (2008)
94. Tanaka, T., Yoshida, A., Saiki, D., Saito, K., Guo, Q., Nishio, M., Yamaguchi, T.: Influence of composition ratio on properties of Cu_2ZnSnS_4 thin films fabricated by co-evaporation. Thin Solid Films **518**, S29–S33 (2010)
95. Vora, N., Blackburn, J., Repins, I., Beall, C., To, B., Pankow, J., Teeter, G., Young, M., Noufi, R.: Phase identification and control of thin films deposited by co-evaporation of elemental Cu, Zn, Sn, and Se. J. Vac. Sci. Technol. A **30**, 051201 (2012)
96. Weber, A., Krauth, H., Perlt, S., Schubert, B., Kotschau, I., Schorr, S., Schock, H.W.: Multi-stage evaporation of Cu_2ZnSnS_4 thin films. Thin Solid Films **517**, 2524–2526 (2009)
97. Das, S., Mandal, K.C.: Comparison of Cu_2ZnSnS_4 thin film properties prepared by thermal evaporation of elemental metals and binary sulfide sources. In: Photovoltaic Specialists Conference (PVSC), 38th IEEE, Austin, Texas, pp. 002674–002678 (2012)
98. Han, S., Hasoon, S.F., Al-Thani, H.A., Hermann, A.M., Levi, D.H.: Effect of Cu deficiency on the optical properties and electronic structure of $CuIn_{1-x}Ga_xSe_2$. J. Phys. Chem. Solids **66**, 1895–1898 (2005)
99. Chalapathy, R.B.V., Jung, G.S., Ahn, B.T.: Fabrication of Cu_2ZnSnS_4 films by sulfurization of Cu/ZnSn/Cu precursor layers in sulfur atmosphere for solar cells. Sol. Energy Mater. Sol. Cells **95**, 3216–3221 (2011)
100. Zoppi, G., Forbes, I., Miles, R.W., Dale, P.J., Scragg, J.J., Peter, L.M.: $Cu_2ZnSnSe_4$ thin film solar cells produced by selenisation of magnetron sputtered precursors. Prog. Photovoltaics Res. Appl. **17**, 315–319 (2009)
101. Momose, N., Htay, M.T., Yudasaka, T., Igarashi, S., Seki, T., Iwano, S., Hashimoto, Y., Ito, K.: Cu_2ZnSnS_4 thin film solar cells utilizing sulfurization of metallic precursor prepared by simultaneous sputtering of metal targets. Jpn. J. Appl. Phys. **50**, 01BG09 (2011)
102. Fernandes, P.A., Salomé, P.M.P., da Cunha, A.F., Schubert, B.: Cu_2ZnSnS_4 solar cells prepared with sulphurized dc-sputtered stacked metallic precursors. Thin Solid Films **519**, 7382–7385 (2011)

103. Ito, K., Nakazawa, T.: Proceedings of the 4th international conference on photovoltaics science and engineering, Sydney, Australia, p. 341 (1989)
104. Fernandes, P.A., Salome, P.M.P., da Cunha, A.F.: Precursors' order effect on the properties of sulfurized Cu_2ZnSnS_4 thin films. Semicond. Sci. Technol. **24**, 105013 (2009)
105. Seol, J.S., Lee, S.Y., Lee, J.C., Nam, H.D., Kim, K.H.: Electrical and optical properties of Cu_2ZnSnS_4 thin films prepared by rf magnetron sputtering process. Sol. Energy Mater. Sol. Cells **75**, 155–162 (2003)
106. Katagiri, H., Jimbo, K., Tahara, M., Araki, H., Oishi, K.: The influence of the composition ratio on CZTS-based thin film solar cells. In: MRS proceedings, 1165-M04-01 (2009). doi:10.1557/PROC-1165-M04-01
107. Yoo, H., Kim, J.: Growth of Cu_2ZnSnS_4 thin films using sulfurization of stacked metallic films. Thin Solid Films **518**, 6567–6572 (2010)
108. Liu, F., Zhang, K., Lai, Y., Li, J., Zhang, Z., Liu, Y.: Growth and characterization of Cu_2ZnSnS_4 thin films by dc reactive magnetron sputtering for photovoltaic applications. Electrochem. Solid-State Lett. **13**, H379–H381 (2010)
109. Jimbo, K., Kimura, R., Kamimura, T., Yamada, S., Maw, W.S., Araki, H., Oishi, K., Katagiri, H.: Cu_2ZnSnS_4-type thin film solar cells using abundant materials. Thin Solid Films **515**, 5997–5999 (2007)
110. Chrisey, D.B., Hubler, G.K.: Pulsed laser deposition of thin films, vol. 14. Wiley, New York (1994)
111. Sekiguchi, K., Tanaka, K., Moriya, K., Uchiki, H.: Epitaxial growth of Cu_2ZnSnS_4 thin films by pulsed laser deposition. Phys. Status Solidi C **3**, 2618–2621 (2006)
112. Moriya, K., Tanaka, K., Uchiki, H.: Fabrication of Cu_2ZnSnS_4 thin-film solar cell prepared by pulsed laser deposition. Jpn. J. Appl. Phys. **46**, 5780–5781 (2007)
113. Moriya, K., Tanaka, K., Uchiki, H.: Cu_2ZnSnS_4 thin films annealed in H_2S atmosphere for solar cell absorber prepared by pulsed laser deposition. Jpn. J. Appl. Phys. **47**, 602–604 (2008)
114. Pawar, S.M., Moholkar, A.V., Kim, I.K., Shin, S.W., Moon, J.H., Rhee, J.I., Kim, J.H.: Effect of laser incident energy on the structural, morphological and optical properties of Cu_2ZnSnS_4 (CZTS) thin films. Curr. Appl. Phys. **10**, 565–569 (2010)
115. Sun, L., He, J., Kong, H., Yue, F., Yang, P., Chu, J.: Structure, composition and optical properties of Cu_2ZnSnS_4 thin films deposited by pulsed laser deposition method. Sol. Energy Mater. Sol. Cells **95**, 2907–2913 (2011)
116. Moholkar, A.V., Shinde, S.S., Babar, A.R., Sim, K., Lee, H., Rajpure, K.Y., Patil, P.S., Bhosale, C.H., Kim, J.H.: Synthesis and characterization of Cu_2ZnSnS_4 thin films grown by PLD: solar cells. J. Alloy. Compd. **509**, 7439–7446 (2011)
117. Moholkar, A.V., Shinde, S.S., Babar, A.R., Sim, K.-U., Kwon, Y., Rajpure, K.Y., Patil, P.S., Bhosale, C.H., Kim, J.H.: Development of CZTS thin films solar cells by pulsed laser deposition: influence of pulse repetition rate. Solar Energy **85,** 1354–1363 (2011)
118. Moholkar, A.V., Shinde, S.S., Agawane, G.L., Jo, S.H., Rajpure, K.Y., Patil, P.S., Bhosale, C.H., Kim, J.H.: Studies of compositional dependent CZTS thin film solar cells by pulsed laser deposition technique: an attempt to improve the efficiency. J. Alloy. Compd. **544**, 145–151 (2012)
119. Panthani, M.G., Akhavan, V., Goodfellow, B., Schmidtke, J.P., Dunn, L., Dodabalapur, A., Barbara, P.F., Korgel, B.A.: Synthesis of $CuInS_2$, $CuInSe_2$, and $Cu(In_xGa_{1-x})Se_2$ (CIGS) nanocrystal "Inks" for printable photovoltaics. J. Am. Chem. Soc. **130**, 16770–16777 (2008)
120. Allen, P.M., Bawendi, M.G.: Ternary I–III–VI quantum dots luminescent in the red to near-infrared. J. Am. Chem. Soc. **130**, 9240–9241 (2008)
121. Hernandez-Pagan, E.A., Wang, W., Mallouk, T.E.: Template electrodeposition of single-phase p- and n-type copper indium diselenide ($CuInSe_2$) nanowire arrays. ACS Nano **5**, 3237–3241 (2011)
122. Guo, Q., Kim, S.J., Kar, M., Shafarman, W.N., Birkmire, R.W., Stach, E.A., Agrawal, R., Hillhouse, H.W.: Development of $CuInSe_2$ nanocrystal and nanoring inks for low-cost solar cells. Nano Lett. **8**, 2982–2987 (2008)

123. Steinhagen, C., Panthani, M.G., Akhavan, V., Goodfellow, B., Koo, B., Korgel, B.A.: Synthesis of Cu_2ZnSnS_4 nanocrystals for use in low-cost photovoltaics. J. Am. Chem. Soc. **131**, 12554–12555 (2009)
124. Guo, Q., Hillhouse, H.W., Agrawal, R.: Synthesis of Cu_2ZnSnS_4 nanocrystal ink and its use for solar cells. J. Am. Chem. Soc. **131**, 11672–11673 (2009)
125. Riha, S.C., Parkinson, B.A., Prieto, A.L.: Solution-based synthesis and characterization of Cu_2ZnSnS_4 nanocrystals. J. Am. Chem. Soc. **131**, 12054–12055 (2009)
126. Cao, Y., Denny Jr, M.S., Caspar, J.V., Farneth, W.E., Guo, Q., Ionkin, A.S., Johnson, L.K., Lu, M., Malajovich, I., Radu, D., Rosenfeld, H.D., Roy, K., Choudhury, W., Wu, W.: High-efficiency solution-processed $Cu_2ZnSn(S,Se)_4$ thin-film solar cells prepared from binary and ternary nanoparticles. J. Am. Chem. Soc. **134**, 15644–15647 (2012)
127. Kameyama, T., Osaki, T., Okazaki, K., Shibayama, T., Kudo, A., Kuwabata, S., Torimoto, T.: Preparation and photoelectrochemical properties of densely immobilized Cu_2ZnSnS_4 nanoparticle films. J. Mater. Chem. **20**, 5319–5324 (2010)
128. Riha, S.C., Fredrick, S.J., Sambur, J.B., Liu, Y., Prieto, A.L., Parkinson, B.A.: Photoelectrochemical characterization of nanocrystalline thin-film Cu_2ZnSnS_4 photocathodes. ACS Appl. Materi. Interfaces **3**, 58–66 (2011)
129. Shavel, A., Arbiol, J., Cabot, A.: Synthesis of quaternary chalcogenide nanocrystals: stannite $Cu_2Zn_xSn_ySe_{1+x+2y}$. J. Am. Chem. Soc. **132**, 4514–4515 (2010)
130. Lu, X., Zhuang, Z., Peng, Q., Li, Y.: Wurtzite Cu_2ZnSnS_4 nanocrystals: a novel quaternary semiconductor. Chem. Commun. **47**, 3141–3143 (2011)
131. Dai, P., Shen, X., Lin, Z., Feng, Z., Xu, H., Zhan, J.: Band-gap tunable $(Cu_2Sn)_{x/3}Zn_{1-x}S$ nanoparticles for solar cells. Chem. Commun. **46**, 5749–5751 (2010)
132. Cao, M., Shen, Y.: A mild solvothermal route to kesterite quaternary Cu_2ZnSnS_4 nanoparticles. J. Cryst. Growth **318**, 1117–1120 (2011)
133. Shi, L., Pei, C., Xu, Y., Li, Q.: Template-directed synthesis of ordered single-crystalline nanowires arrays of Cu_2ZnSnS_4 and $Cu_2ZnSnSe_4$. J. Am. Chem. Soc. **133**, 10328–10331 (2011)
134. Todorov, T.K., Reuter, K.B., Mitzi, D.B.: High-efficiency solar cell with earth-abundant liquid-processed absorber. Adv. Mater. **22**, E156–E159 (2010)
135. Barkhouse, D.A.R., Gunawan, O., Gokmen, T., Todorov, T.K., Mitzi, D.B.: Device characteristics of a 10.1 % hydrazine-processed $Cu_2ZnSn(Se,S)_4$ solar cell. Prog. Photovoltaics Res. Appl. **20**, 6–11 (2012)
136. Washio, T., Shinji, T., Tajima, S., Fukano, T., Motohiro, T., Jimbo, K., Katagiri, H.: 6 % efficiency Cu_2ZnSnS_4-based thin film solar cells using oxide precursors by open atmosphere type CVD. J. Mater. Chem. **22**, 4021–4024 (2012)
137. Bhattacharya, R.N.: CIGS-based solar cells prepared from electrodeposited stacked Cu/In/Ga layers. Sol. Energy Materials Solar Cells **113**, 96–99 (2013)
138. Ahmed, S., Reuter, K.B., Gunawan, O., Guo, L., Romankiw, L.T., Deligianni, H.: A high efficiency electrodeposited Cu_2ZnSnS_4 solar cell. Adv. Energy Mater. **2**, 253–259 (2012)
139. Ennaoui, A., Steiner, M.L., Weber, A., Ras, D.A., Kotschau, I., Schock, H.W., Schurr, R., Holzing, A., Jost, S., Hock, R., Vob, T., Schulze, J., Kirbs, A.: Cu_2ZnSnS_4 thin film solar cells from electroplated precursors: novel low-cost perspective. Thin Solid Films **517**, 2511–2514 (2009)
140. Araki, H., Kubo, Y., Jimbo, K., Maw, W.S., Katagiri, H., Yamazaki, M., Oishi, K., Takeuchi, A.: Preparation of Cu_2ZnSnS_4 thin films by sulfurization of co-electroplated Cu–Zn–Sn precursors. Phys. Status Solidi C **6**, 1266–1268 (2009)
141. Kurihara, M., Berg, D., Fisher, J., Siebentritt, S., Dale, P.J.: Kesterite absorber layer uniformity from electrodeposited precursors. Phys. Status Solidi C **6**, 1241–1244 (2009)
142. Pawar, S.M., Pawar, B.S., Moholkar, A.V., Choi, D.S., Yun, J.H., Moon, J.H., Kolekar, S.S., Kim, J.H.: Single step electrosynthesis of Cu_2ZnSnS_4 (CZTS) thin films for solar cell application. Electrochim. Acta **55**, 4057–4061 (2010)
143. Chan, C.P., Lam, H., Surya, C.: Preparation of Cu_2ZnSnS_4 films by electrodeposition using ionic liquids. Sol. Energy Mater. Sol. Cells **94**, 207–211 (2010)

144. Schurr, R., Hölzing, A., Jost, S., Hock, R., Voß, T., Schulze, J., Kirbs, A., Ennaoui, A., Lux-Steiner, M., Weber, A., Kötschau, I., Schock, H.-W.: The crystallisation of Cu_2ZnSnS_4 thin film solar cell absorbers from co-electroplated Cu–Zn–Sn precursors. Thin Solid Films **517**, 2465–2468 (2009)
145. Bhattacharya, R.N.: Fabrication of ionic liquid electrodeposited Cu–Sn–Zn–S–Se thin films and method of making, United States Patent Application Publication No.: US 2013/0168825 A1, July 4, 2013
146. Farinella, M., Inguanta, R., Spano, T., Livreri, P., Piazza, S., Sunseri, C.: Electrochemical deposition of CZTS thin films on flexible substrate. Energy Procedia **44**, 105–110 (2014)
147. Bhattacharya, R.N.: 3.6 %-CZTSS Device fabricated from ionic liquid electrodeposited Sn layer. Open Surface Sci. J. **5**, 21–24 (2013)
148. Timmo, K., Altosaar, M., Raudoja, J., Muska, K., Pilvet, M., Kauk, M., Varema, T., Danilson, M., Volobujeva, O., Mellikov, E.: Sulfur-containing $Cu_2ZnSnSe_4$ monograin powders for solar cells. Sol. Energy Mater. Sol. Cells **94**, 1889–1892 (2010)
149. Mellikov, E., Meissner, D., Varema, T., Altosaar, M., Kauk, M., Volobujeva, O., Raudoja, J., Timmo, K., Danilson, M.: Monograin materials for solar cells. Sol. Energy Mater. Sol. Cells **93**, 65–68 (2009)
150. Kauk, M., Muska, K., Altosaar, M., Raudoja, J., Pilvet, M., Varema, T., Timmo, K., Volobujeva, O.: Effects of sulphur and tin disulphide vapour treatments of $Cu_2ZnSnS(Se)_4$ absorber materials for monograin solar cells. Energy Procedia **10**, 197–202 (2011)
151. Katagiri, H.: Cu_2ZnSnS_4 thin film solar cells. Thin Solid Films **480–481**, 426–432 (2005)
152. Jeong, A.R., Jo, W., Jung, S., Gwak, J., Yun, J.H.: Enhanced exciton separation through negative energy band bending at grain boundaries of $Cu_2ZnSnSe_4$ thin-films. Appl. Phys. Lett. **99**, 082103 (2011)
153. Shin, B., Wang, K., Gunawan, O., Reuter, K.B., Chey, S.J., Bojarczuk, N.A., Todorov, T., Mitzi, D.B., Guha, S.: Photovoltaic specialists conference (PVSC), 37th IEEE (2011), pp. 002510–002514
154. Jung, S., Gwak, J., Yun, J.H., Ahn, S.J., Nam, D., Cheong, H., Ahn, S., Cho, A., Shin, K.S., Yoon, K.H.: $Cu_2ZnSnSe_4$ thin film solar cells based on a single-step co-evaporation process. Thin Solid Films **535**, 52–56 (2013)
155. Platzer-Björkman, C., Scragg, J., Flammersberger, H., Kubart, T., Edoff, M.: Influence of precursor sulfur content on film formation and compositional changes in Cu_2ZnSnS_4 films and solar cells. Solar Energy Materials and Solar Cells **98**, 110–117 (2012)
156. Ericson, T., Scragg, J.J., Kubart, T., Törndahl, T., Platzer-Björkman, C.: Annealing behavior of reactively sputtered precursor films for Cu_2ZnSnS_4 solar cells. Thin Solid Films **535**, 22–26 (2013)
157. Lechner, R., Jost, S., Palm, J., Gowtham, M., Sorin, F., Louis, B., Yoo, H., Wibowo, R.A., Hock, R.: Cu2ZnSn(S, Se)4 solar cells processed by rapid thermal processing of stacked elemental layer precursors. Thin Solid Films **535**, 5–9 (2013)
158. Woo, K., Kim, Y., Moon, J.: A non-toxic, solution-processed, earth abundant absorbing layer for thin-film solar cells. Energy Environ. Sci. **5**, 5340–5345 (2012)
159. Ki, W., Hillhouse, H.W.: Earth-abundant element photovoltaics directly from soluble precursors with high yield using a non-toxic solvent. Adv. Energy Mater. **1**, 732–735 (2011)
160. Ford, G.M., Guo, Q., Agrawal, R., Hillhouse, H.W.: Earth abundant element $Cu_2Zn(Sn_{1-x}Ge_x)S_4$ nanocrystals for tunable band gap solar cells: 6.8 % efficient device fabrication. Chem. Mater. **23**, 2626–2629 (2011)
161. Maeda, K., Tanaka, K., Fukui, Y., Uchiki, H.: Influence of H_2S concentration on the properties of Cu_2ZnSnS_4 thin films and solar cells prepared by sol–gel sulfurization. Sol. Energy Mater. Sol. Cells **95**, 2855–2860 (2011)
162. Tanaka, K., Fukui, Y., Moritake, N., Uchiki, H.: Chemical composition dependence of morphological and optical properties of Cu_2ZnSnS_4 thin films deposited by sol–gel sulfurization and Cu_2ZnSnS_4 thin film solar cell efficiency. Sol. Energy Mater. Sol. Cells **95**, 838–842 (2011)

163. Moritake, N., Fukui, Y., Oonuki, M., Tanaka, K., Uchiki, H.: Preparation of Cu_2ZnSnS_4 thin film solar cells under non-vacuum condition. Phys. Status Solidi C **6**, 1233–1236 (2009)
164. Tanaka, K., Oonuki, M., Moritake, N., Uchiki, H.: Cu_2ZnSnS_4 thin film solar cells prepared by non-vacuum processing. Sol. Energy Mater. Sol. Cells **93**, 583–587 (2009)
165. Jiang, M., Li, Y., Dhakal, R., Thapaliya, P., Mastro, M., Caldwell, J.D., Kub, F., Yan, X.: Cu_2ZnSnS_4 polycrystalline thin films with large densely packed grains prepared by sol-gel method. J. Photonics Energy **1**, 019501 (2011)
166. Ilari, G.M., Fella, C.M., Ziegler, C., Uhl, A.R., Romanyuk, Y.E., Tiwari, A.N.: $Cu_2ZnSnSe_4$ solar cell absorbers spin-coated from amine-containing ether solutions. Sol. Energy Mater. Sol. Cells **104**, 125–130 (2012)
167. Zhou, Z., Wang, Y., Xu, D., Zhang, Y.: Fabrication of Cu_2ZnSnS_4 screen printed layers for solar cells. Sol. Energy Mater. Sol. Cells **94**, 2042–2045 (2010)
168. Chen, Q., Cheng, S., Zhuang, S., Dou, X.: Cu_2ZnSnS_4 solar cell prepared entirely by non-vacuum processes. Thin Solid Films **520**, 6256–6261 (2012)
169. Prabhakar, T., Nagaraju, J.: Device parameters of Cu_2ZnSnS_4 thin film solar cell. Photovoltaic Specialists Conference (PVSC), 37th IEEE, Seattle, pp. 001346–001351 (2011)
170. Patel, M., Mukhopadhyay, I., Ray, A.: Structural, optical and electrical properties of spray-deposited CZTS thin films under a non-equilibrium growth condition. J. Phys. D Appl. Phys. **45**, 445103 (2012)
171. Wangperawong, A., King, J.S., Herron, S.M., Tran, B.P., Pangan-Okimoto, K., Bent, S.F.: Aqueous bath process for deposition of Cu_2ZnSnS_4 photovoltaic absorbers. Thin Solid Films **519**, 2488–2492 (2011)

Chapter 3
Cu_2ZnSnS_4, $Cu_2ZnSnSe_4$, and Related Materials

Shiyou Chen

3.1 History of Cu_2ZnSnS_4-Related Semiconductors

3.1.1 Theoretical Design of I_2–II–IV–VI_4 Semiconductors

The theoretical design and experimental synthesis of quaternary I_2–II–IV–VI_4 (I = Cu, Ag, II = Zn, Cd, IV = Si, Ge, Sn, VI = S, Se, Te) started as early as 1950s. In 1958, Goodman showed that "various series of new semiconducting compounds can be derived from known ones by a process of 'cross-substitution', i.e., by replacing one element by pairs from other groups of the Periodic Table while keeping the valence-electron:atom ratio constant" [1]. For example, starting from the diamond-like (adamantine-like, zincblende-like) lattice of ZnS, if two Zn^{2+} cations are replaced by one Cu^{+} and one Ga^{3+} cation, a ternary $CuGaS_2$ compound can be derived, in which the S^{2-} anion is still in the eight-electron full-shell state. This element cross-substitution design of new semiconductors is schematically shown in Fig. 3.1. If two Ga^{3+} cations are further replaced by one Zn^{+} cation and one Ge^{4+} cation, the ternary $CuGaS_2$ mutates into quaternary Cu_2ZnGeS_4. Ge^{4+} can be replaced by isovalent Sn^{4+}, then Cu_2ZnSnS_4 is derived; and if S^{2-} can be replaced by isovalent Se^{2-}, then $Cu_2ZnSnSe_4$ is derived. Through the substitution of the group I, II, IV, and VI elements, a series of I_2–II–IV–VI_4 quaternary compound semiconductors can be designed.

S. Chen (✉)
Key Laboratory for Polar Materials and Devices (MOE), East China Normal University, Shanghai, China
e-mail: chensy@ee.ecnu.edu.cn

S. Chen
Key Laboratory for Computational Material Sciences (MOE), Department of Physics, Fudan University, Shanghai, China

M.P. Paranthaman et al. (eds.), *Semiconductor Materials for Solar Photovoltaic Cells*, Springer Series in Materials Science 218,
DOI 10.1007/978-3-319-20331-7_3

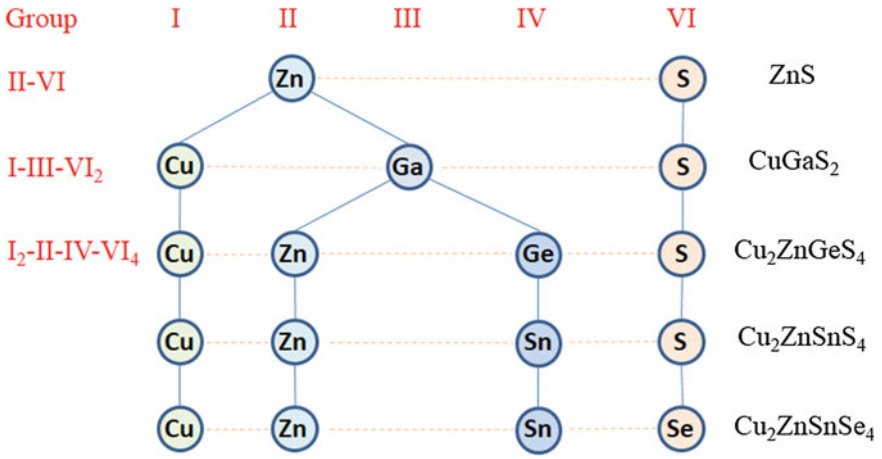

Fig. 3.1 Element-substitution mutation from binary II–VI semiconductors to ternary I–III–VI_2 and quaternary I_2–II–IV–VI_4 compound semiconductors

3.1.2 Synthesis and Fabrication of Solar Cells

Since 1960s, some I_2–II–IV–VI_4 semiconductors including Cu_2ZnSnS_4 have been synthesized by different groups [2–8]. In 1988, Ito and Nakazawa synthesized p-type Cu_2CdSnS_4 and Cu_2ZnSnS_4 thin films with (112) orientation and fabricated a photovoltaic cell of Cu_2ZnSnS_4 with an open-circuit voltage of 165 mV [9]. In 1996, Katagiri et al. fabricated a Cu_2ZnSnS_4 thin-film solar cell with a structure of ZnO:Al/CdS/CZTS/Mo/SLG and reported an open-circuit voltage of 400 mV and an energy-conversion efficiency of 0.66 % [10, 11]. In 1997, Friedlmeier et al. reported the preparation of Cu_2ZnSnS_4 solar cell with 2.3 % energy-conversion efficiency and $Cu_2ZnSnSe_4$ cell with 0.6 % efficiency [12]. Then in the following 10 years, the efficiency increased steadily, and until 2009, an efficiency as high as 6.7 % had been achieved by Katagiri et al. [11].

Since 2009, the thin-film solar cells based on Cu_2ZnSnS_4 and $Cu_2ZnSnSe_4$ have drawn a significantly increasing amount of attention. In 2010, a hydrazine-based deposition process was used to prepare $Cu_2ZnSn(S,Se)_4$ (CZTSSe) solar cells with an efficiency as high as 9.7 % [13]; in 2012, the efficiency was increased to 11.1 % [14]; and in 2013, the efficiency was further increased to 12.6 % [15]. Although the highest-efficiency cell uses the $Cu_2ZnSn(S,Se)_4$ alloys as the absorber layer, the efficiency of the cells using Cu_2ZnSnS_4 or $Cu_2ZnSnSe_4$ compounds as the absorber layers have also increased recently. A 9.2 % efficiency was achieved by Repins et al. [16] and a 9.7 % efficiency was achieved by Brammertz et al. [17] for $Cu_2ZnSnSe_4$ solar cells. An 8.4 % efficiency was achieved by Shin et al. for $Cu_2ZnSnSe_4$ solar cells [18].

Table 3.1 The reported performance parameters (open-circuit voltage V_{oc}, short-circuit current density J_{sc}, fill factor FF, and light to electricity conversion efficiency η) of Cu_2ZnSnS_4, $Cu_2ZnSnSe_4$, and $Cu_2ZnSn(S,Se)_4$-based solar cells with different chemical component as described by the Cu/(Zn + Sn) and Zn/Sn ratios

Component	Cu/(Zn + Sn)	Zn/Sn	V_{oc} (mV)	J_{sc} (mA/cm^2)	FF (%)	η (%)	References
Cu_2ZnSnS_4	0.85	0.93	610	8.59	44	2.29	[23]
Cu_2ZnSnS_4	0.85	1.03	629	12.53	58	4.53	[23]
Cu_2ZnSnS_4	0.88	1.04	633	6.96	47	0.47	[23]
Cu_2ZnSnS_4	0.87	1.14	521	5.53	59	0.59	[23]
Cu_2ZnSnS_4	0.88	1.09	486	5.79	46	0.46	[23]
Cu_2ZnSnS_4	0.85	1.25	610	17.9	62	6.77	[24]
Cu_2ZnSnS_4	0.92	1.17	575	9.69	36.4	2.03	[25]
Cu_2ZnSnS_4	0.97	1.10	442	5.39	36.6	0.87	[25]
Cu_2ZnSnS_4	1.00	1.00	410	3.83	39.1	0.61	[25]
Cu_2ZnSnS_4	0.91	1.10	371	16.2	35	2.1	[21]
Cu_2ZnSnS_4	0.97	1.08	529	15.9	42	3.6	[21]
Cu_2ZnSnS_4	0.98	1.00	486	6.8	31.9	1.2	[21]
Cu_2ZnSnS_4	1.13	0.77	386	4.76	27	0.49	[26]
Cu_2ZnSnS_4	0.94	0.84	188	10.5	37.2	0.73	[27]
Cu_2ZnSnS_4	0.96	1.17	554	6.70	43.4	1.61	[28]
Cu_2ZnSnS_4	0.73	0.86	546	6.78	48	1.74	[29]
Cu_2ZnSnS_4	1.13	1.03	529	10.2	41.6	2.23	[30]
Cu_2ZnSnS_4	1.0	1.1	540	12.6	46.4	3.16	[31]
Cu_2ZnSnS_4	1.01	1.02	541	13.0	59.8	4.1	[32]
Cu_2ZnSnS_4	0.80	1.13	400	24.9	41.2	4.1	[33]
Cu_2ZnSnS_4	0.67	1.45	545	15.4	54.6	4.59	[34]
Cu_2ZnSnS_4	0.82	1.2	587	17.8	65	6.81	[35]
Cu_2ZnSnS_4	~0.78	~1.25	661	19.5	65.8	8.4	[18]
Cu_2ZnSnS_4	0.86	1.04	289	1.79	47.9	0.25	[36]
Cu_2ZnSnS_4	0.808	0.998	110	0.25	29	0.00	[37]
Cu_2ZnSnS_4	0.834	1.054	200	1.05	31	0.70	[37]
Cu_2ZnSnS_4	0.872	1.100	450	2.85	37	0.51	[37]
Cu_2ZnSnS_4	0.881	1.178	485	1.10	38	0.24	[37]
Cu_2ZnSnS_4	0.853	1.197	490	0.50	43	0.12	[37]
Cu_2ZnSnS_4			505.4	24.5	57.83	7.17	[38]
Cu_2ZnSnS_4	0.82	1.20	330	1.8	32	7.55	[39]
Cu_2ZnSnS_4	0.87	1.16	330	1.8	32	6.31	[39]
Cu_2ZnSnS_4	0.83	1.23	330	1.8	32	5.82	[39]
Cu_2ZnSnS_4	0.86	1.04	330	1.8	32	5.60	[39]
Cu_2ZnSnS_4	0.86	1.17	633	21.75	60.11	8.27	[40]
Cu_2ZnSnS_4	0.80	1.17	361	7.5	37.1	1.0	[41]
Cu_2ZnSnS_4	0.86	1.40	243	3.9	38.6	0.37	[41]
Cu_2ZnSnS_4			710	14.71	73.06	7.63	[42]
Cu_2ZnSnS_4	~1.1	~1.5	679.2	4.1	43.8	1.2	[43]
Cu_2ZnSnS_4	0.85	1.2	558	14.10	53	4.21	[44]
$Cu_2ZnSnSe_4$	0.75	1.65	229	18.4	49.4	2.08	[45]

(continued)

Table 3.1 (continued)

Component	Cu/(Zn + Sn)	Zn/Sn	V_{oc} (mV)	J_{sc} (mA/cm^2)	FF (%)	η (%)	References
$Cu_2ZnSnSe_4$	0.64	1.60	302	31.4	33.5	3.17	[45]
$Cu_2ZnSnSe_4$	0.59	0.86	272	36.8	38.2	3.82	[45]
$Cu_2ZnSnSe_4$	0.83	1.15	359	20.7	43.0	3.2	[46]
$Cu_2ZnSnSe_4$	0.86	1.15	377	37.4	64.9	9.15	[16]
$Cu_2ZnSnSe_4$	0.81	1.12	308	23.8	50.0	4.4	[47]
$Cu_2ZnSnSe_4$	0.80	1.60	355	9.75	60.0	2.1	[48]
$Cu_2ZnSnSe_4$	0.80		170	21.9	28.8	1.04	[49]
$Cu_2ZnSnSe_4$			710	14.33	74.11	7.54	[42]
$Cu_2ZnSnSe_4$	0.7	1.0	408	38.9	61.4	9.7	[17]
$Cu_2ZnSn(S,Se)_4$	0.925	1.0	622	15.87	60.0	5.9	[50]
$Cu_2ZnSn(S,Se)_4$	0.79	1.11	420	30.4	52.7	7.2	[51]
$Cu_2ZnSn(S,Se)_4$	0.9	1.1	497	20	0	5.4	[52]
$Cu_2ZnSn(S,Se)_4$	0.8	1.22	562.7	24.07	60.0	8.13	[53]
$Cu_2ZnSn(S,Se)_4$	0.80		230	2.47	40.2	0.22	[49]
$Cu_2ZnSn(S,Se)_4$			700	17.29	72.96	8.83	[42]
$Cu_2ZnSn(S,Se)_4$	0.77	1.20	451	−29.0	64.9	8.5	[54]
$Cu_2ZnSn(S,Se)_4$	0.76	1.17	424	−22.7	62.2	6.0	[54]
$Cu_2ZnSn(S,Se)_4$	0.94	1.08	389	−15.7	33.0	2.0	[54]
$Cu_2ZnSn(S,Se)_4$	0.85	1.24	404	29.5	62.8	7.5	[55]
$Cu_2ZnSn(S,Se)_4$	0.8	1.2	409	32.25	61	8.08	[56]
$Cu_2ZnSn(S,Se)_4$	0.8	1.2	516	28.6	65.0	9.66	[57]
$Cu_2ZnSn(S,Se)_4$	0.8	1.2	517	30.8	63.7	10.1	[58]
$Cu_2ZnSn(S,Se)_4$			459.8	34.5	69.8	11.1	[14]
$Cu_2ZnSn(S,Se)_4$	0.8	1.1	513.4	35.2	69.8	12.6	[15]

3.1.3 *Characteristics of Cu_2ZnSnS_4-Based Solar Cells*

Table 3.1 lists the reported CZTS, CZTSe, and CZTSSe solar cell performance since 2005. One obvious character is that most of the cells are non-stoichiometric, i.e., the ideal ratio of Cu, Zn, Sn, and S (or Se) element is 2:1:1:4, i.e., the ratio Cu/(Zn + Sn) = 1, Zn/Sn = 1, and (Cu + Zn + Sn)/S = 1; however, as listed in Table 3.1, the deviation of the Cu/(Zn + Sn) and Zn/Sn ratios are common in CZTS, CZTSe, and CZTSSe solar cells and can be as large as 30 and 20 %, respectively. In Fig. 3.2, the distribution of Cu/(Zn + Sn) and Zn/Sn ratios for solar cells with different efficiencies is plotted [19]. Obviously, most of the solar cells have Cu/(Zn + Sn) ratio between 0.75 and 1, and Zn/Sn ratio between 1 and 1.25, and most of the cells with efficiencies higher than 8 % have these two ratios around 0.8 and 1.2, respectively. This is mentioned frequently as an empirical rule that the Cu-poor and Zn-rich growth condition gives the highest solar cell efficiency [11, 20].

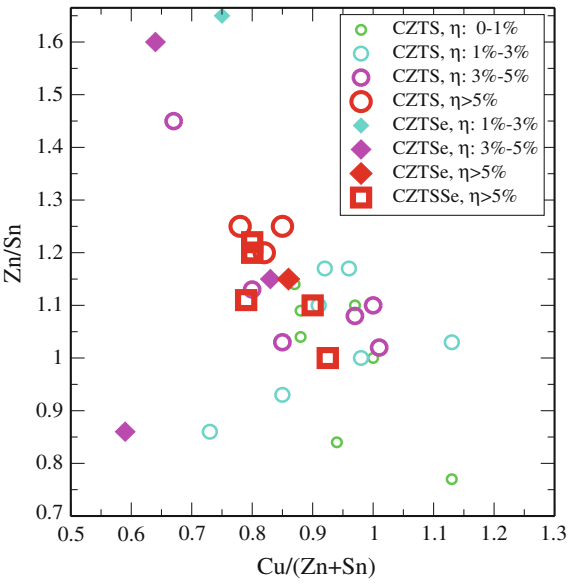

Fig. 3.2 The plot of the Cu/(Zn + Sn) and Zn/Sn element ratio distribution of the Cu_2ZnSnS_4, $Cu_2ZnSnSe_4$, and $Cu_2ZnSn(S,Se)_4$ solar cells with different efficiencies. Adapted from Ref. [19]

3.2 Crystal Structure

3.2.1 II–VI to I–III–VI_2 to I_2–II–IV–VI_4 Structure Mutation

II–VI binary semiconductors (such as ZnS or CdS) crystalize usually in zincblende (Fig. 3.3a) or wurtzite (Fig. 3.4a) structures. When the group II cations are replaced by the group I and III cations, the derived I–III–VI_2 ternary semiconductors keep the structural framework, i.e., the group VI anion sites are not changed, but the group II cation sites are occupied by the group I and III cations.

The occupation of I and III cations (replacement of II by I and III) is not random, but ordered. For example, when ZnS mutates into $CuGaS_2$, the Cu^+ and Ga^{3+} cations are ordered on the original Zn^{2+} sublattice. This order obeys the octet rule, which states that the S anions should be coordinated by the Cu (in +1 valence state) and Ga (in +3 valence state) cations in a way that makes all S anions in eight-electron full-shell state (in −2 valence state), so the local charge neutrality is satisfied around all S anions.

Obeying this octet rule, the binary II–VI zincblende structure mutates into two ternary I–III–VI_2 structures which has an 8-atom primitive cell: The first is the chalcopyrite structure (space group: I-42d, shown in Fig. 3.3b), and the other is the CuAu-like structure (shown in Fig. 3.3c). In both structures, the group VI (S) anions are surrounded by two group I and two group III cations; thus, the local charge neutrality is always satisfied. For $CuGaS_2$ and other I–III–VI_2

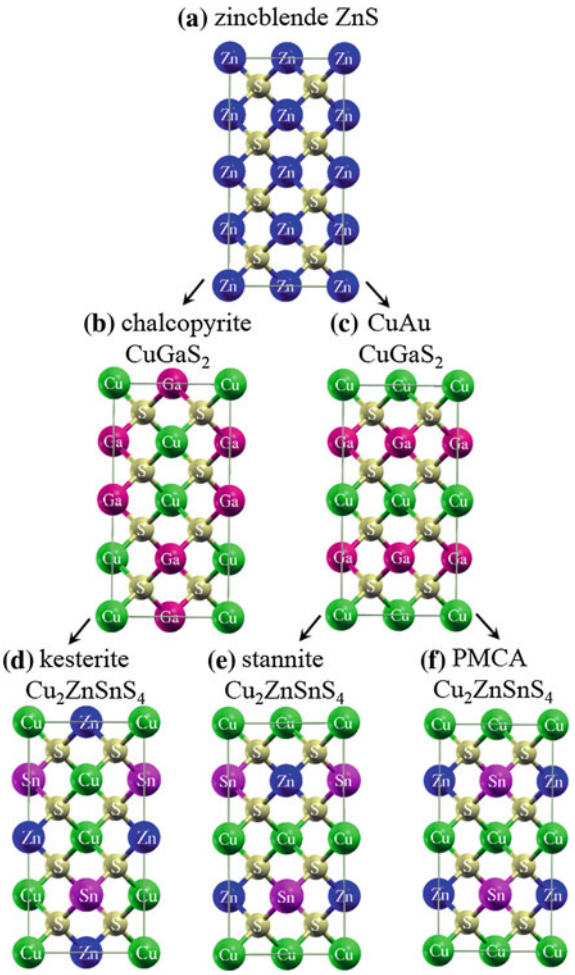

Fig. 3.3 The crystal structure mutation from zincblende ZnS to chalcopyrite $CuGaS_2$ and CuAu-like $CuGaS_2$, then to kesterite Cu_2ZnSnS_4, stannite Cu_2ZnSnS_4, and PMCA–Cu_2ZnSnS_4

semiconductors, the chalcopyrite structure is more stable than CuAu-like structure and thus the ground-state structure of these semiconductors such as $CuInS_2$, $CuInSe_2$, and $CuGaSe_2$.

When I–III–VI_2 ($CuGaS_2$) further mutates into I_2–II–IV–VI_4 (Cu_2ZnSnS_4) with two group III cations (Ga) replaced by group II (Zn) and IV (Sn) cations, the chalcopyrite and CuAu-like structures mutate into three quaternary structures with the smallest 8-atom primitive cell, as schematically plotted in Fig. 3.3. Obeying the octet rule, there is only one possible configuration for the replacement of two Ga by one Zn and one Sn in the chalcopyrite structure, which leads to the quaternary kesterite structure (space group I-4) as shown in Fig. 3.3d. In contrast, there are two possible configurations for the same replacement in the CuAu-like structures, one leading to the stannite structure (I-42 m) as shown in Fig. 3.3e and the other leading to the PMCA structure (P-42 m) as shown in Fig. 3.3f.

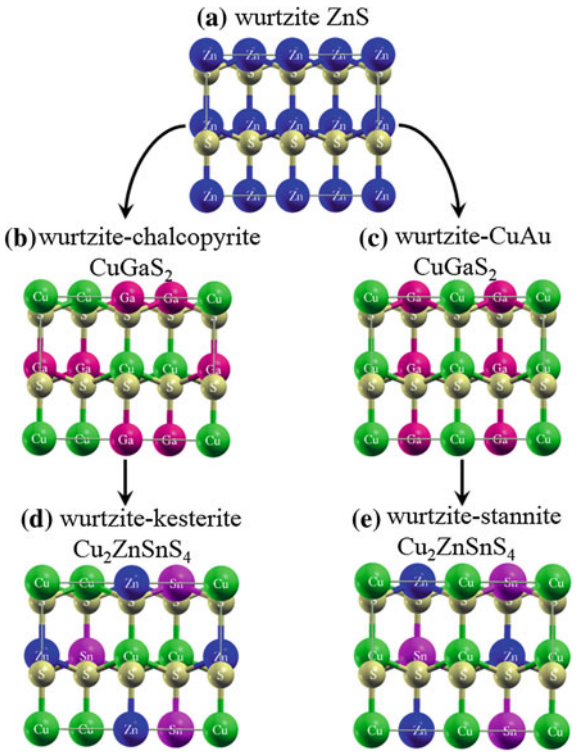

Fig. 3.4 The crystal structure mutation from wurtzite ZnS to chalcopyrite $CuGaS_2$ and CuAu $CuGaS_2$, then to wurtzite-kesterite Cu_2ZnSnS_4 and stannite Cu_2ZnSnS_4

Similar to the mutation in the zincblende structure, the mutation in the binary wurtzite structure also leads to ternary and quaternary structures, which is schematically plotted in Fig. 3.4. Starting from the II–VI wurtzite structure (Fig. 3.4a), two I–III–VI_2 structures and two I_2–II–IV–VI_4 structures are derived. Based on the relationship of wurtzite-derived and zincblende-derived structures, the two I–III–VI_2 wurtzite-derived structures are named wurtzite-chalcopyrite (Fig. 3.4b) and wurtzite-CuAu (Fig. 3.4c), respectively, and the two I_2–II–IV–VI_4 structures are named wurtzite-kesterite (space group Pmn21, Fig. 3.4d) and wurtzite-stannite (Pc, Fig. 3.4e), respectively [59].

3.2.2 *Energetic Stability of Different Quaternary Structures*

Although all these derived quaternary structures, including kesterite, stannite, PMCA, wurtzite-kesterite, and wurtzite-stannite, obey the octet rule and thus are more stable than other structures violating the octet rule, there is still difference in the energetic stability of these structures. First principle calculations based on the density functional theory had shown that Cu_2ZnSnS_4, $Cu_2ZnSnSe_4$, Cu_2ZnGeS_4,

and $Cu_2ZnGeSe_4$ crystalize in zincblende-derived kesterite structure as the ground state, and the stannite, PMCA, or wurtzite-derived structures have higher energy (by several meV/atom) [59]. This indicates that the synthesized samples should crystallize mainly in the kesterite structure. Previously, $Cu_2ZnSnSe_4$ and $Cu_2ZnGeSe_4$ had been reported to crystalize in the stannite structure according to the X-ray diffraction measurement [5, 6, 62, 63], which is in contrast with the theoretically predicted ground-state structure. The reason for this inconsistence will be discussed in Sect. 3.2.3.

When the group I, II, IV, or VI elements change, other structures may become the ground state of I_2–II–IV–VI_4 compounds. For example, Cu_2CdSnS_4 takes stannite structure as the ground state, while Ag_2CdSiS_4, Ag_2CdGeS_4, and Ag_2CdSnS_4 take wurtzite-kesterite structure as the ground state. The relative energy differences between stannite and kesterite and that between low-energy wurtzite-derived structure (kesterite or stannite) and wurtzite-derived structure (wurtzite-kesterite or wurtzite-stannite) for different I_2–II–IV–S_4 are plotted in Fig. 3.5. The energy differences show two general trends: (i) When the size difference in different cations is small, the compound is more stable in kesterite (or wurtzite-kesterite) than stannite (wurtzite-stannite); (ii) when the cations or anions are more ionic, the wurtzite-derived structures become more stable relative to the zincblende-derived structures.

Although the wurtzite-kesterite or wurtzite-stannite structures are not the ground-state structure of Cu_2ZnSnS_4 or $Cu_2ZnSnSe_4$ from the thermodynamic point of view, these metastable phases can still be synthesized given proper kinetic

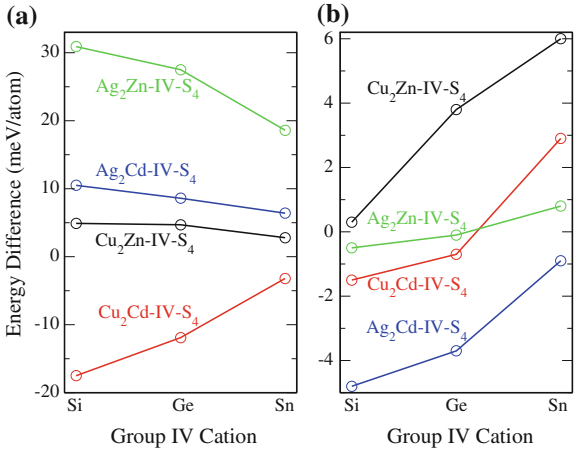

Fig. 3.5 Energy difference **a** between stannite and kesterite, and **b** between low-energy wurtzite-derived structure (kesterite or stannite) and wurtzite-derived structure (wurtzite-kesterite or wurtzite-stannite) of I_2–II–VI–S_4 as the group-IV cations change from Si to Ge to Sn. Adapted from Ref. [59]

control, for example, they can be stabilized in nanocrystal samples [64–67]. Based on the X-ray diffraction pattern, these samples have wurtzite-derived structural framework, but the exact occupation of Cu, Zn, and Sn on the cation sublattice cannot be exactly determined so far, and therefore, it is not clear which wurtzite-derived structure (wurtzite-kesterite, wurtzite-stannite, or other low-energy structures) is dominant in the samples.

3.2.3 *Partial Disorder in Kesterite Structure and Structural Confusion*

As discussed above, kesterite, stannite, and PMCA are three low-energy structures that obey the octet rule and also have only 8 atoms in the primitive cell. If the size of the primitive cell is increased, more structures can be found and they can be considered as the superstructure (mixed structure) of the fundamental kesterite, stannite, and PMCA structures. In Fig. 3.6a, the 16-atom conventional cell of the kesterite structure is plotted. There are four inequivalent (001) layers of cations, /Cu + Zn/Cu + Sn/Zn + Cu/Sn + Cu/ in the order from bottom to top. If we exchange the occupation of Zn and Cu cations in the third layer, leading to /Cu + Zn/Cu + Sn/Cu + Zn/Sn + Cu/, the energy cost is very small, less than one meV/atom, much smaller than the energy difference ($\sim$3 meV/atom) between stannite and kesterite. Considering the small energy cost, the exchange of Cu and Zn cations in (001) layers is thermodynamically inevitable under the growth temperature (which is usually much higher than room temperature), so it is highly possible that the synthesized samples have partially disordered kesterite structure, in which Cu and Zn cations are disordered in the (001) layers, as shown in Fig. 3.6b.

When the Cu and Zn cations are disordered in (001) layers, the symmetry of the partially disordered kesterite structure becomes equivalent to that of the stannite structure, i.e., the disordered Cu/Zn sites become one-element type (we can call it M), then the partially disordered kesterite Cu_2ZnSnS_4 become stannite M_2CuSnS_4. On the other hand, the atomic numbers of Cu and Zn are neighboring, so in the X-ray diffraction measurements, the partially disordered kesterite structure and the stannite structure cannot be distinguished. Early experimental study claimed that the synthesized $Cu_2ZnSnSe_4$ and $Cu_2ZnGeSe_4$ samples were in stannite structure, which we believe should be a confusion between the partially disordered kesterite and stannite structures. Recent neutron scattering experiments by Schorr et al. and synchrotron radiation X-ray diffraction measurement by Washio et al. both confirmed the existence of the Cu/Zn partial disorder in Cu_2ZnSnS_4 and $Cu_2ZnSnSe_4$ [68–70]. The partial disorder is an important character of the quaternary compound semiconductors, at variance to the binary or ternary ones. It is currently not well understood how the partial disorder of the cations influence the photovoltaic performance of the quaternary semiconductors.

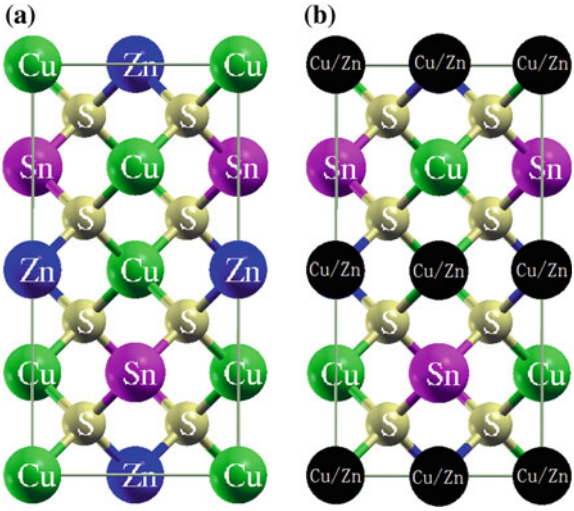

Fig. 3.6 The crystal structure plot of **a** fully ordered kesterite Cu_2ZnSnS_4, and **b** Cu/Zn partially disordered kesterite Cu_2ZnSnS_4. In (**b**) the Cu/Zn-disordered occupation exists only in alternative (001) cation layers, so the symmetry of lattice becomes equivalent to that of the stannite structure

3.3 Electronic Band Structure

3.3.1 Band Structure and Band Gap

Since the crystal structure of Cu_2ZnSnS_4 and $Cu_2ZnSnSe_4$ can be derived from ZnS, ZnSe, $CuGaSe_2$, and $CuInSe_2$, the electronic band structure of Cu_2ZnSnS_4 and $Cu_2ZnSnSe_4$ inherits the direct band gap of the parent binary and ternary semiconductors. In Fig. 3.7, the calculated band structure using the hybrid exchange-correlation functional (HSE) is plotted, where a 1.5-eV direct band gap opens at Γ point. The band structure of $Cu_2ZnSnSe_4$ is similar to that of Cu_2ZnSnS_4, but the band gap size is smaller, at 1.0 eV [60]. In early literature, the band gap of $Cu_2ZnSnSe_4$ had been reported to be around 1.5 eV, close to that of Cu_2ZnSnS_4 [71–73]. Our DFT calculations at the level of the local density approximation (LDA) or generalized gradient approximation (GGA) clearly showed that the gap of the selenide should be about 0.5 eV smaller than that of the sulfide. Calculations using hybrid functionals (e.g., HSE [74]) mixed with Hartree-Fock exchange or at the level of many-body perturbation theory (e.g., GW [75]) also confirmed that the band gap of $Cu_2ZnSnSe_4$ should be around 1.0, 0.5 eV smaller than that of Cu_2ZnSnS_4 at 1.5 eV, which is in good agreement with the photoluminescence spectrum and optical absorption spectrum measurements on high-quality samples [16, 76–78].

In Table 3.2, the calculated lattice parameters, relative energy difference, and band gaps are listed for Cu_2ZnSnS_4 and $Cu_2ZnSnSe_4$. The most stable kesterite structure has the largest band gap among the three structures. For Cu_2ZnSnS_4, the stannite and PMCA structures have gaps about 0.12 eV smaller than kesterite structure, and for $Cu_2ZnSnSe_4$, the difference is about 0.15 eV. This difference is

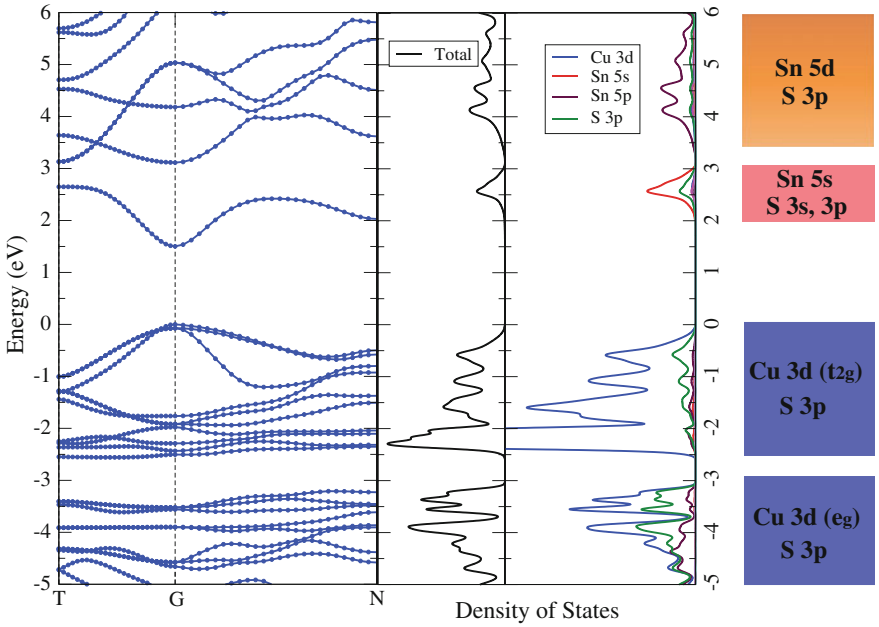

Fig. 3.7 The calculated band structure, total and partial density of states, and the schematic plot of the band component for kesterite Cu_2ZnSnS_4. Adapted from Ref. [79]

determined by the different symmetry of the kesterite and stannite (PMCA) lattice [61]. When the Cu/Zn becomes partially disordered as shown in Fig. 3.6b, the band gap is decreased slightly by 0.04 eV, so the band gap of the partially disordered structure is intermediate between those of kesterite and stannite.

3.3.2 Band Alignment

Relative to ZnS which has a large band gap 3.78 eV, Cu_2ZnSnS_4 has a much smaller band gap 1.5 eV. There is a difference around 2.3 eV, which is contributed by two parts, the valence and conduction band offsets. The calculated band alignment in Fig. 3.8 showed as follows: (i) There is a large valence band offset around 1.1 eV between ZnS- and the Cu-based chalcogenides, as shown in Fig. 3.8a for $ZnS/CuGaS_2$. In Cu-based chalcogenides, the top of valence bands is mainly composed of the antibonding states of Cu-3d/S-3p (or Se-4p) orbitals [80, 81], and Cu-3d states are very shallow (high in eigenenergy and low in binding energy), so the valence band maximum state is pushed up significantly relative to that of ZnS, which explains the large valence band offset. The band component at the top of the valence band is similar for $CuGaS_2$ and Cu_2ZnSnS_4, so the similarly large valence band offset also exist between ZnS/Cu_2ZnSnS_4, which contributes to half of the band

Table 3.2 Calculated lattice constant a, c/2a ratio, energy difference per atom relative to the lowest-energy structure, and direct band gap corrected according to HSE06 calculation

Structure	a (Å)	c/2a	ΔE (meV)	Gap (eV)
Cu_2ZnSnS_4				
Kesterite	5.467	0.999	0	1.50
Stannite	5.458	1.004	2.86	1.38
PMCA	5.459	1.005	3.15	1.35
$Cu_2ZnSnSe_4$				
Kesterite	5.763	0.998	0	0.96
Stannite	5.762	1.000	3.79	0.82
PMCA	5.753	1.004	5.53	0.79

Adapted from Ref. [60]

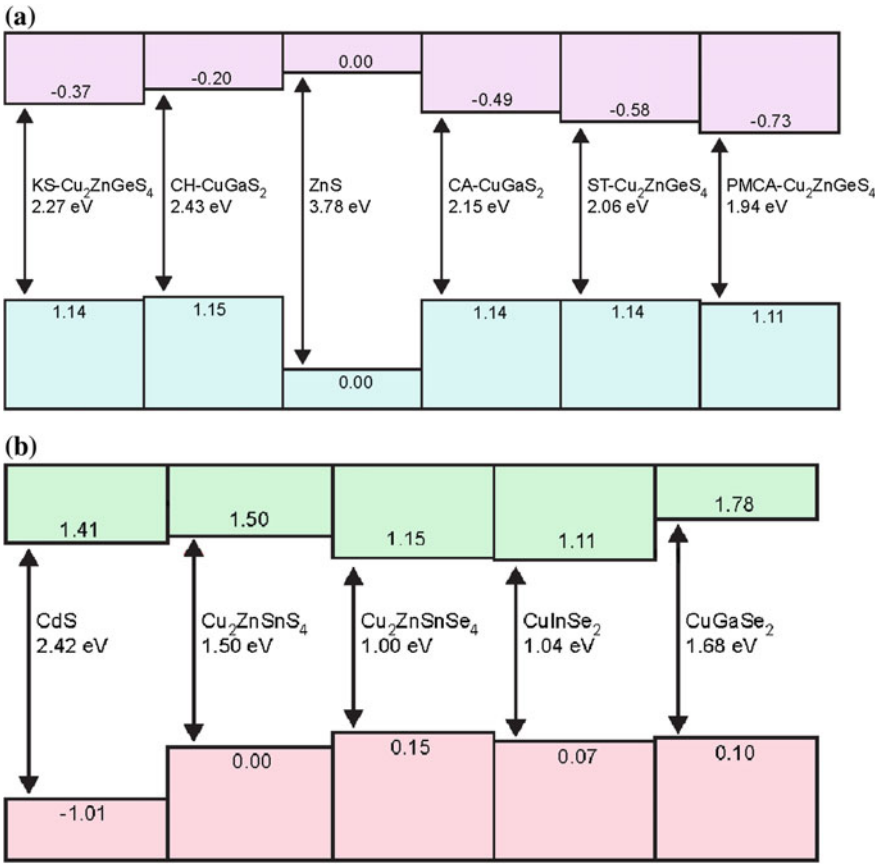

Fig. 3.8 The calculated band alignment for different binary, ternary, and quaternary chalcogenide semiconductors (calculations were performed using the GGA functional, with the spin–orbital interaction considered). Adapted from Ref. [61, 83]

gap decrease. (ii) There is also a large conduction band offset between ZnS- and Ga-, Ge- or Sn-based chalcogenides. In ZnS, $CuGaS_2$, Cu_2ZnGeS_2, and Cu_2ZnSnS_4, the conduction band minimum (CBM) state is mainly the antibonding state of the hybridization between Zn-4s (Ga-4s, Ge-4s, and Sn-5s in order)/S-3s. The Zn-4s, Ga-4s, Ge-4s, and Sn-5s levels shift down in order, so the CBM level also shifts down in order. On the other hand, Sn has a much larger size than Zn, which also weakens the hybridization between Sn-5s/S-3s and shifts down the CBM level.

Based on the similar band component (hybridization) picture, the band gap difference between Cu_2ZnSnS_4 and $Cu_2ZnSnSe_4$ can also be understood. As shown in Fig. 3.8b, the valence band of $Cu_2ZnSnSe_4$ is shifted up relative to that of Cu_2ZnSnS_4, because the 4p level of Se is higher in energy than the 3p level of S; thus, the VBM of the selenides is higher than that of the sulfides; for example, the VBM is 0.52 eV higher for ZnSe than ZnS [82]. On the other hand, the Cu-3d/Se-4p hybridization is weaker than Cu-3d/S-3p as a result of the longer Cu–Se bond than Cu–S bond, so the shiftup of the antibonding VBM level in the selenide is not as large as that in the sulfide. As a result, the valence band offset between $Cu_2ZnSnSe_4$/Cu_2ZnSnS_4 is less than that between ZnSe/ZnS. On the conduction band side, the longer bond length of Sn–Se than Sn–S weakens the Sn-5s/Se-4s hybridization, so the antibonding state of $Cu_2ZnSnSe_4$ is shifted down relative to that of Cu_2ZnSnS_4 [83]. It should be noted that the exact values of the conduction and valence band offsets between Cu_2ZnSnS_4/$Cu_2ZnSnSe_4$ have not been well determined in experiments [84–86], although theoretically calculated values are given in Fig. 3.3b [83, 87].

With the band component analysis, we can predict the band gap change when different group of elements in I_2–II–IV–VI_4 semiconductors are changed:

I: Cu → Ag gap increases,
II: Zn → Cd gap decreases,
III: Si → Ge → Sn gap decreases, and
VI: S → Se → Te gap decreases.

3.3.3 *Band Gap Dependence of $Cu_2ZnSn(S,Se)_4$ and $Cu_2Zn(Ge,Sn)Se_4$ Alloys*

According to the predicted band gap change with the component elements, we can tune the band gap of Cu_2ZnSnS_4 or $Cu_2ZnSnSe_4$ by alloying it with different elements, e.g., tuning the gap from 1.5 to 1.0 eV through $Cu_2ZnSn(S,Se)_4$ alloys, from 1.5 to 2.2 eV through $Cu_2Zn(Ge,Sn)S_4$ alloys, and from 1.0 to 1.5 eV through $Cu_2Zn(Ge,Sn)Se_4$ alloys. High-efficiency solar cells have been fabricated based on $Cu_2ZnSn(S,Se)_4$ and $Cu_2Zn(Ge,Sn)Se_4$ alloys, whose band gaps are both close to the optimal band gap for single-junction solar cells. Although we know that the band gap changes with the alloy composition, S/Se and Ge/Sn ratios, it is unknown how it changes with the composition, linearly or nonlinearly.

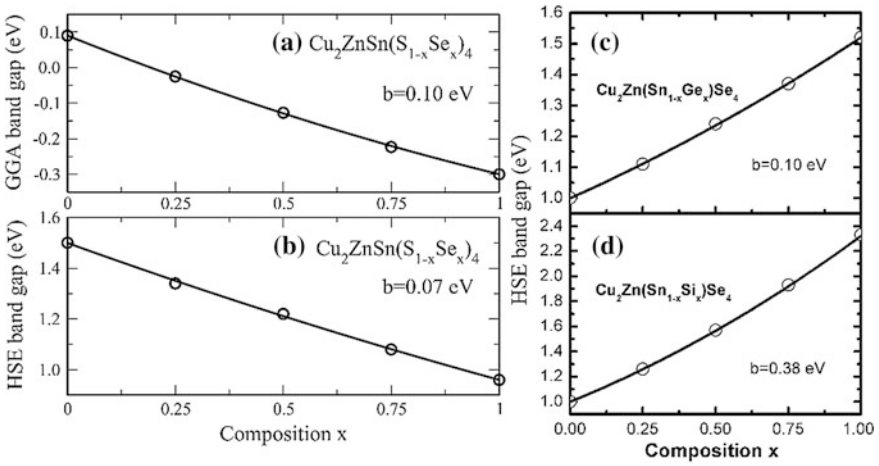

Fig. 3.9 The calculated band gap of $Cu_2ZnSn(S_{1-x}Se_x)_4$ alloys using **a** GGA functional and **b** HSE functional, and of **c** $Cu_2Zn(Ge_{1-x}Sn_x)Se_4$ and **d** $Cu_2Zn(Si_{1-x}Sn_x)Se_4$ alloys at different compositions x. Adapted from Ref. [83, 88]

In Fig. 3.9, the calculated band gap dependence on the composition parameter is plotted for $Cu_2ZnSn(S,Se)_4$, $Cu_2Zn(Si,Sn)Se_4$, and $Cu_2Zn(Ge,Sn)Se_4$ alloys. Obviously, no matter which approximation to the exchange-correlation functional is used, the band gap changes almost linearly with the composition parameter x, i.e., the band gap bowing parameters of these alloys are small, especially for $Cu_2ZnSn(S,Se)_4$ and $Cu_2Zn(Ge,Sn)Se_4$ alloys whose bowing parameters are less than 0.10 eV. Experimentally, linear band gap dependence had also been found in the measured band gaps of $Cu_2ZnSn(S,Se)_4$ alloys [89, 90].

Beside the linear band gap dependence, another interesting property of $Cu_2ZnSn(S,Se)_4$ and $Cu_2Zn(Ge,Sn)Se_4$ alloys is that they have a very small interaction parameter and thus very good miscibility [83, 91]. The alloys with different composition can be synthesized with good component uniformity, and the miscibility temperature is less than 300 K. In contrast, the $Cu_2Zn(Si,Sn)Se_4$ have larger interaction parameter and thus worse miscibility, because of the larger chemical and size difference between Si and Sn than between Ge and Sn; therefore, it is relatively difficult to tune the band gap of $Cu_2Zn(Si,Sn)Se_4$ alloys continuously from 1.0 to 2.4 eV.

3.4 Thermodynamic Stability and Secondary Phases

3.4.1 Stable Region in Chemical Potential Space

Since there are more component elements in Cu_2ZnSnS_4, $Cu_2ZnSnSe_4$ and related quaternary semiconductors, these elements can also form other compounds, e.g., binary or ternary compounds. Experiments have found the coexistence of secondary

phases, such as ZnS, Cu_2SnS_3 (ZnSe, Cu_2SnSe_3), in Cu_2ZnSnS_4 ($Cu_2ZnSnSe_4$) thin films, which cause non-stoichiometry and compositional non-uniformity. Therefore, it is much more difficult to prepare high-quality single-crystal samples of quaternary semiconductors [11, 92, 93].

To study quantitatively the phase competition between the binary, ternary, and quaternary compounds, we can use the elemental chemical potentials to describe the richness of different elements in the synthesis environment. Then under a certain chemical potential condition, one compound is more stable than other competing compounds thermodynamically, so we can plot the stable chemical potential region for different compounds in the chemical potential space, as shown in Fig. 3.10.

The detailed process for plotting the stable chemical potential region of $Cu_2ZnSnSe_4$ is given here as an example (more details are given in Ref. [94–96]): (i) The chemical potential μ_i is defined to describe the richness of the element *i*, and

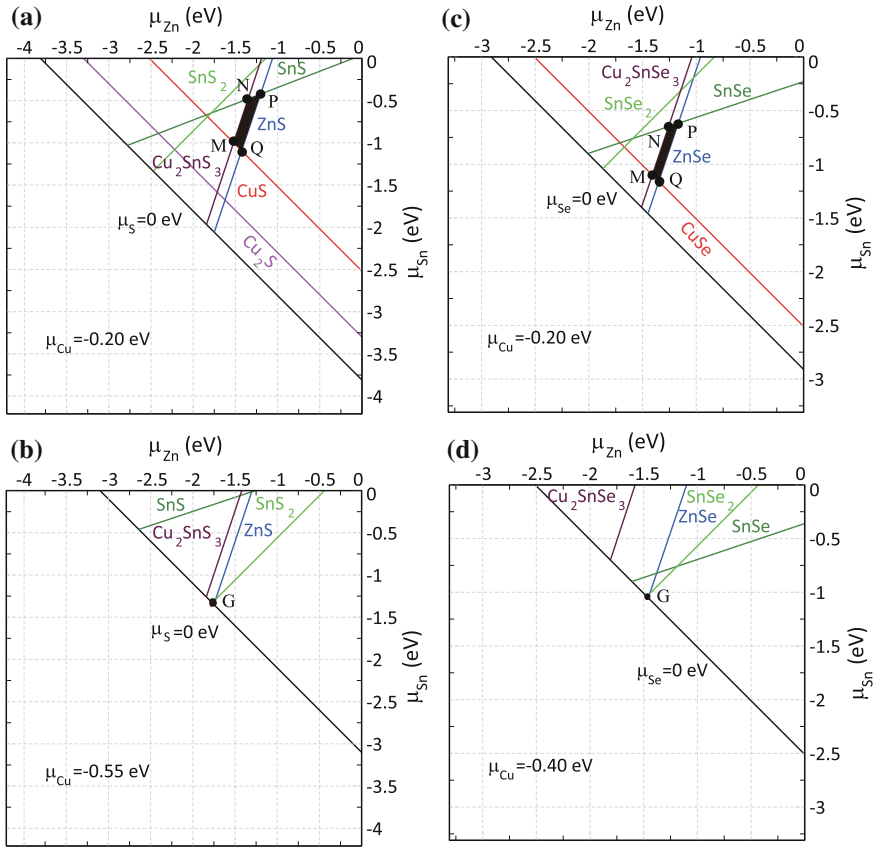

Fig. 3.10 The calculated chemical potential stable region of Cu_2ZnSnS_4 and $Cu_2ZnSnSe_4$ in the μ_{Cu} = −0.20 and −0.55 eV planes (the *black area* and *points* show the stable region). Adapted from Ref. [79]

$\mu_i = 0$ means the element is so rich that their pure solid phase can form; (ii) because pure Cu, Zn, Sn metals, and Se bulk should not be avoided in the synthesized samples, it is required that $\mu_{Cu} < 0$, $\mu_{Zn} < 0$, $\mu_{Sn} < 0$, $\mu_{Se} < 0$; and (iii) the coexistence of secondary phases such as CuSe, ZnSe, SnSe, and Cu_2SnSe_3 should be avoided too; thus the following relations must be satisfied:

$$\begin{aligned}
\mu_{Cu} + \mu_{Se} &< \Delta H_f(CuSe) \\
2\mu_{Cu} + \mu_{Se} &< \Delta H_f(Cu_2Se) \\
\mu_{Zn} + \mu_{Se} &< \Delta H_f(ZnSe) \\
\mu_{Sn} + \mu_{Se} &< \Delta H_f(SnSe) \\
\mu_{Sn} + 2\mu_{Se} &< \Delta H_f(SnSe_2) \\
2\mu_{Cu} + \mu_{Sn} + 3\mu_{Se} &< \Delta H_f(Cu_2SnSe_3)
\end{aligned}$$

where ΔH_f means the calculated formation energy of the compounds. Since the Cu_2ZnSnS_4 crystal should be stable under thermodynamic equilibrium, the chemical potential of Cu, Zn, Sn, and Se must satisfy the following equation:

$$2\mu_{Cu} + \mu_{Zn} + \mu_{Sn} + 4\mu_{Se} = \Delta H_f(Cu_2ZnSnSe_4)$$

With this equation, only three of the four chemical potentials are independent; i.e., μ_{Se} is dependent on μ_{Cu}, μ_{Zn}, and μ_{Sn}. Under these constraints, the chemical potential range of Cu, Zn, and Sn that stabilizes CZTSe is bound in a polyhedron in the three-dimensional (μ_{Cu}, μ_{Zn} and μ_{Sn}) space. In Fig. 3.8, the slices of the polyhedron in two planes are plotted.

Obviously, the stable regions of Cu_2ZnSnS_4 and $Cu_2ZnSnSe_4$ are both narrow. A deviation from the stable region will cause the coexistence of CuSe, ZnSe, SnSe, or Cu_2SnSe_3 (similarly for sulfides). This indicates that the chemical potential control is very important for growing good-quality single crystals.

The region of μ_{Zn} is extremely narrow, because of the strict limit imposed by ZnS and Cu_2SnS_3. In fact, the energy cost of the phase-separation reaction from Cu_2ZnSnS_4 to ZnS and Cu_2SnS_3 is small. Therefore, the control of Zn richness is critical for growing electronic-quality Cu_2ZnSnS_4 crystals, i.e., too rich Zn leads to ZnS while too poor Zn leads to Cu_2SnS_3. Experimental detection of ZnS, ZnSe, Cu_2SnS_3, and Cu_2SnSe_3 secondary phases have been reported [41, 52, 97], which is consistent with the calculated narrow region in the chemical potential space.

3.4.2 Structural Similarity of Secondary Phases

Among the possible secondary compounds, Cu_2S, CuS, SnS, SnS_2, etc., have crystal structures that are significantly different from the zincblende-derived structures, so it is easy to detect the coexistence of these compounds using the standard X-ray diffraction technique. However, it is more challenging to detect ZnS,

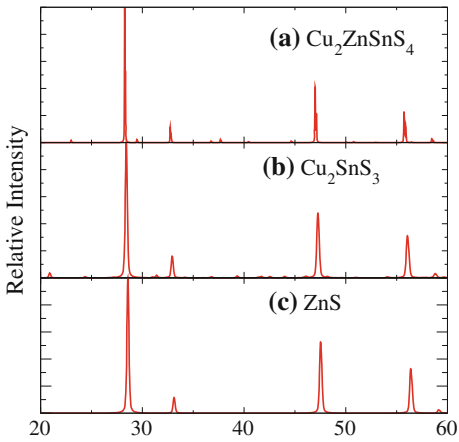

Fig. 3.11 Simulated X-ray (Cu Kα source, $\lambda = 0.15406$ nm) diffraction patterns of kesterite Cu_2ZnSnS_4, Cu_2SnS_3 with the Cc space group and zincblende ZnS. Adapted from Ref. [96]

Cu_2SnS_3, and related non-stoichiometric phases because of the structural similarity. In Fig. 3.11, the simulated X-ray diffraction patterns of Cu_2ZnSnS_4, Cu_2SnS_3, and ZnS are plotted. Obviously, the main peaks and their positions are very similar, which indicates that it is difficult to detect/exclude the coexistence of the secondary and non-stoichiometric phases using the X-ray diffraction technique, especially considering that the quality of thin-film samples are usually poor. Experimentally, Cu_2SnS_3 had been reported to crystalize in many different structures, such as the monoclinic, cubic, and tetragonal phases; however, our recent theoretical study showed that the diverse can all be derived from the zincblende structure with tetrahedral coordination [98]. Therefore, their X-ray diffraction patterns are all similar to that in Fig. 3.11b, which makes the exact characterization of different Cu_2SnS_3 phases also challenging.

3.5 Defect Formation and Ionization

3.5.1 Defect Formation Energy

As the number of component elements increases, the chemical and structural freedom of Cu_2ZnSnS_4 and $Cu_2ZnSnSe_4$ increase significantly, which gives birth to a series of intrinsic defects, such as vacancies, antisites, and interstitials, much more than those in binary and ternary semiconductors.

In Fig. 3.12, the calculated formation energies of different defects are plotted as functions of the Fermi energy (0 means that the Fermi energy is at VBM, while 1.5 or 1.0 eV means that Fermi energy is at CBM). The turning points in the plot show the transition energy levels of defects, at which the defects with two different charge states (the slop of the plot shows the charge state, negative when acceptor defects become ionized, and positive when donor defects become ionized) have the same formation energy, so the electrons/holes can be released.

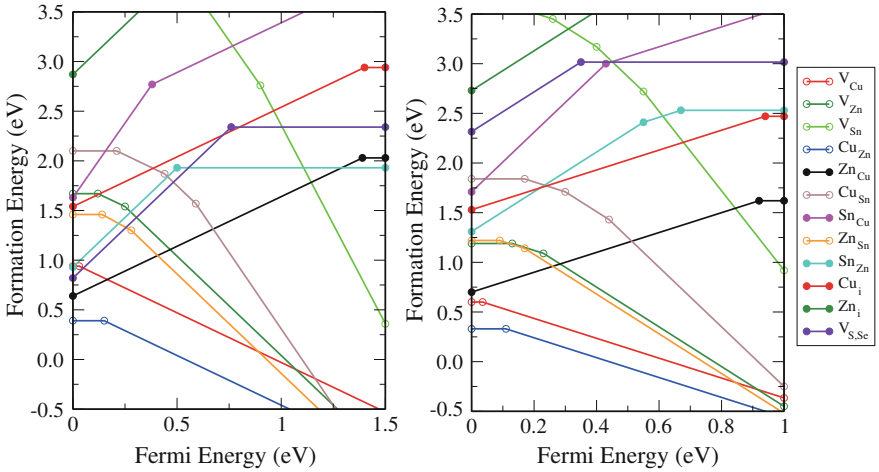

Fig. 3.12 The change in the defect formation energy as a function of the Fermi energy at the chemical potential point A. For each value of the Fermi energy, only the most stable charge state is plotted with the *filled circles* representing a change in charge state (transition energy level). Adapted from Ref. [79]

Obviously, for both CZTS and CZTSe, the Cu_{Zn} antisite defect has the lowest formation energy among all the defects, which means that it is the dominant defect in this quaternary semiconductors and determines the p-type electrical conductivity of samples. This is different from the situation in $CuInSe_2$ or $CuGaSe_2$, where Cu vacancies have lowest formation energy and determines the p-type conductivity. The formation energies of Cu vacancies in $CuInSe_2$, $CuGaSe_2$, Cu_2ZnSnS_4, and $Cu_2ZnSnSe_4$ are comparable [79], but in Cu_2ZnSnS_4 and $Cu_2ZnSnSe_4$, the Cu_{Zn} antisites have lower formation energies than Cu vacancies and thus become dominant.

3.5.2 *Transition Energy Levels*

The transition energy levels of V_{Cu} and Cu_{Zn} are plotted in Fig. 3.13. The (-/0) level of Cu_{Zn} (0.15 eV in CZTS, 0.11 eV in CZTSe) is obviously deeper than that of V_{Cu} (0.01 eV in CZTS, 0.02 eV in CZTSe) [79, 95, 99]. The deeper level of Cu_{Zn} indicates that it is not as benign as V_{Cu} to the photovoltaic performance, and a higher concentration of Cu_{Zn} defects are required to produce a certain amount of hole carriers. This is a negative factor for the CZTS or CZTSe solar cells, which may limit their performance compared to the $CuInSe_2$ or $CuGaSe_2$ solar cells.

Recently, several experimental groups have reported their characterization of the acceptor levels in CZTS and CZTSe. In CZTSSe solar cells with high efficiency and

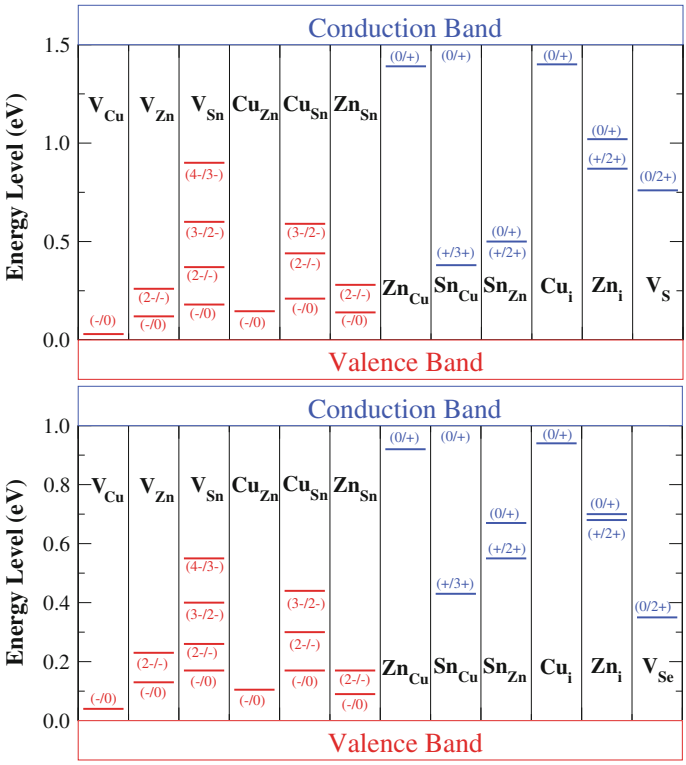

Fig. 3.13 The transition energy levels of different intrinsic defects in the band gaps of Cu_2ZnSnS_4 and $Cu_2ZnSnSe_4$. Adapted from Ref. [79]

band gaps between 1.0 and 1.5 eV, Gunawan et al. observed a dominant acceptor defect with energy level at 0.13–0.2 eV using admittance spectroscopy [100]. This level is close to our calculated Cu_{Zn} (-/0) levels. Using capacitance spectroscopy, Barkhouse et al. observed [58] a dominant defect level at 156 meV in the Cu-poor and Zn-rich CZTSSe solar cells with a 10.1 % efficiency [22]. Fernandes et al. observed [101] two acceptor levels of 45 and 113 meV in Cu_2ZnSnS_4, which are close to our calculated (-/0) levels of V_{Cu} and Cu_{Zn}, respectively. Das et al. observed two dominant deep acceptor levels at 0.12 and 0.32 eV identified as CuZn (-/0) and CuSn (2-/-) antisite defects, respectively [102]. Nagaoka et al. observed [103] an acceptor level at 0.12 eV above VBM, close to the calculated level of Cu_{Zn} too. Through comparing the experimentally observed defect levels to our calculated levels as listed in Fig. 3.13, we may identify possible defects in samples grown under different conditions.

Three donor defects in CZTS also have formation energies lower than 1.0 eV when the samples are p-type and the Fermi energy is close to VBM. They are Zn_{Cu} antisite, S (Se) vacancy, and Sn_{Zn} antisite. Among them, the S vacancy and Sn_{Zn}

antisite produce deep donor levels in the band gap, detrimental to the solar cell performance. In contrast, only Zn_{Cu} which is a shallow donor has low formation energy in CZTSe, as shown in Fig. 3.12. Therefore, the defects in CZTSe are more benign than those in CZTS, which may explain the higher efficiency of CZTSSe solar cells with higher Se content.

Besides isolated acceptor and donor defects, there are a large amount of charge neutral defect clusters in which acceptor and donor defects compensate each other, e.g., V_{Cu} compensated by Zn_{Cu} produces $V_{Cu} + Zn_{Cu}$ defect cluster, two Cu_{Zn} compensated by Sn_{Zn} produce $2Cu_{Zn} + Sn_{Zn}$ defect cluster. Some defect clusters have very high concentration in CZTS and CZTSe, e.g., $Cu_{Zn} + Zn_{Cu}$ (exchange of Cu and Zn sites), $V_{Cu} + Zn_{Cu}$, and $2Cu_{Zn} + Sn_{Zn}$ can have high concentration and even causes non-stoichiometry [19, 104]. The formation of charge neutral defect clusters shifts the valence and conduction band edges, which is shown in Fig. 3.14 (calculated assuming a defect concentration of one defect in a 128-atom supercell). When the conduction (valence) band edge shift is large, the defect cluster may trap the electron (hole) carriers and is detrimental to the solar cell performance, e.g., $2Cu_{Zn} + Sn_{Zn}$. There are also defect clusters which are not charge neutral, e.g., $Cu_{Zn} + Sn_{Zn}$ is a donor defect with a deep level, so it may work as an electron–hole recombination center.

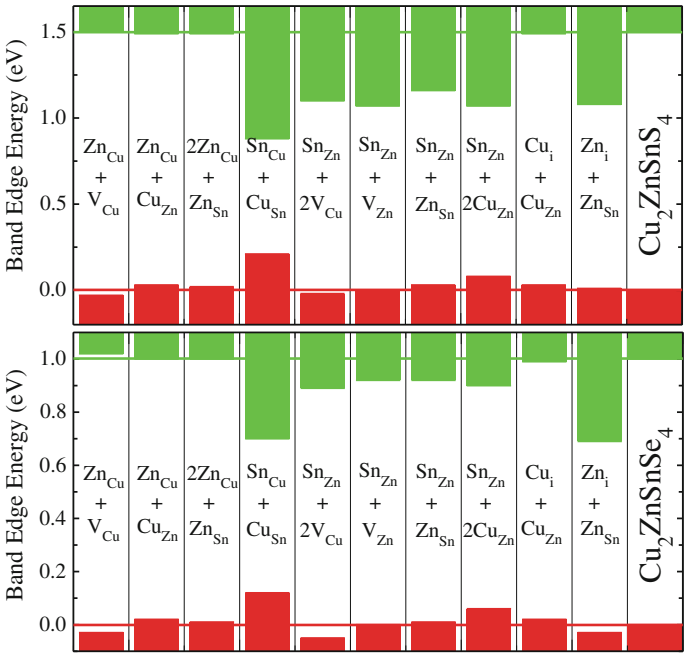

Fig. 3.14 The valence and conduction band shifts caused by different defect clusters in Cu_2ZnSnS_4 (*top panel*) and $Cu_2ZnSnSe_4$ (*bottom panel*). Adapted from Ref. [79]

3.5.3 *Defect and Carrier Concentration*

The formation energies of intrinsic defects also depend on the chemical potential of elements (growth conditions). More detailed discussion can be found in Ref. [79]. To improve the solar cell performance, optimal chemical potential conditions

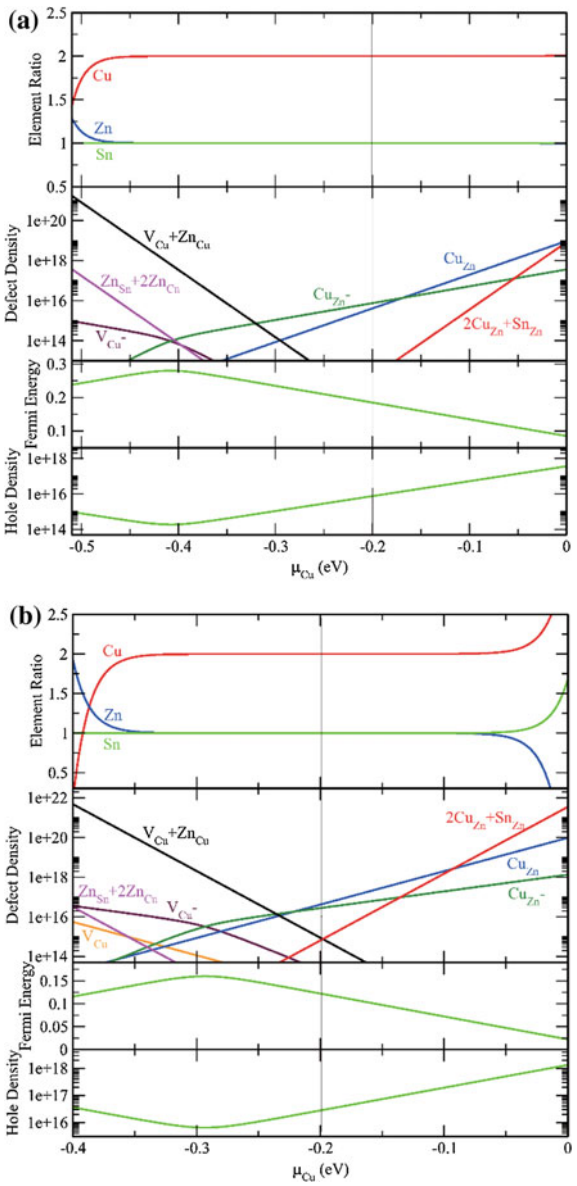

Fig. 3.15 Calculated element ratio, defect density (cm^{-3}), Fermi energy (in eV relative to VBM), and hole density (cm^{-3}) at room temperature as functions of the Cu chemical potential for **a** Cu_2ZnSnS_4 and **b** $Cu_2ZnSnSe_4$. Adapted from Ref. [79]

(Cu poor, Zn rich, and a higher Se content for CZTSSe alloys) should be used to suppress the detrimental defects (Sn_{Zn}, V_S) and defect clusters ($2Cu_{Zn} + Sn_{Zn}$, $Cu_{Zn} + Sn_{Zn}$) and increase the concentration of shallow defect (V_{Cu}) and benign defect clusters ($V_{Cu} + Zn_{Cu}$).

In Fig. 3.15, we calculated the elemental ratio (showing the degree of non-stoichiometry), defect concentration, hole carrier concentration, and Fermi energy as functions of the Cu chemical potential for CZTS and CZTSe. As we can see, when Cu is rich (chemical potential is high) Cu_{Zn} and $2Cu_{Zn} + Sn_{Zn}$ have high concentration. Although high concentration of Cu_{Zn} produces high concentration of hole carriers, high concentration of $2Cu_{Zn} + Sn_{Zn}$ traps the electrons (minority carriers), so the solar cell efficiency under the Cu-rich condition is limited. When Cu becomes poorer, the shallow Cu vacancies become the dominant defects, the concentration of $2Cu_{Zn} + Sn_{Zn}$ drops down dramatically, while the concentration of the benign $Zn_{Sn} + 2Zn_{Cu}$ and $V_{Cu} + Zn_{Cu}$ defect clusters increases to a high level, determining the degree of non-stoichiometry. Obviously, this Cu-poor condition is optimal for fabricating high-efficiency CZTS and CZTSe solar cells. As Cu changes from rich to poor, the hole concentration decreases first (because the concentration of Cu_{Zn} decreases), and then increases (because V_{Cu} becomes dominant and its concentration increases), so there is a minimum hole concentration, on the order of 10^{14} cm^{-3} in CZTS and 10^{15} cm^{-3} in CZTSe. Under the most Cu-poor condition in Fig. 3.15, the hole concentration is on the order of 10^{15} cm^{-3} in CZTS and 10^{16} cm^{-3} in CZTSe. Experimentally, the measured hole concentration in the high-efficiency $Cu_2ZnSn(S,Se)_4$ solar cells is around 5×10^{15} cm^{-3} when Cu/(Zn + Sn) ratio is near 0.8 (Cu poor) [35, 58], which agrees well with our calculated value considering the large margins of error (one or two order of magnitude) in both the experimental and theoretical methods.

3.6 Surfaces

3.6.1 Surface Reconstruction

Surfaces in the thin-film samples play an important role in the separation of photogenerated electron–hole pairs and thus influence the photovoltaic performance. As the synthesized CZTS samples are usually thin films or nanocrystals with high volume/surface ratio, the importance of the surface properties is highlighted. However, the increased number of elements in Cu_2ZnSnS_4 makes it difficult to study the stable surface structure (reconstruction) and surface-induced electronic states, which limits the further improvement of the solar cell performance.

Theoretical calculations [105, 106] and experiments [18, 19] for the ternary $CuInSe_2$ (CISe) told us that the polar (112)/(-1-1-2) surfaces, which are stabilized by charge-compensating defects (V_{Cu}, Cu_{In}, In_{Cu}), are more stable than the non-polar (110)/(-1-10) surfaces. Considering the structural similarity between CISe and CZTSe, one may expect that the polar (112)/(-1-1-2) surfaces are also stable in

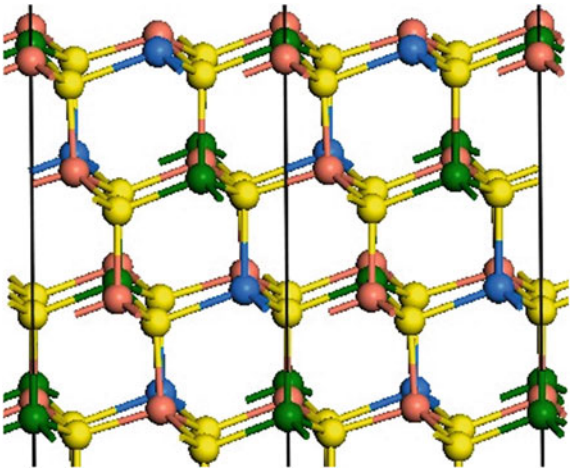

Fig. 3.16 The structures of the cation-terminated (112) (*top*) and anion-terminated (-1-1-2) (*bottom*) surfaces of the kesterite CZTS. The *red*, *green*, *blue,* and *yellow* balls show Cu, Zn, Sn, and S atoms in order. A (2 × 1) surface supercell is shown here. Adapted from Ref. [111]

CZTS. Experiments did find that (112)/(-1-1-2) is the most preferred surface orientation for the CZTS thin films [107–110]; however, the detailed surface reconstruction is unknown.

Similar to the (111)/(-1-1-1) surfaces of the binary zincblende structure, the (112)/(-1-1-2) surfaces of CZTS are terminated by cation/anion layer as shown in Fig. 3.16. Every (112) cation-terminated surface unit cell contains two Cu, one Zn, and one Sn atoms, while every (-1-1-2) S-terminated surface unit cell contains four S atoms. The (112)/(-1-1-2) surfaces belongs to Tasker's type-III polar surfaces [112], so only charge-compensating defects are required to form to stabilize the surfaces.

In Fig. 3.17, we plot the surface reconstruction patterns with different charge-compensating defects formed on the surfaces. According to first principle calculations [111], under Cu-poor and Zn-rich conditions the most stable surface reconstruction patterns for both (112) and (-1-1-2) are with Cu-depleted and Zn-enriched defects. Furthermore, the (-1-1-2) surface is energetically more favorable than (112) surface, so we predict that the anion-terminated (-1-1-2) surfaces have a higher population in the CZTS thin films.

3.6.2 Electronic States of Surfaces

Surfaces will produce electronic states that are different from the electronic states of bulk. When the surface states are beyond the band gap of the bulk, the surfaces have weak influence on the behavior of majority and minority carriers; however, when the surface states fall in the band gap, they may work as the recombination centers

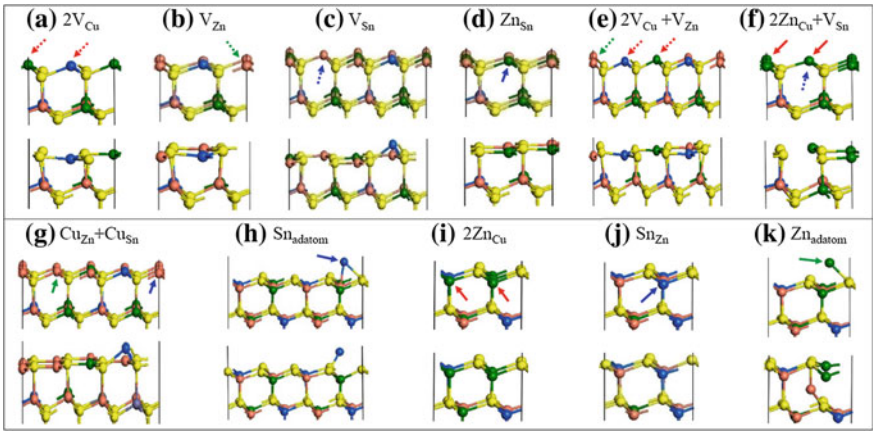

Fig. 3.17 Side view of the kesterite CZTS (112) (**a**)–(**g**) and (-1-1-2) (**h**)–(**k**) surfaces with different surface defects. The *top* and *bottom* parts of each panel show the structures before and after relaxation, respectively. The *arrows* denote the location of the surface defects. Adapted from Ref. [111]

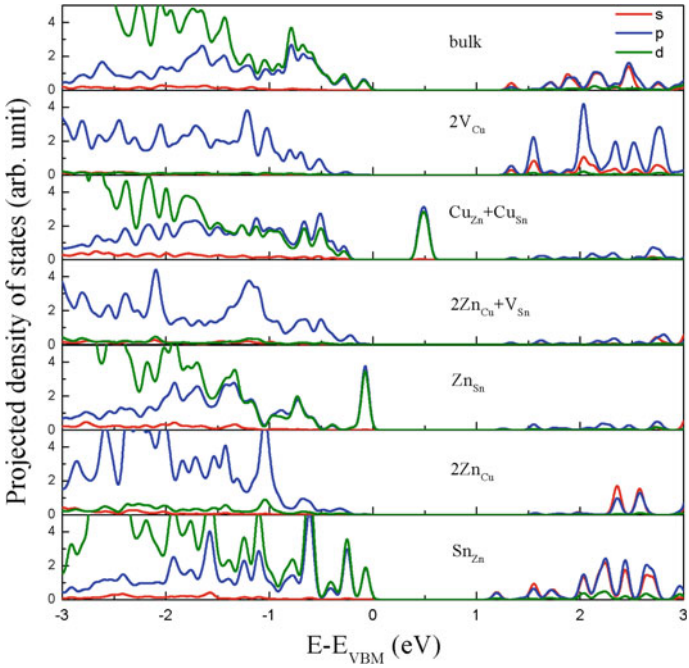

Fig. 3.18 The partial density of states projected on different bilayers of the CZTS slabs with different surface defects. Adapted from Ref. [111]

of electrons and holes. To study the surface states, we plot the calculated partial density of states (PDOS) projected on different bilayers of lowest-energy surfaces in Fig. 3.18.

All the Cu-depleted and Zn-enriched surface defects do not induce valence band edge upshift and conduction band edge downshift, thus producing no states in the gap, so they are benign surfaces. In contrast, the Cu-enriched or Zn-depleted surface defects create deep levels in the band gap, e.g., the electronic energy level of Cu_{Zn} + Cu_{Sn} is in the middle of the band gap and that of Sn_{Zn} is below the conduction band edge of the bulk. These surface defects (surface reconstruction) are detrimental to the solar cell performance. To optimize the influence of surfaces, Cu-poor and Zn-rich conditions should be used for fabricating high-efficiency CZTSSe solar cells, which is consistent with the optimal condition for optimizing the influence of defects.

Acknowledgements I thank Prof. Aron Walsh, Prof. Su-Huai Wei, and Prof. Xin-Gao Gong for their long-term help and inspiring discussion, and Mr. Peng Xu and Mr. Kun Luo for their help in the preparation of this chapter.

References

1. Goodman, C.H.L.: J. Phys. Chem. Solids **6**(4), 305–314 (1958)
2. Hahn, H., Schulze, H.: Naturwissenschaften **52**(14), 426 (1965)
3. Nitsche, R., Sargent, D.F., Wild, P.: J. Cryst. Growth **1**(1), 52–53 (1967)
4. Schleich, D.M., Wold, A.: Mater. Res. Bull. **12**(2), 111–114 (1977)
5. Parasyuk, O.V., Gulay, L.D., Romanyuk, Y.E., Piskach, L.V.: J. Alloy. Compd. **329**(1–2), 202–207 (2001)
6. Parasyuk, O.V., Piskach, L.V., Romanyuk, Y.E., Olekseyuk, I.D., Zaremba, V.I., Pekhnyo, V.I.: J. Alloy. Compd. **397**(1–2), 85–94 (2005)
7. Lee, C., Kim, C.-D.: J. Korean Phys. Soc. **37**, 364 (2000)
8. Schorr, G.W.S., Tovar, M., Sheptyakov, D.: Mater. Res. Soc. Symp. Proc. **1012**, Y03–Y05 (2007)
9. Ito, K., Nakazawa, T.: Jpn. J. Appl. Phys. Part 1 Regul. Pap. Short Notes Rev. Pap. **27**(11), 2094–2097 (1988)
10. H. K. e. al.: In: Presented at the Technical Digest Photovoltaic Science and Engineering Conference-9, Miyazaki (1996) (unpublished)
11. Katagiri, H., Jimbo, K., Maw, W.S., Oishi, K., Yamazaki, M., Araki, H., Takeuchi, A.: Thin Solid Films **517**(7), 2455–2460 (2009)
12. Friedlmeier, N.W.T.M., Walter, T., Dittrich, H., Schock, H.W.: In: Presented at the Proceedings of the 14th European Photovoltaic Solar Energy Conference, Barcelona, Spain (1997) (unpublished)
13. Todorov, T.K., Reuter, K.B., Mitzi, D.B.: Adv. Mater. **22**(20), E156 (2010)
14. Todorov, T.K., Tang, J., Bag, S., Gunawan, O., Gokmen, T., Zhu, Y., Mitzi, D.B.: Adv. Energy Mater. **3**, 34 (2013)
15. Wang, W., Winkler, M.T., Gunawan, O., Gokmen, T., Todorov, T.K., Zhu, Y., Mitzi, D.B.: Adv. Energy Mater. **4**, 1301465 (2013)
16. Repins, I., Beall, C., Vora, N., DeHart, C., Kuciauskas, D., Dippo, P., To, B., Mann, J., Hsu, W.-C., Goodrich, A., Noufi, R.: Sol. Energy Mater. Sol. Cells **101**, 154–159 (2012)

17. Brammertz, G., Buffière, M., Oueslati, S., ElAnzeery, H., Ben Messaoud, K., Sahayaraj, S., Köble, C., Meuris, M., Poortmans, J.: Appl. Phys. Lett. **103**(16) (2013)
18. Shin, B., Gunawan, O., Zhu, Y., Bojarczuk, N.A., Chey, S.J., Guha, S.: Prog. Photovoltaics Res. Appl. **21**(1), 72–76 (2013)
19. Chen, S., Walsh, A., Gong, X.G., Wei, S.H.: Adv. Mater. **25**, 1522 (2013)
20. Wang, H.: Int. J. Photoenergy (2011)
21. Ennaoui, A., Lux-Steiner, M., Weber, A., Abou-Ras, D., Koetschau, I., Schock, H.W., Schurr, R., Hoelzing, A., Jost, S., Hock, R., Voss, T., Schulze, J., Kirbs, A.: Thin Solid Films **517**(7), 2511–2514 (2009)
22. Tanaka, K., Oonuki, M., Moritake, N., Uchiki, H.: Sol. Energy Mater. Sol. Cells **93**, 583 (2009)
23. Katagiri, H.: Thin Solid Films **480**, 426–432 (2005)
24. Katagiri, H., Jimbo, K., Yamada, S., Kamimura, T., Maw, W.S., Fukano, T., Ito, T., Motohiro, T.: Appl. Phys. Express **1**(4) (2008)
25. Tanaka, K., Fukui, Y., Moritake, N., Uchiki, H.: Sol. Energy Mater. Sol. Cells **95**(3), 838–842 (2011)
26. Zhou, Z., Wang, Y., Xu, D., Zhang, Y.: Sol. Energy Mater. Sol. Cells **94**(12), 2042–2045 (2010)
27. Riha, S.C., Parkinson, B.A., Prieto, A.L.: J. Am. Chem. Soc. **131**(34), 12054–12055 (2009)
28. Moritake, N., Fukui, Y., Oonuki, M., Tanaka, K., Uchiki, H.: Physica Status Solidi (c) **6**(5), 1233–1236 (2009)
29. Moriya, K., Tanaka, K., Uchiki, H.: Jpn. J. Appl. Phys. **46**(9R), 5780 (2007)
30. Maeda, K., Tanaka, K., Fukui, Y., Uchiki, H.: Sol. Energy Mater. Sol. Cells **95**(10), 2855–2860 (2011)
31. Araki, H., Kubo, Y., Jimbo, K., Maw, W.S., Katagiri, H., Yamazaki, M., Oishi, K., Takeuchi, A.: Physica Status Solidi (c) **6**(5), 1266–1268 (2009)
32. Schubert, B.-A., Marsen, B., Cinque, S., Unold, T., Klenk, R., Schorr, S., Schock, H.-W.: Prog. Photovoltaics Res. Appl. **19**(1), 93–96 (2011)
33. Ki, W., Hillhouse, H.W.: Adv. Energy Mater. **1**(5), 732–735 (2011)
34. Chalapathy, R.B.V., Jung, G.S., Ahn, B.T.: Sol. Energy Mater. Sol. Cells **95**(12), 3216–3221 (2011)
35. Wang, K., Gunawan, O., Todorov, T., Shin, B., Chey, S.J., Bojarczuk, N.A., Mitzi, D., Guha, S.: Appl. Phys. Lett. **97**(14) (2010)
36. Flynn, B., Wang, W., Chang, C.-H., Herman, G.S.: Physica Status Solidi (a) **209**(11), 2186–2194 (2012)
37. Kurokawa, M., Tanaka, K., Moriya, K., Uchiki, H.: Jpn. J. Appl. Phys. **51**(10S), 10NC33 (2012)
38. Woo, K., Kim, Y., Yang, W., Kim, K., Kim, I., Oh, Y., Kim, J.Y., Moon, J.: Sci. Rep. **3** (2013)
39. Gershon, T., Shin, B., Gokmen, T., Lu, S., Bojarczuk, N., Guha, S.: Appl. Phys. Lett. **103** (19) (2013)
40. Gershon, T., Shin, B., Bojarczuk, N., Gokmen, T., Lu, S., Guha, S.: J. Appl. Phys. **114** (15) (2013)
41. Vigil-Galán, O., Espíndola-Rodríguez, M., Courel, M., Fontané, X., Sylla, D., Izquierdo-Roca, V., Fairbrother, A., Saucedo, E., Pérez-Rodríguez, A.: Sol. Energy Mater. Sol. Cells **117**, 246–250 (2013)
42. Zhu, L., Qiang, Y.H., Zhao, Y.L., Gu, X.Q.: Appl. Surf. Sci. **292**, 55–62 (2014)
43. Lee, D., Yong, K.: Nanotechnology **25**(6), 065401 (2014)
44. Su, Z., Sun, K., Han, Z., Cui, H., Liu, F., Lai, Y., Li, J., Hao, X., Liu, Y., Green, M.A.: J. Mater. Chem. A **2**(2), 500–509 (2014)
45. Jeong, A.R., Jo, W., Jung, S., Gwak, J., Yun, J.H.: Appl. Phys. Lett. **99**(8) (2011)
46. Zoppi, G., Forbes, I., Miles, R.W., Dale, P.J., Scragg, J.J., Peter, L.M.: Prog. Photovoltaics Res. Appl. **17**(5), 315–319 (2009)

47. Kauk-Kuusik, M., Altosaar, M., Muska, K., Pilvet, M., Raudoja, J., Timmo, K., Varema, T., Grossberg, M., Mellikov, E., Volobujeva, O.: Thin Solid Films **535**, 18–21 (2013)
48. Tampo, H., Makita, K., Komaki, H., Yamada, A., Furue, S., Ishizuka, S., Shibata, H., Matsubara, K., Niki, S.: Thin Solid Films **551**, 27–31 (2014)
49. Lee, S.M., Cho, Y.S.: J. Alloy. Compd. **579**, 279–283 (2013)
50. Timmo, K., Altosaar, M., Raudoja, J., Muska, K., Pilvet, M., Kauk, M., Varema, T., Danilson, M., Volobujeva, O., Mellikov, E.: Sol. Energy Mater. Sol. Cells **94**(11), 1889–1892 (2010)
51. Guo, Q., Ford, G.M., Yang, W.-C., Walker, B.C., Stach, E.A., Hillhouse, H.W., Agrawal, R.: J. Am. Chem. Soc. **132**(49), 17384–17386 (2010)
52. Redinger, A., Berg, D.M., Dale, P.J., Siebentritt, S.: J. Am. Chem. Soc. **133**(10), 3320–3323 (2011)
53. Todorov, T., Gunawan, O., Chey, S.J., de Monsabert, T.G., Prabhakar, A., Mitzi, D.B.: Thin Solid Films **519**(21), 7378–7381 (2011)
54. Cao, Y., Denny, M.S., Caspar, J.V., Farneth, W.E., Guo, Q., Ionkin, A.S., Johnson, L.K., Lu, M., Malajovich, I., Radu, D., Rosenfeld, H.D., Choudhury, K.R., Wu, W.: J. Am. Chem. Soc. **134**(38), 15644–15647 (2012)
55. Schnabel, T., Löw, M., Ahlswede, E.: Sol. Energy Mater. Sol. Cells **117**, 324–328 (2013)
56. Yang, W., Duan, H.-S., Bob, B., Zhou, H., Lei, B., Chung, C.-H., Li, S.-H., Hou, W.W., Yang, Y.: Adv. Mater. **24**(47), 6323–6329 (2012)
57. Todorov, T.K., Reuter, K.B., Mitzi, D.B.: Adv. Mater. **22**(20), E156–E159 (2010)
58. Barkhouse, D.A.R., Gunawan, O., Gokmen, T., Todorov, T.K., Mitzi, D.B.: Prog. Photovoltaics **20**(1), 6–11 (2012)
59. Chen, S., Walsh, A., Luo, Y., Yang, J.-H., Gong, X.G., Wei, S.-H.: Phys. Rev. B **82**(19), 195203 (2010)
60. Chen, S., Gong, X.G., Walsh, A., Wei, S.-H.: Appl. Phys. Lett. **94**(4), 041903 (2009)
61. Chen, S., Gong, X.G., Walsh, A., Wei, S.-H.: Phys. Rev. B **79**(16), 165211 (2009)
62. Adhi Wibowo, R., Soo Lee, E., Munir, B., Ho Kim, K.: Physica Status Solidi (a) **204**(10), 3373–3379 (2007)
63. Matsushita, H., Maeda, T., Katsui, A., Takizawa, T.: J. Cryst. Growth **208**(1–4), 416–422 (2000)
64. Pan, D., An, L., Sun, Z., Hou, W., Yang, Y., Yang, Z., Lu, Y.: J. Am. Chem. Soc. **130**(17), 5620–5621 (2008)
65. Wang, J.-J., Hu, J.-S., Guo, Y.-G., Wan, L.-J.: NPG Asia Mater **4**, e2 (2012)
66. Lu, X., Zhuang, Z., Peng, Q., Li, Y.: Chem. Commun. **47**(11), 3141–3143 (2011)
67. Regulacio, M.D., Ye, C., Lim, S.H., Bosman, M., Ye, E., Chen, S., Xu, Q.-H., Han, M.-Y.: Chem. A Eur. J. **18**(11), 3127–3131 (2012)
68. Schorr, S., Hoebler, H.-J., Tovar, M.: Eur. J. Mineral. **19**(1), 65–73 (2007)
69. Schorr, S.: Sol. Energy Mater. Sol. Cells **95**(6), 1482–1488 (2011)
70. Washio, T., Nozaki, H., Fukano, T., Motohiro, T., Jimbo, K., Katagiri, H.: J. Appl. Phys. **110** (7) (2011)
71. Liu, B.W., Zhang, M.J., Zhao, Z.Y., Zeng, H.Y., Zheng, F.K., Guo, G.C., Huang, J.S.: J. Solid State Chem. **204**, 251–256 (2013)
72. Li, D., Bancroft, G.M., Kasrai, M., Fleet, M.E., Feng, X.H., Tan, K.H., Yang, B.X.: J. Phys. Chem. Solids **55**(7), 535–543 (1994)
73. Babu, G.S., Kumar, Y.B.K., Bhaskar, P.U., Raja, V.S.: Semicond. Sci. Technol. **23**(8), 085023 (2008)
74. Heyd, J., Scuseria, G.E.: J. Chem. Phys. **121**(3), 1187–1192 (2004)
75. Hedin, L.: Phys. Rev. **139**, A796 (1965) (Copyright (C) 2010 The American Physical Society)
76. Luckert, F., Hamilton, D.I., Yakushev, M.V., Beattie, N.S., Zoppi, G., Moynihan, M., Forbes, I., Karotki, A.V., Mudryi, A.V., Grossberg, M., Krustokm, J., Martin, R.W.: Appl. Phys. Lett. **99**(6) (2011)

77. Ahn, S., Jung, S., Gwak, J., Cho, A., Shin, K., Yoon, K., Park, D., Cheong, H., Yun, J.H.: Appl. Phys. Lett. **97**(2) (2010)
78. Tanaka, T., Sueishi, T., Saito, K., Guo, Q., Nishio, M., Yu, K.M., Walukiewicz, W.: J. Appl. Phys. **111**(5) (2012)
79. Chen, S., Walsh, A., Gong, X.-G., Wei, S.-H.: Adv. Mater. **25**(11), 1522–1539 (2013)
80. Chen, S., Gong, X.G., Walsh, A., Wei, S.-H.: Phys. Rev. B **79**(16) (2009)
81. Jaffe, J., Zunger, A.: Phys. Rev. B **29**(4), 1882 (1984)
82. Li, Y.-H., Walsh, A., Chen, S., Yin, W.-J., Yang, J.-H., Li, J., Da Silva, J.L.F., Gong, X.G., Wei, S.-H.: Appl. Phys. Lett. **94**(21), 212103–212109 (2009)
83. Chen, S., Walsh, A., Yang, J.-H., Gong, X.G., Sun, L., Yang, P.-X., Chu, J.-H., Wei, S.-H.: Phys. Rev. B **83**(12) (2011)
84. Bär, M., Schubert, B.-A., Marsen, B., Wilks, R.G., Pookpanratana, S., Blum, M., Krause, S., Unold, T., Yang, W., Weinhardt, L., Heske C., Schock, H.-W.: Appl. Phys. Lett. **99**(22) (2011)
85. Haight, R., Barkhouse, A., Gunawan, O., Shin, B., M. Copel, M. Hopstaken and D. B. Mitzi, Appl. Phys. Lett. **98**(25) (2011)
86. Santoni, A., Biccari, F., Malerba, C., Valentini, M., Chierchia, R., Mittiga, A.: J. Phys. D Appl. Phys. **46**(17), 175101 (2013)
87. Botti, S., Kammerlander, D., Marques, M.A.L.: Appl. Phys. Lett. **98**(24) (2011)
88. Shu, Q., Yang, J.-H., Chen, S., Huang, B., Xiang, H., Gong, X.-G., Wei, S.-H.: Phys. Rev. B **87**(11), 115208 (2013)
89. Brivio, F., Butler, K.T., Walsh, A., van Schilfgaarde, M.: Phys. Rev. B **89**(15), 155204 (2014)
90. Levcenco, S., Dumcenco, D., Wang, Y.P., Huang, Y.S., Ho, C.H., Arushanov, E., Tezlevan, V., Tiong, K.K.: Opt. Mater. **34**(8), 1362–1365 (2012)
91. Du, M.H.: J. Mater. Chem. A **2**(24), 9091–9098 (2014)
92. Scragg, J.J., Dale, P.J., Peter, L.M., Zoppi, G., Forbes, I.: Physica Status Solidi B Basic Solid State Phys. **245**(9), 1772–1778 (2008)
93. Ahn, S., Jung, S., Gwak, J., Cho, A., Shin, K., Yoon, K., Park, D., Cheong, H. Yun, J.H.: Appl. Phys. Lett. **97**(2) (2010)
94. Chen, S., Gong, X.G., Walsh, A., Wei, S.H.: Appl. Phys. Lett. **96**, 021902 (2010)
95. Chen, S., Yang, J.-H., Gong, X.G., Walsh, A., Wei, S.-H.: Phys. Rev. B **81**(24) (2010)
96. Walsh, A., Chen, S., Wei, S.-H., Gong, X.-G.: Adv. Energy Mater. **2**(4), 400–409 (2012)
97. Djemour, R., Mousel, M., Redinger, A., Gütay, L., Crossay, A., Colombara, D., Dale, P.J., Siebentritt, S.: Appl. Phys. Lett. **102**(22) (2013)
98. Zhai, Y.-T., Chen, S., Yang, J.-H., Xiang, H.-J., Gong, X.-G., Walsh, A., Kang, J., Wei, S.-H.: Phys. Rev. B **84**(7), 075213 (2011)
99. Chen, S., Gong, X.G., Walsh, A., Wei, S.-H.: Appl. Phys. Lett. **96**(2) (2010)
100. Gunawan, O., Gokmen, T., Warren, C.W., Cohen, J.D., Todorov, T.K., Barkhouse, D.A.R., Bag, S., Tang, J., Shin, B., Mitzi, D.B.: Appl. Phys. Lett. **100**(25) (2012)
101. Fernandes, P.A., Sartori, A.F., Salome, P.M.P., Malaquias, J., da Cunha, A.F., Graca, M.P.F., Gonzalez, J.C.: Appl. Phys. Lett. **100**(23) (2012)
102. Das, S., Chaudhuri, S.K., Bhattacharya, R.N., Mandal, K.C.: Appl. Phys. Lett. **104**(19) (2014)
103. Nagaoka, A., Miyake, H., Taniyama, T., Kakimoto, K., Yoshino, K.: Appl. Phys. Lett. **103** (11) (2013)
104. Chen, S., Yang, J.-H., Gong, X.G., Walsh, A., Wei, S.-H.: Phys. Rev. B **81**, 245204 (2010)
105. Jaffe, J., Zunger, A.: Phys. Rev. B **64**, 241304 (2001)
106. Zhang, S.B., Wei, S.H.: Phys. Rev. B **65**, 081402 (2002)
107. Fernandes, P.A., Salomé, P.M.P., da Cunha, A.F.: Thin Solid Films **517**, 2519 (2009)
108. Yoo, H., Kim, J.: Thin Solid Films **518**, 6567 (2010)
109. Moholkar, A.V., Shinde, S.S., Babar, A.R., Sim, K.-U., Kwon, Y.-B., Rajpure, K.Y., Patil, P. S., Bhosale, C.H., Kim, J.H.: Sol. Energy **85**, 1354 (2011)

110. He, J., Sun, L., Zhang, K., Wang, W., Jiang, J., Chen, Y., Yang, P., Chu, J.: Appl. Surf. Sci. **264**, 133 (2013)
111. Xu, P., Chen, S., Huang, B., Xiang, H.J., Gong, X.-G., Wei, S.-H.: Phys. Rev. B **88**(4), 045427 (2013)
112. Tasker, P.W.: J. Phys. C Solid State Phys. **12**, 4977 (1979)

Chapter 4
ZnO Doping and Defect Engineering—A Review

Faxian Xiu, Jun Xu, Pooran C. Joshi, Craig A. Bridges and M. Parans Paranthaman

4.1 Introduction

Demand for efficient solid-state lighting (SSL) devices has accelerated in recent years and will continue to grow in the foreseeable future. As a result, interest in developing advanced optoelectronic devices such as light-emitting diodes (LEDs), laser diodes, and photodetectors is increasing. These optoelectronic devices require the use of compound semiconductors with a direct bandgap. In the past, this role was mainly dominated by GaAs and InP compound semiconductors. In the early 1990s, however, the wide bandgap semiconductor GaN became the subject of intense technical interest because it can emit light in the visible and ultraviolet range due to its direct wide bandgap. Shortly after Nakamura solved the p-type doping problem [1], GaN became the focus of mainstream solid-state research, leading to the wide commercialization of GaN-based visible LEDs, blue/ultraviolet lasers, and ultraviolet photodetectors.

More recently, the II–VI semiconductor ZnO has been perceived as a promising wide bandgap semiconductor material for next-generation optoelectronics. This new interest is due to several fundamental advantages over its main competitor GaN. ZnO has a much higher free exciton binding energy of 60 meV than that of GaN (21–25 meV), which could lead to highly efficient light-emitting even above room temperature. The large and high-quality ZnO bulk substrate is commercially

One of the coauthors Jun Xu deceased on March 10, 2013.

F. Xiu (✉)
State Key Laboratory of Surface Physics and Department of Physics, Fudan University, Shanghai 200433, China
e-mail: faxian@fudan.edu.cn

J. Xu · P.C. Joshi · C.A. Bridges · M. Parans Paranthaman
Oak Ridge National Laboratory, PO Box 2008, Oak Ridge, TN 37831, USA

M.P. Paranthaman et al. (eds.), *Semiconductor Materials for Solar Photovoltaic Cells*, Springer Series in Materials Science 218,
DOI 10.1007/978-3-319-20331-7_4

available, making it possible to grow homoepitaxial optoelectronic devices on its own substrate. Wet chemical processing is possible for ZnO, which provides an opportunity for fabrication of small-size devices. ZnO has a high resistance to radiation damage, making it a suitable candidate for space application. In addition, ZnO is inexpensive, nontoxic, and compatible with semiconductor manufacturing processes. Importantly, ZnO has been synthesized with variety of nanostructures. The nanoscale p–n junctions can increase the injection rate of carriers many times more than that for a planar ZnO diode. Based on these advantages, ZnO has seen a surge of research interest aiming at achieving high efficiency for ultra-bright LEDs, laser diodes, and ultra-fast photodetectors [2–6]. However, the main obstacle hindering ZnO application is a reliable method for fabricating p-type ZnO material with a high hole concentration, high mobility, and low resistivity. The present work in this chapter is dedicated to reviewing the existing p-type doping techniques and providing insight for future ZnO LED development.

For the development of ZnO-based LED devices, it is indispensable to have both high-quality n-type and p-type ZnO materials. The n-type dopants could be group III elements (Al, Ga, and In), substituting for Zn and therefore releasing electrons to conduction band. The group VII elements, such as F, Cl, Br, and I, could also make high-quality n-type ZnO as they occupy oxygen sites and contribute electrons. In fact, naturally grown ZnO is found to be n-type, possibly due to intrinsic defects or process induced hydrogen impurities. While ZnO can be easily made n-type, unfortunately, p-type doping of ZnO has been found to be much more difficult. To date, tremendous research has focused on using group I (Li and Na), group V (N, P, As, Sb, and Bi), and group IB (Cu and Ag) elements or codoped elements (Al–N, Ga–N, In–N, P–N, Zr–N, Li–N, P–Ga, N–As) as the p-type dopants. However, only limited success has been achieved so far. The stability and reliability of p-type ZnO still present a great challenge, not to mention the commercialization issues for any useful ZnO-based optoelectronic devices. Nevertheless, in parallel with experiments, some theories have been developed to explain ZnO doping asymmetry. In short, p-type doping difficulty could originate for the following reasons:

(a) Low solubility of the dopants and precipitate formation;
(b) Compensation effects. The intrinsic defects and extrinsic impurities can compensate the acceptors;
(c) Deep acceptor levels. Almost all p-type dopants have deep acceptor levels, leading to low hole concentrations;
(d) Formation of stable AX and DX structures [7].

It is important to note that some of these reasons are linked together. For example, to improve the solubility of the acceptor dopants, a Zn-rich growth environment would be ideal. However, the Zn-rich environment can generate extra oxygen vacancies in ZnO, leading to a high probability of compensation effects. To overcome these challenges, new doping methods which involve defect and bandgap engineering, non-equilibrium doping, and alloying techniques have been pursued. In this chapter, we will emphasize these new methods.

4.2 n-type Doping

4.2.1 Intrinsic n-type Conduction

As mentioned earlier, ZnO is naturally n-type. The n-type conductivity of undoped–doped ZnO may originate from the intrinsic defects, such as zinc interstitials (Zn_i), zinc antisite (Zn_O), and/or oxygen vacancies (V_O). From now on, we designate the subscripts I, O, and Zn as interstitial, O lattice site, and Zn lattice site, respectively. It was predicted that both Zn_i and V_O not only have high formation energies in n-type ZnO, but also have deep donor levels, which eliminates the possibility of developing large quantities of these species in ZnO films [8, 9]. Later, this conclusion was challenged by Zhang et al. [10] and Oba et al. [11], who predicted that Zn_i is actually a shallow donor. However, the high formation energy of Zn_i cannot give a reasonable explanation of high electron concentrations in as-grown ZnO films [12]. More recently, two models were established to explain the origin of n-type conductivity in ZnO. One potential source of n-type conductivity is hydrogen impurity. Hydrogen is not amphoteric in ZnO and acts as donor with ionization energy in the range of 30–40 meV [13, 14]. This assumption is valid since hydrogen is always present in all growth methods, and it can be easily incorporated into ZnO in large quantities. In contrast, Look et al. argued that under N ambient, Zn_i–N_O is a stronger candidate than H or any other known impurity for a 30 meV donor, based on evidence from temperature-dependent Hall effect measurements, magnetic resonance experiments, and also density functional theory [15].

4.2.2 Intentional n-type Doping

The group III elements were found to substitute for Zn, while the group VII elements replace O to contribute electrons. Since the high electron concentration ($\sim 10^{20}$–10^{21} cm^{-3}) and low resistivity ($\sim 10^{-4}$ Ω cm) can be easily achieved by doping with Ga [16, 17], Ga–In [18], Al [19], and Ga–Al [20], more research has been focused on identifying the actual donor levels of these impurities. So far, Ga and Al were found to have shallow levels of 55–75 meV [9]. Their associated photoluminescence (PL) emissions are exclusive in the region of 3.36 eV [9]. It is reasonable to conclude that the current n-type doping techniques are well developed, ready to be applied in various applications, such as LEDs and transparent ohmic contacts.

4.3 p-type Doping

Despite of the asymmetric doping in ZnO, many research groups have attempted to grow p-type ZnO by many different dopants using various growth techniques. In the following section, the current status of p doping by these elements and methods are

comprehensively reviewed. The doping mechanisms are also discussed based on the available theoretical models and experimental data.

4.3.1 Group I p-type Doping

The group I elements, Li, Na, and K, were predicted to have relatively shallow acceptor levels of 90, 170, and 320 meV, respectively, assuming that these elements substitute for Zn [7]. From the physical point of view, the valence-band maximum (VBM) state mainly consists of the anion *p* orbitals with small mixing of the cation *p* and *d* orbitals, which gives only small perturbations at the valence-band maximum when replacing Zn by group I elements [7]. In other word, the strain around the dopant atoms is small and couplings between the anion and cation orbitals are weak. Therefore, the acceptor levels are relatively shallow. However, the group I elements (especially Li and Na) prefer the interstitial sites rather than substitutional ones and are therefore likely to form Li_i and Na_i in ZnO, which behave as shallow donors [21]. As the Fermi level becomes closer to the valence-band maximum due to the formation of Li_{Zn} and Na_{Zn} shallow acceptors, the formation of Li_i and Na_i shallow donors becomes more favorable. Eventually, at equilibrium, the Fermi level will sit between the donor and acceptor levels (close to middle of bandgap), leading to the widely observed semi-insulating behavior [22]. The p-type doping with Li and Na is thus limited by the formation of the self-compensating interstitial donors. In terms of K doping, the interstitial K_i is less stable because of its large atomic size. This, to some extent, eliminates the self-compensating problem. However, K_{Zn} has a much deeper acceptor level than Li_{Zn} and Na_{Zn}, and K doping could trigger the formation of V_O–K complexes, which behave as the primary acceptor "killers" and limit p-type doping [7].

To solve the solubility of Li, Lee et al. proposed that a H_i-codoping method can improve the incorporation of Li by forming H_i-acceptor complexes, and the formation of compensating interstitials can be suppressed. Subsequently, after removing H at the relatively low annealing temperature near 500 °C, the low-resistivity p-type ZnO could be produced. The doping mechanism is similar to that of Mg-doped GaN [21]. On the other hand, Wardle et al. suggested that Li_{Zn}–Li_i complexes are likely to be preferentially formed along with others, such as Li_{Zn}–H and Li_{Zn}–AX that passivate the Li_{Zn} acceptors in ZnO. By means of an annealing process at 300 °C, Li_i could be dissociated from the complex, thus activating the material [23].

Despite the formation of self-compensating donors, encouraging experimental results on Li-doped p-type ZnO were reported by Ye et al. by using a dc reactive magnetron sputtering system [24–27]. The optimized p-type ZnO was achieved with a resistivity of 16.4 Ω cm, Hall mobility of 2.65 cm^2/V s, and hole concentration of 1.44×10^{17} cm^{-3}. The stability was tested over a month. Investigation of the Li-doped p-type ZnO PL indicated that the Li_{Zn} acceptor level was located 150 meV above the VBM. Another deeper acceptor state was found at 250 meV,

which increased with increased Li concentration. Finally, X-ray photoelectron spectroscopy demonstrated two chemical bonding states of Li, indicating the formation of two acceptor states. It was also found that growth regions of n- and p-type Li-doped ZnO strictly depend on the amount of Li being introduced into the films. At a Li content of greater than 1.2 at.%, only highly resistive ZnO was obtained. Below this value, the p-type conductivity in ZnO is enhanced by the incorporation of Li. When Li content reached 0.6 at.%, the ZnO film showed optimal p-type conduction. These experiments indicate that proper growth conditions promote the formation of Li acceptors while suppressing Li interstitials [27].

Other groups have also investigated Li acceptor levels. Meyer et al. performed low-temperature PL from a Li-diffused ZnO bulk substrate and a chemical vapor deposition (CVD)-grown ZnO with in situ doping of Li [28, 29]. Both PL spectra showed a donor–acceptor pair (DAP) transition at around 3.0 eV, followed by three DAP transitions coupling to longitudinal optical phonons with an energy separation of 72 meV (Fig. 4.1). Assuming the donor binding energy is about 50 meV, the Li acceptor level can be estimated to be near 300 meV. This level could be the second Li acceptor level as observed by Ye et al. [24–27].

Other group I elements, such as Na and K, have rarely been used for ZnO doping, partially because of the difficulty of handling these elements [14]. Na doping behavior and conduction mechanisms are still unclear. Stable Na-doped p-type ZnO films with an acceptor level of about 164 meV have been fabricated by pulsed-laser deposition technique. Magnetic field dependent Hall effect measurements and rectification behavior of ZnO homojunction diode confirmed p-type conductivity in the ZnO:Na films with lowest resistivity value of 12 Ω cm [30]. Ye et al. claimed the successful fabrication of p-type ZnO using Na as the dopant source. 0.3 at.% of Na was introduced into the ZnO film, yielding a hole concentration of 2.57×10^{17} cm^{-3}, Hall mobility of 0.406 cm^2/V s, and resistivity of 59.9 Ω cm. For the 0.1 and 0.5 at.% Na-doped ZnO films, weak p-type conduction

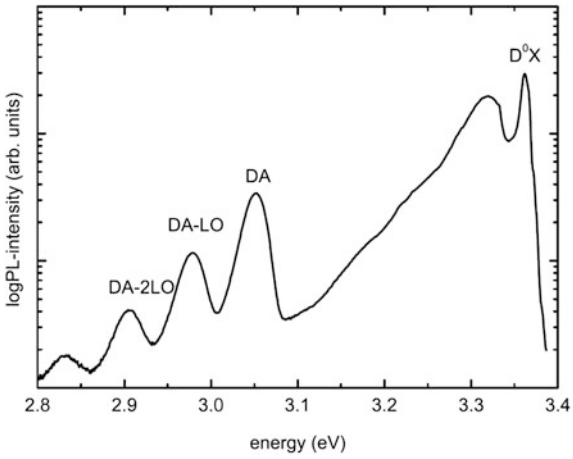

Fig. 4.1 PL spectra of CVD grown ZnO on GaN templates with in situ Li doping (T = 4.2 K, He–Cd laser excitation). The positions of the zero phonon line of the donor–acceptor pair band and its phonon replica are indicated [28]

was found with high resistivity and low carrier concentration, respectively. This can be explained by the deficient and excessive Na concentrations, which result in low number of Na_{Zn} acceptors and formation of Na_{Zn}–Na_i, respectively [31]. These experiments support the fact that, analogous to Li doping, Na could also introduce shallow acceptor state. Excess Na incorporation into ZnO shows an ambiguous carrier type due to increase in the donor-like V_O density indicating that compensation effects limit the hole concentration in Na-doped ZnO films [32].

4.3.2 Group V p-type Doping

After group I element doping studies, most research on p-type-doped ZnO has involved group V elements. The original motivation is that group V elements will substitute for oxygen and therefore capture electrons from the valence band, resulting in p-type conductivity. However, the real scenario seems to be far more complicated than this simple model. Experiments have so far demonstrated that, for different group V elements, the doping mechanism seems to be quite different. It has also been shown that the p-type conduction is sensitive to various growth conditions and techniques. In this section, both the theoretical calculations and experimental results for group V doping are briefly reviewed.

4.3.2.1 Nitrogen Doping

Among all group V elements, N doping has been the most extensively studied [33–37]. The fundamental reason is that N is the one among the group V elements with an atomic size nearest to that of O. So N is believed to be an ideal p-type dopant if N substitutes for O and produces N_O acceptors. Indeed, Look et al., for the first time, successfully fabricated a p-type N-doped ZnO layer with a hole concentration of 9×10^{16} cm^{-3} and a hole mobility of 2 cm^2/V s. The low-temperature PL spectrum for the p-type layer shows a large acceptor-bound exciton (A^0X) at 3.315 eV line, which is attributed to N_O acceptor, as shown in Fig. 4.2. Based on the A^0X energy, the N_O acceptor energy was estimated to be in the range of 170–200 meV [38]. More recently, by fitting the temperature-dependent Hall effect data, Look et al. obtained a more accurate activation energy of 150 meV [22]. These results were further confirmed by Zeuner et al. with a value of 165 ± 40 meV for N_O [24]. It is noted that the assignment of the 3.315 eV peak is still controversial. Many authors attribute the peak to DAP [39, 40]. The main argument against this assignment is the implication of a large Haynes factor [41].

Since the demonstration of the first N-doped p-type ZnO, research interest on N doping has increased. Various types of nitrogen sources were used in different growth techniques, for example N_2, NH_4NO_3, NO, N_2O, NH_3, and Zn_3N_2. A good review in this regard can be found in an article written by Ozgur et al. [42]. However, no matter which nitrogen source and deposition technique are used, the

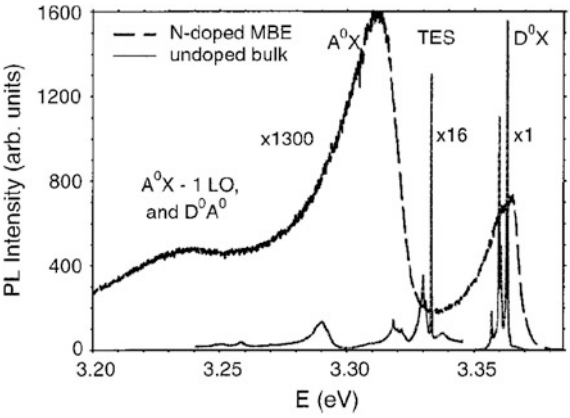

Fig. 4.2 PL spectra, at 2 K, for two ZnO samples, an undoped bulk sample, and an N-doped, MBE-grown epitaxial layer [38]

solubility of N seems to be quite limited, leading to low hole concentrations and high resistivities. In addition, besides the formation of N_O acceptors, the shallow double donors $(N_2)_O$ could also be developed, making the p-type conduction unstable [35, 43]. Fortunately, several approaches were proposed to address the low solubility of N and/or minimize the formation of $(N_2)_O$ defects. Biaxial compressive stress in the deposited films due to lattice mismatch between the substrate and thin film has been ascribed to the origin of the instability of the electrical properties [34]. Reliable and stable nitrogen-doped p-type ZnO films were fabricated by plasma-assisted molecular beam epitaxy on *c*-Al_2O_3 substrates as compared to films deposited on *a*-Al_2O_3 substrates due to lower thermal or lattice mismatch resulting in reduced N_O and increased $N_{2(O)}$ as confirmed by X-ray photoelectron spectroscopy. Tsukazaki et al. [44] first used a repeated temperature modulation epitaxy method for growing high-quality p-type ZnO on insulating and lattice-matched $ScAlMgO_4$ substrates. It was found that the nitrogen concentration decreased from low level of 10^{20} cm^{-3} at 450 °C to about 10^{18} cm^{-3} at 700 °C. This inspired a new method of using low-temperature nitrogen incorporation and subsequent activation at higher temperature. Indeed, this approach successfully meets the requirements of high nitrogen concentration and good crystallinity. As a result (Fig. 4.3), stable p-type ZnO was obtained with a layer-by-layer growth mode, and the hole concentration of 10^{16} cm^{-3} was achieved [44].

Alternatively, Xu et al. [45] proposed a non-equilibrium method by using a pulse thermal processing (PTP) for effectively generating N_O acceptors in ZnO. According to theoretical prediction [46], p-type doping of ZnO under equilibrium conditions is difficult because the penning energy is high, 1.6 eV above the VBM. In other words, as Fermi energy becomes closer to the pinning energy, spontaneous formation of donor-type V_O and Zn_i will take over doping pathways, preventing the generation of acceptors in ZnO. Therefore, in order to produce a high concentration of p-type carriers, non-equilibrium doping methods are plausible. PTP is a non-equilibrium process that generates high-temperature pulses to activate nitrogen dopants (N_O) and simultaneously hinders the diffusion of the dopants out of the

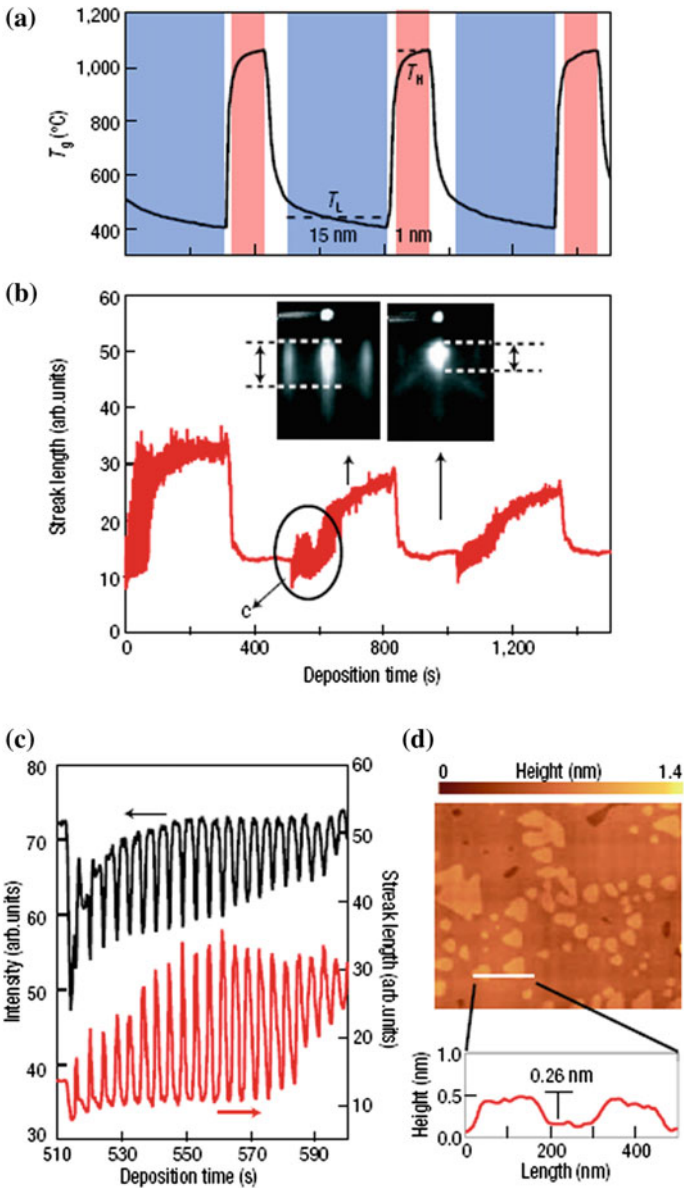
(a)
1,200
1,000
800
600
400
T_g (°C)
T_H
T_L
15 nm
1 nm
(b)
Streak length (arb.units)
60
50
40
30
20
10
0
0
400
800
1,200
Deposition time (s)
c
(c)
Intensity (arb.units)
Streak length (arb.units)
80
70
60
50
40
30
60
50
40
30
20
10
510
530
550
570
590
Deposition time (s)
(d)
0
Height (nm)
1.4
1.0
0.5
0.0
Height (nm)
0.26 nm
0
200
400
Length (nm)

◀ **Fig. 4.3** Atomically smooth ZnO films doped with nitrogen can be grown by a repeated temperature modulation technique. **a** Temporal variation of growth temperature, switching between T_H and T_L, during ZnO thin-film growth. Layers of ZnO:N with high nitrogen concentration (CN) were deposited at T_L in the period colored *blue*. The layers were annealed, and additional ZnO:N layers with low CN that were grown in the period *colored red* in order to activate nitrogen as an acceptor and recover surface smoothness, respectively. **b** Typical RHEED patterns observed during T_L (*left*) and T_H (*right*) periods are shown in the *insets*, representing rather rough and atomically smooth surfaces by *streaky* and *spotty* patterns, respectively. Temporal variation of streak length (defined by *broken lines*) is plotted as a measure of the surface roughness. **c** RHEED intensity (*black*) and streak length (*red*) are plotted for the initial growth of high CN layer at T_L as denoted by *circle* in (**b**). Clear oscillations having a half-phase shift confirm the layer-by-layer growth mode. **d** An AFM image of the surface for a 500-nm-thick ZnO:N film. The step height corresponds to the thickness of a charge-neutral molecular layer of ZnO (0.26 nm) [44]

films. Figure 4.4 shows the PL spectra for a N-doped ZnO film grown at 400 °C before and after PTP. All spectra were measured at 8.8 K. For the as-grown film, a dominant near-band-edge emission peak was observed at 3.364 eV. This emission is associated with the donor-bound exciton (D^0X). Then, the N-doped ZnO film was processed via PTP with a profile of 2 s preheating at 200 A and 50 ms at 900 A. The peak temperature was estimated to be above 600 °C. After processing, PL spectrum peak at 3.364 eV disappeared, while two new dominant peaks were observed at 3.30 and 3.34 eV, which are assigned to DAP and A^0X, respectively. The DAP peak assignment is consistent with previous work [39, 40]. The appearance of both A^0X and DAP indicates that PTP generates nitrogen acceptors in ZnO. On the other hand, under conventional annealing methods, a large amount of N dopants can undergo the formation of N_2 to vapor phase due to the low solubility. Under a non-equilibrium process, the initial nitrogen mix may be in the interstitial sites of as-grown ZnO. PTP thermal pulses activate the interstitial N with an increased solubility in a metastable state.

Many other researchers, however, focused their efforts on studying the defect formation during N-doping processes, such as $(N_2)_O$, No–H, N–C, and $(NC)_O$.

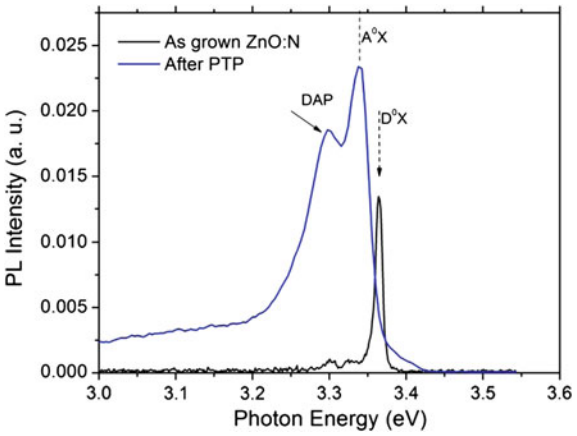

Fig. 4.4 PL spectra before and after PTP processing for a N-doped ZnO film grown at 400 °C. The spectra were measured at 8.8 K [45]

Li et al. [47] studied the role of impurities in N-doped ZnO films to understand the difficulty of p-type ZnO by nitrogen doping. High levels of nitrogen dopants ($\sim 10^{21}$ cm^{-3}) were observed in the ZnO films. However, acceptor concentrations were typically in the lower range of 10^{14}–10^{17} cm^{-3}. XPS and SIMS measurements showed that carbon and hydrogen are the impurities that induce the defect complexes of CH_x, NH_x, and NC_x. From the first-principles calculations, the No–H and $(NC)_O$ complexes were also predicted to passivate the nitrogen acceptors, leading to a low hole concentration [48]. With different approaches, Li and coworkers [47] and Zhang and coworkers [50] investigated the formation of No–H complex. Both papers reported the out-diffusion of H and the activation of nitrogen acceptors during an annealing process. However, the annealing temperature could not be too high because the N may either out-diffuse or recombine to form N_2 bubbles. These experimental results are consistent with those from the soft X-ray absorption near-edge structure spectroscopy (XANES) [51]. Nevertheless, the best p-type ZnO was reported to be made using a N_2O plasma as both nitrogen and oxygen sources. N_2O is a mild oxidizing gas that has a much lower dissociation energy and ionization potential than N_2. By using N_2O flowing through an electron cyclotron resonance source, it was found that nitrogen incorporation was significantly enhanced. The samples showed strong p-type conductivity with a hole concentration of 3×10^{18}–6×10^{18} cm^{-3}, a resistivity of 2–5 Ω cm, and a hole mobility of 0.1–0.4 cm^2/V s [52]. The direct observation of N lattice location was achieved by using N *K*-edge X-ray absorption structure spectroscopy [53]. Absorption spectroscopy revealed that N indeed substitutes for O to act as an acceptor. In another study, ZnO thin films implanted with 70 keV N+ ions at 460 °C showed p-type characteristics with a carrier concentration of 2.4×10^{17} cm^{-3}, resistivity of 18 Ω cm, and mobility of 1.4 cm^2/V s [33]. Ion implantation is attractive for precise control of dopant concentration; however, the process induces undesirable lattice damage. TEM analysis showed that ion implantation at elevated temperature was effective in enhancing the concentration of p-type N dopants while reducing the amount of post-implantation disorder.

One of the most effective methods to verify the quality of p-type ZnO is the fabrication of light-emitting diodes. Several groups have successfully produced UV LEDs based on N doping. Tsukazaki et al. [44] were the first ever to report the room temperature electroluminescence (EL) from a p–i–n ZnO homo-LED. The device structure and electrical characterizations are shown in Fig. 4.5. The threshold voltage is observed to be about 7 V. The high value comes from the high resistivity of the p-type ZnO layer. The EL emission was obtained by feeding a direct current of 20 mA at room temperature. The spectrum reveals luminescence in both the violet and green regions. This experiment, for the first time, demonstrates the possibility of fabricating ZnO homo-LEDs.

Wei et al. [54] also fabricated a ZnO p–n junction consisting of 200-nm-thick nitrogen-doped p-type ZnO and 200-nm-thick n-type layer on top. The p-type ZnO layer has a high hole concentration of 1.2×10^{18} cm^{-3} and a mobility of 1.0 cm^2/V s. The *I*–*V* curve of the ZnO LED showed a rectifying characteristic with a turn-on voltage of about 4.0 V. Under forward injection currents of

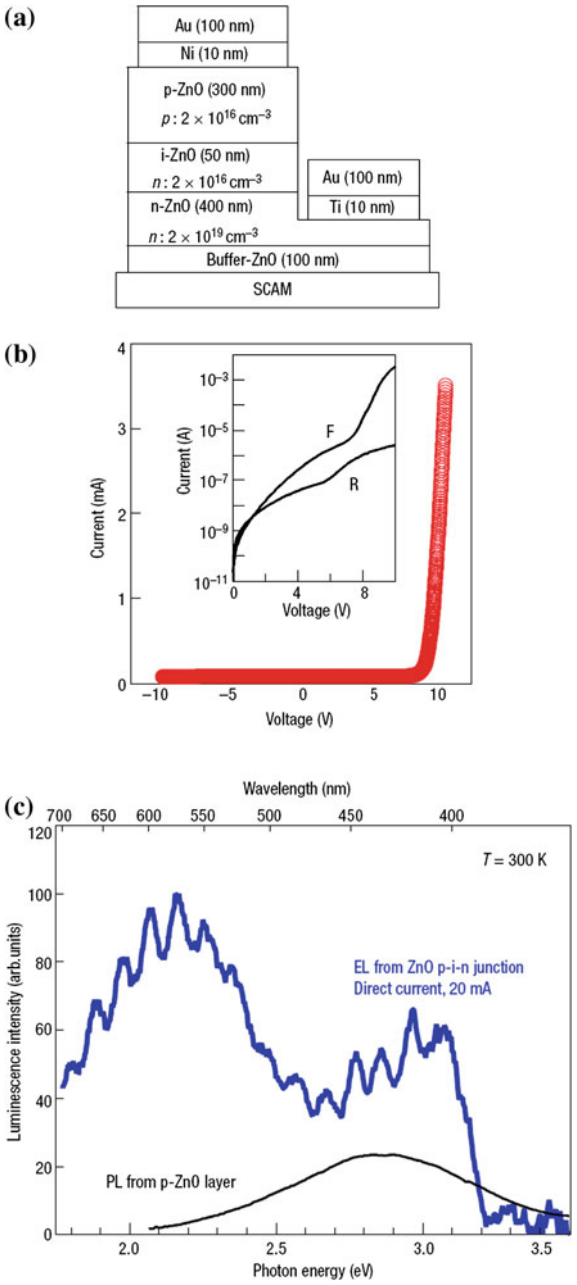

Fig. 4.5 ZnO homostructural p–i–n junction shows rectifying current–voltage characteristics and electroluminescence in forward bias at room temperature. **a** The structure of a typical p–i–n junction LED. **b** Current–voltage characteristics of a p–i–n junction. The *inset* has logarithmic scale in current with F and R denoting forward and reverse bias conditions, respectively. **c** Electroluminescence spectrum from the p–i–n junction (*blue*) and PL spectrum of a p-type ZnO film measured at 300 K. The p–i–n junction was operated by feeding in a direct current of 20 mA [44]

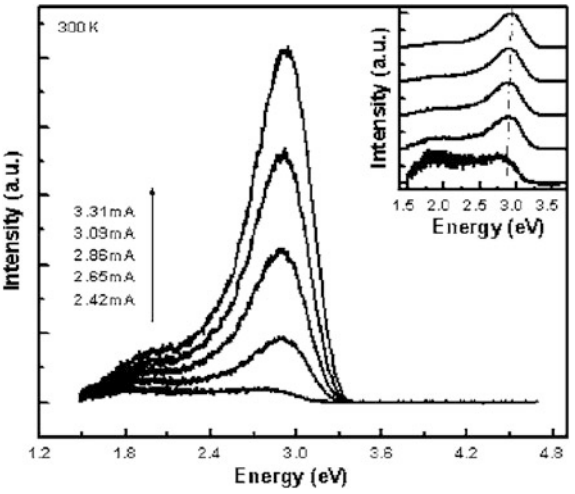

Fig. 4.6 EL spectra of the ZnO LED measured at room temperature under various injection currents. The *inset* shows the normalized EL spectra in which a blue shift of the emission peak with applied current is clearly seen [54]

2.42–3.31 mA, strong EL emission was observed in the blue-violet (~420 nm) and the red regions (~650 nm) (Fig. 4.6).

A ZnO LED with a lifetime of 6.8 h has been reported by Liu et al. [55]. The plasma-assisted molecular beam epitaxy technique was used for the processing of p-$Mg_{0.25}Zn_{0.75}O$: (Li, N)/*n*-type ZnO LED structures. The LEDs showed a near-band-edge emission at around 392 nm with continuous operation for 6.8 h under 20 mA current showing the future possibility of long lifetime devices.

4.3.2.2 Phosphorus Doping

While most studies have focused on nitrogen doping, phosphorus has been investigated as another potential p-type dopant. Density functional theory predicts that phosphorus, with an atomic radius greater than nitrogen, would produce a deep acceptor level of 930 meV if phosphorus replaces oxygen. Furthermore, the phosphorus-related AX centers are stable and could significantly compensate for acceptors [2]. When coupled with the antisite P_{Zn} defects, this compensation effect fundamentally precludes the possibility of phosphorus p-type doping. However, many experiments have demonstrated that phosphorus can be a good p-type dopant since high hole concentration of 10^{18}–10^{19} cm^{-3} has been achieved by using P_2O_5, Zn_3P_2, and GaP dopant sources. To explain the phosphorus doping behavior, models of the defect complexes were proposed. The theory predicted that the formation of P_{Zn}–$2V_{Zn}$ acceptor complexes, similar to the model for As and Sb doping [56], could be the species in causing the p-type conduction [57]. The acceptor energy was predicted to be 0.18 eV above VBM [57]. It is also noted that the formation of this complex requires O-rich conditions, where Zn vacancies are abundant and the P_{Zn}–$2V_{Zn}$ complex is stabilized.

Lee and Yu recently carried out first-principles pseudopotential calculations to determine the best phosphorus dopant source and model the phosphorus doping behavior under different growth conditions [57–59]. Lee et al. reported that by using P_2O_5 under Zn-rich growth conditions, P_O acceptors are compensated by dominant donors such as P_{Zn}, leading to n-type conductivity [57, 58]. Under O-rich conditions, the Zn vacancies are more likely to be formed than P_{Zn}–$2V_{Zn}$, which explains the p-type conductivity. However, the formation of P_{Zn}–$2V_{Zn}$ complex is energetically more favorable and becomes the dominant acceptor when using Zn_3P_2 as phosphorus source. In contrast, Yu et al. [59] predicted that doping ZnO using Zn_3P_2 under zinc-rich conditions would lead to good p-type conduction. The authors postulate that origin of the p-type behavior comes from the formation of P_O being a shallow acceptor at high growth temperatures. Despite these different explanations of origin of p-type conduction, both works support the usage of Zn_3P_2 as the phosphorus doping source.

Experimentally, both P_2O_5 and Zn_3P_2 have been extensively used for fabrication of p-type ZnO [60–72]. Kim et al. [65] reported that the as-grown phosphorus-doped ZnO by using a P_2O_5 source possessed an n-type conductivity. However, after a thermal annealing process at the temperature above 800 °C, the film was converted to p-type via thermal activation of dopants. Specifically, the P_2O_5 dissociated and consequently the phosphorus atoms acted as acceptors. The ZnO films showed p-type behavior with a hole concentration of 1.0×10^{17}–1.7×10^{19} cm^{-3}, a mobility of 0.53–3.51 cm^2/V s, and a low resistivity of 0.59–4.4 Ω cm. Hwang et al. performed a detailed study on the PL of phosphorus-doped p-type ZnO by using P_2O_5 with a RF magnetron sputtering system [48]. It revealed an acceptor-bound exciton peak at 3.355 eV and a conduction band to the acceptor transition at 3.310 eV. The acceptor energy level of phosphorus was estimated to be 127 meV above the valence band. Li et al. [47] also carried out the phosphorus-doped ZnO growth by a pulsed-laser deposition system. They found that increasing the oxygen partial pressure from 20 to 200 mTorr yielded a carrier-type conversion from n- to p-type for films grown at 550 °C. Under an oxygen partial pressure of 150 mTorr, a marginal p-type ZnO film was obtained with a hole concentration of 2.7×10^{16} cm^{-3}, mobility of 8.2 cm^2/V s, and a resistivity of 35 Ω cm.

Many groups have also reported p-type conductivity by using Zn_3P_2. In early 2000, Aoki et al. [67] reported that by depositing a thin layer of Zn_3P_2 on n-type ZnO substrate and subsequently annealing, a homojunction was fabricated with a p-type ZnO layer on the n-type substrate. The light emission from this device at 110 K verified the formation of the real p–n junction. Inspired from this research, Vaithianathan et al. [69] used a pulsed-laser deposition to grow phosphorus-doped ZnO. The results of the Hall effect measurements taken at room temperature show that the 3-mol% phosphorus-doped ZnO films thermally annealed at temperature between 600 and 800 °C exhibit p-type behavior with a hole concentration of 5.1×10^{14}–1.5×10^{17} cm^{-3}, a hole mobility of 2.38–39.3 cm^2/V s, and a resistivity of 17–330 Ω cm. These studies suggest that the conductivity of phosphorus-doped ZnO may depend on growth and annealing conditions.

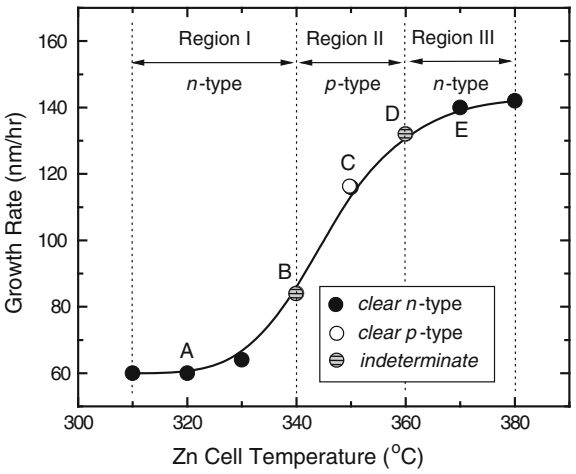

Fig. 4.7 Phosphorus-doped ZnO growth rate as a function of Zn cell temperature. Three regions were identified: Region I, extremely oxygen-rich region (n-type); Region II, oxygen-rich region (p-type); Region III, stoichiometric and Zn-rich region (n-type) [74]

Besides P_2O_5 and Zn_3P_2, GaP could be an alternative phosphorus dopant source. Xiu et al. [73, 74] utilized a solid-source GaP effusion cell to provide phosphorus dopants in a molecular beam epitaxy system. The GaP effusion cell was constructed with a Ga-trapping-cap system, which captures the parasitic Ga atoms upon the decomposition of GaP at high temperature of ~700 °C. As a result, a high purity P_2 beam was generated as the phosphorus dopant. Using this technique, Xiu et al. carried out a series of phosphorus-doped ZnO growth. Three growth regions were identified to generate ZnO films with different conduction types by systematically varying the Zn cell temperatures, as shown in Fig. 4.7. Hall effect and resistivity measurements revealed that, only in the oxygen-rich region (Region II), phosphorus-doped ZnO films exhibit p-type conductivities. A hole concentration of 6.0×10^{18} cm^{-3}, Hall mobility of 1.5 cm^2/V s and resistivity of 0.7 Ω cm were measured for the phosphorus-doped ZnO film. The low-temperature PL spectra reveal a strong peak at 3.317 eV, which was attributed to the phosphorus-associated A^0X emission, and from these data, the activation energy of phosphorus impurities is estimated to be 0.18 eV. Similar impact of the GaP doping on the p-type characteristics has been reported for RF magnetron sputtered ZnO thin films [75]. ZnO films with 2 % GaP content exhibited a resistivity of 2.17 Ω-cm, a hole concentration of 1.8×10^{18} cm^{-3}, and a mobility of 1.60 cm^2/V s. Low-temperature PL (10 K) spectrum exhibited signal corresponding to neutral acceptor-bound exciton recombination confirming p-type conductivity. The presence of high concentration of P than Ga was also confirmed by SIMS.

In spite of the amphoteric nature of phosphorus doping, some hetero- and homojunction LEDs were successfully fabricated by using phosphorus-doped p-type ZnO. Hwang et al. [76] reported the UV emission from a p-type ZnO/n-GaN heterostructure LED. The device consists of a phosphorus-doped p-type ZnO with a hole concentration of 6.68×10^{17} cm^{-3} and a Si-doped GaN with electron concentration of 1.1×10^{18} cm^{-3}. At an injection current of 60 mA, a blue-violet

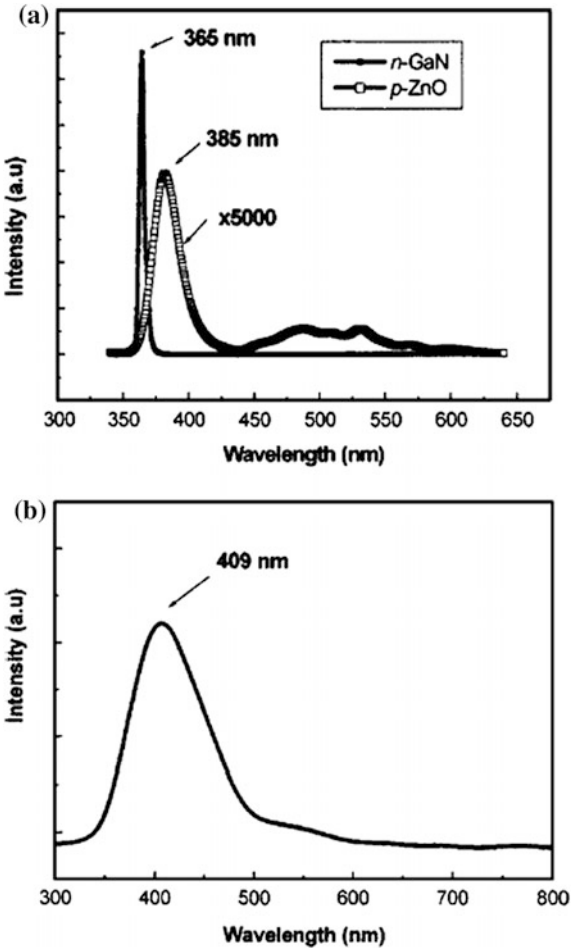

Fig. 4.8 **a** PL spectrum of n-GaN and p-type ZnO layers at room temperature and **b** an EL spectrum of p-type ZnO/n-GaN heterostructure at an injection current of 60 mA [76]

emission was observed at about 409 nm at room temperature. To verify the origin of EL emissions, the EL and PL spectra were compared, as shown in Fig. 4.8. Judging from the peak positions, the EL emission comes from the p-type ZnO region of the LED, instead of GaN. However, the peak positions exhibit a difference. That can be explained by a band offset of 0.13 eV at the valence band of p-type ZnO in the p-type ZnO/n-GaN band diagram.

Using the same doping method, Lim et al. have achieved further success in fabricating a homostructure LED [61]. The p-type ZnO was grown at high temperature of 900 °C by RF sputtering. The hole concentration reached 1.0×10^{19} cm^{-3} and mobility was 1 cm^2/V s. The homojunction ZnO LED showed an excellent rectifying characteristic with a turn-on voltage of 3.2 V, comparable to

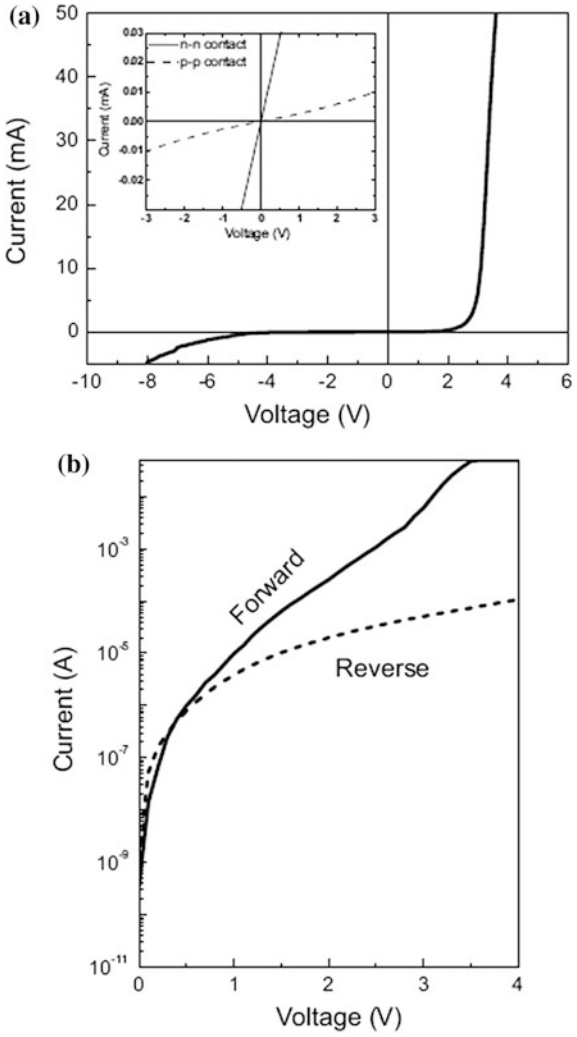

Fig. 4.9 *I–V* characteristics of the p–n homojunction ZnO LED at room temperature. **a** In the linear plot, the threshold voltage is 3.2 V. The *inset* shows the *I–V* characteristics of Ti/Au and NiO/Au ohmic contacts to n-type and p-type ZnO films, respectively. **b** In the semi-logarithmic plot, the current rectification factor is approximately 103 at a bias voltage of ±3.5 V [77]

the ZnO bandgap (Fig. 4.9). The p–n junction was operated at forward currents of 20 and 40 mA. The resultant EL spectra show near-band-edge emissions at 380 nm and deep emission at about 640 nm (Fig. 4.10). The deep-level emission can be further reduced by employing two $Mg_{0.1}Zn_{0.9}O$ layers as energy barriers to confine the carriers in the n-type ZnO. This work proves that phosphorus-doped ZnO by using P_2O_5 could be very promising for fabricating ZnO optoelectronic devices.

Authors would like to draw a special attention that the nanoscale p–n junctions can increase lighting efficiency due to the higher injection rate than planar

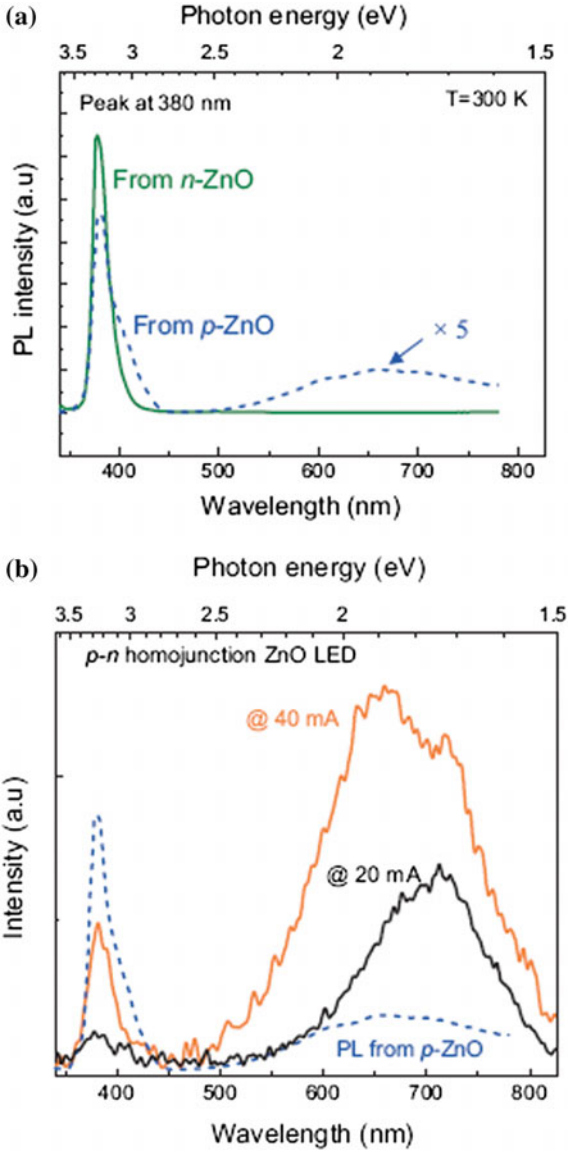

Fig. 4.10 **a** PL spectra of n- and p-type ZnO films at room temperature. The PL spectrum of the p-type ZnO film consists of near-band-edge emission and deep-level emission. **b** EL spectra of p–n homojunction ZnO LED operated at forward currents of 20 and 40 mA; PL spectrum of p-type ZnO obtained at room temperature [77]

junctions. To realize nanowire LEDs, it requires having p-type nanowires. In a recent report, p-type ZnO nanowire arrays were successfully achieved by using P_2O_5 as the dopant source in a simple chemical vapor disposition system [78]. The p-type conduction was confirmed by the low-temperature PL measurements and the electrical transport in single nanowire field-effect transistors. This discovery paves the way toward inexpensive new kind of SSL devices that could compete with today's GaN LEDs.

4.3.2.3 Arsenic Doping

Arsenic (As) has been predicted to have an acceptor level of 1150 meV, much deeper than that of nitrogen and phosphorus, assuming As substitutes for O [7]. However, several groups have reported successfully synthesizing As-doped p-type ZnO [79–92, 97]. For instance, Look et al. [84] prepared As-doped ZnO by an evaporation process. A thin Zn_3As_2 layer was deposited on a fused-quartz substrate, followed by the sputtering of ZnO. Through the As diffusion process, a p-type As-doped ZnO was obtained with a hole concentration of 4×10^{18} cm^{-3} and mobility of 4 cm^2/V s. A stable p-type behavior was reported for RF sputtered ZnO films dually implanted with As and O ions [93]. The ZnO films dually implanted to fluences of 1×10^{15} As cm^{-2} and 1×10^{14} O cm^{-2} exhibited a high hole mobility of 32.9 cm^2/V s and a low resistivity of 4.86×10^{-2} Ω-cm. The observed electrical performance and dominant acceptor-related peaks in PL spectrum suggested that O implantation played a key role in forming p-type ZnO films by reducing the density of oxygen vacancies and facilitating the formation of As-induced acceptors. Ryu et al. [81–83] innovatively grew As-doped ZnO films with a hybrid beam deposition technique. The Hall effect measurements show a hole concentration up to the mid-10^{17} cm^{-3} range. The As activation energy was found to be 120 ± 10 meV. Based on the successful As-doped p-type ZnO, Ryu et al. [81] for the first time demonstrated a ZnO LED employing a BeZnO/ZnO active layer with seven quantum wells (see Fig. 4.11). Two dominant EL emissions were observed at 363 and 388 nm, which arise from localized exciton emission in the quantum wells and from impurity-bound emissions in ZnO, respectively (Fig. 4.12). The broad emission at 550 nm is associated with the green band. Other devices such as photodiodes and p-type field-effect transistors were also fabricated based on the successful As-doped p-type ZnO [82]. The photodiodes exhibited dominant peak at 380 nm that is associated with band-edge absorption (Fig. 4.13). The other peak near 460 nm could be attributed to some deep defect levels. The p-type field-effect transistors showed typical *I–V* characteristics for a normally off MESFET with a p-channel (Fig. 4.14). More recently, Ryu et al. [94] fabricated ultraviolet laser diodes based on ZnO/BeZnO films. The devices demonstrated spontaneous and

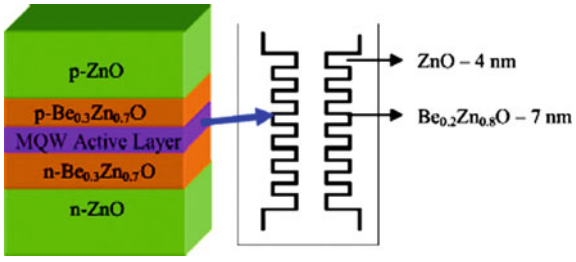

Fig. 4.11 Schematic illustration of the structure of the ZnO-based UV LED devices that employ a BeZnO/ZnO active layer comprised of MQWs [81]

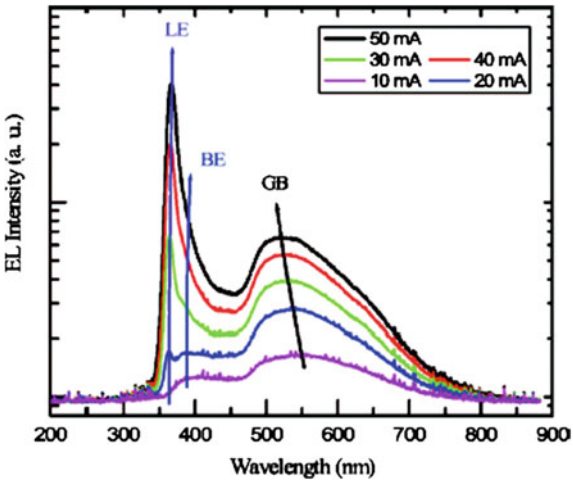

Fig. 4.12 EL spectrum measured at room temperature in continuous current mode of a p–n junction ZnO-based LED with a BeZnO active layer [81]

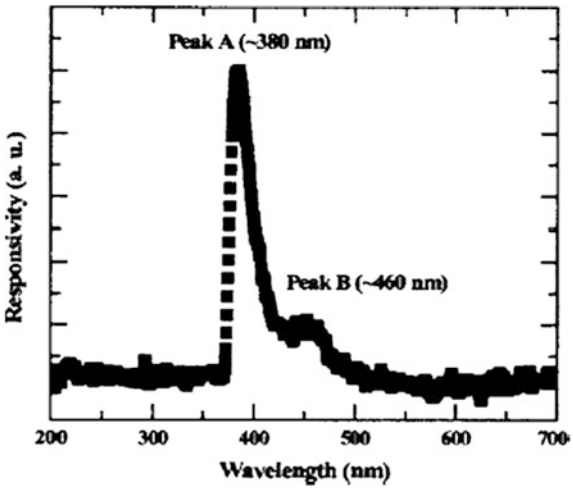

Fig. 4.13 Spectral response for a ZnO photodiode [82]

stimulated emissions from excitons at room temperature. Lasing action was observed both by optical and electrical pumping of these devices.

To explain the doping mechanism, Sukit and coworkers proposed a model for large-size-mismatched group V dopants in ZnO [56]. In this model, the dopants do not occupy the O sites, but rather the Zn sites: Each forms a complex with two spontaneously induced Zn vacancies in a process that involves fivefold As coordination. More importantly, an $As_{Zn}–2V_{Zn}$ complex may have lower formation energy than any of the parent defects. The activation energy of this complex was found to be 150 meV. In fact, several experimental results support this prediction. Wahl et al. [95] performed conversion electron emission channeling from

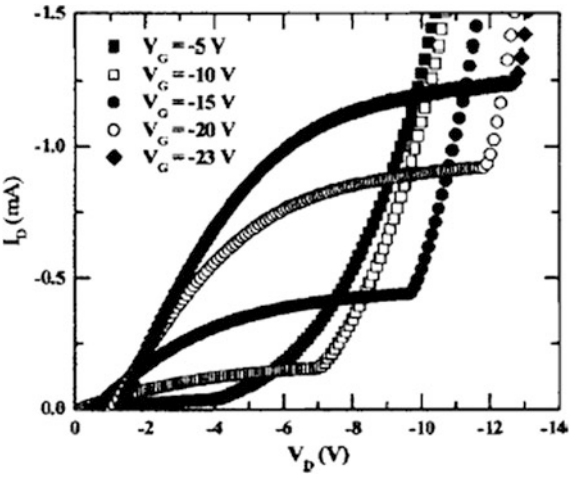

Fig. 4.14 I_D–V_D characteristics for a ZnO MESFET [82]

radioactive to determine the lattice site of As in ZnO. It is found that As does not occupy the oxygen site; instead, it prefers the substitutional Zn sites. This can be understood with the fact that As is more similar in terms of atomic radius with Zn than with oxygen. In 2006, Vaithianathan et al. [86] carried out the XANES spectroscopy to determine the As local structure and its chemical state in the As-doped p-type ZnO. The XANES spectrum of p-type As-doped shows a dominating As^{3-} peak at the photon energy of 11,860 eV besides a small As^0-related absorption peak, which would be expected if a large amount of As substituted for Zn. However, the n-type As-doped ZnO exhibits a dominating As^{5+} peak near 11,873 eV, indicating that As reacts with O to form As_2O_5 compound in n-type films. To compare the experimental results with theory, Sukit and coworkers performed the first-principles calculations to simulate the XANES spectra for various defect formations, such as As_o, As_{Zn}, and As_{Zn}–$2V_{Zn}$ [98]. Among all these species, the As_{Zn}–$2V_{Zn}$ defect complex shows a similar XANES spectrum as seen in the experiments. Therefore, Sukit and coworkers asserted that the formation of As_{Zn}–$2V_{Zn}$ is the cause of p-type conductivity in As-doped ZnO films.

4.3.2.4 Antimony Doping

Similarly, using this model, antimony (Sb) was predicted to produce p-type conductivity with the formation of shallow acceptor complex of Sb_{Zn}–$2V_{Zn}$. The activation energy was predicted to be 160 meV [56]. In accordance with this, several groups have experimentally obtained Sb-doped p-type ZnO [96, 99–102]. Aoki et al. [99] deposited a thin Sb metal film on top of ZnO and subsequently use an excimer laser to drive Sb dopant into the film to produce Sb-doped ZnO. The electrical measurements showed a low resistivity of 8×10^{-3} Ω cm, a hole mobility of 1.5 cm^2/V s, and an acceptor concentration of 5×10^{20} cm^{-3}. But the residual Sb

metal film on top of the ZnO layer and the non-uniformity of Sb doping might be a potential problem for fabricating reliable p-type ZnO and optoelectronic devices. David et al. [100] used a filtered vacuum arc deposition method to grow Sb-doped ZnO films. By incorporating 1.5 ± 0.3 % Sb with a O/Zn ratio of 0.721 ± 0.03, the as-grown films showed p-type conduction with a hole concentration of 1.03–4.65 × 10^{16} cm^{-3}.

More exciting results were reported by using a simple effusion cell to provide Sb dopant source in a molecular beam epitaxy system [96, 101]. Two sets of samples were grown with a systematic variation of Sb cell temperature and annealing temperature. The Hall effect measurements revealed that a hole concentration of 1.7 × 10^{18} cm^{-3} and a mobility of 20.0 cm^2/V s were attained by Sb doping. The temperature-dependent PL study revealed that emissions at 3.296 and 3.222 eV blue shifted with an increase of temperature from 8.5 to 100 K, in a manner consistent with free electron to acceptor (FA) and DAP transitions (Fig. 4.15). The acceptor energy level was estimated to be about 0.14 eV above the VBM. By studying the role of annealing temperatures on dopant activation, the doping mechanism is clarified. Sb prefers to substitute for Zn, instead of O, and simultaneously creates Zn vacancies. Some Zn vacancies connect with Sb_{Zn} to form the complex (Sb_{Zn}–$2V_{Zn}$) and serve as a shallow acceptor with an activation energy of 140 meV, which is close to the theoretical value of 160 meV [41]. The rest of the Zn vacancies are isolated in the films although they cannot contribute to strong p-type conductivity. The homojunction photodiodes based on Sb-doped p-type ZnO were also successfully fabricated on Si substrates [103]. The *I*–*V* measurements showed that the diode has a turn-on voltage of about 2 V (Fig. 4.16). A good response in the UV region was obtained under the reverse-biased condition. These experimental results demonstrate that Sb is a good candidate for p-type doping of ZnO films.

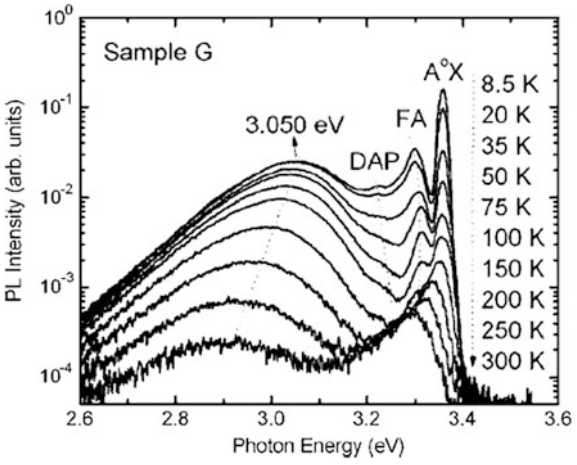

Fig. 4.15 PL spectra measured at several temperatures over the range from 8.5 to 300 K for an Sb-doped p-type ZnO [96]

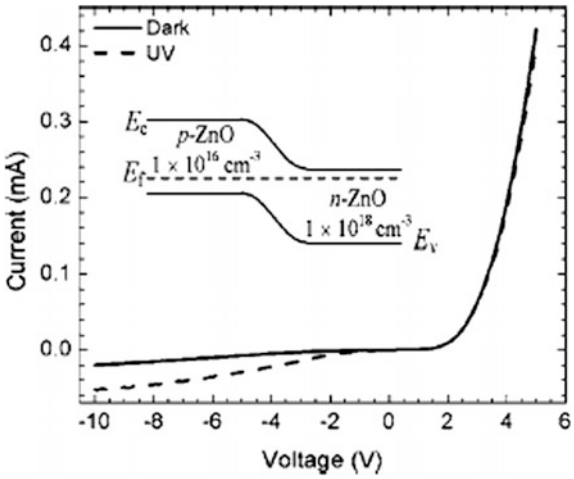

Fig. 4.16 *I–V* characteristics of the Ga-doped ZnO/Sb-doped ZnO p–n homojunction showing clear rectifying behavior. The *I–V* obtained in dark and UV is shown as *solid* and *dashed lines*, respectively. The *inset* shows the band diagram of the homojunction at zero bias [103]

More evidence of Sb_{Zn}–$2V_{Zn}$ formation was provided by Pan et al. [104] using a pulsed-laser deposition system. The X-ray photoemission spectroscopy measurement clearly presented a Sb–O associated peak at 539.9 eV for a Sb-doped p-type ZnO film. This indicated that Sb would occupy the Zn site and Sb_{Zn}–$2V_{Zn}$ could be the most likely candidate for a shallow acceptor. With the same growth method, another group has also succeeded in fabricating p-type Sb-doped ZnO on sapphire substrate [105]. The films grown at 600 °C had hole concentration of 1.9×10^{17} cm^{-3}, Hall mobility of 7.7 cm^2/V s, and resistivity of 4.2 Ω cm. The thermal activation energy for Sb acceptor was found to be 115 ± 5 meV, close to the theoretical prediction [56]. A similar acceptor-like Sb_{Zn}–$2V_{Zn}$ complex formation was observed for Sb-doped ZnO (SZO) thin films fabricated by dual ion beam sputtering technique [106]. The SZO films exhibited hole concentration, mobility, and resistivity values of 1.356×10^{17} cm^{-3}, 6.737 cm^2/V s, and 6.842 Ω-cm, respectively. The XPS analysis further established that Sb^{5+} states were preferable to Sb^{3+} states for Sb_{Zn}–$2V_{Zn}$ formation. These results for Sb-doped p-type ZnO films clearly indicate that the formation of Sb_{Zn}–$2V_{Zn}$ defect complex is the reason of p-type conduction induced by Sb doping.

4.3.2.5 Bismuth Doping

Bi is the last element of group V and has the largest atomic size among others. It is well established that Bi-doped ZnO is an excellent material for fabricating varistors. The typical process involves mixing ZnO and Bi_2O_3 powders and sintering them together at high temperature above 1000 °C. In general, the resultant films have

large concentration of Bi, especially at grain boundaries. These films also usually display phase separations of α- and β-phase Bi_2O_3, which is beneficial for varistor properties. However, the phase separation is not desirable for p-type doping. Duclere et al. [107] incorporated low-percentage Bi ($\sim$1.0 at.%) into ZnO films and tried to make it p-type. Unfortunately, the phase separation developed, giving rise to a high resistivity value from 3 to 350 Ω cm and low electron concentration ($\sim 10^{16}$ cm^{-3}). Xiu et al. [108] attempted to control the Bi concentration well below 1.0 at.% by a molecular beam epitaxy. The room temperature Hall effect measurements showed a significant reduction of electron concentration and an increase of resistivity with an increase in Bi concentration. The low-temperature PL showed a 3.222 eV DAP emission, which was confirmed by the temperature-dependent and excitation-power-dependent PL measurements. This experiment suggested that Bi could introduce acceptor states in ZnO. Eventually, the Bi-doped p-type ZnO was achieved by an electrochemical deposition method [109]. It was found that Bi in the ZnO matrix is mixed into states of Bi^0 (26 %) and Bi^{3+} (74 %). The optimized Bi-doped ZnO layer exhibited p-type conduction with a hole concentration of 1.18×10^{16} cm^{-3} and a mobility of 32.7 cm^2/V s. However, the Bi doping mechanism remains unclear so far.

4.3.3 Group IB p-type Doping

A theoretical study suggested that group IB elements such as Cu and Ag could be good candidates for fabricating p-type ZnO [110]. Between these two elements, Cu could be a better candidate because the size mismatch between Cu and Zn is smaller. Cu has limited thermodynamic equilibrium solubility in ZnO and can act as acceptor when it substitutes for Zn sublattice of ZnO. The group IB elements exhibit lower formation energy for the substitutional sites as compared to interstitial sites, and, thus the compensation effects of the interstitial atoms can be restrained. However, the ionization energy of the group IB elements is usually large to promote p-type conductivity. The addition of S has been shown to cause VB offset bowing in $ZnO_{1-x}S_x$ alloy which can be exploited to enhance the p-type doping efficiency and stability of Cu-doped ZnO films. The ZnO films alloyed with Cu and S showed very stable p-type conductivity with a hole concentration of $4.31–5.78 \times 10^{19}$ cm^{-3}, a resistivity of 0.29–0.34 Ω cm, and a mobility of 0.32–0.49 cm^2/V s. The p-type conductivity was attributed to the substitution of Cu^{1+} for the Zn site, and the ionization energy of the Cu^{1+} was measured to be 53 meV which is significantly lower than the value reported for Cu-doped ZnO films [111]. Guided by the theoretical predictions, Ahn et al. [112] have successfully achieved the Cu-doped p-type ZnO. The Mott–Schottky plot showed a negative slope, indicating a p-type conduction. The hole concentration was evaluated in the range of 10^{19}–10^{20} cm^{-3} more significantly, and the ZnO bandgap was reduced from 3.16 to 3.05 eV by increasing the degree of Cu doping, which might be due to the increase of the valance band and the formation of impurity bands.

Ag could also act as an acceptor in ZnO if incorporated on substitutional Zn sites. Fan and Freer suggested that Ag acted as an amphoteric dopant, existing both on substitutional Zn sites and in the interstitial sites. As a result, Ag doping decreases donor concentration [113]. Kanai [114] reported that Ag behaves as an acceptor with a deep level of 0.23 eV below the conduction band. However, the first-principles calculations revealed that Ag has a relatively shallow acceptor level of 400 meV. The formation energy of Ag_{Zn} is very low, while it is high at the interstitial sites under O-rich conditions [91]. From experiments, Ag-doped p-type ZnO thin films were synthesized by a pulsed-laser deposition [115]. It was found that a narrow window of deposition temperatures existed for p-type ZnO. The hole concentration was obtained in the range of 4.9×10^{16}–6.0×10^{17} cm^{-3}. A neutral acceptor-bound exciton peak of 3.317 eV was also observed in Ag-doped ZnO, which is similar to that of N-doped ZnO at 3.315 eV. Therefore, the Ag acceptor activation energy could be estimated as 170–200 meV.

4.3.4 Codoping

The codoping method with donor (such as Ga, Al, and In) and acceptor (N) incorporated into ZnO was proposed by Yamamoto and Katayama-Yoshida [116–119]. The basic idea of codoping is based on the formation of ion pairs between donor and acceptor ions and a subsequent decrease of Madelung energy by codoping, therefore significantly promoting the incorporation of N in ZnO. Although this method has been found itself to be hardly reproducible and controversial, a number of publications reported the successful fabrication of codoped p-type ZnO [120–137].

4.3.4.1 Ga-N Codoping

A second ion mass spectroscopy study on the solubility limits of Ga and N in ZnO showed the enhancement of N solubility by a factor of 400 as compared to that in N-implanted ZnO [42]. By using N_2O gas as an effective N source and Ga as the donor dopants, Joseph et al. [137] have grown a p-type ZnO with low resistivity of 2.0 Ω cm, a high hole concentration of 4×10^{19} cm^{-3}, and a low mobility of 0.07 cm^2/V s. The XPS analysis revealed the presence of Ga–N type of bonding and the approximate ratio of 1:6 for Ga:N in ZnO. Compared with the XPS results for GaN (1Ga:1N = 1:3.2), the real ratio of Ga:N could be corrected as 1:2 in the codoped p-type ZnO films, which is consistent with the theoretical predictions [138]. For example, (N, Ga) codoped ZnO films with a hole concentration of about 2.41×10^{18} cm^{-3} and a mobility of 4.29 cm^2/V s can be grown using MOCVD. A homojunction was also found to confirm the p-type conduction. It showed a fairly good rectifying behavior with a turn-on voltage of 3.7 V [139]. Unfortunately, some other groups have failed to reproduce p-type conduction based on the Ga–N

codoping method [124, 140, 141], although the presence of Ga–N bond was detected in (N, Ga)-codoped ZnO [140].

4.3.4.2 Al–N Codoping

Al has been extensively used for codoping with N in ZnO [121, 122, 125–128, 135, 136, 142–144]. The electrical properties of the Al–N-codoped ZnO films strongly depend on the activation of Al_{Zn} donor and the N_O acceptor [145]. An increase in hole concentration from 1.0×10^{16} to 1.5×10^{18} cm^{-3} was observed at ambient temperatures ranging from 80 to 300 K for Al–N-codoped ZnO films deposited by sputtering technique. The observed increase in hole concentration indicates significant contribution from shallow acceptors. Secondary ion mass spectroscopy (SIMS) has demonstrated that N incorporation is enhanced by the presence of Al in ZnO [121]. The resistivity, hole concentration, and Hall mobility are typically around 50–100 Ω cm, 1×10^{17}–8×10^{18} cm^{-3}, and 0.1–9.4 cm^2/V s, respectively [135, 145]. EL spectrum was observed with a near-band-edge emission at 3.18 eV and a deep-level emission at 2.58 eV at 110 K. The 3.18 eV emission was believed to be the radiative recombination of donor–acceptor pairs in the p-type ZnO layer. Unfortunately, the EL significantly quenched as the temperature increased, presumably due to the degradation of p-type ZnO [144].

4.3.4.3 In–N Codoping

In codoping with N was also found to dramatically enhance the N incorporation into ZnO [131, 146, 147]. The SIMS experiments were performed on a two-layer-structured film consisting of In–N-codoped ZnO and a N-doped ZnO on top. The N concentration was evidently higher in the codoped layer than that of N-doped layer [131]. The XPS spectra showed that two peaks are associated with N–In and Zn–N at 397.3 and 396.0 eV, respectively. Based on these experiments, it is reasonable to conclude that the presence of In improves the incorporation of N in ZnO by the formation of In–N and Zn–N bonds [147]. The rectifying characteristic of *I–V* curve was also observed in a ZnO-based homostructural p–n junction grown on quartz substrate. A low turn-on voltage of 1.9 V was obtained while the breakdown voltage is about 3.9 V. The EL emission was obtained by growing a ZnO homojunction on GaAs substrate. Unfortunately, only defect-related emission was observed at about 500 nm [148].

4.3.4.4 Other Codoping

Other metal–N-codoped ZnO was realized by using Be (group II) [149], Zr (group IVB) [150], and Te (group VI) [151]. Be was found to bind with N to form Be–N acceptors in p-type ZnO [149]. Zn–Te bond was expected to offer better acceptor

mobility as well as raise the valence-band energy, leading to improved acceptor ionization. The codoping experiments show that Te can be helpful in producing intrinsic ZnO thin films [151]. An increased concentration of Te ions into N-doped ZnO films not only made the acceptor energy level shallower but also resulted in improved crystalline quality and efficient suppression of native donor-like defects [152]. Zr–N codoping method was proved to successfully produce p-type ZnO with excellent electrical properties. A heterojunction based on p-type ZnO/n-type Si showed a rectifying *I–V* characteristic, indicating the formation of p-type ZnO [150]. However, no EL was observed.

4.3.4.5 Dual Acceptor Codoping

It was demonstrated that the donor–acceptor codoping method enhances nitrogen incorporation. However, the extra donors would significantly compromise the p-type conduction by introducing electrons. Therefore, it was proposed that dual acceptor doping might be helpful. Li–N codoping was extensively tried based on the assumption that the formation of Li_{Zn}–N would preclude or at least suppress the generation of Li_i and $(N_2)_O$ donor-like defects, which produce electrons in Li-doped and N-doped ZnO films, respectively [153–156]. Indeed, low-resistive Li–N codoped p-type ZnO was produced by a pulsed-laser deposition. Compared with N- and Li-monodoped ZnO films, the codoping method offers better electrical properties. And most importantly, the p-type conduction lasts over a year, which is far better than monodoping. The improved stability of dual acceptor doping indicates that the formation of compensating defects can be reduced with dual acceptor codoping [155]. XPS data have shown that Li and N are possibly combined to form a Li–N complex with a shallow acceptor level of 126 meV [153].

Besides Li–N codoping, Krost et al. [133] have attempted As–N codoping and studied the local p-type conductivity by means of scanning capacitance microscopy, which is a technique that probes the local conduction with C-V measurements. It was found that the local conductivity correlated to the surface morphology as two-dimensional surfaces has a p-type conduction, while three-dimensional growth yields n-type. In contrast to N or As monodoping, the codoped ZnO film shows stable homogeneous local p-type conduction, disturbed by a few n-type regions [157]. Swapna et al. [154] reported on the 4 at.% ZnO:(Ag,N) thin films exhibiting low resistivity with high hole concentration. The p-type conductivity was attributed to the formation of acceptor–acceptor (Ag_{Zn}–N_o) complex. The peak PL response of the dual acceptor-doped films at 2.56 eV indicated a low density of native defects which is confirmed by Ag and N incorporation in the samples. Based on the reported information in literature, it appears that dual acceptor doping could be a possible approach for p-type ZnO, but the underline mechanisms do not seem to be convincing, at least for now.

4.3.5 *Intrinsic p-type ZnO*

There are several reports on the p-type behavior in nominally undoped ZnO films [158–166]. Zeng et al. [158] reported the growth of intrinsic p-type ZnO films by plasma-assisted metal organic CVD. By increasing oxygen partial pressure, a p-type film was obtained with a resistivity of 12.7 Ω cm, a Hall mobility of 2.6 cm^2/V s, and a hole concentration of 1.88×10^{17} cm^{-3}. Two acceptor states, with energy located at 160 and 270 meV above the VBM, were identified by temperature-dependent PL measurements. The origin of intrinsic p-type behavior was attributed to the formation of zinc vacancies and some complex acceptor centers. Other studies also revealed similar phenomena. That is, by increasing oxygen partial pressure, the conductivity of films can convert from n-type to p-type, meaning that the intrinsic defects, such as V_{Zn}, could dominate the carrier type [164]. The pulsed-laser deposited undoped ZnO films showed a conductivity conversion from n-type to p-type depending on the growth temperature and nature of underlying Si substrate [166]. The ZnO films grown on *n*-type Si substrates exhibited n-type conductivity for all Hall temperatures. However, ZnO films grown on *p*-type Si showed a conductivity conversion from n- to p-type at Hall temperatures between 190 and 250 K. The n-type conductivity is observed at Hall temperatures below 190 K, while p-type conductivity is observed above 250 K. The observed behavior can be attributed to the thermal competition between donor-like defects, mostly oxygen vacancies and hydrogen impurity, and acceptor-like defects such as Zn vacancies and/or oxygen interstitials. From theoretical calculation point of view, V_{Zn} has a lower formation energy and could serve as the dominant acceptor in intrinsic ZnO [10, 56, 167, 168]. Sukit et al. and Lin et al. predicted that V_{Zn} should have a level of 370–390 meV. Recently, positron annihilation spectroscopy was used to identify and quantify the open volume defects in ZnO [169]. It was found that V_{Zn} are the primary acceptors with a concentration of $\sim 2 \times 10^{15}$ cm^{-3}. After irradiation by 2 MeV electrons with a fluence of 6×10^{17} cm^{-3}, the concentration of V_{Zn} increases approximately ten times. Although the direct positron annihilation data are not available for the intrinsic p-type films, it is believed that V_{Zn} species could be the most source of p-type conductivity in the nominally undoped ZnO films.

4.4 Conclusion

In summary, the current status of ZnO p-type doping has been comprehensively reviewed in this work, including the different doping methods and dopant sources. It is reasonable to conclude that up to now, the stability and reproducibility are still great challenges for the ZnO community. The current state of p-type doping of ZnO seems to be similar to that of p-type doping of GaN more than 20 years ago. By then, GaN LED research virtually ceased because it was difficult to produce p-type

carriers in GaN. The materials research director at *Radio Corporation of America*, James Tietjen, stated in 1980 that it was time to "*stop this garbage*" in reference to GaN LED technology [170]. Then, in the next decade, GaN and GaN alloy-based LED technology became the state-of-the-art in terms of lighting efficiency. Therefore, it is believed that, with continuing innovation, the p-doping difficulty in ZnO can be solved. The next-generation high-efficiency SSL devices based on ZnO are promising candidates for commercialization in a wide variety of applications.

Acknowledgements This research was sponsored by the National Young 1000 Talent Plan, Pujiang Talent Plan in Shanghai, National Natural Science Foundation of China (61322407, 11474058), the US Department of Energy, National Nuclear Security Administration, Office of Nonproliferation and Verification Research and Development, and Oak Ridge National Laboratory SEED funding.

References

1. Nakamura, S., Iwasa, N., Senoh, M., Mukai, T.: Hole compensation mechanism of P-type GaN films: Jpn. J. Appl. Phys. **31**, 1258 (1992)
2. Choi, Y.-S., Kang, J.-W., Hwang, D.-K., Park, S.-J.: Recent advances in ZnO-based light-emitting diodes. IEEE Trans. Electron Dev. **57**, 26 (2010)
3. Tynell, T., Karppinen, M.: Atomic layer deposition of ZnO: A review, Semicond. Sci. Technol. **29**, 043001 (2014)
4. Varol, S.F., Sahin, D., Kompitsas, M., Çankaya, G.: The impact of different ZnO growth methods on the electrical and optical properties of a n-ZnO/p-GaN:Mg/c-plane sapphire UV LED. RSC Adv. **4**, 13593 (2014)
5. Chiaria, S., Goano, M., Bellotti, E.: Numerical study of ZnO-based LEDs. IEEE J. Quantum Electron. **47**, 661 (2011)
6. Özgür, Ü., Hofstetter, D., Morkoç, H.: ZnO devices and applications: A review of current status and future prospects. Proc. IEEE **98**, 1255 (2010)
7. Park, C.H., Zhang, S.B., Wei, S.H.: Origin of p-type doping difficulty in ZnO: The impurity perspective. Phys. Rev. B **66**, 073202 (2002)
8. Kohan, A.F., Ceder, G., Morgan, D., Van de Walle, C.G.: First-principles study of native point defects in ZnO. Phys. Rev. B Condens. Matter. Mater. Phys. **61**, 15019 (2000)
9. Look, D.C.: Progress in ZnO materials and devices. J. Electron. Mater. **35**, 1299 (2006) (and the references herein)
10. Zhang, S.B., Wei, S.H., Zunger, A.: Intrinsic n-type versus p-type doping asymmetry and the defect physics of ZnO. Phys. Rev. B: Condens. Matter. Mater. Phys. **63**, 075205 (2001)
11. Oba, F., Nishitani, S.R., Isotani, S., Adachi, H., Tanaka, I.: Energetics of native defects in ZnO. J. Appl. Phys. **90**, 824 (2001)
12. Bunn, C.W.: A comparative review of ZnO materials and devices. Proc. Phys. Soc. London **47**, 836 (1935)
13. Van de Walle, C.G.: Hydrogen as a cause of doping in zinc oxide. Phy. Rev. Lett. **85**, 1012 (2000)
14. Avrutin, V., Silversmith, D.J., Morkoç, H.: Doping asymmetry problem in ZnO: current status and outlook. Proc. IEEE **98**, 1269 (2010)
15. Look, D.C., Farlow, G.C., Reunchan, P., Limpijumnong, S., Zhang, S.B., Nordlund, K.: Evidence for native-defect donors in n-type ZnO. Phys. Rev. Lett. **95**, 225502 (2005)

16. Ko, H.J., Chen, Y.F., Hong, S.K., Wenisch, H., Yao, T., Look, D.C.: Ga-doped ZnO films grown on GaN templates by plasma-assisted molecular-beam epitaxy. Appl. Phys. Lett. **77**, 3761 (2000)
17. Park, S.M., Ikegami, T., Ebihara, K.:Effects of substrate temperature on the properties of Ga-doped ZnO by pulsed laser deposition. Thin Solid Films **513**, 90 (2006)
18. Le, H.Q., Chua, S.J.: Gallium and Indium co-doping of epitaxial ZnO thin films grown in water at 90°C. J. Phys. D Appl. Phys. **44**, 125104 (2011)
19. Kim, K.K., Tampo, H., Song, J.O., Seong, T.Y., Park, S.J., Lee, J.M., Kim, S.W., Fujita, S., Niki, S.: Effect of rapid thermal annealing on Al doped n-ZnO films grown by RF-magnetron sputtering. Japanese J. Appl. Phys. **44**, 4776 (2005)
20. Seo, K.-W., Shin, H.-S., Lee, J.-H., Chung, K.-B., Kim, H.-K.: The effects of thickness on the electrical, opticcal, structural and morphological properties of Al and Ga co-doped ZnO films grown by linear facing target sputtering. Vacuum **101**, 250 (2014)
21. Lee, E.C., Chang, K.J.: Possible p-type doping with group-I elements in ZnO. Phys. Rev. B **70**, 115210 (2004)
22. Look, D.C., Claflin, B.: P-type doping and devices based on ZnO. Phys. Status Solidi B **241**, 624 (2004)
23. Wardle, M.G., Goss, J.P., Briddon, P.R.: Theory of Li in ZnO: A limitation for Li-based p-type doping. Phys. Rev. B **71**, 155205 (2005) (and the reference herein)
24. Zeng, Y.J., Ye, Z.Z., Xu, W.Z., Chen, L.L., Li, D.Y., Zhu, L.P., Zhao, B.H., Hu, Y.L.: Realization of p-type ZnO films via monodoping of Li acceptor. J. Cryst. Growth **283**, 180 (2005)
25. Zeng, Y.J., Ye, Z.Z., Lu, J.G., Xu, W.Z., Zhu, L.P., Zhao, B.H., Limpijumnong, S.: Identification of acceptor states in Li-doped p-type ZnO thin films. Appl. Phys. Lett. **89**, 042106 (2006)
26. Zeng, Y.J., Ye, Z.Z., Xu, W.Z., Li, D.Y., Lu, J.G., Zhu, L.P., Zhao, B.H.: Dopant source choice for formation of p -type ZnO: Li acceptor. Appl. Phys. Lett. **88**, 062107 (2006)
27. Lu, J.G., Zhang, Y.Z., Ye, Z.Z., Zeng, Y.J., He, H.P., Zhu, L.P., Huang, J.Y., Wang, L., Yuan, J., Zhao, B.H., Li, X.H.: Control of p- and n-type conductivity in Li-doped ZnO thin films. Appl. Phys. Lett. **89**, 112113 (2006)
28. Meyer, B.K., Stehr, J., Hofstaetter, A., Volbers, N., Zeuner, A., Sann, J.: On the role of group I elements in ZnO. Appl. Phys. A **88**, 119 (2007)
29. Meyer, B.K., Sann, J., Zeuner, A.: Lithium and sodium acceptors in ZnO. Superlattice Microstruct. **38**, 344 (2005)
30. Lin, S.S., Lu, J.G., Ye, Z.Z., He, H.P., Gu, X.Q., Chen, L.X., Huang, J.Y., Zhao, B.H.: p-type behavior in Na-doped ZnO films and ZnO homojunction light-emitting diodes. Solid State Commun. **148**, 25 (2008)
31. Yang, L.L., Ye, Z.Z., Zhu, L.P., Zeng, Y.J., Lu, Y.F., Zhao, B.H.: Fabrication of p-type ZnO thin films via DC reactive magnetron sputtering by using Na as the dopant Source. J. Electron. Mater. **36**, 498 (2007)
32. Lai, J.-J., Lin, Y.-J., Chen, Y.-H., Chang, H.-C., Liu, C.-J., Zou, Y.-Y., Shih, Y.-T., Wang, M.-C.: Effects of Na content on the luminescence behavior, conduction type, and crystal structure of Na-doped ZnO films. J. Appl. Phys. **110**, 013704 (2011)
33. Myers, M.A., Myers, M.T., General, M.J., Lee, J.H., Shao, L., Wang, H.: P-type ZnO thin films achieved by N+ ion implantation through dynamic annealing process. Appl. Phys. Lett. **101**, 112101 (2012)
34. Chen, X., Zhang, Z., Yao, B., Jiang, M., Wang, S., Li, B., Shan, C., Liu, L., Zhao, D., Shen, D.: Effect of Compressive Stress on Stability of N-doped p-type ZnO. Appl. Phys. Lett. **99**, 091908 (2011)
35. Lyons, J.L., Janotti, A., Van de Walle, C.G.: Why nitrogen cannot lead to p-type conductivity in ZnO. Appl. Phys. Lett. **95**, 252105 (2009)
36. Wang, Z., Yue, Y., Cao, Y.: Preparation and properties of nitrogen doped p-type zinc oxide films by reactive magnetron sputtering. Vacuum **101**, 313 (2014)

37. Look, D.C., Reynolds, D.C., Litton, C.W., Jones, R.L., Eason, D.B., Cantwell, G.: Characterization of homoepitaxial p-type ZnO grown by molecular beam epitaxy. Appl. Phys. Lett. **81**, 1830 (2002)
38. Zuener, A., Alves, H., Hofmann, D.M., Meyer, B.K., Hoffmann, A., Haboeck, U., Strassburg, M., Dworzak, M. Optical properties of the nitrogen acceptor in epitaxial ZnO. Phys. Status Solidi B **234**, R7 (2002)
39. Lu, J., Zhang, Y., Ye, Z., Wang, L., Zhao, B., Huang, J.: p-type ZnO films deposited by DC reactive magnetron sputtering at different ammonia concentrations. Mater. Lett. **57**, 3311 (2003)
40. Nakahara, K., Takasu, H., Fons, P., Yamada, A., Iwata, K., Matsubara, K., Hunger, R., Niki, S.: Interactions between gallium and nitrogen dopants in ZnO films grown by radical-source molecular-beam epitaxy. Appl. Phys. Lett. **79**, 4139 (2001)
41. Look, D.C.: Electrical and optical properties of p-type ZnO. Semicond. Sci. Technol. **20**, S55 (2005)
42. Ozgur, U., Alivov, Y.I., Liu, C., Teke, A., Reshchikov, M.A., Dogan, S., Avrutin, V., Cho, S.-J., Morkoc, H.: A comprehensive review of ZnO materials and devices. J. Appl. Phys. **98**, 041301 (2005) (and the references herein)
43. Yan, Y.F., Zhang, S.B.: Control of doping by impurity chemical potentials: Predictions for p-type ZnO. Phys. Rev. Lett. **86**, 5723 (2001)
44. Tsukazaki, A., Ohtomo, A., Onuma, T., Ohtani, M., Makino, T., Sumiya, M., Ohtani, K., Chichibu, S.F., Fuke, S., Segawa, Y., Ohno, H., Koinuma, H., Kawasaki, M.: Repeated temperature modulation epitaxy for p-type doping and light-emitting diode based on ZnO. Nat. Mater. **4**, 42 (2005)
45. Xu, J., Ott, R., Sabua, A.S., Pan, Z., Xiu, F., Liu, J., Erie, J., Norton, D.: unpublished
46. Zunger, A.: Practical doping principles. Appl. Phys. Lett. **83**, 57 (2003)
47. Li, X., Asher, S.E., Limpijumnong, S., Keyes, B.M., Perkins, C.L., Barnes, T.M., Moutinho, H.R., Luther, J.M., Zhang, S.B., Wei, S.H., Coutts, T.J.: Impurity effects in ZnO and nitrogen-doped ZnO thin films fabricated by MOCVD. J. Cryst. Growth **287**, 94 (2006)
48. Limpijumnong, S., Li, X., Wei, S.H., Zhang, S.B.: Probing deactivations in Nitrogen doped ZnO by vibrational signatures: A first principles study. Phys. B **376–377**, 686 (2006)
49. Lu, J.G., Fujita, S., Kawaharamura, T., Nishinaka, H.: Roles of hydrogen and nitrogen in p-type doping of ZnO. Chem. Phys. Lett. **441**, 68 (2007)
50. Zhang, Y., Lu, J., Chen, L., Ye, Z.: Properties of N-doped ZnO thin films in annealing process. Solid State Commun. **143**, 562 (2007)
51. Fons, P., Tampo, H., Niki, S., Kolobov, A.V., Ohkubo, M., Tominaga, J., Friedrich, S., Carboni, R., Boscherini, F.: Soft X-ray XANES of N in ZnO: N–Why is doping so difficult? Nucl. Instrum. Meth. Phys. Res. B **246**, 75 (2006)
52. Guo, X.L., Tabata, H., Kawai, T.: Pulsed laser reactive deposition of p-type ZnO film enhanced by an electron cyclotron resonance source. J. Crystal Growth **223**, 135 (2001)
53. Fons, P., Tampo, H., Kolobov, A.V., Ohkubo, M., Niki, S., Tominaga, J., Carboni, R., Boscherini, F., Friedrich, S.: Direct observation of nitrogen location in molecular beam epitaxy grown nitrogen-doped ZnO. Phys. Rev. Lett. **96**, 045504 (2006)
54. Wei, Z.P., Lu, Y.M., Shen, D.Z., Zhang, Z.Z., Yao, B., Li, B.H., Zhang, J.Y., Zhao, D.X., Fan, X.W., Tang, Z.K.: Room temperature pn ZnO blue-violet light-emitting diodes. Appl. Phys. Lett. **90**, 042113 (2007)
55. Liu, J.S., Shan, C.X., Shen, H., Li, B.H., Zhang, Z.Z., Liu, L., Zhang, L.G., Shen, D.Z.: ZnO light-emitting devices with a lifetime of 6.8 hours. Appl. Phys. Lett. **101**, 011106 (2012)
56. Limpijumnong, S., Zhang, S.B., Wei, S.H., Park, C.H.: Doping by large-size-mismatched impurities: the microscopic origin of arsenic-or antimony-doped p-type zinc oxide. Phys. Rev. Lett. **92**, 155504 (2004)
57. Lee, W.J., Kang, J., Chang, K.J.: Electronic structure of phosphorus dopants in ZnO. Phys. B **376–377**, 699 (2006)
58. Lee, W.J., Kang, J., Chang, K.J.: Defect properties and p-type doping efficiency in phosphorus-doped ZnO. Phys. Rev. B **73**, 024117 (2006)

59. Yu, Z.G., Gong, H., Wu, P.: Dopant sources choice for formation of p-type ZnO: Phosphorus compound sources. Chem. Mater. **17**, 852 (2005)
60. Chen, F.G., Ye, Z.Z., Xu, W.Z., Zhao, B.H., Zhu, L.P., Lv, J.G.: Fabrication of p-type ZnO thin films via MOCVD method by using phosphorus as dopant source. J. Cryst. Growth **281**, 458 (2005)
61. Yu, Z.G., Gong, H., Wu, P.: Study on anomalous n-type conduction of P-doped ZnO using P2O5 dopant source. Appl. Phys. Lett. **86**, 212105 (2005)
62. Li, Y.J., Heo, Y.W., Kwon, Y., Ip, K., Pearton, S.J., Norton, D.P.: Transport properties of p-type phosphorus-doped (Zn, Mg) O grown by pulsed-laser deposition. Appl. Phys. Lett. **87** (07), 2101 (2005)
63. Hwang, D.K., Kim, H.S., Lim, J.H., Oh, J.Y., Kim, K.K., Look, D.C., Park, Y.S.: Study of the photoluminescence of phosphorus-doped p-type ZnO thin films grown by radio-frequency magnetron sputtering. Appl. Phys. Lett. **86**, 151917 (2005)
64. Miao, Y., Ye, Z.Z., Xu, W.Z., Chen, F.G., Zhou, X.C., Zhao, B.H., Zhu, L.P., Lu, J.G.: p-Type conduction in phosphorus-doped ZnO thin films by MOCVD and thermal activation of the dopant. Appl. Surf. Sci. **252**, 7953 (2006)
65. Kim, K.K., Kim, H.S., Hwag, D.K., Lim, J.H., Park, S.J.: Realization of p-type ZnO thin films via phosphorus doping and thermal activation of the dopant. Appl. Phys. Lett. **83**, 63 (2003)
66. Yang, H., Li, Y., Norton, D.P., Pearton, S.J., Jung, S., Ren, F., Boatner, L.A.: Characteristics of unannealed ZnMgO/ZnO pn junctions on bulk (100) ZnO substrates. Appl. Phys. Lett. **86**, 172103 (2005)
67. Aoki, T., Hatanaka, Y., Look, D.C.: ZnO diode fabricated by excimer-laser doping. Appl. Phys. Lett. **76**, 3257 (2000)
68. Ko, Y.D., Jung, J., Bang, J.H., Park, M.C., Huh, K.S., Myoung, J.M., Yun, I.: Characteristics of ZnO/Si prepared by Zn3P2 diffusion. Appl. Surf. Sci. **202**, 266 (2002)
69. Vaithianathan, V., Lee, B.T., Kim, S.S.: Pulsed-laser-deposited p-type ZnO films with phosphorus doping. Appl. Phys. Lett. **98**, 043519 (2005)
70. Tampo, H., Shibata, H., Fons, P., Yamada, A., Matsubara, K., Iwata, K., Tamura, K., Takasu, H., Niki, S.: The effects of thermal treatments on the electrical properties of phosphorus doped ZnO layers grown by MBE. J. Cryst. Growth **278**, 268 (2005)
71. Vaithianathan, V., Lee, B.T., Kim, S.S.: Growth of phosphorus doped ZnO thin films by pulsed laser deposition. Phys. Status Solidi A **201**, 2837 (2004)
72. Bang, K.H., Hwang, D.K., Park, M.C., Ko, Y.D., Yun, I., Myoung, J.M.: Formation of p-type ZnO film on InP substrate by phosphor doping. Appl. Surf. Sci. **210**, 177 (2003)
73. Xiu, F.X., Yang, Z., Mandalapu, L.J., Liu, J.L., Beyermann, W.P.: p-type ZnO films with solid-source phosphorus doping by molecular-beam epitaxy. Appl. Phys. Lett. **88**, 052106 (2006)
74. Xiu, F.X., Yang, Z., Mandalapu, L.J., Liu, J.L.: Donor and acceptor competitions in phosphorus-doped ZnO. Appl. Phys. Lett. **88**, 152116 (2006)
75. Gowrishankar, S., Balakrishnan, L., Balasubramanian, T., Gopalakrishnan, N.: Fabrication of n-Zn1−xGaxO/p-(ZnO)1−x(GaP)x thin films and homojunction. Mater. Sci. Eng. B **178**, 31 (2013)
76. Hwang, D.K., Kang, S.H., Lim, J.H., Yang, E.J., Oh, J.Y., Yang, J.H., Park, S.J.: p-ZnO/n-GaN heterostructure ZnO light-emitting diodes. Appl. Phys. Lett. **86**, 222101 (2005)
77. Lim, J.H., Kang, C.K., Kim, K.K., Park, I.K., Hwang, D.K., Park, S.J.: UV electroluminescence emission from ZnO light-emitting diodes grown by high-temperature radiofrequency sputtering. Adv. Mater. **18**, 2720 (2006)
78. Xiang, B., Wang, P., Zhang, X., Dayeh, S.A., Aplin, D.P.R., Soci, C., Yu, D., Wang, D.: Rational synthesis of p-type zinc oxide nanowire arrays using simple chemical vapor deposition. Nano Lett. **7**, 323 (2007)
79. Ryu, Y.R., Zhu, S., Look, D.C., Wrobel, J.M., Jeong, H.M., White, H.W.: Synthesis of p-type ZnO films. J. Cryst. Growth **216**, 330 (2000)

80. Ryu, Y.R., Lee, T.S., White, H.W.: Properties of arsenic-doped p-type ZnO grown by hybrid beam deposition. Appl. Phys. Lett. **83**, 87 (2003)
81. Ryu, Y.R., Lee, T.S., Lubguban, J.A., White, H.W., Kim, B.J., Park, Y.S., Youn, C.J.: Next generation of oxide photonic devices: ZnO-based ultraviolet light emitting diodes. Appl. Phys. Lett. **88**, 241108 (2006)
82. Ryu, Y.R., Lee, T.S., Lubguban, J.A., White, H.W., Park, Y.S., Youn, C.J.: ZnO devices: Photodiodes and p-type field-effect transistors. Appl. Phys. Lett. **87**, 153504 (2005)
83. Ryu, Y.R., Lee, T.S., White, H.W.: A technique of hybrid beam deposition for synthesis of ZnO and other metal oxides. J. Cryst. Growth **261**, 502 (2004)
84. Look, D.C., Renlund, G.M., Burgener II, R.H., Sizelove, J.R.: As-doped p-type ZnO produced by an evaporation/sputtering process. Appl. Phys. Lett. **85**, 5269 (2004)
85. Vaithianathan, V., Lee, B.T., Kim, S.S.: Preparation of As-doped p-type ZnO films using a Zn3As2/ZnO target with pulsed laser deposition. Appl. Phys. Lett. **86**, 062101 (2005)
86. Vaithianathan, V., Lee, B.T., Chang, C.H., Asokan, K., Kim, S.S.: Characterization of As-doped, p-type ZnO by x-ray absorption near-edge structure spectroscopy. Appl. Phys. Lett. **88**, 112103 (2006)
87. Braunstein, G., Muraviev, A., Saxena, H., Dhere, N., Richter, V., Kalish, R.: p type doping of zinc oxide by arsenic ion implantation. Appl. Phys. Lett. **87**, 192103 (2005)
88. Jeong, T.S., Han, M.S., Youn, C.J., Park, Y.S.: Raman scattering and photoluminescence of As ion-implanted ZnO single crystal. J. Appl. Phys. **96**, 175 (2004)
89. Jeong, T.S., Han, M.S., Kim, J.H., Youn, C.J., Ryu, Y.R., White, H.W.: Crystallinity-damage recovery and optical property of As-implanted Zno crystals by post-implantation annealing. J. Cryst. Growth **275**, 541 (2005)
90. Lee, W., Jeong, M.C., Joo, S.W., Myoung, J.M.: Arsenic doping of ZnO nanowires by post-annealing treatment. Nanotechnology **16**, 764 (2005)
91. Xu, N., Xu, Y.L., Li, L., Shen, Y.Q., Zhang, T.W., Wu, J.D., Sun, J., Ying, Z.F.: Arsenic doping for synthesis of nanocrystalline p-type ZnO thin films. J. Vac. Sci. Technol. A **24**, 517 (2006)
92. Lee, W., Jeong, M.C., Myoung, J.M.: Optical characteristics of arsenic-doped ZnO nanowires. Appl. Phys. Lett. **85**, 6167 (2004)
93. Kim, C.O., Shin, D.H., Kim, S., Choi, S.-H., Belay, K.: Effect of (O, As) dual implantation on p-type doping of ZnO films. J. Appl. Phys. **110**, 103708 (2011)
94. Ryu, Y.R., Lubguban, J.A., Lee, T.S., White, H.W., Jeong, T.S., Youn, C.J., Kim, B.J.: Excitonic ultraviolet lasing in ZnO-based light emitting devices. Appl. Phys. Lett. **90**(13), 1115 (2007)
95. Wahl, U., Rita, E., Correia, J.G., Marques, A.C., Alves, E., Soares, J.C.: Direct evidence for as as a Zn-site impurity in ZnO. Phys. Rev. Lett. **95**(21), 5503 (2005)
96. Xiu, F.X., Yang, Z., Mandalapu, L.J., Zhao, D.T., Liu, J.L.: Photoluminescence study of Sb-doped p-type ZnO films by molecular-beam epitaxy. Appl. Phys. Lett. **87**, 252102 (2005)
97. Braunstein, G., Muraviev, A., Saxena, H., Dhere, N., Richter, V., Kalish, R.: p type doping of zinc oxide by arsenic ion implantation. Appl. Phys. Lett. **87**, 192103 (2005)
98. Limpijumnong, S., Smith, M.F., Zhang, S.B.: Comment on "Characterization of As-doped, p-type ZnO by x-ray absorption near-edge structure spectroscopy: Theory". Appl. Phys. Lett. **89**, 222113 (2006)
99. Aoki, T., Shimizu, Y., Miyake, A., Nakamura, A., Nakanishi, Y., Hatanaka, Y.: p-type ZnO layer formation by excimer laser doping. Phys. Status Solidi B **229**, 911 (2002)
100. David, T., Goldsmith, S., Boxman, R.L.: Dependence of zinc oxide thin film properties on filtered vacuum arc deposition parameters. J. Phys. D: Appl. Phys. **38**, 2407 (2005)
101. Xiu, F.X., Yang, Z., Mandalapu, L.J., Zhao, D.T., Liu, J.L., Beyermann, W.P.: High-mobility Sb-doped p-type ZnO by molecular-beam epitaxy. Appl. Phys. Lett. **87**, 152101 (2005)
102. Friedrich, F., Sieber, I., Klimm, C., Klaus, M., Genzel, C., Nickel, N.H.: Sb-doping of ZnO: Phase segregation and its impact on p-type doping. Appl. Phys. Lett. **98**, 131902 (2011)

103. Mandalapu, L.J., Yang, Z., Xiu, F.X., Zhao, D.T., Liu, J.L.: Homojunction photodiodes based on Sb-doped p-type ZnO for ultraviolet detection. Appl. Phys. Lett. **88**, 092103 (2006)
104. Pan, X., Ye, Z., Li, J., Gu, X., Zeng, Y., He, H., Zhu, L., Che, Y.: Fabrication of Sb-doped p-type ZnO thin films by pulsed laser deposition. Appl. Surf. Sci. **253**, 5067 (2007)
105. Guo, W., Allenic, A., Chen, Y.B., Pan, X.Q., Che, Y., Hu, Z.D., Liu, B.: Microstructure and properties of epitaxial Antimony-doped p-type ZnO films fabricated by pulsed laser deposition. Appl. Phys. Lett. **90**, 242108 (2007)
106. Pandey, S.K., Pandey, S.K., Avasthi, V., Gupta, M., Deshpande, U.P., Mukherjee, S.: Influence of in-situ annealing ambient on p-type conduction in dual ion beam sputtered Sb-doped ZnO thin films. Appl. Phys. Lett. **103**, 072109 (2013)
107. Duclere, J.R., Haire, R.O., Meaney, A., Johnston, K., Reid, I., Tobin, G., Mosnier, J.P., Viry, M.G., Mcglynn, E., Henry, M.O.: Fabrication of P-type doped ZnO thin films using pulsed laser deposition for device applications. J. Mater. Sci. **16**, 421 (2005)
108. Xiu, F.X., Mandalapu, L.J., Yang, Z., Liu, J.L., Liu, G.F., Yarmoff, J.A.: Bi-induced acceptor states in ZnO by molecular-beam epitaxy. Appl. Phys. Lett. **89**, 052103 (2006)
109. Pan, C.J., Cheng, H.Y., Chung, R.J., Li, J.H., Kao, K.F., Chin, T.S.: Bi-doped ZnO layer prepared by electrochemical deposition. J. Electrochem. Soc. **154**, D117 (2007)
110. Yan, Y., Al-Jassim, M.M., Wei, S.H.: Doping of ZnO by group-IB elements. Appl. Phys. Lett. **89**, 181912 (2006)
111. Pan, H.L., Yao, B., Yang, T., Xu, Y., Zhang, B.Y., Liu, W.W., Shen, D.Z.: Electrical properties and stability of p-type ZnO film enhanced by alloying with S and heavy doping of Cu. Appl. Phys. Lett. **97**, 142101 (2010)
112. Ahn, K., Deutsch, T., Yan, Y., Jiang, C., Perkins, C., Turner, J., Al-Jassim, M.: Synthesis of band-gap-reduced p-type ZnO films by Cu incorporation. J. Appl. Phys. **102**, 023517 (2007)
113. Fan, J., Freer, R.: The roles played by Ag and Al dopants in controlling the electrical properties of ZnO varistors. J. Appl. Phys. **77**, 4795 (1995)
114. Kanai, Y.: Admittance Spectroscopy of ZnO Crystals Containing Ag. Jpn. J. Appl. Phys. Part 1 **30**, 2021 (1991)
115. Kang, H.S., Ahn, B.D., Kim, J.H., Kim, G.H., Lim, S.H., Chang, H.W., Lee, S.Y.: Structural, electrical, and optical properties of p-type ZnO thin films with Ag dopant. Appl. Phys. Lett. **88**, 202108 (2006)
116. Yamamoto, T., Katayama-Yoshida, H.: Solution using a codoping method to unipolarity for the fabrication of p-type ZnO. Jpn. J. Appl. Phys. **38**, 166 (1999)
117. Yamamoto, T., Katayama-Yoshida, H.: Control of valence states in ZnO by co-doping method. Mater. Res. Soc. Proc. **623**, 223 (2000)
118. Yamamoto, T., Katayama-Yoshida, H.: Unipolarity of ZnO with a wide-band gap and its solution using codoping method. J. Cryst. Growth **214/215**, 552 (2000)
119. Yamamoto, T.: Codoping for the fabrication of p-type ZnO. Thin Solid Films **420**, 100 (2002)
120. Bian, J.M., Li, X.M., Gao, X.D., Yu, W.D., Chen, L.D.: Deposition and electrical properties of N-In codoped p-type ZnO films by ultrasonic spray pyrolysis. Appl. Phys. Lett. **84**, 541 (2004)
121. Zhu, L.P., Ye, Z.Z., Zhuge, F., Yuan, G.D., Lu, J.G.: Al–N codoping and p-type conductivity in ZnO using different nitrogen sources. Surf. Coat. Technol. **198**, 354 (2005)
122. He, H.P., Zhuge, F., Ye, Z.Z., Zhu, L.P., Wang, F.Z., Zhao, B.H., Huang, J.Y.: Strain and its effect on optical properties of Al-N codoped ZnO films. J. Appl. Phys. **99**, 023503 (2006)
123. Zhang, X., Li, X.M., Chen, T.L., Zhang, C.Y., Yu, W.D.: p-type conduction in wide-gap Zn1-xMgxO films grown by ultrasonic spray pyrolysis. Appl. Phys. Lett. **87**, 092101 (2005)
124. Tsukazaki, A., Saito, H., Tamura, K., Ohtani, M., Koinuma, H., Sumiya, M., Fuke, S., Fukumura, T., Kawasaki, M.: Systematic examination of carrier polarity in composition spread ZnO thin films codoped with Ga and N. Appl. Phys. Lett. **81**, 235 (2002)
125. Lu, J.G., Zhu, L.P., Ye, Z.Z., Zeng, Y.J., Zhuge, F., Zhao, B.H., Ma, D.W.: Improved N-Al codoped p-type ZnO thin films by introduction of a homo-buffer layer. J. Cryst. Growth **274**, 425 (2005)

126. Zeng, Y.J., Ye, Z.Z., Lu, J.G., Zhu, L.P., Li, D.Y., Zhao, B.H., Huang, J.Y.: Effects of Al content on properties of Al–N codoped ZnO films. Appl. Surf. Sci. **249**, 203 (2005)
127. Zhang, Z.H., Ye, Z.Z., Ma, D.W., Zhu, L.P., Zhou, T., Zhao, B.H., Fei, Z.G.: Preparation and characteristic of p-type ZnO films by Al–N codoping technique. Mater. Lett. **59**, 2732 (2005)
128. Lu, J.G., Zhu, L.P., Ye, Z.Z., Zhuge, F., Zhao, B.H., Huang, J.Y., Wang, L., Yuan, J.: p-type ZnO films by codoping of nitrogen and aluminum and ZnO-based p-n homojunctions. J. Cryst. Growth **283**, 413 (2005)
129. Cong, G.W., Peng, W.Q., Wei, H.Y., Han, X.X., Wu, J.J., Liu, X.L., Zhu, Q.S., Wang, Z.G., Lu, J.G., Ye, Z.Z., Zhu, L.P., Qian, H.J., Su, R., Hong, C.H., Zhong, J., Ibrahim, K., Hu, T. D.: Comparison ofvalence band x-ray photoelectron spectrum between Al–N-codoped and N-doped ZnO films. Appl. Phys. Lett. **88**, 062110 (2006)
130. Yan, Z., Song, Z.T., Liu, W.L., Wan, Q., Zhang, F.M., Feng, S.L.: Optical and electrical properties of p-type zinc oxide thin films synthesized by ion beam assisted deposition. Thin Solid Films **492**, 203 (2005)
131. Chen, L.L., Lu, J.G., Ye, Z.Z., Lin, Y.M., Zhao, B.H., Ye, Y.M., Li, J.S., Zhu, L.P.: p-type behavior in In–N codoped ZnO thin films. Appl. Phys. Lett. **87**, 252106 (2005)
132. Yuan, N.Y., Li, J.H., Fan, L.N., Wang, X.Q., Zhou, Y.: Structure, electrical and optical properties of N–In codoped ZnO thin films prepared by ion-beam enhanced deposition method. J. Cryst. Growth **290**, 156 (2006)
133. Krtschil, A., Dadgar, A., Oleynik, N., Blasing, J., Diez, A., Krost, A.: Local p-type conductivity in zinc oxide dual-doped with nitrogen and arsenic. Appl. Phys. Lett. **87**(26), 2105 (2005)
134. Cao, Y.G., Miao, L., Tanemura, S., Tanemura, M., Kuno, Y., Hayashi, Y.: Low resistivity p-ZnO films fabricated by sol-gel spin coating. Appl. Phys. Lett. **88**, 251116 (2006)
135. Lu, J.G., Zhu, L.P., Ye, Z.Z., Zhuge, F., Zhao, B.H., Ma, D.W., Wang, L., Huang, J.Y.: Reproducibility and stability of N–Al codoped p-type ZnO thin films. J. Mater. Sci. **41**, 467 (2006)
136. He, H.P., Ye, Z.Z., Zhuge, F., Zeng, Y.J., Zhu, L.P., Zhao, B.H., Huang, J.Y., Chen, Z.: Carrier localization in codoped ZnO:N:Al films. Solid State Commun. **138**, 542 (2006)
137. Joseph, M., Tabata, H., Kawi, T.: p-Type electrical conduction in ZnO thin films by Ga and N codoping. Jpn. J. Appl. Phys. Part 2 **38**, L1205 (1999)
138. Xie, F.-W., Yang, P., Li, P., Zhang, L.-Q.: First-principle study of optical properties of (N, Ga) codoped ZnO. Opt. Commun. **285**, 2660 (2012)
139. Wang, H., Ho, H.P., Lo, K.C., Cheah, K.W.: Preparation of p-type ZnO films with (N, Ga) co-doping by MOVPE. Mater. Chem. Phys. **107**, 244 (2008) doi:10.1016/j.matchemphys.2007.07.012
140. Ohshima, T., Ikegami, T., Ebihara, K., Asmussen, J., Thareja, R.: Synthesis of p-type ZnO thin films using co-doping techniques based on KrF excimer laser deposition. Thin Solid Films **435**, 49 (2003)
141. Gopalakrishnan, N., Shin, B.C., Lim, H.S., Balasubramanian, T., Yu, Y.S.: Effect of GaN doping on ZnO films by pulsed laser deposition. Mater. Lett. **61**, 2307 (2007)
142. Lu, J.G., Ye, Z.Z., Zhuge, F., Zeng, Y.J., Zhao, B.H., Zhu, L.P.: p-type conduction in N-Al co-doped ZnO thin films. Appl. Phys. Lett. **85**, 3134 (2004)
143. Lu, J.G., Ye, Z.Z., Yuan, G.D., Zhuge, F., Zhu, L.P., Zhao, b.H., Zhang, S.B.: p-type conduction in N-Al co-doped ZnO thin films. Appl. Phys. Lett. **89**(05), 3501 (2006)
144. Ye, Z.Z., Lu, J.G., Zhang, Y.Z., Zeng, Y.J., Chen, L.L., Zhuge, F., Yuan, G.D., He, H.P., Zhu, L.P., Huang, J.Y., Zhao, B.H.: ZnO light-emitting diodes fabricated on Si substrates with homobuffer layers. Appl. Phys. Lett. **91**, 113503 (2007)
145. Yao, S.-L., Hong, J.-D., Lee, C.-T., Ho, C.-Y., Liu, D.-S.: Determination of activation behavior in annealed Al–N codoped ZnO Films. J. Appl. Phys. **109**, 103504 (2011)
146. Chen, L.L., Ye, Z.Z., Lu, J.G., Chu, P.K.: Control and improvement of p-type conductivity in indium and nitrogen codoped ZnO thin films. Appl. Phys. Lett. **89**, 252113 (2006)

147. Chen, L.L., Ye, Z.Z., Lu, J.G., he, H.P., Zhao, B.H., Zhu, L.P., Chu, P.K., Shao, L.: Co-doping effects and electrical transport in In-N doped zinc oxide. Chem. Phys. Lett. **432**, 352 (2006)
148. Du, G.T., Liu, W.F., Bian, J.M., Hu, L.Z., Liang, H., Wang, X.S., Liu, A.M., Yang, T.P.: Room temperature defect related electroluminescence from ZnO homojunctions grown by ultrasonic spray pyrolysis. Appl. Phys. Lett. **89**, 052113 (2006)
149. Sanmyo, M., Tomita, Y., Kobayashi, K.: Preparation of p-type ZnO films by doping of Be-N bonds. Chem. Mater. **15**, 819 (2003)
150. Kim, H., Cepler, A., Osofsky, M.S., Auyeung, R.C.Y., Pique, A.: Fabrication of Zr–N codoped p-type ZnO thin films by pulsed laser deposition. Appl. Phys. Lett. **90**, 203508 (2007)
151. Porter, H.L., Muth, J.F., Narayan, J., Foreman, J.V., Everitt, H.O.: Photoluminescence study of ZnO films codoped with nitrogen and tellurium. J. Appl. Phys. **100**, 123102 (2006)
152. Tang, K., Gu, S., Ye, J., Huang, S., Gu, R., Zhang, R., Zheng, Y.: Temperature-dependent photoluminescence of ZnO films codoped with tellurium and nitrogen. J. Appl. Phys. **112**, 103534 (2012)
153. Wang, X.H., Yao, B., Wei, Z.P., Sheng, D.Z., Zhang, Z.Z., Li, B.H., Lu, Y.M., Zhao, D.X., Zhang, J.Y., Fan, X.W., Guan, L.X., Cong, C.X.: Acceptor formation mechanisms determination from electrical and optical properties of p-type ZnO doped with lithium and nitrogen. J. Phys. D Appl. Phys. **39**, 4568 (2006)
154. Swapna, R., Amiruddin, R., Kumar, M.C.S.: Aging and annealing effects on properties of Ag-N dual-acceptor doped ZnO thin films. AIP Conf. Proc. **1512**, 682 (2013)
155. Lu, J.G., Zhang, Y.Z., Ye, Z.Z., Zhu, L.P., Wang, L., Zhao, B.H., Liang, Q.L.: Low-resistivity, stable p-type ZnO thin films realized using a Li-N dual-acceptor doping method. Appl. Phys. Lett. **88**, 22114 (2006)
156. Wang, X.H., Yao, B., Shen, D.Z., Zhang, Z.Z., Li, B.H., Wei, Z.P., Lu, Y.M., Zhao, D.X., Zhang, J.Y., Fan, X.W., Guan, L.X., Cong, C.X.: Optical properties of p-type ZnO doped by lithium and nitrogen. Solid State Commun. **141**, 600 (2007)
157. Dadgar, A., Krtschil, A., Bertram, F., Giemsch, S., Hempel, T., Veit, P., Diez, A., Oleynik, N., Clos, R., Christen, J., Krost, A.: ZnO MOVPE growth: From local impurity incorporation towards p-type doping. Superlattices Microstruct. **38**, 245 (2005)
158. Zeng, Y.J., Ye, Z.Z., Xu, W.Z., Lu, J.G., He, H.P., Zhu, L.P., Zhao, B.H., Che, Y., Zhang, S. B.: p-type behavior in nominally undoped ZnO thin films by oxygen plasma. Appl. Phys. Lett. **88**, 262103 (2006)
159. Butkhuzi, T.V., Bureyev, A.V., Georgobiani, A.N., Kekelidze, N.P., Khulordava, T.G.: Optical and electrical properties of radical beam gettering epitaxy grown n- and p-type ZnO single crystals. J. Cryst. Growth **117**, 366 (1992)
160. Oh, M.S., Kim, S.H., Seong, T.Y.: Growth of nominally undoped p-type ZnO on Si by pulsed-laser deposition. Appl. Phys. Lett. **87**, 122103 (2005)
161. Xiong, G., Wilkinson, J., Mischuck, B., Tuzemen, S., Ucer, K.B., Williams, R.T.: Control of p-and n-type conductivity in sputter deposition of undoped ZnO. Appl. Phys. Lett. **80**, 1195 (2002)
162. Tan, S.T., Chen, B.J., Sun, X.W., Yu, M.B., Zhang, X.H., Chua, S.J.: Realization of intrinsic p-type ZnO thin films by metal organic chemical vapor deposition. J. Electron. Mater. **34**, 1172 (2005)
163. Ma, Y., Du, G.T., Yang, S.R., Li, Z.T., Zhao, B.J., Yang, X.T., Yang, T.P., Zhang, Y.T., Liu, D.L.: Control of conducti
vity type in undoped ZnO thin films grown by metalorganic vapor phase epitaxy. J. Appl. Phys. **95**, 6268 (2004)
164. Oh, M.S., Kim, S.H., Park, S.J., Seong, T.Y.: Type conversion of intentionally undoped ZnO layers grown by pulsed laser deposition. Superlattices Microstruct. **39**, 130 (2006)
165. Hazra, S.K., Basu, S.: Stable p-ZnO thin films by oxygen control using reverse spray dynamics. Solid State Commun. **133**, 245 (2005)

166. Esmaili-Sardari, S., Berkovich, A., Iliadis, A.A.: Observation of conductivity type conversion in undoped ZnO films grown by pulsed laser deposition on silicon (100) substrates. Appl. Phys. Lett. **100**, 053505 (2012)
167. Lin, B.X., Fu, Z.X., Jia, Y.B.: Green luminescent center in undoped zinc oxide films deposited on silicon substrates. Appl. Phys. Lett. **79**, 943 (2001)
168. Kohan, A.F., Ceder, G., Morgan, D.: First-principles study of native point defects in ZnO. Phys. Rev. B **61**, 15019 (2000)
169. Tuomisto, F., Ranki, V., Saarinen, K., Look, D.C.: Evidence of the Zn vacancy acting as the dominant acceptor in n-type ZnO. Phys. Rev. Lett. **91**, 205502 (2003)
170. Schubert, E.F.: Light-emitting diodes. Cambridge (2005)

Chapter 5
Hydrogen Production and Photodegradation at TiO_2/Metal/CdS Sandwich Using UV–Visible Light

A. Manivannan, Aaron Peterson, Winn Wilson, Bratindranath Mukherjee and Vaidyanathan Ravi Subramanian

5.1 Introduction

As clean energy resources, light and water are abundant and universally available and hence, there is immense interest for energy applications. Hydrogen production utilizing light and water is a sustainable and logical approach for constant energy generation [1–3]. As a well-known photocatalyst, TiO_2 is of interest and has been examined persistently for water splitting and reasons that include wide-ranging pH stability, non-toxicity, and good photoactivity in the presence of UV light [4–6]. The hydrogen generation mechanism on TiO_2 can be summarized as follows [7–10]:

$$TiO_2 \xrightarrow{\text{Sunlight}} TiO_2(e_{cb} + h_{vb}) \tag{5.1}$$

$$2H_2O \xrightarrow{TiO_2(e_{cb}+h_{vb})} 2H_{2,\text{anode}} + O_{2,\text{cathode}} \tag{5.2}$$

A. Manivannan (✉)
Thermal Sciences Division, National Energy Technology Laboratory,
US Department of Energy, 3610 Collins Ferry Road, Morgantown, WV 26507, USA
e-mail: manivana@netl.doe.gov

A. Peterson · B. Mukherjee · V.R. Subramanian (✉)
Chemical and Materials Engineering, University of Nevada, Reno, NV 89557, USA
e-mail: ravisv@unr.edu

W. Wilson
Civil and Environmental Engineering, University of Nevada, Reno, NV 89557, USA

A. Manivannan
Mechanical and Aerospace Engineering, West Virginia University,
Morgantown, WV 26506, USA
e-mail: amanivan@wvu.edu

M.P. Paranthaman et al. (eds.), *Semiconductor Materials for Solar Photovoltaic Cells*, Springer Series in Materials Science 218,
DOI 10.1007/978-3-319-20331-7_5

Electron–hole generation and separation (5.1) leads to hole-enabled water oxidation and an electron-enabled hydrogen formation (5.2) during photoillumination. The redox reaction occurs at different locations in the same particle, if particulate TiO_2 is used. Several literature reviews have discussed photocatalytic water splitting in general [11, 12] and the specific benefits of using TiO_2 [13].

The critical requirements for TiO_2 to perform water splitting and produce hydrogen efficiently are (i) separating photogenerated charges and (ii) absorbing light over a broad range. TiO_2 can photocatalytically perform water splitting, but the absorbance and charge separation capabilities are limited. Metal centers can function as sinks for the photogenerated electrons and help keeping it away from holes during charge separation [8]. Moreover, the addition of visible light receptors such as chalcogenides can assist with enhancing light absorbance and the quantum efficiency of the overall process [14–16]. Thus, photocatalytic water splitting can be performed efficiently using a TiO_2-based photocatalyst by combining these primary entities (metals and light harvesters) as additives.

There have been some studies examining the role of metal and light harvesters on TiO_2. Among metals, most studies have focused on Pt group metals or PGMs [17–22], while chalcogenides as size tunable visible light harvesters have garnered significant attention [23–28]. CdS is a chalcogenide that has been used with Pt to promote photocatalysis [14, 29, 30]. Most studies have focused on the commercially available Degussa P25 [14, 31] as the TiO_2 source, while a few have explored solgel-based TiO_2 [20, 32, 33]. A study comparing the various forms of contacting CdS, Pt, and TiO_2 has been reported [29, 34]. After examining various approaches to combine TiO_2, Pt, and CdS, having Pt and CdS deposits juxtaposed adjacently to one another decorating the TiO_2 surface appears to be an optimal arrangement as it can be expected to promote both hole-mediated oxidation and electron-mediated reduction, effectively. Elsewhere, it has been mentioned that a core–shell architecture comprising of Au core–CdS shell on TiO_2 is highly efficient in artificial photosynthesis [22]. In another related report, the application of Degussa P25 with Pt and CdS to form a nanocomposites film to produce hydrogen from pollutants has been reported [14]. The chapter describes the significant different from the aforementioned one, in that (i) an actual pollutant has been tested instead of sacrificial agents such as azo dye and (ii) the applicability of an IH-TiO_2 with 100 % anatase phase with high surface area is reported instead of commercial P25.

A unique approach to synthesizing TiO_2 with 100 % anatase content and use it as a base to first deposit metal followed by chalcogenide is presented. The effects of Ag, Au, and Pt as the electron-shuttling agent and the chalcogenide CdS as the light harvester on the photocatalytic water splitting are examined. Since CdS is involved, prevention of its hole-driven corrosion assumes a significant challenge. To this end, the effect of a stabilizing agent that scavenges the holes has been examined using two approaches. Firstly, the role of a sulfide ion containing sacrificial agent has been probed. Secondly, a strategy to perform hole-mediated oxidation of an aquatic pollutant as an approach to (i) delay CdS corrosion and (ii) facilitate photodegradation of the pollutant, simultaneously, has also been presented. A systematic study of the effects of (i) PGM metals, (ii) a representative visible light chalcogenide-type

harvester, (iii) a corrosion inhibitor on the photocatalytic hydrogen generation, and (iv) the role of pollutants as electrolyte additives in hydrogen generation is presented.

5.2 Experimental Section

The TiO_2–PGM–chalcogenide composites were synthesized in three steps. The key synthesis information and the conditions for the preparation of TiO_2, metal nanoparticles, and the chalcogenide are summarized in Scheme 5.1 and discussed below.

5.2.1 TiO_2 Synthesis

In-house nanoparticulate TiO_2 was synthesized using a wet chemical approach. In a typical step, a mixture of 5 mL of titanium propoxide (Sigma-Aldrich) and 0.6 mL of hydrofluoric acid (40 w/v%) was taken in a Teflon®-lined autoclave and diluted to 30 ml with DI water. Diluted HF was taken with the goal to accelerate the hydrolysis of Ti precursor, creating large number of nucleation sites and hence smaller particle size. The autoclave is sealed and heated in the oven at 190 °C for 24 h. The resulting TiO_2 is rinsed multiple times with DI water and ethanol to remove impurities. For comparative studies, commercial TiO_2 was obtained from Degussa® corporation (Generic name: Degussa P25) and used without any modification.

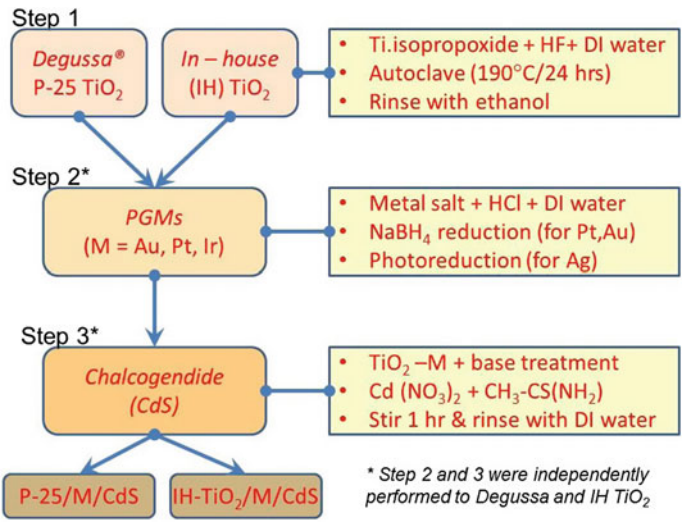

Scheme 5.1 The step-by-step sequence used for the synthesis of the oxide–metal–chalcogenide composite photocatalyst is shown. The key details during each step of the synthesis process are also provided

5.2.2 Pt, Ag, and Au Deposition

Pt and Au deposition on either P25 or the as-prepared TiO_2 was performed by mixing 1-mg Pt salt or Au salt/mL with 20 or 5 % HCl in solution, respectively. A quantity that would give 1wt% coverage on TiO_2 was used. These mixtures were stirred on a hot plate at 80 °C until all the excess water was evaporated. A 1 M $NaBH_4$ solution was then added to the dried samples to ensure the metal ions are reduced to nanoparticles. Aqueous Ag ions were reduced by UV-assisted photogenerated electrons for a loading of 1 wt% on TiO_2. The solution was later stirred at 80 °C until all the excess water was evaporated off.

5.2.3 CdS Deposition

A two-step approach was adapted to ensure the deposition of CdS on TiO_2. The preliminary TiO_2-M (M = Pt, Au, or Ag) powders were immersed in 0.1 M NaOH aqueous solution for 1 h to enhance the number of basic sites on the TiO_2 surface. After this base treatment, the slurries were centrifuged and the excess solution was poured off. The CdS was deposited at room temperature by stirring the pretreated TiO_2-M (M = Pt, Au, or Ag) powders in 10 mM solution of $Cd(NO_3)_2$ and thioacetamide. Calculated amount of $Cd(NO_3)_2$ and thioacetamide was taken to ensure 10 % CdS loading on the catalyst surface. It is anticipated that the surface hydroxyl groups on TiO_2 promote selective deposition of CdS presumably through intermediate formation of $Cd(OH)_2$. A similar procedure was followed with P25–PGMs. Further, separate experiments were conducted with identical CdS content. A known concentration of CdS was deposited on both IH-TiO_2-M and P25-M to ensure that the CdS content was the same.

5.2.4 Synthesis of CdS–Au–TiO_2 Sandwich Nanorod Array

The TiO_2 nanorod array was fabricated on the FTO substrate with a hydrothermal method. Decoration of Au nanoparticles on the TiO_2 nanorods was performed using $HAuCl_4$ with NaOH solution. The TiO_2 nanorod array was immersed into the $HAuCl_4$ aqueous solution for the deposition of Au nanoparticles on the surface of TiO_2 nanorod. Finally, the CdS–Au–TiO_2 sandwich structure was designed by depositing CdS QDs on the surface of the Au-decorated TiO_2 nanorod array with a chemical bath of $CdSO_4$ and thiourea dissolved into ammonia solution. After CdS deposition, the nanorod array was washed with DI water and annealed in a N_2 flow at 400 °C for 2 h.

5.2.5 Techniques Used for the Characterization of the Composites

The characterization of the various catalysts was carried out using several instruments. A Hitachi S-4700 scanning electron microscopy (SEM) and electron dispersive spectrometry (EDS) were used to determine the physical features of the components in the composites and to perform compositional analyses. A Philips 12045 BX-ray diffractometer (XRD) was used at a scan rate of 0.4°/min to identify the phase of the synthesized materials. A Micrometrics 2720 Chemisorb Single-point Brunauer–Emmett–Teller (BET) surface area analyzer was used to determine the surface area of the photocatalyst. A Shimadzu UV-2501PC spectrophotometer was used to perform UV–vis diffuse reflectance measurements (DRUV–vis) and determine the absorbance responses of the photocatalysts.

5.2.6 Film Preparation and Measurements

A suspension of the Degussa® P25–TiO_2 and the IH-TiO_2 of same loading in DI water was used to prepare the films using an established procedure [35]. The P25 and IH-TiO_2 nanoparticulate coatings were prepared on conducting glass slides by syringing out identical volumes of suspension, drop casting them, and performing a mild annealing in an oven at $\sim$300 °C. The photoelectrochemical measurements involved two specific studies: time-dependent current (*I*/*t*) and voltage (*J*/*t*) measurements and Mott–Schottky analysis. Both these measurements were taken using an Autolab® PGSTAT 30 Potentiostat and Galvanostat under illumination using a $\sim$90 mW/cm^2 collimated UV–vis light. The measurements were taken under aerated conditions since most photocatalytic reaction requires aerated conditions. Our earlier work provides complete details on the protocols for performing (*I-t*/*V-t*) [36] and MS analysis [37, 38].

5.2.7 Photocatalytic Measurements

A gas chromatograph equipped with TCD detector (SRI 8610C) was used for quantitatively and qualitatively estimating hydrogen production under UV–vis illumination. The setup comprised of a 500-mL Pyrex vessel with 500 mg of catalyst and was run with and without sacrificial agents. The catalyst dispersion was bubbled with nitrogen for 30 min prior to running the experiment. It was then sealed, and the outlet was fed to a downward displacement gas collection system. The light source was a 500 W xenon lamp with an output equal to one sun. The light consists of $\sim$10 % UV, and the rest visible/infrared. The sacrificial agent was made of either 0.1 M Na_2S and 0.02 M Na_2SO_3 or the pollutant, methyl orange

(MO)—40 μM. A schematic of the setup is shown elsewhere [39, 40]. The photocatalysis was carried out under ambient conditions of temperature and pressure.

5.2.8 Actinometry Measurements

Quantum yield for methyl orange dye degradation is measured using ferrioxalate actinometer using the procedure reported elsewhere [41]. Briefly, 0.6 M of potassium ferrioxalate solution was irradiated by a xenon light source for 90 s, and photoreduced Fe^{2+} concentration is estimated by measuring the absorbance of Fe^{2+} phenanthroline complex at 510 nm. The number of photons entering the reaction system is determined to be 5.376×10^{16}/s using a method discussed elsewhere [42]. Further, at working white light condition, quantum yield for photocomplexation of Fe^{2+} is taken 1.2 and molar absorptivity is that of the Fe^{2+} phenanthroline complex measured from the slope of the Fe^{2+} complex absorbance calibration curve.

5.3 Results

5.3.1 Surface and Photoelectrochemical Characterization

5.3.1.1 Scanning Electron Microscopy

Figure 5.1 shows the SEM images of in-house TiO_2 (IH-TiO_2) and P25–TiO_2. The IH-TiO_2 nanoparticles are much smaller (ϕ = 20 nm) than the P25 nanoparticles ($\phi \sim$ 40–50 nm). Further, the BET surface analysis data shown in Table 5.1 indicate that the surface area of IH-TiO_2 is $\sim$60 % larger compared to the P25.

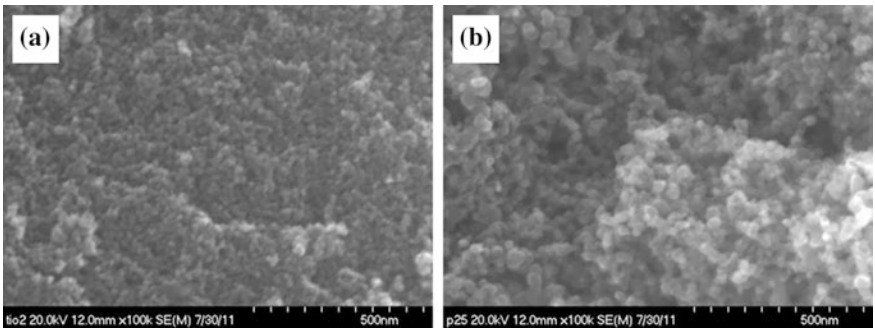

Fig. 5.1 The surface features of the **a** IH-TiO_2 and **b** commercially procured P25 (Degussa® corporation) are observed in these representative images obtained using the scanning electron microscope

Table 5.1 Quantitative analysis of the metal content in the TiO_2–Pt–CdS was performed using EDS

	Surface area (m^2/g)	Metal coding			Rate constant, k_{MO} (min^{-1})[a]		Rate (ml/g/h)[b]	
		Pt (at.%)	Au (at.%)	Ag (at.%)	No Pt/CdS	Pt/CdS	No Pt/CdS	With Pt/CdS
P25– TiO_2	53 + 4 %	0.79	0.85	0.81	0.0041	0.017	–	0.25
IH-TiO_2	130 ± 4 %	0.8	0.78	0.75	0.0063	0.036	–	4.6

The table lists the comparative data of the different element contents in a representative set of samples [M = Pt, Au, or Ag]. The columns in the second half at the far end provide rate information on MO photodegradation and hydrogen generation

[a]MO photodegradation

[b]Hydrogen generation

Smaller particle sizes are desirable as they offer higher surface area per gram of the photocatalyst. This smaller particle size and greater surface area have a number of activity implications that are detailed in later sections. The SEM and XRD analysis images of the samples with metal nanoparticle (Pt, Au, and Ag) deposits are shown in Fig. 5.2. A representative image containing IH-TiO_2 with Pt followed by CdS deposition is shown in Fig. 5.3. While the distinction between the TiO_2, Pt, and CdS nanoparticles is difficult to note from the SEM images, it is observed from the magnified images that the particles in the P25-based samples are much larger

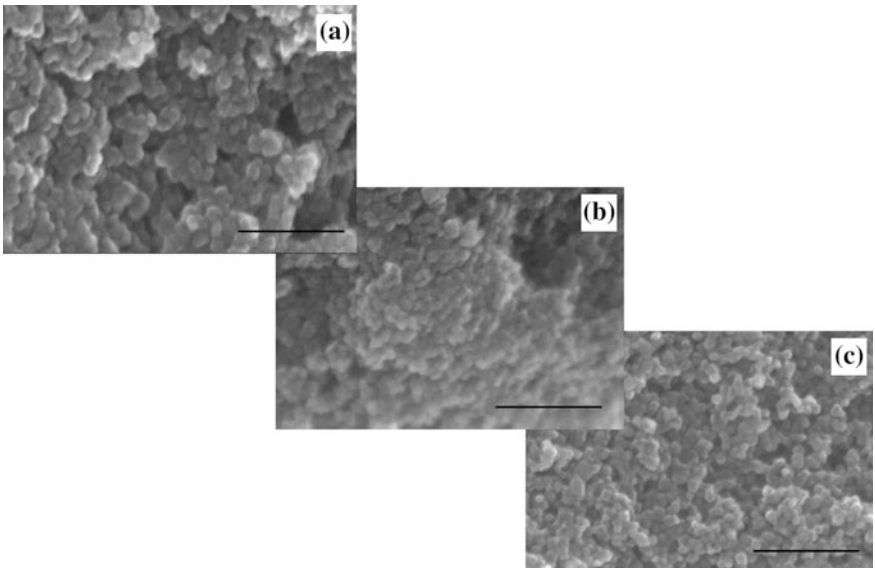

Fig. 5.2 The surface features of the IH-TiO_2 with different metal deposits are shown in these images obtained using the scanning electron microscope. This includes IH-TiO_2 with **a** Pt, **b** Au, and **c** Ag. All the samples have been shown with a scale of 200 nm

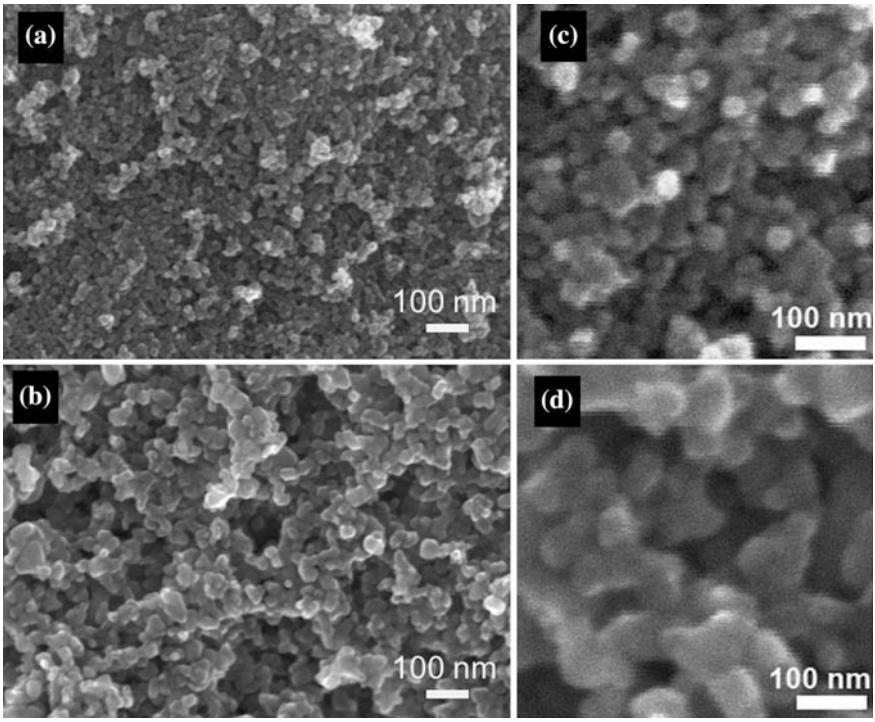

Fig. 5.3 The representative SEM images of the **a** IH-TiO_2–Pt–CdS and **b** P25–Pt–CdS are shown. Higher magnification images of **c** IH-TiO_2–Pt–CdS and **d** P25–Pt–CdS provide more clarity on the particle size, shape, and texture

compared to the IH-TiO_2-based samples. This suggests that CdS and Pt deposit differently on IH-TiO_2 and P25 nanoparticles. Further analysis using XRD and EDS was performed (Sect. 5.3.1.2) to obtain additional details of the photocatalyst surface.

5.3.1.2 XRD and EDS Analyses

XRD analysis was performed on the samples during various stages of synthesis. XRD of representative samples with CdS and Pt is shown in Fig. 5.4. The IH-TiO_2 is exclusively in anatase crystal structure matched with JCPDS#21-1272. The anatase phase has been shown to have a higher photoactivity compared to the mixed anatase/rutile crystal structure [43–45]. The CdS peaks can also be observed along with the XRD of the IH-TiO_2–CdS–Pt. The primary CdS peak (111) overlaps with the anatase TiO_2 peak, but the next CdS peak has no overlap with TiO_2 or metal and

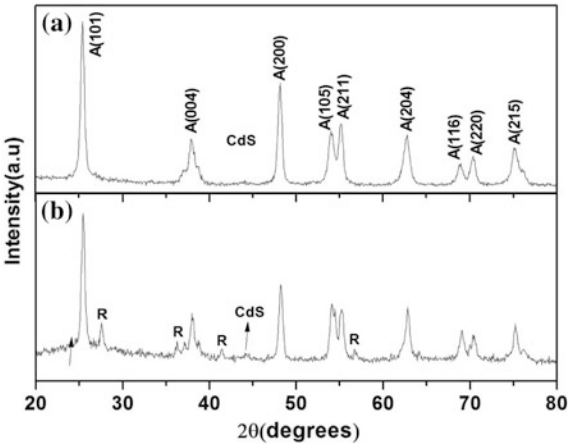

Fig. 5.4 The XRD of the **a** IH-TiO_2–Pt–CdS and **b** P25–Pt–CdS indicating the formation of crystalline TiO_2 is shown. The (hkl) values associated with the different anatase peaks are also shown in the figure. *Note* "A"—anatase, "R"—rutile

can be seen at $2\theta = 43$ corresponding to (220) (JCPDS#65-2887). The XRD of the P25–CdS–Pt structure shows the anatase and rutile peaks as well as the peaks for CdS. EDS analysis was carried out in order to determine its concentration since Pt loading is less than 1 wt%. The EDS results of all metal loaded IH-TIO_2 were performed over identical areas and the results are shown in Table 5.1. The metal loading intended during synthesis was $\sim$1 wt%, while the EDS tests showed that the metal loading was 0.79, 0.85, and 0.81 wt%. The EDS data indicate that the observed PGM loading is very close to the desired levels.

5.3.1.3 Diffuse Reflectance

Diffuse reflectance measurements are used to obtain the absorbance profiles of the samples. As shown in Fig. 5.5, The IH-TiO_2 demonstrates absorbance in the UV

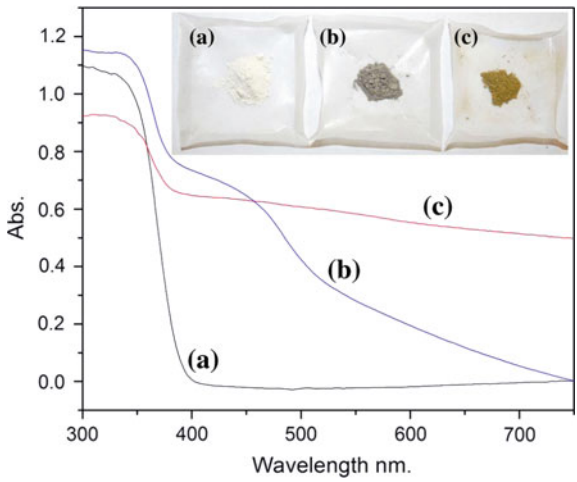

Fig. 5.5 UV–visible diffuse reflectance spectra of **a** IH-TiO_2, **b** Pt deposits on IH-TiO_2, and **c** CdS deposits on IH-TiO_2-Pt. The *inset* shows the photographs of the different samples in the same order

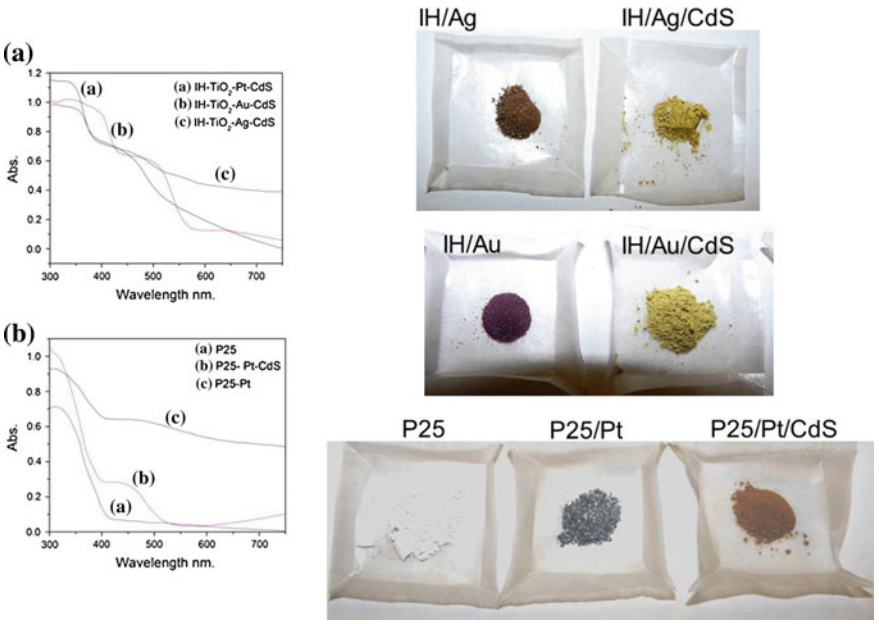

Fig. 5.6 UV–visible diffuse reflectance spectra of other samples prepared in this study are shown. This includes **a** IH-TiO_2-based and **b** P25-based samples. The *photographs* of the different samples are also shown in the figure

with an onset absorbance of ~390 nm. The addition of Pt causes the absorbance onset to shift to ~450 nm, while the characteristic shoulder and a corresponding onset of ~575 nm, which is entirely CdS size-dependent, are also noted. The samples demonstrate corresponding change in color as shown in the inset. The CdS particles are yellow and when added to the IH-TiO_2–Pt, which is gray, the composite becomes dark yellow. The Pt and CdS deposits appear of the same color on Degussa P25. The addition of Au nanoparticle turns the IH-TiO_2 to dark red/violet and creates a blue/green composite, while the addition of Ag nanoparticles results in a gray/brown color, while CdS addition results in a dark yellow composite. From the EDS data and a comparison of the absorbance of the CdS on IH-TiO_2 with P25, a higher and efficient distribution of CdS on IH-TiO_2 is evident. The pictures of actual sample powders and corresponding absorbance spectra of other samples are shown in Fig. 5.6.

5.3.1.4 Transmission Electron Microscopy (TEM)

Figure 5.7a shows a representative bright-field TEM view of the surface of the IH-TiO_2/Pt/CdS photocatalyst. A porous network of TiO_2 grains with an average diameter of ~20 nm decorated with ultra-small particles is evident from the image. Large grains showing lattice fringes match with (101) of anatase, whereas the

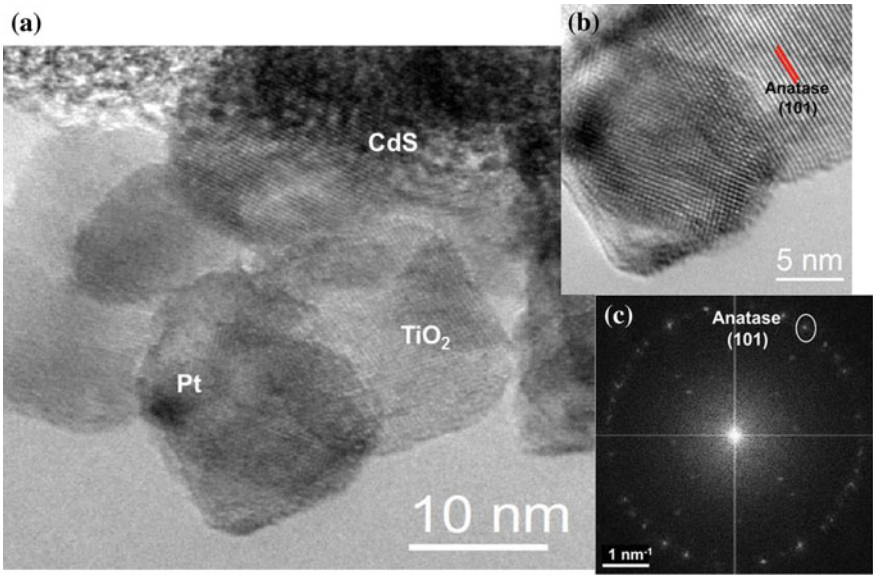

Fig. 5.7 High magnification TEM images of a representative part of the (**a**) IH-TIO_2–Pt–CdS sample. The features corresponding to the anatase (101) plane can be noted in the HRTEM shown in (**b**) as well as the SAED patterns in (**c**)

cluster of ~2-nm particles marked in the image are CdS nanoparticles or a mixture of CdS and Pt nanoparticles. The crystalline nature of the IH-TiO_2 is evident from the HRTEM in Fig. 5.7b. The FFT (Fig. 5.7c) of the HRTEM can be indexed clearly to (101) plane anatase TiO_2 with *d*-value of 0.352 nm.

The smaller diameter of the IH-TiO_2 shown in the SEM images and the higher surface area as evidenced by the BET analysis point to the presence of more active sites relative to Degussa P25. The higher surface area also leads to a higher CdS loading, as evident from the data in Table 5.1. Thus, the synthesis approach demonstrated here results in an efficient CdS utilization and therefore is overall a more cost-effective synthesis process. Further, XRD results showed that the smaller IH-TiO_2 particles are completely in the active photocatalytic anatase phase. The improved photoactivity of IH-TiO_2 than the commercial Degussa P25 has been demonstrated based on the combination of (i) high surface area, (ii) effective CdS distribution, and (iii) predominant anatase crystal structure. These samples were tested for photocatalytic experiments.

5.3.1.5 Photoelectrochemical Analysis

The representative photocurrent (*I*/*t*) results of the P25 and IH-TiO_2 are shown in Fig. 5.8. The inset table shows that both photocurrent and photovoltage are higher with the IH-TiO_2 compared to the P25 for the same loading. This is attributed to the

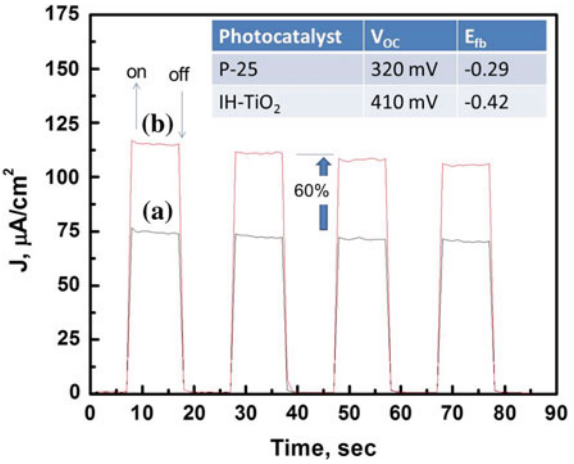

Fig. 5.8 The photocurrent measurements of the **a** commercial (Degussa® P25) and the **b** IH-TiO_2 are shown. The *inset* shows the stabilized values of the chronopotentiometry (V_{OC}/*t*) and the values of the flat-band potential (E_{fb}) for both TiO_2

higher surface area provided by the film by virtue of smaller particle sizes. Further, Mott–Schottky analysis indicates that IH-TiO_2 shows a flat-band potential of −0.42 V, whereas P25 shows a flat-band potential of −0.29 V (Fig. 5.8 inset). The more negative flat-band potential for IH-TiO_2 suggests the presence of larger band bending at the TiO_2/electrolyte interface enhancing better charge separation compared to P25. Thus, both photoelectrochemical measurements indicate the usefulness of the IH-TiO_2 as an effective photocatalyst that promotes high charge generation, separation, and available for utilization. The following section demonstrates the applicability of the IH-TiO_2 as a base material for photocatalysis.

5.3.2 *Photocatalytic Hydrogen Generation*

The applicability of the composites to photo-assisted hydrogen generation from water has been evaluated by performing slurry-based reactions in the presence of two classes of sacrificial agents: (i) a commonly known sulfur-stabilizing polysulfide as a sacrificial compound—Na_2S, +Na_2SO_3, [46] and (ii) a common aquatic pollutant that belongs to the azo dye family group [14]—methyl orange (MO). These results are discussed below.

5.3.2.1 Photocatalytic Hydrogen Generation with Polysulfide as the Sacrificial Agent

Effects of PGM in IH-TiO_2/M/CdS (M = Pt, Ag, Au) Photocatalysis

Photocatalytic hydrogen generation was tested with both the metal and the chalcogenide using IH-TiO_2. As a first screening step, the focus was on the contribution

of the PGMs to photocatalytic water splitting. The tests were performed comparing the hydrogen production rates of IH-TiO_2–Pt–CdS, IH-TiO_2–Au–CdS, and IH-TiO_2–Ag–CdS samples in the presence of sacrificial agent (0.1 M Na_2S, 0.02 M Na_2SO_3). The results shown in Fig. 5.9 indicate that IH-TiO_2–Pt–CdS had the highest production rate, while IH-TiO_2–Au–CdS was less and IH-TiO_2–Ag–CdS was the slowest. Further, the hydrogen production rate is noted to steadily increase over the duration of the experiment. It is important to mention that during the photocatalysis, the IH-TiO_2–Ag–CdS samples particularly become visibly darker during prolonged irradiation.

Comparison of the Pt-Based Catalysts on Photocatalytic Hydrogen Evolution in DI Water

Since Pt was found to be most favorable among the PGMs, the results discussed here focus only on Pt. A series of tests were performed comparing the photocatalytic activities of IH-TiO_2–Pt–CdS, IH-TiO_2–CdS, and P25–Pt–CdS. Photocatalytic hydrogen evolution was tested without any sacrificial agent, just for baseline information. Figure 5.10 shows the results obtained using these three catalysts. The IH-TiO_2–Pt–CdS has the highest hydrogen production rate of 1.4 ml/h. However,

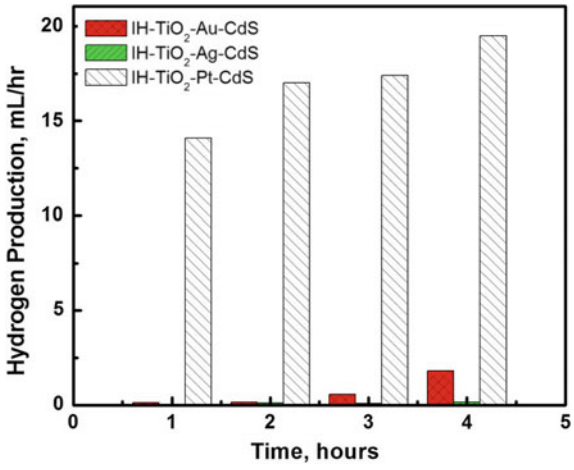

Fig. 5.9 The hydrogen yield obtained in the presence of the different IH-TiO_2-based photocatalysts with Au, Ag, and Pt followed by CdS deposits. The experiments were conducted in the presence of a polysulfide solution as a sacrificial agent using UV–vis illumination (deaeration using N_2 for 30 min, 0.1 M Na_2S + 0.2 M Na_2SO_3)

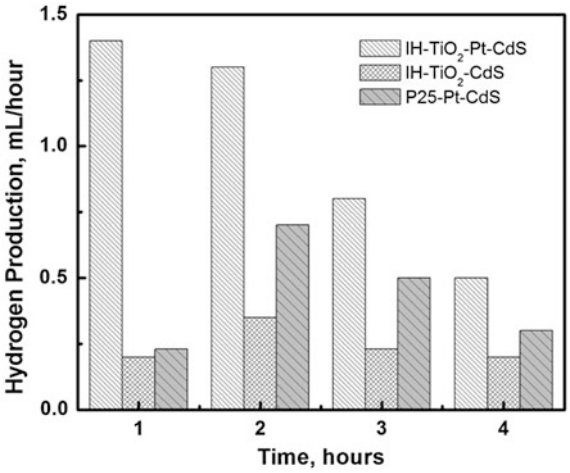

Fig. 5.10 The hydrogen generation obtained in the presence of the different types of TiO_2 including IH-TiO_2 and P25 containing Pt and CdS deposits. The experiments were conducted in DI water using UV–vis illumination (500-mg photocatalyst, deaeration using N_2 for 30 min, no polysulfides were used)

the main aspect to note is the decrease in the hydrogen generation with time and is expected due to (i) very low water splitting occur without sacrificial agents and (ii) CdS corrosion drives the hydrogen generation albeit for a short duration.

Comparison of the Pt-Based Catalysts on Photocatalytic Hydrogen Evolution in Aqueous Na_2S/Na_2SO_3

The photocatalytic activities of the different IH-TiO_2 supported photocatalysts were further examined in the presence of the Na_2S/Na_2SO_3 as shown in Fig. 5.11. It is observed that ~18.5 ml of hydrogen can be produced per hour once the system is operating at a steady state. Two key differences can be observed while overall activity of the catalysts performance is similar to the trend seen in Fig. 5.10 (i.e., IH-TiO_2–Pt–CdS > P25–Pt–CdS > IHTiO_2–CdS). They are as follows: (i) at least one-order higher hydrogen generation rate with all the photocatalysts in the presence of Na_2S/Na_2NO_3 and (ii) unlike the results shown in Fig. 5.10, the hydrogen generation rate does not decrease even after 4 h of continuous illumination. The sacrificial agent is expected to protect the CdS from a predominantly hole-mediated corrosion [47, 48]. Moreover, the IH-TiO_2-based photocatalyst shows at least a twofold enhancement in hydrogen generation compared to the Degussa P25-based photocatalyst. Thus, in the presence of the polysulfide as a sacrificial agent, the IH-TiO_2-based samples demonstrate a higher photoactivity than the P25-based samples.

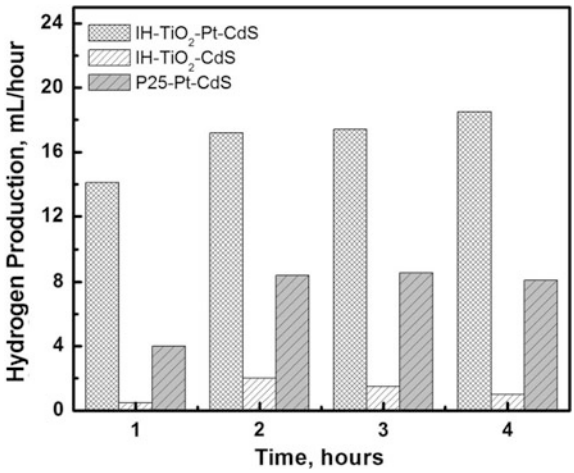

Fig. 5.11 The hydrogen yield obtained in the presence of the different types of TiO_2 including IH-TiO_2 and P25 containing Pt and CdS deposits. The experiments were conducted in the presence of a polysulfide solution as a sacrificial agent using UV–vis illumination (deaeration using N_2 for 30 min, 0.1 M Na_2S + 0.2 M Na_2SO_3)

5.3.2.2 Photocatalytic Hydrogen Generation with Methyl Orange as the Sacrificial Agent

Need for Replacing Stabilizers with Pollutants

The presence of Na_2S/Na_2SO_3 has been shown to improve the activity of TiO_2 with CdS and Pt. However, using Na_2S/Na_2SO_3 as a sacrificial additive has limitations: (i) has to be exclusively introduced with the purpose to remove holes to stabilize CdS, (ii) will require monitoring on a regular basis as it will be consumed (potentially forming S deposits on CdS) [14], and (iii) offers no additional value from an energy production or environmental benefit standpoint. Alternately, should this additive be a pollutant, the added advantage of its decontamination, besides hole scavenging, can also be realized. The quantum yield under exactly same illumination condition (reactor volume exposed and distance of photocell from light source) is found to be 12.45 %. To test the applicability of a pollutant-assisted photocatalytic hydrogen production in the presence of CdS deposits, the organic pollutants MO was used to replace Na_2S/Na_2SO_3.

Photocatalytic Hydrogen Generation in the Presence of MO

MO is a colored compound that belongs to the azo dye family group and is often used in the textile industry as a dying agent [49]. A significant amount of the unused MO is released as waste into the adjoining water bodies destabilizing the

fragile aquatic ecosystem. To mitigate this issue, photodegradation has been considered as a possible pathway to destroy MO [36] and similar colored dyes [50]. MO photodegradation has been well studied by our group [36, 51] as well as by others [52–54]. Blank experiments performed with no photocatalyst and light illumination to examine the photobleaching of MO was carried out and indicated no measureable change as shown in Fig. 5.12. Figure 5.13 shows the results of the UV–vis illumination of a dye solution in the presence of the IH-TiO_2/Pt/CdS composite. The evolution of hydrogen is clearly evident, and it indicates that the system works as per the conceptual expectations. The hydrogen generation is lower compared to the Na_2S/Na_2SO_3 as the electrolyte but more than DI water alone (DI water hydrogen generation is 4 ml). The time-dependent photodegradation of the dye was also examined. The change in the dye concentration was tracked by monitoring the decrease in the peak dye absorbance at 465 nm as shown in Fig. 5.13a. The conversion of the dye is noted to occur over a period of 50 min of continuous illumination. A comparison of the hydrogen yield over time followed using IH-TiO_2–Pt–CdS as the photocatalyst in water and methyl orange as the sacrificial pollutant is presented in Fig. 5.14.

Estimation of the Kinetic Parameters

The photodegradation of MO can be fitted to a pseudo-first-order rate expression: $-r = k[\mathrm{MO}]^n$, where r is rate of consumption of the MO, [MO] is MO concentration, and n is the order of reaction ($n = 1$) as shown in Fig. 5.13b. The rate constant values corresponding to the different photocatalysts are reported in Table 5.1. It is evident that the MO degradation occurs more rapidly in the presence of Pt/CdS on both P25 and IH-TiO_2, from the conversion data in Figs. 5.13 and 5.14 and the corresponding rate constant values in Table 5.1. In studies on hydrogen generation kinetics involving TiO_2/CdS, the focus has been on the

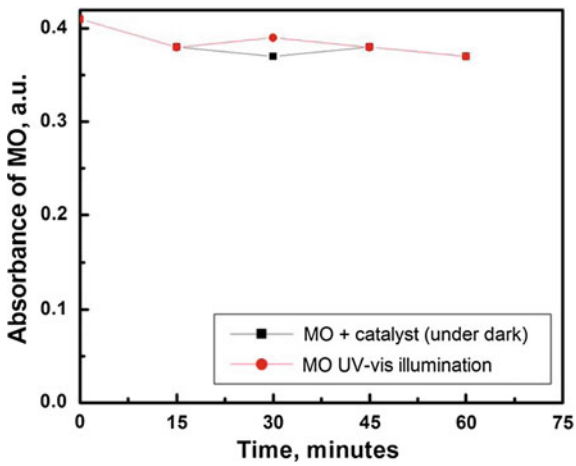

Fig. 5.12 Baseline experiments to demonstrate activity of MO in the absence of light and absence of photocatalyst

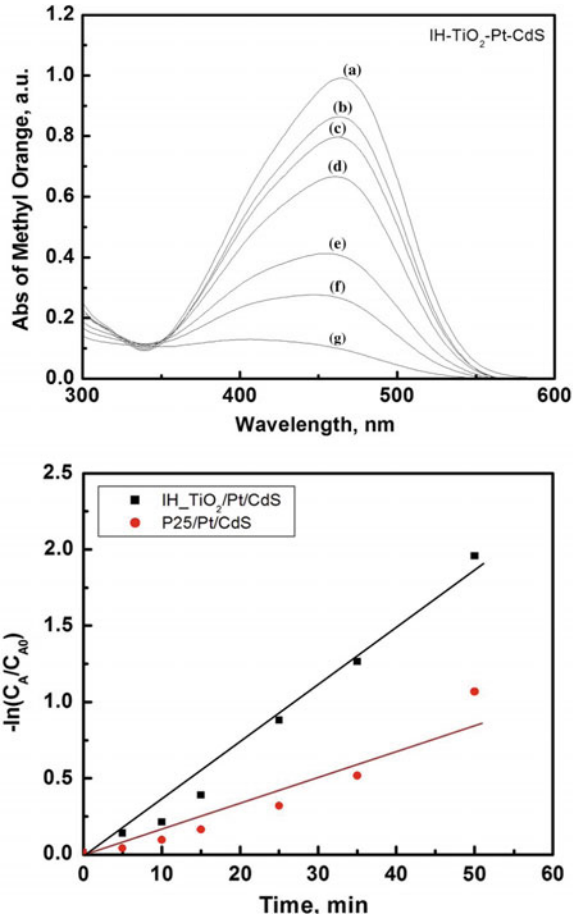

Fig. 5.13 **a** The absorbance spectra of the MO solution was monitored at the end of **a** 0, **b** 5, **c** 10, **d** 15, **e** 25, **f** 35, and **g** 50 min to determine the fractional conversion of the methyl orange dye during the simultaneous production of hydrogen. **b** A pseudo-first-order linearized kinetic model was applied to the absorbance data to determine the rate constant. The linear fit indicates that the photodegradation follows the first-order kinetics

hydrogen yield from sulfide-based electrolytes alone [55, 56]. We have chosen to apply the general rigorous approach of using the differential form of the power-law model [57] to estimate the rate parameters. The hydrogen generation rate is also shown in Table 5.1. The values are higher with the IH-TiO_2 and +Na_2SO_3 are reflective of the trend noted with MO degradation indicating that higher MO degradation leads to greater hydrogen yields.

The rate limiting step(s) could be any one of the following: (i) dye concentration, (ii) catalyst loading, (iii) light intensity, and (iv) charge transfer from photocatalyst to surrounding electrolyte across the catalyst–electrolyte double layer. In an unrelated system, it has been shown that these parameters can influence photocatalytic reactions and conversion yields [35]. Other parameters such as catalyst size, adsorption mechanism, and light type can also critically influence the photoconversion process in such systems [58]. It is important to optimize these parameters in order to get deeper insights into the role of each of these contributing factors.

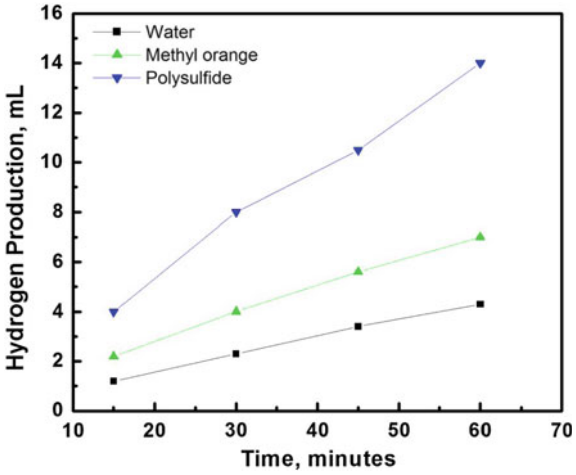

Fig. 5.14 A comparison of the hydrogen yield over time followed using IH-TiO_2–Pt–CdS as the photocatalyst in water and methyl orange as the sacrificial pollutant. The experiments were conducted in the presence of a 40 μM of methyl orange using UV–vis illumination (deaeration using N_2 for 30 min)

5.3.3 *CdS–Au–TiO_2 Sandwich Nanorod Array Enhanced with Au Nanoparticle as Electron Relay and Plasmonic Photosensitizer*

Instead of utilizing quantum dots and nanocomposites, plasmonic metal nanostructures can be used as the photosensitizer, where the energy stored in the plasmon can be transferred to a semiconductor [59] by direct electron transfer (DET) [60, 61] or plasmon-induced resonant energy transfer (PIRET). Localized surface plasmon resonance (LSPR) is the collective oscillation of surface electrons, with an oscillation frequency depending on size, shape, and metal of the nanostructure. The energy stored in the plasmon can be transferred to a semiconductor [59] by DET or PIRET [62]. Transfer of plasmonic hot electrons over the interfacial Schottky barrier occurs via DET [60, 61, 63–67]. PIRET involves the non-radiative dipole–dipole coupling between the plasmon in the metal and electron–hole pairs in the semiconductor [62, 68, 69].

Here, we would like to show hydrogen generation on a vertically aligned CdS–Au–TiO_2 nanorod array on a fluorine-doped tin oxide (FTO) substrate. Figure 5.15 shows the single-crystalline rutile TiO_2 nanorod arrays grown on a FTO substrate with a hydrothermal process. TiO_2 nanorods were $\sim$2.5 μm high and 150–200 nm in a diameter (Fig. 5.15b, c). Au nanoparticles (10 nm) were deposited on the TiO_2 nanorod with a photoreduction method following a uniform 15-nm-thick CdS QD layer deposition using a cadmium precursor chemical bath to form a sandwich nanorod structure. Here, CdS–Au–TiO_2 is the photoanode. The dual role of gold

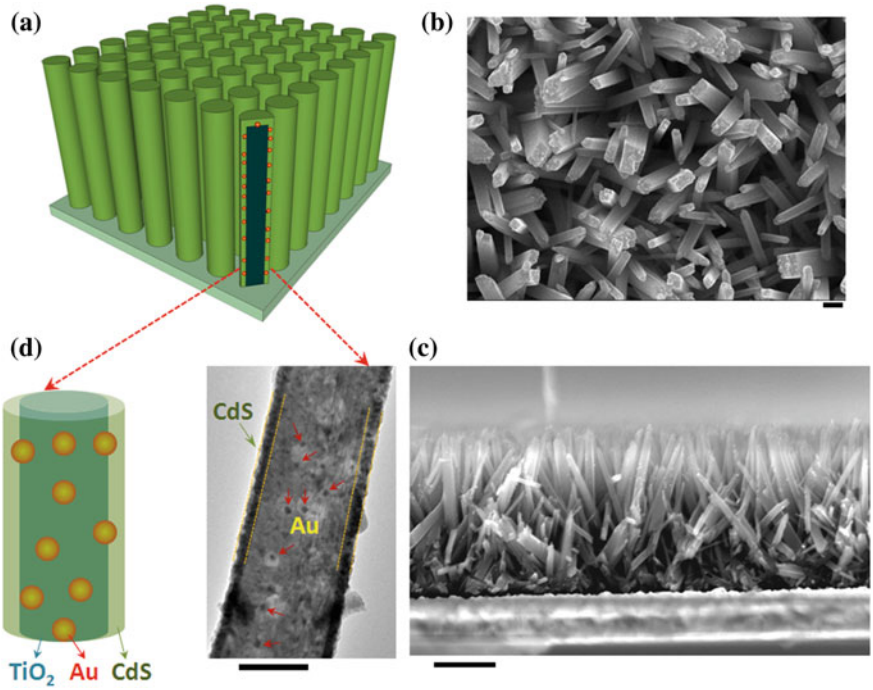

Fig. 5.15 Microstructure of the CdS–Au–TiO_2 sandwich nanorod array. **a** Scheme for the sandwich nanorod array on the FTO substrate, **b** *Top-view*, and **c** *cross-sectional view* of CdS–Au–TiO_2 nanorod array, **d** TEM image of a single sandwich nanorod. Scale bars: **b** 200 nm, **c** 1 μm, and **d** 100 nm [69]

nanoparticles sandwiched between the TiO_2 nanorod and the CdS quantum dot (QD) layer enhanced the solar-to-hydrogen conversion efficiency. Au nanoparticles act as an electron relay facilitating charge transfer between the CdS and TiO_2. Moreover, the Au nanoparticles function as a plasmonic photosensitizer helping photoconversion in the visible region (725 nm). Detailed interfacial trap states in the present heterostructure, charge transfer through trap-based Auger scattering with back-transfer, or increased charge separation occurring on the long-timescale are explained in a recent paper [69].

Increase in rate transfer into the CB of TiO_2, decrease in back-transfer rate, and the reduction in the trap-based Auger scattering rate have been observed independent of excitation wavelength. This is due to the presence of Au nanoparticle in the CdS–Au–TiO_2 heterostructure. It has been demonstrated that the Au acts as both an electron sink and transfer channel. Thus, the plasmonic electron transfer is via DET into the TiO_2 subject to the hot electron distribution energy relative to the Schottky barrier depending on the spectral position of the plasmon. The mechanism of interfacial charge transfer in CdS–TiO_2 heterostructure is essential for the PEC efficiency which will help optimizing the QD-sensitized heterostructures.

5.3.4 *Dual Role of Au Nanoparticle*

Figure 5.8 represents the best description of the PEC performance based on the observations made from inversion analysis method for transient-absorption spectroscopy (i) the interfacial trap states play in the CdS–TiO_2, (ii) the effect of Au on interfacial transfer, and (iii) the effect of the plasmonic hot electron energy relative to the interfacial Schottky barrier. This analysis method is the key inhibiting the critical role of interfacial trap states occur in the CdS–TiO_2 heterostructure, the influence of Au on interfacial transfer and long-timescale back transfer, and the impact of the plasmonic hot electron energy relative to the interfacial Schottky barrier.

UV–visible absorption spectra were collected for TiO_2 nanorod and the CdS–TiO_2 arrays with and without Au nanoparticles. Pure TiO_2 nanorod array displays a sharp absorption edge at around 410 nm matching the rutile titanium oxide bandgap. At longer wavelength, the absorption has a background from the ITO which is below the energy of the bandgap of both TiO_2 and CdS–TiO_2. Addition of CdS QDs improves the absorption up to 525 nm (2.36 eV). Enhanced absorption has been observed at wavelengths shorter than the band edge of CdS extending absorption up to 725 nm due to the inclusion of Au nanoparticles in between TiO_2 and CdS. LSPR due to Au nanoparticles corresponds to the strong absorption band centered at 610 nm, and it is sensitive to size, shape, and the surrounding environment. A redshift to 550 nm is detected for Au–TiO_2 compared to LSPR peak which is typically centered at 520 nm for Au nanoparticles in aqueous solution. The absorption peak is further shifted to 610 nm when the Au nanoparticles are deposited in-between TiO_2 and CdS which can be explained due to the large refractive index of the CdS layer.

For excitation wavelengths below 525 nm, the photocurrent enhancement is not due to the LSPR of Au nanoparticles since they are not excited. But the charge carriers are created in the CdS QDs (Fig. 5.16) due to photoexcitation and subsequently transferred to TiO_2 via the Au nanoparticles as represented in Fig. 5.17a.

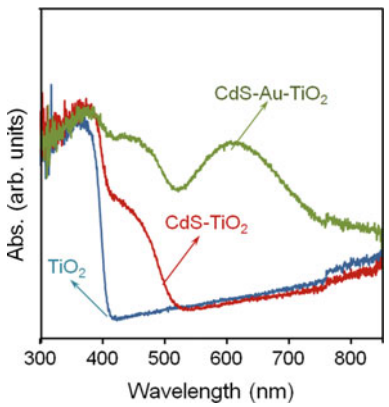

Fig. 5.16 UV–visible absorption spectra obtained from the CdS–TiO_2 nanorod arrays with and without Au nanoparticles [68]

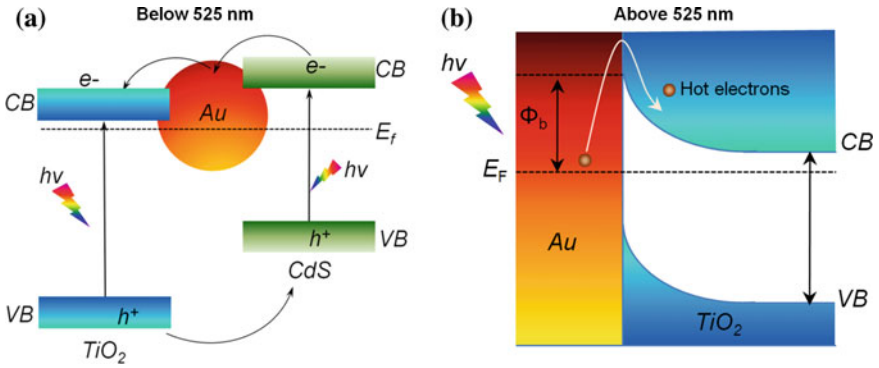

Fig. 5.17 The wavelength dependent dual role of Au nanoparticles in the CdS–Au–TiO_2 sandwich structure. **a** Electron relay effect of Au nanoparticles that facilitate charge transfer from CdS QDs to TiO_2 nanorod. **b** Plasmonic energy transfer from excited Au nanoparticles to TiO_2 through the hot electron transfer. CB = Conduction band, VB = Valence band, E_f = Fermi energy level, and Φ_B = Schottky barrier [69]

The light energy is insufficient to create carriers in the TiO_2 or CdS for wavelengths higher than 525 nm and therefore no charge transfer from CdS to TiO_2. The Au nanoparticles are excited via LSPR, and hot electrons are excited and can be transferred from the plasmonic metal to the conduction band of TiO_2 (Fig. 5.17b). Here, the Au nanoparticles play a major role as the plasmonic photosensitizer, increasing photoconversion from 525- to 725-nm wavelength region [69].

5.4 Discussions

An analysis of the observations and results presented in Sect. 5.3 is discussed below.

5.4.1 Pt, Au, and Ag Noble Metal Ad-Atoms

The addition of a noble metal reduces electron/hole recombination since the metal functions as electron sinks [19, 21, 70]. To facilitate electron–hole separation, three noble metals Ag, Au, and Pt were individually tested and Pt was noted to be the most effective, while Au and Ag were less effective. The IH-TiO_2 with Au as well as Ag indicated a gradual change in color following photoillumination. Such a color change indicates possible undesirable side reaction which could be the basis for the observed lowering in photoactivity. In fact, it has been shown that Au at the

interface with an oxide semiconductor exists in a dynamic equilibrium with its oxidation states [71–73]. Photogenerated holes oxidize Au, while the electron reduces them resulting in the existence of a dynamic equilibrium as shown below [72]:

$$\mathrm{Au} \xrightarrow{n\mathrm{h}^+} \mathrm{Au}^{n+} \tag{5.3}$$

$$\mathrm{Au}^{n+} \xrightarrow{n\mathrm{e}^-} \mathrm{Au} \tag{5.4}$$

Such a dynamic interface can function as trap centers consuming photogenerated electrons and holes resulting in reduced availability of these charges for redox reactions. Likewise, variation in Ag–Ag_2O ratio under illumination in a related study suggests the presence of a dynamic metal–metal ion interface [74]. Further, oxidation of Ag to Ag ions can lead to the formation of Ag_2O or Ag_2S [74–76] These in situ reactions could decrease the role Ag particles are expected to play, i.e., preventing e^-/h^+ recombination.

5.4.2 *Mechanism of the Photocatalytic Hydrogen Generation*

The UV–vis illumination will produce electron–hole pairs in the composite across the valence and conduction bands, respectively, of the TiO_2 and CdS. The holes participate in multiple reactions including water oxidation (rxn-1), hydroxyl radical formation (rxn-2), and in the oxidation of the polysulfide (rxn-3) or the pollutant MO/4-CP (rxn-4) resulting in intermediate degradation products. It is important to note that the oxidizing power of the holes from TiO_2 can lead to the formation of hydroxyl radicals. Every step that participates in hole utilization directly facilitates ensuring the longevity of the CdS deposits on the TiO_2 surface. The favorable energetics between the TiO_2 and CdS allows for the transfer of the photogenerated electrons from the CdS to the TiO_2. Electrons can be drawn to the Pt sites due its electron affinity. These charges will then participate in reactions leading to hydrogen generation (rxn-5). The protons can also yield hydroxyl radicals (rxn-6). The different steps that occur on the composite surface are summarized in Scheme 5.2.

5.4.3 *Comparison of the Photocatalytic Hydrogen Generation with Other Reported Systems*

Due to the popularity of Pt–CdS–TiO_2 as a composite photocatalyst for hydrogen generation, a review of the literature discussing the photoactivity of composites

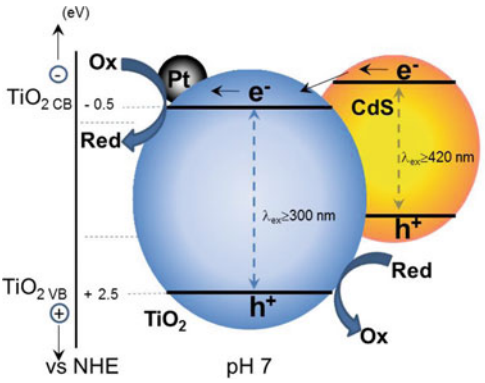

Redox reactions	
$H_2O+2h^+ \rightarrow 2H^+ + ½O_2$	1
$OH + h^+ \rightarrow OH^•$	2
$2S^{2-} + 2h^+ \rightarrow S_2^{2-}$	3
$MO \rightarrow h^+/(OH^•) \rightarrow$ Intermediates	4
$2H^+ + 2e^- \rightarrow H_2$	5
$H^+ + HO_2^• \rightarrow 2OH^•$	6
$O_2 + e^- \rightarrow O_2^{•-}$	7

Scheme 5.2 The figure shows the process of photocatalytic hydrogen evolution with simultaneous stabilization of the CdS via either hole scavenging by the polysulfides or by the pollutant MO. The common redox reactions that occur on the surface of the composite photocatalyst under aerated and deaerated conditions are shown in the *adjacent table*

prepared by bringing them together using various synthesis strategies has been performed and compared. It is important to mention that the experimental conditions are different and hence a direct comparison has limitations. We have strictly limited our comparison specifically to the amount of hydrogen generated with respect to the CdS loading. Table 5.2 shows the key parameters in this comparison. If unavailable, relevant information has been estimated from the available data. Of particular interest in this work is the hydrogen generation per unit mass of CdS per hour. At 140 μmol/1 % CdS, the IH-TiO_2–Pt–CdS composite studied here demonstrates a H_2 generation very close to the current best sample reported

5.4.4 *Photocatalytic Hydrogen Generation with CdS–Au–TiO_2*

Increase in rate transfer into the CB of TiO_2, decrease in back-transfer rate, and the reduction in the trap-based Auger scattering rate have been observed independent of excitation wavelength. This is due to the presence of Au nanoparticle in the CdS–Au–TiO_2 heterostructure. It has been demonstrated that the Au acts as both an electron sink and transfer channel. Thus, the plasmonic electron transfer is via DET into the TiO_2 subject to the hot electron distribution energy relative to the Schottky barrier depending on the spectral position of the plasmon. The mechanism of interfacial charge transfer in CdS–TiO_2 heterostructure is essential for the PEC efficiency which will help optimizing the QD-sensitized heterostructures [69].

Table 5.2 The table shows a comparative analysis of the hydrogen yield using different TiO_2–Pt–CdS samples reported in the literature (references shown)

Sample	Major electrolyte	Hydrogen yield (μM H_2/1 % CdS)	Sacrificial agent	CdS loading (%)	References
Pt(CdS–TiO_2)	Water	28.5	Na_2S/Na_2SO_3	10	[14]
CdS(bulk)–TiO_2–Pt	Water	120	Na_2S/Na_2SO_3	20	[34]
CdS–Pt–TiO_2	Water	167 (Optimized)*	Na_2/Na_2SO_3	2.8	[30]
CdS–Pt–TiO_2	Water	57.08	Na_2S/Na_2SO_3	11.3	[20]
Pt–(CdS–TiO_2)	Water	8.5	EDTA	1	J. Mol. Catal. A: Chemi., 129 1998. 61
IH-TiO_2–Pt–CdS	Water	140.3 (Unoptimized)*	Na_2S/Na_2SO_3	5.7	This work
Pt–CdS–TiO_2		0.142	Na_2S/Na_2SO_3	63	[29]

Key parameters such as electrolyte content, type of sacrificial agent, as well as the CdS loading are reported. As a benchmark for comparison, the hydrogen yield is normalized to unit weight of CdS

5.5 Conclusion

In conclusion, a wet chemical approach to synthesis anatase-only TiO_2, incorporate PGMs, and subsequently deposit a chalcogenide to form a unique high surface area nanocomposite has been presented in this chapter. Optical, microstructural, and photoelectrochemical studies have shown that the IH-TiO_2 has a particle size of 20 nm, demonstrates 60 % higher surface area compared to the commercial TiO_2, and exhibits superior photoelectrochemical responses (e.g., 60 % increase in photocurrent), indicating that it is a promising base material for preparing visible light active composites. Among the three PGMs studied for photocatalytic hydrogen generation, Pt of ~0.79 wt% on IH-TiO_2 is noted to be most useful: attributable at least in part to its known stability relative to other PGMs during photocatalysis. MO can be used as a replacement for polysulfide stabilizers with the dual benefit of its photodegradation as well as hydrogen generation. Hydrogen generation with all the catalysts over various time intervals in the presence of MO increases with time. Inclusion of Au nanoparticles in the CdS–Au–TiO_2 heterostructure decreases the rate of trap-based Auger recombination, increases the rate of transfer as well as the number of charge carriers transferred, and leads to efficient charge separation. Au nanoparticles sandwiched between the TiO_2 nanorod and CdS QD shell layer play a dual role in enhancing the solar-to-chemical energy conversion efficiency of PEC.

Acknowledgements RSV thanks the Department of Energy and the Office of the Vice-President for Research at the University of Nevada, and Reno junior faculty research startup for funding this project. RSV would also like to thank Degussa® Corporation for samples of P25. RSV would like to thank the NSF for supporting this work partially through the grant NSFCBET1134486.

References

1. Ni, M., Leung, M.K.H., Leung, D.Y.C., Sumathy, K.: Renw. Sust. Energy Rev. **11**, 401–425 (2007)
2. Park, H., Holt, J.K.: Energy. Environ. Sci. **3**, 1028–1036 (2010)
3. Ma, Y., Xu, Q., Zong, X., Wang, D.G., Wu, G.P., Wang, X., Li, C.: Energy Environ. Sci. **5**, 6345–6351 (2012)
4. Fujishima, A., Rao, T.N., Tryk, D.A.: J. Photochem. Photobiol. C **1**, 1–21 (2000)
5. Gerischer, H.: Electrochim. Acta **40**, 1277–1281 (1995)
6. Tran, P.D., Wong, L.H., Barber, J., Loo, J.S.C.: Energy Environ. Sci. **5**, 5902–5918 (2012)
7. Aroutiounian, V.M., Arakelyan, V.M., Shahnazaryan, G.E.: Sol. Energy **78**, 581–592 (2005)
8. Tang, J., Durrant, J.R., Klug, D.R.: J. Am. Chem. Soc. **130**, 13885–13891 (2008)
9. Alexander, B.D., Kulesza, P.J., Rutkowska, L., Solarska, R., Augustynski, J.: J. Mater. Chem. **18**, 2298–2303 (2008)
10. Rajeshwar, K.: J. Appl. Electrochem. **37**, 765–787 (2007)
11. Maeda, K., Domen, K.: J. Phys. Chem. Lett. **1**, 2655–2661 (2010)
12. Chen, X., Shen, S., Guo, L., Mao, S.S.: Chem. Rev. **110**, 6503–6570 (2010)
13. Cowan, A.J., Tang, J., Leng, W., Durrant, J.R., Klug, D.R.: J. Phys. Chem. C **114**, 4208–4214 (2010)
14. Daskalaki, V.M., Antoniadou, M., Puma, G.L., Kondarides, D.I., Lianos, P.: Environ. Sci. Technol. **44**, 7200–7205 (2010)
15. Lee, Y.-L., Chi, C.-F., Liau, S.-Y.: Chem. Mater. **22**, 922–927 (2009)
16. Li, G.-S., Zhang, D.-Q., Yu, J.C.: Environ. Sci. Technol. **43**, 7079–7085 (2009)
17. Chiarello, G.L., Aguirre, M.H., Selli, E.: J. Catal. **273**, 182–190 (2010)
18. Awazu, K., Fujimaki, M., Rockstuhl, C., Tominaga, J., Murakami, H., Ohki, Y., Yoshida, N., Watanabe, T.: J. Am. Chem. Soc. **130**, 1676–1680 (2008)
19. Choi, H., Chen, W.T., Kamat, P.V.: ACS Nano. **6**, 4418–4427 (2012)
20. Qi, L., Yu, J., Jaroniec, M.: Phys. Chem. Chem. Phys. **13**, 8915–8923 (2011)
21. Subramanian, V., Wolf, E.E., Kamat, P.V.: J. Am. Chem. Soc. **126**, 4943–4950 (2004)
22. Tada, H., Mitsui, T., Kiyonaga, T., Akita, T., Tanaka, K.: Nat. Mater. **5**, 782–786 (2006)
23. Peng, Z.A., Peng, X.G.: J. Am. Chem. Soc. **123**, 183–184 (2001)
24. Robel, I., Subramanian, V., Kuno, M.K., Kamat, P.V.: J. Amer. Chem. Soc. **128**, 2385–2393 (2006)
25. Zlateva, G., Zhelev, Z., Bakalova, R., Kanno, I.: Inorg. Chem. Commun. **46**, 6212–6214 (2007)
26. Kongkanand, A., Tvrdy, K., Takechi, K., Kuno, M., Kamat, P.V.: J. Am. Chem. Soc. **130**, 4007–4015 (2008)
27. Weller, H.: Adv. Mater. **5**, 88–95 (1993)
28. Li, L.S., Hu, J.T., Yang, W.D., Alivisatos, A.P.: Nano Lett. **1**, 349–351 (2001)
29. Park, H., Choi, W., Hoffmann, M.R.: J. Mater. Chem. **18**, 2379–2385 (2008)
30. Park, H., Kirn, Y.K., Choi, W.: J. Phys. Chem. C **115**, 6141–6148 (2011)
31. Lu, H.Q., Zhao, J.H., Li, L., Gong, L.M., Zheng, J.F., Zhang, L.X., Wang, Z.J., Zhang, J., Zhu, Z.P.: Energy Environ. Sci. **4**, 3384–3388 (2011)
32. Kim, J., Monllor-Satoca, D., Choi, W.: Energy Environ. Sci. **5**, 7647–7656 (2012)
33. Patsoura, A., Kondarides, D.I., Verykios, X.E.: Appl. Catal. B-Environ. **64**, 171–179 (2006)
34. Jang, J.S., Choi, S.H., Kim, H.G., Lee, J.S.: J. Phys. Chem. C **112**, 17200–17205 (2008)
35. Subramanian, V., Kamat, P.V., Wolf, E.E.: Ind. Eng. Chem. Res. **42**, 2131–2138 (2003)
36. Smith, Y., Kar, A., Subramanian, V.R.: Ind. Eng. Chem. Res. **48**, 10268–10276 (2009)
37. Raja, K., Smith, Y., Kondamudi, N., Manivannan, A., Misra, M., Subramanian, V.: Electrochem. Solid State Lett. **14**, F5–F8 (2010)
38. Mukherjee, B., Peterson, A., Subramanian, V.: Chem. Comm. **48**, 2415–2417 (2012)

39. Jaeger, V., Wilson, W., Subramanian, V.: Appl. Catal. B **110**, 6–13 (2011)
40. Murugesan, S., Huda, M.N., Yan, Y., Al-Jassim, M.M., Subramanian, V.: J. Phys. Chem. C **114**, 10598–10605 (2010)
41. Hatchard, C.G., Parker, C.A.: Proc. R. Soc. Lond. A **235**, 518–536 (1956)
42. Gomes, C., Silva, R., Juárez, T., Marino, R., Molinari, H.: García. J. Am. Chem. Soc. **133**, 595–602 (2010)
43. Toyoda, M., Nanbu, Y., Nakazawa, Y., Hirano, M., Inagaki, M.: Appl. Catal. B-Environ. **49**, 227–232 (2004)
44. Sivalingam, G., Nagaveni, K., Hegde, M.S., Madras, G.: Appl. Catal. B-Environ. **45**, 23–38 (2003)
45. Chan, C.K., Porter, J.F., Li, Y.G., Guo, W., Chan, C.M.: J. Am. Ceram. Soc. **82**, 566–572 (1999)
46. Jang, J.S., Ji, S.M., Bae, S.W., Son, H.C., Lee, J.S.: J. Photochem. Photobiol. Chem. **188**, 112–119 (2007)
47. Lee, Y.-L., Chang, C.-H.: J. Power Sour. **185**, 584–588 (2008)
48. Chakrapani, V., Baker, D., Kamat, P.V.: J. Amer. Chem. Soc. **133**, 9607–9615 (2011)
49. Baiocchi, C., Brussino, M.C., Pramauro, E., Prevot, A.B., Palmisano, L., Marci, G.: Int. J. Mass Spectrom. **214**, 247–256 (2002)
50. Stathatos, E., Petrova, T., Lianos, P.: Langmuir **17**, 5025–5030 (2001)
51. Kar, A., Smith, Y.R., Subramanian, V.: Environ. Sci. Technol. **43**, 3260–3265 (2009)
52. Arabatzis, I.M., Stergiopoulos, T., Andreeva, D., Kitova, S., Neophytides, S.G., Falaras, P.: J. Catal. **220**, 127–135 (2003)
53. Bao, N.Z., Feng, X., Yang, Z.H., Shen, L.M., Lu, X.H.: Environ. Sci. Technol. **38**, 2729–2736 (2004)
54. Comparelli, R., Fanizza, E., Curri, M.L., Cozzoli, P.D., Mascolo, G., Passino, R., Agostiano, A.: Appl. Catal. B-Environ. **55**, 81–91 (2005)
55. Priya, R., Kanmani, S.: Sol. Energy **83**, 1802–1805 (2009)
56. Hatchard, S.N., Upadhyay, S.N., Sinha, A.S.K.: Int. J. Hydro. Energ. **24**, 130–137 (2009)
57. Fogler, H.S., Gurmen, M.N.: Elements of Chemical Reaction Engineering. Prentice Hall, Upper Saddle River (2006)
58. Kansal, S.K., Singh, M., Sud, D.: J. Hazard. Mater. **141**, 581–590 (2007)
59. Cushing, S.K., Wu, N.: Q. Interface **22**, 63–67 (2013)
60. Tian, Y., Tatsuma, T.: J. Am. Chem. Soc. **127**, 7632–7637 (2005)
61. Tian, Y., Tatsuma, T.: Chem. Commun. 1810–1811 (2004)
62. Cushing, S.K., Li, J., Meng, F., Senty, T.R., Suri, S., Zhi, M., Li, M., Brristow, A.D, Wu, N.Q: J. Am. Chem. Soc. **134**, 15033–15041 (2012)
63. Chen, H., Chen, C.K., Chen, C.J., Cheng, L., Wu, P., Cheng, B., Ho, Y., Tseng, M., Hsu, Y., Chan, T., Lee, J., Liu, R., Tsai, D.: ACS Nano. **6**, 7362–7372 (2012)
64. Chen, H., Chen, C.K., Tseng, M., Wu, P., Chang, C., Cheng, L., Huang, H., Chan, T., Huang, D., Liu, R., Tsai, D.: Small **9**, 2926–2936 (2013)
65. Mubeen, S., Hernandez-Sosa, G., Moses, D., Lee, J., Moskovits, M.: Nano Lett, **11**, 5548–5552 (2011)
66. Liu, Z., Hou, W., Pavaskar, P., Aykol, M., Cronin, S.B.: Nano Lett. **11**, 1111–1116 (2011)
67. Warren, S., Thimsen, E.: Energy Environ Sci **5**:5133–5146 (2012)
68. Li, J., Cushing, S., Bright, J., Meng, F., Sentry, T.R., Zheng, P., Bristow, A.D., Wu, N.Q.: ACS Catal. **3**, 47–51 (2013)
69. Li, J., Cushing, S.K., Zheng, P., Senty, T., Meng, F., Bristow, A.D., Manivannan, A., Wu, N.: J. Am. Chem. Soc. **136**(23), 8438–8449 (2014)
70. Tian, Y., Tatsuma, T.: J. Am. Chem. Soc. **127**, 7632–7637 (2005)
71. Lahiri, D., Subramanian, V., Shibata, T., Wolf, E.E., Bunker, B.A., Kamat, P.V.: J. Appl. Phys. **93**, 2575–2582 (2003)
72. Subramanian, V., Wolf, E.E., Kamat, P.V.: Langmuir **19**, 469–474 (2003)

73. Subramanian, V., Roeder, R.K., Wolf, E.E.: Ind. Eng. Chem. Res. **45**, 2187–2193 (2006)
74. Park, M.S., Kang, M.: Mater. Lett. **62**, 183–187 (2008)
75. Kuo, Y.L., Chen, H.W., Ku, Y.: Thin Solid Films **515**, 3461–3468 (2007)
76. Zhang, W.X., Zhang, L., Hui, Z.H., Zhang, H.M., Qian, Y.T.: Solid State. Ionics. **130**, 111–114 (2000)

Chapter 6
Organic Photovoltaics

Dean M. DeLongchamp

6.1 Introduction to Organic Photovoltaics

Organic photovoltaics (OPV) describes a group of technologies wherein the active layer of a solar cell is composed of hydrocarbon-based organic materials [1–3]. OPV occupies a special niche among solar energy technologies in that it could potentially satisfy the growing energy needs of the world with a product that is sustainable, elementally abundant, and cheaply manufactured. OPV cells have recently seen a dramatic uptick in reported efficiencies, with power conversion efficiencies reaching ≈11 %, as shown in Fig. 6.1 [4, 5]. These increases in power conversion efficiency have largely been driven by the development and discovery of new OPV active layer materials and new ways to process them. The technology has gained significant commercial attention over the past decade, as its unique attributes merit consideration for a place in the landscape of distributed energy generation devices [6]. Some of OPV advantages include a flexible form factor and facile processing, either from fluids or from vacuum deposition.

At least two different device designs are often regarded as OPV technologies. The first is based on a solid-state OPV cell, having typically two organic semiconductors in a bilayer or distributed heterojunction arrangement. The second type, which will not be addressed in this chapter, is more typically called a dye-sensitized solar cell (DSSC) [7], which relies on a mesoporous electron conductor that is typically inorganic, a sensitizing dye, and an ion-conducting redox electrolyte. Unlike organic heterojunctions, the DSSC contains liquid and thus faces challenges in packaging and limited flexibility.

The first report of a solid-state OPV cell was as early as 1959, when a photovoltaic effect in ≈10-μm-thick anthracene crystals was reported [8]. The efficiency

D.M. DeLongchamp (✉)
Materials Science and Engineering Division, National Institute of Standards and Technology, Gaithersburg, MD 20899, USA
e-mail: dean.delongchamp@nist.gov

M.P. Paranthaman et al. (eds.), *Semiconductor Materials for Solar Photovoltaic Cells*, Springer Series in Materials Science 218,
DOI 10.1007/978-3-319-20331-7_6

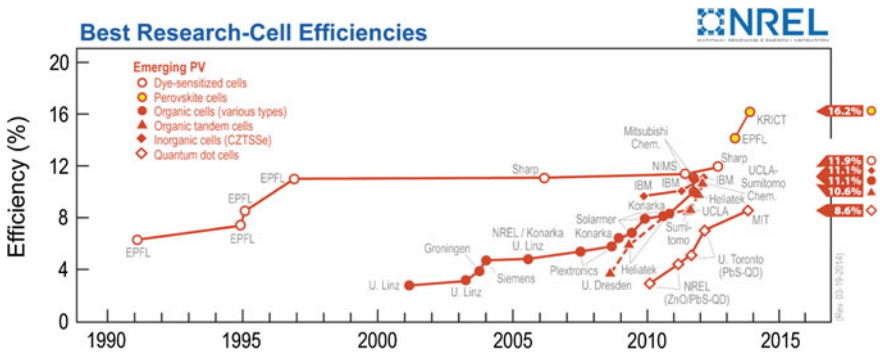

Fig. 6.1 Best research cell efficiencies for emerging photovoltaics technologies. OPV is indicated by *filled circles*. Both single-cell and tandem OPV efficiencies are approaching 12 % [4]

was very poor. The reasons for this were several, but the most prominent was likely that the exciton that forms upon photon absorption in pure organic semiconductors has a high binding energy, far higher than 25 meV [9–12], and therefore, it will rarely spontaneously split into a hole and electron pair. Thus, a critical difference between modern heterojunction OPV devices and most inorganic solar cells is that the OPV active layer is not often composed of a single semiconductor. The typical approach is to combine two organic semiconductors, one an electron donor and one an electron acceptor. This approach was demonstrated by Tang in 1986, with the construction of what is often considered the first OPV cell to resemble modern ones [13] (though it is clear that the potential of the technology was recognized earlier [14], even with predictions of 10 % single-junction efficiency). The active layer consisted of a bilayer with one layer being copper phthalocyanine and the other being a perylene tetracarboxylic derivative. It exhibited a power conversion efficiency of ≈1 %.

In a typical OPV active layer, one or both phases will absorb light to create excitons; the bandgaps of the two semiconductors will determine their optical absorption. The offset in lowest unoccupied molecular orbitals (LUMOs), as illustrated in Fig. 6.2, is exploited to split the exciton. Before the exciton can be split, it must first diffuse to the interface between the two materials. For facile exciton separation, the two phases must be separated in a length scale similar to the organic semiconductor exciton diffusion length of <10 nm [15–17].

Because the exciton diffusion length is significantly smaller than the typical desired optical path for efficiency harvesting of solar light, a bilayer approach may not be suitable for the highest efficiency photovoltaics. The need to reconcile a large optical path and a small exciton diffusion length has led to the bulk heterojunction (BHJ) concept [18], as illustrated in Fig. 6.3, where the two phases are blended in a single nanocomposite film. The discovery and advancement of the BHJ concept accompanied an emerging understanding that there could be ultrafast charge

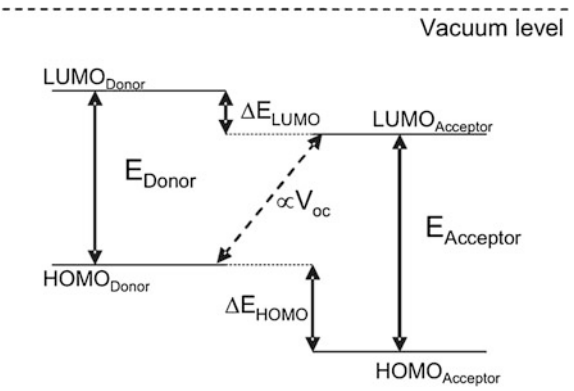

Fig. 6.2 Donor and acceptor energy-level schemes [3]

electron transfer from a donor to an acceptor in a blend [19–21]. In this electron transfer work, the electron acceptor was invariably a fullerene and the electron donor a polymer. The first intentional construction of a polymer–fullerene BHJ for solar energy harvesting appears to have been in 1995 [22]. A BHJ is most commonly created by simultaneous casting of the donor and acceptor materials, either in solution or during vacuum deposition. The nanoscale structure (typically called morphology) of the BHJ may be intrinsically linked to its power conversion efficiency, because it could influence processes such as exciton diffusion, electron and

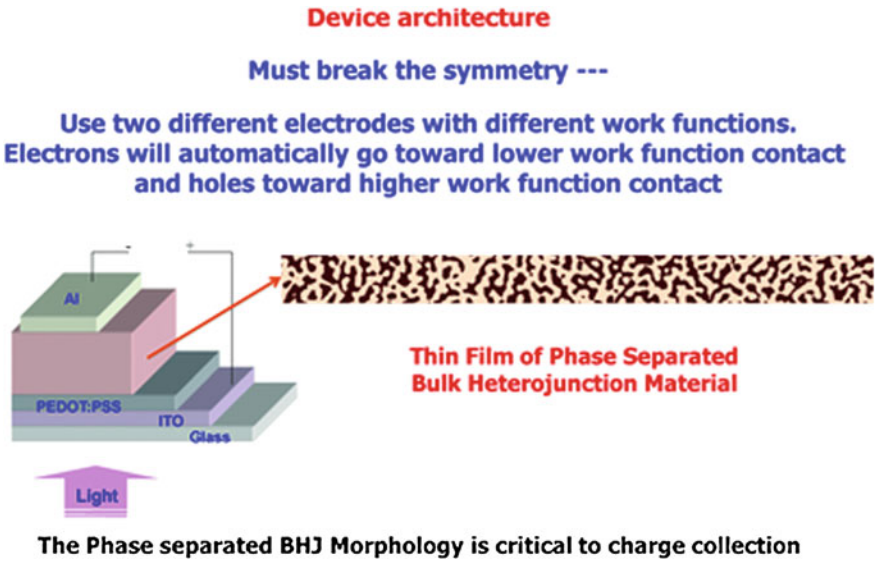

Fig. 6.3 The BHJ concept [18]

hole percolative conduction, and bimolecular recombination. The morphology of a BHJ can depend strongly on the two components used and the casting conditions [23]. Morphology studies of BHJ systems are thus very common in the field, although there is considerable disagreement about what morphological features should lead to the highest performing solar cells [24–26].

The ultimate power conversion efficiency of an OPV cell is determined by its component electron donor and electron acceptor materials. Since the electron acceptor is so often a specific fullerene (PCBM, discussed at length in Sect. 6.2.1.2), the routes to higher power conversion efficiency are often considered solely through the properties of the electron donor. Of particular importance are the highest occupied molecular orbital (HOMO), the lowest occupied molecular orbital, and bandgap between them. A calculation of how the power conversion efficiency of an OPV cell depends on these parameters is shown in Fig. 6.4. Intrinsic to this model is the expectation that the open-circuit potential will be proportional to the difference between the HOMO energy of the donor and the LUMO energy of the acceptor, less 0.3 V [27]. This lost potential is an empirical factor that is thought to compensate for dark current and electric field dropping losses.

In this chapter, I will discuss the current state of OPV technology. Because the technology is so dependent on materials, the selection and development of new materials will be a key focus. Other sections will include measurements of OPV materials structure and a discussion of the state-of-the art in commercial OPV fabrication.

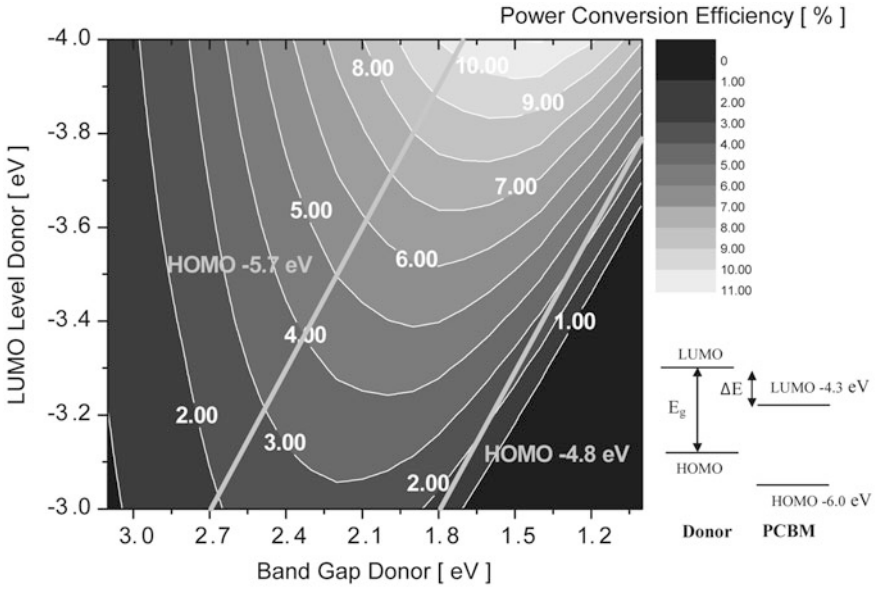

Fig. 6.4 Dependence of power conversion efficiency on bandgap and LUMO level of donor polymer [27]

6.2 OPV Materials

Modern OPV active layers are typically described as being either solution-processed or vacuum-deposited. All materials used for the active layer are conjugated organic molecules, which have extensive delocalized pi electron networks. The chemical structures of conjugated organics are characterized by extensive series of alternating single and double bonds. Aromatic moieties, including fused ring structures, are also common. The pace of new organic semiconductor development is extremely rapid, and the synthetic diversity is extraordinary, prompting topical reviews every few years [28]. In this section, I will describe some of the organic semiconductors that have seen extensive use in OPV active layers. The ones featured should be regarded more as examples of widely used materials or material families rather than an exhaustive list.

6.2.1 Solution-Processable OPV Materials

There is great interest in solution-processable OPV materials as a route toward the large-scale manufacture of OPV modules. The general arguments in favor of solution processing involve its ambient pressure and (generally) low temperature, which are argued to promote a lower overall fabrication cost. The concept of adapting solution web coating techniques, such as those used for the now-defunct chemical photography film, to OPV fabrication has proven especially attractive. Solution processing does have some significant disadvantages, however. The solvents that organic semiconductors are most commonly processed from halogenated aromatic solvents are not environmentally friendly. Care has to be taken when subsequent layers are deposited in multilayer structures such that the application does not dissolve underlying layers. And how to control the materials structure of solution-deposited organic semiconductors is still not well-understood. Finally, the chemical design of solution-processable organic semiconductors results in some curious idiosyncrasies: Since the conjugated core (the semiconducting part) has very few conformational degrees of freedom, it is almost never soluble in solution by itself, so the chemist adds a variety of solubilizing groups, which are typically branched or linear alkane chains. This chemical modification can further influence the development of material structure, and therefore OPV performance, because it affects how the molecule can pack in crystals. The development of new materials is therefore quite complex, and very few of the materials that are chemically synthesized eventually show significant promise in OPV devices.

6.2.1.1 Solution-Processable Electron Donors

The most common solution-deposited donor material family in OPV devices is the polythiophenes. Highly regioregular poly(3-hexylthiophene) (P3HT) in particular is

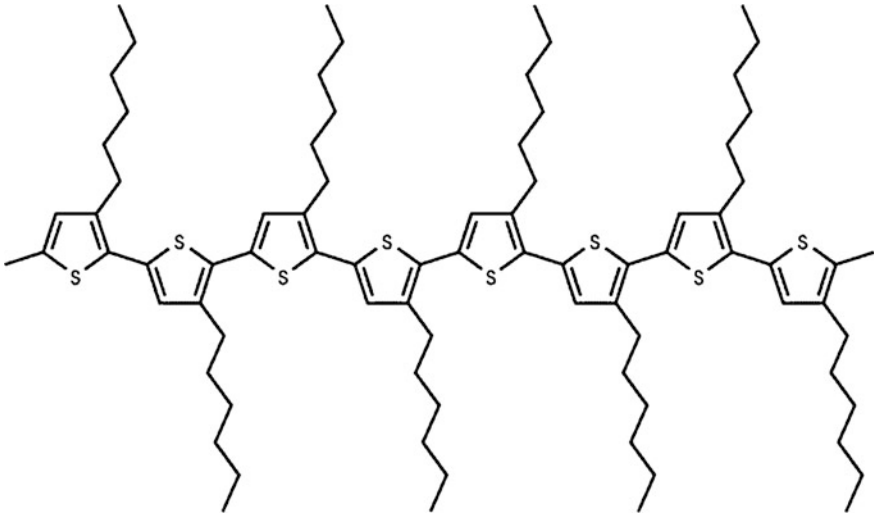

Fig. 6.5 A short oligomer of P3HT

commonly recognized as the most commonly used donor material [29, 30]. The structure of P3HT is shown in Fig. 6.5. Regiorandom poly(3-alkylthiophenes) were first synthesized in the late 1980s [31], but synthetic routes for regioregular P3HT and other poly(3-alkylthiophenes) were established later, in independent contributions by McCullough [32] and Rieke [33]. The later development of the Grignard metathesis route by McCullough [34] produced what is today the most common synthesis of the ubiquitous P3HT donor. P3HT is now widely commercially available.

Whereas regiorandom P3HT tends to be amorphous, regioregular P3HT tends to be highly crystalline [35, 36]. This crystallinity may be very important to its function in solar cells as it improves the polymer's hole mobility. Although other regioregular poly(3-alkylthiophenes) are readily available, none has the cachet or ubiquitous application that P3HT has seen. The issue of regioregularity is less prevalent in other solution-deposited donor materials. Typical P3HT-based OPV cells exhibit efficiencies between 2 and 4 %, although an enormous breadth of performance has been reported [29]. P3HT-based active layers, and most other OPV active layers, are processed using either 1-chlorobenzene (CB) or 1,2-dichlorobenzene (DCB) as primary solvents. The electron acceptor in these and most other OPV active layers is a fullerene (PCBM) that will be described later in this chapter. The efficiency of P3HT-based OPV cells is limited by P3HT's light absorption, which is somewhat too high energy for good overlap with the solar spectrum.

To achieve lower energy light absorption, most modern solution-processed donor polymers for OPV are based on a push-pull chromophore system where the repeat unit has two parts, each of which may have multiple separate or fused rings

[37, 38]. Some examples of these polymers are given in Fig. 6.6. Because of their complex repeats, these polymers are typically referred to using acronyms, which themselves have become fairly complex. Several common donor polymers with their acronyms are shown in Fig. 6.6.

Poly[*N*-9′-heptadecanyl-2,7-carbazole-alt-5,5-(4′,7′-di-2-thienyl-2′,1′,3′-benzothiadiazole)] (PCDTBT) was first reported in 2007, synthesized by Leclerc and co-workers [39]. This material is now commonly available and has seen wide use

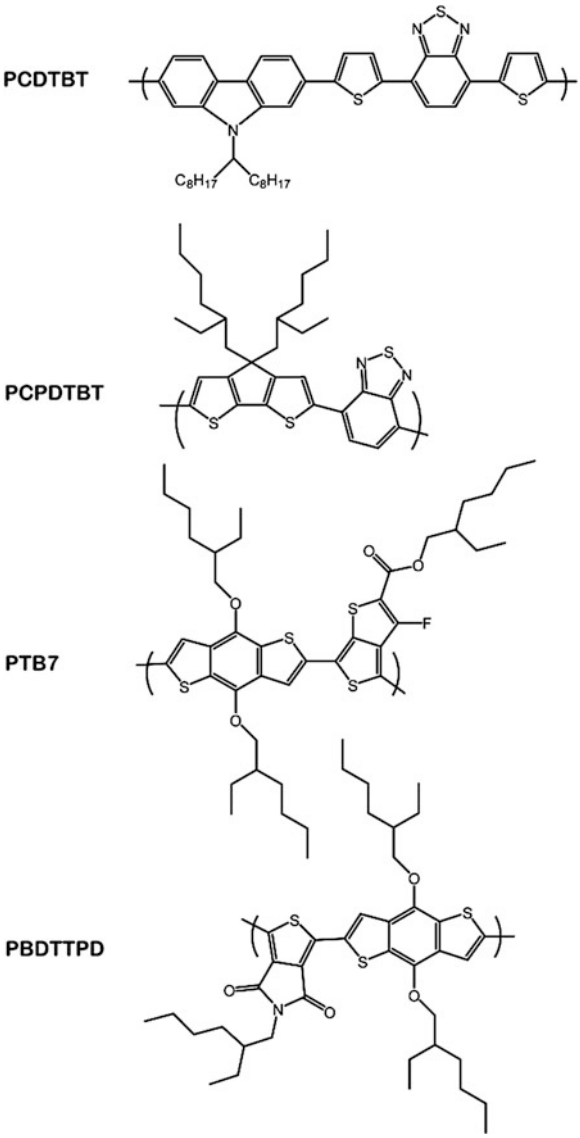

Fig. 6.6 Some commonly used donor polymers

[40]. Cells using PCDTBT have achieved power conversion efficiencies up to 7.5 % [41], with efficiencies above 6 % being common [40, 42]. PCDTBT is different than P3HT and other donor polymer in several ways. Unlike for P3HT, cells containing PCDTBT are generally not amenable to heating schedules to improve power conversion efficiency, implying that PCDTBT does not further crystallize with heating. The X-ray diffraction strength of PCDTBT is also remarkably small [42] unless it is prepared in an unusual way, suggesting that its typical crystallinity is lower than most other semiconducting polymers.

Poly[2,6-(4,4-bis-(2-ethylhexyl)-4H-cyclopenta[2,1-b;3,4-b′]-dithiophene)-alt-4,7-(2,1,3-benzothiadiazole)] (PCPDTBT) was first introduced by Bazan and co-workers in 2007 [43]. PCPDTBT has an acronym regrettably similar to PCDTBT, and they are sometimes confused. This material was notable because its high efficiency was discovered by the use of low-volatility additives that have now become common in OPV formulation [44]. As shown in Fig. 6.7, the principal effect of the additive in PCPDTBT-based devices is to increase the nanoscale domain size. Interestingly, a synthetic variant of this polymer called Si-PCPDTBT, which differs only in having a silicon bridge across the dithiophene rather than PCPDTBT's carbon bridge, has similar performance and morphology to PCPDTBT-based active layers even without the formulation additive [45].

Because of the discoveries surrounding the introduction and optimization of PCPDTBT, the practice of formulating OPV casting solutions using low-volatility additives is now commonplace. Common additives include 1,8-diiodo octane (DIO), 1,8-octanedithiol (ODT), and 1-chloronaphthalene (CN). If a BHJ material pair fails to perform well using only a CB or DCB solution, a common approach is to add 3 % DIO, which will frequently result in improvement. Although the mechanism by which the additives act on the material is not entirely clear, many

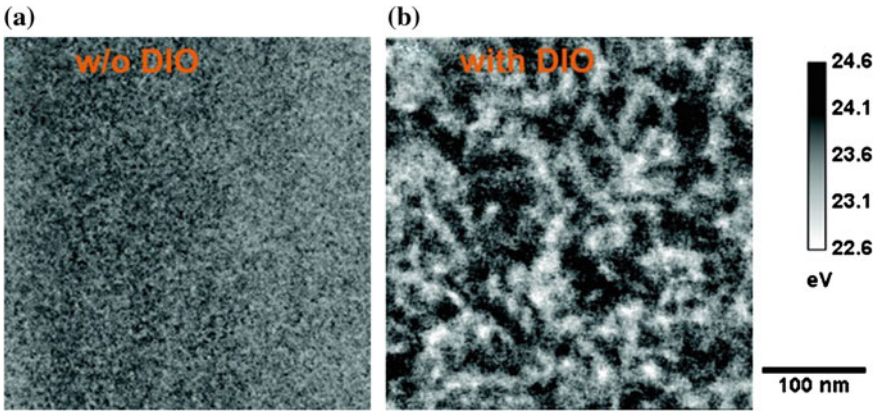

Fig. 6.7 The impact of a formulation additive on the nanoscale morphology of PCPDTBT-based active layers [146]. The contrast is generated from the plasmon loss in energy-filtered transmission electron microscopy

additives such as DIO and ODT are poor solvents for the polymer but good solvents for the electron acceptor (typically a fullerene). Additives such as CN may work by a different mechanism because they are good solvents for both the electron donor and the electron acceptor. All additives do degrade the solvent quality to some extent, leading to earlier aggregation [46].

The polymer PTB7, which is based on ester-substituted thieno[3,4-b]thiophene and benzodithiophene units, was introduced by Yu and co-workers in 2010 [47]. Solar cells of PTB7 exhibit power conversion efficiencies greater than 7 % [47], with extremely high efficiencies greater than 9 % reported for some device designs [48]. As for PCPDTBT, the efficiency of PTB7-based devices is improved using low-volatility formulation additives. PTB7 has a fluorine substituent on one of its rings, which creates a large local dipole moment that is thought to be responsible for low bimolecular recombination rates in the solar cell [49]. This theme of fluorination leading to high efficiency absorbers has also been seen in other polymers [50–52] and small molecules [53], although the specific site of fluorination seems to be incredibly important. The morphology of PTB7 is often described as "hierarchical," [54, 55] having multiple length scales of characteristic structure, although some measurements indicate that it can also be more uniform [56–58].

The poly(benzo[1,2-b:4,5-b′]dithiophene–thieno[3,4-c]pyrrole-4,6-dione) (PBDTTPD) polymers were introduced by Frechet around 2010 [59] as a family of materials having efficiency up to 8.5 % that depends strongly on the choice of side chain substituents [60]. Aside from its high efficiency, PBDTTPD is notable among lower-bandgap polymers in that its linear side chain variants have a relatively high X-ray diffraction strength [60], suggesting that its crystallinity is significantly higher than typical lower-bandgap polymers such as PCDTBT and PTB7, and perhaps similar to that of P3HT.

An important new class of absorbers in OPV active layers are soluble conjugated small molecules [61]. High efficiency small-molecule absorbers appeared around 2011, in syntheses described by Bazan and co-workers [53]. It has been suggested that small-conjugated molecules may be intrinsically easier to synthesize and purify than conjugated polymers. One of the highest power conversion efficiency small-molecule absorbers (p-DTS(FBTTh$_2$)$_2$) is shown in Fig. 6.8. The power conversion efficiencies of cells using this material can exceed 8 % [62].

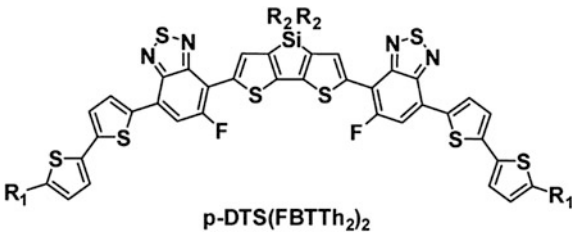

Fig. 6.8 The chemical structure of a very high-performance small-molecule absorber for OPV active layers [53]. R_1 = n-hexyl, R_2 = 2-ethylhexyl

The nanoscale domain size within of active layers containing the small-molecule p-DTS(FBTTh$_2$)$_2$ is very sensitive to the amount of DIO additive in its formulation. If too much is added, the domain size can grow too large, and efficiency suffers, presumably because the absorber domain size exceeds the exciton diffusion length. TEM images of p-DTS(FBTTh$_2$)$_2$-based films prepared in different ways are shown in Fig. 6.9.

The solution-deposited acceptors are the most synthetically diverse subset of materials in OPV technology, and this section of this chapter cannot provide exhaustive coverage. Some other materials of interest include the diketopyrrolopyrrole (DPP)-based systems, which have been developed as both polymers [63] and as small molecules [64]. Polymers based on benzodithiophene-fluorinated benzotriazole pairs (PBnDT−FTAZ) are remarkable because they exhibit high fill factors even for films that are relatively thick, which is a rare trait among OPV

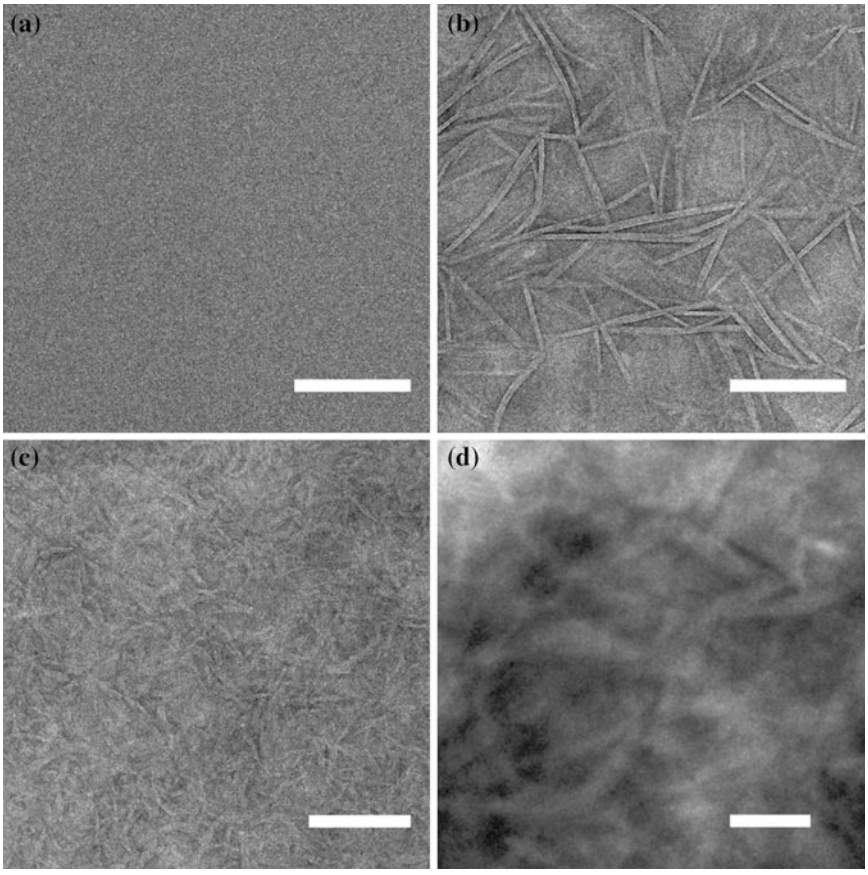

Fig. 6.9 Bright-field TEM showing domain size in p-DTS(FBTTh$_2$)$_2$-based films **a** as cast, **b** thermally annealed, **c** with 0.4 % DIO additive, and **d** with 1 % DIO additive [147]

active layers [50]. The PBnDT−FTAZ materials also exhibit a diverse nanoscale morphology that their power conversion efficiency seems largely independent from [65]. The isoindigo (iI)-based small molecules [66] and polymers [67, 68] are remarkable because in addition to providing efficiencies in excess of 6 % [67], the iI moiety is synthesized primarily from a naturally derived and widely available dye, which may have important ramifications for scale-up and the ultimate cost of the absorber polymer in manufactured cells.

6.2.1.2 Solution-Processable Electron Acceptors

By far the most common acceptor to be used in OPV cell active layers is [6,6]-phenyl-C_{61}-butyric acid methyl ester (PCBM), which is shown in Fig. 6.10. PCBM is based on the C_{60} fullerene. The potential for C_{60} fullerene-based BHJ layers was recognized in 1992 [19], and the synthesis of PCBM by Hummelen and Wudl [69] as well as its BHJ demonstration with Heeger [22] was published in 1995. An enormous variety of functionalized fullerenes has now been synthesized [70–72], primarily motivated by the search for a PCBM replacement. Despite this effort, only the C_{70} variant of PCBM [73] has enjoyed similar ubiquitous interest and use, primarily because it has more extensive light absorption across the visible range than does the C_{60} variant. In polymer-fullerene cells containing $PC_{70}BM$, hole transfer from the fullerene to the polymer is a power conversion channel equally important to electron transfer; the shorthand jargon terms “donor” and “acceptor” become less meaningful (without further qualification) in such a scheme, even though they are still extensively used.

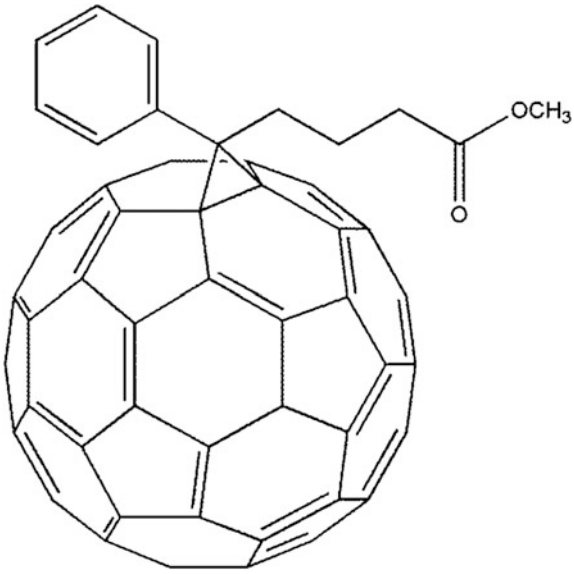

Fig. 6.10 The electron acceptor PCBM

One of the remarkable features of PCBM is that it generally does not crystallize in a BHJ. It instead remains amorphous, a glass at room temperature. Its X-ray diffraction typically produces a broad ring without distinctive peaks. The broadness of this feature suggests that the coherent domain size is a few fullerene molecules. If peaks in the X-ray diffraction are present, they are usually caused by micron-scale PCBM crystals that grow when the PCBM glass is heated above its glass transition temperature, especially on certain substrates [74], which is considered detrimental to the power conversion efficiency. Interestingly, the published crystal structures of PCBM contain solvent molecules, when either CB or DCB is used [75]. But it seems unlikely that PCBM crystals exist within mainstream polymer–fullerene BHJs, at least from the X-ray evidence [76], although it bears mentioning that pre-crystalline aggregates may occur that have energy-level properties distinct from those of molecularly dispersed PCBM [77]. The only crystalline phase in a polymer–fullerene BHJ is typically the polymer crystal.

Fullerene bisadducts are increasingly popular because they can substantially raise the open-circuit voltage of OPV devices [78, 79]. The most common of the fullerene adducts is the indene bisadduct of fullerene (ICBA) [80]. ICBA performs quite well when blended with P3HT, with power conversion efficiencies up to 6.5 % [81], but more poorly when blended with other polymers. A blend of P3HT and ICBA has been sold under the trade name PV2000 by Plextronics Inc., for several years as of this writing.

There has been an extensive synthetic effort across the OPV community to develop electron acceptors that are not fullerenes. The most extensive of these efforts has been in polymers, and in particular in the consideration of polymers that make excellent n-type organic semiconductors for transistors [82]. An interesting aspect of replacing fullerenes with polymers is that the electron-accepting polymer can often absorb light quite strongly, so it becomes a hole donor as well and an important channel for power conversion. Some of the earliest work in this area focused on cyanated phenylenevinylene acceptor polymers. The most well studied of these were CN-PPV [83] and MEH-CN-PPV [84, 85]. Although the power conversion efficiencies of these materials were very low by modern standards, they did exhibit high photovoltage, and the studies of them were essential to developing early understanding of charge separation processes in OPV blends.

More recently, polymers based on perylene diimide and naphthalene diimide have been used successfully as electron acceptors in OPV cells. The earliest report of this type of polymer was in 2007 by the Marder group, with the introduction of P(PDI2DD-DTT) shown in Fig. 6.11a [86]. Although polymers of this type exhibit extended two-dimensional conjugation within each monomer, the selection of appropriate side chains renders them soluble in common solvents. Polymers based on perylene diimide have been used in bulk heterojunction solar cells to reach power conversion efficiencies of just over 2 % [87, 88]. Interestingly, the electron donor polymers that perform best when paired with these acceptor polymers are generally different than those that perform best when paired with fullerenes. This phenomenon has generally been attributed to morphological considerations [88]. The most well-known naphthalene diimide-based polymer, P(NDI2OD-T2), was

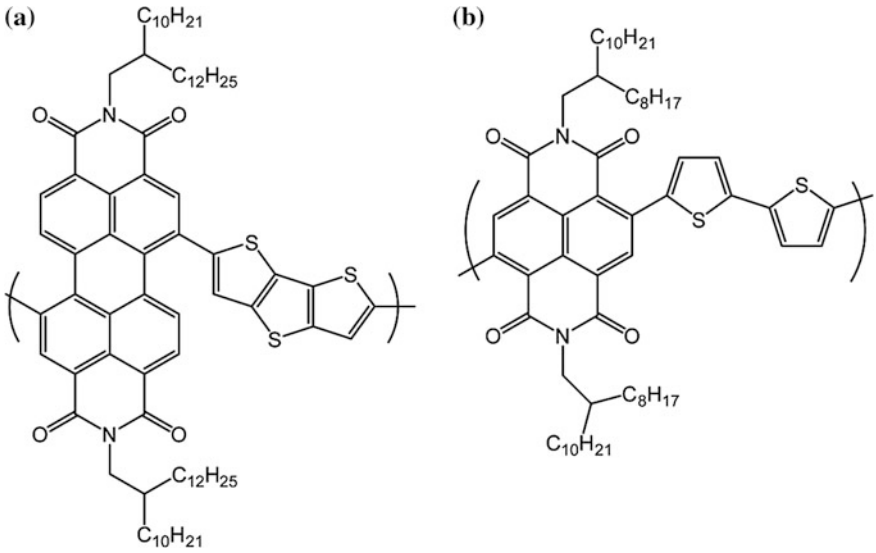

Fig. 6.11 The n-type semiconducting polymers (**a**) and (**b**)

introduced in 2009 as a revolutionary new electron-transporting material for transistors [89]. With electron mobilities of up to 0.85 cm^2/Vs, its capability for electron transport far exceeded other polymeric materials at the time, though there were many polymers that exhibited hole mobility of similar magnitude. The excellent charge transport of P(NDI2OD-T2) was generally attributed to its very high crystallinity [90, 91]. Despite the excellent charge transport of P (NDI2OD-T2), the power conversion efficiencies of OPV cells incorporating them were generally quite low, less than 1 % [92, 93]. The general conclusion was that the higher crystallinity led to impractically large domain sizes. Recent work has shown that the optimization of domain length scale using careful solvent selection and processing protocols can result in power conversion efficiencies higher than 1 % [94]. Pairing P(NDI2OD-T2) with an undisclosed, optimized donor polymer has resulted in efficiencies as high as 4.2 %, and other, presumably related polymer acceptors have produced all-polymer cells having more than 6 % single-cell efficiency, as reported by the Polyera Corporation [95].

6.2.2 Vacuum-Deposited Materials

Vacuum-deposited small-molecule OPV cells were some of the first organic solar cells in the 1970s, and their continued development has been extremely active. The arguments in favor of vacuum deposition generally point out that the technique is not as expensive as commonly believed; in fact vacuum deposition is used routinely

on disposable items such as food packaging. The high level of structural control, and particularly the fact that solvent is not present, gives the deposition technique significant advantages in the fabrication of extremely complex multilayer stacks. The technique can also leverage of the wealth of deposition knowledge and tooling from organic light-emitting diode (OLED) technology. OLEDs are fast-becoming the display material of choice for handheld devices such as smart phones. The multilayer stacks of an OLED are quite similar to the layers required for small-molecule OPV cells. It is thus straightforward to use vacuum deposition to make tandem cells, and vacuum-deposited tandems have achieved 12 % efficiency or greater in recent years [96].

Most of the materials development in vacuum-deposited OPV materials is invested in the donor material because the acceptor is invariably a fullerene (C_{60} or C_{70} rather than PCBM), which are quite well adapted to the deposition technique. Vacuum-deposited absorbers are generally more recognizable as common synthetic dyes or pigments (or variations on them) than are solution-deposited materials. They cannot be polymers because a lower molecular mass is required for the material to thermally evaporate, and they usually lack the characteristic alkane side groups common to solution-processed materials.

The most common early material used as an acceptor in vacuum-deposited OPV devices was the metal phthalocyanines (Pc), as shown in Fig. 6.12a. These had been synthesized for hundreds of years, but their application in 1986 as a light absorber in a two-layer cell essentially launched the field of modern OPV [13]. Early power conversion efficiencies of single-layer Pc-based devices were quite poor [14],

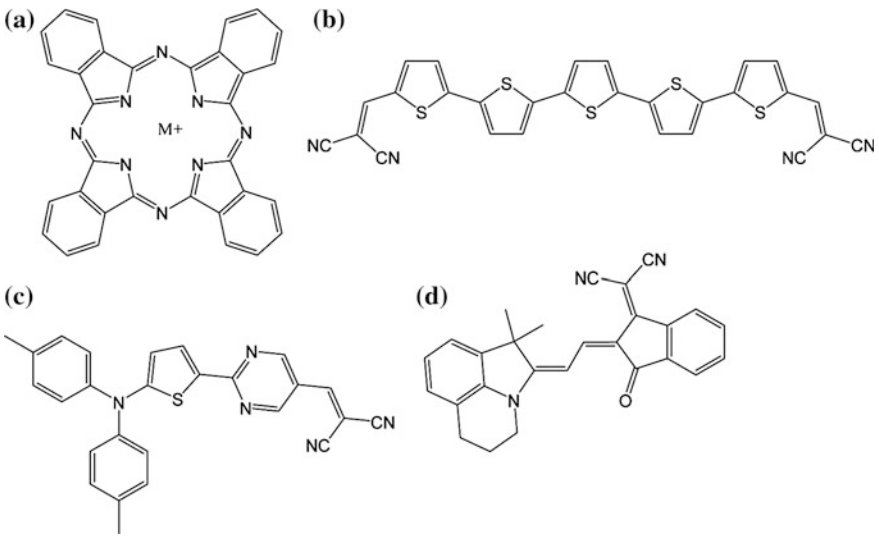

Fig. 6.12 The vacuum-deposited absorbers **a** phthalocyanines, where M is typically copper or zinc, **b** dicyanovinylene-substituted quinquethiophene (DCV-5T), **c** diphenylaminothienyl-pyrimidine-dicyanovinyl-based dye, and **d** merocyanine dye

before Tang's inclusion of a second layer to accept electrons and split the exciton. By the early 2000s, the CuPc-based cells were incorporated into successful tandems with power conversion efficiencies of nearly 6 % [97, 98]. During this era, the straightforward tandem fabrication in vacuum-deposited cells put their demonstrated efficiencies significantly higher than solution-cast cells, although they have now reached nominal parity.

An important absorber family in thermally evaporated OPV systems has been the dicyanovinyl-substituted oligothiophenes, exemplified by the quinquethiophene material shown in Fig. 6.12b. This family of materials has been especially important as a model system for the study of how conjugation length (number of thiophene units in the backbone) affects OPV device performance [99]. The bandgap was decreased with increasing molecular length by an increasing HOMO level and a relatively stable LUMO. The "sweet spot" in terms of device performance was the pentamer, which had a power conversion efficiency of ≈4 %. A slightly modified chemical structure was used in a later study [100], which also identified the pentamer as the most successful material, having an efficiency of ≈5.2 % in bulk heterojunction cells that required considerable optimization of film thickness and adjacent layer work function.

It has also been common in thermally evaporated OPV materials design to consider dyes using a push-pull chromophore system like that we describe for advanced polymer absorbers in Sect. 6.2.1.1. Materials such as that shown in Fig. 6.12c have been considered for this purpose. In cells with C_{70} as the electron acceptor, this chromophore based on an electron-donating ditoluylaminothienyl moiety and an electron-withdrawing dicyanovinylene moiety has demonstrated promising efficiencies up to ≈5.8 % [101]. Chemically similar dyes have achieved efficiencies of ≈6.4 % [102]. The dimerization of the dye into very close π-stacks, as measured by X-ray diffraction, was considered an important contribution to the high efficiency of this system.

Merocyanine dyes have recently become important candidate absorber materials for vacuum-deposited OPV systems. These dyes are relatively recent inventions and are known for their intense coloration and fluorescence. A power conversion efficiency of ≈4.9 % has been achieved using the merocyanine dye shown in Fig. 6.12d in a conventional device stack [103]; the efficiency was increased to ≈5.8 % using an inorganic hole-collecting layer instead. The dimerization of the merocyanine dyes is well known, and this habit was suggested to play a role in the high efficiency of these systems by its potential impacts on the separation of materials phases within the bulk heterojunction materials structure [103].

6.3 Materials Structure in OPV

The importance of the materials structure in the BHJ is a unique facet of OPV technology, and the many approaches used to measure it deserve some mention. Materials structure, which is often called morphology in the OPV community, has

become a well-studied OPV subtopic [24, 26, 76, 104–106]. The importance of BHJ morphology may be obvious when considering the mismatch between the length scale of exciton diffusion and the thickness of the typical OPV active layer. Additional considerations are related to order within domains, and charge transport throughout the active layer. It is thought that there may be an impact of morphology on recombination behaviors as well. Because the OPV active layer is a blend, and furthermore a non-equilibrium structure with ambiguous extents of order and orientation within nanoscale phases, its measurement can be complicated and challenging.

6.3.1 Order: Local and Long Range

Because the polymer is typically the only phase that is crystalline in a typical BHJ, the assessment of order focuses on the electron donor. Most of the electron donors described in Sect. 6.2.1 that exhibit reasonable or high power conversion efficiencies also exhibit some measurable extent of order, either local or long range. None is provably amorphous. Greater order within the electron donor (or any light-absorbing phase) is thought to lead to larger exciton diffusion lengths and better change transport.

Local order is most typically measured using optical methods such as ultraviolet–visible (UV–Vis) spectroscopy. Typical signatures of increased order in an absorbing conjugated organic material include a red-shifted absorption spectrum from increased conjugation length, or the appearance of new narrow features that can be attributed to vibronic transitions or the intermolecular excitation phenomena commonly termed aggregates [107]. The assessment of local order by optical means is most mature for P3HT, which exhibits a radically changed UV-Vis absorption spectrum when local order is present [107–110]. Modeling of these emergent absorption features is shown in Fig. 6.13 [111]. Local-order measurements by optical methods are less common for more modern push-pull polymer systems, which often lack significant fine structure features in their absorption spectra.

Long-range order is more typically identified as crystallinity. Crystallinity is common in OPV materials, particularly in the absorbing materials. X-ray diffraction (XRD) is the most common method for assessing crystallinity in OPV materials, most commonly using a synchrotron source. Unlike in some inorganic photovoltaics, which may include large or monolithic crystals, the crystals in OPV materials tend to be very small, of submicron size. It is typically not possible to determine an explicit packing arrangement of the molecules within these crystals using XRD. What is usually collected instead are interplanar “d-spacings” within the lattice, which occasionally bring insight into the intermolecular and intramolecular arrangements within the crystal, crystal orientation distributions, and relative crystallinity information. XRD analysis of organic semiconductors has become such a widespread practice that there are now authoritative review articles discussing its proper application [104]. The most common experimental setup for

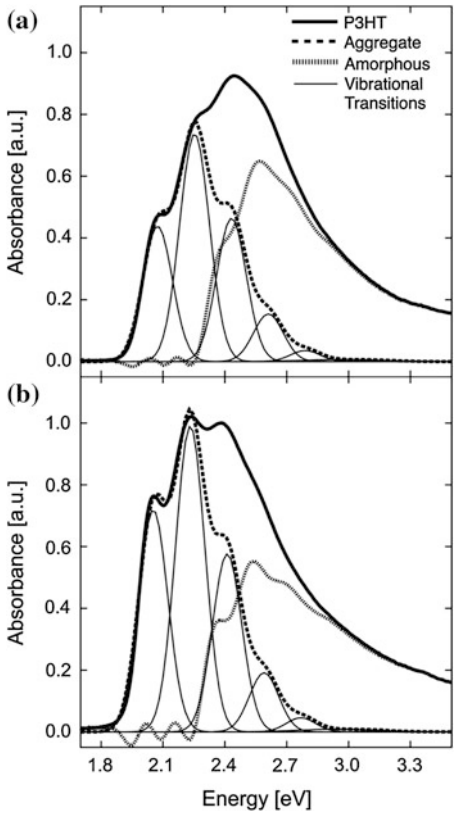

Fig. 6.13 Optical measurement of local order in P3HT. Spectra shown are the P3HT component of the absorption spectrum for **a** a film cast from a volatile solvent (less ordered) and **b** a film cast from a low-volatility solvent (more ordered) [111]

OPV XRD is the grazing-incidence X-ray diffraction (GIXD) geometry. GIXD is particularly valuable for thin-film samples, because it produces a full diffraction pattern from a single exposure at a shallow incident angle. Because the geometry has the scattering vector aligned with respect to the thin-film sample, it also can be interpreted in terms of crystal orientation distribution. Typically, it is found that crystals of OPV materials are highly anisotropic within the film. Spectroscopic ellipsometry is an alternative optical means to evaluate this anisotropy [112]. Quite often, it is found that the optical transition dipoles serendipitously orient parallel to the substrate plane, which should enhance the absorption of normally incident light.

The relative X-ray diffraction strength is often used as a means to compare relative crystallinities in OPV materials. This is only a valid practice if the materials are compositionally the same and from the same crystals. In OPV, materials variations and crystalline polymorphs are quite common, so often it is not possible to compare relative crystallinity between different films. Recent advancements of XRD application to OPV have focused on the identification and measurement of defects in the crystals by mathematical treatments of the diffraction peak widths [113, 114].

6.3.2 Nanoscale Structure

Transmission electron microscopy (TEM) is generally considered the most appropriate technique to measure the shape, size, composition, and connectivity of domains in bulk heterojunction films. With its high resolution, various contrast modes, and three-dimensional structure measurement (via tomography), the technique has proven to be a powerful tool for OPV development. Early applications of TEM to OPV materials focused on the bright-field contrast modes (BF-TEM), with a mass-thickness contrast mechanism that highlights electron density differences between materials. Highly resolved images of polymer–fullerene bulk heterojunction structures resolve whether the domains are nodular or fibrilar [115–117]. More recently, the contrast mechanism of choice appears to be energy-filtered TEM (EF-TEM), which has direct chemical contrast. The most common implementation involves the selection of energy windows on either side of the ≈25-eV bulk plasmon region [118–120]. Some images generated using the EF-TEM method are shown in Fig. 6.14. EF-TEM can also be practiced at the elemental edges, using the sulfur as a unique identifier of the polymer, although this practice may be limited to thinner films [121]. The analysis of TEM images showing OPV nanoscale structure is not straightforward; usually, a length scale or scales of compositional heterogeneity is reported, often along with an impression of the potential for percolative charge transport. Approaches that go beyond an appraisal of the domain shape and size include graph theory-based analysis of tomograms [122, 123] and device physics models such as Monte Carlo [124, 125], continuum [126, 127], or analytical [128, 129].

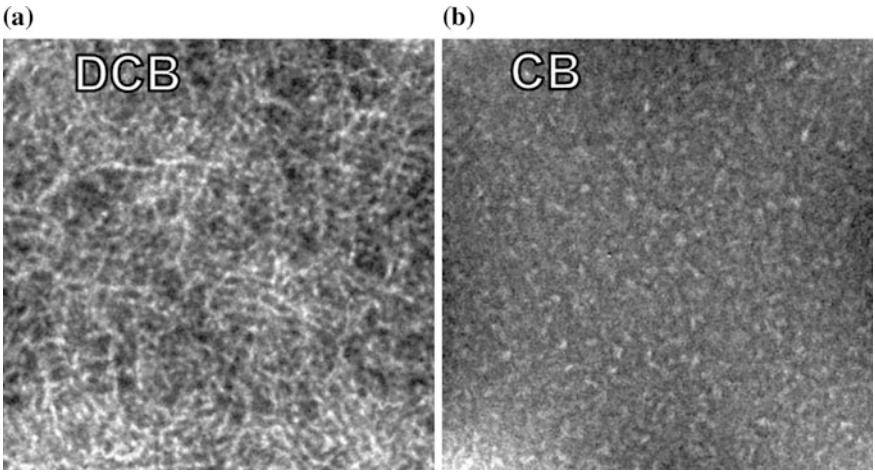

Fig. 6.14 EF-TEM measurements of a P3HT/PCBM BHJ for **a** a film cast from a low-volatility solvent (fibrillar) and **b** a film cast from a more volatile solvent (nodular)

Small-angle scattering is a powerful alternative to TEM for examining the nanoscale structure of OPV materials. With hard X-rays (SAXS), the implementation is similar to GIXD as described above. The contrast in scattering length density between polymer and fullerene often is sufficient to provide interpretable scattering [121, 130]. A more recent method is to exploit chemical contrast using resonant soft X-ray scattering (R-SoXS) [131–133]. R-SoXS exploits differences in scattering length density that appear near significant X-ray absorption features across an elemental edge, most commonly the carbon K-edge. R–SoXS may be able to detect orientational heterogeneities in compositionally homogeneous media, which provides an interesting new measurement capability with relevance to OPV. Because fullerenes typically lack a significant number of protons compared to the polymer, a polymer–fullerene bulk heterojunction has natural contrast in small-angle neutron scattering (SANS), and the technique has been extensively practiced on BHJ photovoltaics [130, 134, 135]. As with TEM, the analysis of small-angle scattering data on OPV materials remains a challenge. A model is typically required to interpret the features of the scattering pattern, and the multiple length scales and potential fractal qualities of the bulk heterojunction make it a very challenging system to analyze, although some progress is being made [121].

6.4 The Outlook for OPV

Because of the global energy needs that emerge from an increasing population and an ever-increasing standard of living, new photovoltaic technologies are extremely important contributions to our mixed energy production. Some key advantages for OPV include their production from earth-abundant elements, the potential for low-cost solution processing at speeds similar to graphics arts printing, and a high degree of customizability with regard to color, transparency, and form factor. The energy payback time—the operation time required to pay back the energy cost of module production—could become as low as 10 days in the near future [136]. Given such advantages, a strong case can be made for continued investment in OPV technology development, as has very recently been shown [137].

OPV manufacturing has been reduced to practice by several organizations within the last decade. Perhaps, the most comprehensive attempt was by Konarka, which declared bankruptcy in 2012 [138] but before that substantially pushed the technology forward, particularly with respect to high-volume manufacturing, and semitransparent, building-integrated photovoltaic applications (tinted “solar windows” [139]). Companies in OPV as of this writing include Heliatek GmbH, Solarmer Energy, Polyera, and NEXT Energy Inc. Heliatek, which focuses on small-molecule evaporated OPV, have recently announced world record triple-junction efficiencies of ≈12 % [96], and have publically announced multi-junction efficiency targets of ≈15 % in the midterm, which would begin to approach the efficiencies available from today’s commercial crystalline silicon modules.

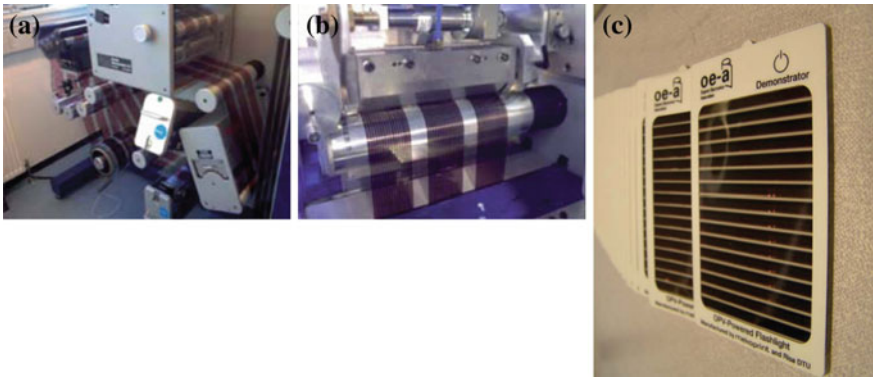

Fig. 6.15 Demonstrator fabrication by Krebs and co-workers [142]

Some of the most comprehensive publically disclosed demonstrations of OPV manufacturing have been made by Krebs and co-workers [136, 140–142]. In a recent demonstration, shown in Fig. 6.15, an OPV module with integrated light and power storage was constructed. The OPV module was made by roll-to-roll-based methods that were comprehensively described [142]. Aspects of the processing such as the moving foil with the bulk heterojunction applied (Fig. 6.15a), and slot-die coating of additional layers (Fig. 6.15b), were shown. The final module was packaged with an off-the-shelf light-emitting diode and lithium pouch cell to create the demonstrator shown in Fig. 6.15c.

Krebs has also shown that slot-die coating can be manipulated to be a combinatorial optimization platform that has the potential to exceed the typical batch processing optimization that is done on spin-coated cells [143]. This approach and its results are illustrated in Fig. 6.16. Some of the unique aspects of OPV, such as solution processing and high throughput, enable this kind of innovative experimentation, which could mitigate the well-known process sensitivity and time-consuming optimization needs that are typical of OPV formulation and processing.

It is difficult to predict the ultimate costs and competitiveness of OPV technologies until a mature industry is achieved. For raw materials, it is likely that the bulk heterojunction components will be a negligible expense compared to the transparent conducting substrate and encapsulation. Production costs and margins are also uncertain, and the competitiveness of other solar cell technologies is also changing rapidly, particularly with the recent decrease in silicon module cost. New technologies such as the perovskite-based solar cells [144], which are also flexible and solution processable [145], have also recently emerged. The unique merits of OPV technology, however, will likely ensure that it continues to see investment and development, and a significant future role in our increasingly diverse energy production portfolio.

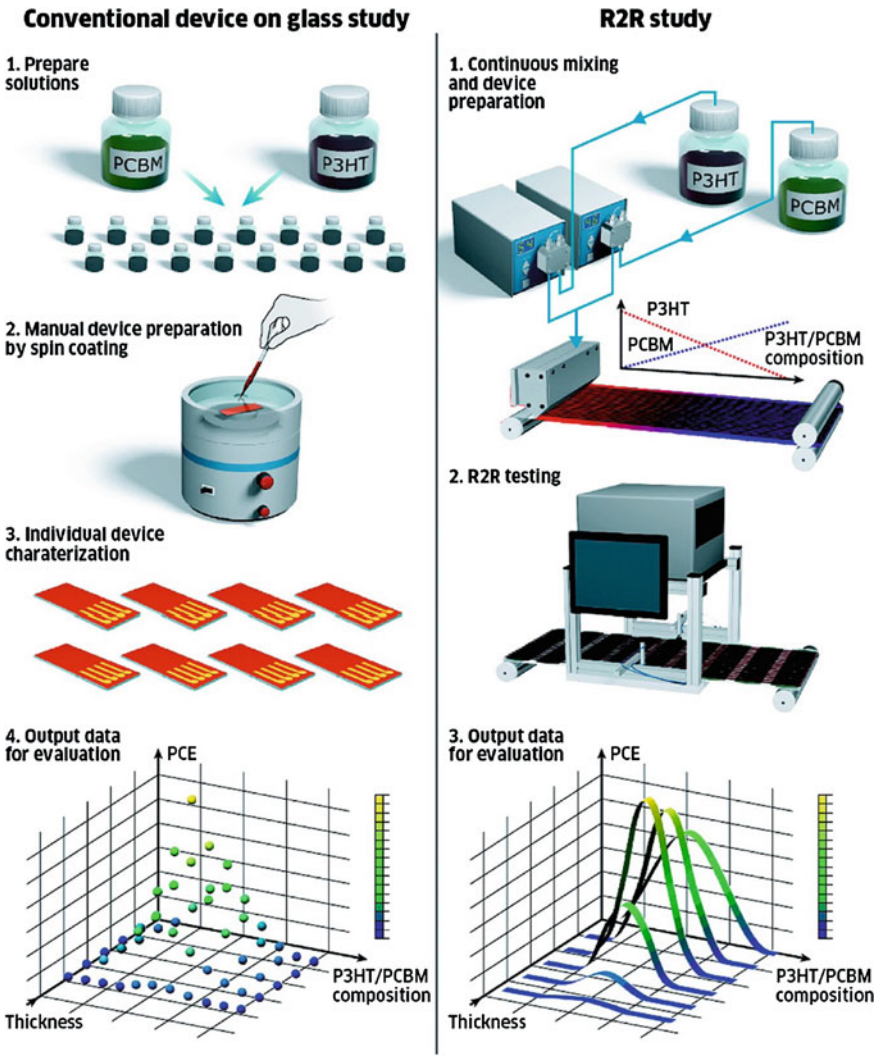

Fig. 6.16 Comparison of conventional small-scale OPV device optimization versus R2R optimization [143]

References

1. Brabec, C.J.: Organic Photovoltaics: Concepts and Realization. Springer, Berlin (2003)
2. Brabec, C., Scherf, U., Dyakonov, V.: Organic Photovoltaics: Materials, Device Physics, and Manufacturing Technologies. John Wiley & Sons, Hoboken (2011)
3. Dennler, G., Scharber, M.C., Brabec, C.J.: Polymer-fullerene bulk-heterojunction solar cells. Adv. Mater. **21**, 1323–1338 (2009)
4. Kazmerski, L.: Best research-cell efficiencies. at http://www.nrel.gov/ncpv/

5. You, J., et al.: A polymer tandem solar cell with 10.6 % power conversion efficiency. Nat. Commun. **4,** 1446 (2013)
6. Brabec, C.J., et al.: Polymer-fullerene bulk-heterojunction solar cells. Adv. Mater. **22**, 3839–3856 (2010)
7. O'Regan, B., Grätzel, M.: A low-cost, high-efficiency solar cell based on dye-sensitized colloidal TiO_2 films. Nature **353**, 737–740 (1991)
8. Kallmann, H., Pope, M.: Photovoltaic effect in organic crystals. J. Chem. Phys. **30**, 585–586 (1959)
9. Gomes da Costa, P., Conwell, E.M.: Excitons and the band gap in poly(phenylene vinylene). Phys. Rev. **B 48**, 1993–1996 (1993)
10. Brédas, J.-L., Cornil, J., Heeger, A.J.: The exciton binding energy in luminescent conjugated polymers. Adv. Mater. **8**, 447–452 (1996)
11. Barth, S., Bässler, H.: Intrinsic photoconduction in PPV-type conjugated polymers. Phys. Rev. Lett. **79**, 4445–4448 (1997)
12. Alvarado, S.F., Seidler, P.F., Lidzey, D.G., Bradley, D.D.C.: Direct determination of the exciton binding energy of conjugated polymers using a scanning tunneling microscope. Phys. Rev. Lett. **81**, 1082–1085 (1998)
13. Tang, C.W.: Two-layer organic photovoltaic cell. Appl. Phys. Lett. **48**, 183–185 (1986)
14. Chamberlain, G.A.: Organic solar cells: a review. Sol. Cells **8**, 47–83 (1983)
15. Halls, J.J.M., Pichler, K., Friend, R.H., Moratti, S.C., Holmes, A.B.: Exciton diffusion and dissociation in a poly(p-phenylenevinylene)/C60 heterojunction photovoltaic cell. Appl. Phys. Lett. **68**, 3120–3122 (1996)
16. Markov, D.E., Tanase, C., Blom, P.W.M., Wildeman, J.: Simultaneous enhancement of charge transport and exciton diffusion in poly(p-phenylene vinylene) derivatives. Phys. Rev. B **72**, 045217 (2005)
17. Markov, D.E., Amsterdam, E., Blom, P.W.M., Sieval, A.B., Hummelen, J.C.: Accurate measurement of the exciton diffusion length in a conjugated polymer using a heterostructure with a side-chain cross-linked fullerene layer. J. Phys. Chem. A **109**, 5266–5274 (2005)
18. Heeger, A.J.: 25th anniversary article: bulk heterojunction solar cells: understanding the mechanism of operation. Adv. Mater. **26**, 10–28 (2014)
19. Sariciftci, N.S., Smilowitz, L., Heeger, A.J., Wudl, F.: Photoinduced electron transfer from a conducting polymer to buckminsterfullerene. Science **258**, 1474–1476 (1992)
20. Kraabel, B., et al.: Ultrafast photoinduced electron transfer in conducting polymer–buckminsterfullerene composites. Chem. Phys. Lett. **213**, 389–394 (1993)
21. Brabec, C.J., et al.: Tracing photoinduced electron transfer process in conjugated polymer/fullerene bulk heterojunctions in real time. Chem. Phys. Lett. **340**, 232–236 (2001)
22. Yu, G., Gao, J., Hummelen, J.C., Wudl, F., Heeger, A.J.: Polymer photovoltaic cells: enhanced efficiencies via a network of internal donor-acceptor heterojunctions. Science **270**, 1789–1791 (1995)
23. Shaheen, S.E., et al.: 2.5 % efficient organic plastic solar cells. Appl. Phys. Lett. **78**, 841–843 (2001)
24. DeLongchamp, D.M., Kline, R.J., Herzing, A.: Nanoscale structure measurements for polymer-fullerene photovoltaics. Energy Environ. Sci. **5**, 5980–5993 (2012)
25. Vandewal, K., Himmelberger, S., Salleo, A.: Structural factors that affect the performance of organic bulk heterojunction solar cells. Macromolecules 130807112515002 (2013). doi:10.1021/ma400924b
26. Vakhshouri, K., Kesava, S.V., Kozub, D.R., Gomez, E.D.: Characterization of the mesoscopic structure in the photoactive layer of organic solar cells: a focused review. Mater. Lett. **90**, 97–102 (2013)
27. Scharber, M.C., et al.: Design rules for donors in bulk-heterojunction solar cells—towards 10 % energy-conversion efficiency. Adv. Mater. **18**, 789–794 (2006)
28. Beaujuge, P.M., Fréchet, J.M.J.: Molecular design and ordering effects in π-functional materials for transistor and solar cell applications. J. Am. Chem. Soc. **133**, 20009–20029 (2011)

29. Dang, M.T., Hirsch, L., Wantz, G.: P3HT:PCBM, best seller in polymer photovoltaic research. Adv. Mater. **23**, 3597–3602 (2011)
30. Marrocchi, A., Lanari, D., Facchetti, A., Vaccaro, L.: Poly(3-hexylthiophene): synthetic methodologies and properties in bulk heterojunction solar cells. Energy Environ. Sci. **5**, 8457–8474 (2012)
31. Hotta, S., Rughooputh, S.D.D.V., Heeger, A.J., Wudl, F.: Spectroscopic studies of soluble poly(3-alkylthienylenes). Macromolecules **20**, 212–215 (1987)
32. McCullough, R.D., Lowe, R.D.: Enhanced electrical conductivity in regioselectively synthesized poly(3-alkylthiophenes). J. Chem. Soc. Chem. Commun. 70–72 (1992). doi:10.1039/C39920000070
33. Chen, T.-A., Wu, X., Rieke, R.D.: Regiocontrolled synthesis of poly(3-alkylthiophenes) mediated by Rieke Zinc: their characterization and solid-state properties. J. Am. Chem. Soc. **117**, 233–244 (1995)
34. Loewe, R.S., Khersonsky, S.M., McCullough, R.D.: A simple method to prepare head-to-tail coupled, regioregular poly(3-alkylthiophenes) using grignard metathesis. Adv. Mater. **11**, 250–253 (1999)
35. Prosa, T.J., Winokur, M.J., Moulton, J., Smith, P., Heeger, A.J.: X-ray structural studies of poly(3-alkylthiophenes): an example of an inverse comb. Macromolecules **25**, 4364–4372 (1992)
36. Joseph Kline, R., McGehee, M.D., Toney, M.F.: Highly oriented crystals at the buried interface in polythiophene thin-film transistors. Nat. Mater. **5**, 222–228 (2006)
37. Zhan, X., Zhu, D.: Conjugated polymers for high-efficiency organic photovoltaics. Polym. Chem. **1**, 409 (2010)
38. Inganäs, O., et al.: Polymer photovoltaics with alternating copolymer/fullerene blends and novel device architectures. Adv. Mater. **22**, E100–E116 (2010)
39. Blouin, N., Michaud, A., Leclerc, M.: A low-bandgap poly(2,7-carbazole) derivative for use in high-performance solar cells. Adv. Mater. **19**, 2295–2300 (2007)
40. Beaupré, S., Leclerc, M.: PCDTBT: en route for low cost plastic solar cells. J. Mater. Chem. A **1**, 11097–11105 (2013)
41. Wang, D.H., et al.: Transferable graphene oxide by stamping nanotechnology: electron-transport layer for efficient bulk-heterojunction solar cells. Angew. Chem. Int. Ed. **52**, 2874–2880 (2013)
42. Peters, C.H., et al.: High efficiency polymer solar cells with long operating lifetimes. Adv. Energy Mater. **1**, 491–494 (2011)
43. Peet, J., et al.: Efficiency enhancement in low-bandgap polymer solar cells by processing with alkane dithiols. Nat. Mater. **6**, 497–500 (2007)
44. Lee, J.K., et al.: Processing additives for improved efficiency from bulk heterojunction solar cells. J. Am. Chem. Soc. **130**, 3619–3623 (2008)
45. Morana, M., et al.: Nanomorphology and charge generation in bulk heterojunctions based on low-bandgap dithiophene polymers with different bridging atoms. Adv. Funct. Mater. **20**, 1180–1188 (2010)
46. Shin, N. et al.: Effect of processing additives during solidification of blade-coated polymer/fullerene blend films via in-situ structure measurements. Adv. Funct. Mater. (2013)
47. Liang, Y., et al.: For the bright future—bulk heterojunction polymer solar cells with power conversion efficiency of 7.4 %. Adv. Mater. **22**, E135–E138 (2010)
48. He, Z., et al.: Enhanced power-conversion efficiency in polymer solar cells using an inverted device structure. Nat. Photonics **6**, 591–595 (2012)
49. Carsten, B., et al.: Examining the effect of the dipole moment on charge separation in donor-acceptor polymers for organic photovoltaic applications. J. Am. Chem. Soc. **133**, 20468–20475 (2011)
50. Price, S.C., Stuart, A.C., Yang, L., Zhou, H., You, W.: Fluorine substituted conjugated polymer of medium band gap yields 7 % efficiency in polymer−fullerene solar cells. J. Am. Chem. Soc. **133**, 4625–4631 (2011)

51. Albrecht, S., et al.: Fluorinated copolymer PCPDTBT with enhanced open-circuit voltage and reduced recombination for highly efficient polymer solar cells. J. Am. Chem. Soc. **134**, 14932–14944 (2012)
52. Stuart, A.C., et al.: Fluorine substituents reduce charge recombination and drive structure and morphology development in polymer solar cells. J. Am. Chem. Soc. **135**, 1806–1815 (2013)
53. Van der Poll, T.S., Love, J.A., Nguyen, T.-Q., Bazan, G.C.: Non-basic high-performance molecules for solution-processed organic solar cells. Adv. Mater. **24**, 3646–3649 (2012)
54. Chen, W., et al.: Hierarchical nanomorphologies promote exciton dissociation in polymer/fullerene bulk heterojunction solar cells. Nano Lett. **11**, 3707–3713 (2011)
55. Liu, F. et al.: Understanding the morphology of PTB7:PCBM blends in organic photovoltaics. Adv. Energy Mater. **4,** n/a–n/a (2014)
56. Hammond, M.R., et al.: Molecular order in high-efficiency polymer/fullerene bulk heterojunction solar cells. ACS Nano **5**, 8248–8257 (2011)
57. Hedley, G.J. et al.: Determining the optimum morphology in high-performance polymer-fullerene organic photovoltaic cells. Nat. Commun. **4** (2013)
58. Guo, S., et al.: Influence of Solvent and Solvent Additive on the Morphology of PTB7 Films Probed via X-ray Scattering. J. Phys. Chem. B **118**, 344–350 (2014)
59. Piliego, C., et al.: Synthetic control of structural order in n-alkylthieno[3,4-c] pyrrole-4,6-dione-based polymers for efficient solar cells. J. Am. Chem. Soc. **132**, 7595–7597 (2010)
60. Cabanetos, C., et al.: Linear side chains in benzo[1,2-b:4,5-b′]dithiophene–thieno[3,4-c] pyrrole-4,6-dione polymers direct self-assembly and solar cell performance. J. Am. Chem. Soc. **135**, 4656–4659 (2013)
61. Lin, Y., Li, Y., Zhan, X.: Small molecule semiconductors for high-efficiency organic photovoltaics. Chem. Soc. Rev. **41**, 4245 (2012)
62. Kyaw, A.K.K., et al.: Intensity dependence of current-voltage characteristics and recombination in high-efficiency solution-processed small-molecule solar cells. ACS Nano **7**, 4569–4577 (2013)
63. Bronstein, H., et al.: Thieno[3,2-b]thiophene−diketopyrrolopyrrole-containing polymers for high-performance organic field-effect transistors and organic photovoltaic devices. J. Am. Chem. Soc. **133**, 3272–3275 (2011)
64. Walker, B., et al.: Nanoscale phase separation and high photovoltaic efficiency in solution-processed, small-molecule bulk heterojunction solar cells. Adv. Funct. Mater. **19**, 3063–3069 (2009)
65. Tumbleston, J.R., Stuart, A.C., Gann, E., You, W., Ade, H.: Fluorinated polymer yields high organic solar cell performance for a wide range of morphologies. Adv. Funct. Mater. **23**, 3463–3470 (2013)
66. Mei, J., Graham, K.R., Stalder, R., Reynolds, J.R.: Synthesis of isoindigo-based oligothiophenes for molecular bulk heterojunction solar cells. Org. Lett. **12**, 660–663 (2010)
67. Wang, E., et al.: An easily accessible isoindigo-based polymer for high-performance polymer solar cells. J. Am. Chem. Soc. **133**, 14244–14247 (2011)
68. Stalder, R., Grand, C., Subbiah, J., So, F., Reynolds, J.R.: An isoindigo and dithieno [3,2-b:2′,3′-d]silole copolymer for polymer solar cells. Polym. Chem. **3**, 89 (2012)
69. Hummelen, J.C., et al.: Preparation and characterization of fulleroid and methanofullerene derivatives. J. Org. Chem. **60**, 532–538 (1995)
70. Wudl, F.: Fullerene materials. J. Mater. Chem. **12**, 1959–1963 (2002)
71. Giacalone, F., Martín, N.: New concepts and applications in the macromolecular chemistry of fullerenes. Adv. Mater. **22**, 4220–4248 (2010)
72. He, Y., Li, Y.: Fullerene derivative acceptors for high performance polymer solar cells. Phys. Chem. Chem. Phys. **13**, 1970 (2011)
73. Wienk, M.M., et al.: Efficient methano[70]fullerene/mdmo-ppv bulk heterojunction photovoltaic cells. Angew. Chem. Int. Ed. **42**, 3371–3375 (2003)
74. He, C., et al.: Influence of substrate on crystallization in polythiophene/fullerene blends. Sol. Energy Mater. Sol. Cells **95**, 1375–1381 (2011)

75. Rispens, M.T., et al.: Influence of the solvent on the crystal structure of PCBM and the efficiency of MDMO-PPV:PCBM 'plastic' solar cells. Chem. Commun. 2116–2118 (2003). doi:10.1039/B305988J
76. Collins, B.A., Tumbleston, J.R., Ade, H.: Miscibility, crystallinity, and phase development in P3HT/PCBM solar cells: toward an enlightened understanding of device morphology and stability. J. Phys. Chem. Lett. **2**, 3135–3145 (2011)
77. Jamieson, F.C., et al.: Fullerene crystallisation as a key driver of charge separation in polymer/fullerene bulk heterojunction solar cells. Chem. Sci. **3**, 485 (2012)
78. Lenes, M., et al.: Fullerene bisadducts for enhanced open-circuit voltages and efficiencies in polymer solar cells. Adv. Mater. **20**, 2116–2119 (2008)
79. Faist, M.A., et al.: Effect of multiple adduct fullerenes on charge generation and transport in photovoltaic blends with poly(3-hexylthiophene-2,5-diyl). J. Polym. Sci. Part B Polym. Phys. **49,** 45–51 (2011)
80. Laird, D.W., et al. Organic photovoltaic devices comprising fullerenes and derivatives thereof (2010)
81. Zhao, G., He, Y., Li, Y.: 6.5 % efficiency of polymer solar cells based on poly (3-hexylthiophene) and Indene-C60 bisadduct by device optimization. Adv. Mater. **22**, 4355–4358 (2010)
82. Anthony, J.E., Facchetti, A., Heeney, M., Marder, S.R., Zhan, X.: n-type organic semiconductors in organic electronics. Adv. Mater. **22**, 3876–3892 (2010)
83. Halls, J.J.M., et al.: Efficient photodiodes from interpenetrating polymer networks. Nature **376**, 498–500 (1995)
84. Yu, G., Heeger, A.J.: Charge separation and photovoltaic conversion in polymer composites with internal donor/acceptor heterojunctions. J. Appl. Phys. **78**, 4510–4515 (1995)
85. Granström, M., et al.: Laminated fabrication of polymeric photovoltaic diodes. Nature **395**, 257–260 (1998)
86. Zhan, X., et al.: A high-mobility electron-transport polymer with broad absorption and its use in field-effect transistors and all-polymer solar cells. J. Am. Chem. Soc. **129**, 7246–7247 (2007)
87. Mikroyannidis, J.A., Stylianakis, M.M., Sharma, G.D., Balraju, P., Roy, M.S.: A novel alternating phenylenevinylene copolymer with perylene bisimide units: synthesis, photophysical, electrochemical, and photovoltaic properties. J. Phys. Chem. C **113**, 7904–7912 (2009)
88. Zhou, E., et al.: All-polymer solar cells from perylene diimide based copolymers: material design and phase separation control. Angew. Chem. Int. Ed. **50**, 2799–2803 (2011)
89. Yan, H., et al.: A high-mobility electron-transporting polymer for printed transistors. Nature **457**, 679–686 (2009)
90. Rivnay, J., et al.: Unconventional face-on texture and exceptional in-plane order of a high mobility n-type polymer. Adv. Mater. **22**, 4359–4363 (2010)
91. Rivnay, J., et al.: Drastic control of texture in a high performance n-type polymeric semiconductor and implications for charge transport. Macromolecules **44**, 5246–5255 (2011)
92. Fabiano, S., et al.: Role of photoactive layer morphology in high fill factor all-polymer bulk heterojunction solar cells. J. Mater. Chem. **21**, 5891 (2011)
93. Moore, J.R., et al.: Polymer blend solar cells based on a high-mobility naphthalenediimide-based polymer acceptor: device physics, photophysics and morphology. Adv. Energy Mater. **1**, 230–240 (2011)
94. Schubert, M., et al.: Influence of aggregation on the performance of all-polymer solar cells containing low-bandgap naphthalenediimide copolymers. Adv. Energy Mater. **2**, 369–380 (2012)
95. Facchetti, A.: Polymer donor–polymer acceptor (all-polymer) solar cells. Mater. Today **16**, 123–132 (2013)
96. Ali-Oettinger, S.: Heliatek announces world record for organic cell. Pv Mag. at http://www.pv-magazine.com/news/details/beitrag/heliatek-announces-world-record-for-organic-cell_100009859/

97. Xue, J., Uchida, S., Rand, B.P., Forrest, S.R.: 4.2 % efficient organic photovoltaic cells with low series resistances. Appl. Phys. Lett. **84**, 3013–3015 (2004)
98. Xue, J., Uchida, S., Rand, B.P., Forrest, S.R.: Asymmetric tandem organic photovoltaic cells with hybrid planar-mixed molecular heterojunctions. Appl. Phys. Lett. **85**, 5757–5759 (2004)
99. Schueppel, R., et al.: Optimizing organic photovoltaics using tailored heterojunctions: a photoinduced absorption study of oligothiophenes with low band gaps. Phys. Rev. B **77**, 085311 (2008)
100. Fitzner, R., et al.: Dicyanovinyl-substituted oligothiophenes: structure-property relationships and application in vacuum-processed small molecule organic solar cells. Adv. Funct. Mater. **21**, 897–910 (2011)
101. Lin, L.-Y., et al.: A low-energy-gap organic dye for high-performance small-molecule organic solar cells. J. Am. Chem. Soc. **133**, 15822–15825 (2011)
102. Chiu, S.-W., et al.: A donor–acceptor–acceptor molecule for vacuum-processed organic solar cells with a power conversion efficiency of 6.4 %. Chem. Commun. **48**, 1857 (2012)
103. Kronenberg, N.M., et al.: Direct comparison of highly efficient solution- and vacuum-processed organic solar cells based on merocyanine dyes. Adv. Mater. **22**, 4193–4197 (2010)
104. Rivnay, J., Mannsfeld, S.C.B., Miller, C.E., Salleo, A., Toney, M.F.: Quantitative determination of organic semiconductor microstructure from the molecular to device scale. Chem. Rev. **112**, 5488–5519 (2012)
105. Vandewal, K., Himmelberger, S., Salleo, A.: Structural factors that affect the performance of organic bulk heterojunction solar cells. Macromolecules (2013). doi:10.1021/ma400924b
106. Dang, M.T., Hirsch, L., Wantz, G., Wuest, J.D.: Controlling the morphology and performance of bulk heterojunctions in solar cells. Lessons learned from the benchmark poly(3-hexylthiophene):[6,6]-phenyl-c61-butyric acid methyl ester system. Chem. Rev. **113**, 3734–3765 (2013)
107. Spano, F.C.: The spectral signatures of frenkel polarons in H- and J-aggregates. Acc. Chem. Res. **43**, 429–439 (2010)
108. Clark, J., Silva, C., Friend, R.H., Spano, F.C.: Role of intermolecular coupling in the photophysics of disordered organic semiconductors: aggregate emission in regioregular polythiophene. Phys. Rev. Lett. **98**, 206406 (2007)
109. Spano, F.C.: Modeling disorder in polymer aggregates: the optical spectroscopy of regioregular poly(3-hexylthiophene) thin films. J. Chem. Phys. **122,** 234701–234701–15 (2005)
110. Clark, J., Chang, J.-F., Spano, F. C., Friend, R.H., Silva, C.: Determining exciton bandwidth and film microstructure in polythiophene films using linear absorption spectroscopy. Appl. Phys. Lett. **94**, 163306–163306–3 (2009)
111. Turner, S.T., et al.: Quantitative analysis of bulk heterojunction films using linear absorption spectroscopy and solar cell performance. Adv. Funct. Mater. **21**, 4640–4652 (2011)
112. Germack, D.S., et al.: Interfacial segregation in polymer/fullerene blend films for photovoltaic devices. Macromolecules **43**, 3828–3836 (2010)
113. Rivnay, J., Noriega, R., Kline, R.J., Salleo, A., Toney, M.F.: Quantitative analysis of lattice disorder and crystallite size in organic semiconductor thin films. Phys. Rev. B **84**, 045203 (2011)
114. Rivnay, J., et al.: Structural origin of gap states in semicrystalline polymers and the implications for charge transport. Phys. Rev. B **83**, 121306 (2011)
115. Van Bavel, S.S., Sourty, E., de With, G., Loos, J.: Three-dimensional nanoscale organization of bulk heterojunction polymer solar cells. Nano Lett. **9**, 507–513 (2009)
116. Van Bavel, S.S., Sourty, E., de With, G., Veenstra, S., Loos, J.: Three-dimensional nanoscale organization of polymer solar cells. J. Mater. Chem. **19**, 5388–5393 (2009)
117. Van Bavel, S.S., Bärenklau, M., de With, G., Hoppe, H., Loos, J.: P3HT/PCBM bulk heterojunction solar cells: impact of blend composition and 3D morphology on device performance. Adv. Funct. Mater. **20**, 1458–1463 (2010)

118. Herzing, A.A., Richter, L.J., Anderson, I.M.: 3D nanoscale characterization of thin-film organic photovoltaic device structures via spectroscopic contrast in the TEM 1. J. Phys. Chem. C **114**, 17501–17508 (2010)
119. Pfannmöller, M., et al.: Visualizing a homogeneous blend in bulk heterojunction polymer solar cells by analytical electron microscopy. Nano Lett. **11**, 3099–3107 (2011)
120. Drummy, L.F., et al.: Molecular-scale and nanoscale morphology of P3HT:PCBM bulk heterojunctions: energy-filtered TEM and low-dose HREM†. Chem. Mater. **23**, 907–912 (2011)
121. Kozub, D.R., et al.: Polymer crystallization of partially miscible polythiophene/fullerene mixtures controls morphology. Macromolecules **44**, 5722–5726 (2011)
122. Wodo, O., Tirthapura, S., Chaudhary, S., Ganapathysubramanian, B.: A graph-based formulation for computational characterization of bulk heterojunction morphology. Org. Electron. **13**, 1105–1113 (2012)
123. Wodo, O., Roehling, J.D., Moule, A., Ganapathysubramanian, B.: Quantifying organic solar cell morphology: a computational study of three-dimensional maps. Energy Environ. Sci. (2013). doi:10.1039/C3EE41224E
124. Watkins, P.K., Walker, A.B., Verschoor, G.L.B.: Dynamical Monte Carlo modelling of organic solar cells: the dependence of internal quantum efficiency on morphology. Nano Lett. **5**, 1814–1818 (2005)
125. McNeill, C.R., Westenhoff, S., Groves, C., Friend, R.H., Greenham, N.C.: Influence of nanoscale phase separation on the charge generation dynamics and photovoltaic performance of conjugated polymer blends: balancing charge generation and separation. J. Phys. Chem. C **111**, 19153–19160 (2007)
126. Buxton, G.A., Clarke, N.: Predicting structure and property relations in polymeric photovoltaic devices. Phys. Rev. B **74**, 085207 (2006)
127. Kodali, H.K., Ganapathysubramanian, B.: Computer simulation of heterogeneous polymer photovoltaic devices. Model. Simul. Mater. Sci. Eng. **20**, 035015 (2012)
128. Ray, B., Lundstrom, M.S., Alam, M.A.: Can morphology tailoring improve the open circuit voltage of organic solar cells? APL Org. Electron. Photonics **5**, 7 (2012)
129. Ray, B., Alam, M.A.: Random vs regularized OPV: Limits of performance gain of organic bulk heterojunction solar cells by morphology engineering. Sol. Energy Mater. Sol. Cells **99**, 204–212 (2012)
130. Chen, D., Liu, F., Wang, C., Nakahara, A., Russell, T.P.: Bulk heterojunction photovoltaic active layers via bilayer interdiffusion. Nano Lett. **11**, 2071–2078 (2011)
131. Swaraj, S., et al.: Nanomorphology of bulk heterojunction photovoltaic thin films probed with resonant soft X-ray scattering. Nano Lett. **10**, 2863–2869 (2010)
132. Collins, B.A., Tumbleston, J.R., Ade, H.: Miscibility, crystallinity, and phase development in P3HT/PCBM solar cells: toward an enlightened understanding of device morphology and stability. J. Phys. Chem. Lett. **2**, 3135–3145 (2011)
133. Collins, B.A., et al.: Absolute measurement of domain composition and nanoscale size distribution explains performance in PTB7:PC71BM solar cells. Adv. Energy Mater. **3**, 65–74 (2013)
134. Yin, W., Dadmun, M.: A new model for the morphology of P3HT/PCBM organic photovoltaics from small-angle neutron scattering: rivers and streams. ACS Nano **5**, 4756–4768 (2011)
135. Kiel, J.W., Eberle, A.P.R., Mackay, M.E.: Nanoparticle agglomeration in polymer-based solar cells. Phys. Rev. Lett. **105**, 168701 (2010)
136. Søndergaard, R., Hösel, M., Angmo, D., Larsen-Olsen, T.T., Krebs, F.C.: Roll-to-roll fabrication of polymer solar cells. Mater. Today **15**, 36–49 (2012)
137. Darling, S.B., You, F.: The case for organic photovoltaics. RSC Adv. **3**, 17633–17648 (2013)
138. Herndon, A., Pettersson, E.: Thin-film solar panel maker Konarka files for bankruptcy. Bloomberg (2012). at http://www.bloomberg.com/news/2012-06-02/thin-film-solar-panel-maker-konarka-files-for-bankruptcy.html

139. Tracy W.: Konarka and arch aluminum and glass announce unique solar curtain wall pilot project. Business Wire (2009). http://www.businesswire.com/news/home/20091110005343/en/Konarka-Arch-Aluminum-Glass-Announce-Unique-Solar#.U-JFD_ldV5I
140. Krebs, F.C., Tromholt, T., Jørgensen, M.: Upscaling of polymer solar cell fabrication using full roll-to-roll processing. Nanoscale **2**, 873 (2010)
141. Krebs, F.C., Fyenbo, J., Jørgensen, M.: Product integration of compact roll-to-roll processed polymer solar cell modules: methods and manufacture using flexographic printing, slot-die coating and rotary screen printing. J. Mater. Chem. **20**, 8994 (2010)
142. Krebs, F.C., et al.: The OE-A OPV demonstrator anno domini 2011. Energy Environ. Sci. **4**, 4116 (2011)
143. Alstrup, J., Jørgensen, M., Medford, A.J., Krebs, F.C.: Ultra fast and parsimonious materials screening for polymer solar cells using differentially pumped slot-die coating. ACS Appl. Mater. Interfaces **2**, 2819–2827 (2010)
144. Ball, J.M., Lee, M.M., Hey, A., Snaith, H.J.: Low-temperature processed meso-superstructured to thin-film perovskite solar cells. Energy Environ. Sci. **6**, 1739–1743 (2013)
145. Docampo, P., Ball, J.M., Darwich, M., Eperon, G.E., Snaith, H.J.: Efficient organometal trihalide perovskite planar-heterojunction solar cells on flexible polymer substrates. Nat. Commun. **4** (2013)
146. Albrecht, S., et al.: On the field dependence of free charge carrier generation and recombination in blends of PCPDTBT/PC70BM: influence of solvent additives. J. Phys. Chem. Lett. **3**, 640–645 (2012)
147. Love, J.A., Proctor, C.M., Liu, J., Takacs, C.J., Sharenko, A., van der Poll, T.S., Heeger, A. J., Bazan, G.C., Nguyen, T.-Q.: Film morphology of high efficiency solution-processed small-molecule solar cells. Adv. Funct. Mater. **23** 5019 (2013)

Chapter 7
Nanophase Engineering of Organic Semiconductor-Based Solar Cells

Bin Yang, Ming Shao, Jong Keum, David Geohegan and Kai Xiao

7.1 Introduction

Organic photovoltaic (OPV) technology is among the most promising for next-generation clean energy harvesting due to many attractive characteristics, such as flexibility, light weight, low-cost, and low-temperature-solution-processing capability. The power conversion efficiency (PCE) of OPV solar cells has been advanced commercially to 12 % in tandem cells [1], which is an exciting milestone on the road to the commercialization of organic photovoltaics. Equally important to high efficiency in practical applications is the long-term device stability, which has been demonstrated to be more than three years on rooftops by multiple industrial companies [1, 2].

Conjugated organic materials play a central role in achieving high-performance devices [3–6]. In these conjugated materials, two separated energy states, the bonding π-orbital and the antibonding π*-orbital, are formed as a result of overlap between the electron wave functions of the p_z orbitals. The bonding π-orbital and the antibonding π*-orbital are usually referred as the highest occupied molecular orbital (HOMO) and the lowest unoccupied molecular orbital (LUMO), respectively [7]. However, due to the weak molecular interaction in most conjugated organic materials [8], excitons typically recombine quickly, and diffuse only 10–20 nm [9] before they recombine. Exciton dissociation must therefore be accomplished rapidly; however, excitons with large binding energy (>100 meV) are hard to dissociate under thermal activation at room temperature [10]. To resolve this problem, the bulk heterojunction (BHJ) device, designed by Heeger et al. [11], has been the most successful strategy to maximize donor/acceptor interfacial areas for efficient exciton dissociation and has greatly influenced the design of the most highly efficient OPV devices today [1, 2]. Devices with BHJ structures are

B. Yang · M. Shao · J. Keum · D. Geohegan · K. Xiao (✉)
Center for Nanophase Materials Sciences,
Oak Ridge National Laboratory, Oak Ridge, TN 37831, USA
e-mail: xiaok@ornl.gov

M.P. Paranthaman et al. (eds.), *Semiconductor Materials for Solar Photovoltaic Cells*, Springer Series in Materials Science 218,
DOI 10.1007/978-3-319-20331-7_7

fabricated on conductive transparent electrode substrates, such as indium tin oxide (ITO) or fluorine-doped tin oxide (FTO), which must be designed for maximal transmission of the incident sunlight. The active layer, a film mixture of both donor and acceptor materials, is sandwiched between the cathode and anode, as shown in Fig. 7.1a. In order to generate favorable nanoscale phase separation for efficient exciton dissociation and charge transport, the active layer films generally must be processed further, including thermal annealing, solvent annealing, and other treatments [12–14]. In BHJ OPV devices, incident photons with sufficient energy can excite electrons from ground states to excited states in the donors and/or acceptors (step 1), followed by a thermal relaxation (step 2), as shown in Fig. 7.1b. Stable excitons, consisting of the electrons in the LUMO and holes in the HOMO, can be formed in a single molecule. If these excitons diffuse to reach the donor/acceptor interface before they recombine (step 3), exciton dissociation (i.e., the electron transfer process from donor to acceptor) can occur (step 4), given that the band offset between the donor and the acceptor exceeds the exciton binding energy. The electron–hole pairs (i.e., charge transfer excitons) with much smaller binding energy [7] at the donor/acceptor interfaces are subsequently separated into free charges, which are eventually swept out to external electrical circuit under the built-in internal electric field (step 5). The open circuit voltage (V_{OC}) is determined by the offset between the HOMO of the donor and the LUMO of the acceptor (E_{DA}) [15] as shown in Fig. 7.1b. More specific description about the OPV operation process under illumination can be found in review articles (Refs. [7, 15]).

The rapid progress in the worldwide development of OPVs can largely be credited to the innovative synthesis of novel photoactive materials with lower, tunable bandgaps and a new focus on the importance of controlling the structure, morphology, and interfaces of conjugated materials in devices [16]. This race to the ~10 % threshold where OPVs approach commercially viable [1] has revealed the scientific roadblocks which must be answered by basic research for further progress. Issues are not only the syntheses of new organic semiconductor materials

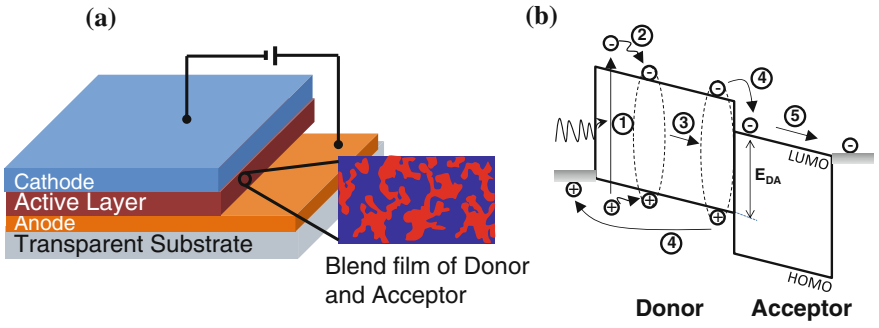

Fig. 7.1 **a** A typical bulk heterojunction OPV device structure; **b** working principle of OPVs under illumination: step 1, incident photons with sufficient energy excite electrons from ground states to excited states in the donors and/or acceptors; step 2, thermal relaxation of excited states to form excitons; step 3, exciton diffusion; step 4, exciton dissociation; step 5, charge extraction to two respective electrodes. E_{DA} is the offset between the HOMO of the donor and the LUMO of the acceptor

to maximize charge separation, recombination, and transport, but also the structural heterogeneity between the donor/acceptor blend in active layers [17–23]. First, molecular structure design aims to narrow both the optical bandgaps of organic semiconductors in order to enable the absorption of photons with longer wavelength [5, 10, 24–27], while tuning the LUMO and HOMO levels to reduce the energy level offset between donor and acceptor for enhanced V_{OC} [5]. Second, the film morphology has a critical effect on both charge separation and charge collection. At the nanoscale, the separation of donor and acceptor nanophases in interpenetrating networks should match characteristic exciton diffusion lengths for efficient exciton dissociation. In addition, the formation of long-range charge transport pathways is of equal importance in order to achieve efficient charge extraction and charge collection [28]. Unlike the case for crystalline silicon, for example, organic films normally have a fraction of amorphous phase present. Compared to the crystalline domains, these amorphous regions are undesirable traps for charge carriers and lead to exciton recombination [29–35]. Therefore, understanding and controlling phase separation, molecular orientation, crystallinity, and film morphology for successful exciton diffusion and reduced recombination loss is a major fundamental challenge [36–39]. Third, suitable energy level alignment at active layer/electrode interfaces and donor/acceptor interfaces is critically important to realize efficient interfacial charge transfer to suppress unnecessary energy loss. For example, the LUMO offset between the donor and the acceptor must be larger than the exciton binding energy for efficient photoinduced charge transfer, however, not large enough to cause significant energy loss during the charge transfer process [40, 41]. As a result, the V_{OC} in most high-efficiency OPVs amounts to smaller than half of the optical bandgaps of the conjugated organic donors [42–48].

In this chapter, recent progress in synthetic control of novel conjugated organic donors, as well as fullerene acceptors, will be discussed. Strategies will be reviewed how to tune phase separation, molecular orientation, crystallinity, and morphology through film treatments such as thermal annealing, solvent annealing, and adding a small amount of processing additives or diblock copolymer compatibilizers. Then, methods to tune the energy level alignment at active layer/electrode interfaces and donor/acceptor interfaces for optimized charge transfer will be examined. Finally, a brief summary and an outlook on future directions of organic photovoltaics will conclude the chapter.

7.2 Synthesis of Conjugated Molecules for High-Efficiency Organic Photovoltaics

The chemical synthesis of photoconductive organic molecules forms the foundation of organic photovoltaics. The synthetic design of low-bandgap-conjugated polymers with energy levels that match the energy levels of fullerene derivative acceptors is crucial to optimize charge transfer for high-efficiency devices. Conversely, in addition to the fullerene derivatives that are typically used, the

synthetic design of versatile acceptors with improved functionalities, such as high electron mobility, and strong complementary absorption is also a challenge. This section reviews progress in these two areas.

7.2.1 Donors

The remarkable success of organic photovoltaics relies on the design and synthesis of novel donors with low optical bandgaps and suitable energy levels, because the conjugated polymers typically used as donors are the tunable building blocks for light absorption. The most successful low-bandgap polymers and small molecules incorporate fused rings as building blocks, such as thienothiophene, benzodithiophene, cyclopenta-dithiophene, and carbazole [42–50]. Based on these building blocks, the optoelectronic properties can be controlled by manipulating the conjugation length. In addition, branched alkyl chains were introduced as substituents on main chains in order to tune the solubility of conjugated polymers. Figure 7.2 lists several low-bandgap polymers under intensive study recently. The strategy

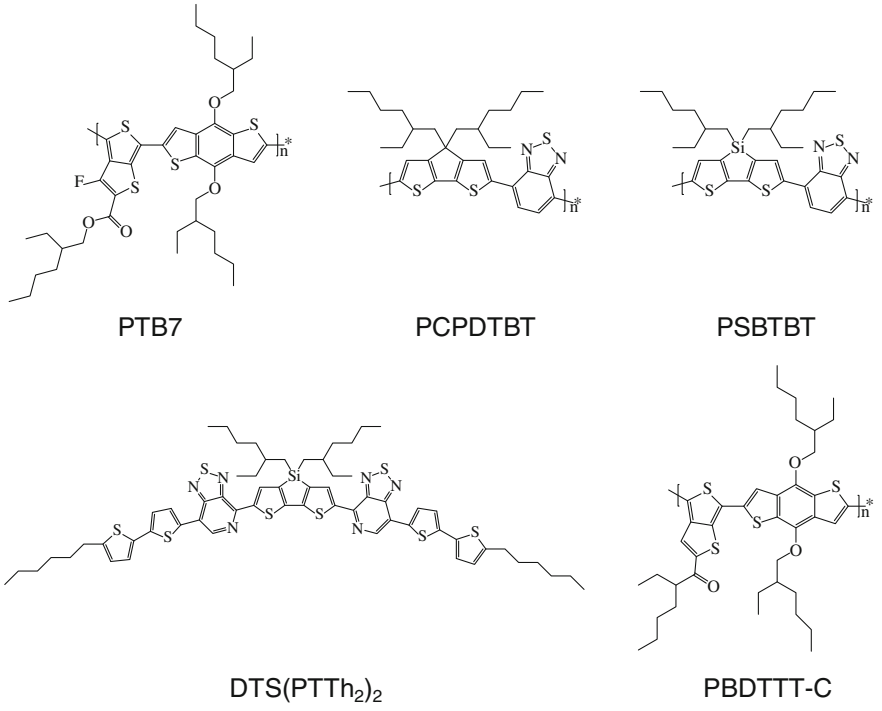

Fig. 7.2 Molecular structure of the typical low-bandgap-conjugated polymers and small molecules: PTB7 (1.84 eV), PCPDTBT (E_g = 1.46 eV) [23], PSBTBT (E_g = 1.45 eV) [25], DTS ($PTTh_2$)$_2$ (E_g = 1.6 eV) [50], PBDTTT-C (E_g = 1.77 eV) [43]

successfully used to tune the energy levels in these polymers is the substitution of fluorine atoms for hydrogen atoms on the polymer backbone. Yu et al. found that by introducing fluorine into the main chains of a low-bandgap polymer, the HOMO level can be significantly reduced [45]. Moreover, by changing the number of introduced fluorine atoms, both HOMO and LUMO levels can be tuned [45]. This important finding enabled an approach to maximize the V_{OC} by decreasing the HOMO level without sacrificing other optoelectronic properties such as the optical bandgaps of conjugated polymers. Based on this scenario, an attractive low-bandgap polymer Poly({4,8-bis[(2-ethylhexyl)oxy]benzo[1,2-b:4,5-b′]dithiophene-2,6-diyl}{3-fluoro-2-[(2-ethylhexyl)carbonyl]thieno[3,4-b]thiophenediyl}) (PTB7) was designed with introduction of fluorine atoms into the thieno[3,4-b]thiophene and benzodithiophene polymers (PTBs) [3]. He et al. [49] used PTB7 as donor and [6,6]-phenyl-C71-butyric acid methyl ester $PC_{71}BM$ as acceptor to make inverted single junction structure devices, which yielded V_{OC} of 0.754 V, short circuit current density (J_{SC}) of 17.46 mA/cm^2, fill factor (FF) of 70 %, and the highest reported PCE of 9.2 % in single junction OPVs at that time.

7.2.2 Acceptors

Despite the rapid development in organic donors, the synthesis of acceptors still far lags behind. The commonly used acceptors are fullerene-based materials, such as C_{60}, C_{70}, and fullerene derivatives such as [6,6]-phenyl-C_{61}-butyric acid methyl ester ($PC_{61}BM$) and $PC_{71}BM$. However, the characteristically low LUMO levels in these fullerene acceptors incur unnecessary energy loss during the photoinduced charge transfer from donor to acceptor [51]. In order to raise the LUMO in fullerene-based materials and avoid energy losses during the charge transfer process, thereby enhancing V_{OC}, trimetallic nitride endohedral fullerene derivatives, $Lu_3N@C_{80}$, were synthesized [52, 53]. In another approach, He et al. [54] designed a novel fullerene derivative, indene-C_{60} bisadduct (ICBA), which has two substituents on the fullerene, leading to increased LUMO levels (Fig. 7.3). However,

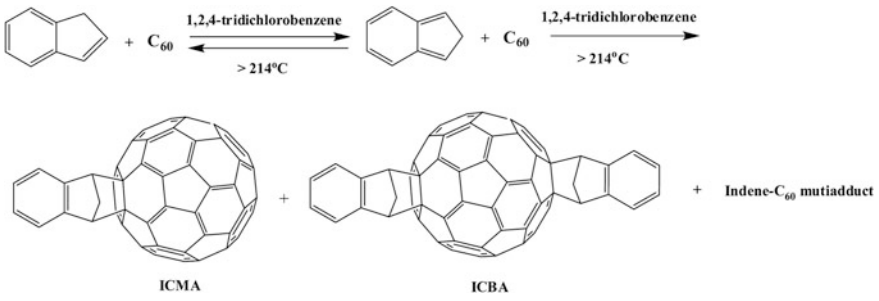

Fig. 7.3 Synthesis route of ICBA acceptor. Reprinted with permission from He et al. [54]. © Copyright (2010) American Chemical Society

this approach produces a fullerene side-product also, indene-C_{60} monoadduct (ICMA), which only raises the LUMO energy level slightly, and therefore, a purification process to separate ICBA and ICMA is required. Since the V_{OC} is determined by the energy difference between the LUMO of the acceptor and the HOMO of the donor (E_{DA}), both ICBA and ICMA acceptors with higher LUMO energy levels showed increased V_{OC}, and ICBA significantly enhanced V_{OC} from 0.58 V to 0.84 V because of the strong reduction in E_{DA} compared to PCBM and side-product ICMA. Consequently, the devices with P3HT:ICBA films showed a much higher PCE (5.4 %) than regular P3HT:PCBM-based devices ($\sim$4 %). Furthermore, a combination of solvent annealing and thermal annealing treatments was applied to optimize the film morphology through the formation and separation of preferable nanophases in ICBA:P3HT blend films, and the devices yielded V_{OC} of 0.84 V, J_{SC} of 10.61 mA/cm^2, FF of 72.7 %, and PCE of 6.5 % [55].

However, to underscore the complexity and flexibility of synthetic design, although the increased LUMO levels in ICBA led to higher V_{OC} in ICBA: poly (3-hexylthiophene) (P3HT) devices, a reduction in electron mobility was found that resulted in decreased J_{SC} and external quantum efficiency (EQE). Moreover, ICBA showed similar adverse effects in devices when utilized with low-bandgap polymers such as PTB7 [56–58]. The specific reasons for the poor device performance are unclear but appeared due to unfavorable phase separations and film morphologies. In an attempt to resolve these issues, He et al. designed another synthesis route to synthesize a C_{70}-based fullerene derivative ICBM by replacing the fullerene with an endohedral fullerene, leading to both enhanced LUMO levels for larger V_{OC} and improved charge transport properties for high J_{SC} [59]. Moreover, this fullerene acceptor ICBM could be not only blended with P3HT polymer donor for improved efficiency, but was also compatible with low-bandgap polymers (e.g., PTB7) for enhanced device performance.

An important direction in OPV's is the design of non-fullerene acceptors with complementary absorption and suitable energy levels for charge transfer. Very recently, boron subphthalocyanine chloride (SubPc) or chloroboron (III) sub naphthalocyanine (SubNc) were employed as acceptors with a-6T donor layer. These non-fullerene acceptor-based devices showed higher V_{OC} and J_{SC} compared to the device with C_{60} fullerene as an acceptor. By designing a cascade structure (a-6T/SubNc/SubPc), the devices showed high PCE of 8.4 % without employing any fullerene or fullerene derivatives [60]. Alternative polymer acceptors based on cyanated poly(phenylenevinylene), benzothiadiazole, perylene-, and naphthalene-diimide with a wide range of tunability of electronic properties are also under intensive study [61]. Compared to the fullerene-based devices, the devices based on polymer acceptors showed lower photocurrents and efficiencies because of reduced electron mobility and inefficient charge separation [61, 62].

7.3 Optimizing Film Morphology and Phase Separation in Polymer Photovoltaics

Optimizing the nanoscale phase separation plays a key role in ensuring the successful exciton dissociation at donor/acceptor interfaces and formation of charge extraction pathways for efficient charge collection. However, the precisely tuning of film phase separation, morphology, molecular orientation, and crystallinity is still a challenge. A broad range of film treatments, including thermal annealing, solvent annealing, and adding a small amount of processing additives or compatibilizers, were proposed to realize these goals.

7.3.1 Thermal Annealing

Thermal annealing is critical for many organic photovoltaic thin films because it can enhance crystallinity and phase separation of donor/acceptor blends. The success of OPVs is based on the formation of heterojunctions between donors and acceptors at the nanoscale. However, the addition of fullerene acceptor would hinder the crystallinity of donor polymers [63]. As a result, thermal annealing is resorted to further improve the phase separation, which could increase the interchain interactions such as π–π stacking, and thus enhances the crystallinity in P3HT polymer domains for more efficient charge transport in solar cells [64].

In order to understand the impact of thermal annealing on the morphology (especially vertical composition profiles of D/A) of the electron donor/acceptor blends, different experimental techniques such as variable-angle spectroscopic ellipsometry (VASE), cross sectional transmission electron microscopy (TEM), depth-profiled X-ray photoelectron spectroscopy (XPS), secondary ion mass spectrometry (SIMS), and neutron reflectometry have been used to obtain insight into vertical composition profiles of BHJ films. X-ray reflectivity (XRR) has been used to investigate the vertical composition profiles of donor and acceptor in OPV blend films [65–67]. However, the natural X-ray scattering length density (*x*SLD) contrast between organic donor and acceptor is often very low and hence neutron reflectivity (NR) has recently been used to investigate the vertical phase depth profiles of donor and acceptor. The donor and acceptor in film naturally exhibit a large natural contrast in neutron scattering length density (*n*SLD) due to the large difference in proton content between the proton-poor fullerene and the proton-rich-conjugated polymer. Therefore, donor and acceptor BHJs are an excellent system to elucidate the phase structure using NR and to correlate the effects of structure and actual photovoltaic device efficiency. In NR measurement, slit-collimated neutron beam impinges onto the flat surface and interface of film at shallow incidence angles α_i's and, at each α_i, only the reflected beams of which exit

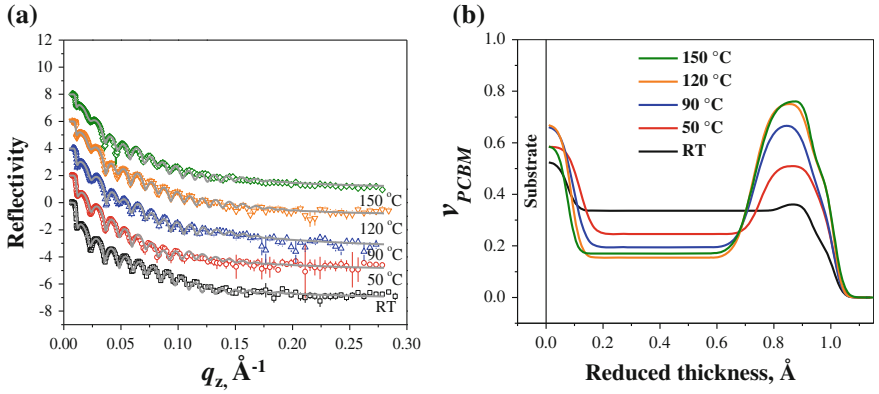

Fig. 7.4 **a** Fits to raw neutron reflectivity data taken on as-cast and annealed P3HT/$PC_{61}BM$ film are used to derive **b** volume fraction profiles of $PC_{61}BM$ (v_{PC61BM}) in the film, which reveals that with increasing annealing temperature the PCBM is stratified more to the substrate and air interfaces. Reprinted with permission from Keum et al. [20]. © (2013) AIP Publishing LLC

angle (α_f) is identical to α_i are recorded to explore the vertical depth profile of sample film. As usual in neutron scattering experiment, where the phase information is lost, the analysis of measured reflectivity curve is generally carried out by a construction of model *n*SLD profile from which the calculated reflectivity profile using Parratt formalism [68] is fit to the experimental reflectivity data until a goodness of fit with least χ^2 is attained. Using obtained *n*SLD, the composition profiles of constituents are deduced by the expressions described in Refs. [20, 65]. Using NR, Keum et al. [20] have recently demonstrated that the film stratification occurring during film formation and thermal annealing process can be due to the unique crystallization habit of P3HT in thin film and the partial miscibility between amorphous P3HT and $PC_{61}BM$. Figure 7.4 shows the measured and modeled neutron reflectivity curves for as-spun and annealed P3HT/$PC_{61}BM$ films deposited on silicon (Si) substrate, and the volume fraction profiles of $PC_{61}BM$, v_{PC61BM}'s are obtained from the neutron reflectivity modeling. From the changes in v_{PC61BM}, it is evident that spin-casting P3HT/$PC_{61}BM$ onto Si substrate results in stratified morphology with $PC_{61}BM$ accumulations near the free surface and Si interface. It is also seen that increasing annealing temperature accompanies increased stratification. Based on the NR results, it has been proposed that since P3HT remains less crystalline in the two interfacial regions (free surface and substrate interface) than in the bulk region and $PC_{61}BM$ is miscible with amorphous P3HT, $PC_{61}BM$ preferentially diffuses to the two interfacial regions and accumulates resulting in the stratification. The three-phase-morphology (P3HT phase, $PC_{61}BM$ phase, and a homogenous mixture of the two) [69, 70], which recently is believed to be dominating morphology in most highly efficient BHJ OPVs device delivering better charge separation and suppressed bimolecular charge recombination [69, 71, 72].

7.3.2 Solvent Annealing

Solvent annealing is shown to be another effective approach to induce the self-organization in conjugated polymer films, such as P3HT, because the solvent vapor allows the P3HT polymers to self-organize into a more ordered structure by slowing down the drying speed of the spin-coated wet P3HT:$PC_{61}BM$ films. As illustrated in Fig. 7.5a, the solvent annealed films showed very a similar absorption spectrum to the thermal annealed film, and the characteristic absorption shoulder of the P3HT polymer is also evident in the solvent annealed films, which indicates the formation of crystalline P3HT domains. The growth of P3HT crystallinity as function of solvent (e.g., tetrahydrofuran, chloroform) annealing time in P3HT:$PC_{61}BM$ blend films was observed with grazing-incidence X-ray scattering. The polymer self-reorganization due to solvent annealing could induce nanoscale phase separation and the resulted domain size as a function of solvent annealing time was also clearly obtained.

Recently, Hedge et al. [73] studied the effect of solvent annealing on the P3HT:$PC_{61}BM$ thin film properties and photovoltaic performance. It was found that exposure of this bulk heterojunction to carbon disulfide (CS_2) vapor alters the crystallinity and depth profile of D/A blend very effectively, presumably by inducing mobility of the components as the solvent plasticizes the mixture. The crystallinity and crystal size of the P3HT increase initially with solvent vapor pressure and annealing time, but longer exposure to solvent decreases P3HT crystallinity and photovoltaic efficiency. Neutron reflectivity indicates that the $PC_{61}BM$ segregates to the Si substrate in the as-cast thin film, but distributes throughout the film with solvent annealing. The changes in crystallinity and the depth profile of the P3HT:$PC_{61}BM$ mixture differ from those induced by thermal annealing. Controlled solvent exposure provides a more controllable annealing process than thermal annealing and takes less time than thermal annealing.

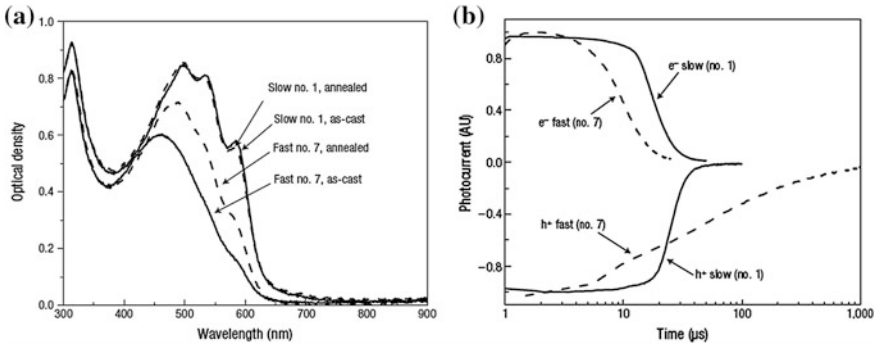

Fig. 7.5 Variation in absorption spectra (**a**) and time of flight measurement results (**b**) with different film processing conditions. Reprinted with permission from Li et al. [12]. © (2005) Nature Publishing Group

The combination of thermal annealing and solvent annealing could not only enhance the crystallinity of P3HT polymer domains, but also promote the phase separation between donor and acceptor in the solution casted P3HT:$PC_{61}BM$ films [12]. The time of flight technique was applied to study the charge transport properties in the films after thermal annealing and solvent annealing treatment. For the fast drying method prepared P3HT:$PC_{61}BM$ films, the electron and hole mobility was 1.1×10^{-4} cm^{-2} V^{-1} s^{-1} and 5.1×10^{-6} cm^{-2} V^{-1} s^{-1}, respectively, whereas for the slow drying method prepared P3HT:$PC_{61}BM$ films, the hole mobility was increased by one order to 5.1×10^{-6} cm^{-2} V^{-1} s^{-1}. More balanced electron–hole mobility was obtained after both thermal annealing and solvent annealing (Fig. 7.5b), which is beneficial to reduce the charge recombination.

7.3.3 Processing Additives

Both thermal annealing and solvent annealing were demonstrated to effectively tune the phase separation and enhance crystallinity in donor/acceptor blend films; however, the phase-separated morphology is not thermodynamically stable. It is well-known that including a third component to modify interfaces in a binary blend provides abundant opportunities to achieve useful microstructures and thermodynamically stable morphology. In terms of ternary blends for organic solar cell active layers, there are two major approaches that rely on either (i) processing solvent additives or (ii) block copolymer compatibilizers to tune morphology. The former approach is aimed at increasing the polarity difference between donor- and acceptor-rich domains to avoid thermal annealing steps, while the latter approach is used to stabilize donor–acceptor interfaces, especially after thermal annealing. Interestingly, processing additives can precisely control the target crystal growth and further tune the blend film morphology. To successfully control the morphology, the chosen solvent additives should meet two prerequisites: (1) The solvent additive should have higher boiling point than the major solvent, and (2) the solvent additive should have selective solubility of one component of the BHJ. Previous studies have agreed that processing additives enhance the overall crystallinity and the size of crystalline domains of the conjugated polymer donors. However, the relative variation in the size of the fullerene domains (either increasing or decreasing) upon adding various processing additives is strongly materials dependent. For example, the processing additive 1,8-octanedithiol (ODT) can promote the aggregation of fullerene-rich domains in PCPBDTBT/$PC_{61}BM$ BHJ films, whereas the solvent additive 1,8-diiodooctane (DIO) reduces oversized fullerene-rich domains (from ~hundreds of nanometers to tens of nanometers) in PTB7/$PC_{61}BM$ BHJ films. The opposite structural evolution upon adding additive is determined by distinctive initial states without additives processing, which is related with the intrinsic factors of solubility, crystallization ability, and miscibility between BHJ components.

Shao et al. [19] observed that both lateral and vertical morphology of the PBDTTT-C-T:$PC_{71}BM$ blend films could be optimized by using a small amount of additive of 3 % DIO. Low-voltage energy filter transmission electron microscopy (EF-TEM) was applied to reveal the phase and morphology in PBDTTT-C-T:$PC_{71}BM$ blend films with DIO and without DIO. EF-TEM with elastic energy of 19 ± 4 eV was applied to image donor-rich regions, while 30 ± 4 eV was applied to image acceptor-rich area, which evidently suggested enhanced phase segregation in the films with adding 3 % DIO.

Besides lateral phase morphology, the vertical phase profile is also very critical to the device performance. Shao et al., employ the neutron reflectometry to investigate the effect of solvent additive DIO on the vertical distributions of the blend components. As shown in Fig. 7.6, all the films exhibited Kiessig fringes, a characteristic of the interference of reflected neutrons. For the NR curve of PBDTTT-C-T:$PC_{71}BM$/DCB film, the best goodness of fit is achieved using a single layer model. This implies that the phase-separated $PC_{71}BM$ domains are distributed homogeneously through the thickness direction of the film. In the PBDTTT-C-T:$PC_{71}BM$/DCB:DIO film, however, the best fit using a 4-layer morphology imply that PBDTTT-C-T and $PC_{71}BM$ are distributed in different proportions through the thickness of the film. This result indicates that the DIO additive also induces a strong vertical phase separation. Specifically, the results indicate that $PC_{71}BM$-depleted layers form preferentially at the top surface of the blend film made from DCB/DIO, meaning that more polymers are enriched at the top interface. Thus, using inverted device structure is expected to achieve higher device performance for the PBDTTT-C-T and $PC_{71}BM$ blend due to the improved charge transport and collection near the anode interface.

Shao et al. [19] also found that the DIO additives could significantly facilitate the molecular ordering in the spin-coated films. Two-dimensional (2D) grazing-

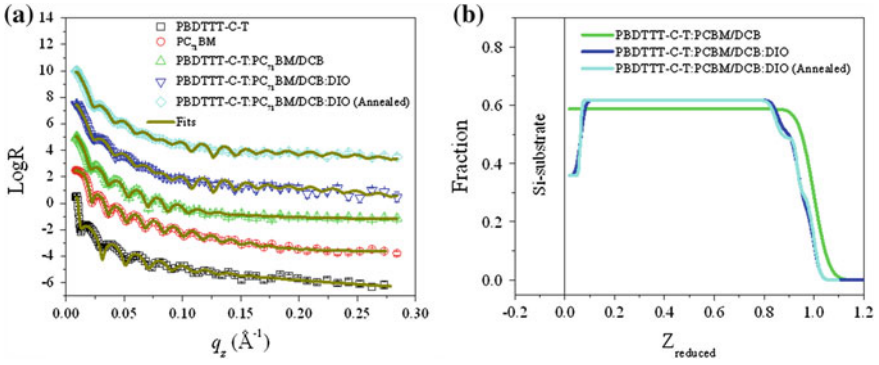

Fig. 7.6 **a** Experimental and modeled NR curves for PBDTTT-C-T, PC71BM, PBDTTT-C-T:$PC_{71}BM$/DCB, PBDTTT-C-T:$PC_{71}BM$/DCB:DIO, and annealed PBDTTT-CT:$PC_{71}BM$/DCB:DIO film. **b** Volume fraction profile of PCBM calculated from the SLD profiles. Reprinted with permission from Shao et al. [19]. © (2014) WILEY-VCH Verlag GmbH & Co. KGaA, Weinheim

incidence wide-angle X-ray scattering (GIWAXS) was applied to reveal the molecular orientation, molecular ordering, as well as polymer crystallinity of the PBDTTT-C-T:$PC_{71}BM$ blend films. The GIWAXS patterns of pure PBDTTT-C-T film, PBDTTT-C-T:$PC_{71}BM$ blend film, and PBDTTT-C-T:$PC_{71}BM$ blending with adding 3 % DIO are shown in Fig. 7.7. In-plane (100) and out-of-plane (010) reflections of PBDTTT-C-T crystals were clearly observed in PBDTTT-C-T:$PC_{71}BM$ blend films with adding 3 % DIO. This observation indicates that PBDTTT-C-T have a face-on molecular orientation which is a beneficial characteristic for hole transporting along the perpendicular direction to ITO substrates. In addition, higher degree of crystallinity in PBDTTT-C-T:$PC_{71}BM$ films with 3 % DIO additives was also identified by comparing the GIWAXS patterns between the PBDTTT-C-T:$PC_{71}BM$ film with and without DIO. The higher crystallinity in PBDTTT-C-T polymer domains also facilitates charge transport in OPVs. EF-TEM and GIWAXS measurements conclusively showed that the efficiency improvement in the OPVs with adding DIO additives is because of the preferable phase separation, molecular ordering, and higher crystallinity.

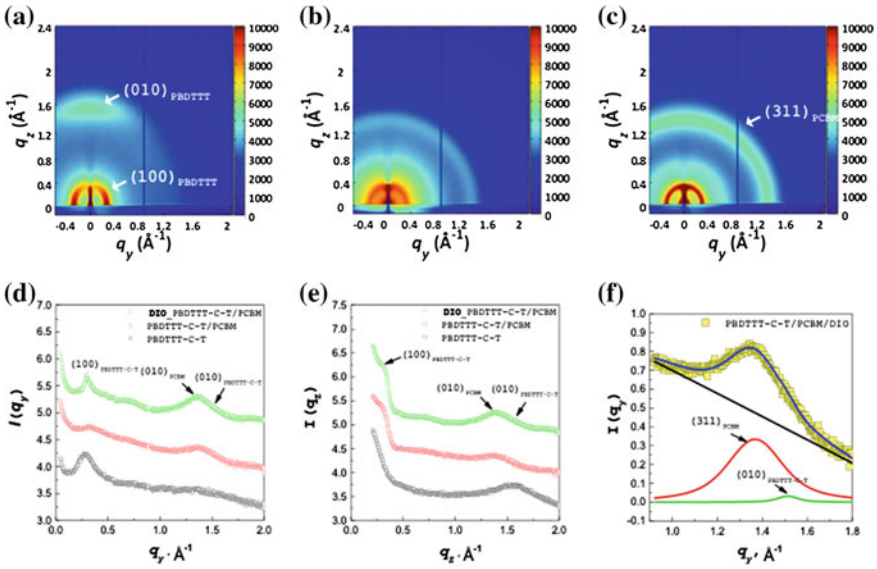

Fig. 7.7 2D GIWAXS patterns of **a** pristine PBDTTT-C-T polymer film, **b** PBDTTT-C-T:$PC_{71}BM$ blend film, and **c** PBDTTT-C-T:$PC_{71}BM$:DIO blend film. **d**, **e** in-plane and out-of-plane GIWAXS profiles extracted from the respective 2D GIWAXS patterns. **f** A curve-fit result showing the existence of (311) reflection of $PC_{71}BM$ and (100) of PBDTTT crystal. Reprinted with permission from Shao et al. [19]. © (2014) WILEY-VCH Verlag GmbH & Co. KGaA, Weinheim

7.3.4 Compatibilizers

Generally, the binary donor/acceptor blend film is not thermo-dynamically stable. The film morphology and nanoscale phase separation were found to change with time [72]. The compatibilizers can significantly reduce interfacial tension and suppress coalescence [74]. Therefore, interfacial compatibilizers are introduced into donor and acceptor blend film to enhance the long-term stability and also reduce the donor/acceptor domain size within exciton diffusion length.

Chen et al. [75] found that diblock copolymer, poly(3-hexylthiophene)-b-poly (ethylene oxide) (P3HT-b-PEO), to systematically tune the P3HT polymer and $PC_{61}BM$ fullerene derivative domain sizes at the nanoscale. With increasing the amount of P3HT-b-PEO compatibilizers, the domain sizes were significantly reduced to the length of the scale within exciton diffusion length. However, the J_{SC} was greatly reduced with introducing 5 wt% P3HT-b-PEO compatibilizers, resulting in decreased PCE because charge transfer between donor and acceptor is blocked by the insulating PEO component at the P3HT/$PC_{61}BM$ interface. Therefore, appropriate design of diblock copolymer architecture is very critical to warranty efficient charge transfer at donor/acceptor interfaces and still maintain optimized film morphology and thermal stability.

Sun et al. [17] found that diblock copolymer, polystyrene-block-poly (3-hexylthiophene) (PS-b-P3HT), could effectively control domain size in the P3HT:$PC_{61}BM$ blend films while the advantages of optimized phase separation and thermal stabilization of the ternary blend film could be maintained. Figure 7.8 shows AFM phase images of the different loading ratio of PS-b-P3HT compatibilizer in the P3HT:$PC_{61}BM$ blend films. 5 wt% PS-b-P3HT compatibilizers were found to promote the formation of the most homogenous morphology with

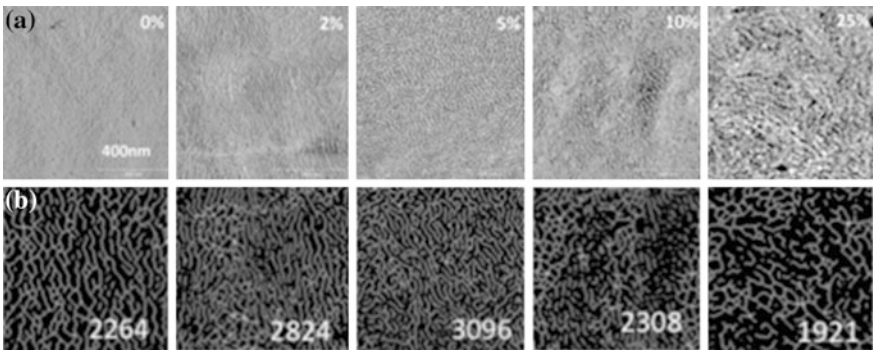

Fig. 7.8 **a** AFM phase images of P3HT:$PC_{61}BM$ blend films with 0 wt%, 2 wt%, 5 wt%, 10 wt%, 25 wt% PS-b-P3HT compatibilizers. **b** The features in the mid-frequency range after Fourier transform for corresponding AFM phase images. 5 wt% of PS-b-P3HT compatibilizers showed the best ordering of P3HT polymer and penetrating network. Reproduced with permission from Sun et al. [17]. © (2011) WILEY-VCH Verlag GmbH & Co. KGaA, Weinheim

interpenetrating nanoscale domains, which significantly improved charge separation and charge extraction efficiency.

The crystallinity variation in P3HT:$PC_{61}BM$ films with adding different amount of the PS-b-P3HT compatibilizers was also examined by Sun et al. with 2D GIXS measurements. As shown in Fig. 7.9, the (100), (200), (300) planes showed an evident crystalline peaks. This observation indicated that the P3HT aromatic planes have a face-on orientation, which means the P3HT planes are aligned parallel with the substrate surface. As the amount of the PS-b-P3HT compatibilizers increased, both the peak intensity and crystal size reached maximum at 5 wt%. Therefore, a small amount of 5 wt% PS-b-P3HT compatibilizers could not only optimize the phase separation, but also increase crystallinity in P3HT polymer domains.

Neutron reflectivity was also applied to reveal vertical phase morphology with adding amount of PS-b-P3HT compatibilizers. The vertical concentration profile in the P3HT:$PC_{61}BM$ films could be obtained according to large scattering length density (SLD) difference between P3HT and $PC_{61}BM$. The neutron reflectivity profile in P3HT:$PC_{61}BM$ films with different PS-b-P3HT compatibilizers loading ratio is shown in Fig. 7.10. A standard iterative formula combining with a proposed multilayer model was used to fit the neutron data and approximate the SLD data. The

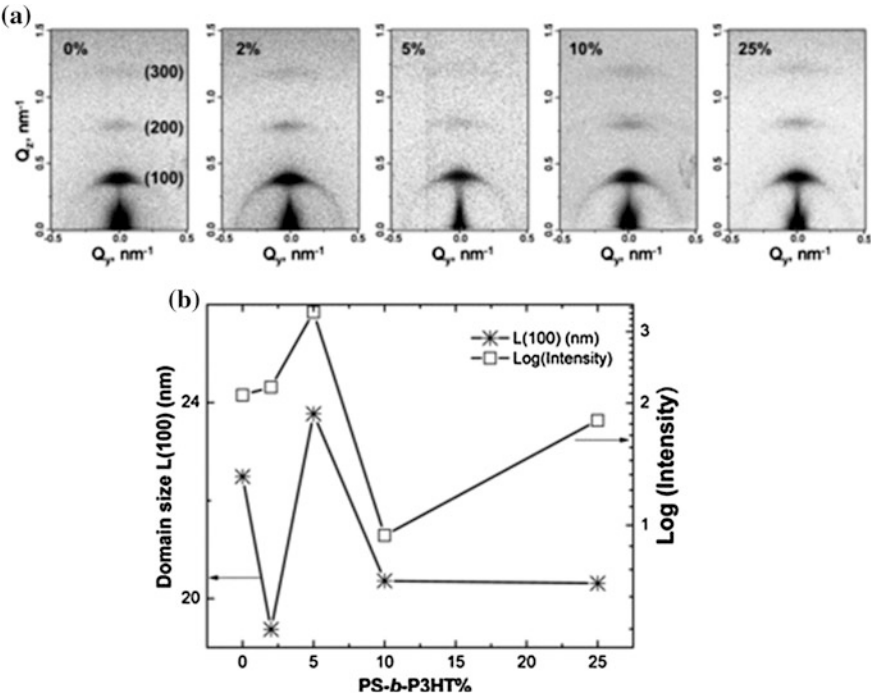

Fig. 7.9 **a** 2D GIXS patterns of the P3HT:$PC_{61}BM$ blend films with adding 0 wt%, 2 wt%, 5 wt%, 10 wt%, and 25 wt% of PS-b-P3HT compatibilizers. Q_z and Q_y are the perpendicular and parallel wave vectors transfer with respect to substrate surface. **b** The domain size and normalized peak intensity of (100) extracted from 1D GIXS measurement. Reprinted with permission from Sun et al. [17]. © (2011) WILEY-VCH Verlag GmbH & Co. KGaA, Weinheim

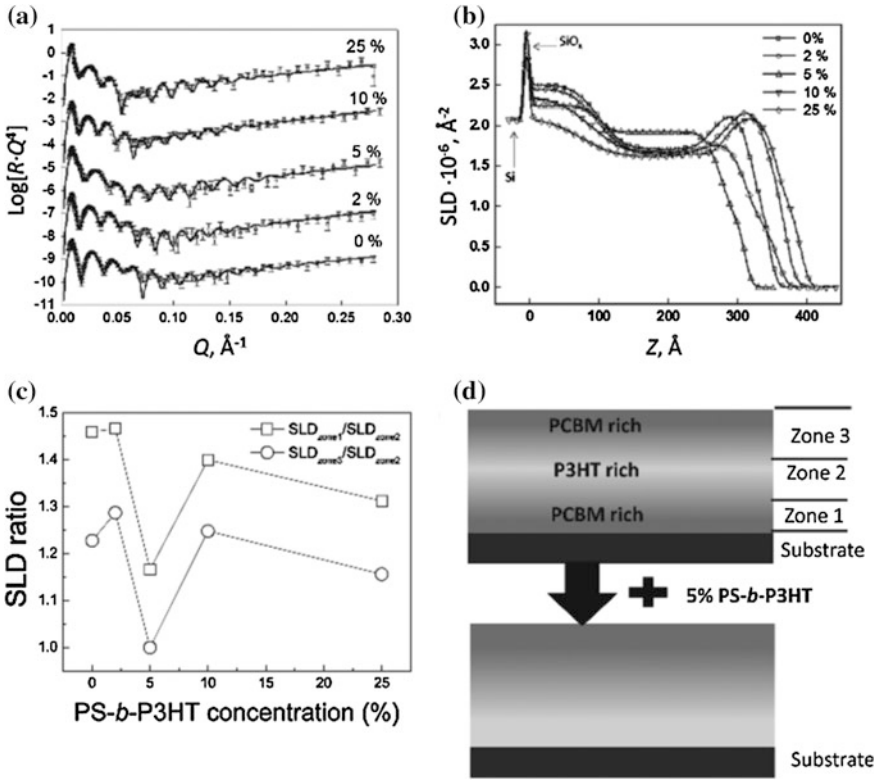

Fig. 7.10 **a** Fits to raw neutron reflectivity data taken on thin P3HT/PCBM films made with different loading ratios of PS-b-P3HT compatibilizers are used to derive (**b**) scattering length density (SLD) profiles versus depth which are used to model the fraction of PCBM and P3HT for different depths in the film, **c** SLD ratio as a function of PS-b-P3HT concentration, empty square represents the ratio of SLDzone1/SLDzone2, while empty circle represents the ratio of SLD zone3/SLD zone2. schematically diagramed in (**d**), which reveals that under most circumstances the PCBM migrates to the substrate and air interfaces, except for the 5 wt% compatibilizer ratio which makes a more uniform blend. Reprinted with permission from Sun et al. [17]. © (2011) WILEY-VCH Verlag GmbH & Co. KGaA, Weinheim

neutron data obtained from films with 0 wt%, 2 wt%, 10 wt%, 25 wt% PS-b-P3HT compatibilizers could be well fitted with three-layer model; however, films with 5 wt % PS-b-P3HT compatibilizers could only be fitted with two-layer model (Fig. 7.10d). And also, the neutron reflectivity showed that more $PC_{61}BM$ sit on the top and more P3HT locating on the bottom in the 5 wt% PS-b-P3HT compatibilizers film, which is favorable for charge transport and charge extraction in OPVs. In summary, adding 5 wt% PS-b-P3HT compatibilizers to P3HT:$PC_{61}BM$ films could improve the phase separation, polymer crystallinity, and vertical phase morphology. The P3HT:$PC_{61}BM$ OPVs with adding 5 wt% PS-b-P3HT compatibilizers yielded the highest efficiency of 3.8 %, which is consistent with the morphological study.

7.3.5 *Layer-by-Layer Processing for Optimized Film Morphology and Reduced Charge Recombination*

As-processed donor/acceptor blend BHJ films from solution usually have many dead ends, which often act as charge trapping centers. Recently, layer-by-layer processing was shown to be an effective approach to fabricate BHJ films [76–78]. Compared to one-step solution processing, the sequential layer-by-layer processing should be easier to control over the individual components and interfaces between the donor and acceptor during the film formation [79]. Typically, the donor conducting polymer was first spin-coated on the substrate, and then the PCBM acceptor layer was spin-coated by using immiscible solvents with donor polymers followed by thermal annealing treatment. This approach has been successfully applied to fabricate polymer-based devices such as P3HT [80], poly{2,6-(4,4-bis [2-ethylhexyl]-4*H*-cyclopenta[2,1-*b*;3,4-*b*′]dithiophene)-*alt*-4,7-(2,1,3-benzothiadiazole)} (PCPDTTBT) [81], which showed comparable or even better performance to the single-step-fabricated OPVs. Yang et al. [82] fabricated the P3HT:PCBM BHJ OPVs via bilayer interdiffusion and the devices exhibited a *PCE* of 5.1 %, which is better than that of the blend solution-processed BHJ counterparts. The reason for the device efficiency improvement is that richer $PC_{61}BM$ domains sit close to the cathode and more P3HT polymers are close to the anode in the BHJ films, as revealed by Russell et al. [77].

In order to understand the underlying physical mechanism of the formation of favorable vertical film morphology for improved device performance by using layer-by-layer processing approach, the time-delayed collection field (TDCF) method was applied to characterize the amount of long-lived photogenerated charges (>1 μs) to explore the charge generation and recombinations [82]. It was found that the amount of long-lived photogenerated charges was slightly enhanced by about 5 % in the thermally annealed bilayer devices. However, through characterizing the average charge carrier lifetime as a function of applied bias in single-step fabricated devices and thermally annealed bilayer devices by using impedance spectroscopy, Yang et al. found that the average lifetime was much longer in the thermally annealed bilayer devices than the single-step fabricated counterparts. In addition, the thermally annealed bilayer devices have significantly longer carrier lifetime than in the single-step fabricated BHJ devices. The bimolecular recombination coefficient was strongly decreased by threefold with transient photovoltage/photocurrent measurements, demonstrating that the significantly reduced bimolecular recombination loss is a major contribution to the increased efficiency in the thermally annealed bilayer OPVs.

7.3.6 *Isotopic Effects of Deuteration on Film Morphology, Phase Separation, and Optoelectronic Properties of Conducting Polymers*

The OPV device performance is significantly dependent on the optoelectronic properties of the conducting polymers. In order to achieve attractive optoelectronic properties, it is crucial to manipulate and control the intra- and inter-polymer chain interactions. Isotopic effect of deuteration has been shown to strongly affect optoelectronic properties such as electroluminescence [83]. However, how isotopic substitution affects the film morphology, phase separation, and optoelectronic properties in OPV devices is still an unresolved question.

Shao et al. [84] found that selective deuteration on P3HT polymer has a remarkable contribution to the morphology, phase separation, and charge transport properties in OPVs. Figure 7.11a shows the main chain deuteration and side chain deuteration on P3HT polymers. Interestingly, selective deuterations on the different position of P3HT result in distinct optoelectronic response in P3HT/PCBM solar cells. Specifically, the main chain deuterated polymer (MD-P3HT) reduced the J_{SC}, whereas the side chain deuterated polymer (SD-P3HT) decreased the V_{OC} (Fig. 7.11b). Through examining the absorption spectra, the absorption decreased significantly in MD-P3HT (Fig. 7.11c), which could be a reason for reduced J_{SC}.

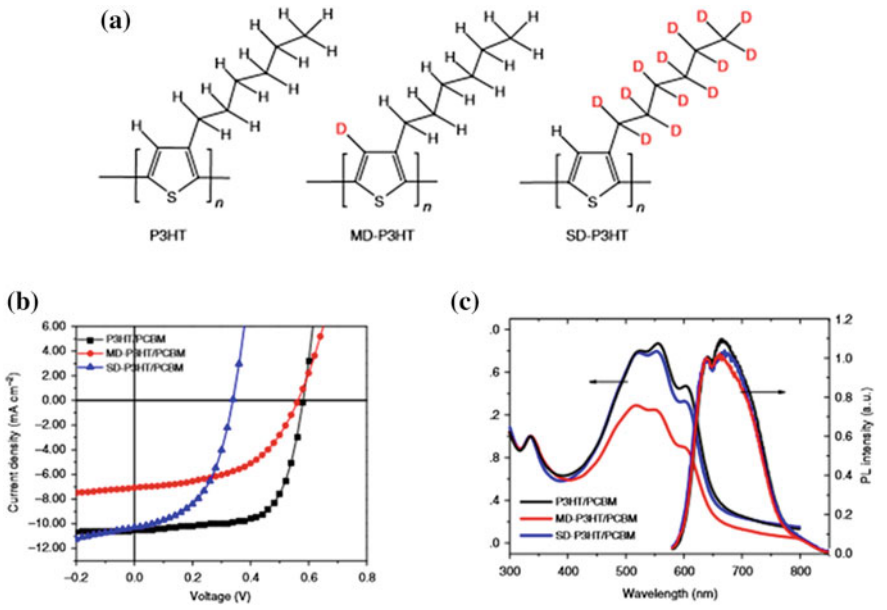

Fig. 7.11 **a** Chemical structure of P3HT, MD-P3HT, and SD-P3HT; *J–V* curves under illumination of 100 mW/cm^2 (**b**) and absorption spectra (**c**) of the three P3HT isotopes blended with PCBM. Reprinted with permission from Shao et al. [84]. © (2014) Nature Publishing Group

Shao et al. [84] also examined deuteration effect on film morphology and crystallinity of P3HT. Nanofibrillar structures were observed in both P3HT/$PC_{61}BM$ and SD-P3HT/$PC_{61}BM$ films in AFM phase images (Fig. 7.12a), which indicates highly crystalline P3HT domains in both blend films. However, no evident P3HT crystalline fibril was found in the MD-P3HT/$PC_{61}BM$ film, which suggests that the MD-P3HT is less crystalline or perhaps amorphous. Energy-filtered TEM was applied to identify whether the deuteration affects the phase separation. The bright regions in Fig. 7.12b correspond to P3HT-rich domains. It was observed that the interpenetrating network is better in both P3HT/$PC_{61}BM$ and SD-P3HT/$PC_{61}BM$ films than the MD-P3HT/$PC_{61}BM$ films. In addition, the domain size in the MD-P3HT/$PC_{61}BM$ films is in the range of 29 nm, which is much larger than exciton diffusion length. As a result, the interfacial area between donor and acceptor is reduced, leading to inefficient charge separation and charge extraction.

The deuteration effect on the P3HT molecular ordering and interchain packing in blend films was examined with GIWAXS measurements using a synchrotron X-ray radiation source as shown in Fig. 7.13. The q_y and q_z refer to in-plane and out-of-plane scattering wave vectors. The GIWAXS profiles from both non-deuterated and deuterated blend films show the out-of-plane diffraction patterns

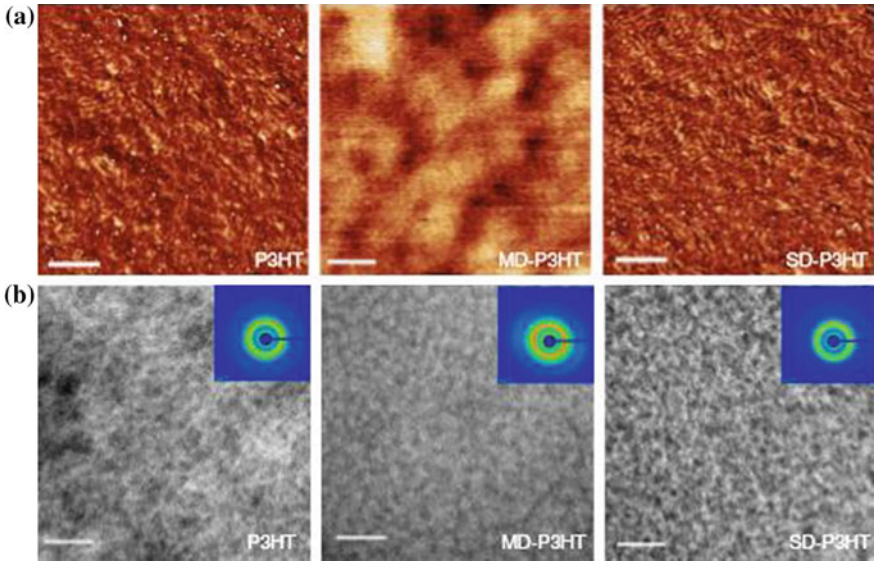

Fig. 7.12 Morphology characterizations. **a** AFM phase images of P3HT, MD-P3HT, and SD-P3HT blended with $PC_{61}BM$ after thermal annealing (scale bar, 200 nm). **b** Energy-filtered TEM images of P3HT, MD-P3HT, and SD-P3HT blended with $PC_{61}BM$ after thermal annealing (scale bar, 100 nm). Each film is imaged with 19 ± 4 eV, where inelastic scattering is more intense for P3HT. *Insets* of (**b**) show the selected area electron diffraction patterns. Reprinted with permission from Shao et al. [84]. © (2014) Nature Publishing Group

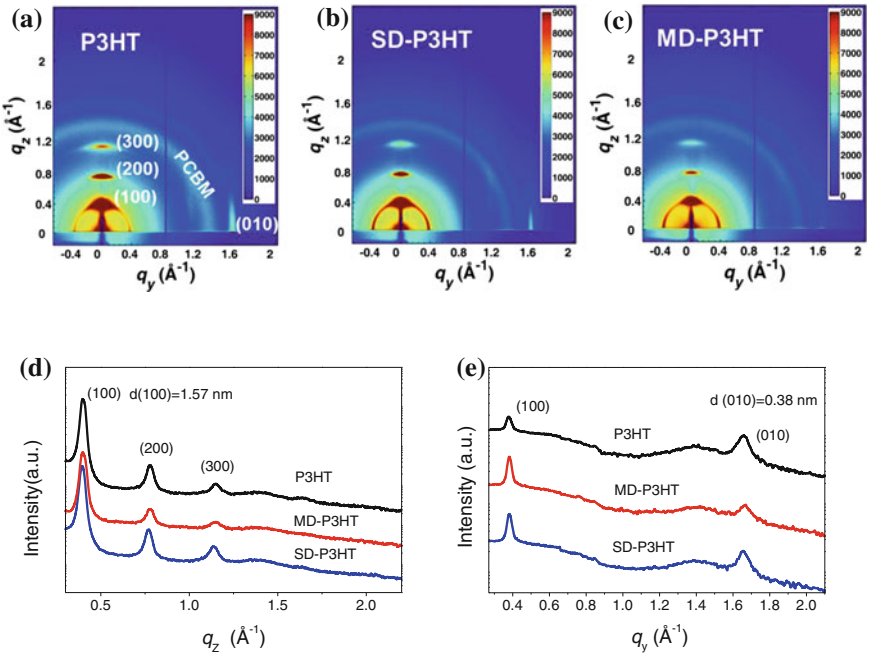

Fig. 7.13 Two-dimensional GIWAXS plots of **a** P3HT:$PC_{61}BM$, **b** SD-P3HT:$PC_{61}BM$, and **c** MD-P3HT:$PC_{61}BM$ film annealed at 120 °C. **d** Out-of-plane and **e** in-plane GIWAXS slices extracted from the corresponding 2D GIWAXS patterns. q_z and q_y are the perpendicular and parallel wave vectors transfer with respect to substrate surface. Reprinted with permission from Shao et al. [84]. © (2014) Nature Publishing Group

of (l00) reflections and the in-plane (010) reflection patterns, indicating a well-organized lamellar structure with edge-on orientation on the substrate. MD-P3HT exhibits the lowest crystallinity among three, which can be inferred by the weakest (100) and (010) diffraction intensities. This observation is consistent with TEM results. The intensity ratios of out-of-plane (100) to in-plane (100) were found to be 239, 32, and 90 for P3HT/$PC_{61}BM$, MD-P3HT/$PC_{61}BM$, and SD-P3HT/$PC_{61}BM$ implying that the population of edge-on crystallites for deuterated P3HT is much less than that for protonated P3HT. Moreover, random oriented crystallites will lead to lower carrier mobility, and probably results in a small J_{SC} and worse photovoltaic performance.

GISAXS is a high resolution, nondestructive scattering technique suitable to characterize the lateral and vertical phase structure of OPV blend layer. Shao et al. have investigated the lateral domain morphologies of $PC_{61}BM$ dispersed in various P3HT matrices using GISAXS [84], where the in-plane GISAXS profiles (intensity vs. q_y) were modeled using a combined model of Guinier-Porod [85] and polydisperse hard-sphere model with Schulz distribution [86] as shown in Fig. 7.14. In the model fits, Guinier-Porod and polydisperse hard-sphere models account for the

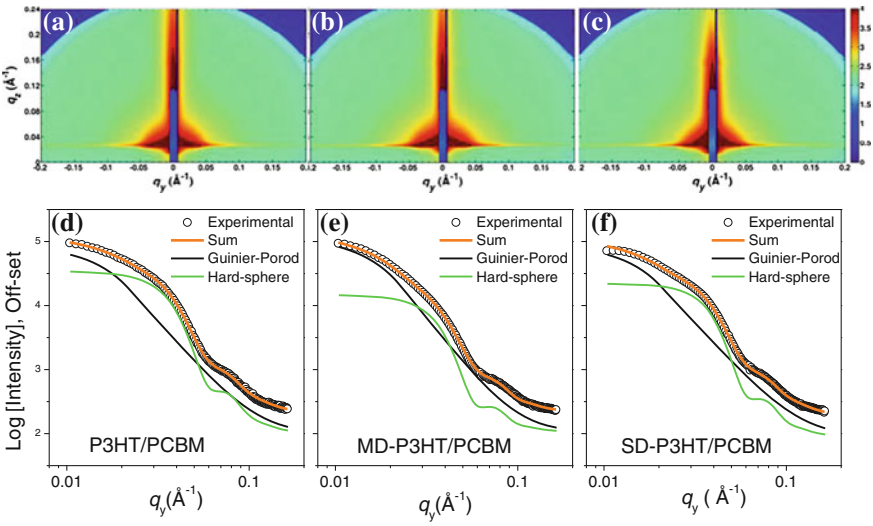

Fig. 7.14 Measured 2D GISAXS of P3HT/$PC_{61}BM$ (**a**), SD-P3HT/$PC_{61}BM$ (**b**), and MD-P3HT/$PC_{61}BM$ (**c**) films, and corresponding in-plane 1D profiles of P3HT/$PC_{61}BM$ (**d**), SD-P3HT/$PC_{61}BM$ (**e**), and MD-P3HT/$PC_{61}BM$ (**f**) films. The *solid lines* represent the SAXS intensities calculated by the DAB model. Reprinted with permission from Shao et al. [84]. © (2014) Nature Publishing Group

Table 7.1 Structural parameters determined by combined polydisperse sphere and Guinier-Porod model fitting

Samples	Hard-sphere model with Schulz distribution		Guinier-Porod	
	$R_{g,1}$, Å	Polydispersity	$R_{g,2}$, Å	Porod exponent
P3HT/PCBM	54.9	0.16	99.7	3.2
SD-P3HT/PCBM	54.8	0.15	95.5	3.1
MD-P3 HT/PCBM	56.2	0.14	97.1	3.5

Reprinted with permission from Shao et al. [84]. © (2014) Nature Publishing Group

phase-separated $PC_{61}BM$ domains with largely two different sizes, i.e., Guinier-Porod model for large domains (low-q_y region) and hard-sphere model for small domains (high-q_y region). The fit results are summarized in Table 7.1. As shown in Fig. 7.14 and Table 7.1, GISAXS results indicate that the $R_{g,1}$'s (54.8–56.2 Å) and $R_{g,2}$ (95.5–99.7 Å), corresponding to $PC_{61}BM$ domains with largely two different sizes, were essentially identical with slight differences in protonated and deuterated P3HT/$PC_{61}BM$ blend system. This implies that deuterium substitution of P3HT does not significantly affect the size of $PC_{61}BM$ domains in the blend films.

Combined with structural and morphology study, MD-P3HT shows the lowest film crystallinity, the weakest intermolecular packing, and more random crystallites

in P3HT/$PC_{61}BM$ blends, which are responsible for the reduced J_{SC} and OPV efficiency. However, the significant V_{OC} loss observed in SD-P3HT/$PC_{61}BM$ was further attributed to a higher saturation dark current and the larger recombination of interfacial charge transfer state.

7.4 Tailoring the Structure and Orientation of Conjugated Molecular at Interface for High-Performance Photovoltaics

It is still a great challenge to enhance the charge collection efficiency and suppress the charge recombination loss in the bulk films or interfaces for achieving high-efficiency devices by interfacial control and assembly. In this part, we will discuss how to tailor the structure and molecular orientation at the different interfaces in organic photovoltaics to maximize charge collection gain and minimize charge recombination loss.

7.4.1 Interfacial Control at the Interfaces Between the Active Layer and Electrodes

Tailoring the interfaces between the active layer and electrodes is crucial to maximize charge collection gain and minimize charge recombination loss. The interfacial layer between active layer and electrodes is usually used to generate a strong interface dipole which could shift the vacuum levels to tune the work function of transparent electrodes, such as ITO [87]. The self-assembling monolayers (SAMs) of dipole molecules were also applied to modify the work function of metals and metal oxides [88–90]. For example, the saturated carboxylic acids with dipole moments and terminal groups are widely used as SAMs to tune the work function of metal electrodes [90]. Yuan et al. [91] applied two monolayers of the Langmuir–Blodgett (LB) ferroelectric copolymer film, polyvinylidene fluoride (70 %)-tetrafluoroethylene (30 %), P(VDF-TrFE), between the cathode and active layer to introduce an permanent electric field for improved charge separation and charge extraction efficiency. The device efficiency was increased from 1–2 % in the reference cells to 4–5 % in the cells with poled two monolayer P(VDF-TrFE).

Despite the use of SAMS for tuning the work function of ITO and metal electrodes, the obtained V_{oc} is still low. Recently, increasing the Schottky barrier height between the fullerene acceptor and anode was proposed to output larger V_{OC}. Yang et al. [92] found that the OPV devices with solution-processed fullerene (e.g., C_{60}, $PC_{61}BM$, ICBA) as the active layer can output a V_{OC} of around 0.86 V, which is higher than that of most BHJ devices. The variation trend of the obtained V_{OC} follows the LUMO of fullerene levels. These devices have a simple device structure

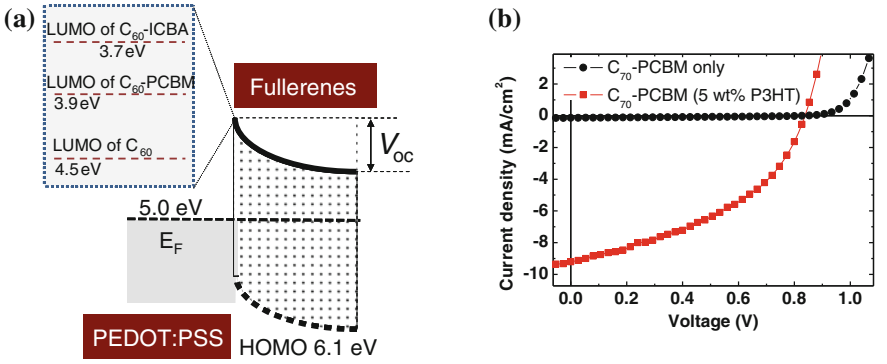

Fig. 7.15 **a** Schematic energy diagram showing the variation of V_{OC} following the LUMO of fullerene levels. **b** Device performance comparison between devices based on pristine $PC_{71}BM$ and devices based on $PC_{71}BM$ with adding 5 wt% P3HT. Reprinted with permission from Yang et al. [92]. © (2012) WILEY-VCH Verlag GmbH & Co. KGaA, Weinheim

of ITO/PEDOT:PSS/fullerene/bathocuproine (BCP)/Al. The Schottky barrier is expected to form at the fullerene/PEDOT:PSS contact as shown in Fig. 7.15a. The V_{OC} is determined by the LUMO of fullerene and work function of the anode. In these pure fullerene-based Schottky-junction OPVs, the photocurrent is as low as 1 mA/cm^2 due to poor hole extraction property. In order to extract the holes in the active fullerene films, 5 wt% donors was added into the fullerene film and a PCE of 3.3 % was achieved in these fullerene-based Schottky-junction devices (Fig. 7.15b). Yang et al. also found that V_{OC} in the devices with adding 5 wt% donors is still governed by the Schottky barrier height between the fullerene and anode [93].

7.4.2 *Interfacial Control at the Interfaces Between the Donor and the Acceptor*

Despite the fact that LUMO offset between the donor and the acceptor should be larger than the exciton binding energy for efficient photoinduced charge transfer, too large LUMO offset leads to unnecessary energy loss during the charge transfer process [40–48]. In order to reduce the LUMO offsets, modification of molecular structure in the donor and the acceptor by chemical approach was applied, which showed significant V_{OC} enhancement [94]. However, the chemical modification changed the chemical structure of the donor and thus altered the optoelectronic properties, resulting in degraded device performance.

In order to tailor the relative energy level offsets between the donor and the acceptor to enhance the V_{OC} without changing the molecular structure of donor and acceptor, Yang et al. introduced a thin ferroelectric dipole layer between the donor and the acceptor layers to tune the LUMO offset between the donor and the

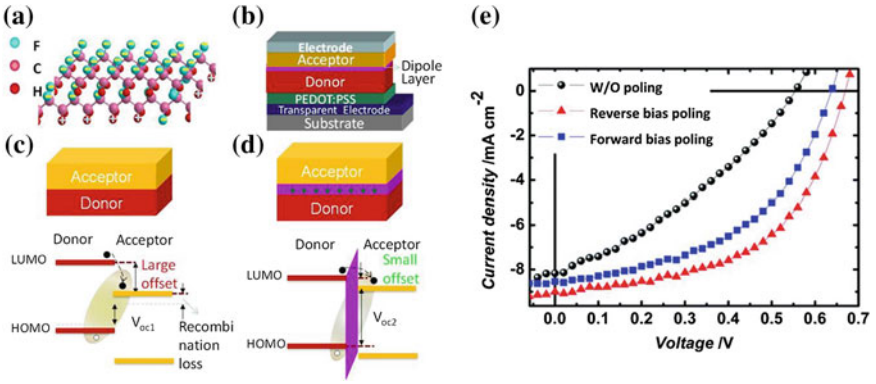

Fig. 7.16 **a** The molecular structure of a ferroelectric P(VDF-TrFE) dipole layer, **b** the device structure with a dipole layer inserted between the acceptor and the donor layers, the working principle to tune relative energy levels is shown in **c** bulk heterostructure without and **d** with a dipole layer inserted between the acceptor and the donor layers. **e** Tunable *J*–*V* curves with reverse bias poling and forward bias poling. Reprinted with permission from Yang et al. [51]. © (2012) WILEY-VCH Verlag GmbH & Co. KGaA, Weinheim

acceptor [51]. A ferroelectric dipole layer P(VDF-TrFE) can shift the relative energy levels of the donor and the acceptor (Fig. 7.16), because of the high polarization charge density originated from the large electron affinity difference between the fluorine (F) and hydrogen (H) atoms. One monolayer P(VDF-TrFE) (thickness of ~1.7 nm) was grown by LB deposition method [95].

By tuning the ferroelectric dipole direction, the relative energy levels can be tuned to reduce the LUMO offset between the donor and the acceptor to an optimized value for both efficient charge transfer and reduced energy loss. As a result, the energy level difference between the HOMO of the donor and the LUMO of the acceptor could be maximized, resulting in an enhanced V_{OC} [96, 97]. Yang et al. sandwiched the one monolayer P(VDF-TrFE) in the P3HT/$PC_{61}BM$ system and found that the V_{OC} increased from 0.55 to 0.67 V with poling by a large reverse bias to align the ferroelectric dipoles. In order to show the switching capability of P(VDF-TrFE) dipoles, the piezoelectric force microscopy (PFM) measurement was applied on these three-layer films. The PFM tip can detect the piezoelectric signal on the sample surface or even under a thin layer such as 20 nm PCBM. Figure 7.17a, b evidenced that the P(VDF-TrFE) layer was non-continuous on P3HT layer, because of the surface energy mismatch between the P(VDF-TrFE) (51 mJ m^{-2}) [98] and P3HT (26.9 mJ m^{-2}) [99]. As shown in Fig. 7.17c, d, the polarization was confirmed by the hysteresis loops of PFM phase and amplitude of P(VDF-TrFE). In addition, the polarization direction of P(VDF-TrFE) dipole could be fully switched by applying −6 V (Fig. 7.17e, f), which is a good evidence to show the switching behavior of inserted P(VDF-TrFE).

The electrostatic force microscopy (EFM) is a useful tool to characterize the surface potential change by measuring the electrostatic force between the tip and

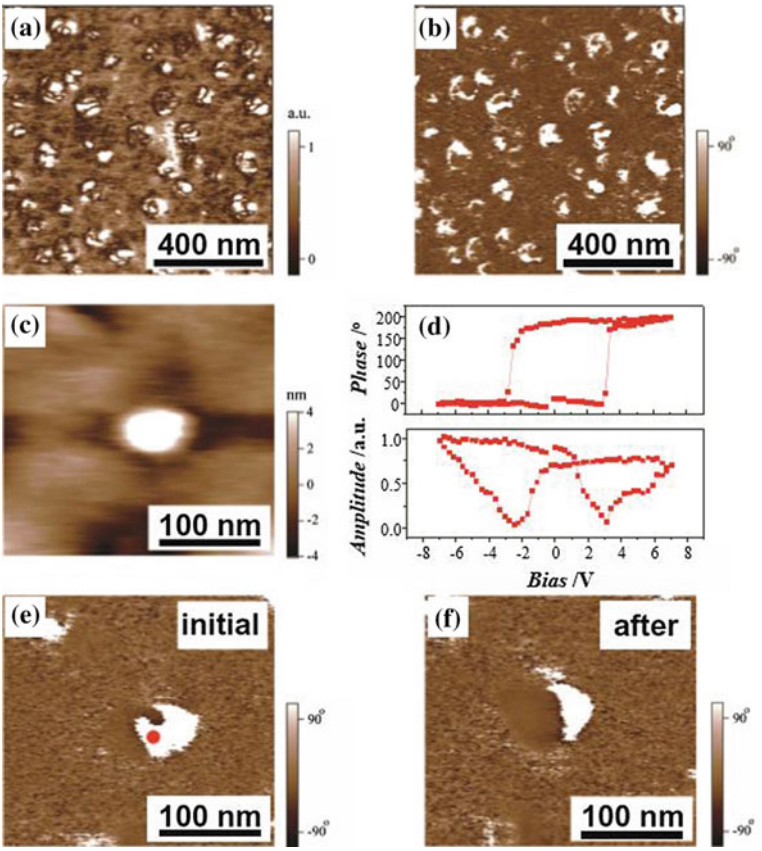

Fig. 7.17 **a**, **b** PFM images took on the films with ferroelectric P(VDF-TrFE) thin layer sandwiched between P3HT layer and PCBM layer (1.0 μm × 1.0 μm): **a** PFM amplitude, **b** PFM phase image; **c**–**f** show the ferroelectric switching of a P(VDF-TrFE) nanoisland: **c** topographic image of a single P(VDF-TrFE) nanoisland; **d** PFM hysteresis loops (phase and amplitude) of the P(VDF-TrFE) nanoisland (**c**); **e**, **f** PFM phase images of the P(VDF-TrFE) nanoisland before and after applying the voltage pulse (−6 V, 2 s). The *dark dot* in **e** marks the location of the PFM tip during voltage pulse application. Reprinted with permission from Yang et al. [51]. © (2012) WILEY-VCH Verlag GmbH & Co. KGaA, Weinheim

sample surface. Yang et al. [51] used EFM to confirm the tuning of relative energy levels between the P3HT and the $PC_{61}BM$. Approximate 100 mV surface potential change was observed on the surface of P(VDF-TrFE)/P3HT film after the voltage bias of 4 V was applied between the tip and the substrate to align the dipoles (Fig. 7.18). The change of 100 mV in surface potential on P(VDF-TrFE)/P3HT film is consistent with the tuned V_{OC} of 0.12 V.

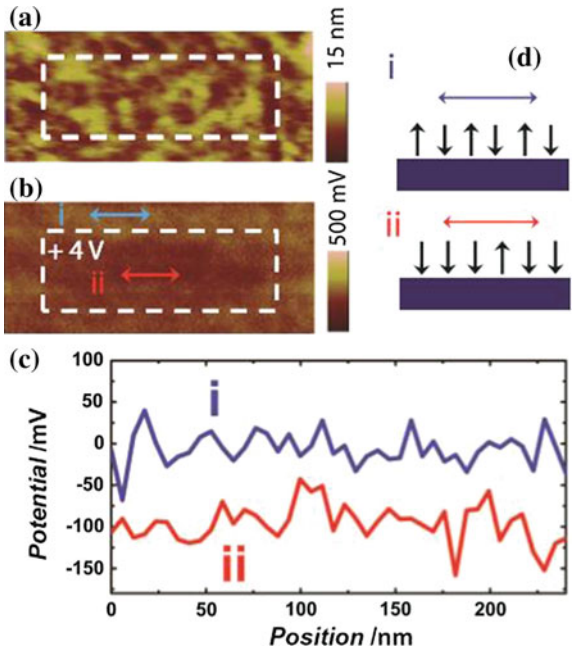

Fig. 7.18 Electrostatic force microscopy study on P(VDF-TrFE)/P3HT films: **a** topography and **b** surface potential map. The *white dotted rectangular* region was poled by +4 V voltage bias applied by the PFM tip (Image size is 1.0 μm × 3.0 μm), **c** cross-sectional analysis of the surface potential map along the *i* and *ii* lines as labeled in (**b**), **d** schematic illustration of the origin of the potential difference. Reprinted with permission from Yang et al. [51]. © (2012) WILEY-VCH Verlag GmbH & Co. KGaA, Weinheim

7.4.3 *Understanding Substrate-Assisted Alignment and Assembly of Conjugated Molecules for Organic Photovoltaics*

For OPVs, efficient light absorption, exciton diffusion, and dissociation in thin films rely upon aligning planar molecules facedown to the substrate. In this orientation, the transition dipole moment of the planar molecule, which is typically along its long axis, is in alignment with the electric field of the incident light. The simultaneous optimization of exciton and charge transport relies upon the microstructure and morphology determined by the molecular stacking at both the molecular scale and mesoscale. However, organic semiconductor molecules in films usually tend to exhibit an edge-on orientation on the surface of widely used substrates (e.g., SiO_2, ITO, or PEDOT/PSS). Therefore, controlling the orientation of molecules at hybrid interfaces is an ongoing challenge, and a carefully modified substrate can be a powerful tool. Recently, Xiao et al. [100] found that both natively grown graphene on copper substrates and graphene transferred onto a Si substrate act as effective

templates to orient and pack copper phthalocyanine (CuPc) molecules to a face-on orientation within thin films, which is the ideal structure for high-performance OPVs. Graphene, a large π-system with a monolayer of carbon atoms tightly packed into a two-dimensional honeycomb lattice, can promote the orientation of π-conjugated molecules through strong π–π interactions between the conjugated backbones and the graphene substrate. Scanning tunneling microscope (STM) measurements of the alignment of CuPc molecules on Si and graphene show quite different orientations. On Si substrates, CuPc is vertically aligned, like books on a shelf, while on graphene CuPc lies down in face-on orientation, like tiles on a roof. Moreover, CuPc tends to self-assemble at graphene grain boundaries, where defects provide additional charge density. CuPc molecules grown on graphene at room temperature exhibit a face-on orientation. However, following nucleation into islands and coalescence by edge growth into a continuous thin film CuPc molecule start to tilt up to and edge-on orientation. Higher growth temperatures are able to overcome this orientation change to maintain a fully face-on molecular orientation, forming extremely large, monocrystalline grains of CuPc on graphene within micro-meters-size, strip-like crystals. These types of CuPc crystals may potentially enable high mobility for a significant improvement of device properties in organic photovoltaics [100]. Kim et al. similarly found two different configurations (edge-on and face-on) for P3HT molecule formation on graphene and ITO substrates due to specific π–π interaction and van der Waals interaction between P3HT and a graphene monolayer, while only edge-on configurations of P3HT were found on the ITO [101].

In order to significantly improve the performance of OPVs, it is crucial to create an ordered BHJ structure with directional, long-range exciton diffusion and high charge carrier mobility along the optimal direction of the photovoltaic. Therefore, generating an ordered "nanostructured BHJ" that guarantees an adequate percolation of charges is the ultimate goal. Inorganic nanowires (NWs) have been widely combined with organic counterparts for hybrid solar cells, but exhibit low efficiency due to interfacial mismatches between organics and inorganics. Crystalline organic nanowires are a new and promising building block for organic electronics, which innately possess highly crystalline order for long-range, one-dimensional transport. This is a significant advantage compared to the morphological disorder and low charge mobility of polymers. Moreover, this quasi-one-dimensional morphology promises to also overcome the anisotropic transport limitations of small-molecule thin films, offering much higher mobilities and directional transport for improved photovoltaic efficiencies. Recently, Xiao et al. [102] synthesized organic crystalline nanowires of CuPc and metal-7,7,8,8-tetracyanoquinodimethane (TCNQ) [103] with highly efficient charge transport and effective optical absorption in a well-controlled manner using different vapor-phase techniques, including vapor-solid chemical reactions and vapor-phase deposition [102, 103]. The nanowires grow with the planar molecules π–π stacked along their length and could be grown in aligned arrays with these conducting axes aligned perpendicularly to the substrate in a suitable direction for carrier transport required for photovoltaic cells [104]. Their long-range crystalline order should result in increased exciton diffusion

length and carrier mobility several orders of magnitude higher than comparable organic thin films typically used in OPVs, where the conductive axis is aligned parallel to the substrate. Moreover, the direct electrical pathways provided by the organic nanowire ensure the rapid collection of carriers generated throughout the device. The nanoscale nanowires diameters coupled with their high aspect ratio are ideal for highly efficient charge separation, reduced surface optical reflection and enhanced absorption, and efficient carrier transport and collection for high-efficiency organic photovoltaics.

7.5 Summary

In summary, different chemical synthesis approaches were highlighted to illustrate how synthetic control of both low-bandgap polymer acceptors and fullerene derivative acceptors can be accomplished to tune and match their respective electronic energy levels for optimized charge transfer in OPV's. The importance of processing strategies to optimize the film morphologies using solvent annealing, thermal annealing, processing additives, and compatibilizers was also reviewed. Processing additives and interfacial compatibilizers were shown to have a great influence on the lateral and vertical film morphology, phase separation, molecular orientation and alignment, and polymer crystallinity. Finally, different strategies were introduced to show how to engineer the interfaces between the active layer and electrodes in concert with the donor/acceptor interfaces in order to modify the work functions and alignment of energy levels across the device taking advantage of various strategies for the self-assembly of molecular dipoles.

The development of OPV's for widespread commercialization is still in progress. The various important strategies, described in this chapter, such as design of molecular structure, optimization of film morphology, interfacial control and manipulation, are under intensive investigation. Controlling the ideal film morphology to realize efficient charge generation and charge separation, a nanoscience problem governing the formation of a network of bicontinuous interpenetrating nanophases, remains critically important to achieve competitive OPV device performance.

Very recently, organometal halide perovskite solar cells have emerged with PCEs rapidly increasing to over 20 % within a very short time [105–109]. The remarkable success of organic–inorganic hybrid perovskites is based upon the combination of the advantages of organic materials, such as low-cost, solution-processing capability, and flexibility, coupled with the advantages of inorganic semiconductors, such as high crystallinity and excellent charge transport properties. The versatile design and synthesis of organic molecules offers a wide range of tunability for the basic material structure, optoelectronic properties, and resulting film morphology which together promise to enhance the efficiency of organic/inorganic hybrid perovskite solar cells ever higher. Similar strategies as reviewed in this chapter, such as the design of conjugated polymers or

small-molecule donors and fullerene derivative acceptors, could be included as complementary absorbers in the perovskite solar cells. Ultimately, commercial synthetic and processing strategies that optimize the combination of efficiency, lifetime, and cost of OPV devices will determine the optimal organic solar cells of the future.

Acknowledgement This research was conducted at the Center for Nanophase Materials Sciences (CNMS) and the Spallation Neutron Source (SNS) which are sponsored at Oak Ridge National Laboratory by the Scientific User Facilities Division, Office of Basic Energy Sciences, US Department of Energy.

References

1. http://www.heliatek.com/
2. http://www.solarmer.com
3. Xu, T., Yu, L.: How to design low bandgap polymers for highly efficient organic solar cells. Mater. Today **17**, 11–15 (2014)
4. Kyaw, A.K.K., et al.: Efficient solution-processed small-molecule solar cells with inverted structure. Adv. Mater. **25**, 2397–2402 (2013)
5. Brabec, C.J., Durrant, J.R.: Solution-processed organic solar cells. MRS Bull. **33**, 670–675 (2008)
6. Mayer, A.C., Scully, S.R., Hardin, B.E., Rowell, M.W., McGehee, M.D.: Polymer-based solar cells. Mater. Today **10**, 28–33 (2007)
7. Deibel, C., Dyakonov, V.: Polymer–fullerene bulk heterojunction solar cells. Rep. Progr. Phys. **73**, 096401 (2010)
8. Menke, S.M., Luhman, W.A., Holmes, R.J.: Tailored exciton diffusion in organic photovoltaic cells for enhanced power conversion efficiency. Nat. Mater. **12**, 152–157 (2013)
9. Clarke, T.M., Durrant, J.R.: Charge photogeneration in organic solar cells. Chem. Rev. **110**, 6736–6767 (2010)
10. Günes, S., Neugebauer, H., Sariciftci, N.S.: Conjugated polymer-based organic solar cells. Chem. Rev. **107**, 1324–1338 (2007)
11. Yu, G., Gao, J., Hummelen, J., Wudl, F., Heeger, A.: Polymer photovoltaic cells: enhanced efficiencies via a network of internal donor-acceptor heterojunctions. Science **270**, 1789–1790 (1995)
12. Li, G., et al.: High-efficiency solution processable polymer photovoltaic cells by self-organization of polymer blends. Nat. Mater. **4**, 864–868 (2005)
13. Kim, Y., et al.: A strong regioregularity effect in self-organizing conjugated polymer films and high-efficiency polythiophene: fullerene solar cells. Nat. Mater. **5**, 197–203 (2006)
14. Campoy-Quiles, M., et al.: Morphology evolution via self-organization and lateral and vertical diffusion in polymer: fullerene solar cell blends. Nat. Mater. **7**, 158–164 (2008)
15. Kippelen, B., Brédas, J.-L.: Organic photovoltaics. Energy Environ. Sci. **2**, 251–261 (2009)
16. Schultz, O., Glunz, S., Willeke, G.: Short communication: accelerated publication: Multicrystalline silicon solar cells exceeding 20 % efficiency. Prog. Photovoltaics Res. Appl. **12**, 553–558 (2004)
17. Sun, Z., et al.: PS-b-P3HT copolymers as P3HT/PCBM interfacial compatibilizers for high efficiency photovoltaics. Adv. Mater. **23**, 5529–5535 (2011)
18. Lee, J.K., et al.: Processing additives for improved efficiency from bulk heterojunction solar cells. J. Am. Chem. Soc. **130**, 3619–3623 (2008)

19. Shao, M., et al.: Understanding how processing additives tune the nanoscale morphology of high efficiency organic photovoltaic blends: from casting solution to spun-cast thin film. Adv. Funct. Mater. **24**, 6647–6657 (2014)
20. Keum, J.K., et al.: Morphological origin for the stratification of P3HT: PCBM blend film studied by neutron reflectometry. Appl. Phys. Lett. **103**, 223301 (2013)
21. Staniec, P.A., et al.: The nanoscale morphology of a PCDTBT: PCBM photovoltaic blend. Adv. Energy Mater. **1**, 499–504 (2011)
22. Peet, J., Heeger, A.J., Bazan, G.C.: "Plastic" solar cells: self-assembly of bulk heterojunction nanomaterials by spontaneous phase separation. Acc. Chem. Res. **42**, 1700–1708 (2009)
23. Peet, J., et al.: Efficiency enhancement in low-bandgap polymer solar cells by processing with alkane dithiols. Nat. Mater. **6**, 497–500 (2007)
24. Cheng, Y.-J., Yang, S.-H., Hsu, C.-S.: Synthesis of conjugated polymers for organic solar cell applications. Chem. Rev. **109**, 5868–5923 (2009)
25. Hou, J., et al.: Synthesis of a low band gap polymer and its application in highly efficient polymer solar cells. J. Am. Chem. Soc. **131**, 15586–15587 (2009)
26. Zhou, J., et al.: Small molecules based on benzo [1, 2-b: 4, 5-b′] dithiophene unit for high-performance solution-processed organic solar cells. J. Am. Chem. Soc. **134**, 16345–16351 (2012)
27. Zhou, H., Yang, L., You, W.: Rational design of high performance conjugated polymers for organic solar cells. Macromolecules **45**, 607–632 (2012)
28. Park, S.H., et al.: Bulk heterojunction solar cells with internal quantum efficiency approaching 100&percnt. Nat. Photonics **3**, 297–302 (2009)
29. Maurano, A., et al.: Recombination dynamics as a key determinant of open circuit voltage in organic bulk heterojunction solar cells: a comparison of four different donor polymers. Adv. Mater. **22**, 4987 (2010)
30. Cowan, S.R., Roy, A., Heeger, A.J.: Recombination in polymer-fullerene bulk heterojunction solar cells. Phys. Rev. B **82**, 245207 (2010)
31. Garcia-Belmonte, G., et al.: Charge carrier mobility and lifetime of organic bulk heterojunctions analyzed by impedance spectroscopy. Org. Electron. **9**, 847–851 (2008)
32. Vandewal, K., Tvingstedt, K., Gadisa, A., Inganäs, O., Manca, J.V.: On the origin of the open-circuit voltage of polymer–fullerene solar cells. Nat. Mater. **8**, 904–909 (2009)
33. Cowan, S.R., Banerji, N., Leong, W.L., Heeger, A.J.: Charge formation, recombination, and sweep-out dynamics in organic solar cells. Adv. Funct. Mater. **22**, 1116–1128 (2012)
34. Maurano, A., et al.: Recombination dynamics as a key determinant of open circuit voltage in organic bulk heterojunction solar cells: a comparison of four different donor polymers. Adv. Mater. **22**, 4987–4992 (2010)
35. Street, R., Cowan, S., Heeger, A.: Experimental test for geminate recombination applied to organic solar cells. Phys. Rev. B **82**, 121301 (2010)
36. Koster, L., Mihailetchi, V., Blom, P.: Bimolecular recombination in polymer/fullerene bulk heterojunction solar cells. Appl. Phys. Lett. **88**, 052104 (2006)
37. Shuttle, C., et al.: Bimolecular recombination losses in polythiophene: Fullerene solar cells. Phys. Rev. B **78**, 113201 (2008)
38. Groves, C., Greenham, N.: Bimolecular recombination in polymer electronic devices. Phys. Rev. B **78**, 155205 (2008)
39. Koster, L., Kemerink, M., Wienk, M.M., Maturová, K., Janssen, R.A.: Quantifying bimolecular recombination losses in organic bulk heterojunction solar cells. Adv. Mater. **23**, 1670–1674 (2011)
40. Kirchartz, T., Taretto, K., Rau, U.: Efficiency limits of organic bulk heterojunction solar cells. J. Phys. Chem. C **113**, 17958–17966 (2009)
41. Vandewal, K., Tvingstedt, K., Manca, J.V., Inganas, O.: Charge-transfer states and upper limit of the open-circuit voltage in polymer: fullerene organic solar cells. IEEE J. Sel. Top. Quantum Electron. **16**, 1676–1684 (2010)
42. Amb, C.M., et al.: Dithienogermole as a fused electron donor in bulk heterojunction solar cells. J. Am. Chem. Soc. **133**, 10062 (2011)

43. Chen, H.Y., et al.: Polymer solar cells with enhanced open-circuit voltage and efficiency. Nat. Photonics **3**, 649–653 (2009)
44. He, Z., et al.: Simultaneous enhancement of open circuit voltage, short circuit current density, and fill factor in polymer solar cells. Adv. Mater. **23**, 4636 (2011)
45. Liang, Y., et al.: For the bright future-bulk heterojunction polymer solar cells with power conversion efficiency of 7.4 %. Adv. Mater. **22**, E135–E138 (2010)
46. Loser, S., et al.: A naphthodithiophene-diketopyrrolopyrrole donor molecule for efficient solution-processed solar cells. J. Am. Chem. Soc. **133**, 8142 (2011)
47. Park, S.H., et al.: Bulk heterojunction solar cells with internal quantum efficiency approaching 100 % percent. Nat. Photonics **3**, 297–302 (2009)
48. Price, S.C., Stuart, A.C., Yang, L., Zhou, H., You, W.: Fluorine substituted conjugated polymer of medium band gap yields 7 % efficiency in polymer-fullerene solar cells. j. Am. Chem. Soc. **133**, 4625 (2011)
49. He, Z., et al.: Enhanced power-conversion efficiency in polymer solar cells using an inverted device structure. Nat. Photonics **6**, 591–595 (2012)
50. Sun, Y., et al.: Solution-processed small-molecule solar cells with 6.7 % efficiency. Nat. Mater. **11**, 44–48 (2012)
51. Yang, B., et al.: Tuning the energy level offset between donor and acceptor with ferroelectric dipole layers for increased efficiency in bilayer organic photovoltaic cells. Adv. Mater. **24**, 1455–1460 (2012)
52. Ross, R.B., et al.: Endohedral fullerenes for organic photovoltaic devices. Nat. Mater. **8**, 208–212 (2009)
53. Ross, R.B., et al.: Tuning conversion efficiency in metallo endohedral fullerene-based organic photovoltaic devices. Adv. Funct. Mater. **19**, 2332–2337 (2009)
54. He, Y., Chen, H.-Y., Hou, J., Li, Y.: Indene-C60 bisadduct: a new acceptor for high-performance polymer solar cells. J. Am. Chem. Soc. **132**, 1377–1382 (2010)
55. Zhao, G., He, Y., Li, Y.: 6.5 % efficiency of polymer solar cells based on poly (3-hexylthiophene) and Indene-C60 Bisadduct by Device Optimization. Adv. Mater. **22**, 4355–4358 (2010)
56. Cheng, Y.-J., Hsieh, C.-H., He, Y., Hsu, C.-S., Li, Y.: Combination of indene-C60 bis-adduct and cross-linked fullerene interlayer leading to highly efficient inverted polymer solar cells. J. Am. Chem. Soc. **132**, 17381–17383 (2010)
57. Nelson, J.: Polymer: fullerene bulk heterojunction solar cells. Mater. Today **14**, 462–470 (2011)
58. Credgington, D., Durrant, J.R.: Insights from transient optoelectronic analyses on the open-circuit voltage of organic solar cells. J. Phys. Chem. Lett. **3**, 1465–1478 (2012)
59. He, Y., Shao, M., Xiao, K., Smith, S.C., Hong, K.: High-performance polymer photovoltaics based on rationally designed fullerene acceptors. Sol. Energ. Mat. Solar Cells **118**, 171–178 (2013)
60. Cnops, K. et al.: 8.4 % efficient fullerene-free organic solar cells exploiting long-range exciton energy transfer. Nat. Commun. **5** (2014)
61. Facchetti, A.: Polymer donor–polymer acceptor (all-polymer) solar cells. Mater. Today **16**, 123–132 (2013)
62. McNeill, C.R., et al.: Photophysics and photocurrent generation in polythiophene/polyfluorene copolymer blends. Adv. Funct. Mater. **19**, 3103–3111 (2009)
63. Vanlaeke, P., et al.: P3HT/PCBM bulk heterojunction solar cells: relation between morphology and electro-optical characteristics. Sol. Energ. Mat. Solar Cells **90**, 2150–2158 (2006)
64. Li, G., Shrotriya, V., Yao, Y., Yang, Y.: Investigation of annealing effects and film thickness dependence of polymer solar cells based on poly (3-hexylthiophene). J. Appl. Phys. **98**, 043704 (2005)
65. Liu, H.-J., et al.: Surface and interface porosity of polymer/fullerene-derivative thin films revealed by contrast variation of neutron and X-ray reflectivity. Soft Matter **7**, 9276–9282 (2011)

66. Kirschner, S.B., et al.: X-ray and neutron reflectivity and electronic properties of PCBM-poly (bromo) styrene blends and bilayers with poly (3-hexylthiophene). J. Mater. Chem. **22**, 4364–4370 (2012)
67. Ruderer, M.A., et al.: Thin films of photoactive polymer blends. ChemPhysChem **10**, 664–671 (2009)
68. Parratt, L.G.: Surface studies of solids by total reflection of X-rays. Phys. Rev. **95**, 359 (1954)
69. Collins, B.A., et al.: Molecular miscibility of polymer-fullerene blends. J. Phys. Chem. Lett. **1**, 3160–3166 (2010)
70. Parnell, A.J., et al.: Nanoscale phase separation of P3HT PCBM thick films as measured by small-angle X-ray scattering. Macromolecules **44**, 6503–6508 (2011)
71. Jamieson, F.C., et al.: Fullerene crystallisation as a key driver of charge separation in polymer/fullerene bulk heterojunction solar cells. Chem. Sci. **3**, 485–492 (2012)
72. Collins, B.A., Tumbleston, J.R., Ade, H.: Miscibility, crystallinity, and phase development in P3HT/PCBM solar cells: toward an enlightened understanding of device morphology and stability. J. Phys. Chem. Lett. **2**, 3135–3145 (2011)
73. Hegde, R., et al.: The impact of controlled solvent exposure on the morphology, structure and function of bulk heterojunction solar cells. Sol. Energ. Mat. Solar Cells **107**, 112–124 (2012)
74. Galloway, J.A., Jeon, H.K., Bell, J.R., Macosko, C.W.: Block copolymer compatibilization of cocontinuous polymer blends. Polymer **46**, 183–191 (2005)
75. Chen, J., et al.: Ternary behavior and systematic nanoscale manipulation of domain structures in P3HT/PCBM/P3HT-b-PEO films. J. Mater. Chem. **22**, 13013–13022 (2012)
76. Wang, D.H., et al.: Sequential processing: control of nanomorphology in bulk heterojunction solar cells. Nano Lett. **11**, 3163–3168 (2011)
77. Chen, D., Liu, F., Wang, C., Nakahara, A., Russell, T.P.: Bulk heterojunction photovoltaic active layers via bilayer interdiffusion. Nano Lett. **11**, 2071–2078 (2011)
78. Moon, J.S., Takacs, C.J., Sun, Y., Heeger, A.J.: Spontaneous formation of bulk heterojunction nanostructures: multiple routes to equivalent morphologies. Nano Lett. **11**, 1036–1039 (2011)
79. Ayzner, A.L., Tassone, C.J., Tolbert, S.H., Schwartz, B.J.: Reappraising the need for bulk heterojunctions in polymer-fullerene photovoltaics: the role of carrier transport in all-solution-processed P3HT/PCBM bilayer solar cells. J. Phys. Chem. C **113**, 20050–20060 (2009)
80. Lee, K.H., et al.: Morphology of all-solution-processed "bilayer" organic solar cells. Adv. Mater. **23**, 766–770 (2011)
81. Huang, J.-H., et al.: Efficient bilayer polymer solar cells possessing planar mixed-heterojunction structures. J. Mater. Chem. **20**, 3295–3300 (2010)
82. Yang, B., Yuan, Y., Huang, J.: Reduced bimolecular charge recombination loss in thermally annealed bilayer heterojunction photovoltaic devices with large external quantum efficiency and fill factor. J. Phys. Chem. C **118**, 5196–5202 (2014)
83. Tong, C.C., Hwang, K.C.: Enhancement of OLED efficiencies and high-voltage stabilities of light-emitting materials by deuteration. J. Phys. Chem. C **111**, 3490–3494 (2007)
84. Shao, M., et al.: The isotopic effects of deuteration on optoelectronic properties of conducting polymers. Nat. Commun. **5**, 3180 (2014)
85. Hammouda, B.: A new guinier-porod model. J. Appl. Crystallogr. **43**, 716–719 (2010)
86. Griffith, W., Triolo, R., Compere, A.: Analytical scattering function of a polydisperse Percus-Yevick fluid with Schulz-(Γ-) distributed diameters. Phys. Rev. A **35**, 2200 (1987)
87. Zhou, Y., et al.: A universal method to produce low–work function electrodes for organic electronics. Science **336**, 327–332 (2012)
88. Yip, H.-L., Hau, S.K., Baek, N.S., Ma, H., Jen, A.K.-Y.: Polymer solar cells that use self-assembled-monolayer-modified ZnO/metals as cathodes. Adv. Mater. **20**, 2376–2382 (2008)
89. de Boer, B., Hadipour, A., Mandoc, M.M., van Woudenbergh, T., Blom, P.W.: Tuning of metal work functions with self-assembled monolayers. Adv. Mater. **17**, 621–625 (2005)

90. Tseng, C.-T., et al.: Study of anode work function modified by self-assembled monolayers on pentacene/fullerene organic solar cells. Appl. Phys. Lett. **91**, 233510 (2007)
91. Yuan, Y., et al.: Efficiency enhancement in organic solar cells with ferroelectric polymers. Nat. Mater. **10**, 296–302 (2011)
92. Yang, B., et al.: Solution-processed fullerene-based organic Schottky junction devices for large-open-circuit-voltage organic solar cells. Adv. Mater. **25**, 572–577 (2013)
93. Yang, B., Xiao, Z., Huang, J.: Polymer aggregation correlated transition from Schottky-junction to bulk heterojunction organic solar cells. Appl. Phys. Lett. **104**, 143304 (2014)
94. Tada, A., Geng, Y., Wei, Q., Hashimoto, K., Tajima, K.: Tailoring organic heterojunction interfaces in bilayer polymer photovoltaic devices. Nat. Mater. **10**, 450–455 (2011)
95. Bune, A.V., et al.: Two-dimensional ferroelectric films. Nature **391**, 874–877 (1998)
96. Brabec, C.J., et al.: Origin of the open circuit voltage of plastic solar cells. Adv. Funct. Mater. **11**, 374–380 (2001)
97. Scharber, M.C., et al.: Design rules for donors in bulk heterojunction solar cells towards 10 % energy conversion efficiency. Adv. Mater. **18**, 789–794 (2006)
98. Wi, S., Senthilkumar, N., Rhee, S.-W.: Characterization of poly (vinylidene fluoride-trifluoroethylene) 50/50 copolymer films as a gate dielectric. J. Mater. Sci. Mater. Electron. **19**, 45–50 (2008)
99. Germack, D.S., et al.: Substrate-dependent interface composition and charge transport in films for organic photovoltaics. Appl. Phys. Lett. **94**, 233303 (2009)
100. Xiao, K., et al.: Surface-induced orientation control of CuPc molecules for the epitaxial growth of highly ordered organic crystals on graphene. J. Am. Chem. Soc. **135**, 3680–3687 (2013)
101. HwanáKim, D., SugáLee, H.: Graphene surface induced specific self-assembly of poly (3-hexylthiophene) for nanohybrid optoelectronics: from first-principles calculation to experimental characterizations. Soft Matter **9**, 5355–5360 (2013)
102. Xiao, K., et al.: Metastable copper-phthalocyanine single-crystal nanowires and their use in fabricating high-performance field-effect transistors. Adv. Funct. Mater. **19**, 3776–3780 (2009)
103. Xiao, K., Yoon, M., Rondinone, A.J., Payzant, E.A., Geohegan, D.B.: Understanding the metal-directed growth of single-crystal M-TCNQF4 organic nanowires with time-resolved, in situ X-ray diffraction and first-principles theoretical studies. J. Am. Chem. Soc. **134**, 14353–14361 (2012)
104. Xiao, K., et al.: Single-crystal organic nanowires of copper–tetracyanoquinodimethane: synthesis, patterning, characterization, and device applications. Angew. Chem. Int. Ed. **119**, 2704–2708 (2007)
105. Yang, B., et al.: Perovskite solar cells with near 100 % internal quantum efficiency based on large single crystalline grains and vertical bulk heterojunctions. J. Am. Chem, Soc. **137**, 9210–9213 (2015)
106. Sanjib, D., et al.: High-performance flexible perovskite solar cells by using a combination of ultrasonic spray-coating and low thermal budget photonic curing. ACS Photonics **2**, 680–685 (2015)
107. Yang, W.S., et al.: High-performance photovoltaic perovskite layers fabricated through intramolecular exchange. Science **348**, 1234–1237 (2015)
108. Burschka, J., et al.: Sequential deposition as a route to high-performance perovskite-sensitized solar cells. Nature **499**, 316–319 (2013)
109. Liu, M., Johnston, M.B., Snaith, H.J.: Efficient planar heterojunction perovskite solar cells by vapour deposition. Nature **501**, 395–398 (2013)

Chapter 8
Solar Cell Characterization

Behrang H. Hamadani and Brian Dougherty

8.1 Introduction

The solar cell characterizations covered in this chapter address the electrical power generating capabilities of the cell. Some of these covered characteristics pertain to the workings within the cell structure (e.g., charge carrier lifetimes), while the majority of the highlighted characteristics help establish the macro-performance of the finished solar cell (e.g., spectral response, maximum power output). Specific performance characteristics of solar cells are summarized, while the method(s) and equipment used for measuring these characteristics are emphasized.

The most obvious use for solar cells is to serve as the primary building block for creating a solar module. As such, a key pursuit is to manufacture a solar module, or more correctly, to manufacture each unique model or product line of photovoltaic (PV) module, using cells that perform as similarly as possible. To achieve that end, manufacturers conduct quick measurements of mass-produced cells and then allocate them into a few groups or "bins" based on those measurements. The key cell characteristic(s) used for binning are embodied in the cell's electrical current versus voltage (I–V) relationship, Fig. 8.1. From these curves, the cell's maximum power output, short-circuit current , and open-circuit voltage, in particular, are identified.

Additional cell parameters and relationships are used to more fully characterize a solar cell. These additional characteristics include, but are not limited to, spectral response, fill factor, series resistance, temperature coefficients, and quantum efficiency. Knowledge of these additional parameters is helpful, for example, when developing, evaluating, and fine tuning a new cell design and manufacturing process. Characterizations that focus on maximizing accuracy, moreover, are especially important for the purpose of creating reference cells. Reference cells serve as transfer standards that can be used by manufacturers and third-party testing

B.H. Hamadani (✉) · B. Dougherty
National Institute of Standards and Technology, Gaithersburg, MD 20899, USA
e-mail: behrang.hamadani@nist.gov

M.P. Paranthaman et al. (eds.), *Semiconductor Materials for Solar Photovoltaic Cells*, Springer Series in Materials Science 218,
DOI 10.1007/978-3-319-20331-7_8

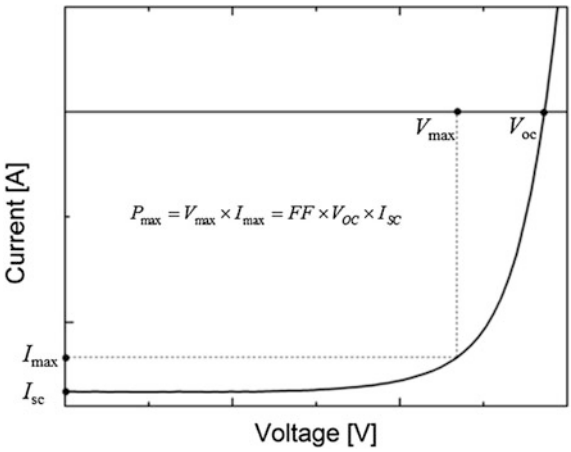

Fig. 8.1 A generic *I–V* curve of a solar cell under sun illumination

laboratories to generate and verify, respectively, published ratings of production cells and modules. Most primary PV characterization laboratories aim to achieve overall uncertainties of better than 1 % on their standard reference cells, while the secondary laboratories aim to achieve better than 2 % overall uncertainties when calibrating cells for customers.

8.2 *I–V* Curves: Features and Uses

Measurements of the electrical current versus voltage (*I–V*) curves of a solar cell or module provide a wealth of information. Solar cell parameters gained from every *I–V* curve include the short-circuit current, I_{sc}, the open-circuit voltage, V_{oc}, the current I_{max} and voltage V_{max} at the maximum power point P_{max}, the fill factor (FF) and the power conversion efficiency of the cell, η [1–5]. These parameters are shown in the Fig. 8.1 *I–V* curve for a generic single-junction cell when subjected to a specific level of solar illumination and otherwise operated at a specific set of conditions. Notably, the FF is an indication of internal losses that is visually communicated by how much the *I–V* characteristic curve deviates from a rectangular shape in the shown 4th current–voltage quadrant.

The electrical generation of a photovoltaic cell (or module), as revealed in its *I–V* curves, depends on many factors, including, but not limited to, the incident solar radiation spectrum, the orientation of the cell relative to the beam component of that solar input, the resulting operating temperature of the cell, and the applied electrical load that completes the DC circuit. To readily allow comparisons between cells, *I–V* curves are measured and reported based on common sets of operating conditions. The primary set of operating conditions is the standard reporting conditions (SRC), which are also called standard test conditions (STC). The standard reference spectrum for SRC is an air mass 1.5 global (AM 1.5G) solar spectrum

with a total irradiance of 1000 W/m^2 [6]. This spectrum corresponds to what would typically be observed at the surface of the earth for mid-latitudes and it contains a direct radiation component of about 88 % of the total irradiance with the rest in diffuse irradiance originating from hemispheric sky and ground reflections and scattering of light. The SRC-specified device operating temperature is 25 °C. Finally, when the power rating of a cell or module is reported and used to market the product, it almost always corresponds to the current–voltage pair along the SRC *I–V* curve that yields the highest power.

From a practical point of view, it is difficult to obtain SRC in an outdoor setting. Therefore, most testing laboratories perform these electrical measurements under simulated sunlight in an indoor environment. Indoor testing under a solar simulator has several advantages over outdoor measurements; indoor testing, however, also introduces some measurement challenges, as discussed below.

Solar simulator *I–V* curve measurements of cells are typically carried out in the testing laboratory by employing a second cell, a calibrated reference cell. This reference cell is used to monitor and measure the total irradiance of the solar simulator during *I–V* testing. Based on this measurement, the output of the solar simulator can be adjusted to provide the approximate intensity required (e.g., 1000 W/m^2 for SRC) and to normalize the output from the device under test to this nominal rating condition. A commonly used reference cell is a Si cell packaged based on the World Photovoltaic Scale (WPVS) design [7]. Reference cells can be purchased directly from commercial vendors or, in some cases, obtained directly from a certified secondary laboratory. Vendors, who package the reference cells but lack in-house calibration capabilities, will have the cell calibrated by the certified secondary laboratory or, in some cases, by a primary calibration laboratory such as the National Renewable Energy Laboratory in the USA.

If the reference cell has very similar characteristics (e.g., spectral response) to the cell under test, then *I–V* testing is relatively straightforward. However, that scenario is not often the case, such as when one is trying to measure the *I–V* curve of a CdTe solar cell, and the only available reference cell is Si-based. In such cases, a deviation arises from the *mismatch* between the responsivity of the two cells. For example, the reference cell may indicate an irradiance of 1000 W/m^2 even if the spectrum deviates from the nominal AM 1.5 spectrum. If the device under test is not responsive in the part of the simulator's spectrum that deviates from AM 1.5, a scaling to 1000 W/m^2 will not be representative of the test cell's actual performance under AM 1.5. Furthermore, since the majority, if not all, of the solar simulators do not generate a true irradiance match to the SRC spectrum or may not have the same level of light collimation as designated in the standard, an additional source of error is introduced into the electrical measurements. The resulting adverse impact on the *I–V* measurement may become significant with second- and third-generation PV cell technologies when the operator primarily uses a single crystalline silicon cell as the reference cell. Fortunately, there is a way to compensate for these deviations, by calculating a spectral mismatch factor, *M*, and using it to correct each electrical current value from the raw *I–V* curve data [2]. Furthermore, the temporal stability of the light source during the course of the measurement and the uniformity of the

illumination at the measurement plane can also introduce errors. Key steps for determining a mismatch factor, along with other useful information that aids in performing successful *I–V* measurements of single-junction solar cells and modules, are described in the below chapter subsections.

8.3 Solar Simulator Performance

A solar simulator is a light source with a broadband optical output similar to that of the sun over the response range of different solar cell technologies. Solar simulators can be used for electrical characterization of solar cells as well as irradiance exposure of materials and devices. A solar simulator operates in either a steady-state mode or a pulsed mode. The type of lamp used in the simulator can vary among different models. Xenon arc lamps, metal halide arc lamps, quartz tungsten halogen lamps, and light-emitting diodes (LEDs) have all been used in simulators, with Xe lamps being the most common [3]. Regardless of the type, a solar simulator is currently [8] evaluated based on three unique criteria: (1) spectral match to the reference spectrum over a certain wavelength range, (2) non-uniformity of the irradiance within the measurement test plane, and (3) temporal instability of the irradiance during the course of the measurement. Irradiance represents the power of the electromagnetic radiation per unit area of the incident surface and is expressed in units of watts per meter squared (W/m^2). When the irradiance measurement is expressed as a function of the wavelength, it is called *spectral irradiance* and has units of W/m^3, or more commonly, $W/m^2/nm$.

Figure 8.2 shows the irradiance spectrum of a Xe flash solar simulator compared to the industry standard AM 1.5 global tilt spectrum. Although the Xe simulator provides a reasonably good match to the sun spectrum, the match is not without substantial deviations, particularly at wavelengths greater than 800 nm. As per the

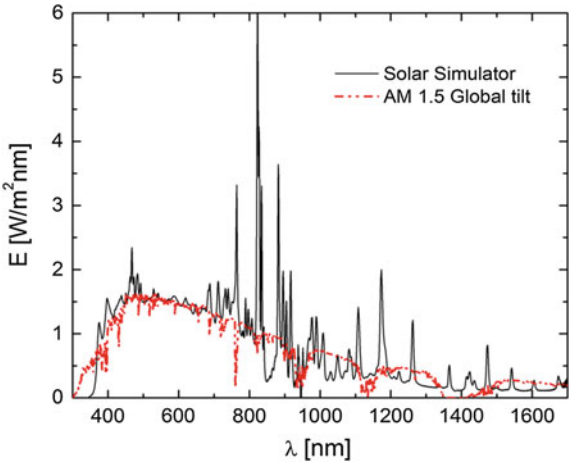

Fig. 8.2 The irradiance spectrum of a Xe flash solar simulator. For comparison, the AM 1.5G spectrum is also plotted

Table 8.1 Example of the spectral mismatch rating determination for the Xe solar simulator

Wavelength range (nm)	Measured percentages (%)	IEC standard percentages (%)	IEC ratio	Class rating
400–500	18.8	18.4	1.02	A
500–600	18.3	19.9	0.92	A
600–700	16.9	18.4	0.92	A
700–800	16.9	14.9	1.13	A
800–900	15.4	12.5	1.24	A
900–1100	13.7	15.9	0.86	A

current IEC standard for evaluating a solar simulator [8], the radiant energy delivered at the test plane by the simulator for 6 contiguous wavelength intervals is first determined. The irradiance for each interval is then divided by the total 6-interval irradiance, and the resulting measured percentages are compared with the percentages for the reference spectrum. This comparison is achieved by calculating the ratio of the percentage from the simulator to the corresponding percentage for the reference spectrum. A letter grade is assigned for each wavelength interval based on the magnitude of the ratio relative to limits prescribed in the consensus standard. For example, a ratio between 0.75 and 1.25 constitutes an "A" rating, while a "B" rating is assigned if the ratio falls outside the A range but within 0.6 and 1.4. The overall spectral grade of the solar simulator is assigned based on the lowest grade for any interval. Thus, for a simulator to achieve a Class A rating with respect to spectrum, a ratio between 0.75 and 1.25 must be achieved for all 6 intervals. This calculation is demonstrated for the simulator data of Fig. 8.2 in Table 8.1. This simulator obtains a rating of A for spectral match although it can be seen that the 800 nm to 900 nm interval is on the A/B class borderline (1.25).

Regarding the nonuniformity of irradiance, a rating of A is given to a simulator with better than 2 % for its "non-uniformity of irradiance percentage" as calculated below. The limit for a class B rating is 5 %, while the limit for a class C rating is 10 %. The non-uniformity is evaluated by dividing up the test area into at least 64 equal blocks and using a detector to measure irradiance. A broadband detector having the needed small footprint, while being stable, sufficiently fast, and having a linear response over the range of the measured irradiances is recommended. If the temporal stability of the light source is questionable over the course of completing the set of irradiance measurements, then the measurements should be performed all at one time using an array of calibrated detectors. The non-uniformity is obtained from the relation:

$$\text{Non-uniformity } (\%) = \left[\frac{\text{max irradiance} - \text{min irradiance}}{\text{max irradiance} + \text{min irradiance}}\right] \times 100 \qquad (8.1)$$

where max and min correspond to the maximum and minimum irradiance levels across the measured test plane.

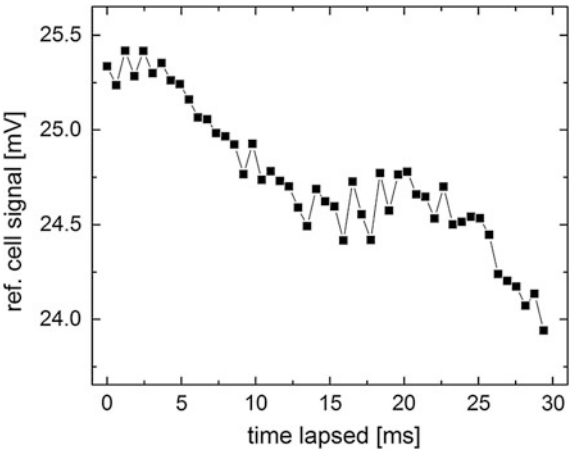

Fig. 8.3 The temporal stability of a flash solar simulator during the course of a 30 ms *I–V* measurement

The temporal instability of the simulator must also be evaluated and involves both short-term and long-term instabilities. Short-term instability is evaluated over the sampling interval of each unique data set (voltage, current, irradiance) during the *I–V* measurement whereas long-term instability considers the variation in the simulator's generated irradiance over the entire *I–V* curve measurement. Interestingly, long-term temporal instability is calculated using the exact same equation as given above for non-uniformity—only now using data collected during the actual *I–V* curve measurement—with the grading limits also being the same (i.e., 2 % for A, 5 % for B, and 10 % for C). Figure 8.3 shows an example of long-term temporal instability monitoring for a flash solar simulator during a 30-ms time interval when an entire *I–V* sweep was performed (with a total flash duration of 36 ms). These data reveal a temporal instability of just under 3 %, for a B rating. In cases such as this, normalizing each *I–V* data pair to the instantaneous measured irradiance by using the corresponding irradiance measurement is recommended in order to reduce the uncertainty in the final curve. Alternatively, other actions (such as changing the light bulb and servicing the power supply electronics) can be pursued in an effort to minimize the issue. Otherwise, one must accept the larger uncertainty associated with the *I–V* measurement.

8.4 Spectral Irradiance Measurements

The spectral output of a solar simulator or any light source is measured using a calibrated spectroradiometer [9, 10]. Nowadays, these instruments are typically spectrographs equipped with fast photodiode arrays or Si charge-coupled devices (CCD) that provide sensitive and reliable information regarding the spectrum and intensity of the light. In order to obtain a sufficiently wide spectral range, two or more types of detector arrays might be necessary, such as Si- and InGaAs-based

arrays. Furthermore, correct measurements of irradiance require the spectroradiometer to be calibrated against a known light source such as a calibrated 1000-W FEL lamp [9]. An FEL lamp is an ANSI standard 1000-W tungsten halogen incandescent lamp, and its calibration is based on the absolute radiometric determination of the freezing temperature of gold. The calibrated reference lamp needs to be operated under a set of very precise conditions. The most important of these operational conditions are as follows: (1) the use of a very stable, high accuracy power supply with a feedback mechanism for precise control of the lamp's current (typically 8.2 A) and (2) the proper alignment and placement of the spectroradiometer collection optics at a specified distance from the center of the bulb filament. Since an output accuracy of better than 0.1 % is typically required, the lamp's input current has to be set and maintained to better than 0.01 % during the course of the calibration.

Periodic calibration of the spectroradiometer is necessary to ensure an overall low uncertainty budget. Additionally, the irradiance characteristics of the simulator must be measured on a regular basis because, as the lamps age, the shape of their spectral output changes as well. A change in the shape of the spectrum not only can affect the overall class rating of the solar simulator but also can significantly impact the corrected *I–V* curve, as elaborated later in this chapter.

8.5 Spectral Response Measurements of Solar Cells

The spectral responsivity of a solar cell, *R*,—which quantifies the wavelength dependence of the cell's photocurrent generation when normalized for the input irradiance or the radiant power of the incident monochromatic radiation—is a very informative and thus useful photovoltaic characteristic [11–18]. Cell spectral responsivity (SR), for example, is used to calculate quantum efficiency, which indicates the cell's electron generation to incident photon conversion efficiency as a function of wavelength. The absolute determination of the SR of a solar cell, if done under appropriate conditions such as uniform overfill illumination and proper light biasing, can be used to predict the short-circuit current, I_{sc}, of the test device under any incident spectral irradiance, including the standard AM 1.5 solar spectrum [11]. One advantage of this absolute SR approach is that it provides a direct route for SI traceability of the I_{sc} measurement via a cryogenic electrical substitution radiometer, a route that differs from the more common approach of having traceability to the World Radiometric Reference (WRR) scale. Another leading use of relative (or absolute) SR data of PV cells is to adjust *I–V* data to account for spectral differences between spectrum of the actual illumination source and the chosen reference. Finally, SR curves can be used in modeling and simulations to provide important physical quantities such as the charge carrier diffusion length or for studying bandgap defect densities within the active layer of the device [19]. These physical parameters are an important indication of the quality of the semiconductor material comprising the active layer.

The differential spectral responsivity (DSR) method is the most widely used method for measuring the SR of a solar cell. Using this technique, a small modulated (quasi) monochromatic light beam and a more intense steady-state white light source (the light bias) simultaneously illuminate the solar cell, producing a photocurrent that is the sum of these two sources: a small pulsed signal superimposed on a larger steady current. The pulsed signal is separated, amplified, and detected using a lock-in amplifier that is synced with the user-selected modulation rate of the chopped monochromatic beam. A small portion of the monochromatic beam is diverted toward a monitor photodetector in order to measure the beam's radiant power. This radiant power, which is recorded by the same or by a separate lock-in amplifier, coupled with the cell's pulsed current and the monochromator's known passed wavelength, collectively define each discrete SR data point. The set of these discrete points, in turn, is used to construct the overall SR curve. As for the radiant power of the bias light and the resulting steady dc current of the cell, the impact on the SR measurement has been described previously, particularly for certain types of solar cells [14, 15, 20].

The spectral response measurements of a PV device can be performed in either the power-mode or the irradiance-mode, and each measurement can be either a relative or an absolute measurement. Power-mode measurements require the knowledge of the monochromatic beam's radiant power, typically obtained using a calibrated, SI-traceable reference photodetector. For power-mode, the monochromatic beam is sized such that it illuminates only part of the reference photodetector and then only a smaller part of the test cell (i.e., underfilling). For the irradiance-mode, the irradiance or incident power per unit area of the monochromatic beam is required. Irradiance can be determined by fully illuminating (i.e., overfilling) a very spatially uniform reference photodetector with the incident monochromatic radiation and then dividing the measured beam power by the aperture area of the detector. The incident beam should have a very spatially uniform irradiance profile. The absolute SR in power-mode has SI units of A W^{-1}, whereas the absolute SR in irradiance-mode is reported in units of A m^2 W^{-1}.

Figure 8.4a shows a schematic of a simple monochromator-based SR measurement system designed to measure the spectral response data in the power-mode. A mechanical chopper placed within the light path of the monochromator causes the excitation light to be in the form of a square wave, generating a pulsed signal in the device under test. The cell is simultaneously illuminated with a set of bias lights operated in a steady dc mode. The pulsed signals from both the cell and the monitor photodiode are measured by a lock-in amplifier sequentially for each wavelength. The spectral response data can be constructed from these individual measurements. Figure 8.4b shows the design of a system where the entire cell area is uniformly illuminated by the monochromatic beam. If the irradiance of this beam is measured using a calibrated reference detector, then the irradiance-mode SR data can be obtained using this setup. To achieve an overfilling monochromatic beam, interference filters can be used to narrow down the broadband beam into a quasi-monochromatic one; afterward, an optical lens assembly can be used to project this light on to the test cells. Other types of light sources such as LEDs and

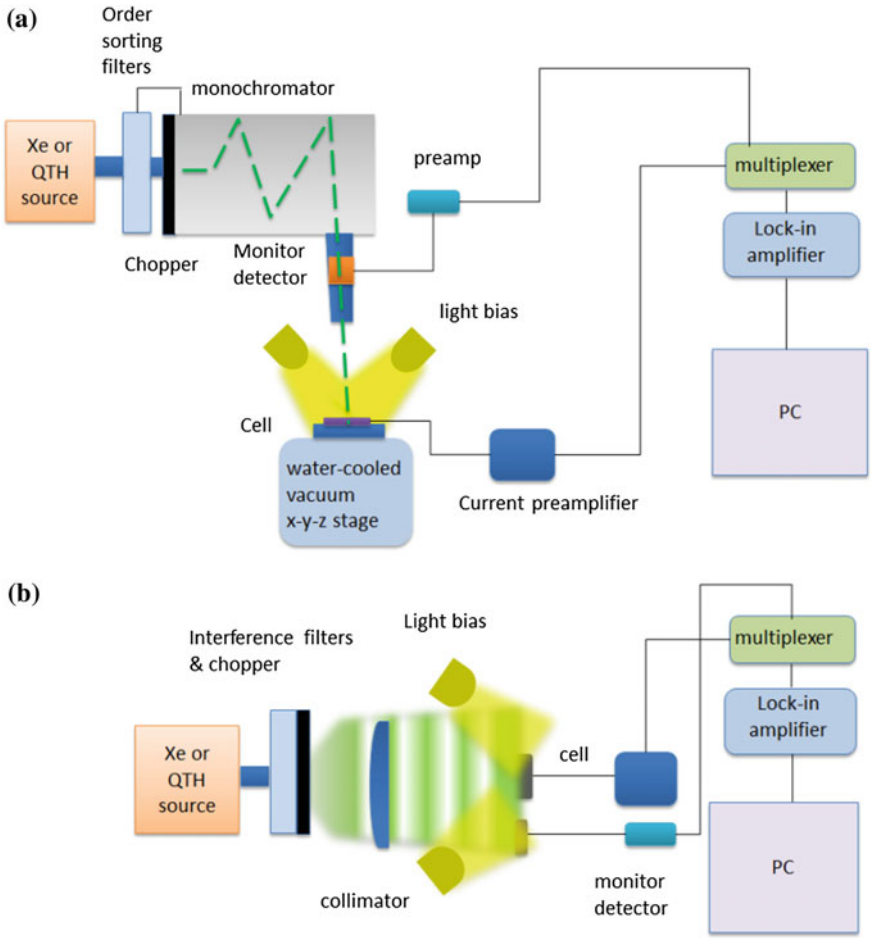

Fig. 8.4 **a** Schematics of a monochromator-based SR measurement system where the probe beam underfills the cell. **b** An example of an SR measurement system where the beam overfills the cell

lasers can also be used as monochromatic sources [21–23]. With respect to these two measurement options, the more accurate and viable route for obtaining the I_{sc} of a solar cell are achieved using the irradiance-mode SR curve of the cell. The lack of spatial material uniformity across the cell and/or the presence of metal fingers on the front surface of the cell can lead to variances in the cell's overall spectral response if measured using the underfilled power responsivity measurements. These particular complications are avoided when using the overfilled irradiance responsivity measurements; the impacts of such cell features are accounted for in the method because the test setup is consistent with the eventual overfill deployment in a solar simulator or outside in the sun.

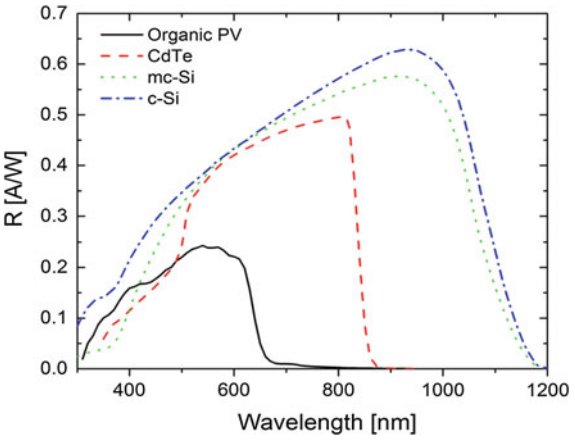

Fig. 8.5 Power-mode spectral response curves of a few different types of solar cells

Figure 8.5 shows the spectral response curves of a few different types of single-junction solar cells, obtained in power-mode. As shown, the spectral response can vary significantly among different photovoltaic materials. The higher wavelength cutoff is directly related to the bandgap of the absorber layer. Also, the actual magnitude of each curve is directly proportional to the total photocurrent generation under illumination. For the purpose of evaluating the mismatch factor M (discussed in the next section), relative SR curves (normalized to 1) or absolute SR curves in power-mode such as those plotted here are generally sufficient, as long as the local spatial variations of SR do not cause the overall shape of the curve to change. If there is a significant change in the shape of the curve when the probe beam is moved across the surface of the cell, then either an averaging algorithm must be applied to estimate the correct shape or the SR must be re-evaluated in the irradiance (overfill) mode.

Figure 8.6 shows the irradiance-mode SR data for three solar cells. From these data, the I_{sc} of the cells subjected to AM 1.5 global tilt spectrum can be directly

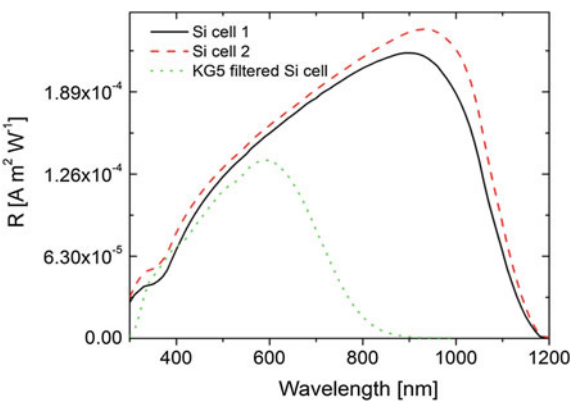

Fig. 8.6 Irradiance-mode spectral response curves of a few solar cells

calculated, provided the spectral response, R, is measured under short-circuit conditions:

$$I_{sc} = \int R_{irrdmode}(\lambda) \cdot E_{AM1.5}(\lambda)\, d\lambda \tag{8.2}$$

where $E_{AM1.5}(\lambda)$ is the spectral irradiance associated with AM 1.5 global tilt conditions. Care must be taken to ensure that the irradiance spectral response of the cell is representative of the cell's responsivity under the SRC. This typically implies that a light bias must be used during DSR measurements.

8.6 Spectral Mismatch Factor

The spectral mismatch factor, M, corrects for (1) the mismatch between the spectral response of the PV test cell and the PV reference cell and (2) the mismatch between the illumination source and the reference spectrum (e.g., AM 1.5G). This correction factor is evaluated using:

$$M = \frac{\int_{\lambda 1}^{\lambda 2} E_s(\lambda) R_t(\lambda) d\lambda}{\int_{\lambda 3}^{\lambda 4} E_s(\lambda) R_r(\lambda) d\lambda} \times \frac{\int_{\lambda 3}^{\lambda 4} E_r(\lambda) R_r(\lambda) d\lambda}{\int_{\lambda 1}^{\lambda 2} E_r(\lambda) R_t(\lambda) d\lambda} \tag{8.3}$$

where $E_s(\lambda)$ is the spectral irradiance of the source, $E_r(\lambda)$ is the reference spectral irradiance, $R_t(\lambda)$ is the spectral response of the test cell, and $R_r(\lambda)$ is the spectral response of the reference cell [2]. The integrals should be evaluated over the full range of the device's responsivity. Additionally, it is noted that only relative irradiance and responsivity data are required to perform this calculation as multiplicative factors in the numerator and denominator cancel out. This relative option is a particularly favorable aspect of this calculation because maintaining the absolute scale is a major challenge for most secondary laboratories, especially with regard to the irradiance measurements.

Prior to reporting or using any type of I–V test curve, the mismatch factor associated with the test setup must be calculated and applied. Table 8.2 shows a few examples of this calculation for various combinations of test cells, reference cells, and simulator sources. Notably, even nominal monocrystalline Si cells have sufficiently different spectral response curves among each other so that M will not be exactly 1. For example, the calculation provided in row 1 shows M = 1.007, which can cause a 0.7 % error in current measurements during I–V testing if not taken into account. Among typical solar simulators, such as a Xe flash-based simulator and a Xe steady-state simulator, noteworthy differences can result. For example, a CdTe solar cell measured under a Xe flash simulator yields a M = 1.03, while under a steady-state Xe simulator, M = 1.10. These differences, which originate from differences in the irradiance spectrum, may not necessarily be due to the Xe source

Table 8.2 Examples of spectral mismatch factor calculations for different combinations of solar cells, references, and solar simulator sources

Cell type	Reference cell	Simulator type	*M* factor
m-Si	m-Si	Xe flash	1.00685
CIGS	m-Si	Xe flash	0.998028
CdTe	m-Si	Xe flash	1.03383
CdTe	m-Si	Xe steady state	1.10333
OPV	m-Si	Xe flash	0.975193
OPV	m-Si	Xe steady state	1.15999
OPV	KG5-filtered Si	Xe steady state	1.00692
OPV	m-Si	White LED	2.1222
OPV	KG5-filtered Si	White LED	1.1377

itself but rather related to the filters that manufacturers design and install in front of the light source to make them better match to the sun's spectrum. The calculations with the organic PV cell under various combinations are also revealing.

The third OPV calculation, for instance, shows that if the reference cell used is a KG5-filtered Si cell instead of a regular Si cell, the mismatch error will only be 0.7 %, as compared to the 16 % for the combination of the Xe simulator and a m-Si reference cell. Finally, if a white LED light source is used as the solar simulator, then the error in *I–V* measurements with an OPV test cell and a m-Si reference cell exceeds a factor of 2. Here again, the error can be substantially reduced (to $M = 1.14$) if the reference m-Si cell was replaced by a KG5 filtered Si cell.

8.7 Measuring *I–V* Curves

The correct setup for performing *I–V* measurements on a solar cell is based on a 4-wire connection (also known as Kelvin configuration) as depicted in Fig. 8.7. These connections are sometimes referred to as source leads and sense leads [24]. The current flows through the source leads and the device under test, and the voltage across the device is measured by sense leads. Since the input impedance of the sense leads are very high, the source current will not flow through the sense

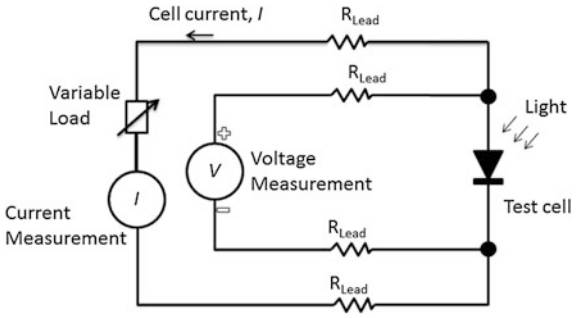

Fig. 8.7 4 wire *I–V* measurement schematic

leads, and therefore, only the voltage across the device is measured. By comparison, if a simple 2-wire connection were used to take the *I–V* data, the current flowing through the leads will cause a voltage drop in the leads in addition to the potential drop across the device; hence, the voltage measurement across the circuit will not be that of the voltage across the cell. This effect can be particularly significant for larger area solar cells where a large photocurrent is generated in the cell under SRC or comparable illumination. With this large current, the voltage drop due to lead resistance will be more significant, hence pointedly altering the shape of the *I–V* curve.

Figure 8.8a shows the 4-wire versus 2-wire *I–V* curve data for a 2 cm by 2 cm Si solar cell under 1-sun illumination intensity. For this measurement, the parameter more noticeably affected by the 2-wire measurement is the *FF*, showing a slight reduction. This reduction impacts the measured power conversion efficiency of the

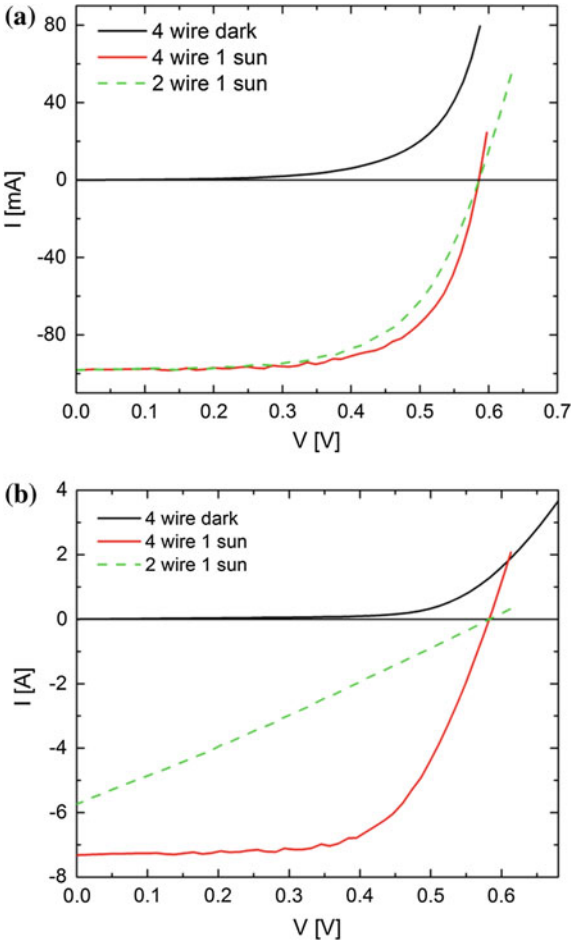

Fig. 8.8 **a** Comparison between 2 wire and 4 wire *I–V* measurements on a small 4 cm^2 solar cell. **b** Same comparison on a larger cell with an area of 219 cm^2. The *I–V* curves measured in the dark are also plotted for both solar cells

device, although the I_{sc} and the V_{oc} are relatively unaffected. In Fig. 8.8b, the 2- and 4-wire *I–V* curves for a copper indium gallium diselenide (CIGS) cell with an area of ≈219 cm^2 are shown under illumination. The series resistance-inflicted potential drop is so significant that the entire shape of the *I–V* curve is altered (dashed line), leading to a completely unsatisfactory and inaccurate measurement. These results illustrate the importance of performing 4-wire *I–V* measurements on solar cells, particularly for large area cells or on cells with relatively low internal series resistance. It is noted that if the device itself presents a large series resistance to current flow (such as by having poor contacts), then the effect of the circuit resistance on the *I–V* curve might be less pronounced. Only in cases like this, the use of 2-wire measurements may be acceptable.

Prior to obtaining solar cell *I–V* measurements, the series resistance R_s of the cell must be determined unless the total irradiance is expected to be within ±2 % of the SRC [4]. Additionally, the cell temperature must be measured to be within ±1 °C of the SRC. The reference cell temperature must also be measured, and a correction must be applied to its output if it is different from the temperature of the SRC. This correction would require knowledge of the temperature coefficient of the reference cell. Under the simplified assumptions that the operating temperature is at the standard reference temperature and the total irradiance is very near the standard reporting irradiance, E_0, (i.e., 1000 W m^{-2}), each *I–V* data point measured under the illumination source should be corrected by:

$$I_0 = \frac{I \cdot E_0 \cdot C}{M \cdot I_r} \tag{8.4}$$

$$V_0 = V - R_s(I_0 - I) \tag{8.5}$$

where $C = I_{sc,r}/E_0$ is the calibration constant of the reference cell, $I_{sc,r}$ is the short-circuit current of the reference cell measured under SRC by a primary or certified laboratory, I_r is the monitored current of the reference cell during the course of the measurement, and I_0 and V_0 are the corrected current and voltage measurements for reporting under the SRC. I_r must be monitored for each *I–V* data pair if the long-term temporal instability of the light source is greater than 0.1 %. R_s determination is not needed if the measured total irradiance remains to within ±2 % of the standard reporting total irradiance [4]. It can be seen that the parameter *M* plays an important role in the correct evaluation of the *I–V* curve as described earlier.

From the full set of corrected I_0–V_0 data, the four parameters I_{sc}, V_{oc}, V_{max}, and I_{max} are extracted. The fill factor, *FF*, is given by:

$$FF = \frac{I_{max} V_{max}}{I_{sc} V_{oc}} \tag{8.6}$$

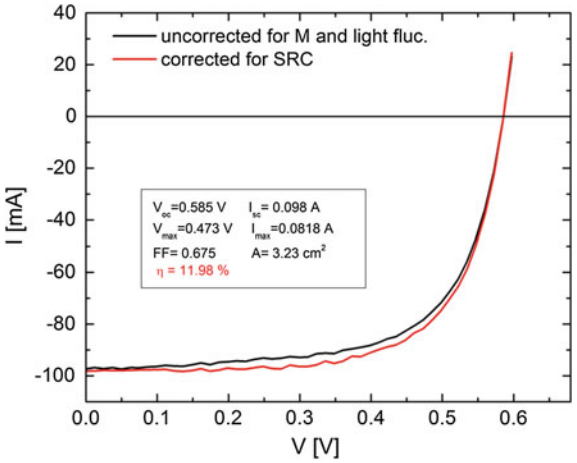

Fig. 8.9 *I–V* curves for a solar cell before and after correction of the raw measurement to standard reporting conditions. The reason for the noise in the data is related to the short-term fluctuations in the lamp's intensity profile

and the power conversion efficiency, η, is determined from:

$$\eta\,[\%] = 100\frac{(I_{sc}/A)V_{oc}FF}{E_0} \tag{8.7}$$

where A is the cell total frontal area including contacts and E_0 = 1000 W m^{-2} for AM 1.5G illumination conditions.

Figure 8.9 shows the *I–V* curve for a small solar cell both before and after correction by Eq. 8.3 (without V_0 correction). These data were recorded under a solar simulator with temporal stability as shown in Fig. 8.3. Since the total irradiance levels changed during the course of the measurement, the correction of the measured current by Eq. 8.3 was necessary for every data point in order to obtain the correct form of the *I–V* curve. Additional device parameters and the calculated power conversion efficiency under AM 1.5G conditions are shown next to the plot.

8.8 Additional Remarks

The aim of the various sections outlined in this chapter is to present a clear and coherent picture for performance measurements and characterization of solar cells. The presented list of challenges and requirements is by no means comprehensive, and there are various other issues in addition to those mentioned previously that can complicate the measurement process. For example, recent measurements by the author and by other groups have revealed that the degree of light collimation from the solar simulator incident upon the test and the reference cell specimen may influence the spectral response and the *I–V* measurement results [25]. This effect has been found to originate from the differences in the angular response (cosine

response) of the two cells. Overall, the more collimated the light source is, the lower the error associated with this angular mismatch. Ideally, primary reference cells are calibrated either outdoors or when subject to conditions similar to the level of collimation achieved from the sun (88 % direct incidence for the AM 1.5 global reference).

Finally, the light-level correction errors which were addressed by Eqs. 8.4 and 8.5 in the previous section become more significant if the *I–V* measurement are performed substantially below or above (>±5 %) the standard irradiance (i.e., 1000 W m^{-2}). In such case, additional corrections are recommended [26]. In general, all the uncertainties affecting the various aspects of the measurement should be considered and reported with the performance parameters.

8.9 Summary

A detailed review of the various steps and requirements needed to achieve accurate photovoltaic performance measurements was presented. Characteristics of the indoor solar simulator have been presented, and the steps needed to verify the class rating of the simulator were discussed in detail. Solar simulators should provide for a uniformly illuminated test plane that qualifies as Class A. Additionally, the irradiance spectrum of the simulator must be measured and compared with the standard reference spectrum. For cases where the reference solar cell has a different spectral response behavior than the test cell, a parameter called the spectral mismatch factor needs to be calculated based on the measurements of the irradiance and the spectral response of both the reference and the test cells. The irradiance and the spectral response measurement systems should be calibrated against light sources of known irradiance and reference photodiodes with known spectral response. The current versus voltage (*I–V*) measurements must be performed in four-wire configuration and ideally at total irradiance levels near the standard reference conditions. The light source temporal stability must also be monitored during these measurements and a correction applied to the collected data if the source is not perfectly stable. The objective of most primary and secondary certification laboratories is to maintain a total relative uncertainty of less than 1 % for smaller sized cells and 2 % for cells up to 15 cm in size. Other testing laboratories should aim for uncertainties of generally less than 5 % within a 95 % confidence interval.

References

1. Emery, K., Osterwald, C.: Measurement of photovoltaic device current as a function of voltage, temperature, intensity and spectrum. Sol cells **21**, 313–327 (1987)
2. Emery, K.: Photovoltaic efficiency measurements. Proc SPIE **5520**, 36–44 (2004). doi:10.1117/12.562712

3. Emery, K.A.: Solar simulators and I-V measurement methods. Sol Cells **18**, 251–260 (1986)
4. ASTM Stand. E948-09: Standard test method for electrical performance of photovoltaic cells under simulated sunlight. (2009)
5. IEC Stand. 60904-1: Photovoltaic devices—part 1: measurements of photovoltaic current-voltage characteristics. (1987)
6. ASTM Stand. G173-03: Standard tables for reference solar spectral irradiances: direct normal and hemispherical on 37 degrees tilted surface. ASTM International, West Conshohocken (2012)
7. Osterwarld, C.R., Anevsky, S., Bucher, K., et al.: The world photovoltaic scale: an international reference cell calibration program. Prog Photovolt Res Appl **7**, 287–297 (1999)
8. IEC Stand. 60904-9: Solar simulator performance requirements, 2nd edn. (2007)
9. Yoon, H.W., Gibson, C.E.: Spectral irradiance calibrations. Maryland, NIST Special Publications, pp. 250–89 (2011)
10. Cannon, T.W.: Spectral solar irradiance instrumentation and measurement techniques. Sol Cells **18**, 233–241 (1986). doi:10.1016/0379-6787(86)90122-5
11. Hamadani, B.H., Roller, J., Dougherty, B., et al.: Absolute spectral responsivity measurements of solar cells by a hybrid optical technique. Appl. Opt. **52**, 5184–5193 (2013)
12. ASTM Stand E1021-12: Standard test method for spectral responsivity measurements of photovoltaic devices. 12.02, pp. 502–511 (2012)
13. Metzdorf, J., Winter, S., Wittchen, T.: Radiometry in photovoltaics: calibration of reference solar cells and evaluation of reference values. Metrologia **37**, 573–578 (2000)
14. Winter, S., Wittchen, T., Metzdorf, J.: Primary reference cell calibration at the PTB based on an improved DSR facility. Proc 16th European Photovoltaic Solar Energy Conference, pp. 1–4 (2000)
15. Boivin, L., Budde, W., Dodd, C., Das, S.: Spectral response measurement apparatus for large area solar cells. Appl. Opt. **25**, 2715–2719 (1986)
16. Ciocan, R., Li, Z., Han, D., et al.: A fully automated system for local spectral characterization of photovoltaic structures. In: 35th IEEE PVSC, pp. 1675–1677 (2010)
17. Metzdorf, J.: Calibration of solar cells. 1: the differential spectral responsivity method. Appl. Opt. **26**, 1701–1708 (1987). doi:10.1364/AO.26.001701
18. Hartman, J.S., Lind, M.A.: Spectral response measurements for solar cells. Sol Cells **7**, 147–157 (1982)
19. Chopra, K.L., Das, S.R.: Thin film solar cells. Plenum, New York (1983)
20. Kreinin, L., Bordin, N.: Significance of bias light spectral composition for accurate measurement of silicon solar cell spectral response. In: 33rd IEEE PV Specialists Conference, San Diego, CA, pp. 1329–1332 (2008)
21. Zaid, G., Park, S.-N., Park, S., Lee, D.-H.: Differential spectral responsivity measurement of photovoltaic detectors with a light-emitting-diode-based integrating sphere source. Appl. Opt. **49**, 6772–6783 (2010)
22. Hamadani, B.H., Roller, J., Dougherty, B., Yoon, H.W.: Versatile light-emitting-diode-based spectral response measurement system for photovoltaic device characterization. Appl. Opt. **51**, 4469–4476 (2012)
23. Young, D.L., Egaas, B., Pinegar, S., Stradins, P.: A new real-time quantum efficiency measurement system. In: PVSC 33rd IEEE, pp. 1–3 (2008)
24. Overview of two-wire and four-wire (kelvin) resistance measurements. In: Appl. note 3176. http://www.keithley.com
25. Winter, S., Friedrich, D., Gerloff, T.: Effect of the angle dependence of solar cells on the results of indoor and outdoor calibrations. In: Proceeding 25th EU-PVSEC, pp. 4304–4306. doi:10.4229/25thEUPVSEC2010-4AV.3.97 (2010)
26. Campanelli, M., Emery, K.: Device-dependent light-level correction errors in photovoltaic I-V performance measurements. In: IEEE PV Spec. Conf. p (To be published) (2013)

Chapter 9
Applications

F.L. Chen, D.J. Yang and H.M. Yin

9.1 Introduction

Solar cell technology exhibits many advantages compared to traditional fuel-based energy sources, such as widely available free energy source, zero emission, no noise, safe, and versatility. It also has certain disadvantages: Energy source is thin and diffussive, lack of economic energy storage system, and high installation cost. With the technology improvement and government incentives, solar photovoltaic (PV) cells become viable in more applications, including space and terrestrial power sources for space station, satellite, building, car, and various consumer electronics. It has been producing broad impacts on human life and changing the engineering practice in the past decade.

The solar power generation market has been experiencing rapid and vast growth. With the worldwide revolution toward sustainable development, alternative energy has become a top priority. Solar power is at the forefront of alternative energy sources because of its immense potential and availability. Currently, there are three generations of solar cell types: bulk silicon, thin-film, and organic. Bulk silicon PV cells have been invented for decades and is the most common material for solar panels; thin-film cells are a relatively new technology and they are entering the market with success; and finally, organic solar cells are still in the research phase and some challenging problems in efficiency and durability are to be solved before becoming commercially viable. Overall, nine types of solar cells were reviewed:

F.L. Chen · H.M. Yin (✉)
Columbia University, New York, USA
e-mail: yin@civil.columbia.edu

F.L. Chen
e-mail: fangliang.chen@columbia.edu

D.J. Yang
OmniVison Technologies, Inc., Santa Clara, CA, USA
e-mail: dajiangyang@gmail.com

M.P. Paranthaman et al. (eds.), *Semiconductor Materials for Solar Photovoltaic Cells*, Springer Series in Materials Science 218,
DOI 10.1007/978-3-319-20331-7_9

monocrystalline silicon (c-Si), multicrystalline silicon (mc-Si), ribbon silicon, amorphous silicon (a-Si), cadmium telluride (CdTe), copper indium gallium selenide (CIGS), gallium arsenide multijunction (GaAs), dye-sensitized solar cells (DSSCs), and polymer solar cells (PSCs).

Solar energy is one of the fastest growing US industries. In 2010, the US solar market grew to a $6 billion industry, up by 67 % from $3.6 billion in 2009 [1]. PV installations grew 76 % over 2011, to total 3313 MW in 2012, with an estimated market value of $11.5 billion [2]. It is expected that a 4.4 GW of PV and 912 MW of concentrating solar power (CSP) will be installed in 2013, up from 3.4 GW of PV and zero CSP in 2012 [3]. Analysts predict that the USA will become the world's largest solar market within the next few years [1]. Initial results from the 2012 census found that the solar industry employs 119,016 Americans across all 50 states, having grown 13.2 % over last year during difficult economic times across the nation [4].

The solar power industry is now the fastest growing industry in America. It is growing faster than wind energy, telecommunications, and even the mortgage foreclosure industry. Solar, even in the toughest economic times, is creating jobs faster than the rest other industries of America [5]. Today, there are over 1.5 million households using solar water heating and enough solar electricity to power 730,000 homes [6]. Solar power is becoming more affordable with technology innovation, scaled-up manufacturing, faster installation techniques, and new financing options. The consistent decline in the cost of PV systems has continued to improve the solar value proposition to commercial users. The price of solar panels dropped 40 % between 2010 and 2011 [1], and the average price of a completed commercial PV project has dropped by 30 % since the beginning of 2011 making solar panels more affordable than ever for American business. The dramatic fall in prices is encouraging more and more companies to open their investment portfolios to on-site solar energy systems [6].

While the cost of solar energy has declined rapidly in the recent years, it remains much higher than the cost of conventional energy technologies. However, similarly to many renewable energy technologies, solar energy benefits from fiscal and regulatory incentives, including tax credits and exemptions, feed-in tariff, preferential interest rates, renewable portfolio standards, and voluntary green power programs in many countries. Additionally, the potential expansion of carbon credit markets also would provide additional incentives to solar energy deployment. However, despite the huge technical potential, development and large-scale, market-driven deployment of solar energy technologies worldwide still have to overcome a number of technical and economical barriers. If these barriers are not overcome, maintaining and increasing electricity supplies from solar energy will require continuation of potentially costly policy supports [7].

The daunting challenge of energy policy decision makers across the globe has been to make the cost of renewable energy competitive with the mature conventional energy. Historically, householders or energy companies who wanted to install

solar panels have been faced with a lengthy payback time. Consumers have been forced to make a choice based on ethics rather than economics. Without increased consumer demand and political measures to facilitate access to the market, manufacturers of solar PV panels cannot produce the unit volumes needed to bring prices down and drive technological innovation. The feed-in tariff (FIT) has proven to be the most effective policy instrument in overcoming these barriers, and close to 75 % of the world's residential solar PV installations have occurred with the support of national, state, or provincial FIT policies [8].

This chapter will firstly introduce the major applications of solar cells in space engineering, power stations, building envelopes, electrical facilities, and self-power supplies; then, some key specifications to application, such as efficiency, cost, and lifetime, will be reviewed for existing solar cells, and finally, the state of the practice of solar energy industry will be discussed.

9.2 Early Applications in Space Engineering

A space solar array must be extremely reliable in the adverse conditions of space environment. The demand for a reliable, long-lasting power source was the major reason for application of solar cell. The first practical application of solar cells was developed for space applications, starting with US satellite "Vanguard" in 1958, which was equipped with a dual power system of chemical batteries and silicon solar cells, of which the batteries failed after a week while the silicon solar cells kept the satellite communicating with Earth for years [9, 10]. Since then, PV solar generators have been remained as the best choice for providing electrical power to satellites in an orbit around the Earth.

Almost all communication satellites, military satellites, and scientific space probes have been solar-powered. Figure 9.1 shows the NASA photograph of a solar panel array of the international station [11]. In addition, other satellites, Magellan, Mars Global Surveyor, and Mars Observer, used solar power as does the Earth-orbiting, Hubble Space Telescope. Solar power for propulsion was also used on the European lunar mission SMART-1 with a Hall effect thruster [12]. The satellite power requirements have evolved from few watts to several kilowatts, with arrays approaching 100 kW being planned for a future space station.

For material side, the higher efficiency and stability of the silicon solar cells assured their preeminence in satellite power for the next three decades. The state-of-the-art (SOA) space solar cells available today are triple-junction III–V semiconductor cells [13]. There were some researches on low-cost thin-film cells, such as CdS and CuS_2, for space applications [14]. CdTe cells were developed reaching efficiencies of 12 % [15]. Unfortunately, their use was affected by the severe degradation over time.

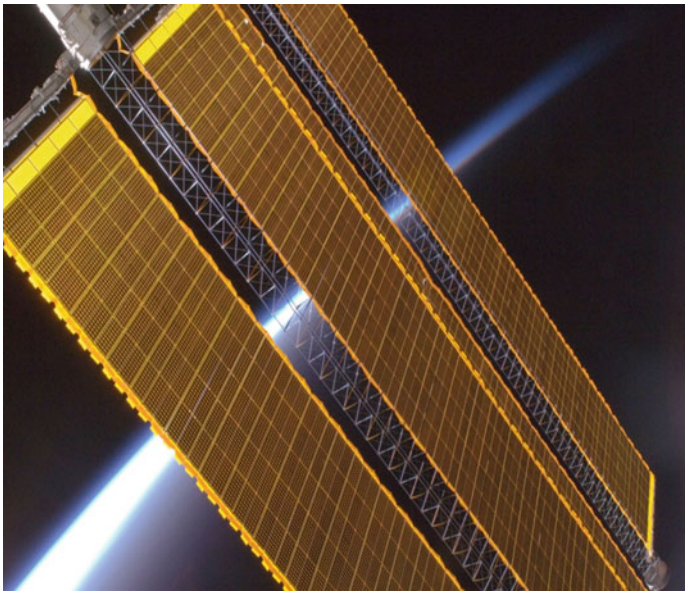

Fig. 9.1 A solar panel array of the International Space Station [11]

9.3 Terrestrial Application

9.3.1 PV Power Stations

Solar power is the conversion of sunlight into electricity, either directly using PVs or indirectly using concentrated solar power (CSP). PVs were initially, and still are, used to power small- and medium-sized applications, from the calculator powered by a single solar cell to off-grid homes powered by a PV array. They are an important and relatively economic choice of electrical energy where grid power is inconvenient, unreasonably expensive to connect, or simply unavailable. A PV power station feeds the generated power instantaneously into the utility distribution network (the "grid") by means of one or more inverters and transformers. The first PV power station was built at Hesperia in southern California in 1982 with nominal power specification 1 MW, using crystalline silicon modules mounted on a 2-axis tracking system. The array of united flexible solar panel was installed in California in 2003 to help power oil field operation (500 kWp installed power). The facility comprised 4800 flexible solar panels [16]. The 250 MW Agua Caliente Solar Project in the USA and the 221 MW Charanka Solar Park in India are among the world's largest PV power stations.

CSP systems use lenses or mirrors and tracking systems to focus a large area of sunlight into a small beam. Commercial CSP plants were first developed in the 1980s. The 354 MW SEGS CSP installation is the largest solar power plant in the

world, located in the Mojave Desert of California. Other large CSP plants include the Solnova Solar Power Station (150 MW) and the Andasol solar power station (150 MW), both in Spain.

9.3.2 Conventional BIPV

Building-integrated photovoltaics (**BIPV**) are photovoltaic materials that are used to replace conventional building materials in parts of the building envelope such as the roof, skylights, or facades [17]. PV applications for buildings began in the 1970s. Aluminum-framed PV modules were connected to or mounted on buildings that were usually in remote areas without access to an electric power grid. In the 1980s, PV module add-ons to roofs began being demonstrated. These PV systems were usually installed on utility-grid-connected buildings in areas with centralized power stations. In the 1990s, BIPV construction products specially designed to be integrated into a building envelope became commercially available [18].

PVs are increasingly being incorporated into the construction of new buildings as a principal or ancillary source of electrical power, although existing buildings may be retrofitted with similar technologies. In addition to the power supply function, the advantage of BIPV over more common non-integrated systems is that the initial cost can be offset by reducing the amount spent on building materials and labor that would normally be used to construct the part of the building that the BIPV modules replace. The modules usually have a 20-year power output warranty and can be structurally and esthetically integrated as roofing for façade elements. These advantages make BIPV one of the fastest growing segments of the PV industry.

9.3.3 Hybrid BIPV

The next generation of BIPV roofing panels needs to pursue high efficiency of energy utilization, low cost of manufacturing and construction, and excellent durability in long-term service. Although emerging nanotechnologies and novel polymeric materials make it possible to significantly improve the performance of the above three solar energy utilization approaches, each of the individual technologies has its limitations that may seriously hinder their applications. In the spectrum of solar irradiation, the PV and illumination technologies can only transfer a part of solar energy into manageable form for energy efficiency. Although the heat utilization can cover the whole spectrum, the efficiency is limited by the temperature and the Carnot efficiency. While the combination of two or three of the approaches is not a simple superposition of the materials and cost, it does provide a viable solution to significantly increase the overall energy utilization efficiency while alleviating the disadvantages of each approach [19]. PV-thermal collectors enable heat harvesting while improving the PV utilization efficiency by controlling the temperature of PV

modules. PV–TE hybrid systems were proposed to utilize the full spectrum of solar radiation and thus obtain higher efficiencies. Thermo-photovoltaic conversion cells were originally made for nuclear electric generation and used with solar concentrator to transfer infrared photons into electricity.

Recently, Yang and Yin [20] from Columbia University invented the hybrid solar panel incorporated with thermal electric module and functional graded material that greatly facilitate the overall energy efficacy. The detailed structure is shown in Fig. 9.2.

A PV surface layer and the thermoelectric (TE) layer below transfer the photoelectric and thermoelectric energy into electricity, respectively. The TE layer is bonded to a plastic lumber plate through a functionally graded material (FGM) interlayer. The FGM contains aluminum (Al) powder dispersed in a high-density polyethylene (HDPE) matrix with a graded microstructure seen in the left top of Fig. 9.2. Water pipelines are cast within the FGM to control the panel's temperature. The plastic lumber, made of recycled polymeric materials, provides mechanical loading support and heat insulation of the building skin as a structural substrate. To be in compliance with the fire code for commercial buildings, the structural substrate has been replaced with fiber reinforced lightweight concrete. The innovations of the design are summarized as follows:

- Due to temperature control by the water flow, the PV module can work at lower temperatures in the summer and thus stably obtain a higher efficiency for PV utilization.
- The temperature difference between the PV module and the water tubes provides a considerable temperature gradient within the TE layer for a higher efficiency of TE utilization.

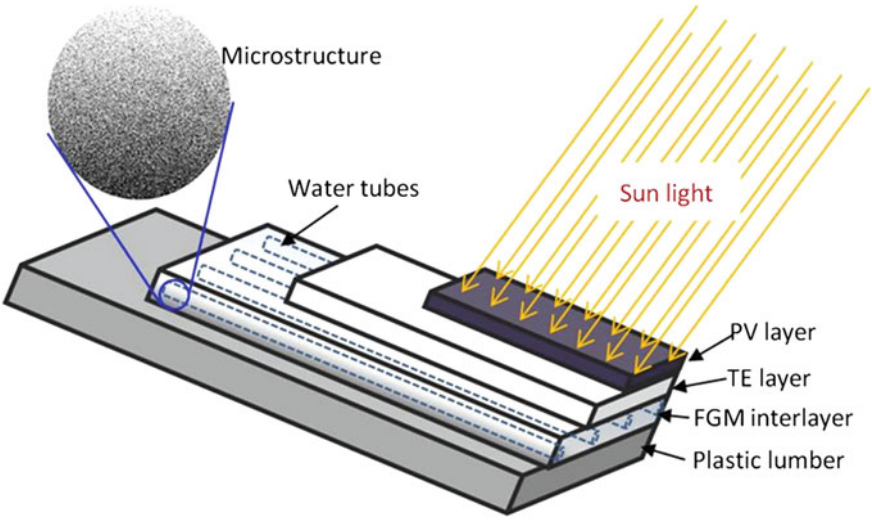

Fig. 9.2 Schematic illustration of novel hybrid solar panel

- The hot water, whose temperature is partially controlled by the flow rate, can be directly utilized by water heating systems for domestic usage.
- Due to the temperature control on the roof, the room temperature can be significantly reduced and thermal comfort in the building can be much improved.
- The various materials and components will be chemically and physically compatible to assure a durable end product.
- A high percentage of aluminum (Al) powder rapidly transfers heat into the water tubes, but below them, the heat conduction is blocked by the HDPE and the plastic lumber substrate.
- The thin-film PV layer improves the heat conduction and structural integrity within the panel and protects the polymer materials underneath from UV radiation.
- The plastic lumber substrate provides the mechanical and structural support for the upper layers and thermal insulation for indoor air as well as to prevent water condensation.

In addition, the design of this roofing panel can be generalized, such that new high-efficient PV and TE modules can be easily integrated into this structure. Because plastic lumber is mainly made of recycled HDPE, at the end of their lifetime, solar panels can be recycled into plastic lumber again [20].

Figure 9.3 shows the cross section of the residential system with the integrated hybrid solar panel. The innovations illustrated above create synergistic benefits on energy saving and generation:

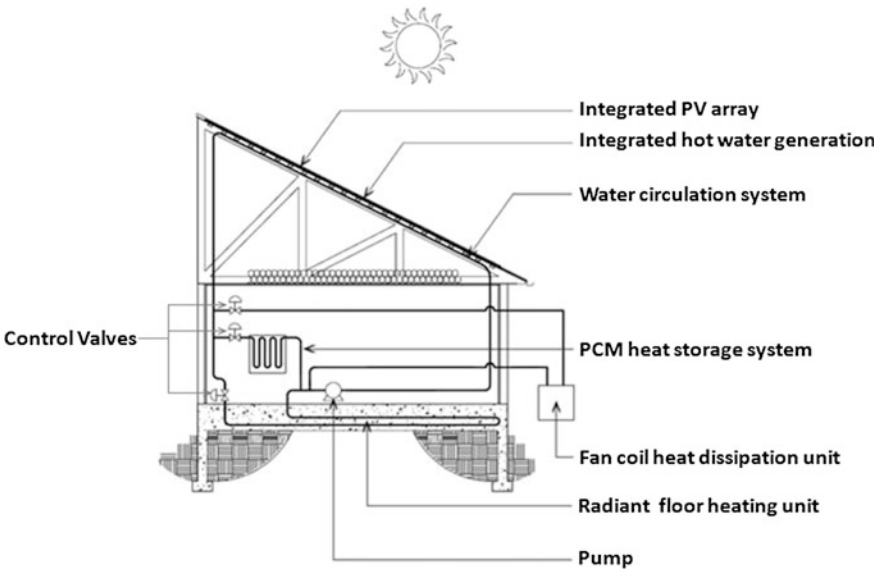

Fig. 9.3 Cross section of residential system

- Reduced cooling demand—During the hot months, because of the temperature control of water flow and the excellent heat insulation performance of the panel, high indoor thermal comfort can be obtained and cooling demand can be significantly reduced.
- Efficient in all climates—When the nighttime ambient temperatures are still too high to allow effective radiation of excess heat through the roof, a traditional fan coil unit will be used to reject the heat and cool the water.
- Snow and ice removal—In winter, warm water can be circulated to remove ice and snow on the roof, clearing the panels and restoring solar energy utilization.

In addition, the performance of this system is significantly affected by the water flow. Using an accurate temperature sensing system and water flow rate control, we can optimize the energy efficiency of the roofing system. When days are warm and nights are cool, the heat captured by the water will be stored in a Phase Change Material Heat Storage Unit, similar to the units used for peak load balancing in commercial buildings. At night, this stored heat can be used in a radiant floor system or rejected to the cool night air by circulating the water through the panels, which will act as a massive flat plate heat exchanger. The substrate of the panel is designed as an integrated part of the building skin, allowing the panel to serve as both structural sheathing and waterproofing, eliminating material redundancies and the embodied carbon associated with those materials. The integration of the panel into the building skin eliminates the waterproofing concerns associated with the roof penetrations required to mount conventional panels. The PV layer protects the underlying polymer materials from UV radiation by transferring high-energy photons into electricity. The design of the substrate can be varied and optimized to suit the various wind and snow load conditions that occur throughout the USA and the world without adversely affecting the performance of the power generating elements [21].

9.3.4 Semitransparent Solar Panel

Transparent solar panels use a tin oxide coating on the inner surface of the glass panels to conduct current out of the cell. The cell contains titanium oxide that is coated with a photoelectric dye [22]. Most conventional solar cells use visible and infrared light to generate electricity. In contrast, the innovative new solar cell also uses ultraviolet radiation. Used to replace conventional window glass, or placed over the glass, the installation surface area could be large, leading to potential uses that take advantage of the combined functions of power generation, lighting, and temperature control.

Transparent solar panel can achieve significant cost reductions when they are used as part of the building envelope and thereby offset the cost of the building materials they replace. Figure 9.4 shows a typical transparent PV panel integrated with atrium. The overall efficiency of the systems involving this technology is higher than the non-integrated standalone systems. Much of the work has been

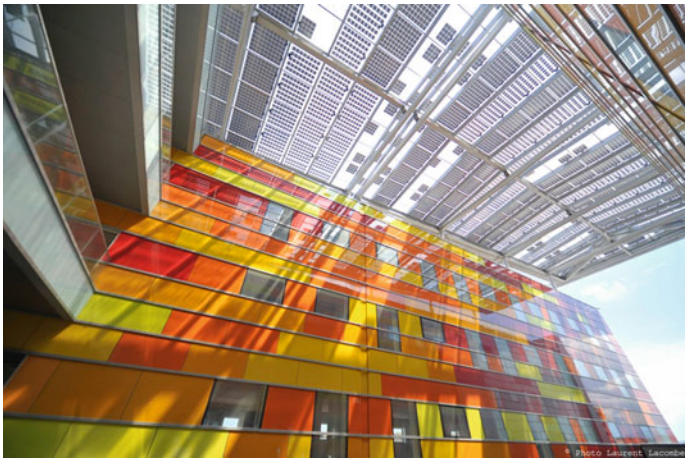

Fig. 9.4 Typical transparent PV panel integrated with atrium [24]

carried out for further improvement in the technology. Guiavarch and Peuportier [23] observed that the overall efficiency is higher for semitransparent than opaque PV collector in case of preheating the ventilation air of the building.

9.4 Power Source for Electrical Facilities

9.4.1 Solar Vehicles

Solar cars have been proposed and tested in the last twenty years, which can be powered by solar energy partially or completely. Although they have not become a practical or economic transportation option yet, in the future they may play a promising role in reducing the consumption on fossil fuels such as petrol and diesel. Solar vehicles combine technologies typically used in the aerospace, bicycle, alternative energy, and automotive industries. The design of a solar vehicle is severely limited by the amount of energy input into the car. Most solar cars have been built for the purpose of solar car races, with some exceptions including solar-powered cars and utility vehicles.

The main cost is due to the large number of expensive and delicate PV solar panels that are needed to power the vehicle. Also, many of the solar-powered cars used in races today are composed of expensive, lightweight materials such as titanium composites. Carbon fiber and glass fiber are also increasingly used for the bodywork. Most of the cars used in races are made in house by specialist teams, which adds to the expense. However, a solar-powered vehicle can only run efficiently when the sun shines, whereas most vehicles of this type require a battery backup. Electricity is stored in the batteries when the sun is shining, and this power can be used when sunlight is restricted (cloudy). Solar-powered cars normally

operate in a range of 80–170 V. To reduce friction with the ground, the wheels are extremely narrow and there are usually only three. The battery pack in a typical solar car is sufficient to allow the car to run up to 250 miles (400 km) without sun and allow the car to continuously travel at speeds of 60 mph (97 km/h).

9.4.2 Solar Power for Other Electrical Device/Equipment

Solar cells are also widely used for variety of consumer products—electronic watches, calculators, power for leisure equipment, and tourism—there is an extensive range of applications where solar cells are already viewed as the best option for electricity supply. In addition, power supply to remote houses or villages, electrification of the healthcare facilities, irrigation, water supply, and treatment are more examples of such applications. These applications usually have the following advantages: stand-alone; there are no fuel costs or fuel supply problems; the equipment can usually operate unattended; and solar cells are very reliable and require little maintenance. The economics of PV systems compares favorably with the usual alternative forms of rural electricity supply, grid extension, and diesel generators. The extension and subsequent maintenance of transmission lines over a long distance can be relatively expensive, particularly if the loads are small. On the other hand, diesel generators require regular fuel supplies, which are often consuming in rural areas; in addition, the maintenance of the generating equipment is another regular cost.

Therefore, PV systems are increasingly used in new applications. For example, more than 10,000 PV-powered water pumps are known to be successfully operating throughout the world by 2013. Solar pumps are used principally for two applications: village water supply (including livestock watering) and irrigation. In terms of the number of installations, lighting is presently the largest application of PVs. They are mainly used to provide lighting for domestic or community buildings, such as schools or health centers. PV is also being increasingly used for lighting streets and tunnels and for security lighting.

PV modules have proved to be a good source of power for high-reliability remote industrial use in inaccessible locations, or where the small amount of power required is more economically met from a stand-alone PV system than from mains electricity. Typical examples of these applications include ocean navigation aids—where many lighthouses and most buoys are now powered by solar cells; telecommunication systems—radio transceivers on mountain tops, or telephone boxes in the country can often be solar-powered; and remote monitoring and control—where scientific research stations, seismic recording, weather stations, etc., use very little power which, in combination with a reliable battery, is powered by a small PV module. Figure 9.5 shows some typical remote monitoring and control devices, such as a secured box with scientific instruments inside located at the IBM Almaden Research Lab in San Jose, CA (left), and a solar-powered paring meter on East Street in Davis, CA (right).

Fig. 9.5 Typical solar power remote monitoring and control devices [25, 26]

9.5 Solar Cell Efficiency, Life, and Cost

Solar cell efficiency is the amount of energy received from the sun that is converted into usable energy. This is often the most important parameter of a solar cell and the most difficult to improve. Taking information from various sources, we have come up with an average efficiency for each type of solar cell. Manufacturers, laboratories, and organizations will have different values for efficiencies because of the inherent differences in methods, equipment, etc. Therefore, we have taken average values for each type of cell to come to a representative efficiency. Crystalline silicon PV cells are the most common solar cells used in commercially available solar panels, representing 87 % of world PV cell market sales in 2011. Crystalline silicon PV cells have laboratory energy conversion efficiencies as high as 25 % for single-crystal cells and 20.4 % for multicrystalline cells. However, industrially produced solar modules currently achieve efficiencies ranging from 18 to 24 % [27]. GaAs multijunction cells have attained the greatest efficiencies by far, the current record of 43.5 % set by Solar Junction [28] in the middle of 2011 by using concentrated PVs with a dilute nitride cell architecture, and it is expected that within the coming years concentrated multijunctions for commercial use will reach efficiencies of 50 %. PSCs have the lowest efficiencies, 8.7 %, but are still in the very early stages of research and have much room for growth and development [29].

Table 9.1 Energy efficiency of different solar cells

Photovoltaic cell	Laboratory efficiency	Production efficiency
Monocrystalline silicon (c-Si)	25 % [27]	21.5 % [30]
Multicrystalline silicon (poly-Si or mc-Si)	20.5 % [27]	14.91 % [31]
Ribbon silicon	18.3 % [32]	13–14.8 % [32]
Amorphous silicon (a-Si)	12.5 % [33]	2.34 %–12.35 % [33]
Cadmium telluride (CdTe)	19.6 % [34]	5%–11.11% [35]
Copper indium gallium selenide (CIGS)	20.8 % [36]	7.03 %–11.55 % [37]
Gallium arsenide multijunction (GaAs)	43.5 % [28]	N/A
Dye-sensitized solar cells (DSSCs)	15 % [38, 39]	14.1 % [39]
Polymer solar cells (PSCs)	8.62 % [29]	10.6 % [40]

9.5.1 Laboratory Efficiency Versus Production Efficiency

It is important to make the distinction between laboratory efficiency and production efficiency because of the different conditions in each setting. In most cases, the laboratory efficiencies are greater than production efficiencies. However, for polymer solar cells, it was shown that the production efficiency is slightly larger than the laboratory efficiency. Table 9.1 shows current energy efficiency of typical conventional solar cells. For the purposes of life cycle cost analyses, production efficiencies are the ones that matter. Those cells that are still in the research phases have N/A marked for production efficiency.

9.5.2 Efficiency Versus Temperature

Solar cells typically have an optimal temperature at which they operate, and any deviation from this temperature will affect the efficiency of the cell. Both the electrical efficiency and the power output of a PV module depend linearly on the operating temperature [41]. Generally, the more sunshine the solar cells get, the hotter the panels get and this in turns counteracts the benefit of the sun. For example, the temperature coefficient of a Suntech 190 W (monocrystalline) solar panel is −0.48 %. What this means is that for each degree over 25 °C, the maximum power of the panel is reduced by 0.48 %. Conversely, on a sunny day in the spring, fall, or even winter—when temperatures are lower than 25 °C, the amount of electricity produced would actually increase above the maximum rated level [42]. To quantify the effect of temperature on efficiency, there is a temperature coefficient. As King et al. [43] described in their paper, "Temperature coefficients provide the rate of change (derivative) with respect to temperature of different PV performance parameters."

Table 9.2 Temperature coefficients of energy efficiency of different solar cells

Photovoltaic cell	Temperature coefficient (/°C)
Monocrystalline silicon (c-Si)	−0.40 % [44] to −0.54 % [45]
Multicrystalline silicon (poly-Si or mc-Si)	−0.45 % [46]
Ribbon silicon	N/A
Amorphous silicon (a-Si)	−0.12 % [47] to −0.3 0 % [48]
Cadmium telluride (CdTe)	-0.31 % [49]
Copper indium gallium selenide (CIGS)	−0.36 % [50] to −0.45 % [51]
Gallium arsenide multijunction (GaAs)	N/A
Dye-sensitized solar cells (DSSCs)	−0.26 % to −0.33 % [52]
Polymer solar cells (PSCs)	N/A

In the case used here, temperature coefficients measure the rate of change of power with respect to temperature. Those cells that do not yet have temperature coefficients available are marked with N/A (Table 9.2).

9.5.3 Service Life

Service life is also a very important parameter to measure when performing a life cycle cost analysis. Where an exact service life could not be found, a manufacturer's warranty period is given. In general, manufacturer warranties cover the power output of Solar PV panels at roughly 20–25 years, and so the life is usually expected for 20–25 years [53]. The warranty conditions for PV panels typically guarantee that panels can still produce at least 80 % of their initial rated peak output after 20 years (or sometimes 25). Unfortunately, exact degradation patterns could not be found for most cell types since only a small proportion of all PV panels installed is older than 10 years over the world (Table 9.3).

Table 9.3 Life cycle of different solar cells

Photovoltaic cell	Service life
Monocrystalline silicon (c-Si)	90 % output for 25 years [44]
Multicrystalline silicon (poly-Si or mc-Si)	80 % output for 25 years [46]
Ribbon silicon	N/A
Amorphous silicon (a-Si)	90 % output for 10 years 80 % output for 25 years [47]
Cadmium telluride (CdTe)	90 % output for 10 years 80 % output for 25 years [49]
Copper indium gallium selenide (CIGS)	80 % output for 25 years [51]
Gallium arsenide multijunction (GaAs)	N/A
Dye-sensitized solar cells (DSSCs)	80 % output for 10–20 years [54, 55]
Polymer solar cells (PSCs)	N/A

9.5.4 Cost

It is very difficult to objectively compare the costs of different types of solar cells because different retailers or companies may present different prices since most manufacturers price their cells based on the type of system, size of system, location, and competitive levels, etc. As a result, the price of solar cells is very dynamic. For cells in the research phase, cost values will also not be available to reflect the market status. In general, the first-generation cell types (such as c-Si, mc-Si) are currently the most prevalent in the market and have relatively plateaued in terms of efficiency and cost because they have existed for a long period. Based on a retail price summary report updated in March 2012 [56], 329 solar modules, 34 % of the total survey, were priced below $2.00/W. The lowest retail price for a multicrystalline silicon solar module is $1.06/W from a German retailer. The lowest retail price for a monocrystalline silicon module is $1.10/W, also from a German retailer. Brand, technical attributes, and certifications are also factors in affecting the retail price. The lowest thin-film module price is $0.84/W from a Germany-based retailer. As a general rule, it is typical to expect thin-film modules to be at a price discount to crystalline silicon (like for module powers). This thin-film price is for a 105/W module.

Generally, thin-film cells (ribbon, a-Si, CdTe, CIGS) hold a promising future because they are less expensive to manufacture and still have some room for efficiency and cost improvements. The third-generation cells (such as GaAs, DSSCs, PSCs) are still in the research phase and therefore have much room for growth. These cells have the potential to be much less expensive and more efficient than the cells currently in production. As an example, tests have shown that DSSCs can produce 10–20 % more electric energy than single-crystal silicon modules with the same capacity and are just getting ready for commercialization [55]. Made from organic materials, PSCs are low cost, low weight, easy processing, and flexibility compared to inorganic counterparts [57].

9.6 Solar Industry and Market

The US solar industry is sectored by both technology and application. Application sectors include Distributed and Central/Utility, while technology sectors include PV, Solar Heating and Cooling (SHC), and CSP.

PV technologies consist of the following:

- **Crystalline silicon (c-Si) modules** represent 85–90 % of the global annual market today. C-Si modules are further subdivided into two main categories: (i) single crystalline (sc-Si) and (ii) multicrystalline (mc-Si).
- **Thin films** currently represent roughly 10–15 % of global PV module sales. These films are subdivided into three main families: (i) amorphous (a-Si) and

micromorph silicon (a-Si/μc-Si), (ii) cadmium telluride (CdTe), and (iii) copper indium diselenide (CIS) and copper indium gallium diselenide (CIGS).
- **Emerging technologies** include advanced thin films and organic cells. The latter technologies are about to enter the market via niche applications.
- **Concentrator technologies (CPV)** use an optical concentrator system that focuses solar radiation onto a small high efficiency cell. The CPV technology is currently being tested in pilot applications.
- **Novel PV concepts** aim at achieving ultra-high-efficiency solar cells via advanced materials and new conversion concepts and processes and are currently the subject of basic research [58].

Noted below are four end-use sectors with distinct markets for PV:

- Residential systems (typically up to 20 kW systems on individual buildings/dwellings).
- Commercial systems (typically up to 1 MW systems for commercial office buildings, schools, hospitals, and retail).
- Utility-scale systems (starting at 1 MW, mounted on buildings or directly on the ground).
- Off-grid applications (varying sizes) [58].

The majority of national PV markets are focused on a particular market segment. In Japan, the residential market dominates, while large-scale PV systems drive the majority of demand in Spain and Italy. In Germany, residential and small commercial systems lead the markets. The USA is led by the markets of utility, non-residential and residential installations, with each segment contributing to 53.8, 31.5, and 14.7 % of the total US installations in 2012, respectively [2].

9.6.1 Solar Industry

Solar PV manufacturing is rapidly maturing into a global industry dominated by a far smaller number of producers. PV systems do not require complex machinery and thousands of parts. In fact, most PV systems have no moving parts at all. They also have long service lifetimes, typically ranging from 10 to 30 years, with some minor performance degradation over time. In addition, PV systems are modular; to build a system to generate large amounts of power, the manufacturer essentially joins together more components than required for a smaller system. These characteristics make PV manufacturing quite different from production of most other types of generating equipment. In particular, PV systems offer little opportunity for manufacturers to make customized, higher value products to meet unique needs. Cell manufacturers typically have proprietary designs that seek to convert sunlight into electricity at the lowest total cost per kilowatt hour. Vertical integration is becoming more important among the world's largest solar cell and module manufacturers, but

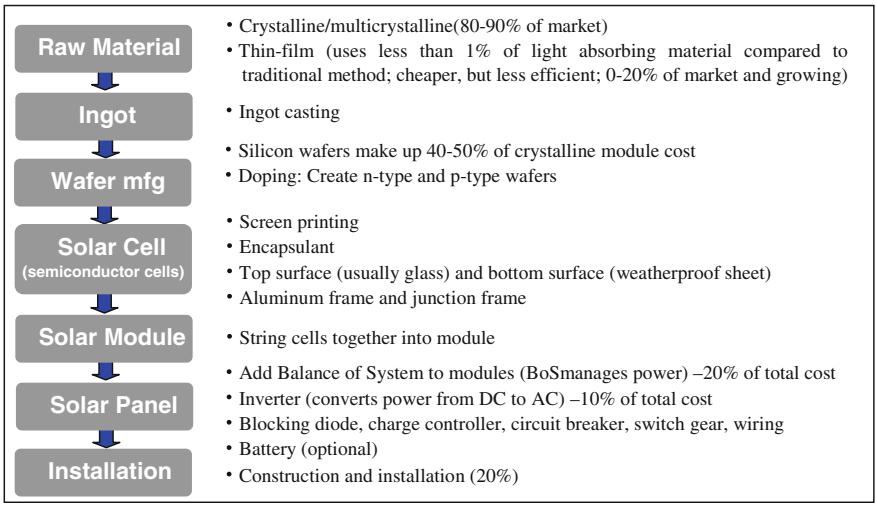

Fig. 9.6 Typical PV manufacturing flow. *Source* Overview of the solar energy industry and supply chain, Stone & Associates. January 2011, p. 21 [60]

many still rely on extensive supply chains for components such as wafers, glass, wires, and racks [59]. A typical manufacturing process is shown in Fig. 9.6.

PV companies include PV capital equipment producers, cell manufacturers, panel manufacturers, and installers. Solar modules, as the final products to be installed to generate electricity, are regarded as the major components to be selected by customers' willing to choose solar PV energy. The solar PV market has been growing for the past few years. The top 10 companies added up to 12.5 GW of module production, a significant share at 44 % of the 2011 total global module production [61]. According to IHS research [62], the PV module supplier base further consolidated in 2012 with the top 10 manufactures collectively accounted for nearly half of all solar panels produced in 2012. The continued consolidation of solar PV manufacturers is creating opportunities for the leading tier 1 module suppliers, and the market share of the top 20 module suppliers increased significantly in Q1 of 2013 to 70 %, up from 58 % in Q1 of 2012 [63].

Table 9.4 shows the top 10 global solar module suppliers in 2012. In a year (2012) that proved very challenging for the entire PV industry, Yingli Green Energy managed to increase its merchant shipment volumes by 43 % year over year to compete the Suntech and First Solar which were the two largest suppliers of 2011. First Solar managed to defend its position as the No. 2 module manufacturer, while Suntech lost significant ground and was displaced to fifth position behind Trina Solar and Canadian Solar. REC Group, the only top 10 supplier headquartered in Europe, grew faster than most of its Chinese competitors in 2012. Increasing its module shipments by 31 % year over year to 757 MW, REC strengthened its position as a leading player in a highly competitive environment [64].

Table 9.4 Top 10 global solar module suppliers

2012 ranking (change from 2011)	Manufactures	Module production in 2012 (MW)	Module production in 2011 (MW)
1 (+2)	Yingli Green Energy	2300	1554
2 (−1)	First Solar	1800	2001
3 (+1)	Trina Solar	1600	1395
4 (+1)	Canadian Solar	1550	1363
5 (−3)	Suntech Power	1500	1866
6 (−)	Sharp	1050	1155
7 (+1)	Jinko Solar	900	782
8	Sunpower	850	
9	REC Group	750	
10 (−3)	Hanwha SolarOne	750	825

Sources 2011 top 10 module manufacturers [61]; top 10 solar PV module suppliers of 2012 overview [65]

9.6.2 Solar Market

Solar energy has become and will continue to be one of the fastest growing technologies in the global energy industry as a consequence of rising energy prices, volatility of fuel costs, and government incentives for renewable energy [66]. Solar power in the USA includes utility-scale solar power plants as well as local distributed generation, mostly from rooftop PVs. In mid-2013, the USA passed 10 GW of installed PV capacity with an additional 0.5 GW of CSP. In the twelve months through September 2013, utility-scale solar power plants generated 7.4 million megawatt-hours, 0.18 % of total US electricity [67].

9.6.2.1 PV Market Growth

Worldwide solar PV demand reached 15 GW through the first six months of 2013, roughly a 9 % increase from 2012, and cumulative solar PV installations are about 116.5 GW. In each scenario, more than half (60 %) comes from four countries: Germany, China, Japan, and the USA. In the second half of 2013, China and Japan should account for nearly half of the solar PV demand all by themselves. By contrast, in 2012 Europe made up half of global demand, while three years ago, China and Japan contributed less than 10 % of second-half-annual demand [68].

Figure 9.7 shows the worldwide solar PV growth from 2007 to 2013, where the bars represent the actual annual installed amount of PV solar systems by manufacturers expressed in gigawatts (1 GW = 1 billion watts), which shows that the solar industry has seen a remarkable rebound from the 2009 recession. The five-year growth rate from 2007 to 2012 was approximately 55 % per year.

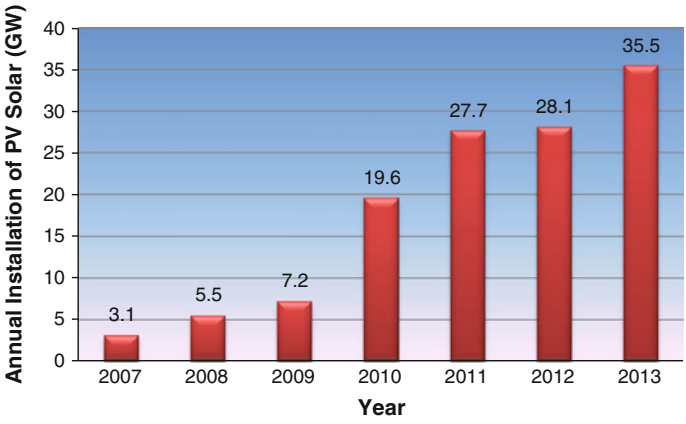

Fig. 9.7 Worldwide solar PV annual installation growth. *Source* Solar markets around the world [70]

The reason for the growth rate of only 1.6 % in 2012 was due to major reductions of incentives in several European countries, namely Italy and Germany [69]. The 28 or so gigawatts installed in 2011 and 2012 were just a fraction of one percent of the total amount of electricity that was being generated by all sources worldwide. The 2013 growth rate is estimated to be about 26 % due mainly to increases in China, Japan, and the USA. After 2013, the long-term growth estimates generally range from 15 to 25 %.

Table 9.5 shows the PV solar installations at different countries in the past three years. It indicates that Germany has historically been the leader in solar power. Germany has a goal to discontinue all nuclear power by the year 2022 and replace it with renewable resources. However, as the price of solar power has decreased and Germany is on target to meet its goals, they have reduced their solar incentives

Table 9.5 PV solar installations (GW) at different countries

Country	2011	2012	2013
Germany	7.5	7.6	5.8
Italy	6.7	3.3	3.0
China	2.8	3.5	6.0
USA	1.9	3.3	4.5
Japan	1.3	2.0	5.0
France	1.8	1.2	1.4
Australia	0.8	0.8	0.9
India	0.6	1.0	2.0
ROTW	4.3	5.4	6.9
Total market	27.7	28.1	35.5

Source Solar markets around the world [63]

prompting their installations to peak in 2012. The same thing occurred in Italy in 2011. In 2013, China, who has over 50 % of the world's manufacturing capacity, has begun to focus on its own internal needs for clean power and is forecast to be number one in installations in 2013.

There was about 100 GW of PV solar installed in the world at the end of 2012. It is roughly divided into three parts: residential rooftops, commercial buildings such as hotels or malls, and utility plants connected to the grid. The utility market has just recently been taking off. This is the market segment that has been the most influential in the growth rates over the last few years.

At the national level, 2012 was another record-breaking year with solar energy being the fastest growing energy source by powering homes, businesses, and utility grids across the nation. PV installations grew 76 % over 2011, to total 3313 MW in 2012, with an estimated market value of $11.5 billion [2]. Of the 3313 MW installed in 2012, 1300 MW (39.2 %) came online in the fourth quarter, making the quarter by far the largest in the history of the US solar market [69]. According to the US Solar Market Quarter reports in 2013 [3, 70, 71], 723 MW were installed in Q1 2013, which accounted for over 48 % of all new electric capacity installed in the USA that quarter and represented the best first quarter of any given year for the industry, while 832 MW was installed in Q2 2013, representing 15 % over the preceding quarter of this year; In Q3 2013, the USA installed 930 MW, up by 20 % over Q2 2013 and 35 % over Q3 2012. This represents the second largest quarter in the history of the US solar market and the largest quarter ever for residential PV installations. Even more importantly, 2013 is likely to be the first time in more than 15 years that the USA installs more solar capacity than world leader Germany, according to GTM Research forecasts.

Overall, US solar installations have grown dramatically in the last few years as utilities have come on strong. Both the residential and utility markets experienced their largest quarter ever. Figure 9.8 shows the US solar PV annual installation growth and global market share from 2000 to 2012.

At the state level, California became the first state to install over 1000 MW in one year, with growth across all market segments. Arizona came in as the second largest market and led by large-scale utility installations, while New Jersey experienced growth in the state's non-residential market. Table 9.6 shows the top 10 largest state solar markets in 2012, where California became the first state to install over 1000 MW in one year, with growth across all market segments. Arizona came in as the second largest market and led by large-scale utility installations, while New Jersey experienced growth in the state's non-residential market [2].

The residential market continues its rapid growth. Through Q3 2013, residential PV installations were up by 45 % year over year, driven largely by increasingly attractive economics and by fair net metering policies. The non-residential segment, which includes commercial, governmental, and nonprofit systems, installed more than 1000 MW in 2012. However, its market has seen the most difficulty in 2013 with installations forecasted to stay flat over 2011. Nevertheless, the utility market continues its consistently strong installation numbers and is forecasted to exceed 1 gigawatt (GW) of installations in the Q4 2013 [71]. Abengoa's Solana, the world's

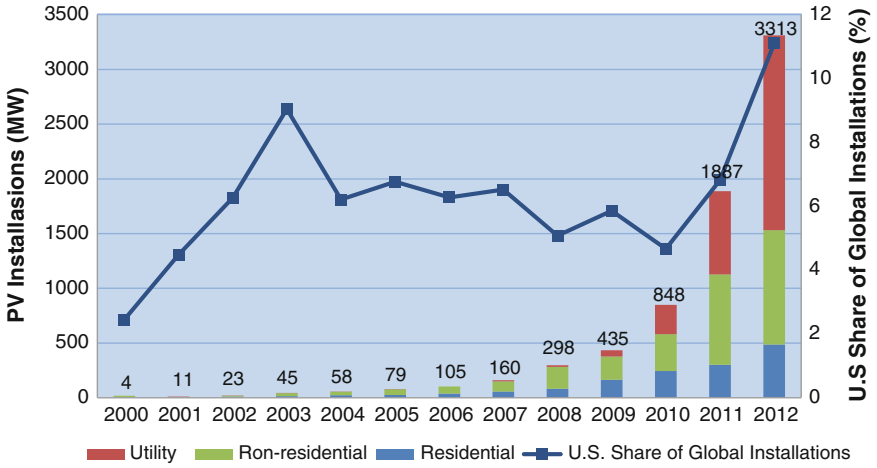

Installations (MWdc)	2000	2001	2002	2003	2004	2005	2006	2007	2008	2009	2010	2011	2012
Residential	1	5	11	15	24	27	38	58	82	164	246	302	488
Ron-residential	2	3	9	27	32	51	67	93	200	213	336	826	1043
Utility	0	3	2	3	2	1	0	9	16	58	267	760	1781
Total Installations	4	11	22	45	58	79	105	160	298	435	848	1887	3313

Fig. 9.8 US PV installations and global market share, 2000–2012. *Source* US solar market insight: year in review 2012 [2]

Table 9.6 Top 10 states by annual PV installations in the USA

2012 ranking (change from 2011)	State	Installations (2012)	Installations (2011)
1 (−)	California	1033	577
2 (+1)	Arizona	710	273
3 (−1)	New Jersey	415	313
4 (+6)	Nevada	198	44
5 (+3)	North Carolina	132	55
6 (+6)	Massachusetts	129	31
7 (+4)	Hawaii	109	40
8 (+5)	Maryland	74	22
9 (−)	Texas	64	44
10 (−3)	New York	60	60

Source US solar market insight: year in review 2012 [2]

largest parabolic trough CSP plant in the U.S., is able to generate electricity for six hours without the concurrent use of the solar field, which is considered as a turning point for renewable energy in the U.S. and a tangible demonstration that solar energy can be stored and dispatched upon demand.

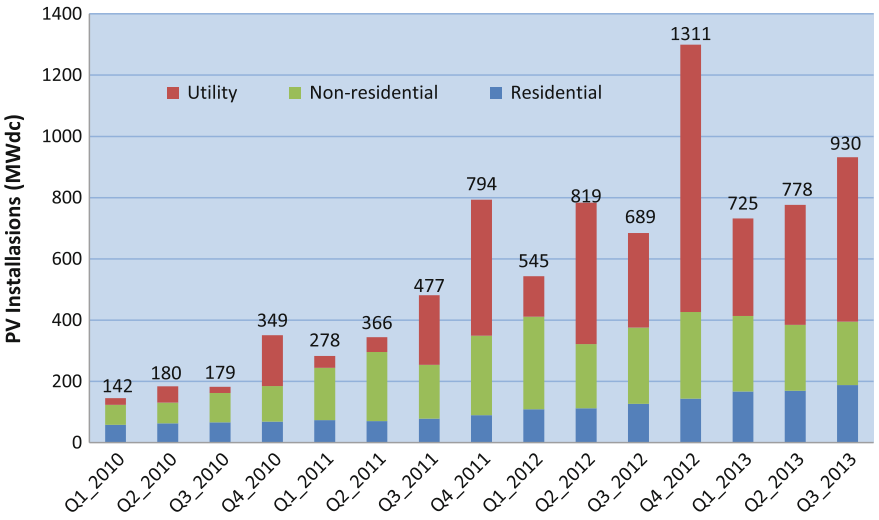

Fig. 9.9 US PV installations by market segment, 2010–2013 PV market restraint: cost. *Source* US solar market insight: year in review 2012; solar market insight 2013 Q3

Meanwhile, the USA is financing the largest rooftop solar project in the country. "Project SolarStrong" is expected to double the number of residential solar systems in the USA by installing 160,000 rooftop systems at 124 military housing developments. The leading contractor on the effort is SolarCity, which will build, own, and operate the solar installations, expected to generate about 371 MW of new solar capacity. It is anticipated that project SolarStrong will create over $1 billion in solar projects across 33 states [72].

Figure 9.9 shows the quarterly PV installations growth for utility, non-residential and residential, during the period of 2010–2013. SEIA and GTM Research [2] expect the growth to continue, the residential and non-residential markets are expected to gain market share as system prices decline, the industry becomes even more efficient, and new financing channels arise.

The key restraint stopping US homeowners from putting solar panels on their roofs is cost. Solar systems are relatively expensive, ranging from $20,000 to $25,000 or more, depending upon the system size and other factors [73]. While prices for solar panels are steadily coming down, they are not yet low enough to prompt the masses to move to solar system. Such solar systems may hold the potential to end up paying for themselves in the long run, and upfront costs of thousands of dollars can be prohibitive for most families.

Large projects and "utility" projects have dominated the market since 2010 because they are more cost-effective to build. Small projects on a single home or business can tend to cost more than double the larger utility projects, often as much as $6–$7/W. Moreover, costs for residential and small commercial solar system can be about 50 % more expensive than comparable installations in Germany, the world's largest solar market [74].

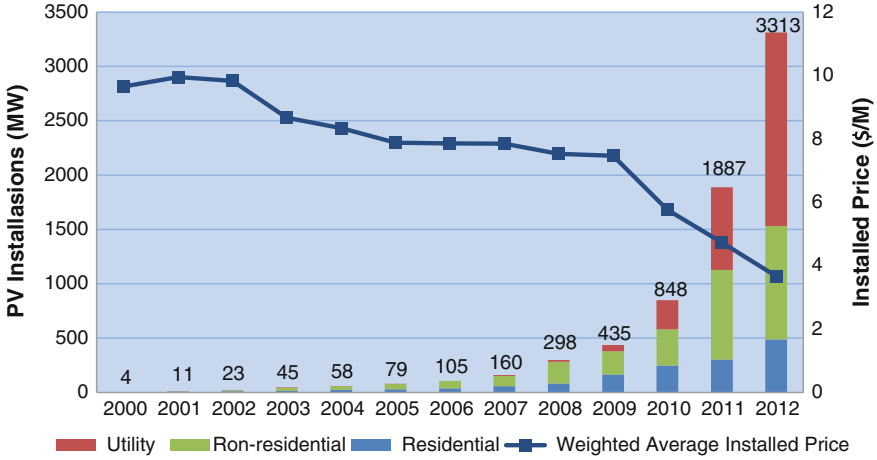

Fig. 9.10 US PV installations and weighted average installed price. *Source* US solar market insight: year in review 2012 [2]

The US PV installations and weighted average installed price over the past decades are depicted in Fig. 9.10, and it shows that the installed prices kept relatively stable during the first three years and began to decline after 2002. Since 2009, installed prices have fallen precipitously as upstream cost reductions—principally PV module cost reductions—worked their way through to end consumers, and as state and utility PV incentive programs continued to ramp down their incentives [75]; 2012 was another banner year for installed price reductions for all types of installations in the USA. Year over year, the national average price declined by 26.6 %, from $4.10/W to $3.01/W. Q3 2013 saw continued average installed price declines across all market segments in the USA compared to one year ago. Quarter over quarter, the national average system price declined by 4.2 %, falling from $3.13/W to $3.00/W, while dropping 16.4 % from $3.59/W one year ago. This capacity-weighted number is heavily impacted by the volume of utility-scale solar power plants installed in a given quarter. For the second straight quarter, utility PV capacity accounted for more than half of all new capacity installed, and for that reason, it had a relatively larger impact on the blended average system price. Individually, the residential and utility segments saw price decreases on a quarter-over-quarter basis, while the non-residential market increased quarter over quarter. (It should be noted that prices reported in this section are weighted averages based on all systems that were completed in Q3 across many locations and that the weight of any individual location can influence the average.)

- From Q3 2012 to Q3 2013, residential system prices fell 9.7 %, from $5.22/W to $4.72/W. Quarter over quarter, installed costs declined by 2 %. Installed prices came down in most major residential markets including California, Arizona, and New Jersey.

- Non-residential system prices fell 6.1 % year over year, from $4.22/W to $3.96/W. Although quarter-over-quarter installed costs increased by 6.5 %, the Q3 national weighted average masks quarterly reductions seen in most established state markets, which ranged from 2 to 10 %.
- Utility system prices once again declined quarter over quarter and year over year, down from $2.40/W in Q3 2012 and $2.10/W in Q2 2013, settling at $2.04/W in Q3 2013.

Overall, however, installed PV prices vary greatly not only state to state, but also project to project. Common residential system prices ranged from less than $3.00/W to just above $7.00/W. Non-residential prices hit levels as low as $1.85/W and as high as $7.75/W. Utility prices also display high variability: a 50-MW plus fixed tilt installation will be significantly less expensive than a 1 MW pilot project that employs dual-axis tracking. Note that the lowest installed cost of power does not necessarily yield the lowest cost of energy, an important metric for measuring project returns, due to factors such as differing amounts of sunlight striking the exact same type of solar system installed in different geographic regions.

In general, cost reductions in modules play a considerable role in reducing the installed prices. The pricing variances for polysilicon and PV components (Wafer, Cell, and Module) from 2012 to Q3 2013 are depicted in Fig. 9.11, and it shows that pricing for both the polysilicon and PV components continued to fall over the

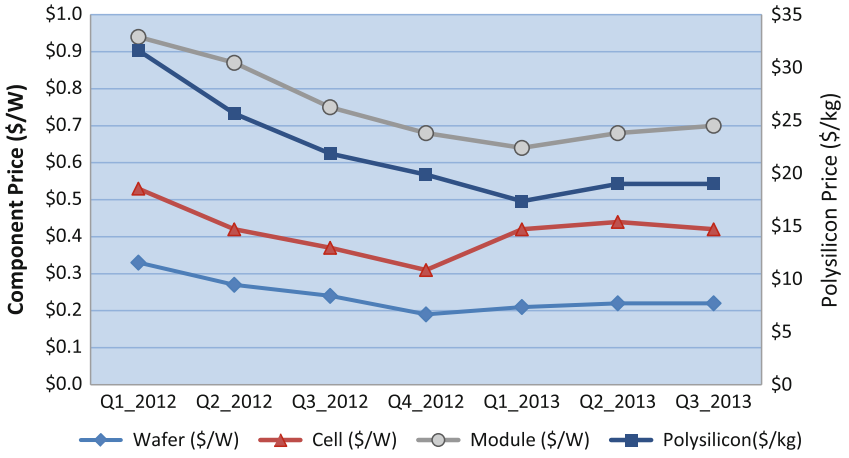

	Q1_2012	Q2_2012	Q3_2012	Q4_2012	Q1_2013	Q2_2013	Q3_2013
Polysilicon($/kg)	$31.62	$25.65	$21.85	$19.88	$17.36	$19.00	$19.00
Wafer ($/W)	$0.33	$0.27	$0.24	$0.19	$0.21	$0.22	$0.22
Cell ($/W)	$0.53	$0.42	$0.37	$0.31	$0.42	$0.44	$0.42
Module ($/W)	$0.94	$0.87	$0.75	$0.68	$0.64	$0.68	$0.70

Fig. 9.11 US polysilicon, wafer, cell, and module prices. *Source* US solar market insight: year in review 2012; solar market insight 2013 Q3

four quarters in 2012; however, it was stable and even slightly increased in the first three quarters in 2013 due to strong demand pickup from Japan, the EU, and China, as well as a more consolidated supply chain [71].

9.6.3 PV Market Driver

The driving force for the solar cell development and application is the realization that the traditional fossil energy resource, such as coal, oil, and gas, is not only limited, but also contributes to the emission of carbon dioxide for environmental pollution. Perhaps most importantly, clean, reliable, affordable solar system is continuing a major growth pattern that has made it a potential leading source of new electricity across the world that is increasingly competitive with conventional electricity across dozens of states today.

Though the solar systems are relatively expensive compared to conventional energy sources, financial incentives, government renewable energy deployment targets and technology cost reduction were and still will be the most important drivers of the solar PV market. According to the research analyst with Navigant Research [76], by the end of 2020, solar PV is expected to be cost-competitive with retail electricity prices, without subsidies, in a significant portion of the world and the global solar PV market will be worth US$134 billion by 2020.

Among industrialized countries, the German and Japanese governments have led the way in legislating high incentives to stimulate development of their domestic solar markets. The German FIT model has been increasingly used in countries around Europe, including Italy and France. As a result, the industry structure has evolved, leading to strong distributor and dealer networks with well-trained installers and good customer support capabilities. Government policy is designed to reduce CO_2 emissions via solar deployment and to create high-tech jobs through the development of a strong national solar industry. In the USA, utilities have played a stronger role in market development [77].

Overall, regional solar energy demand where the solar energy is connected to the electricity grid is driven by the following:

- Incentive programs led by national or state governments: Subsidies allow customers/investors to gain a financial return on the PV system by selling solar electricity at preferential rates.
- Enthusiasm of customers for green energy, especially solar.
- Local electricity tariffs: High electricity rates encourage alternative sources of energy.
- Sunlight conditions: Solar electricity prices fall as sunlight levels increase.
- Marketing strategies by solar companies.
- Delivery infrastructure, which is the number of local suppliers and qualified installers.

By far, the most impressive information was the extent to which the industry is growing in new markets. The influence of Europe, which kicked off the solar PV boom nearly a decade ago with its FITs, is fading. China, Japan, and the USA are competing for domination in the coming years. In addition, strong markets in the rest of Asia, Africa, and South America are also emerging [78].

- In South Africa, the government has already signed contracts for 1 GW of solar PV and is currently holding an auction for another 400 MW of PV capacity. The provincial government of Gauteng announced earlier this month that it would spend $1 billion installing 300 MW of solar PV on the rooftops of all state-owned buildings.
- In Zimbabwe, solar developer Twalumba has signed to develop eight solar farms totaling 600 MW over the next 15 months. Saudi Arabia is gearing up to make a massive investment in solar PV, along with other Gulf and North African countries. On a smaller level, Ethiopia is halfway through a World Bank-sponsored program to bring distributed solar PV to 25,000 households not connected to the grid. Private companies offer similar programs in Africa and Asia to some of the 1.6 billion people who do not have electricity.
- In Asia, India is working its way through its ambitious program to have 20GW of solar PV by 2022, Pakistan has just announced plans for 700 MW of solar capacity in Punjab province, and Bangladesh already has installed a million off-grid solar systems and has announced plans for another 500 MW deployment.

9.7 Summary

The various applications of solar cell technology are reviewed. First of all, the important applications in space were discussed, including the history, development, and material consideration of solar panel in space. The widely used terrestrial application is solar power generation for grid utilities. The BIPV is the fast growth application with large market, and the latest development in hybrid solar and transparent solar panel is discussed. In addition, solar cells have also been used in automotives and public electric facilities, such as road lighting, water pump, vending machine, and various consumer electronics such as watch and hand calculators. The solar cell efficiency, life cycle, and cost of different kinds are reviewed. Finally, the most updated solar panel technology and major solar panel manufacturers are reviewed, and current and potential solar market is discussed.

Acknowledgements This work has been sponsored by the Department of Energy STTR DE-SC0003347 and the National Science Foundation CMMI 0954717, whose support is gratefully acknowledged. The authors are also grateful to Dr. Jack Thatcher and Ms. Theresa Pipher and their company—Dawnbreaker Inc. They worked with Dr. Yin during 2011–2012 on solar energy market and business analysis. Much market information in this chapter can be traced back to that work with the update of market information up to 2013, Quarter 3. In addition, Ms. Carmen Marin

has participated in the literature review of the three generations of PV cells, whose help is highly appreciated. Author Yin also appreciates the support of the Henry Mitchell Weitzner Research Fund, which has been and will be used in his research on solar energy applications and technologies.

References

1. CleanTechnica: U.S. solar energy in 2011. Retrieved January 14, 2014 from http://cleantechnica.com/2011/12/23/u-s-solar-energy-in-2011
2. U.S. solar market insight 2012 year in review. Retrieved January 14, 2014 from http://www.seia.org/research-resources/us-solar-market-insight-2012-year-review (2013)
3. Solar market insight report 2013 Q2. Retrieved January 14, 2014 from http://www.seia.org/research-resources/solar-market-insight-report-2013-q2 (2013)
4. U.S. solar energy jobs increase by more than 13 Percent. Retrieved January 14, 2014 from http://www.seia.org/news/us-solar-energy-jobs-increase-more-13-percent (2012)
5. Medium: State of the solar union in 2012—solar power. Retrieved January14, 2014 from https://medium.com/solar-power/16fb5116c282 (2012)
6. Commercial Solar Users: Solar means business 2013: top U.S. Retrieved January 14, 2014 from http://www.seia.org/research-resources/solar-means-business-2013-top-us-commercial-solar-users (2013)
7. Timilsina, G.R., Kurdgelashvili, L., Narbel, P.A.: A review of solar energy : markets, economics and policies. (The World Bank 2011). Retrieved July 14, 2015 from http://ideas.repec.org/p/wbk/wbrwps/5845.html
8. Gregg, J.: Feed in tariffs—the devil lies in the details. Retrieved July 14, 2015 from http://www.shapingtomorrowsworld.org/greggFeedins.html (2011)
9. Möller, H.J.: Semiconductors for solar cells. Artech House (1993)
10. Pagliaro, M., Ciriminna, R., Palmisano, G.: Flexible solar cells, vol. 1, pp. 880–891. Wiley-VCH Verl. GmbH Co KGaA Weinh (2008)
11. International Space Station Imagery. Retrieved July 14, 2015 from http://spaceflight.nasa.gov/gallery/images/station/crew-17/html/iss017e012652.html
12. Wikipedia, the free encyclopedia: Solar panels on spacecraft. Retrieved July 14, 2015 from http://en.wikipedia.org/wiki/Solar_panels_on_spacecraft
13. Torchynska, T., Polupan, G.: High efficiency solar cells for space applications. Superf. Vacío **17**, 21–25 (2004)
14. Reynolds, D., Leies, G., Antes, L., Marburger, R.: Photovoltaic effect in cadmium sulfide. Phys. Rev. **96**, 533–534 (1954)
15. Romeo, A., Bätzner, D., Zogg, H. & Tiwari, A. Potential of CdTe thin film solar cells for space applications. In: 17th European Photovoltaic Solar Energy Conference, pp. 2183–2186 (2001)
16. Poortmans, J., Arkhipov, V.: Thin film solar cells: fabrication, characterization and applications, vol. 5. Wiley, New York (2006)
17. Strong, S.: Building integrated photovoltaics (BIPV). Whole Building Design Guide (2010), Retrieved July 14, 2015 from http://www.wbdg.org/resources/bipv.ph
18. Eiffert, P., Kiss, G.J.: Building-integrated photovoltaic designs for commercial and institutional structures: a sourcebook for architects. DIANE Publishing, Darby (2000)
19. Zondag, H.A.: Flat-plate PV-Thermal collectors and systems: a review. Renew. Sustain. Energy Rev. **12**, 891–959 (2008)
20. Yang, D., Yin, H.: Energy conversion efficiency of a novel hybrid solar system for photovoltaic, thermoelectric, and heat utilization. Energy Convers. IEEE Trans. On **26**, 662–670 (2011)

21. Yin, H.M., Yang, D.J., Kelly, G., Garant, J.: Design and performance of a novel building integrated PV/thermal system for energy efficiency of buildings. Sol. Energy **87**, 184–195 (2013)
22. West, M.: Energy Efficiency and Environmental News (Florida Energy Extension Service, Florida Cooperative Extension Service, Institute of Food and Agricultural Sciences, University of Florida) (1992)
23. Guiavarch, A., Peuportier, B.: Photovoltaic collectors efficiency according to their integration in buildings. Sol. Energy **80**, 65–77 (2006)
24. Wikipedia Free Encyclopedia: Building-integrated photovoltaics. Retrieved July 14, 2015 from https://en.wikipedia.org/w/index.php?title=Building-integrated_photovoltaics&oldid=574773135 (2013)
25. Solar Powered Scientific Instrument Box—San Jose, CA—Solar Power on Waymarking.com. Retrieved July 14, 2015 from http://www.waymarking.com/waymarks/WMB68A_Solar_Powered_Scientific_Instrument_Box_San_Jose_CA
26. Solar Power Parking Meter—Davis, CA—Solar Power on Waymarking.com. Retrieved July 14, 2015 from http://www.waymarking.com/waymarks/WMB55Z_Solar_Power_Parking_Meter_Davis_CA
27. SunShot initiative: crystalline silicon photovoltaics research. Retrieved January 14, 2014 from http://www1.eere.energy.gov/solar/sunshot/pv_crystalline_silicon.html
28. Sabnis, V., Yuen, H., Wiemer, M.: High-efficiency multijunction solar cells employing dilute nitrides. In: AIP Conference Proceedings, vol. 1477, pp. 14–19. AIP Publishing, New York (2012)
29. Guo, X., Zhou, N., Lou, S.J., Smith, J., Tice, D.B.: Polymer solar cells with enhanced fill factors. Nat. Photonics **7**, 825–833 (2013)
30. SunPower: X-Series solar panels. Retrieved January 14, 2014 from http://us.sunpowercorp.com/homes/products-services/solar-panels/x-series
31. Posharp. Solar Panel Database, Retrieved July 14, 2015 from http://www.posharp.com/photovoltaic/solarpanel.aspx?pid=229a79dd-fc33-4379-a7a3-f469103fd4a8
32. Wikipedia Free Encyclopedia: String ribbon. Retrieved July 14, 2015 from http://en.wikipedia.org/w/index.php?title=String_ribbon&oldid=526567612 (2013)
33. SunShot Initiative: Amorphous silicon. Retrieved July 14, 2015 from http://www.posharp.com/photovoltaic/database.aspx?ctype=1&sort=eff&dt=Desc
34. Green, M.A., Emery, K., Hishikawa, Y., Warta, W., Dunlop, E.D.: Solar cell efficiency tables (version 42). Prog. Photovolt. Res. Appl. **21**, 827–837 (2013)
35. SunShot Initiative: Cadmium telluride. Retrieved July 14, 2015 from http://www.posharp.com/photovoltaic/database.aspx?ctype=5&sort=eff&dt=Asc
36. Pv Magazine: Manz secures 20.8 % CIGS cell technology. Retrieved July 14, 2015 from http://www.pv-magazine.com/news/details/beitrag/manz-secures-208-cigs-cell-technology_100013264
37. SunShot Initiative: Copper indium gallium diselenide. Retrieved July 14, 2015 from http://www.posharp.com/photovoltaic/database.aspx?ctype=18&sort=eff&dt=asc
38. Burschka, J., et al.: Sequential deposition as a route to high-performance perovskite-sensitized solar cells. Nature **499**, 316–319 (2013)
39. Posts—New Record Efficiency for Dye Solar Cells. http://www.dyesol.com/posts/new-record-efficiency-for-dye-solar-cells
40. UCLA Newsroom: UCLA engineers create tandem polymer solar cells that set record for energy-conversion. Retrieved July 14, 2015 from http://newsroom.ucla.edu/portal/ucla/ucla-engineers-create-tandem-polymer-228468.aspx
41. Skoplaki, E., Palyvos, J.A.: On the temperature dependence of photovoltaic module electrical performance: a review of efficiency/power correlations. Sol. Energy **83**, 614–624 (2009)
42. Solar Panel Temperature—Facts and Tips. Retrieved July 14, 2015 from http://www.solar-facts-and-advice.com/solar-panel-temperature.html

43. King, D.L., Kratochvil, J.A., Boyson, W.E.: Temperature coefficients for PV modules and arrays: measurement methods, difficulties, and results. In: Twenty Sixth IEEE Photovoltaic Specialists Conference, pp. 1183–1186 (1997). doi:10.1109/PVSC.1997.654300
44. Posharp. Solar Panel Database, Retrieved July 14, 2015 from http://www.posharp.com/ac-135m156-40s-solar-panel-from-axitec-gmbh_p1602044445d.aspx
45. Posharp. Solar Panel Database, Retrieved July 14, 2015 from http://www.posharp.com/axn-m6t190-solar-panel-from-auxin-solar_p1694948233d.aspx
46. Posharp. Solar Panel Database, Retrieved July 14, 2015 from http://www.posharp.com/photovoltaic/solarpanel.aspx?pid=229a79dd-fc33-4379-a7a3-f469103fd4a8
47. Posharp. Solar Panel Database, Retrieved July 14, 2015 from http://www.posharp.com/mpe-80-al-01-solar-panel-from-schuco-international_p2106210288d.aspx
48. Posharp. Solar Panel Database, Retrieved July 14, 2015 from http://www.posharp.com/ac-52cis75-2x39-lv-s-solar-panel-from-axitec-gmbh_p675169754d.aspx. accessed 7/14/2015
49. Posharp. Solar Panel Database, Retrieved July 14, 2015 from www.posharp.com/ab1-70-solar-panel-from-abound-solar_p2142354797d.aspx
50. Posharp. Solar Panel Database, Retrieved July 14, 2015 from http://www.posharp.com/photovoltaic/solarpanel.aspx?pid=abe6f770-7b1d-4f0f-90c9-c8251b076856
51. Posharp. Solar Panel Database, Retrieved July 14, 2015 from http://www.posharp.com/mr100-solar-panel-from-miasol_p1554053452d.aspx
52. Raga, S.R., Fabregat-Santiago, F.: Temperature effects in dye-sensitized solar cells. Phys. Chem. Chem. Phys. **15**, 2328 (2013)
53. Bosco, N.: Reliability concerns associated with PV technologies. National Renewable Energy Laboratory, California (2010)
54. Reijnders, L.: Design issues for improved environmental performance of dye-sensitized and organic nanoparticulate solar cells. J. Clean. Prod. **18**, 307–312 (2010)
55. Kislenko, S.A., Amirov, R.K., Popel', O.S., Samoilov, I.S.: Dye-sensitized solar cells: present state and prospects for future development. Therm. Eng. **57**, 969–975 (2010)
56. Solarbuzz: Module pricing. Retrieved July 14, 2015 from http://www.solarbuzz.com/facts-and-figures/retail-price-environment/module-prices (2012)
57. Eom, S.H., et al.: High efficiency polymer solar cells via sequential inkjet-printing of PEDOT: PSS and P3HT:PCBM inks with additives. Org. Electron. **11**, 1516–1522 (2010)
58. IEA—Publication: Technology roadmap: solar photovoltaic energy. Retrieved July 14, 2015 from http://www.iea.org/publications/freepublications/publication/name,3902,en.html
59. Platzer, M.: US solar photovoltaic manufacturing: industry trends, global competition, federal support Congressional Research Service, Library of Congress, Washington D.C. (2012)
60. BlueGreen Alliance: Overview of the solar energy industry and supply chain. Retrieved July 14, 2015 from http://solarthermalworld.org/content/overview-solar-energy-industry-and-supply-chain-2011 (2011)
61. Business Wire: Lux research reveals 2011 top 10 module manufacturers. Retrieved July 14, 2015 from http://www.businesswire.com/news/home/20120314005088/en/Lux-Research-Reveals-2011-Top-10-Module (2012)
62. Solar energy value chain that sets solarworld apart. Retrieved July 14, 2015 from http://www.solarworld-usa.com/about-solarworld/value-chain#Silicon
63. CleanTechnica: Top 20 solar module manufacturers up to 70 % of market share in Q1'13. http://www.solarbuzz.com/news/recent-findings/top-20-solar-photovoltaic-module-suppliers-grab-70-market-share-q1-13
64. 10 Top solar module manufacturers. In: 2012 (IHS Report). Retrieved July 14, 2015 from http://solarlove.org/10-top-solar-module-manufacturers-in-2012-ihs-report
65. Zipp, K.: Top 10 solar PV module suppliers of 2012. Sol. Power World. Retrieved July 14, 2015 from http://www.solarpowerworldonline.com/2013/04/top-10-solar-pv-module-suppliers-of-2012

66. Yahoo Finance: Research and markets: analysis of the global solar power market report 2013–2016—PV installations make progress in becoming mainstream energy source. Retrieved July 14, 2015 from http://finance.yahoo.com/news/research-markets-analysis-global-solar-140000237.html (2013)
67. Wikipedia Free Encyclopedia: Solar power in the United States. Retrieved July 14, 2015 from http://en.wikipedia.org/w/index.php?title=Solar_power_in_the_United_States&oldid=586112805 (2013)
68. Renewable. Energy World: US joins 10-GW solar PV club, prepares for liftoff. Retrieved July 14, 2015 from http://www.renewableenergyworld.com/rea/news/article/2013/07/us-joins-10-gw-solar-pv-club-prepares-for-liftoff
69. Solar markets around the world. Retrieved July 14, 2015 from http://solarcellcentral.com/markets_page.html
70. U.S. solar market insight Q1 2013. Retrieved January 14, 2014 from http://www.seia.org/research-resources/us-solar-market-insight-q1-2013
71. Solar market insight 2013 Q3. Retrieved January 14, 2014 from http://www.seia.org/research-resources/solar-market-insight-2013-q3
72. Military installs largest US residential solar project in history. Retrieved July 14, 2015 from http://www.sustainablebusiness.com/index.cfm/go/news.display/id/22877
73. A solar panel on every roof? In: Levitan (ed.) U.S., still a distant dream. Yale Environment 360. Retrieved July 14, 2015 from http://e360.yale.edu/feature/a_solar_panel_on_every_roof_in_us_still_a_distant_dream/2434
74. Daily, M.: Analysis: as solar panels eclipsed, installers in limelight. Retrieved July 14, 2015 from http://www.reuters.com/article/2012/02/17/us-solar-installers-idUSTRE81G27520120217 (2012)
75. Barbose, G., Darghouth, N., Weaver, S., & Wiser, R. Tracking the sun VI:An Historical Summary of the Installed Price of Photovoltaics in the United States from 1998 to 2012. LBNL-6350E. Berkeley, CA: Lawrence Berkeley National Laboratory. http://emp.lbl.gov/sites/all/files/lbnl-6350e.pdf (2013)
76. PV-Tech: Global solar PV market to top US$134 billion by 2020. Retrieved July 14, 2015 from http://www.pv-tech.org/news/global_solar_pv_market_to_top_us134bn_by_2020
77. Solarbuzz: Solar energy market growth. Retrieved July 14, 2015 from http://www.solarbuzz.com/facts-and-figures/markets-growth/market-growth
78. CleanTechnica: How the solar PV industry became a global phenomenon. Retrieved July 14, 2015 from http://cleantechnica.com/2013/09/12/how-the-solar-pv-industry-became-a-global-phenomenon

Index

M.P. Paranthaman et al. (eds.), *Semiconductor Materials for Solar Photovoltaic Cells*, Springer Series in Materials Science 218,
DOI 10.1007/978-3-319-20331-7